Use of high resolution remote sensing and GIS to parameterise spatially-distributed soil erosion models

Hashem, Nadeem

THE USE OF HIGH RESOLUTION REMOTE SENSING AND GIS TO PARAMETERISE SPATIALLY-DISTRIBUTED SOIL-EROSION MODELS

by

Nadeem Hashem

April 2002

A thesis submitted to the University of London for the degree of Doctor of Philosophy

Department of Geography,
King's College London.

ABSTRACT

South-east Spain is subject to soil erosion and land degradation as a result of natural and human-induced factors such as the change in landuse pattern, coupled with a semi-arid climate. Estimates of soil erosion are needed by decision makers in order to quantify the soil loss under various scenarios and different landuse patterns so that policies of sustainable use of land resources can be developed and implemented. The purpose of this study is to explore the potential of using high resolution aerial photography and GIS to derive the parameters controlling the soil loss spatially at the local scale and then implement and validate a soil-erosion model. This enables the automation of the process of soil-erosion modelling to make it cost effective and less labour intensive.

The Thornes model was selected for soil-erosion modelling in this study because it can be implemented in a spatially distributed manner and it needs little data to parameterise. Four factors control the soil loss in the Thornes equation: slope, vegetation cover, soil erodibility, and overland-flow. A Digital Elevation Model (DEM) was derived from the aerial photographs using digital photogrammetry techniques and slope was then calculated from the DEM. Various methods of classification and vegetation indices were reviewed to map the vegetation cover and the mixture modelling method was implemented because in this method the shade can be mapped and consequently removed from the vegetation map. A co-occurrence matrix and image texture analysis was used to correct the vegetation errors in a few pixels. Soil erodibility was calculated using Wischmeier's equation.

The Carson and Kirkby model was used to estimate the overland flow because it was shown by other studies to produce satisfactory results in the study area. Deterministic and stochastic approaches were used for overland-flow modelling and the first approach produced results of higher accuracy and, thus, was implemented. The parameters controlling the soil loss were then integrated according to Thornes equation in a GIS environment producing the soil loss map. This map was validated against measured values resulted from rainfall simulation experiments and the accuracy was satisfactory. The effect of landuse change by ploughing on soil loss was assessed and it was shown that ploughing may increase soil loss by up to 500%.

ACKNOWLEDGEMENT

I would like to express my sincere gratitude and appreciation to all organisations and individuals whose help and support have given me the strength to successfully complete this thesis.

I am indebted to my first supervisor Dr. Nick Drake for his great help, support and guidance, as well as for his criticism which was constructive (most of the time!). Throughout the time of this study I felt privileged to work with Nick for the fruitful discussions we had, for his wealth of knowledge and for being there for me when help was needed. I am also very grateful for my second supervisor Dr. John Wainwright whose constant support and bright ideas were lighting my way during my study. John's extensive knowledge in hydrology, geomorphology and statistics made a remarkable contribution to the results of this study.

I also would like to acknowledge the support and help of a long list of people who added a lot to my life at King's College London at the personal, social and academic level. My thanks go to Professors John Thornes and Keith Hoggart for engaging with, and understanding the problems of, Ph.D. students as heads of department. Special thanks to Dr. Shatish Kundaiker for his valuable and unlimited support, to Mr. John Harper for the nice laughter and to Miss. Roma Beaumont, Mr. Peter Howard and Ms. Alison Green. And to you my dears: Waleed, Mustafa, Elias, Nasos, Alistair, Hung-Fei, Peter, Zhang Zhong, Shen and Shijun, thank you all.

My sincere gratitude goes to the sponsors of this Ph.D. study whose funding and financial support is highly appreciated and acknowledged. The funding for the tuition fees and maintenance came from the University of Aleppo and the Ministry of Higher Education in Syria. The Arab-British Chamber Charitable Foundation provided me with a hardship grant and sponsored the fieldwork in Spain. Al-Tajir Trust financial contribution was very appreciated towards the end of my study.

Last but not least I am very grateful to my parents for their support and unconditional love, every time I visited them in the holiday their first question was: when are you going to finish this Ph.D. so you can enjoy life!. My thanks to my sisters Nadima and Fadila and to my brothers Ibrahim, Omar, Ghassan, Mamoun, and Osama.

And from the heart the warmest thanks to my wife Dr. Sheila Qureshi, for her support and motivation, and to my son Karam for being the rose of my life. Karam was born amid the stress and pressure of my Ph.D. work and his arrival changed a lot of things in my life, he gave it a special meaning.

This thesis is dedicated to my mother Mrs. Ayoush Hashem and to my wife Dr. Sheila Qureshi.

Nadeem Hashem

TABLE OF CONTENTS

Abstract 2

Acknowledgements 3

Table of Contents 5

List of Figures 12

List of Tables 18

CHAPTER 1: INTRODUCTION

1.1 Overview 20

1.2 The Study Area 28

1.3 Aims And Objectives 34

1.4 The Structure Of The Thesis 35

CHAPTER 2: REMOTE SENSING, GIS, AND THE PROCESSES OF SOIL EROSION

2.1 Introduction 40

2.2 Understanding The Soil-Erosion Processes 42

2.2.1 Raindrop Impact 43

2.2.2 Overland Flow 45

2.2.3 Rill Erosion 48

2.2.4 Gully Erosion 50

2.2.5 Soil Erodibility 50

2.2.6 Vegetation Cover 53

2.2.7 Topography 57

2.2.8 Soil Compaction 59

2.3 Remote Sensing Systems And GIS For Monitoring And Modelling Soil erosion 60

2.3.1 Remote Sensing Platforms 65

2.3.1.1 AVHRR 65

2.3.1.2 Landsat TM 66
2.3.1.3 High Spatial Resolution Remote Sensing 67
2.3.1.4 Selecting a Remote Sensing Data Collection System 71
2.3.2 Geographic Information Systems (GIS) For Soil-Erosion Modelling 71
2.4 Conclusion 73

CHAPTER 3: SOIL-EROSION AND OVERLAND-FLOW MODELS

3.1 Introduction 75
3.2 Soil-Erosion Models 76
3.2.1 Introduction 76
3.2.2 Empirical (Or Black Box) Models 78
3.2.2.1 Universal Soil Loss Equation (USLE) 78
3.2.2.2 The SELEMA Model 80
3.2.3 Process-Based Models 80
3.2.3.1 ANSWERS (Areal Non-Point Source Watershed Environment Response Simulation) 82
3.2.3.2 European Soil-Erosion Model (EUROSEM) 82
3.2.4 Process-Based Models With Empirical Elements 83
3.2.4.1 The Morgan, Morgan And Finney Method 84
3.2.4.2 Thornes Soil-Erosion Model 85
3.2.5 Selecting The Soil-Erosion Model 87
3.3 Overland-Flow Modelling 89
3.3.1 Introduction 89
3.3.2 An Overview Of Overland-Flow Models 89
3.3.2.1 SCS Model 91
3.3.2.2 Philip Infiltration Model 92
3.3.2.3 Carson And Kirkby Model 93
3.3.3 Selecting The Overland-Flow Model 94
3.4 Conclusion 95

CHAPTER 4: FIELD SURVEYING, IMAGE GEO-REFERENCING AND SLOPE MAPPING

4.1 Introduction 97

4.2 Field Surveying 98

4.2.1 Introduction 98

4.2.2 The Principles Of Surveying 99

4.2.2.1 Control Survey 100

4.2.2.2 Global Positioning System (GPS) 101

4.2.3 Surveying In Study Area 102

4.2.3.1 Altitude Calculations Of The Control Stations 104

4.2.3.2 Ground Control Points (GCPs) 107

4.2.3.3 Red And Grey Soil Transects. 108

4.3 Topographic Mapping Of The Slope 110

4.3.1 Introduction 110

4.3.2 Digital Photogrammetry And The DEMs Creation 110

4.3.3 The Principles Of Photogrammetry: 111

4.3.3.1 The Principle Of Collinearity 111

4.3.3.2 The Principle Of Coplanarity 113

4.3.3.3 Analytical Aerotriangulation. 114

4.4 DEM Extraction Using Digital Photogrammetric Techniques. 115

4.4.1 Block Tool Processes 116

4.4.1.1 Camera Editor 116

4.4.1.2 Frame Editor 117

4.4.1.3 Ground Control Editor. 118

4.4.1.4 Aerotriangulation. 119

4.4.2 DEM Tool Processes 121

4.5 Slope Calculation From The DEM 123

4.6 Summary And Conclusion 125

CHAPTER 5: VEGETATION COVER AND LAND-USE MAPPING

5.1 Introduction 127

5.2 Mapping The Vegetation Cover 128

5.2.1 Introduction 128

5.2.2 The Spectroscopy Of Vegetation 130

5.2.3 Geometrical Optical Models and Vegetation indices To Map Vegetation Cover 133

5.2.3.1 Geometrical Optical Models 133

5.2.3.2 vegetation Indices 135

5.2.3.3 Investigating The Correlation Between Red Band Reflectance And The Vegetation Cover 138

5.2.4 Methodology of Vegetation Cover Mapping Using Mixture Modelling 141

5.2.4.1 Classification Techniques For Vegetation Mapping 141

5.2.4.2 Fuzzy Classification 142

5.2.4.3 Mixture Modelling 143

5.2.4.4 Linear And Non-Linear Mixture Modelling. 144

5.2.4.5 The Linear Mixture Model 147

5.2.4.6 Endmembers Extraction For Linear Mixture Modelling. 151

5.2.4.6.1 Endmembers Derived From Principal Components Analysis 153

5.2.5 Implementation Of Mixture Modelling 155

5.2.5.1 Endmembers Extraction From The Aerial Photograph 155

5.2.5.2 Mixture Modelling Implementation 160

5.2.6 Re-Scaling Vegetation Map To Remove The Shade Effect 164

5.2.6.1 Implementation Of Re-Scaling Algorithm 167

5.2.7 Co-Occurrence Matrix Methods To Rectify Blank Vegetation Pixels 172

5.3 Mapping The Land Use 183

5.3.1 The Effect Of Land Use On Soil erosion 183

5.3.2 Methodologies Of Land-Use Mapping 186
5.3.2.1 Image Classification 186
5.3.2.2 Classification Methods 186
5.3.3 Implementation Of Classification For Land-Use Mapping 191
5.3.3.1 Maximum Likelihood Land-Use Classification 191
5.3.3.2 Accuracy Assessment Of Land-Use Map 199
5.3.3.3 Land-Use Classes Collapse For Improving Classification Accuracy 206
5.3.3.4 Alternative Methods For Land-Use Mapping: Image Interpretation 215
5.4 Summary And Conclusion 220

CHAPTER 6: SOIL ANALYSIS AND SOIL MAPPING

6.1 Introduction 225
6.1.1 Published Versus Remote Sensing-Derived Soil Maps 227
6.1.2 Spectroscopic Characteristics Of Soils And The Soil Colour 231
6.2 Mapping Soil Types Using Linear Mixture Modelling 233
6.2.1 Re-Scaling The Mixture Modelling Soil Maps To Remove The Shade And Vegetation Effect 234
6.2.2 Results Of The Re-Scaling Process And The Soil Map Generation 238
6.3 Soil Sampling And Analysis 242
6.3.1 Soil Sampling 242
6.3.2 Field Methods 245
6.3.3 Soil Analysis 247
6.3.3.1 Pre-Treatment And Organic Matter Removal 248
6.3.3.2 Particle-Size Analysis – Sieving 249
6.3.3.3 Particle-Size Analysis – Sedimentation 250
6.3.3.4 Bulk Density Measurement 251
6.3.4 Results Of Soil Analysis 252
6.4 Statistical Methods For Mapping Soil Properties 254
6.4.1 Investigating The Probability Distributions Of Soil Properties 255

6.4.2 Investigating The Correlation Between Soil Properties And Soil Fractions To Spatially Map The Soil Properties 265

6.4.3 Geostatistical Analysis Of Soil Properties 269

6.4.3.1 Results Of Mapping Soil Properties Using Geostatistical Techniques 272

6.4.4 Mapping Soil Properties Based On The Principles Of Hydrological Response Units 274

6.5 The Construction Of The Soil Properties Maps 277

6.6 Summary And Conclusion 282

CHAPTER 7: IMPLEMENTATION AND VERIFICATION OF SOIL-EROSION AND OVERLAND-FLOW MODELS IN THE STUDY AREA

7.1 Introduction 286

7.2 Implementation Of Carson And Kirkby Model To Predict Overland Flow 287

7.2.1 Precipitation And Validation Of Overland-Flow Model Using Rainfall Simulation 288

7.2.2 Water Storage Capacity (R_c) Parameter 289

7.2.3 Initial Soil Moisture Parameter 291

7.2.4 Implementation Of Carson And Kirkby Model 292

7.2.4.1 The Deterministic Approach 292

7.2.4.2 The Stochastic Approach 297

7.2.5 Discussion Of The Results Of Carson And Kirkby Model 307

7.2.6 Assessing The Overland-Flow Errors Introduced By Using The Hydrological Response Units Method 310

7.2.7 Sensitivity Analysis Of Carson And Kirkby Model 311

7.3 Soil Erodibility Estimation 313

7.4 Modelling Soil erosion 316

7.4.1 Implementation Of The Thornes Soil-Erosion Model 316

7.4.2 Discussion Of Results 320

7.4.3 Investigating The Effect Of Land-Use Change On Soil Erosion 322

7.4.4 Sensitivity Analysis Of The Thornes Soil-Erosion Model 326

7.5 Summary And Conclusion 328

CHAPTER 8: CONCLUSIONS AND FURTHER WORK

8.1 Introduction 331

8.2 Discussion Of The Outcomes Of This Study 331

8.3 Suggestions For Further Work 339

BIBLIOGRAPHY 342

APPENDICES 362

Appendix A 363

Appendix B 376

Appendix C 380

LIST OF FIGURES

CHAPTER 1:

1.1. A world map showing the average yearly sediment loss (mm year^{-1}) due to soil erosion (from Walling 1996). 22

1.2. The aerial photograph of the study area collected by NERC, before applying geometric corrections. The NERC air campaign took place on the 9th of April 1996. 26

1.3. The RC-10 Aerial Camera which has been used in the NERC air campaign in the Southern-east of Spain. 27

1.4. A map showing the location of the study area in Vélez Rubio, Murcia, South-east Spain. The red dot in the magnified map indicates the location. 29

1.5. The average monthly rainfall and minimum, maximum, and average temperature in the study area of Velez Rubio. 30

1.6. The ploughing of agricultural land in the study area where the matorral is removed to prepare the land for almond. 32

1.7. The effect of overgrazing on the vegetation cover. The figure shows the location where goats are brought to drink water. 33

1.8. A flow diagram showing the inputs and outputs of the overland-flow and soil-erosion models. 36

CHAPTER 2:

2.1. A generalised model of factors involved in the land degradation and soil erosion in semi-arid regions of south-east Spain. 41

2.2. Critical shear velocity in overland flow for soil particle detachment as a function of particle size (after Savat 1982). 47

2.3. Comparison between the characteristics of rill and gully erosion, compared to the interrill erosion (after Brady, 1990) 49

2.4. Nomograph showing how to calculate the soil erodibility (after Wischmeier, Johnson and Cross, 1971). 52

2.5. A part of the study area where the natural vegetation cover (Matorral) is removed in order to plant almond and olive trees. 54

2.6. The effect of vegetation cover on runoff and soil loss in arable land and for different vegetation cover values (from Elwell 1976). 56

2.7. The conversion of remote sensing raw data into standardised thematic information layers. 64

2.8. The effect of the Forward Movement Compensation on the clarity of the aerial photography. 68

2.9. The first panchromatic image taken by the IKONOS satellite with 1 metre spatial resolution, showing fine details of land cover, Washington D.C. The bottom image is a zoomed-in sub-area. 69

CHAPTER 3:

3.1. Flow chart explaining the four processes of soil erosion by water in a process-based model (after Meyer and Wischmeier 1969) 81

CHAPTER 4:

4.1. Showing the locations of the control stations (Temp points) in the study area. The frame shows the borders of the area. 103

4.2. A sketch showing the Case A. 105

4.3. A sketch showing the Case B. 106

4.4. The collinearity condition (after Wolf 1983). 113

4.5. The coplanarity condition (after Wolf 1983). 114

4.6. The aerial photograph of the study area georeferenced to the UTM-30N projection system. 120

4.7. The resultant DEM of the study area, along with the shaded relief for visual assessment. 122

4.8. The topographic slope image derived from the DEM. The slope values are in degrees. 125

CHAPTER 5:

5.1. Typical green vegetation spectrum. Upper plot is an enlargement of the boxed region in the lower plot. The figure shows the pigment absorption in the visible bands. 130

5.2. Reflectance spectra of some dry vegetation materials in semiarid areas. Spectra are displaced vertically to avoid overlap (after Elvidge, 1990). 133

5.3. The location of the vegetation plots where vegetation cover has been measured in the field. 139

5.4. Regression of red band reflectance of the aerial photograph that covers the study area against the vegetation fractions measured in the field. Red band reflectance is re-scaled from 0-255 to 0-100% 140

5.5. A sketch showing the differences between the A) linear and B) non-linear mixture of light reaching the sensor after interacting with ground covers. 146

5.6. Three new images resulted from the PCA transformation. 156

5.7. Scatterplots of PCA components against one another showing the selected endmembers. Scatterplot of PC1 and PC2 158

5.8. The cover fraction maps resulted from the linear mixture modelling before re-scaling to remove the shade and veg effect. 161

5.9. A zoomed-in area of almond field and matorral showing the effect of shade on vegetation cover. 163

5.10. The relationship between observed and estimated vegetation cover before re-scaling to remove the shade effect. 164

5.11. Vegetation cover and shade maps resulted from mixture modelling. The association of shade fraction to the underestimation of vegetation cover in areas of high vegetation density is demonstrated. 165

5.12. Re-scaling the vegetation cover by removing the shade effects in an almond field. A) is before and B) is after re-scaling. The oval-shaped objects are almond trees. 168

5.13. Sensitivity analysis of the algorithm of shade removal from the vegetation map to the of soil fractions present in a given pixel. Three values of soil fractions are analysed: 0.01, 0.03, and 0.05. 169

5.14. Re-scaling the vegetation cover by removing the shade effects in the matorral. A) is before and B) is after re-scaling. 170

5.15. The relationship between observed and estimated vegetation cover before and after re-scaling to remove the shade effect. 171

5.16. The process of extracting the co-occurrence matrix using an example of a simple operator. 175

5.17. The bow-tie operator which was used to extract the co-occurrence matrix for the vegetation cover map. 175

5.18. A) sketch and B) diagram showing the plot of co-occurrence matrix. 176

5.19. The binary mask representing the vegetation objects which was created from the co-occurrence matrix methodology. 178

5.20. The relationship between observed and estimated vegetation cover after applying the co-occurrence matrix analysis. 180

5.21. The effect of applying co-occurrence matrix method on the vegetation cover map in areas of bushes, olive and almond trees. 181

5.22. The effect of applying co-occurrence matrix method on the vegetation cover map in areas of matorral. 182

5.23. A sub-image of the high resolution aerial photograph study area showing different vegetation types. 187

5.23b. Showing the land use/land cover classes at various stages of classification and amalgamation 192

5.24 Histograms and statistics of the spectral signature of the training site of grey soil matorral in the blue, green, and red bands. 195

5.25. The signature comparison chart of the 11 training sites in the study area. "tm1resa" is the blue band, "tm2resa" is the green band, and "tm3resa" is the red band. 198

5.26. The maximum likelihood supervised classification result with A) equal prior probability and B) defined prior probability. 200

5.27. The A) equal prior probability and B) the defined prior probability maximum likelihood classifications. 207

5.28. The A) equal prior probability and B) defined prior probability maximum likelihood classification. 213

5.29. The initial land-use map of the study area derived by image interpretation. 218

5.30. The final land-use map of the study area derived by image interpretation and land-use class amalgamation. 219

CHAPTER 6:

6.1. A digitised soil map of the study area as a subset from the published soil map of Vélez Rubio, Ministry of Agriculture, Spain with a scale of 1:100000. 229

6.2. Spectroscopic analysis of the soil reflectance for grey (Phyllite) and red (Quartzite/Quartz Mica-Schist) soils in the study area. 232

6.3. The soil fraction maps resulted from the linear mixture modelling before re-scaling to remove the shade and vegetation effects. 235

6.4. The effect of vegetation and shade presence on the grey soil map resulted from the mixture modelling. 236

6.5. The effect of vegetation and shade presence on the red soil map resulted from the mixture modelling. 237

6.6. Re-scaling the grey soil map by removing the shade and vegetation effects. 239

6.7. Re-scaling the red soil map by removing the shade and vegetation effects. 240

6.8. The geo-referenced soil map showing the spatial distribution of red and grey soil in the study area. 241

6.9. The locations of grey soil (top) and red soil (lower) samples in the study area of Velez Rubio. 246

6.10. The sieving processor to separate stones (larger than 2000 μm), sand (2000-125 μm), very fine sand (125-63 μm), and silt & clay (below 63 μm) 249

6.11. The Micromeretics Sedigraph 5100 which was used for X-ray sedimentation for particle-size analysis. 251

6.12. The histograms, with the normal distribution curve, of the soil properties samples in both red and grey soil types. 257

6.13. The models of the clay semivariogram, grey soil semivariogram, and their cross-variogram needed for the interpolation process. 273

6.14. The hydrological response units map which will be used as a base map to spatially distribute the soil properties. GS and RS stand for grey soil and red soil respectively. 278

6.15. Spatially distributed soil properties maps generated using the principle of the hydrological response units. 279

CHPTER 7:

7.1. The locations of the nine rainfall simulation plots in the study area. 289

7.2. The effect of soil type and soil particle size on the water storage capacity. 290

7.3. The map of overland flow OF1 generated from a 124 mm rainstorm. The unit is mm per event of 30 minutes. 293

7.4. The accuracy assessment of the results of Carson and Kirkby overland-flow model. 293

7.5. The map of overland flow OF2 generated from a 124 mm rainstorm with the soil depth constrained to 30 cm. The unit is mm per event of 30 minutes. 294

7.6. The accuracy assessment of the Carson and Kirkby overland-flow model results after soil depth is constrained to 300 mm. 294

7.7. Showing the difference in the resultant overland-flow maps as a result of constraining the soil depth to a maximum of 300 mm. 295

7.8. The randomly generated frequency distributions of soil properties for the plots P5 and P6. 298

7.9. The randomly generated frequency distributions of soil properties for the plot P3. 299

7.10. The randomly generated frequency distributions of soil properties for the plots P1, P2, and P8. 300

7.11. The randomly generated frequency distributions of soil properties for the plots P7, P9, and P11. 301

7.12. The frequency distribution of the overland flow in the plots p5 and p6 using the stochastic approach with (OF3) and without (OF4) constraining the soil depth to a value of 300 mm. 302

7.13. The frequency distribution of the resultant overland flow in plot p3 using the stochastic approach with (OF3) and without (OF4) constraining the soil depth to a maximum value of 300 mm. 303

7.14. The frequency distribution of the resultant overland flow in plots p1, p2, and p8 using the stochastic approach with (OF3) and without (OF4) constraining the soil depth to a value of 300 mm. 304

7.15. The frequency distribution of the resultant overland flow in plots p7, p9, and p11 using the stochastic approach with (OF3) and without (OF4) constraining the soil depth to a value of 300 mm. 305

7.16. The accuracy assessment of the results of Carson and Kirkby overland-flow model using the stochastic approach. OF3 is before and OF4 is after soil depth is constrained to 300 mm. 306

7.17. Assessment of the prediction accuracy of Carson and Kirkby overland-flow model using soil properties data collected at the nine verification plots. 311

7.18. Sensitivity analysis of the Carson and Kirkby overland-flow model. 312

7.19. The map of the soil erodibility factor calculated from the Wischmeier's equation. 314

7.20. The predicted soil-erosion map using Thornes model. The units are (mm/event) where the event is 30 minutes in this case. 317

7.21. The accuracy assessment of the results of Thornes soil-erosion model. The rate of the soil loss is calculated in mm/event where the event equals to 30 minutes period of the rainfall simulation. 319

7.22. Showing the location of the regions which have been recently ploughed. The green polygons delineate these regions. 323

7.23. Soil-erosion map after the consideration of the ploughed area (mm/event). A) is the predicted soil-erosion map, and B) is the difference map. 325

7.24. The difference soil-erosion map between before and after the land-use change. The map unit is percentage change as a result of land ploughing. 326

7.25. The sensitivity analysis of the Thornes soil-erosion model. A) is for all model parameters and B) is for parameters excluding the vegetation cover for illustration purposes. 327

LIST OF TABLES

CHAPTER 1:

1.1. Showing the four bands and their wavelengths of the IKONOS sensor. 25

CHAPTER 4:

4.1 Showing the Temp points accurate altitude calculations from the EDM observations. V and D stand for vertical angle and distances respectively. Unit is metre for all measurements. 106

4.2. Showing the calculation of the Easting, Northing, and Altitude of the twenty-one selected GCPs. 107

4.3. Showing the Eastings and Northings calculation of the red soil samples. 108

4.4. Showing the Eastings and Northings calculation of the grey soil samples. 109

4.5. The camera calibration parameters (obtained from the Hunting Aerofilms Certificate of the Camera). 117

4.6. Showing the ground control points which could not been identified on the aerial photograph. 118

CHAPTER 5:

5.1. The statistical results of the PCA transformation applied to the bands of the aerial photograph. 156

5.2. The four endmembers digital numbers. 160

5.3. Comparison of the results of different techniques used to replace the vegetation fraction values of the pixels of zero vegetation in the shade-free mixture modelling vegetation cover. 180

5.4. Values of runoff coefficient and soil-erosion rate under different land use practices in the Mediterranean region. The table shows the effect of land use on soil loss (after Kosmas *et al.*, 1997). 185

5.5. The spectral signatures of the classes used by the supervised maximum likelihood classification. 197

5.6. The error matrix analysis to assess the accuracy of the landuse maps using eleven classes. MAKLIKE and MAXLIKE2 are the results of maximum likelihood classifications using the equal and defined prior probability approaches respectively. 203

5.7. The error matrix analysis to assess the accuracy of the landuse maps using seven and five classes. 208

CHAPTER 6:

6.1. A comparison of soil properties between the published (see Proyecto Lucademe, 1992) and measured (average) values from the fieldwork. 228

6.2. A range of bulk density and porosity values for a variety of soils (after Marshall *et al.*, 1996). 252

6.3-1. Soil analysis results for the red soil samples. 253

6.3-2. Soil analysis results for the grey soil samples. The sand is classified >0.10 mm. Very fine sand (VFS) is classified between 0.05-0.10 mm. 254

6.4. The results of testing the normality (chi-square, central tendency, skewness, and the kurtosis) of the two groups of red and grey soil samples. 263

6.5. The results of testing the normality, skewness, and the kurtosis of the two groups of red and grey soil samples after transformation by applying the square-root. 264

6.6. Showing the improvement of the normality indicators (mean-median differences and chi-square tests), skewness, and kurtosis of the distributions of the samples representing the red and grey soil types after applying the transformation. 265

6.7. The results of the regression between soil properties and the mixture modelling soil fractions. The sign "*" means that the regression is significant at 95% level. 266

6.8. The results of the regression between soil properties and the mixture modelling soil fractions after taking the land-use type into consideration. 268

6.9. Summary statistics of the two-samples t test. The two samples come from different populations when the significance value is greater than (0.05) so the hypothesis H_0 is rejected. 275

6.10. The results of analysis of variance (ANAOV). The four sub-samples come from different populations when the significance value P is smaller than (0.05) and the H_0 hypothesis is rejected. 276

CHAPTER 7:

7.1. The land use types for the rainfall simulation plots. The numbers 1, 2, 3 and 4 represent ploughed grey soil, ploughed red soil, unploughed grey soil and unploughed red soil respectively. 289

CHAPTER 1

INTRODUCTION

1.1 OVERVIEW
1.2 THE STUDY AREA
1.3 AIMS AND OBJECTIVES
1.4 THE STRUCTURE OF THE THESIS

> **The history of civilizations is a record of struggles against the progressive desiccation of civilized lands. The more ancient the civilization, the drier and more wasted, usually, are the supporting countries... .Recently, the archeologists have turned back the pages of history, not merely centuries, but thousands of years. Their post-mortems on buried civilizations suggest that it has been the hand of man, more than climatic change, which has reduced once rich and populous regions to desolation and poverty. After long struggles, a civilization either died or its people migrated to more productive regions. Many ancient civilizations, once reveling in a golden age of prosperity, are crumbling in ruins or lie buried in sands and debris, largely caused by the destructive treatment of the lands on which they were dependent for sustenance. If modern peoples are to escape a similar fate by man-induced impoverishment and the desiccation of their lands, it would seem well to take a measure of these destructive processes and forces, and by intelligent land planning and land use provide for the sustained productivity of agricultural lands and the protection of grasslands and forests for food, textiles, raw materials and continued water supply.**
>
> (Lowdermilk, *Man-Made Deserts*, 1935)

1.1 OVERVIEW

As early as 1949, a geomorphologist called Auberville noticed the phenomenon of land degradation that seemed to be extending north into semi-arid and sub-humid regions of North Africa from the more arid zones of the Sahara and called this problem "desertification" (Auberville, 1949). However, this problem had been observed in the Mediterranean area nearly two millennia ago by the Roman Cicero

who spoke of the destruction of the North African forests and their replacement by barren, desert-like areas. In recent times, the devastating Sahel droughts of the 1968-1973 period and the apparent accelerated southward advance of the Sahara Desert led to extensive international discussion of the problem and the formation of the United Nations Conference on Desertification (UNCOD).

At one of their conferences during 1977 in Nairobi, Kenya, the UNCOD defined desertification as "The diminution or destruction of the biological potential of land, and can lead ultimately to desert-like conditions. It is an aspect of the widespread deterioration of ecosystems, and has diminished or destroyed the biological potential, i.e. plant and animal production, for multiple use purposes at a time when increased productivity is needed to support growing populations in quest for development." (UNEP, 1978).

During the following years various agencies, scientific institutions and individual scientists have found the above UNCOD's definition to be inadequate (UNEP, 1992). In response various groups developed their own definitions, which led to a significant amount of confusion. In addition to that, cyclic oscillations of vegetation productivity in semiarid regions related to climate fluctuations had been observed in satellite data, and there was a need to differentiate between desertification and these cyclic climatic oscillations (UNEP, 1992). In 1992 the UNCOD reconsidered the definition of desertification as "land degradation in arid, semi-arid, and dry sub-humid areas resulting mainly from adverse human impact." (UNEP, 1992). In this new definition the UNCOD emphasised on human impact, rather than the climatic fluctuation, as the source of land degradation. However, it should be mentioned that climatic fluctuations can magnify the damage caused by human activities.

One of the most severe forms of the land degradation is erosion. Reports by the World Resources Institute (1992, 1993) indicate that soil erosion is the most serious form of land degradation on a global scale. Soil erosion can be described as the process in which the quantity and quality, and consequently the productivity, of the soil deteriorate over the time by the act of water or wind. In another definition the

UNEP (1992) describes soil erosion as the process causing a gradual loss of the capacity of land to support the sustainable development of existing ecosystems or, more specifically, the growth of vegetation that is essential for human and animal life. This soil-erosion phenomenon is also manifested by the deterioration of the physical, chemical, biological and economic properties of the soil (United Nations, 1994). Figure 1.1 shows an overview map of the problem of sediment loss due to soil-erosion in various regions around the world where regions of higher than 0.37 mm/year are at high risk of soil erosion.

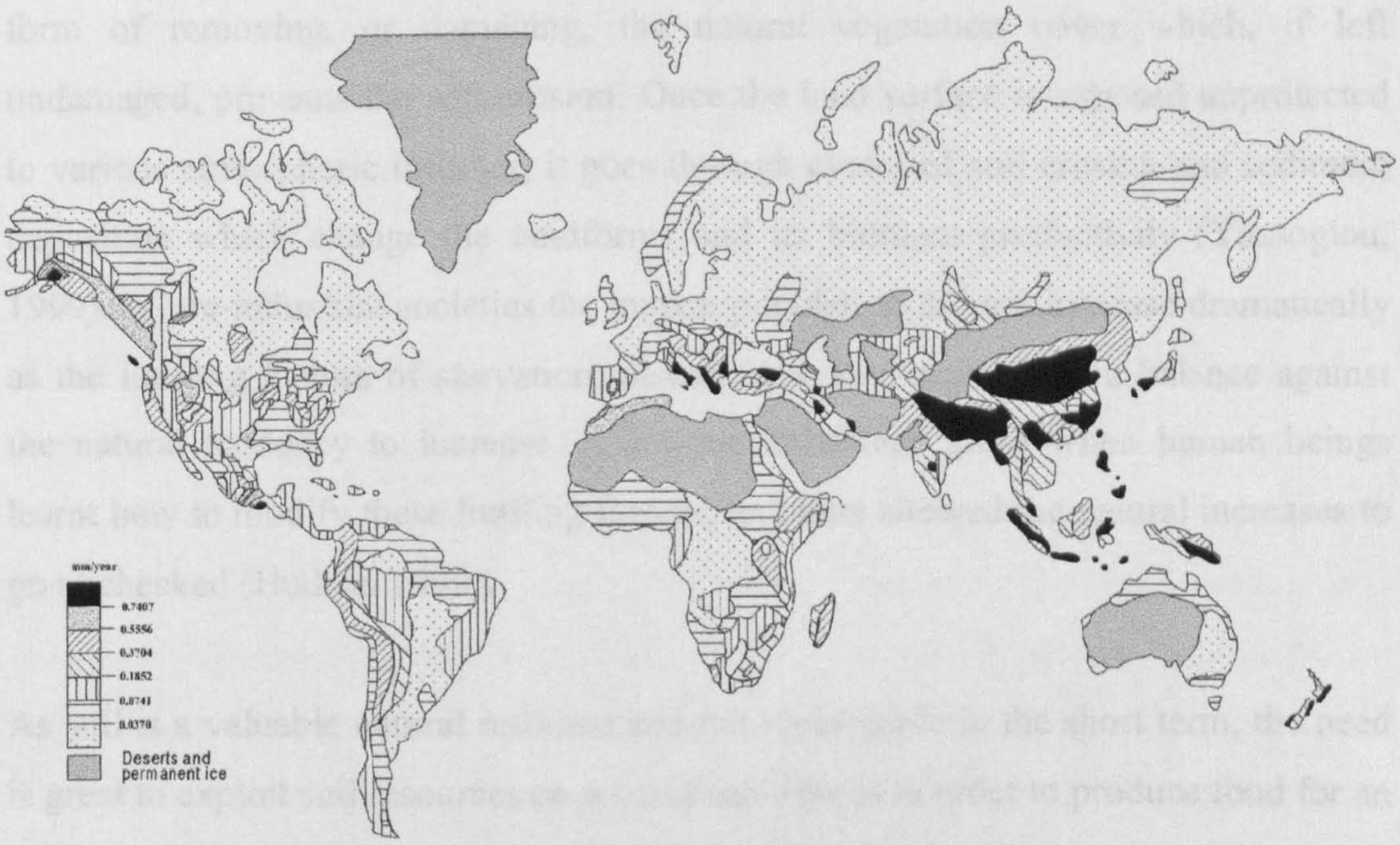

Figure 1.1. A world map showing the average yearly sediment loss (mm year^{-1}) due to soil-erosion (from Walling 1996).

The causes of soil erosion can be attributed to a variety of factors but the two dominant ones are the climate and human activities. The soil erosion caused by climate is a normal process representing erosion of the land surface in its natural environment without the influence of human beings. Bolle (1999) explain how dramatic climate changes in the past have produced conditions that resulted in the conversion of flourishing landscapes into desert. Temperature and precipitation are

considered to be the main controlling factors causing the variability of climate. For example, droughts, which are the results of high temperature and shortage of precipitation, have a very distinctive significance in damaging the vegetation cover, and consequently, in controlling the soil-erosion processes.

Although the land undergoes continuous transformations at low soil-erosion rates under natural conditions, human activities can accelerate these transformations to higher rate by using advanced technology. An example of such activities is the process of preparing land for the production of food, settlements, industries and transport facilities. Human-induced land-transformation processes usually take the form of removing, or damaging, the natural vegetation cover which, if left undamaged, prevents the soil erosion. Once the land surface is exposed unprotected to various atmospheric influxes, it goes through cycles of soil erosion and sediment deposition which change the landforms and its biomass productivity (Yassoglou, 1999). In pre-industrial societies the human population did not increase dramatically as the limiting factors of starvation, disease and war, maintained a balance against the natural tendency to increase. A serious imbalance arose when human beings learnt how to modify these limiting factors, and thus allowed the natural increases to go unchecked (Hudson 1995).

As soil is a valuable natural resource and not replaceable in the short term, the need is great to exploit soil resources on a sustainable basis in order to produce food for an exponentially growing population. The increase in human demands from land places a greater strain upon the soil resources and if these demands become too great, the land is then prone to soil erosion and degradation. As soil is the basis of all terrestrial ecosystems, a degraded soil means lower fertility and reduced productivity and leads to human poverty (Bridges and Oldeman, 1999). According to the Food and Agriculture Organisation (FAO) reports, land degradation and soil erosion are closely linked to poverty in the majority of the developing countries. Poverty in such countries is both a consequence of soil erosion and one of the causes because poor people, with no resources to fall back on, are forced to put immediate needs before the long-term quality of the land (FAO, 2000).

In a study about the extent of the land degradation and soil-erosion problems, Oldeman (1994) shows that 1094 million hectares are affected globally, among which 43 % is caused by deforestation and removal of natural vegetation, 29% by overgrazing, 24 % by improper management of the agricultural land and 4% as a result of over-exploitation of natural vegetation. This implies that human-induced soil erosion is fast becoming recognised as a key issue for soil conservation approaches (Barrow 1991, Van Lynden 1995). The World Resources Institute (1992) reports that "over the past 45 years, about 11 percent of the Earth's vegetated soils have become degraded to the point that their original biotic functions are damaged, and reclamation may be costly or in some cases impossible". The UNCOD stated that as of 1992 land degradation affects 70 percent of the world's drylands (3.6 billion hectares) or nearly one-fourth of the total land area of the planet (UNEP, 1992).

Thus, conservation of the soil resources from soil erosion is vital to achieve a sustainable use of land, especially in the semi-arid regions which are more prone to the problem of soil-erosion and land degradation. In semi-arid Mediterranean North Africa for example, the Romans developed excellent water conservation and irrigation techniques through the use of extensive systems of terraces, enabling them to cultivate this low rainfall area effectively and sustain the soil resources. However, when the empire collapsed, the irrigation and terrace systems were abandoned. Some of the land returned to its original state, but most of it was eroded away leaving a wasteland riddled by dunes and gullies (Bennett, 1939). The Egyptians and Phoenicians also developed terrace systems that fell into disrepair and suffered severe soil erosion (Stallings, 1957).

Soil resources conservation and soil-erosion prevention can be achieved by first identifying those areas which are prone to soil erosion and then developing strategies to exploit sustainably the natural resources in these areas. Soil-erosion modelling can potentially provide a key tool in the soil conservation processes where the most sensitive areas to erosion, and areas that are already most eroded, can be identified

by integrating remotely sensed imagery with other sources of information such as meteorological, soil, and vegetation data.

The number of studies investigating the use of remotely sensed data in soil-erosion modelling is increasing. Due to the fact that parameters governing soil erosion, such as vegetation cover, soil properties and topography, vary spatially and temporally, the demand for an efficient and relatively inexpensive data-collection system is high. Remote sensing techniques provide a powerful tool for collecting data at regular time intervals and with sufficient temporal and spatial resolution. For example, the cover and crop management factor for various environments in the Universal Soil Loss Equation (USLE), which is related to land cover, has been successfully interpreted by using SPOT and Thematic Mapper (TM) (Fenton 1982, Horvath *et al.* 1983, Jürgens and Fander 1993, Price 1993, Metternicht and Zinck 1998).

Remotely sensed data and remote sensing techniques can be used to determine soil types and several soil properties which can be used to parameterise soil-erosion models (Drake *et al.*, 1999). An example of this approach is detecting the change in soil structure where the change appears in the visible wavelengths of the electromagnetic radiation (EMR) as changes of soil surface colour. According to Escadafal *et al.* (1989) soil colour has been found to be related to soil spectral characteristics in the visible wavelengths of EMR.

Band number	Band type	Spectral range
1	Blue	445-516 nm
2	Green	506-595 nm
3	Red	632-698 nm
4	NIR	757-853 nm

Table 1.1. Showing the four bands and their wavelengths of the IKONOS sensor.

The launch of the new generation of high spatial resolution satellites opens the door to a new era of more accurate, spatially distributed environmental modelling. Examples of this generation of satellites are IKONOS and Quickbird which were launched in 1999. IKONOS, for instance, has the capacity to collect data with either multispectral or panchromatic bands with spatial resolution of 4 and 1 metre respectively. Table 1.1 shows the spectral specifications of the four bands of the IKONOS sensor.

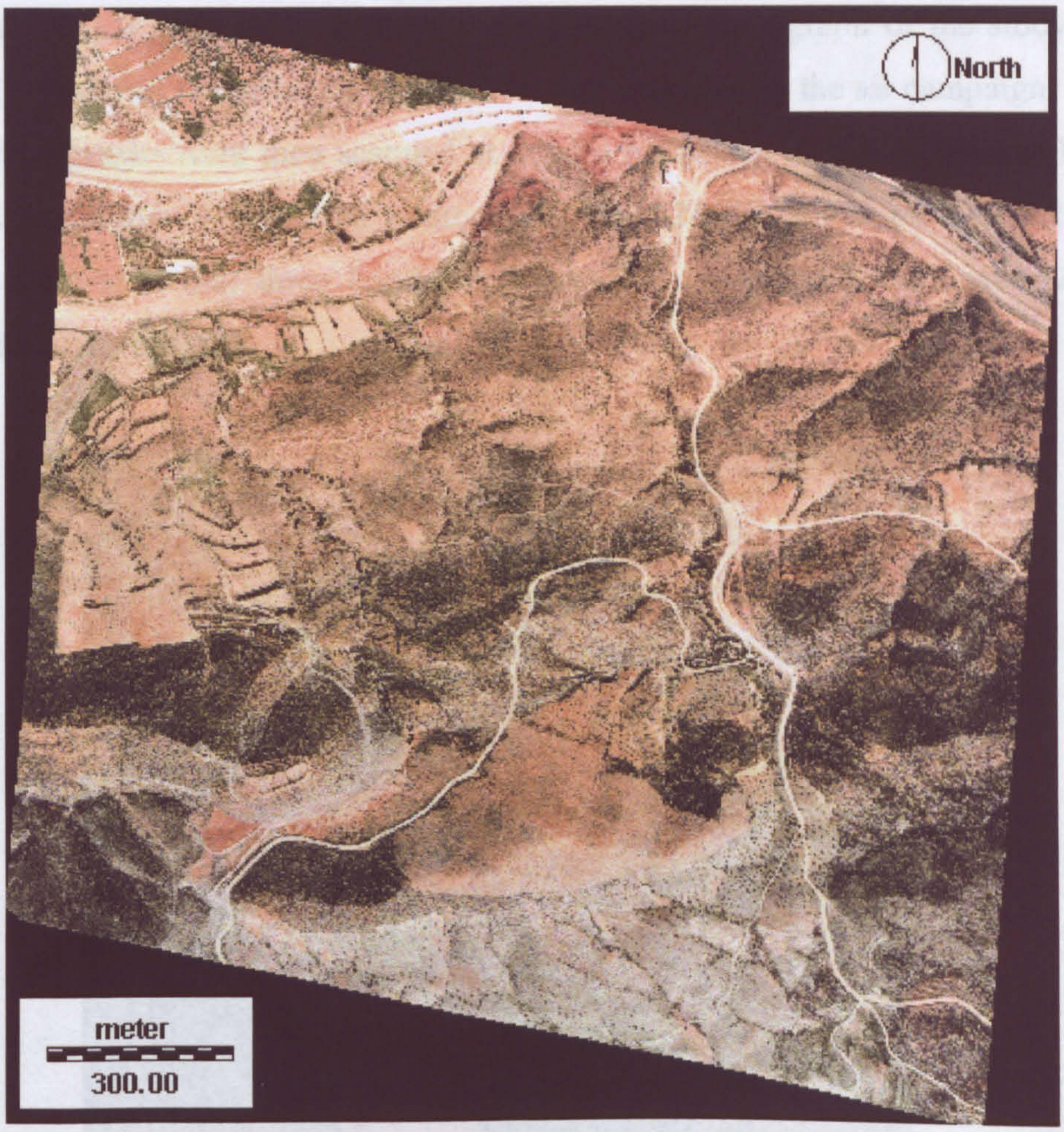

Figure 1.2. The aerial photograph of the study area collected by NERC, after georeferencing and applying geometric corrections (the processes of image georeferencing and geometric corrections are explained later on in chapter 4). The NERC air campaign took place on the 9th of April 1996.

In this research, however, we investigate the use of NERC (Natural Environment Research Council) aerial photographs as a high spatial resolution data collection system for extracting soil-erosion parameters and facilitating the implementation of a spatial soil-erosion model. These aerial photographs are used in this research instead of the high spatial resolution imagery from the above-mentioned sensors because the research was initiated before the launch of these sensors. The true colour aerial photographs were collected on the 9th of April 1996 during NERC air campaign in the South-east Spain, giving 0.55 metre spatial resolution. Three aerial photographs are used in this study which consist of the main one covering the study area and the two adjacent ones that will be used in the process of creating the Digital Elevation Model (DEM). Figure (1.2) displays the main aerial photograph of the study area. Figure (1.3) shows the aerial camera RC-10 that was used in the air campaign. These aerial photographs were then scanned at 600dpi resolution (which is defined by the original resolution of the aerial photographs) into 24 bit colour images and these images were split into three bands of 8 bit (red, blue, and green) using Adobe Photoshop software.

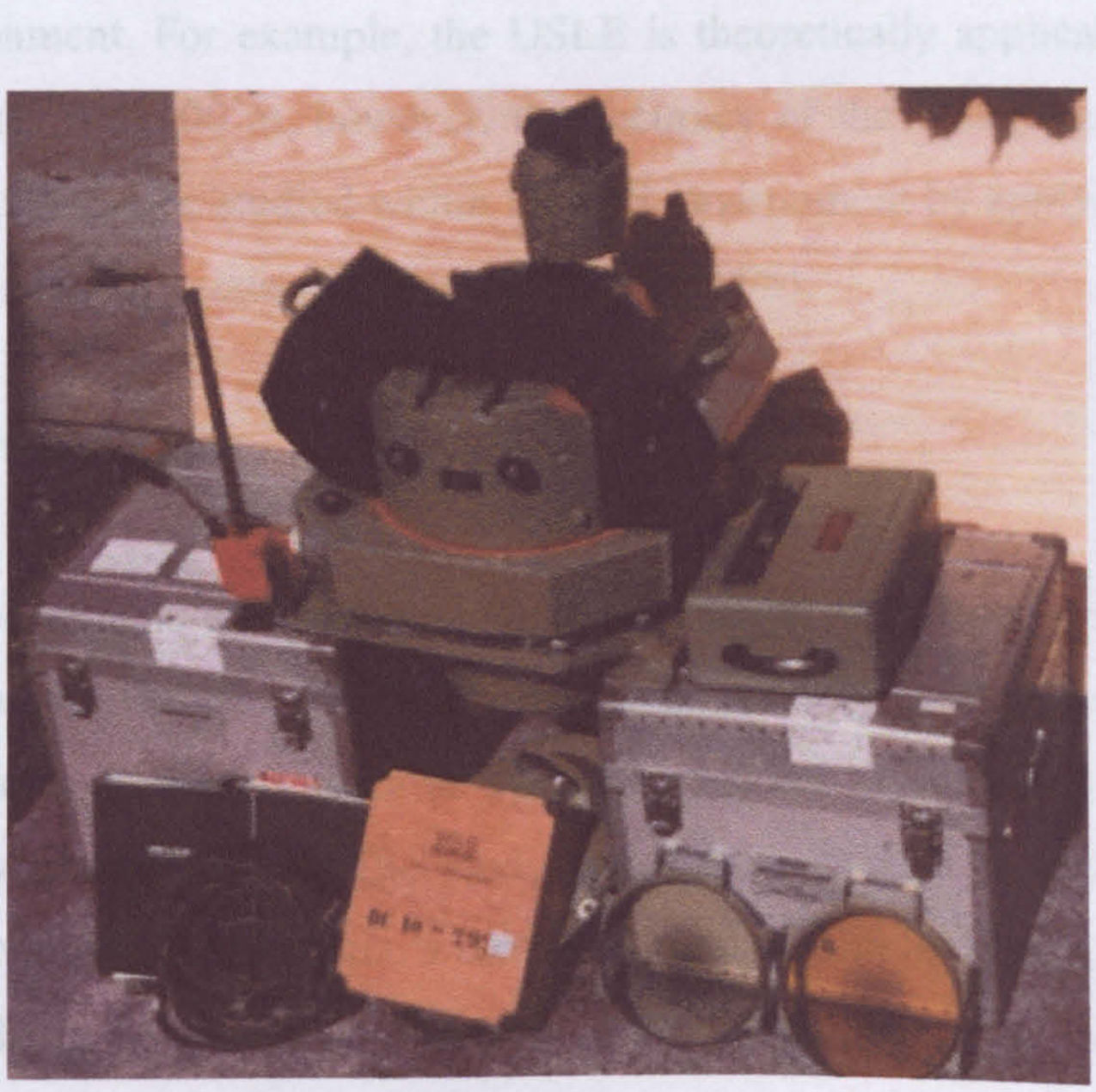

Figure 1.3. The RC-10 Aerial Camera which has been used in the NERC air campaign in the Southern-east of Spain (http://www.nts-info.com).

In this research Geographic Information System (GIS) techniques will be utilised to collect, integrate and analyse the data required by the soil-erosion model and to present the final results. A geographic information system (GIS) can be defined as a tool used to analyse the spatial properties and potential relationships of objects and events. In essence, a GIS is a collection of tools for mapping and analysing things that occur in space and time. In addition, a GIS can integrate all the temporal and spatial information as well as other ancillary data such as the physiographic and soil parameter information. Furthermore, GIS also provides an opportunity for rapid updating of the databases, monitoring, and forecasting soil erosion dynamically and quickly. GISs have also been used in fields as diverse as environmental management, urban and regional planning, emergency response, and agriculture.

Many aspects of land-management and soil-erosion studies can currently be approached using GIS. Today, GIS has the capabilities to facilitate spatially distributed hydrological and geomorphological studies at a desired spatial scale in a raster environment. For example, the USLE is theoretically applicable only at grid sizes less than 100x100 m, however, the accuracy of the USLE calculations using larger grid sizes can be studied within the GIS environment by applying the equation at a wide range of cell sizes (Molnar and Julien, 1998).

1.2 THE STUDY AREA

The semi-arid regions of South-east Spain are subject to extensive soil erosion and land degradation (Thornes, 1976). These regions are very susceptible to soil-erosion due to a number of factors, such as high drainage density, intense rainfall patterns and sparse vegetation cover. The study area of this project is located near Vélez Rubio, in the province of Murcia, a semi-arid rural area in South-east Spain which is defined by the geographical co-ordinates of 37°37'43"-37°38'42" N and 2°02'50"-2°04'02" W and by the size 1.8 by 1.9 km (figure 1.4). This area was selected because it represents different patterns of soils, vegetation cover, land use and

topography so that the effects of these various parameters on the hydrology and soil loss can be assessed.

Figure 1.4. A map showing the location of the study area in Vélez Rubio, Murcia, South-east Spain. The red dot in the magnified map indicates the location.

The main feature of the Mediterranean climate of south-east Spain is the alteration of a rainy season in the cold months and a dry season in the warmest months, which is known as the summer drought (Tomaselli, 1977). Rainfall occurs in this region over two seasons: the first season is between April to May and the second season is between September to October (Garg & Harrison, 1992) (figure 1.5).

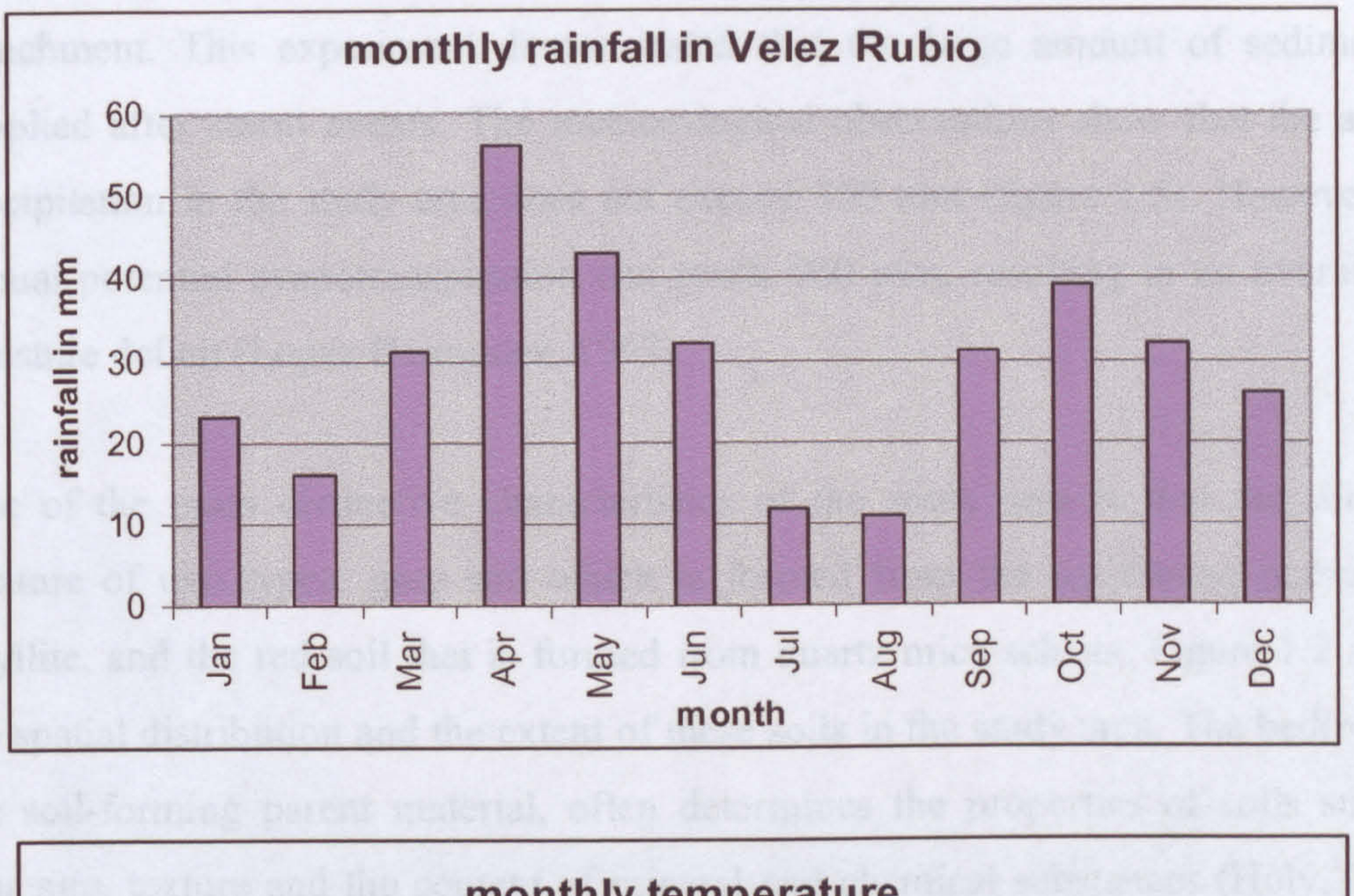

Figure 1.5. The average monthly rainfall and the minimum, maximum, and average temperature in the study area of Velez Rubio (adapted from Proyecto Lucademe, 1992).

Because of the irregularity of the precipitation pattern in the study area, most of the monthly rainfall volumes are due to a few days with high rainfall volumes leading to high number of floods (Lopez-Bermudez *et al.*, 1999). For example, in the neighbouring area of Embalse de Puentes, 24% of the annual precipitation fell in two days in 1987 (Lopez Bermudez, 1997). Navas (1991) carried out an experiment on a cultivated land to analyse the relationship between the precipitation and the sediment detachment. This experiment demonstrated that the large amount of sediment is supplied after storm events. The meteorological observations show that the annual precipitation in the study area does not exceed 350 mm (figure 1.5). However, the annual potential evapotranspiration can reach 900 mm, resulting in an overall soil moisture deficit (Lopez Bermudez, 1997).

One of the main distinctive characteristics of the study area is that the soil is a mixture of two types: grey soil which is formed from the underlying bedrock of phyllite, and the red soil that is formed from quartz mica schists. Figure 1.2 shows the spatial distribution and the extent of these soils in the study area. The bedrock, as the soil-forming parent material, often determines the properties of soils such as structure, texture and the content of mineral and chemical substances (Holý, 1980). For example, soils formed on limestone and dolomite formations are relatively resistant to washing, while soils on igneous rocks and various sediments are less resistant. Thus, mapping the soil types of the study area is significant as the soil is an important factor controlling overland-flow generation and the sediment yield.

The aerial photograph in figure 1.2 shows the nature and spatial distribution patterns of the vegetation cover in the study area. The natural vegetation cover (called matorral) exists in areas that have not experienced agricultural activities and it is dominated by cistus, anthyllis and rosemary. In areas of human agricultural activities the vegetation cover is dominated by almond and olive plantations. Generally, plant distributions are patchy with bare soil exposed. The soil is poorly developed with a large amount of surface stones.

Historically in pre-Neolithic time, 96% of the Iberian Peninsula was covered by forest: 83% evergreen, 8% conifer, and 4% riparian (Conacher and Sala, 1998). Due to the long period of human settlement in the area, little of the indigenous vegetation now remains. Forest clearing started with agriculture and fire was used to convert dense forests into more open wood and shrublands (Naveh and Vernet, 1991). Clearance continued with human settlement, industrialisation and war, when considerable portions of forest were cleared for ship building (Tomaselli, 1977).

Figure 1.6. The ploughing of agricultural land in the study area where the matorral is removed to prepare the land for almond plantation.

Overgrazing, deforestation and intensive agricultural use (such as land cultivation to plant almond and olive trees) has destroyed most of this vegetation cover in the area (figure 1.6). Grazing is considered to be an important factor when talking about the destruction of vegetation cover in the study area. In their study which was carried out in the same region, Lopez-Bermudez *et al.* (1999) show that the grazing has been more severe than in the past due to the growing number of sheep and goats which are

the only significant livestock in the region. Figure 1.7 shows an area of extreme overgrazing around a permanent water point where goats return at least once a day.

The recent land-use evolution in the region shows a decrease of natural land uses and dryland crops in favour of irrigated crops. Growth in irrigable land was estimated to exceed 300% during the 20th century (Lopez-Bermudez *et al.*, 1999). These newly irrigated lands have experienced a huge change in the landscape causing a disruption in the topsoils and destruction of the vegetation cover. As a result of weakening and destroying the vegetation cover in the area, the soil has lost its structure and most of its organic matter which has led the area to severe soil erosion. Research carried out in a similar environment to model the soil erosion (Quine *et al.*, 1994) showed that steeper slopes under vegetation cover are significantly less affected by erosion than very gentle slopes on which agricultural activities are the main factor causing erosion and this demonstrates the effect of land use on accelerating soil erosion.

Figure 1.7. The effect of overgrazing on the vegetation cover. The figure shows the location where goats are brought to drink water.

However, since the middle of the last century, human action has started to reverse forest decline and land clearance. In the Iberian Peninsula, forests have been re-introduced to 13% of the land (Conacher and Sala, 1998). In addition, social and economic changes, such as accelerated industrialisation, have led to large scale abandonment of rural areas, accompanied by the regeneration of vegetation cover (Le Houerou, 1981). The positive impact of this rural abandonment has been in the increase of the land covered by matorral. For example, Ruecker *et al.* (1998) found in eastern Spain that although soil degraded immediately after land is abandoned, 20 years later high density matorral has successfully regenerated. Regeneration was aided by the presence of terraces which limited erosion and improved water infiltration (Hawkes, 1998). Douglas *et al.* (1994) recorded the same improvement in terraces abandoned in southern Spain, despite the fact that these terraces were grazed. Another case of the effect of land abandonment in southern Spain was studied by Faulkner (1995). In this area marginal cropland was abandoned in the 1970s and 1980s. In 1987, the introduction of an EU policy encouraging the cultivation of certain crops led to the cultivation of almonds on previously uncultivated land. However, because of the problems of accessibility, the almond trees were not planted on the abandoned slopes, but on more accessible steeper slopes, never cultivated in the past, creating a large problem of soil-erosion (Hawkes, 1998). However, it was noticed during the fieldwork of this study in 1998 that some parts of the study area, which were covered with matorral, have been ploughed after the aerial photographs were taken in 1996 in order to plant almond and olive trees as a consequence of change in the EU subsidies.

1.3 AIMS AND OBJECTIVES

With the advancement of the remote sensing technology and the availability of a new generation of remote sensors capable of acquiring data at higher spatial scales, the door is open for more accurate, process-based environmental modelling. This study aims primarily to evaluate the potential of high spatial resolution remote sensing, namely aerial photography, and Geographical Information Systems (GIS) in

parameterising spatially distributed soil-erosion models at the field scale. In general, we can summarise the study objectives in the following points:

- To review the available soil-erosion models, both empirical and process-based models, and assess the parameters impacting soil-erosion so that the appropriate spatially distributed model for this study, which incorporates remotely sensed data, can be selected.

- To produce a method of soil-erosion mapping that can be automated as much as possible, relying mainly on remotely sensed data in order to minimise the field sampling, time, effort, and financial expenses necessary for the model implementation.

- To evaluate the utility of applying image processing techniques, that have been developed for application with low resolution systems, to high spatial resolution aerial photography.

- To assess and implement the methodologies of mapping the vegetation cover and topographic slope parameters, of the selected soil-erosion model, from the high spatial resolution aerial photographs.

- To investigate various approaches of continuous and discrete methods to map soil properties, which are needed to calculate the overland flow and soil erodibility, using remotely sensed data and GIS techniques with the aid of field data.

- To implement the selected spatially distributed soil-erosion model by integrating its controlling parameters, which were derived from the remotely sensed data, in a GIS environment. The resultant soil-erosion map can be validated against the field data resulting from the rainfall simulations.

Figure 1.8 summarises the input data required by the overland-flow and soil-erosion models, as well as their outputs.

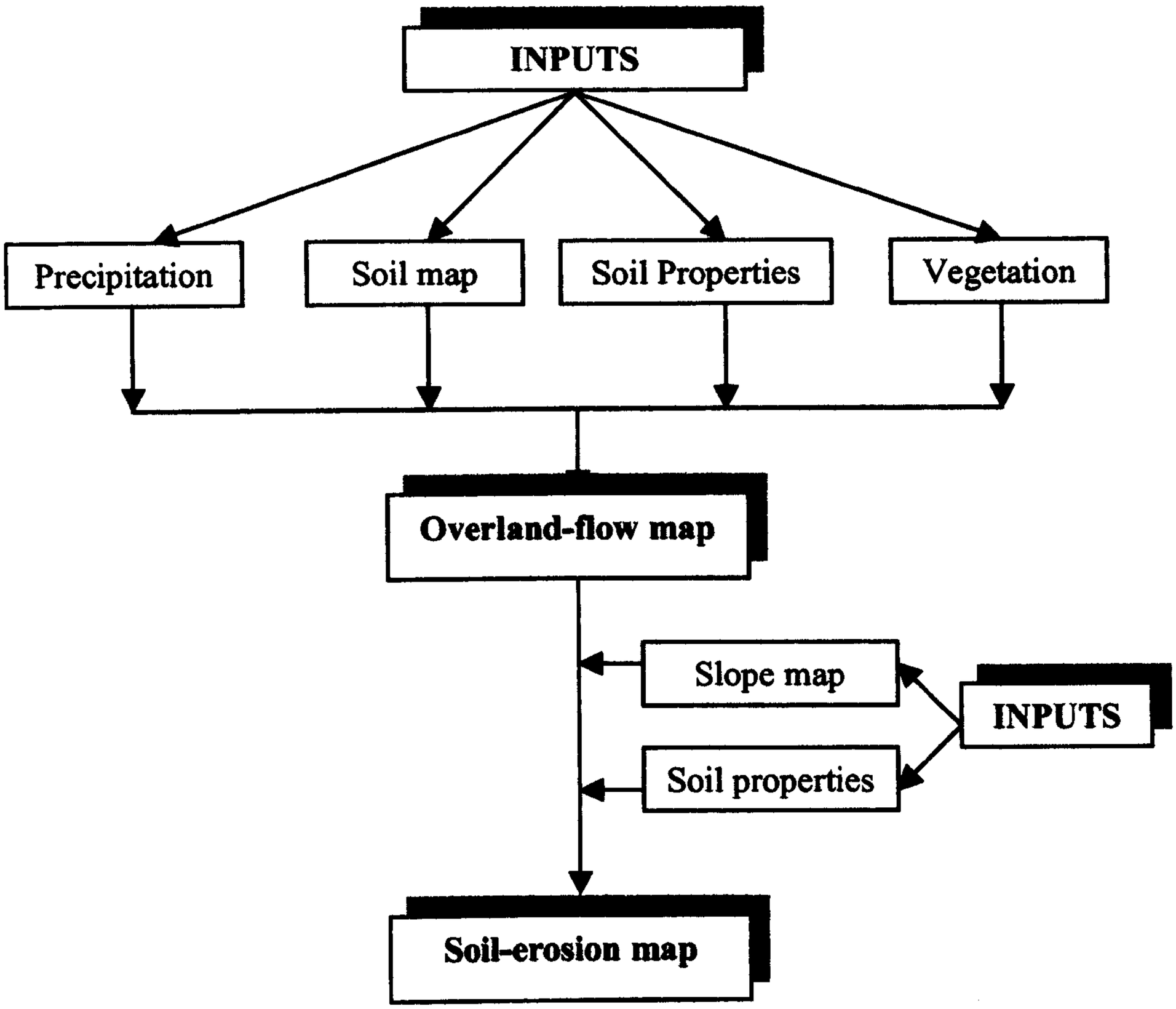

Figure 1.8. A flow diagram showing the inputs and outputs of the overland-flow and soil-erosion models.

1.4 THE STRUCTURE OF THE THESIS

Chapter one gives an overview about the problem of soil-erosion and land degradation, their causes and consequences. The need to understand the processes of soil-erosion in order to model their effects on the environment is outlined. The geography, geology, geomorphology and climate of the study area are described, as well as the nature, extent, and the spatial distribution of soils and vegetation cover.

Chapter two reviews the literature of implementing the remote sensing and Geographical Information Systems (GIS) in soil-erosion modelling. The advantages and limitations of using remote sensing techniques, as data collection systems, are

discussed and compared with the conventional techniques such as field surveys. The factors affecting the soil-erosion and overland flow (e.g. soil erodibility, vegetation cover and topography) are reviewed in order to gain a proper understanding of their impact on runoff generation and sediment yield.

Chapter three concentrates on studying and investigating the characteristics of some of the available soil-erosion and overland-flow models. There are two types of soil-erosion model: the empirical and the process-based models. Since this study emphasises the use of remotely sensed data and GIS techniques, the process-based spatially distributed soil-erosion models are of special interest and the Thornes model is selected. In addition, some empirical and spatially distributed overland-flow models are analysed and the Carson & Kirkby (1972) model is selected because it can be integrated in a GIS environment and can be easily implemented in the Thornes soil-erosion model.

In chapter four the conventional surveying methods and GPS techniques are discussed and their implementation in the field to collect the location data for Ground Control Points (GCPs) and the soil sampling locations is explained. The Digital Elevation Model (DEM) is constructed in ERDAS Imagine OrthoMAX software using the GCPs. The topographic parameter of slope for the Thornes soil-erosion model is then extracted from the DEM.

In chapter five various methodologies are discussed to extract the vegetation information from the remotely sensed data such as the vegetation indices, red band reflectance, and the soft classification techniques. The constrained linear mixture modelling technique is used because the vegetation cover information can then be extracted at the sub-pixel level. Because the shade obscures the vegetation cover, an algorithm is proposed to re-scale the mixture modelling vegetation cover by removing the shade effect. Co-occurrence matrix analysis was implemented to isolate pixels that are assigned a value of zero vegetation, where high fraction of vegetation is expected to exist in those pixels, and the appropriate values are assigned to them. The accuracy of the resultant vegetation cover map is assessed. The methods of hard

classification and image interpretation are investigated to map the land use and the second method is implemented because the hard classification method produced a land-use map of a poor accuracy.

In chapter six the soil maps resulting from the mixture modelling are re-scaled to remove the effects of shade and vegetation and then the binary soil map is produced by hardening. Different sampling methodologies are compared and the appropriate method of soil mapping in the study area is described. Field soil samples were collected and analysed in the soil laboratory to extract the bulk density, organic matter, soil depth, and soil texture. Various statistical methodologies are investigated to distribute the soil properties spatially and the hydrological response units method is used for this purpose employing the binary soil and the land-use maps.

In chapter seven the processes of parameterising and validating both the Carson and Kirkby overland-flow model and the Thornes soil-erosion model are explained. The process of estimating the erodibility factor (K) from the Wischmeier equation using the soil texture and organic matter information is shown. The overland-flow and soil-erosion models are then implemented by integrating their controlling parameters in a GIS environment using IDRISI software. The sensitivity analysis is carried out for both models in order to investigate the variations of the model's outputs as a result of changes in the controlling parameters. The maps resulting from the implementation of these models have been validated by cross checking against the data collected in the field during the rainfall simulations.

Chapter eight sums up the methodologies used in this study and summarises the results of the overland-flow and soil-erosion models in order to draw the final conclusions. These conclusions are drawn in light of the aims and objectives set in chapter one to evaluate the potentials of high spatial resolution remote sensing and GIS for soil-erosion modelling. The future work that would be carried out in order to further the aims and objectives of this research is also outlined.

CHAPTER 2

REMOTE SENSING, GIS, AND THE PROCESSES OF SOIL EROSION

"To gain control over the soil is the greatest achievement of which mankind is capable. The organisation of civilised societies is founded upon the measures taken to wrest control of the soil from the wild nature, and not until complete control has passed into human hands can a stable superstructure of what we call civilisation be erected on the land ... . Soil erosion is altering the course of world history more radically than any war or revolution. Erosion is humbling mighty nations, re-sharing the domestic and external policies and once and for all it has barred the way to the "El Dorado" that a few years ago seemed almost within reach"

(Jacks, 1939)

2.1 INTRODUCTION

2.2 UNDERSTANDING THE SOIL-EROSION PROCESSES

- 2.2.1 Raindrop Impact
- 2.2.2 Overland flow
- 2.2.3 Rill Erosion
- 2.2.4 Gully Erosion
- 2.2.5 Soil Erodibility
- 2.2.6 Vegetation Cover
- 2.2.7 Topography
- 2.2.8 Soil Compaction

2.3 REMOTE SENSING SYSTEMS AND GIS FOR MONITORING AND MODELLING SOIL EROSION

- 2.3.1 Remote Sensing Platforms
  - 2.3.1.1 AVHRR
  - 2.3.1.2 Landsat TM
  - 2.3.1.3 High Spatial Resolution Remote Sensing
  - 2.3.1.4 Selecting a Remote Sensing Data Collection System
- 2.3.2 Geographic Information Systems (GIS) for Soil-erosion Modelling

2.4 CONCLUSION

2.1 INTRODUCTION

Soil is described by the International Soil Society as "a limited and irreplaceable resource and the growing degradation and loss of soil mean that the expanding population in many parts of the world is pressing this resource to its limits. In its absence the biospheric environments of human beings will collapse with devastating results for humanity" (Zhang, 1999). Morgan (1995) defines soil erosion as a natural, and human induced, hazard traditionally associated with agriculture in tropical and semi-arid areas and is important for its long-term effects on soil productivity and sustainable agriculture and land resources.

Soil erosion is mostly caused by human activities and mismanagement of the land natural resources such as the destruction of the natural vegetation cover and cultivating the hillslopes. These practices lead to changes in the physical and chemical resistance of soils and the ease and speed with which water runs over the land surface (Thornes 1976). With the exponential increase of the world population especially in less developed countries, the demand for food, fuel and cloths will increase pressure on the land resources. Figure 2.1 shows how various natural and anthropic factors interact and contribute to the problem of soil erosion where climate, socio-economic and political factors are regarded as the driving factors in accelerating soil erosion.

The Food and Agriculture Organisation (FAO) analysis suggests that 200 million hectares of additional land will be required to produce sufficient food for the world population for the next 20 years (Dudal 1981). This will lead most of the countries, especially those with a high population growth coupled with poor agricultural practices, to intensify their exploitation of soil for rapid agricultural and economic development to meet their needs. This will put more pressure on land resources and will lead to soil degradation.

In order to take corrective measures for preventing soil loss and for the proper management of land for optimal utilisation for agriculture, information on the nature, extent and magnitude of the soil-erosion problem is needed.

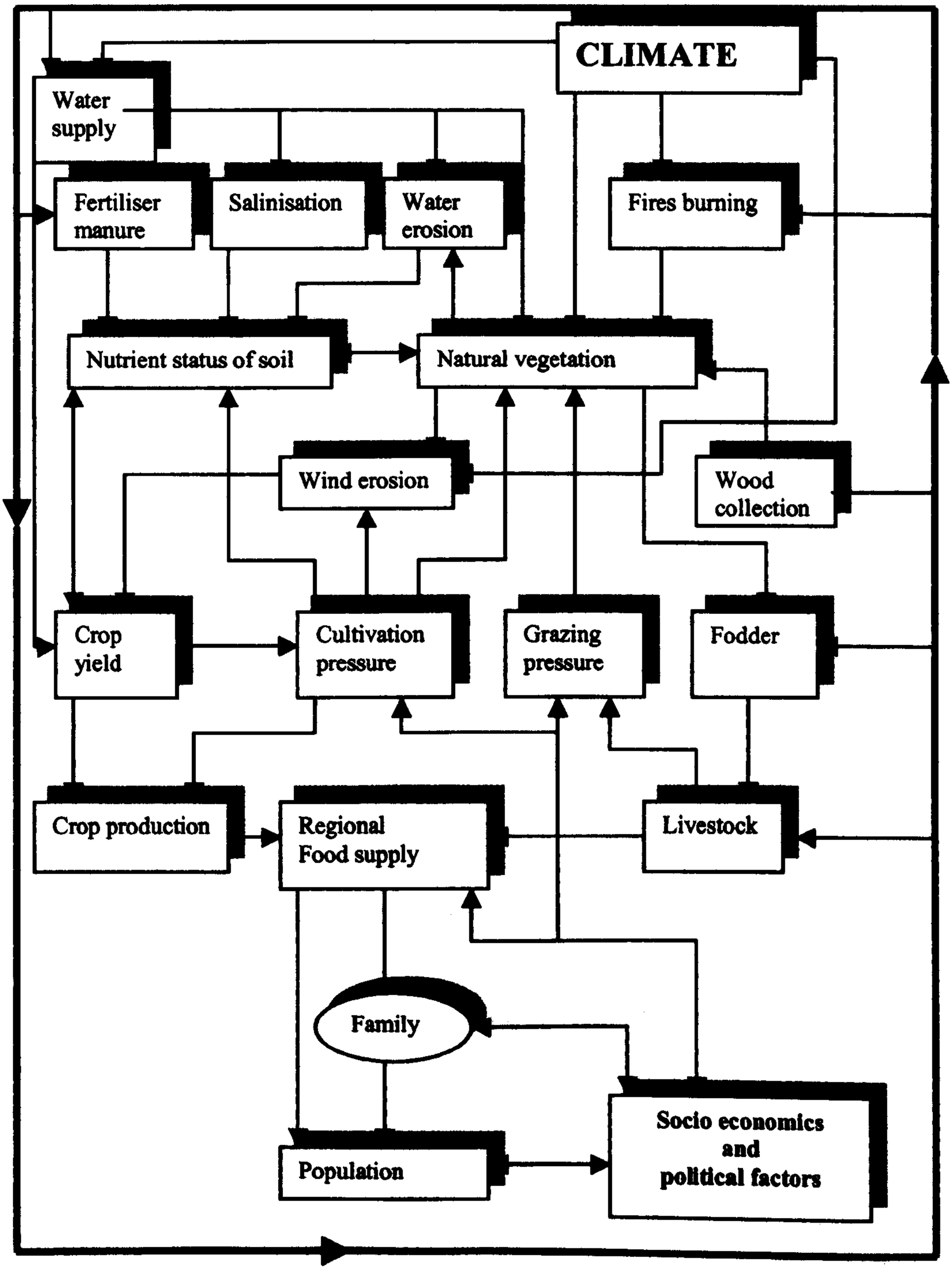

Figure 2.1. A generalised model of factors involved in the land degradation and soil erosion in semi-arid regions of south-east Spain (after Garg & Harrison, 1992).

2.2 UNDERSTANDING THE SOIL-EROSION PROCESSES

In recent years there has been a large amount of research, undertaken by a wide variety of scientists, regarding the processes related to runoff generation and to soil erosion by water. For example, physical geographers have investigated the soil-erosion processes at different scales and in various environments in order to improve our understanding of the fundamentals of these processes and the factors affecting them. However, the soil scientists have observed and measured the sedimentation and soil loss on a simple slope and a field scale in order to select crop-management options which minimise the loss of soil. In contrast, the agricultural and water resources engineers have monitored and modelled soil erosion and sediment transport on slopes, fields and watersheds in an attempt to predict what happened, when and where (Guy *et al.*, 1992). If we look at these different research areas we find that they integrate to form a holistic picture of the soil-erosion phenomenon.

Soil erosion is a two-phase process consisting of the detachment of individual particles from the soil mass and their transport by erosive agents such as running water or wind. When sufficient energy is no longer available to transport the particles, a third phase, deposition, occurs (Morgan, 1995). Hudson (1981) defines the soil-erosion process as a smoothing and levelling process, with soil and rock particles being carried, rolled, or washed down by force of gravity. Water and wind are the main agents which loosen, break down and transport the particles. However, erosion by water is one of the most common degradation phenomena and comprises generally two types of erosion: rill and interrill erosion (Buckman & Brady, 1971) where the rills are initiated at a critical distance downslope when the overland flow becomes channelled.

The controlling factors of soil-erosion processes comprise climate, vegetation cover, soil physical and chemical properties (such as texture, organic matter content etc.) and topographical properties of the landscape (De Jong 1994). Topography, as reflected by landform, gradient and length of slope and the nature of relief, in

conjunction with soil conditions influences soil erosion to a great extent. The vegetation depending upon its extent and coverage intercepts precipitation resulting in the significant loss of kinetic energy of rain drops which leads to considerable protection of soil. The removal or destruction of the vegetation cover upsets this balance and accelerates soil erosion (Dwivedi *et al.*, 1997).

Thus, a thorough and comprehensive understanding of the processes of soil erosion and of the external and internal factors influencing these processes seems mandatory for an accurate and realistic approach to modelling the soil erosion. The following is an analysis and description for these processes and factors.

2.2.1 Raindrop Impact

Sharma *et al.* (1993) describe that the erosive potential of rainfall, which is referred to in the literature as rainfall erosivity, depends on three main factors; the raindrop size distribution, fall velocity and total mass. According to Morgan (1995), the raindrop impact has two effects on soil erosion. First, raindrop impact provides a consolidation force, which compacts the soil and forms a surface crust. Second, raindrop impact provides a disruptive force, which destroys soil aggregates and can launch soil particles into the air. The World Meteorological Organisation (1983) stated that a 4 mm diameter raindrop strikes the ground with enough energy to throw a 0.1 cm^3 volume of sand having a density of 2.65 g cm^{-3} to a height of 6 cm.

Epstein and Grant (1973) explain that two mechanisms are important in the formation of the soil crust by raindrop impact. First, the raindrops falling on a bare soil break the surface aggregates into finer particles which, in turn, fill the voids of the soil. The second mechanism is that the raindrops compact the particles on the soil surface. Le Bissonais (1990) shows the complexity of soil-surface crusting processes by simulating different methods of aggregate breakdown such as immersion with and without stirring, wetting by capillarity action and rainfall simulation. The different mechanisms of aggregate breakdown distinguished are total breakdown by slaking, mechanical breakdown and dispersion (De Jong, 1994). Through his rainfall

simulation, Le Bissonais (1990) also found that two different effects of rainfall on aggregate breakdown are important. First, if aggregates are saturated before rainfall, the rate of breakdown of aggregates is due to contact between water and aggregates, and the most important processes are slaking and micro-cracking. Second, if aggregates are dry before rainfall, the breakdown intensity is due to rainfall kinetic energy and the most important processes are mechanical breakdown, splash and surface compaction.

Crusting, caused by the raindrop impact, can take one of two types: structural crusts caused by compaction and depositional crusts built up of several layers of sediment. Crusts at the soil surface have several adverse effects (Valentin and Bresson, 1992):

- The infiltration capacity of the soil is reduced which causes the generation of runoff and, consequently, rill and gully formation.
- Germination and the development of vegetation are hampered.
- The water retention capacity of the topsoil is reduced.
- Soil aeration is reduced, which holds back root development.
- Downslope soil erosion occurs through sheetwash and rill formation.

Levy *et al.* (1993) relate crust formation to aggregate stability which is, in turn, used as a measure of the susceptibility of the soil to crust formation. The processes that destroy aggregates comprise the impact of falling raindrops and the scouring action of flowing water during surface runoff (De Jong, 1994). On the other hand, Hillel (1980) argues that drying processes cause shrinkage and increase aggregate stability by making the aggregates more dense and adhesive.

The disruption force, caused by the raindrop impact on the bare soil surface, can destroy the soil aggregates and launch the soil into the air which causes transport of soil particles. The severity of this transport depends on the topography where on steep slopes the raindrops transport more soil particles downslope than upslope. However, in flat landscapes, the upslope transport of soil particles balances the downslope transport and the net transport is negligible. De Jong (1994) argues that the effectiveness of splash erosion is very variable and depends on the impact force

of raindrops, on direction of rainfall, on physical characteristics of the soil (soil erodibility) and on site-specific factors such as vegetation cover, slope angle and ground cover.

The studies on the impact of raindrops on the soil surface show that there is an exponential relationship between the kinetic energy of the rain and the slope of the landscape and the detachment rate of soil particles by rainsplash (Sharma *et al.*, 1993; Wischmeier & Smith, 1978). This kinetic energy is a function of the intensity, velocity and diameter of the raindrops.

2.2.2 Overland flow

The integrity of the models predicting soil erosion depends upon an understanding of the hydraulics and erosion mechanics of overland flow. It is, of course, impossible to separate the generation and routing of overland flow from its erosive effects. Since the former determine the latter, any physical modelling of soil erosion by overland flow must begin with overland flow.

Overland flow occurs on hillslopes during a rainstorm when surface-depression storage and either, in the case of prolonged rain, soil-moisture storage or, with intense rain, the infiltration capacity of the soil are exceeded (Morgan, 1995). Thus, there are two main types of overland flow on hillslopes: saturation and Hortonian. The saturation overland flow occurs when the soil layers beneath the soil surface are saturated by water and the rising water tables intersect the soil surface. As a result of this the excessive surface water cannot infiltrate into the soil and takes the type of overland flow. The second type of overland flow is the Hortonian which occurs when rainfall intensity exceeds the surface infiltration rate.

Saturation overland flow is usually common in footslopes that are marginal to stream channels, in topographic hollows and to areas covered with a thin soil layer. In contrast, Hortonian overland flow most often occurs where sparse vegetation permits

surface sealing or where bedrock outcrops limit the infiltration (Anthony *et al.*, 1992). Hortonian overland flow is thus widespread in arid and semi-arid landscapes.

The factors that constrain overland flow can be divided into two types. Some of them such as precipitation, evapotranspiration and soil moisture vary not only in time but also in space because of different climatic conditions and their seasonal variation. Other factors, such as soil type, vegetation type and in some cases land use and management, may change considerably from one catchment to another, or even in the same catchment, but in the same area they can usually be taken as stable at short time scales (Zhang, 1999). These factors all affect overland flow through changing the infiltration rates and the available soil-moisture storage.

One of the most important characteristics of overland flow, which greatly influences soil-erosion processes, is the flow velocity. In order for soil erosion by overland flow to take place, the flow velocity should reach a certain level where it can detach the particles. The detachment of an individual soil particle from the soil mass occurs when the forces exerted by the overland flow exceed the forces keeping the particle in its place (Morgan, 1995). However, along with the shear velocity of the overland flow, the initiation of a soil-particle movement is accelerated by factors like the effect of gravity on steeper slopes, the effects of raindrop impact on the flow, the angle in which the soil particle rests on the surface, and the cohesion of the soil.

For the larger soil particles, the critical shear velocity of the overland flow increases as the particle size increases. However, for the finer particles (such as silt and clay) the critical shear velocity increases with decreasing particle size due to the fact that they are cohesive (see figure 2.2). Once the critical conditions for particle movement are exceeded, soil particles may be detached from the soil mass at a rate which is dependent on the shear velocity of the overland flow and the unit discharge (Govers and Rauws, 1986). However, this situation is only true for completely smooth, bare soil surfaces. In practice, resistance due to the microtopographic form of the soil surface and the plant cover is usually more important and grain resistance may be as

little as 5 per cent of the total resistance offered to the overland flow (Abrahams *et al.*, 1992).

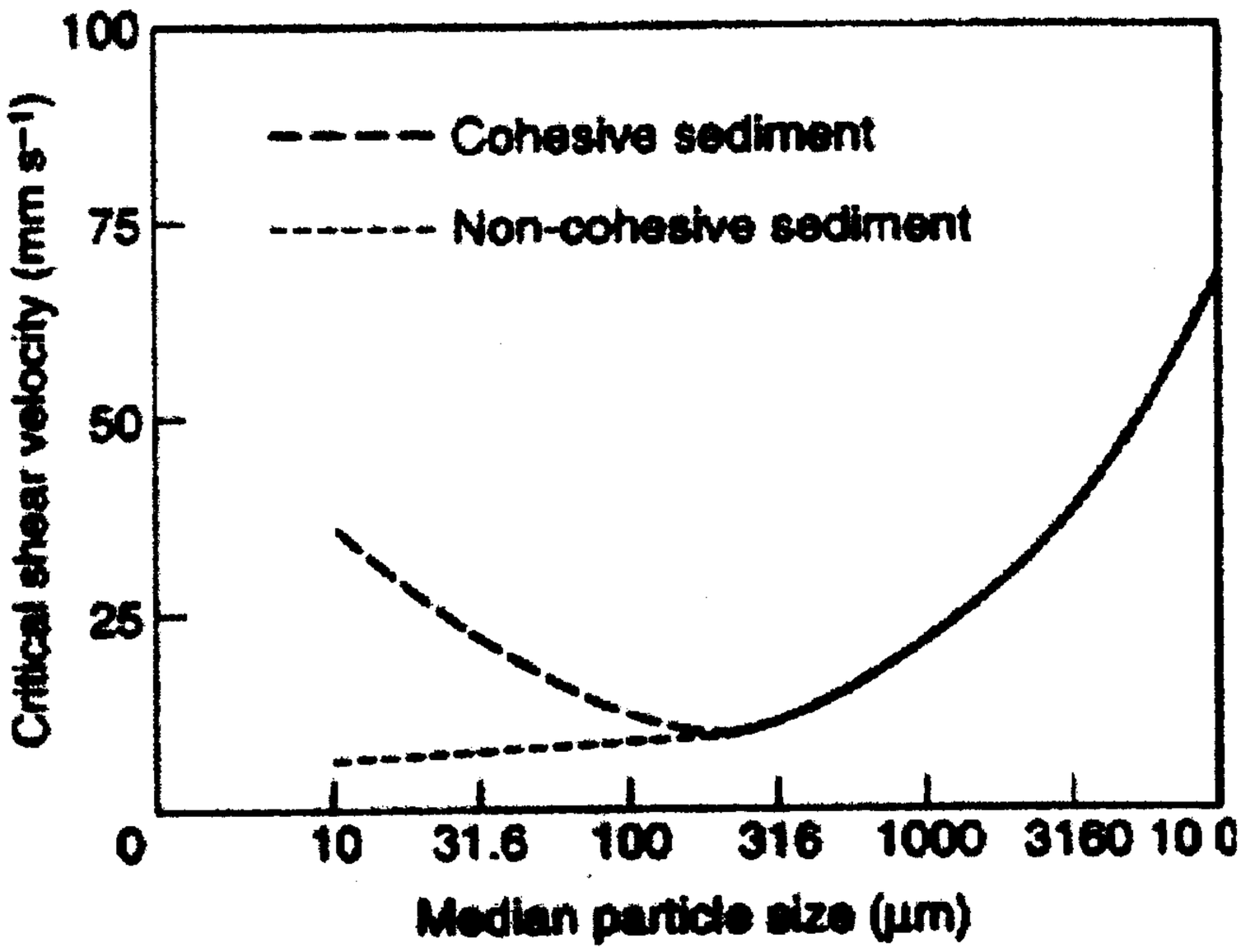

Figure 2.2. Critical shear velocity in overland flow for soil particle detachment as a function of particle size (after Savat 1982).

The modelling of hillslope erosion by overland flow depends on our understanding of three major phases, which have implications for model building, field experimentation and model testing (Scoging 1992). The first phase is determining the way in which the runoff in a certain location in the landscape is generated after the infiltration or saturation has taken place. This also includes predicting spatially variable times to runoff, and the decline in infiltration rate as a result of filling the soil moisture store. Second, routing the overland flow and understanding its hydraulics, temporal distribution and spatial concentration. Third, converting the overland-flow characteristics into erosion mechanics. In this study, however, only the first and third phases are taken into consideration because the second phase of routing is beyond the scope of this study.

2.2.3 Rill Erosion

Rills are ephemeral features occurring at a critical distance downslope where overland flow tends to concentrate and starts forming small channels (Bryan, 1987). Morgan (1995) shows that change from overland flow to rill flow passes through four stages: unconcentrated sheet flow, overland flow with concentrated flow paths, micro-channels without headcuts and micro-channels with headcuts. Studies on the initiation of the rills suggest that a rill starts to initiate when the shear velocity of the overland flow exceeds a certain level. Another approach relates rill initiation to a critical value of the ratio between the shear stress exerted by the flow and the shear strength of the soil. Once rills have been formed, their migration upslope occurs by the retreat of the headcuts on the steep banks at the top of the channels. The rate of the retreat is controlled by various factors such as the cohesiveness of the soil, the height and the angle of the headwall slope, and the discharge and velocity of the flow (De Ploey, 1989). Downslope extension of the rill is controlled by the shear stress exerted by the flow and the strength of the soil.

Since raindrop impact increases the transport capacity of the flow and, through the detachment of the soil particles, causes higher sediment concentration, Savat (1979) argues that the interaction of rainfall with the overland flow would enhance the probability of rilling. Quansah (1982) and Dunne and Aubry (1986), however, found that the particles detached by rain filled in micro-channels as fast as they could form, so that rilling was inhibited. This finding means that the two sets of processes compete so that either the micro-channels are short-lived because they drain away the overland flow, become laterally isolated and fill in, or the concentration of flow increases its erosive power and the channels deepen, widen and migrate both upslope and downslope (Morgan, 1995).

Rill erosion is the detachment and transport of soil by hydraulic processes occurring in flow concentrated by small channels which can by removed by tillage. Rill erosion accounts for the bulk of the sediment removed from a hillside, depending on the spacing of the rills and the extent of the area affected. Govers and Poesen (1988)

found that the material transported in rills accounted for 54-78 per cent of the total soil erosion. The rill erosion has a set of controls that is similar to the interrill erosion such as vegetation cover and slope steepness. In addition, tillage plays a major role in increasing erodibility by reducing soil consolidation. Soil just below the tillage zone can restrict rill depth by acting as a non-erodible layer. Rill erosion will not be considered in this study because it is based on routing the overland flow which is not one of the objectives of this study.

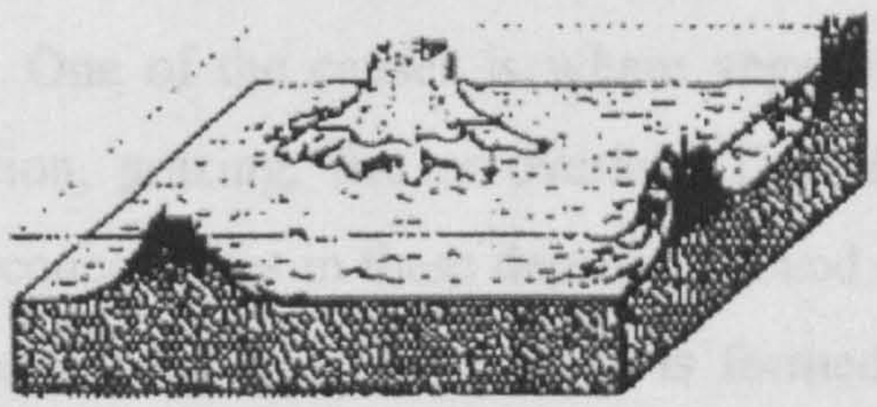

(a) Interrill Erosion

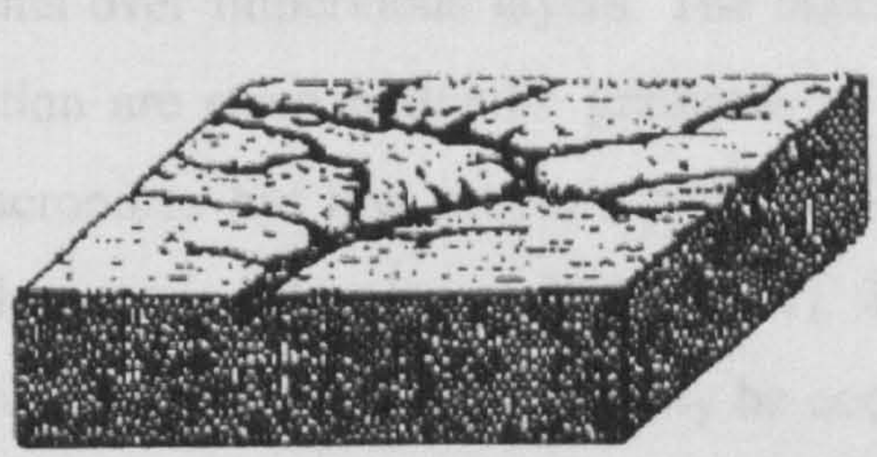

(b) Rill Erosion

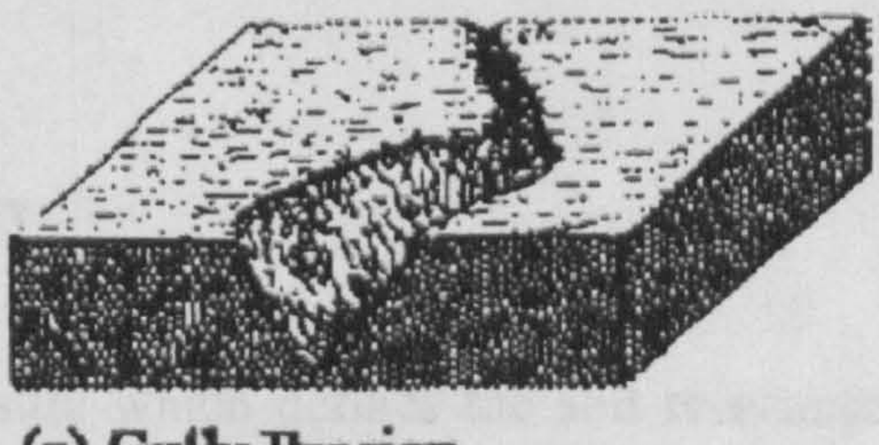

(c) Gully Erosion

Figure 2.3. Comparison between the characteristics of rill and gully erosion, compared to the interrill erosion (after Brady, 1990)

2.2.4 Gully Erosion

A gully is defined as a permanent steep-sided eroding watercourse which is subject to intermittent flash floods (Hudson, 1981). Compared with stable river channels, gullies are characterised by a headcut and various steps or knick-points along their course. Gullies also have relatively greater depth and smaller width than stable channels, carry larger sediment loads and display very erratic behaviour so that the relationship between sediment discharge and runoff are frequently poor (Heede, 1975).

De Jong (1994) shows that there are at least four different reasons and causes for the initiation of gullies. One of the causes is where vegetation cover is weakened by means of deforestation, grazing, fire or overland flow forming depressions. As a result of that, water concentrates in these depressions and enlarges them until several depressions coalesce and an incipient channel is formed. Second, gullies are also initiated by collapsing subsurface pipes and tunnels, or headward erosion in weakly consolidated sediments over impervious layers. The essential requirements for this type of gully formation are steep hydraulic gradients in a soil of high infiltration capacity through macropores but low intrinsic permeability so that water does not move readily into the matrix (Bryan and Yair, 1982). Third, gullies are initiated where landslides leave deep-sided scars which may be occupied by running water in subsequent storms. Forth, some of the rills may develop to form a gully (Figure 2.3). Like the case of rill erosion, gully erosion will not be dealt with in this study for the same reasons.

2.2.5 Soil Erodibility

Erodibility is a measure which defines the soil resistance to both detachment and transport. Erodibility varies with soil texture, aggregate stability, shear strength, infiltration capacity and organic matter content (Morgan, 1995). The way soil texture affects the soil erodibility is not straightforward and this is due to the fact that both large and very fine particles of the soil are more resistant to erosion, whereas the

least resistant particles to erosion are silts and fine sands. Some authors, such as Evans (1980), use the clay content in the soil as an indicator of the soil erodibility. This is due to the fact that clay, when combined with organic matter content, forms large aggregates which play an important role in soil stability against erosion.

The second factor affecting the soil erodibility is aggregate stability. Aggregate stability depends on a wide range of factors such as organic matter, clay content, the presence of iron and aluminium oxides, and the moisture condition of the aggregate (Farres, 1980; Marshall *et al.*, 1996). Wetting of the soil weakens the aggregates because it lowers their cohesiveness, soften the cements and causes swelling as the water is adsorbed on the clay particles (Morgan, 1995). The wetting of initially dry soils results in greater aggregate breakdown than if the soil is already moist because in latter case, less air becomes trapped in the soil (Truman *et al.*, 1990). Although most clays lose strength when first wetted because the free water releases the bonds between the particles, some clays, under moist but unsaturated conditions, regain strength over time. This process occurs because the hydration of clay minerals and the adsorption of free water promote hydrogen bonding (Grissinger and Asmussen, 1963).

The shear strength of the soil is another factor that affects the soil erodibility. Shear strength is regarded as a measure of soil cohesiveness and resistance to shearing forces, flowing water and mechanical pressure. The cohesiveness, in turn, depends on soil texture, soil moisture, and organic matter content. The shear strength is derived from the frictional resistance of particles when forces are exerted on them to slide over one another or to move out of their position. In this case forces are absorbed by solid-to-solid contact among the particles, by cohesive forces related to chemical bonding of the clay minerals, and by surface tension forces within the unsaturated soils (Morgan, 1995). As the soil moisture gradually increases, the shear strength of the soil decreases until the soil totally loses the shear strength and starts to flow under its own weight, and this is called the soil liquid limit.

The other factor affecting the soil erodibility is the infiltration capacity of the soil. The infiltration capacity, which is defined as the maximum rate at which soil can absorb water, is influenced by pore size, pore stability and the soil profile (De Jong, 1994). Soils with stable aggregates maintain their pore spaces better whilst soils with swelling clays or minerals that are unstable in water tend to have low infiltration capacities. The infiltration capacity of a soil plays a positive role in determining how erosive a soil is. The greater the infiltration capacity of the soil is, the less the erodibility of the soil will be due to the decrease in the overland-flow generation.

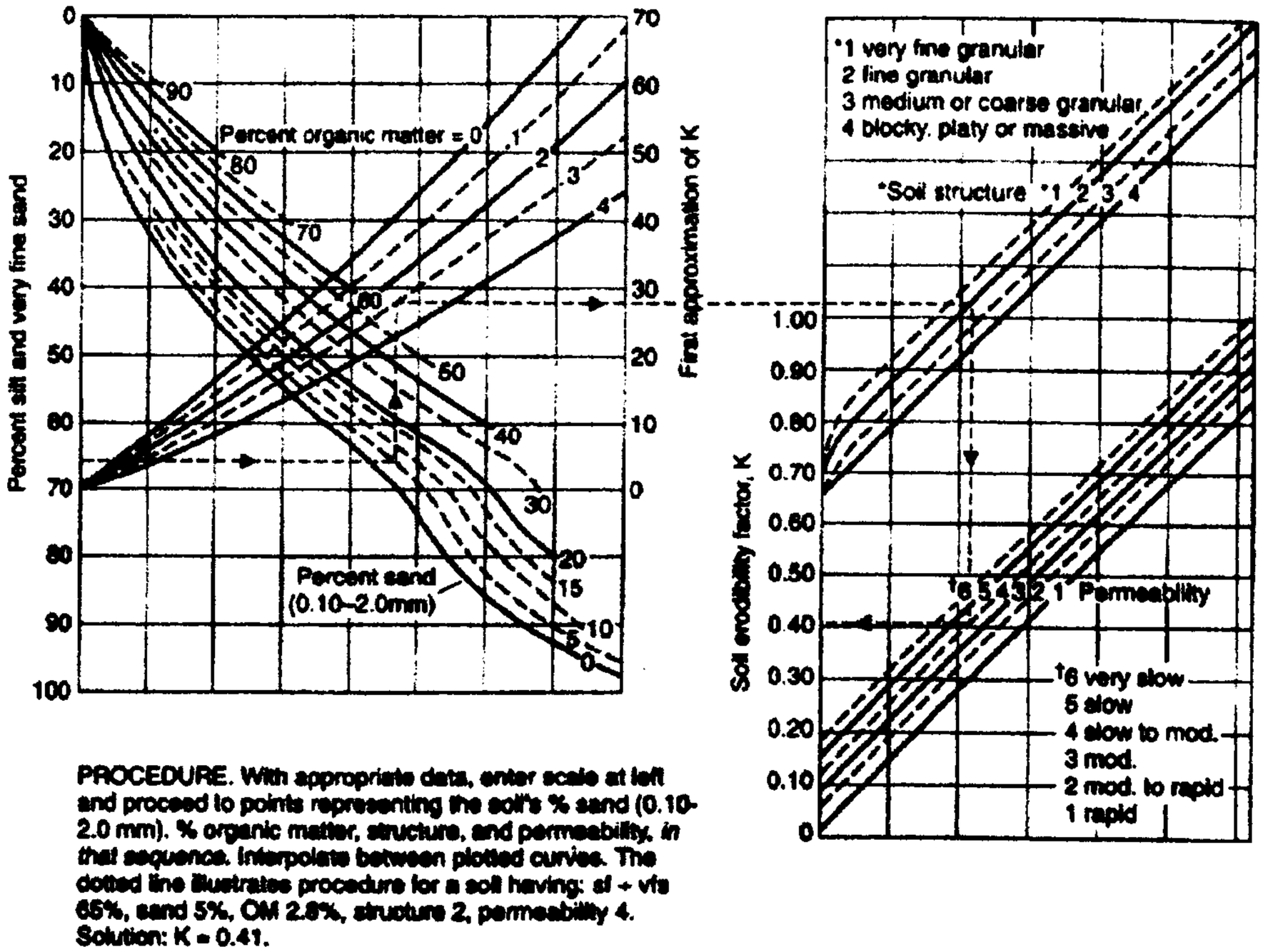

Figure 2.4. Nomograph showing how to calculate the soil erodibility (after Wischmeier, Johnson and Cross, 1971).

As has been explained above, the organic content of the soil is considered to be an important factor affecting the soil erodibility because of its influence on aggregate stability. The organic content of a soil gives a strong indication about the erodibility of that soil. Voroney *et al.* (1981) suggest that soil erodibility decreases linearly with increasing organic content over the range of 0 to 10 per cent whereas Ekwue (1990)

found that soil detachment by raindrop impact decreased exponentially with increasing organic content over a 0 to 12 per cent range.

Due to the significance of the soil erodibility in understanding and modelling the soil erosion, extensive work by different researchers has been carried out in order to define an index of the soil erodibility (Evans, 1980; Wischmeier and Smith, 1978; Carson and Kirkby, 1972). Bryan (1968) found that the aggregate stability is the most efficient index of erodibility. He uses the proportion of water-stable non-primary aggregate larger than 0.5 mm contained in the soil as an indicator of erodibility. However, the most widely used soil erodibility index is the K-factor which was developed by Wischmeier *et al.* (1971). In order to simplify the calculation of the K-factor, Wischmeier provided a nomograph where K can be calculated in a graphical way based on grain size distribution, organic matter content, structure and permeability of the soil (Figure 2.4).

2.2.6 Vegetation Cover

Vegetation acts as a protective layer between the atmosphere and the soil. The above-ground components, such as leaves and stems, absorb some of the energy of falling raindrops, running water and wind, so that less is directed at the soil, whilst the below-ground components, comprising the root system, contribute to the mechanical strength of the soil (Morgan, 1995). In general, the effects of vegetative cover on soil erosion comprise four main processes (De Jong, 1994). First, the interception process which accounts for the change in volume and energy of the rainfall reaching the ground surface as a result of interception of rainfall by plant cover. Its main effect is a decrease in the amount of the soil detached.

The second process is the evapotranspiration where the plant cover extracts some of the soil moisture and releases it to the atmosphere resulting in soils with drier conditions. This process can decrease the runoff, and consequently the soil erosion, after a rainstorm because the soil is drier and has higher storage capacity. Third, as a result of the plant roots penetrating the soil layers, the soil pores around these roots

become larger allowing higher infiltration capacity which leads to a reduction of the generation of runoff. Fourth, the vegetation cover plays an important role in decreasing the velocity and kinetic energy of the overland flow due to the friction between the flowsheet and the plant cover which, in turn, decreases the ability of the overland flow to transport the soil particles.

Vegetation growth in arid and semi-arid areas is moisture-affected and is also influenced by soil type, nutrient availability and the extent of grazing. Moisture availability is a function of rainfall and evaporation and it varies spatially due to redistribution by runoff and runon, both of which are function of topography (Stafford Smith and Pickup, 1993). Soil type and nutrient availability also vary spatially, and it is common to find that depositional areas provide an environment more conducive to plant growth than eroding or stable areas in the landscape (Pickup and Chewings, 1996).

Figure 2.5. A part of the study area where the natural vegetation cover (Matorral) is removed in order to plant almond and olive trees. The surface soil is left prone to soil erosion as evident from the rills in the picture.

The vegetation cover in arid and semi-arid regions is a major determinant of sediment availability, soil-erosion rate and runoff (Johns 1983, Eldridge and Rothon, 1992). The close link between plant cover and soil moisture and erosion status makes it logical to use vegetation cover as an indicator of hydrologic and erosion processes. Vegetation cover is an important factor in determining the resistance of soil to erosion processes where when the canopy increases, the erosion risk decreases. As a result of this correlation between soil erosion and vegetation, most of the up-to-date research on soil erosion and land degradation has been considering the status of vegetation cover as the main factor to infer the degree of the soil erosion. The removal of the vegetation cover from hillslopes, such as by tilling and ploughing, enables a higher rate of detachment of soil particles by raindrops and their transportation through overland flow. However, the degree of soil loss under such conditions depends to a large extent on the slope gradient and length of terrain, soil texture, structure, etc. (Figure 2.5).

Some of the researchers studying the process of soil erosion and conservation have investigated the effect of vegetation cover on the soil loss, in an attempt to find a mathematical formula to relate the second to the first. For example, Elwell (1981) shows that the soil loss, as a result of erosion, decreases exponentially when the percentage of the canopy cover increases. This increase in the vegetation cover results in more rainfall energy being absorbed before it reaches the soil layer, preventing soil loss significantly. Foster (1982) attributes the exponential form of relationship for cover in proximity to the ground to the ponding of water behind the plant elements which reduces the effectiveness of raindrop impact. He argues that since most soil surfaces have depressions and these are filled totally or partially by water during rainstorms, especially where they lie beneath leaf drips, an exponential relationship could be expected to apply to the canopy effect too (Morgan 1995). Hudson (1957) demonstrated the importance of the vegetation canopy to the soil-erosion process by comparing the soil loss and runoff from a tilled, weed-free treatment to that from a plot covered with mosquito-gauze. The mosquito-gauze was placed at 150 mm above the soil surface and it simulated a full vegetation canopy by destroying raindrop energy while allowing majority of the rainfall to reach the soil

surface (Elwell and Stocking, 1976). The result shows the substantial influence of vegetation canopy on runoff generation and soil erosion (figure 2.6).

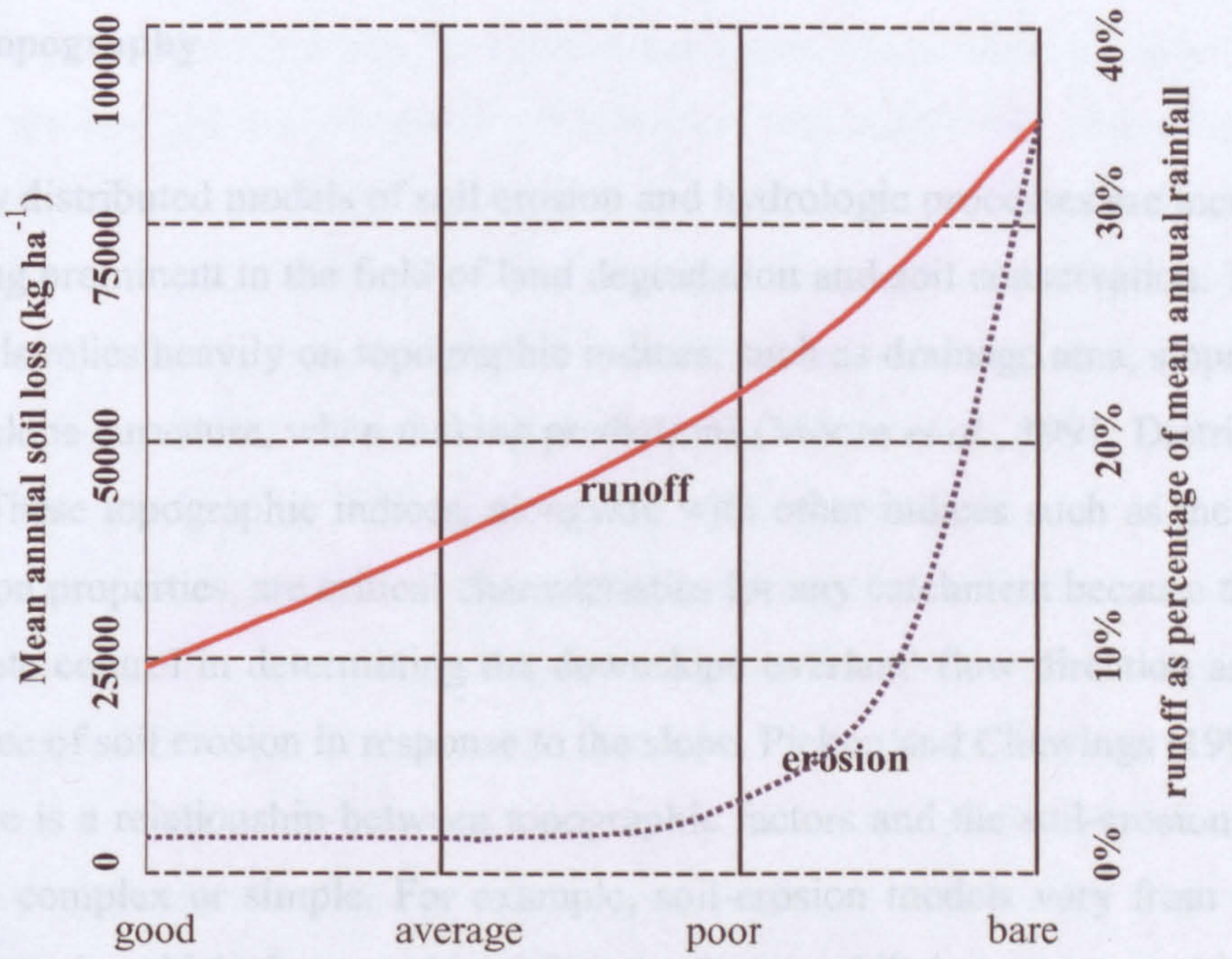

Figure 2.6. The effect of vegetation cover on runoff and soil loss in arable land and for different vegetation cover values where average and poor vegetation cover ratings represent 65% and 30% respectively (from Elwell 1976).

In an attempt to assess the effects of vegetation cover on soil erosion and to model the relationship between them, several researchers have developed various models that predict the soil loss under various vegetation cover conditions. These models vary from simple and easy to use to more complex models. For example, Thornes (1990) developed a model based on simple equations. This model is spatially distributed and can be used in a wide range of different cases of vegetation growth and grazing.

Satellite-based remote sensing and aerial photography are the most widespread and practical ways of monitoring vegetation cover at the spatial scale and temporal frequency necessary to spatially model the soil erosion in arid and semi-arid rangelands. In the recent years, the advances made in developing high spectral and spatial resolution remote sensing devices have considerably improved and enabled

certain techniques that use remote sensing technology to map the vegetation cover which is critical for soil-erosion modelling.

2.2.7 Topography

Spatially distributed models of soil erosion and hydrologic processes are increasingly becoming prominent in the field of land degradation and soil conservation. This type of models relies heavily on topographic indices, such as drainage area, slope, aspect, and hillslope curvature, when making predictions (Moore *et al.*, 1991; Dietrich *et al.*, 1993). These topographic indices, alongside with other indices such as the soil and vegetation properties, are critical characteristics for any catchment because they have immediate control in determining the downslope overland-flow direction as well as the degree of soil erosion in response to the slope. Pickup and Chewings (1996) show that there is a relationship between topographic factors and the soil-erosion whether they are complex or simple. For example, soil-erosion models vary from complex procedures, in which the equations of water flow on hillslopes are combined with sediment-transport equations, to much simpler procedures based on topographic characteristics and the continuity equation for sediment transport.

Soil-erosion rate is strongly correlated with the slope in a way that steeper and longer slopes generate overland flow with greater power, due to the gravity factor. In addition, the raindrops falling on the slopes, which strike the bare soil surface, splash the soil particles downslope aiding the increase of the erosion rate. Steeper slopes cause more soil particles to be transported downslope. The general relationship between the soil erosion and slope index can be expressed in the following general equation:

$$E \alpha \tan^{m}\theta \, L^{n} \qquad 2.1$$

Where: E is the soil erosion, θ is the slope angle, L is the slope length, and (m) & (n) are coefficients.

The equation 2.1 demonstrates the exponential nature of the relationship between the slope angle and the soil-erosion rate. However, the coefficient (m) changes, and consequently the slope effect on the soil-erosion rate changes, according to other factors. For example, Gabriels *et al.* (1975) show that the value of (m) is positively correlated with the grain size of the material. The coefficient (m) can be taken to be 0.6 for particles of 0.05 mm size and increases to 1.7 for particles of 1.00 mm size. Another factor affecting the value of (m) is the slope steepness. The study by Horvath and Erodi (1962) explains the negative correlation between (m) and the slope steepness. Their study shows that m = 1.6 for slopes between 0 and 2.5° , m = 0.7 for slopes between 3 and 6.5° , and m = 0.4 for slopes over 6.5° . One explanation to the fact that (m) decreases, and consequently soil erosion decreases, when slope increases is that the soil layer is gradually replaced by rock surfaces. These rocky surfaces decreases soil-erosion rate by decreasing the amount of soil supply to the overland flow. Zingg (1940) found, from a study on experimental stations of the United States Soil Conservation Services, that the coefficient values can be expressed as (m) = 1.4 and (n) = 0.6.

Another factor affecting the (m) value is the slope shape. D'Souza and Morgan (1976) examined the soil loss from 3m long plots on slopes of average steepness between 2 and 8° under simulated rainfall. They obtained values of (m) = 0.5 for convex slopes, 0.4 for straight slopes and 0.14 for concave slopes (Morgan 1995).

The second topographic factor affecting the soil-erosion rate in equation 2.1 is the slope length L. As it has been demonstrated above, Zingg (1940) expressed the exponential nature of the relationship between soil-erosion rate and slope length with the constant value of (n) = 0.6 (see equation 2.1). However, (n) deviates dramatically from the value 0.6 according to the steepness and the length of the slope. For example, Wischmeier and Smith (1978) argue that (n) is negatively correlated with the slope steepness and they suggest values of n = 0.4 for slopes of 3°, 0.3 for slopes

of 2°, 0.2 for slopes of 1°, and 0.1 for slopes of less than 1°. Another factor influencing the value of (n) is the slope length. Kirkby (1971) suggests different values for (n) in the equation 2.1 according to the distance from the summit (or in other words, according to the slope length). He suggests a value for n = 0 for soil creep and soil splash (i.e. near the summit), a range for n between 0.3-0.7 for overland flow (half way down the slope), and a range for n between 1.0-2.0 for rills.

2.2.8 Soil Compaction

The volume of a typical cultivated silt loam soil is 50 percent soil particles, 30 percent water and 20 percent air. Air and water content in soil are constantly changing. An applied load that reduces the total volume of soil, air and water causes compaction. Because the soil particles and water are relatively incompressible, compaction causes reorientation of soil particles and reduces the volume of air. This slows down water and air movement and reduces the water-holding capacity of the soil.

Soil compaction is caused by the pressure exerted on the soil by raindrop impact, animal hooves, repetitive large changes in the water state of the soil, and from the pressure exerted on the soil by tractors and other agricultural machinery (USDA, 1993). Compaction caused solely by repetitive large changes in the water state of the soil is called "water compaction", while compaction caused by the pressure of machines and animals, as well as the impact of raindrops, is called "mechanical compaction" by the United States Department of Agriculture Soil Conservation Service (USDA, 1993).

Compacted layers of soil constrict the infiltration of water into the soil, and help accelerate overland-flow generation and interrill erosion of the soil during periods of rain on sloping land (Hillel, 1982; Dregne, 1983). In addition, reduced infiltration will cause water ponding for longer periods following rainfall on a field with surface depressions. Once depressions are full, there will be more surface runoff because of the slower infiltration rate.

The lack of water penetration into the soil will make the soil effectively more arid than would be expected due to climate alone (Dregne, 1983). Compacted surface layers may prevent seedlings from penetrating the soil surface, while deeper compacted layers restrict root growth into deeper layers of the soil (Hillel, 1982; Dregne, 1983). In research about the causes of land degradation and the decline of agricultural yields in Southern Africa, Byers (1997) found that about 2 per cent of the soils are damaged by physical degradation caused by compaction of topsoils. This compaction has led to the sealing and crusting of the topsoil and a reduction of available soil water.

2.3 REMOTE SENSING SYSTEMS AND GIS FOR MONITORING AND MODELLING SOIL EROSION

The awareness of the soil-erosion phenomenon goes back to the beginning of the 20th century. Since then a substantial amount of research has been carried out in order to understand and develop strategies and solutions to the soil-erosion problem. Soil erosion was approached, in two different ways, by two groups of scientists: engineers and geomorphologists. In the first approach the soil erosion was considered to be an engineering problem and a technical solution has to be found to this problem. However, the geomorphologists argue that soil-conservation strategies must find a solution to the erosion problem through an understanding of the actual processes of the soil erosion rather than looking at it in an engineering perspective (Morgan 1995).

The evolution of such strategies must accord with local economic, social, demographic and political circumstances. In addition, it is clear that soil erosion and land degradation is a socially constructed problem because it mainly results from changes in land use which is a socially controlled activity. This means that the social dimension of the solution to the soil-erosion problem cannot be ignored even though the definition of the extent, severity and dynamics of the problem can only be undertaken by natural science (Graetz 1994).

Since the beginning of the 1980s the awareness of soil erosion has grown significantly and this phenomenon has become an important issue because of its consequences on the environment and human life. As a result, many countries have taken various measures to control the soil-erosion problem and developed strategies and policies to ensure the sustainable use of their lands. The aims of any policy dealing with sustainable use of soils are to maintain soil quality, properties, processes and diversity. However, soil erosion continues to degrade the global land resource base with approximately 30 per cent of the present cultivated area having been substantially affected (Morgan 1995). There are many interactive factors such as economic, social, environmental, demographic and political factors which contribute to the phenomenon of soil erosion, for example, increasing population with decreasing resources as can be seen in figure 2.1.

In order to seek solutions for the soil-erosion problem and prevent land degradation, soil-erosion processes should be analysed monitored, and modelled. One of the biggest problems with modelling is how to obtain necessary information at the relevant temporal and spatial scale. Data requirements of soil-erosion models are large and include vegetation cover, topographical information, meteorological data, and soil properties which can be measured directly in the field or can be derived from other kinds of data such as data supplied by remote sensing systems.

Field surveys are labour intensive and expensive and give only information for one geographical location where the measurement has taken place. In addition, the processes of land degradation and soil erosion can be difficult to assess from observations on the ground because such observations may quickly show that soil is being eroded from a certain field, however, this single observation does not indicate the state of erosion and sediment deposition a few kilometres away. For larger areas, field surveys are often not feasible and in these cases remote sensing technology may prove a useful alternative for collecting data.

In order to balance the advantages and disadvantages of remote sensing as a data collection system it should be compared to other traditional systems such as field surveys. De Jong (1994) designed a list of criteria for a suitable data-collection system to monitor and to model soil-erosion processes at a landscape scale:

1. The data-collection system should cover large areas;
2. Data should be collected at regular time intervals;
3. It should have sufficient spatial and temporal resolution;
4. It should provide data on the required attribute accurately;
5. It should provide data in a format suitable for further processing;
6. It should be cost effective.

Apart from the fact that the field survey is a better way to collect accurate information on the variables controlling the soil erosion, the field surveys do not fulfil the other criteria for a suitable data-collection system. It is the remote sensing technology that is capable of collecting spatially continuous data for large areas and on regular repetitive time intervals. This may provide a sound database for change detection, status, extent, and spatial distribution of the soil erosion. Warren and Agnew (1988) stated that one of the main problems in our understanding of the soil erosion was "the ignorance in establishing trends and speeds, because trends and speeds require sequential surveys". Remotely sensed data can be a powerful tool to acquire such information.

Remote sensing from satellites offers a potential means to survey and collect appropriate data about all erosion-threatened areas around the globe. However, remote sensing cannot entirely replace the use of ground observation as was widely believed in the 1970s and early 1980s (Mainguet, 1994). However, satellite remote sensing can provide a powerful addition to ground observations by extending in time and space field observations made at a single point in a given region. Satellite remote sensing thus can monitor much larger areas than ground surveys and aid in targeting key ground observations. In this way, ground observations anchor satellite observations, with the satellite remote sensing effectively multiplying the value of

the data acquired on the ground and identifying the specific locations where additional and repeat ground surveys are most needed so that these ground surveys can be most cost and time-effective.

Mainguet (1994) cites the importance of "remote sensing supported by verifications on the ground for a better perception of the extent and processes of soil erosion". The information stored in the remote sensing databases can be manipulated, analysed and classified using remote sensing techniques in order to extract the relevant land features and physical properties of the landscape under study. Examples of this are extracting the land use by applying the supervised classification, applying soft classification, such as mixture modelling, to extract thematic maps of the vegetation cover and so on. In addition, one of the most powerful characteristics of the remote sensing systems is that they provide important information outside the visible range of the spectrum (e.g., infra-red, thermal channels). This information can be important for monitoring rocks, water, soil and vegetation (the calculation of vegetation indices is an example of this). However, in this study we have been restricted to the use of the visible range of the spectrum due to the nature of the aerial photographs.

Alongside the advantages of the remote sensing technology as a data collection system for soil-erosion modelling, it has some weaknesses and limitations. Murphy and Wadge (1994) argue that data collection of the surface soils and features using remote sensing techniques are limited by three main factors. First, a great proportion of the Earth's surface is covered by vegetation, the spectral signature of the material underlying the vegetation, such as soils and rocks, is obscured and cannot reach the sensor. Secondly, most rocks and soils are aggregates of a variety of minerals, some of these minerals have distinct spectral characteristics, but others are not distinct and, thus, cannot be readily mapped by remote sensing. The third factor is the atmospheric conditions which weaken the spectral signature of the surface materials reaching the sensor.

Modelling the soil-erosion phenomenon is restricted by problems of parameterising models over large areas. This is due to the large size of data, such as the

meteorological, vegetation and soil data, required by soil-erosion models. Remote sensing technology provides powerful solutions to these problems as it allows distributed models to be applied over wide areas at a number of different scales (Drake *et al.*, 1995). Remote sensing approaches for monitoring environmental changes have the ability to provide a standardised characterisation of surface conditions (e.g. soil map, land use and so on) and vegetation cover over time. Figure 2.7 shows the process of standardising thematic indices from the remotely sensed data with the aid of ancillary data.

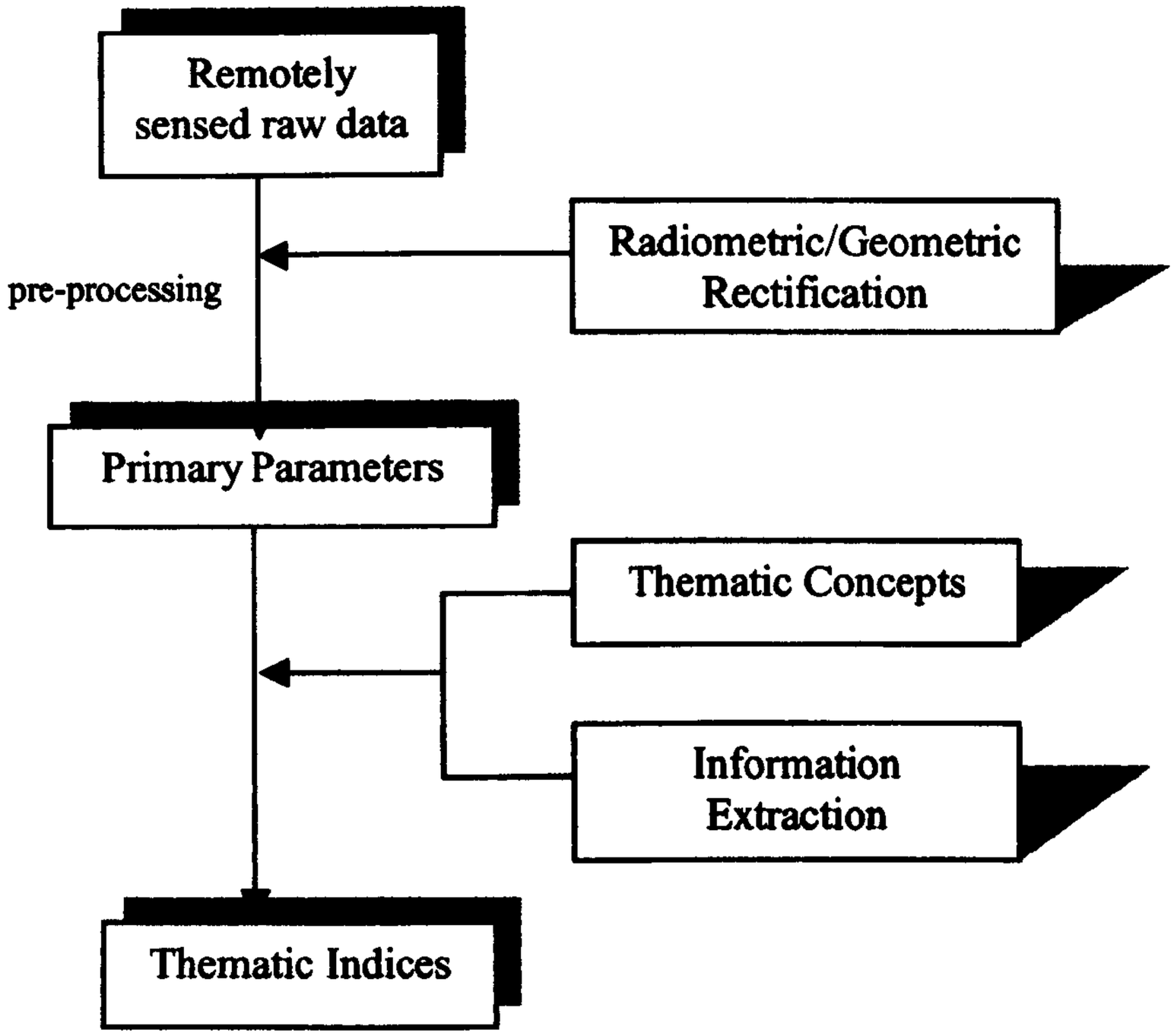

Figure 2.7. The conversion of remote sensing raw data into standardised thematic information layers.

More research in the field of soil erosion and land degradation is being based on earth observation satellite data and on the spectral reflectance of known surface materials and canopy characteristics. Satellite remote sensing has become increasingly popular recently because it can provide inexpensive large area mapping (Jurgens and Fander 1993). As a result, purely empirical methods of image processing are increasingly being replaced by approaches which are more closely

related to the physics of the remotely sensed signal (e.g., the principles of mixture modelling which will be explained in the later chapters) (Hill 1994).

These new approaches have potential to produce a systematic shift to remote sensing techniques as a data collection system. The remote sensing approaches to soil erosion concentrate on the fact that an improved understanding of soil-erosion processes requires meaningful data over space and time which is difficult to collect using more traditional methods such as field surveys.

2.3.1 Remote Sensing Platforms

There are different remote sensing data-collection systems available for Earth observation studies such as satellite-based and aircraft-based systems. The spatial, as well as the temporal, resolution of the data acquired using these remote sensing systems ranges from very coarse (such as the case of AVHRR sensor) to medium (Landsat MSS & TM sensors) to very high resolution (e.g. IKONOS, AVIRIS, ATM and CASI). The process of selecting the appropriate data depends on the application intended by the study. Although the number of remote sensors providing Earth observation data is large, the following describes well-known sensors which are commonly used for land-degradation and environmental studies.

2.3.1.1 AVHRR

The advanced very high resolution radiometer (AVHRR), launched in 1978 as TIROS-N (later, NOAA-6), provides regional-scale coverage (2800 to 4000 km swath width) at a 1 and 4 km spatial resolution. AVHRR sensor provides four or five spectral bands (depending on sensor version) covering the ranges 0.55-0.68 μm, 0.725-1.1 μm, 3.55-3.93 μm, 10.3-11.3 μm, and 11.5-12.5 μm (Kruse, 1999). The principal use of AVHRR sensor is for measuring cloud cover and vegetation indices, however, the sensor can provide valuable data for basic surface geologic, hydrologic, oceanographic and meteorological information over regional scales. Despite the fact that data provided by AVHRR sensor are coarse, they have a wide range of

applications in soil-erosion studies because the data availability over a long time makes it possible to carry out time series analysis. Lambin (1999), for example, used the AVHRR data to monitor and model the soil erosion in tropical regions, and Del Valle *et al.*, (1998) used these data to determine the extents and distributions of land degradation in semi-arid areas.

Although AVHRR sensors offer good temporal resolution for land degradation and soil-erosion studies, their spatial resolution, which is very coarse of 1 and 4 km, causes problems in this type of studies. In most cases, the vegetation cover is heterogeneous and the 1 km AVHRR pixel contains several types of land use which are radiometrically different and the pixel is mixed. Consequently, the spectral reflectance measured by the sensor is in fact an average value and does not represent a value for each vegetation class present in the pixel (Cherchali *et al.*, 2000).

2.3.1.2 Landsat

The Landsat satellite was originally launched in 1972 with two sensor systems, the three-channel Return Beam Vidicon (RBV) and the four-channel multispectral scanner (MSS) (Lillesand and Kiefer, 2000). The RBV bands were designated as bands 1, 2, and 3, while the MSS bands were designated as bands 4, 5, 6, and 7. When the Landsat 4 was launched in 1982, a new Thematic Mapper (TM) sensor was included on board, along with the MSS sensor where the MSS bands were re-designated from 4-7 to 1-4. The Thematic Mapper includes seven spectral bands covering the spectrum from the visible to the thermal infrared with wavelengths of 0.45-0.52 μm for band 1, 0.52-0.60 μm for band 2, 0.63-0.69 μm for band 3, 0.76-0.90 μm for band 4, 1.55-1.75 μm for band 5, 10.40-12.50 μm for band 6, and 2.08-2.35 μm for band 7 (Kruse, 1999). The IFOV of the TM sensor is 28.5 m for bands 1, 2, 3, 4, 5, & 7, and 120 m for band 6 and the size of the area captured by a scene is 185 km ×185 km.

There is a wide range of environmental applications for the data collected by the Thematic Mapper (TM), especially in land degradation and soil-erosion modelling.

The visible and near infrared information provided by the TM sensor is very useful when studying vegetation patterns and changes at different scales. An example of the applicability of TM imagery in soil erosion is the study by Ringrose *et al.*, (1997) which implemented the data collected by TM sensor to determine the extent and the possible causes of the soil-erosion problem in the Northern areas of Botswana. However, some problems arise when the TM data are implemented to map vegetation cover and land use/land cover in semi-arid areas. These problems are because the pixel size in the TM images is 900 m^2 and vegetation cover in semi-arid areas is mostly heterogeneous, which makes it difficult to derive vegetation cover by applying a hard classifier or by extracting endmembers for mixture modelling. In addition, the process of mapping land use and land cover from TM images of semi-arid areas, by using hard classification, may also be problematic because in such areas the land-use/land-cover types change sharply over distances smaller than the TM pixel size.

Since the launch of Landsat-1 in July 1972 which was followed by Landsat series 2, -3, -4 and –5; SPOT-1, 2 and 3, space borne multi-spectral data in the optical region of the electromagnetic spectrum have been extensively used in conjunction with aerial photographs and other relevant information supported by ground truth for deriving information on erosion phenomenon (Pickup and Chewings 1988). However, since spaceborne sensors have a much poorer spatial resolution than aerial photography they are unable sometimes to show ground details which are relevant to soil erosion such as the sharp land-use/land cover changes which characterise semi-arid areas.

2.3.1.3 High Spatial Resolution Remote Sensing

Until the 1950s, the information necessary to model the soil erosion has been collected by conventional surveys. During the 1960s and early 1970s, aerial photographs were used to derive information on land degraded by various processes including soil erosion (Iyer *et al.*, 1975).

Aerial photography can be used to acquire high spatial resolution images from relatively low flying altitudes and has many advantages over other remote sensing systems. An example of such advantages is that it is easier to decide on the date when the flight is taking place, as well as controlling the time of the day when conditions are ideal for image acquisition (e.g. midday when the shade cast by vegetation and topographic relief is minimal). Garg and Harrison (1992), for example, used a series of aerial photographs, in conjunction with GIS techniques, for monitoring the land-use change in the south-east Spain over a period of 30 years, as well as for assessing the risk of soil erosion in that area.

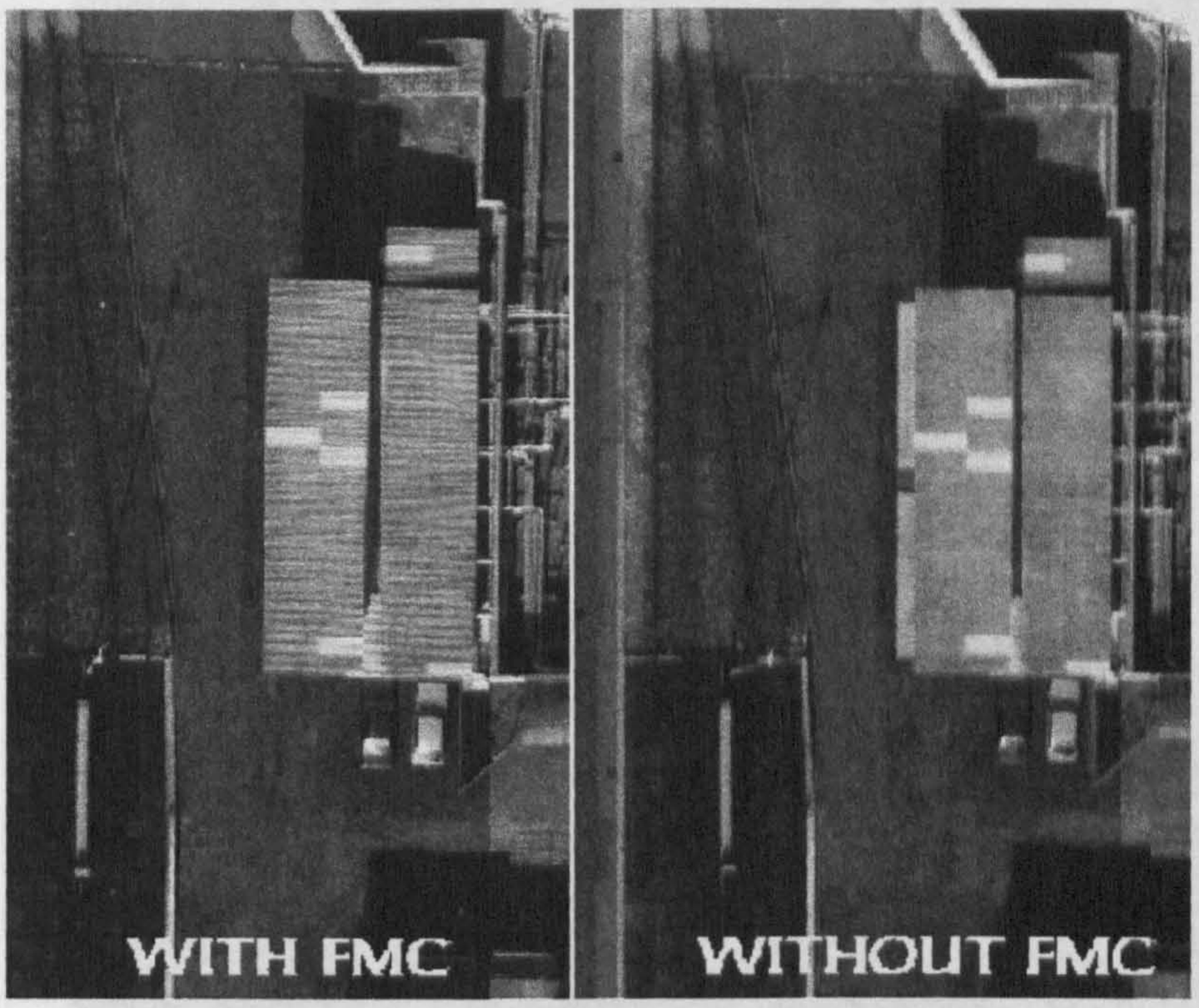

Figure 2.8. The effect of the Forward Movement Compensation on the clarity of the aerial photography (http://www.keystoneaerialsurveys.com)

However, there is problem associated with the acquisition of aerial photography. Since the aerial photographs are taken at a relatively low altitude with high speed, the airplane forward motion may lead to distortions and reduction in the resolving power of the resulting aerial photographs. To overcome this problem aerial cameras are fitted with a Forward Motion Compensation (FMC) mechanism. On account of the forward motion of the aircraft, the area terrain projected on the image plane moves in the flight direction during the exposure time. Figure 2.8 demonstrates the difference of the quality of aerial photographs with and without the FMC.

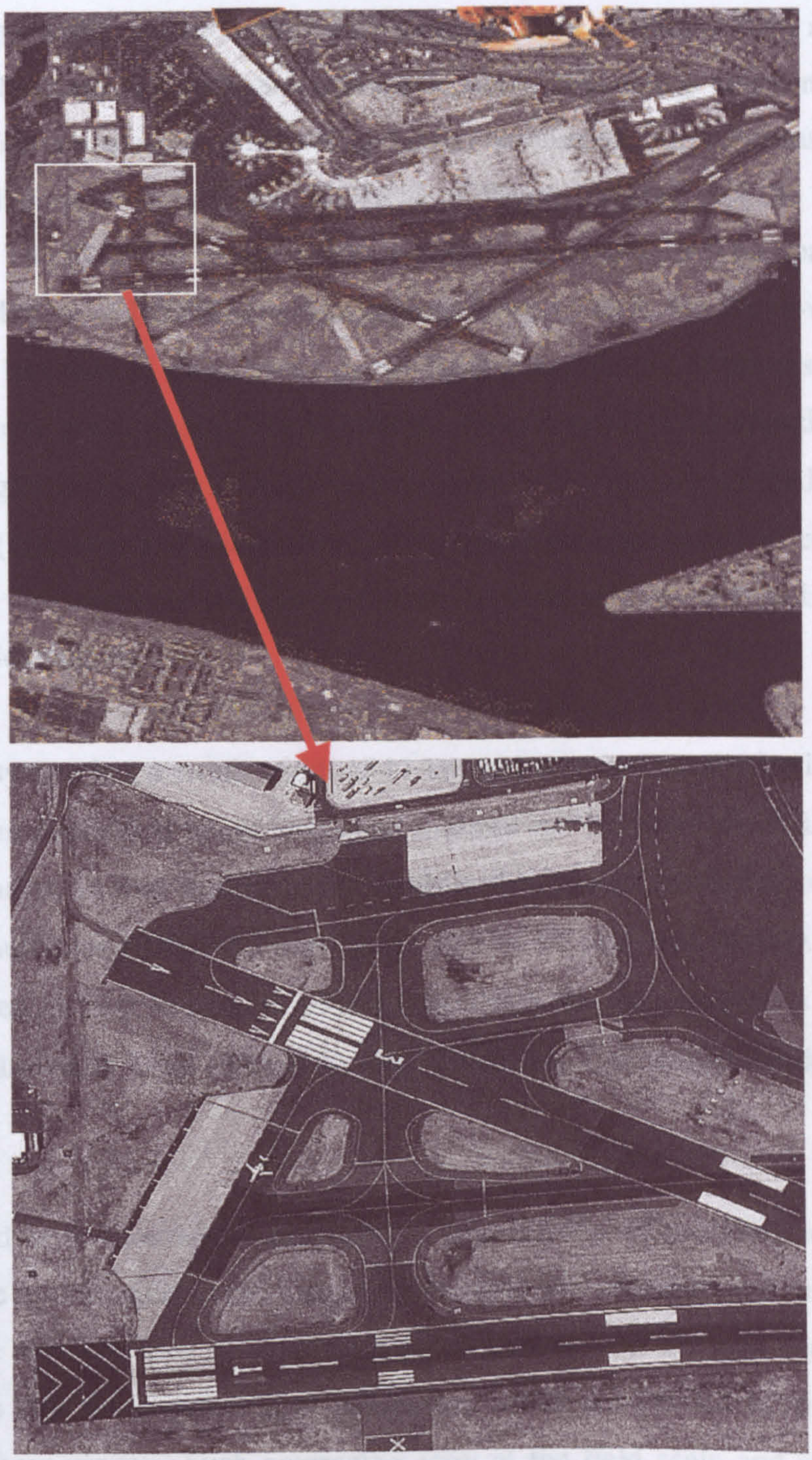

Figure 2.9. The first panchromatic image taken by the IKONOS satellite with 1 metre spatial resolution, showing fine details of land cover, Washington D.C. The bottom image is a zoomed-in sub-area of the top image. (the image is downloaded from Spaceimaging, IKONOS satellite homepage: http://www.spaceimaging.com/ikonos/firstimage.htm).

The late 1990s witnessed the launch of very high spatial resolution remote sensing satellites and within the next few years more of these satellite will be available for commercial use and for environmental applications. This new generation of satellites sensors holds considerable promises to further the use of remotely sensed data. An example of these sensors is the IKONOS of Space Imaging and the PAN/MS of Quickbird. The IKONOS sensor was launched in September 1999 by Space Imaging. The ground track of IKONOS system repeats every 11 days, but the re-visit time for imaging is less than 11 days, based on the latitude and the tilt of the system selected to acquire any given image. The IKONOS system includes the capacity to collect data at angles of up to 45° from vertical both in the cross-track and along-track directions (Lillesand and Kiefer 2000). This offers the opportunity to cover a given area more frequently as well as collection of both side-by-side and fore-and-aft stereoscopic imagery.

IKONOS system has a swath width of 11 km and a typical scene size is 11×11 km, however, user-specified image strips and mosaics can be also collected. The system collects images in four multispectral bands with a spatial resolution of 4 m. these bands include blue (0.45-0.52 μm), green (0.52-0.60 μm), red (0.63-0.69 μm), and near infrared (0.76-0.90 μm). In addition, IKONOS has the capabilities to collect an extra panchromatic band (0.45-0.90 μm) which has 1 m spatial resolution (figure 2.9).

In the field of environmental modelling a large variety of processes are addressed such as the hydrological cycle, evapotranspiration, soil moisture and runoff. Despite substantial developments of environmental modelling over the past years, the main problem is still the acquisition of parameters which are needed to implement and calibrate these models. Such parameters vary at the field scale and undergo rapid changes with time. In principle, remote sensing is the ideal method to acquire spatial distribution as well as temporal development of parameters. With the availability of hyperspectral sensors, such as the AVIRIS (Airborne Visible/Infrared Imaging Spectrometer) and ATM (Airborne Thematic Mapper), there is an opportunity to

map a large number of parameters, such as vegetation cover and soil types, more accurately. AVIRIS, for example, is an advanced imaging system that records reflected light in 224 visible and near-infrared wavelengths from a NASA (National Aeronautics and Space Administration) high-altitude aircraft. This high-spectral resolution allows detection of subtle spectral features that are diagnostic of specific minerals and plant characteristics.

2.3.1.4 Selecting a Remote Sensing Data Collection System

Since the aim of this study is to investigate the potential of high spatial resolution remote sensing for soil-erosion modelling at the field scale, the coarse and medium resolution remote sensing system are excluded because of their limitations to map vegetation and soils in a semiarid environment characterised by heterogeneity. This heterogeneity results in pixels that are mixture of more than one type of surface cover. Although the high spectral resolution sensors such as the AVIRIS and CASI and the high spatial resolution sensors such as IKONOS are more suitable than aerial photography for the purpose of this study, data availability was a decisive factor to use the aerial photography in this research. Thus, the three aerial photographs produced from NERC air campaign will be used in this study.

2.3.2 Geographic Information Systems (GIS) for Soil-Erosion Modelling

Over the last few years there has been a remarkable progress in the development of tools for studies of slope processes, soil erosion and land degradation due to the improvement in IT and computing capabilities. These developments enhanced the capabilities to estimate overland flow in complex terrain, as well as the development of distributed, process-based simulations of soil erosion, sediment transport and deposition.

One of the difficulties encountered by conventional soil-erosion models is their inability to handle the spatial nature of erosion parameters. In the recent past, Geographical Information Systems (GIS) are increasingly being used by the soil

erosion and conservation community as sophisticated database-management systems for efficient storage, retrieval, manipulation, analysis and display of spatially referenced data (Burrough, 1990). To fulfil the need for better understanding of spatial and temporal distributions of phenomena resulting from landscape processes, empirical overland-flow and soil-erosion models based on lumped, averaged parameters are being replaced by process-based, distributed models supported by Geographic Information Systems (Maidment, 1996). A GIS provides an ideal data structure to model the distributed nature of erosion processes and its framework is particularly useful in integrating large amounts of data from different sources of information over a period of time.

Most of the recent soil erosion and land degradation studies show that the erosion can be assessed with satellite data and ancillary digital data in a geographical information system. The various input parameters into a soil-erosion model, such as land use, soil erodibility factor (K), slope, soil depth etc., can be stored in separate layers in a raster (or sometimes vector) environment to be further processed in a GIS. These layers should be first geocoded to a common reference system and co-registered to each other. For each pixel that is represented in all data layers it is possible to determine the soil-erosion rate by application of the desired soil-erosion model. Since all pixels are geocoded it is possible to guide soil-erosion prevention precisely (Jurgens and Funder, 1993). A GIS not only permits the overlay of several data files in a form defined by the user but also it aids in the analysis of large volumes of data which normally is very time consuming.

The interpretation and usability of remotely sensed data in land degradation, vegetation, and soil-erosion modelling studies can be greatly improved by liking analysis with a GIS database. Digital elevation models (DEMs), slope and aspect, for example, can readily be combined with image data sets in a GIS environment to assess topographic patterns and investigate spatial correlations of occurring overland-flow generation, sedimentation and deposition. For instance, Warner *et al.* (1989) combined AVHRR data with DEM in a GIS to assess the soil erosion and drought conditions in areas of East Africa. Smith *et al.*, (1990) developed functions between

elevation and mean vegetation cover and surface temperature, then compared the Landsat Thematic Mapper (TM)-derived estimates of vegetation density and temperature to find vegetation distribution anomalies related to soil conditions and water availability. In addition, other ancillary data in a GIS can be used to improve relationships and spatial dependency using geostatistical methods such as Kriging and Co-Kriging.

2.4 CONCLUSION

In this chapter the processes of soil erosion and the external and internal parameters influencing these processes have been explored for more accurate and realistic modelling of soil erosion. In addition, the potential of using the remotely sensed techniques as a data collection system and the Geographical Information systems (GIS) for overland-flow and soil-erosion modelling have been discussed.

Various factors influencing the processes of soil erosion have been reviewed and their magnitudes have been explored. Raindrop impact has a great effect on soil aggregates and on the detachment of soil particles prior to transportation by the overland flow. The generation of overland flow is controlled by many factors such as precipitation, evapotranspiration, soil moisture, soil type and vegetation type, which all vary spatially and temporally. The overland flow may later develop into rills at the footslopes and these rills could become deeper gullies. Erodibility measures the resistance of soil to detachment and transport and is controlled by the size of soil particles, chemical and organic content, and the aggregate stability.

The vegetation cover acts as a protective agent against soil detachment and sediment loss and it is negatively correlated with the soil-erosion rate. The slope angle is exponentially significant in increasing the soil loss in the soil-erosion equation because the steeper the slope, the higher is the kinetic energy and erosive power of the overland flow. It is also important to understand the soil compaction factor because when the soil is compacted, the infiltration capacity of soil is reduced resulting in larger overland-flow generation and sediment loss.

It has been shown in this chapter that remote sensing techniques provide unique data collection systems, when compared to the traditional methods of field surveys, for environmental modelling in general and for soil-erosion modelling specifically. This is because remotely sensed data have the ability to cover large areas and these data can be collected at regular and repetitive time intervals. In addition, these data have a sufficient temporal and spatial resolution for soil-erosion modelling and are far more cost and time effective than the traditional data collection systems.

The advancement in the technology of manufacturing remote sensors in the recent years produced a new generation of satellite sensors capable of acquiring Earth-observation data with very high spatial resolution of up to 1 to 4 metres in the panchromatic and multispectral bands. This new generation of these satellites sensors holds considerable promises to further the use of remotely sensed data in soil-erosion and land degradation studies especially in semi-arid regions as they are capable of capturing very fine details on the ground such as vegetation objects and sudden land-use changes. Aerial photography, which is a form of these high spatial resolution data, is used in this study to model the soil erosion.

The applicability and potentials of the GIS for the soil-erosion modelling have also been explored. GIS offer a solution to the traditional difficulties encountered by conventional soil-erosion models and strengthen their ability to handle the spatial nature of soil-erosion parameters. In addition, GIS facilitate the implementation of more sophisticated soil-erosion models which are built on a thorough understanding of the processes of soil erosion.

CHAPTER 3

SOIL-EROSION AND OVERLAND-FLOW MODELS

3.1 INTRODUCTION
3.2 SOIL-EROSION MODELS
3.2.1 Introduction
3.2.2 Empirical (or Black Box) Models
3.2.2.1 Universal Soil Loss Equation (USLE)
3.2.2.2 The SELEMA Model
3.2.3 Process-Based Models
3.2.3.1 ANSWERS (Areal Non-point Source Watershed Environment Response Simulation)
3.2.3.2 European Soil-Erosion Model (EUROSEM)
3.2.4 Process-Based Models With Empirical Elements
3.2.4.1 The Morgan, Morgan and Finney Method
3.2.4.2 Thornes Soil-Erosion Model
3.2.5 Selecting The Soil-Erosion Model
3.3 OVERLAND-FLOW MODELLING
3.3.1 Introduction
3.3.2 An Overview of Overland-flow Models
3.3.2.1 SCS Model
3.3.2.2 Philip Infiltration Model
3.3.2.3 Carson and Kirkby Model
3.3.3 Selecting The Overland-flow Model
3.4 CONCLUSION

3.1 INTRODUCTION

As a result of the overland flow generated by the rainfall excess, soil particles can be detached, eroded, transported and deposited through the processes of soil erosion. Although erosion, transport and deposition of the soil material are natural processes, erosion and sedimentation processes in most inhabited regions of the world are strongly affected by human activities (Summer *et al.*, 1998). Thus, it is important to model the processes of soil erosion, and their hydrological component of overland flow, for better understanding and better management of the land and natural resources.

A model is a simplified representation of reality, which describes the object or the process in a formal, structured way because the scientific knowledge is lacking to describe that process exactly. Over the last few decades, scientists have been trying to model soil erosion in order to acquire a better understanding of its natural occurrence and to develop strategies in order to combat the soil-erosion effects of the land resources. These attempts tend to break the natural processes of soil erosion down into a number of parameters which influence these processes. This helps the geomorphologists and land-conservation workers to understand the effects and the sensitivity of these parameters on the resulting soil erosion. Thus, efficient soil-conservation systems can be developed and implemented based on this understanding.

The aim of this chapter is to review, analyse, and compare some of the widely used soil-erosion models which best describe the erosional processes of detachment, transportation, and deposition of soil. One of these models will be selected based on criteria of temporal and spatial scales and data availability, as well as the model applicability for use with the remotely sensed data. This model will then be used to quantify the soil erosion in the study area of Vélez Rubio. Modelling the hydrological component of overland flow in the soil-erosion model is also discussed and its parameters are reviewed and the appropriate overland-flow model is selected. Different methodologies of modelling soil erosion and overland flow are investigated and the trend of moving from empirical towards more process-based modelling approaches is discussed.

3.2 SOIL-EROSION MODELS

3.2.1 Introduction

Over the last few decades, a wide range of soil-erosion models have been developed, with various degrees of complexity, to predict the sediment yield and soil loss in different conditions and environments. Depending on the objective of the soil-

erosion modelling, decisions need to be taken on the suitable level of complexity or simplicity when selecting an appropriate model (Morgan 1995). For example, the need of decision makers, politicians and planners is for a simplified model where a minimum input and effort is needed to predict the soil-erosion rate. However, the scientists' need for soil-erosion modelling is different in that they need a more comprehensive and complex model that describes the details of system functionality, that gives more understanding and depicts the natural processes in a more comprehensive manner.

When predicting soil erosion, Morgan (1995) argues that decisions need to be made on the time and spatial scales, that is whether the prediction should be for a year, a day, a storm or for short time periods within a storm and whether it should be for a field, a hillslope or a drainage basin. These decisions are important because they define the relevant models and the type of input data that will be needed when implementing the specified soil-erosion model. In addition, such decisions are needed because at different spatial scales, different soil-erosion processes tend to become dominant so that the effective focus of the models also changes accordingly. For example, if the erosion study is concerned about the loss of the soil depth or the deterioration of the soil productivity, soil-erosion prediction is needed for a long period of 20 to 30 years. However, if the erosion modelling is designed to study the effect of one incidence, such as a rainstorm, on the erosion rate then an event erosion model is the more appropriate choice.

Models, in general, can be divided into scale, conceptual and mathematical models (Steyaert, 1993). Scale models involve the reduction in scale of the system under study. Conceptual models are used to identify the major components of a system and possible relationships between them without quantifying those relationships, therefore, they cannot be used for prediction. Mathematical models attempt to quantify the relationships within a system and use algebraic equations to predict the system outcomes, thus, this type of models is used in this study.

According to the way that a model depicts the natural processes and mathematically describes the soil erosion, we can distinguish between two main types of models: empirical and process-based models. A third type of soil-erosion models is described by a combination of process-based elements that have physical meaning and empirical elements which help to improve the model outputs.

3.2.2 Empirical (or Black Box) Models

Empirical soil-erosion models are often simple and are used by decision makers and planners for soil-erosion prediction purposes. These models are developed and designed under certain conditions and constraints which make them applicable within these limitations. An example of these conditions is the period in which the soil-erosion loss will be estimated such as average annual, during a storm, for short-time periods within a storm, etc.. . Another example of the limitations of empirical models is that these models cannot be used to extrapolate soil loss outside the specified range of the input data, nor outside the geographical and the topographic specifications. As a result of these pre-defined conditions, countries which are different in terms of the above mentioned constraints and conditions are required to develop their own empirical soil-erosion models which suit their own constraints and conditions.

There are many empirical soil-erosion models that are used worldwide. Some of the most well known models are reviewed below.

3.2.2.1 Universal Soil Loss Equation (USLE)

This model is the most widely used empirical soil-loss prediction model. The core of the USLE was a very simple model of Zingg (1940) who related erosion to slope steepness and slope length (Morgan 1995). Several stages of development to the Zingg model led to the creation of USLE model by adding more input coefficients which have an immediate effect on the rate of erosion such as crop factor, conservation factor, soil erodibility factor and the rainfall erosivity factor. The USLE

model is based on the statistical analysis of a data set of more than 10000 plot years of data of interrill and rill erosion on plots and small watersheds in the Eastern USA. It provides an estimate of long-term average annual soil loss from segments of arable lands under various cropping conditions. The USLE model is expressed in the following equation:

$$E = R.K.L.S.C.P \qquad 3.1$$

Where: E is the average annual soil loss in tonnes per hectare;

R is a measure of the erosive forces of rainfall and runoff;

K is the soil erodibility factor, a number which reflects the susceptibility of a soil type to erosion, that is the reciprocal of the soil resistance to erosion;

L is the length factor, a ration which compares the soil loss with that from a field of specified length of 22.6 metres;

S is the slope factor, a ratio which compares the soil loss with that from a field under a standard treatment of cultivated bare fallow;

C is the cover and crop management factor;

P is the conservation practice factor, a ratio which compares the soil loss with that from a field with no conservation practice.

Because it has a reasonable level of reliability, the USLE has become a standard model to be used by soil-conservation planners. One of the advantages of the USLE is that it can be used to estimate the slope length that keeps the erosion rate at its acceptable level or to calculate the crop factor in order to choose a suitable cropping practice.

The USLE model is designed to predict long term mean annual soil-erosion rates, however, it is often used by scientists and planners to predict the soil loss in single storm events resulting in less accurate soil loss predictions. Another disadvantage of the USLE model is the fact that its use is restricted, because of the nature of its database, to the USA east of the Rocky Mountains and to slopes ranging between 0 to 7° (Morgan, 1995). Using the model outside these restrictions to predict soil erosion may generate large errors in the results.

3.2.2.2 The SELEMA Model

SELEMA model was developed in order to evaluate the soil erosion resulting from different farming systems so that appropriate conservation measures could be recommended (Elwell, 1981). The model has since been adopted by many countries to assess the risk of soil erosion and develop their strategies for soil conservation. This model is described in the following equation:

$$Z = KXC \qquad 3.2$$

Where Z is the annual soil loss (t ha^{-1}), X is a dimensionless combined slope length and steepness factor, C is a dimensionless crop management factor, and K is the mean annual soil loss from a standard field plot (t ha^{-1}). The field plot is 10 by 30 m with a 2.5° slope for a soil of known erodibility under a weed-free, bare fallow.

The value for K is similar to that in the USLE and is determined by relating mean annual soil loss to main annual rainfall energy. The topographic factor X adjusts the value of soil loss calculated for the standard condition to that for the actual conditions of slope steepness and slope length. The procedure is modified if contour ridges are used as a conservation measure. The crop management factor C adjusts the value of soil loss for the standard bare soil condition to that from a cropped field.

3.2.3 Process-Based Models

Process-based soil-erosion models are able to explain mathematically each of the separate physical processes of soil loss and then combine their separate effects. This type of soil-erosion model is different from the empirical type in a way that process-based models are used by scientists and researchers to improve our understanding and broaden our knowledge about the process of soil erosion and their use and is not limited to simple soil loss prediction. Furthermore, the process-based models provide a tool to predict the sediment and the runoff during individual storms in addition to total yearly runoff and soil loss.

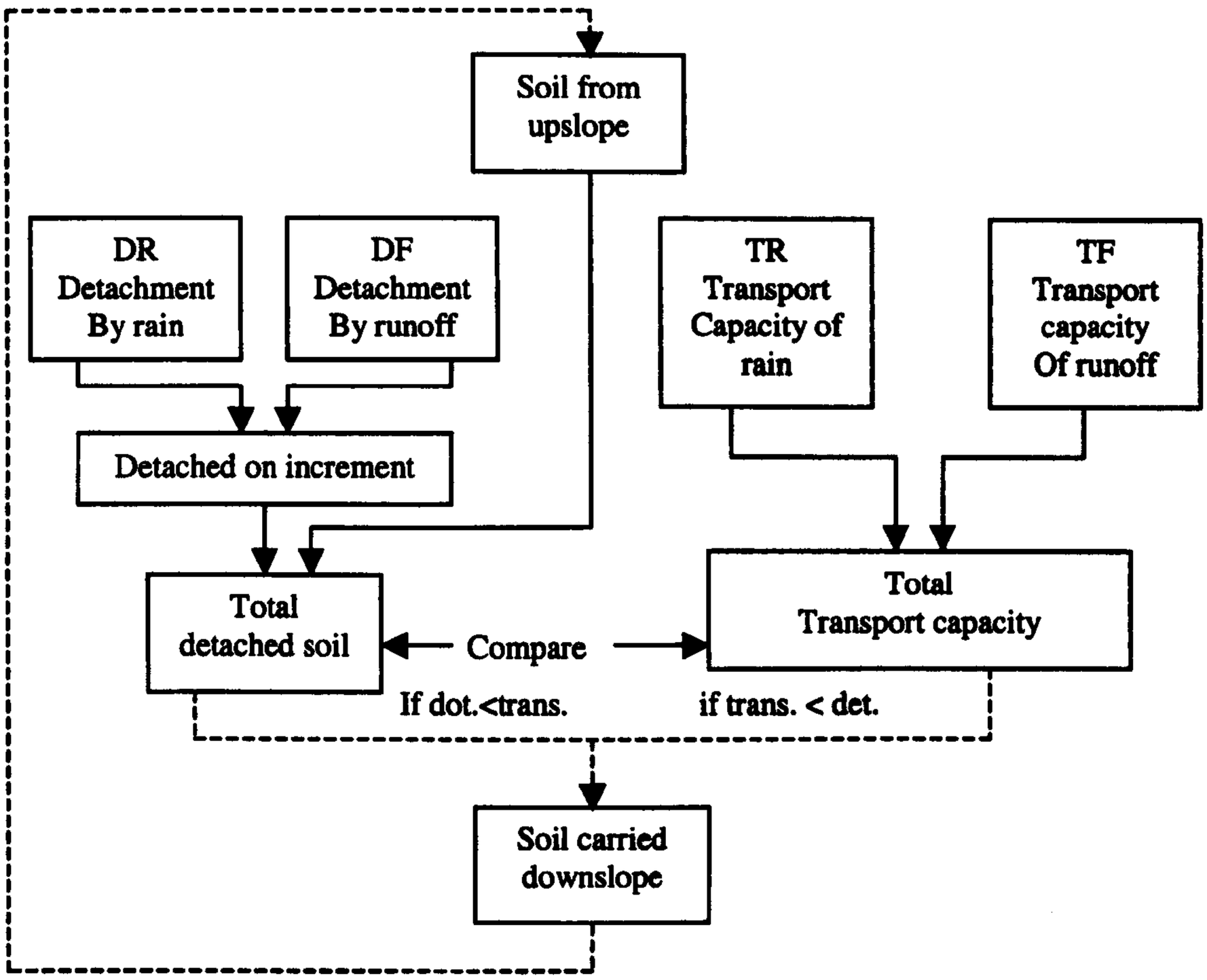

Figure 3.1. Flow chart explaining the four processes of soil erosion by water in a process-based model (after Meyer and Wischmeier 1969)

The original idea of the process-based soil-erosion models was suggested by Meyer and Wischmeier (1969). They suggested that physical processes of the soil erosion consist of four phases of detachment by raindrop splash, transportation by raindrop splash, detachment by surface runoff and transportation by surface runoff (Figure 3.1). These process-based models represent a synthesis of the individual components that affect soil erosion, including the complex interactions between various factors and their temporal variabilities.

3.2.3.1 ANSWERS (Areal Non-point Source Watershed Environment Response Simulation)

From the idea of the Meyer and Wischmeier scheme, many process-based soil-erosion models have been developed. An example of such models is the ANSWERS soil-erosion model which was developed by Beasley, Huggins and Monke (1980). This model is a grid-based distributed model designed to simulate the hydrological and erosional behaviour of agricultural catchments during and immediately following a rainfall event. The ANSWERS model assesses sediment yield from the whole watershed, as opposed to that from field-sized area. Thus it can be implemented at the catchment scale and it can also assesses the cost effectiveness of possible land-use treatments within the watershed.

In this model, several physically based mathematical relationships are used to describe interception, infiltration, surface retention, drainage, overland flow, channel flow, detachment by rainfall, and sediment transport by the overland flow for the inter-rill erosion. When water and sediment reach an element with a channel they are transported to the watershed outlet. The sediment is deposited within a channel when its transport capacity is exceeded.

Sharma and Singh (1995) evaluated the ANSWERS model to predict the runoff and soil loss in three watersheds in arid and semi-arid areas. They found that the model underestimated the soil loss for all the three watersheds. Other studies carried out by various researchers (Bingner *et al.*, 1989, Montas and Madramootoo, 1991) to assess the ANSWERS model confirm the findings of Sharma and Singh (1995).

3.2.3.2 European Soil-Erosion Model (EUROSEM)

Another example of the process-based soil-erosion models is the European Soil-Erosion Model (EUROSEM). This model is a single event model for predicting soil erosion by water from fields and small catchments. The model provides for explicit simulation of inter-rill and rill flow, the effects of vegetation cover on rainfall

interception, infiltration, rainfall energy and flow velocity and the effects of rock fragment cover on infiltration, and splash erosion (Morgan, 1995). This model is a co-operative model-building project carried out by scientists in seven European Community countries and purpose built runoff plots in England and Spain (Folly *et al.*, 1999).

The EUROSEM model can be applied to either individual fields or small catchments. Catchments are represented as a simplified cascading network of elements, which may be either planes or channels. Each plane is considered uniform in its soil, slope, surface microtopography and land cover

The potential of this model has been investigated by Folly *et al.*, (1999) in the Catsop watershed in the Netherlands. In their investigation, the model was calibrated using observed hydrographs and sedigraphs by interactively changing the input parameters of initial soil moisture content, saturated hydraulic conductivity, cohesion, Manning's *n* and the detachability of soil particles. The results show that the soil loss was generally very high and that the model is very sensitive to changes in the initial soil moisture content and Manning's *n*. Because of model high sensitivity and the difficulties of parameterising the model, Folly *et al.*, (1999) concluded that minimum and maximum of the expected output values should be included in the input data in order to prevent extreme overestimation.

3.2.4 Process-Based Models With Empirical Elements

This type of soil-erosion model combines the complexity and mathematical expressions of the process-based models with the simplicity of the empirical models in order to achieve higher prediction accuracy with a simpler approach and a smaller number of input parameters. An advantage of this type of model is that they maintain a description of the physical processes of the soil erosion in a clear and understandable way, while their implementation is easier and more straightforward than the process-based models. However, these models inherit some of the limitations associated with the empirical soil-erosion models in that their use is

restricted by the specified range of the input data and by their geographical and the topographic specifications.

3.2.4.1 The Morgan, Morgan and Finney Method

This model was developed by Morgan, Morgan and Finney (1984) to predict the annual soil loss at the field scale. The model consists of a water phase and a sediment phase. In the water phase, the annual rainfall is used to determine the energy of the rainfall for splash detachment and the volume of runoff, assuming that runoff occurs whenever the daily rainfall exceeds a critical value representing moisture storage capacity. The sediment phase considers the detachment of soil particles by raindrop impact and the transportation of those particles by overland flow (Morgan, 1995). The model is expressed by the following two phases:

1- Water phase

$$E = R(11.9 + 8.7\log_{10} I) \qquad 3.3$$

$$Q = R\exp(-R_c / R_o) \qquad 3.4$$

Where $R_c = 1000MS.BD.RD(E_t / E_o)^{0.5}$

$R_o = R / R_n$

Where E is kinetic energy of rainfall (J m^{-2}), R is the rainfall amount in the year (mm), I is intensity of erosive rain (mm h^{-1}), Q is volume of overland flow (mm), MS is soil moisture content (w w^{-1}%), BD is bulk density (mg m^{-3}), RD is top soil rooting depth (m), E_t is actual evaporation, and E_0 is potential evaporation.

2- Sediment phase

$$F = K(Ee^{-aA})^b.10^{-3} \qquad 3.5$$

$$G = CQ^d \sin S.10^{-3} \qquad 3.6$$

Where F is rate of soil detachment by raindrop impact (kg m^{-2}), K is soil detachability index (g J^{-1}), A is percentage rainfall contributing to permanent

interception, G is transport capacity of overland flow (kg m^{-2}), C is the crop cover management factor, S is slope steepness factor. Coefficients are empirically defined as: $a = 0.05$, $b = 1.0$, $d = 2.0$.

One of the limitations of Morgan, Morgan and Finney model is that the predictions obtained by this model are most sensitive to changes in annual rainfall and soil parameters when erosion is transport-limited and to changes in rainfall interception and annual rainfall when erosion is detachment-limited (Morgan, 1995). In addition, this soil-erosion model requires fifteen input parameters to be implemented which may prove to be a disadvantage in studies where available data are limited.

3.2.4.2 Thornes Soil-Erosion Model

The Thornes soil-erosion model, which was developed by Thornes (1985, 1990), is another example of the process-based models that have empirical elements. This model contains a hydrological component, based on a simple storage-type analogy (Gilman and Thornes 1985), a sediment transport component, and a vegetation growth component. This model is expressed in the following equation:

$$E = K\, OF^{m}\, S^{n}\, e^{bVc} \qquad 3.6$$

Where E is erosion (mm T^{-1} where T is a rainstorm duration), K is soil erodibility (defined empirically), OF is overland flow (mm T^{-1}), S is the topographic parameter of slope (%), Vc is the vegetation cover (%), and "m", "n" and "b" are coefficients that can be defined empirically (their values are discussed later on in this section).

As can be seen in Thornes' model, the main components affecting soil erosion are combined in four simple parameters where each one of the parameters has its own clear physical meaning. These parameters can be measured in a simple way either in the field or derived from remotely sensed data. Thornes' model has the advantage of applicability in a spatially distributed manner in order to predict the soil loss at all locations of a hillslope. Drake *et al.*, (1999) and Zhang (1999), for example,

implemented Thornes' soil-erosion model spatially in the south-east of Spain and reported good results.

The parameter *K*, which represents the soil erodibility in Thornes' model, depends on the nature of material entrained in the flow and relies to some extent on the soil texture (e.g. clay, silt, and sand content), organic matter content, soil porosity, and soil structure. There is a general consensus among geomorphologists that fine material with high clay content tends to be more stable and less susceptible to erosion, yielding a low value for the erodibility parameter *K*. The natural resistance to erosion of such materials is attributed to their cohesiveness and the bonding of their minerals. On the other hand, silt and fine sands are usually considered the most erodible materials because of their relatively small size and the lack of cohesion among the individual grains. Coarser sands are considered more stable, because of their heavier weight, giving a low value of erodibility.

The values of the coefficients "m" and "n" in the soil-erosion equation have been estimated by different researchers. Most of the studies suggest that "m" changes between 0.24-1.66 and "n" between 0.91-2.07 and that "n" can change with the grain size and the slope. For example, Gabriels *et al.* (1975) show that the value of "n" increases with the grain size of material, from 0.6 for particles of 0.05 mm to 1.7 for particles of 0.1 mm. Horvath and Erodi (1962) found from their laboratory studies that n = 1.6 for slopes between 0° and 2.5°, 0.7 for slopes between 3° and 6.5°, and 0.4 for slopes over 6.5°. Thornes (1976) discussed the suitable values for "m" and "n" in the model (equation 3.6) and suggested values of the coefficients of m = 2.0 and n = 1.66 for semi-arid environment.

Relatively low rates of soil erosion are observed in well-vegetated areas compared with the catastrophic rates which can arise when vegetation is cleared (Styczen and Morgan 1995). This is due to the fact that the vegetation cover is a significant parameter in controlling and minimising the risk of soil erosion. Thornes (1985) suggests that down to about 40 per cent vegetation cover the effect of cover is far less significant than below that level where soil loss increases dramatically. Morgan

(1982) found an exponential relationship between soil loss and percentage cover where "b" ranged between –0.03 and –0.07. Thornes (1990) also found that erosion is reduced exponentially in relation to the bare soil value by increased vegetation cover and he used the value –0.07.

3.2.5 Selecting The Soil-Erosion Model

In order to develop an applicable strategy for soil conservation based on the prediction and modelling of the soil erosion, it is critical to choose and implement the most suitable soil-erosion model with consideration to the available data. Most soil-erosion models tend to simplify the complexity of the real world by selectively exaggerating the fundamental aspects of a system. Krenkel and Novotny (1979) have suggested simple general rules for selection and use of models. First, the problem must be clearly defined and the simplest model, which provides acceptable accuracy, should then be adopted. Secondly, the model should be appropriate to the problem, and not vice versa. Thirdly, the assumptions and limitations of the model structure should always be remembered, and the degree of uncertainty associated with model predictions should always be known. More complex models are clearly more versatile, but such models may also be difficult to use widely due to the fact that such models are controlled by a large number of parameters. The range of complexity between the various models is paralleled by the size of the resource base needed to support development, calibration and operation of the model. Far more limiting constraints face the soil-erosion modeller, regardless of location, in terms of the presence or absence of available data. The availability of data will often determine which model is selected because data collection is time-consuming and is often faced by limited financial resources (Anderson and Burt 1985).

Since the focus of this research is to investigate the potential use of the high spatial resolution remote sensing data in soil-erosion modelling, models that integrate remotely sensed and ancillary field data as inputs are of great importance to this study. In the context of soil-erosion modelling, remote sensing is becoming an increasingly important tool for collecting many of the key parameters, such as

vegetation cover and land use, because it expresses the highly non-uniform spatial distribution of model parameters more effectively and covers large areas in fine spatial detail. Furthermore, since the spatial resolution of the data used in this research is high, the ideal soil-erosion model must accommodate the spatial scale of this study.

If an empirical model is to be implemented in this study, then an extensive data set is needed in order to calibrate and parameterise the specified model and to make it applicable to the study area. Since the data set in this study was limited, such calibration processes seem impossible. In addition, empirical soil-erosion models are developed to predict long-term soil loss such as for annual or monthly duration. However, an event-based soil-erosion prediction is needed in this study so the results of such model can be validated against field measurements of a rainfall simulation event. Thus, the empirical soil-erosion models were rejected. On the other hand, if a complex, process-based model is to be implemented for this study, a large data set is also needed to describe the many parameters and their complex interactions in such model. If such a complex model is implemented with few data, the output results from the model can be very unreliable (De Roo, 1993).

In order to satisfy all the above-mentioned criteria, a relatively simple and process based model which needs a limited number of parameters seems to be a reasonable choice. Thornes' (1985, 1990) soil-erosion model satisfies these requirements because it simply combines the soil-erosion factors, it has a clear physical definition, it is relatively easy to parameterise, and thus can be implemented and operated without any major problems. In addition, all the data needed to implement this model in this study are available and this is a crucial element when selecting the appropriate model. The implementation of Thornes' model gave good results during the simulation of the erosion at the Early Bronze site of Laval de la Bretonne situated at the sub-catchment of the Montagne d'Alaric (Wainwright 1994), as well as in quantifying the soil erosion in a semi-arid catchment in southern Spain (Obando 1996).

3.3 OVERLAND-FLOW MODELLING

3.3.1 Introduction

According to the equation 3.6, Thornes' soil-erosion model requires overland flow as an input and this parameter also needs to be modelled. Thus, it is necessary to select a suitable overland-flow model. Over the years a large number of models have been developed for quantifying the overland-flow generation resulting from the rainfall precipitation. The objective of this section is to review a range of the available hydrological overland-flow models with a special emphasis on their spatial distribution capabilities. Some of the widely used overland-flow models, both empirical and process-based, are discussed below and an appropriate model for this study is selected.

3.3.2 An Overview of Overland-flow Models

In order to be able to model the overland flow, it is important to understand the hydrological and the meteorological conditions required for the initiation of the overland flow over various geomorphic units of the catchment under study. Most overland-flow models are based on one of the following two processes. The first is that saturation overland flow occurs when rising water tables intersect the soil surface, generating exfiltration for each rainstorm. The second is that Hortonian overland flow occurs when the rainfall intensity exceeds the infiltration rate of the soil (Freeze 1972).

Investigating the spatial distribution of overland-flow generation, alongside runoff-producing properties, is equally significant in modelling the overland flow more accurately. For example, in a study on an experimental watershed, Yair (1992) shows that rocky, upper valley-side slopes frequently produce runoff, but that this runoff is absorbed by lower colluvial slopes, thus the slope as a whole generates no overland flow. In contrast, overland flow in rocky headwater areas that lead directly into the channel is not infiltrated. Scoging (1992) recognises that overland-flow hydraulics

depends upon how runoff is generated at a point and how that runoff is routed (Anthony *et al.*, 1992). In Scoging's cell-based, distributed model, runoff generation is determined for individual cells, based upon fitting the parameters of an infiltration equation to some measurable ground-surface properties of the cells. The runoff is routed out of the cells according to their slope vector.

This type of distributed runoff generation and overland-flow models requires a considerable amount of hydrological and physical soil parameters data at a high spatial and temporal scale. Since it is almost impossible to collect these data in the field, especially if the data needed are from the past, remote sensing technology is considered to be the alternative and the most adequate solution for data collection. Remote sensing may provide the data in the desired spatial and temporal resolution. In addition, the remote sensing techniques provide the user with analytical tools in order to derive some parameters, such as land use and soil texture, necessary to run the overland-flow models.

One of the advantages of using spatially distributed overland-flow models is their ability to be integrated in the Geographical Information Systems (GIS). GIS techniques are increasingly used by the hydrological community as sophisticated database-management systems for efficient storage, retrieval, manipulation, analysis and display of spatially referenced data (Mattikalli *et al.*, 1996, Burrough 1990). GIS provide an ideal data structure to model the distributed nature of overland flow in a catchment (Schultz 1993). The GIS framework is particularly useful in integrating large amounts of data of rainfall, land-use, soils and topography for hydrological modelling.

As in the case of modelling soil erosion, there are two types of overland-flow model: empirical and process-based. Examples of these two types of models and the process of selecting the appropriate model are outlined below.

3.3.2.1 SCS Model

The SCS (Soil Conservation Service 1972) model is an empirical overland-flow model based on the Hortonian theory where overland flow occurs when the rainfall intensity exceeds the soil infiltration rate. The model is widely used for estimating excess precipitation or direct runoff (*OF*) on a small to medium-sized catchment. No runoff occurs until rainfall equals an initial abstraction (*Ia*). After allowing for *Ia*, the depth of runoff *OF* is the residual after subtracting the water retained in the watershed (*Fa*). The hypothesis of the SCS method is that the ratio of runoff (*OF*) to effective storm rainfall *Pe* is equal to that of the water retained in the watershed (*Fa*) and to the potential retention (*Sc*) (Zhang 1999).

$$P = OF + Ia + Fa \qquad 3.7$$

$$\frac{Fa}{Sc} = \frac{OF}{Pe} \qquad 3.8$$

In order to simplify this equation and after studying the results from many small experimental watersheds, an empirical relationship was developed (Soil Conservation Service 1972).

$$Pe = P\text{-}Ia \qquad 3.9$$

$$Ia = 0.2Sc \qquad 3.10$$

Then

$$OF = \frac{(P-0.2Sc)^2}{(P+0.8Sc)} \qquad 3.11$$

For convenience and to standardise the application of this equation, the potential retention is expressed in the form of a dimensionless runoff curve number *CN*. The curve number and *Sc* are related by:

$$Sc = \frac{1000}{CN} - 10 \text{ (inch)} \quad = \quad \frac{25400}{CN} - 254 \text{ (mm)} \qquad 3.12$$

Curve numbers have been tabulated by the Soil Conservation Service on the basis of soil type and land use (Pilgrim and Cordery 1993, Rawls *et al.*, 1993).

3.3.2.2 Philip Infiltration Model

The Philip infiltration model is based on the Hortonian assumption where overland flow occurs when the rainfall intensity exceeds the infiltration rate of the soil. According to Darcy's law, water movement through a one dimensional unsaturated, vertical soil column is mathematically expressed as (Morgan *et al.*, 1984):

$$q = K(h_p)\frac{dH}{dz} = K(h_p)\frac{dh_p}{dz} - K(h_p) \qquad 3.13$$

Where q is the water flux (mm s^{-1}) and $K(h_p)$ is the hydraulic conductivity (mm s^{-1}), H is the hydraulic potential, h_p is the matric potential (mm) and z is the gravitational potential or height above a reference level (mm).

For the vertical co-ordinate oriented positively downward from the soil surface located at $z=0$, Richards' equation in its diffusivity form is expressed as:

$$\frac{\partial Q}{\partial t} = \partial\left(D(Q)\frac{\partial Q}{\partial z}\right)/\partial z - \frac{dK}{dQ}\frac{\partial Q}{\partial z} \qquad 3.14$$

Where Q is volumetric water content (m^3 m^{-3}) and t is time (s), $D(Q)$ is soil water diffusivity (mm^2 s^{-1}).

An approximate solution of the Richards' equation for vertical infiltration into a homogeneous soil with water completely saturated at the soil surface and a uniform initial water content was given by Philip (1957) as:

$$I = St^{1/2} + At \qquad 3.15$$

$$q = dI/dt = 0.5St^{-1/2} + A \qquad 3.16$$

Where I is cumulative infiltration (mm), q is infiltration rate (mm s^{-1}), A is a parameter which is a fraction of the saturated hydraulic conductivity Ks (mm s^{-1}). It is expected that $A=mKs$. Although m is taken as 1 by some researches (Hanks 1992), the most frequently used value of m is 2/3 but its value ranges between 0.2-0.67 (Philip 1987). S is soil sorptivity (mm $s^{-0.5}$) and t is rainfall duration in seconds (s).

3.3.2.3 Carson and Kirkby Model

The Carson and Kirkby model was developed in (1972) as an overland-flow equation to predict the annual volume of overland flow. Later on, this model was developed further by Kirkby (1976). The model assumes that the overland flow occurs when the daily rainfall total exceeds a critical value which represents the soil water storage, and that the frequency distribution of rainfall in excess of the critical value is exponential. This basic concept has been applied to calculate seasonal overland flow (Kirkby and Neale 1987) and cumulative erosion potential (Kirkby and Cox 1995). In this model, Kirkby states that if each day's rainfall (r) is assumed to fall onto a soil which has water storage capacity (r_c), of which an average depth (h) is already occupied by surface water, then the following cases may be distinguished (Kirkby 1976):

I. If $r \geq r_c - h$ then the excess ($r + h - r_c$) will flow rapidly overland, an amount e_0 (estimated < r_c always) will be released as evapotranspiration, and the balance of ($r_c - e_0$) will contribute to subsurface flow.

II. If $r_c - h > r \geq - e_0 h$ then there will be no overland flow, an amount e_0 will evapotranspire, and the balance ($r - e_0$) will contribute to subsurface flow.

III. If $e_0 - h > r \geq 0$ then there will be no overland flow, the amount ($h + r$) will evapotranspire, and there will be a contribution of $-h$ to subsurface flow.

It can be assumed that once rainfall occurs, the precipitation becomes either infiltration or overland flow since the evapotranspiration may be very small during a rainfall event (Zhang, 1999). Hence, the amount of infiltration I in a rainfall event can be calculated as:

$$I = P - OF \quad 3.17$$

Thus, the Carson and Kirkby overland-flow model can be described in the following equation:

$$OF = P\text{-}(r_c\text{-}Q_{iT}) \quad 3.18$$

Where

$$r_c = 10\ \phi\ h \quad 3.19$$

$$Q_{iT} = 10\ Qi\ h \quad 3.20$$

$$\phi = (1 - \frac{BD}{PD})(1 - fs) \quad 3.21$$

Where OF is the overland flow (mm event^{-1}), P is the amount of rainfall during an event (mm), r_c is the water storage capacity (mm), Q_{iT} is the initial soil moisture (mm), Qi is the volume water content (cm^3 cm^{-3}), h is the soil depth (cm), ϕ is the soil porosity (percentage), BD is the soil bulk density (g cm^{-3}), PD is the particle density (g cm^{-3}), and fs is the stone fraction in the soil (percentage).

3.3.3 Selecting the Overland-flow Model

De Lima (1992) argues that a primary consideration in the choice of a model is the data availability and the determination of the physical processes that are important in a particular situation. For instance, one element of this determination is the spatial and temporal scales. Most studies that focus on understanding processes are generally undertaken on a very small scale for practical or conceptual reasons, whereas application of that understanding for predicting soil erosion needs to be at a much larger scale. The other factor is the temporal scale where most overland-flow models are developed to predict the runoff generation during a specific period of time which can be minutes, rainfall event, days, or yearly. In this study the emphasis is to predict the runoff and model the overland flow during a simulated rainfall event so the models which accommodate this time scale are of special interest.

In a study to model soil erosion and its overland-flow component in the study area in the Southern-east of Spain, Zhang (1999) implemented and compared the three different overland-flow models outlined above. Zhang (1999) then assessed the accuracy of these models by comparing their output prediction results against the measurements of overland flow from rainfall simulation experiments. He found that the Carson and Kirkby model produced the best average estimate of overland flow and the lowest average relative error amongst all the models used in the study (Table 3.1). This can be attributed to the fact that the overland-flow generation rates are most sensitive to the bulk density, effective soil depth and antecedent soil moisture which are incorporated in the Carson and Kirkby model. In addition, Zhang (1999) also found that the SCS and Philip models may be useful for predicting average overland flow in a watershed but they are not very sensitive to the individual rainfall simulation plots.

Model	Carson and Kirkby		SCS		Philip		Field Measure
	OF (mm)	RER%	OF (mm)	RER%	OF (mm)	RER%	OF (mm)
Average	58.35	38.52	44.35	39.65	82.14	70.14	59.99

Table 3.1. Comparison of the accuracies and results of implementing Carson and Kirkby, SCS, and Philip overland-flow models in Vélez Rubio. RER is relative error, and OF is overland flow in *mm* (adapted from Zhang, 1999).

Furthermore, the Carson and Kirkby model has another advantage in that it satisfies the prior conditions of this study such as the temporal scale of a rainfall event and the spatial nature of the model and the possibility of implementing it in a GIS environment. Thus, this model will be implemented in this study and its results will be integrated within Thornes model to spatially predict the soil loss.

3.4 CONCLUSION

In this chapter a wide range of existing soil-erosion models have been reviewed and analysed in order to select the most suitable model for this study. This review

included a variety of models ranging from the simple to the more complex and from the empirical to process-based models. It has been demonstrated that data availability to parameterise a model is critical when selecting an appropriate soil-erosion model. Empirical models are the most widely used because of the substantial databases behind them and the simplicity of implementing and parameterising them. However, such models need to be first calibrated and adjusted to the environment, climate, and conditions of the area under study, the fact which is often neglected in some soil-erosion studies and which may become a source of large errors in the model outputs.

On the other hand, process-based models have the advantage of predicting not only the overall soil loss in a watershed but also the soil loss at all locations in the watershed in a spatially distributed manner. The Thornes model has been selected to predict the soil erosion and sediment loss in this study because it is easy to parameterise and can be implemented in a GIS environment which makes integrating all its parameters and producing the soil-erosion map a straightforward task.

One of the main parameters controlling the Thornes soil-erosion model is the hydrological element of overland flow. Different models of Soil Conservation Services (SCS), Philip, and Carson and Kirkby to estimate the overland flow have been reviewed and their hydrological differences have been shown. The Carson and Kirkby model has been selected to predict overland flow in the Thornes model because it was proven to produce the best results and the least errors in a study by Zhang (1999) which was carried out in an area of similar hydrological conditions to those of our study area. In addition to its accuracy, this model is simple and easy to implement because the data needed to parameterise it are available.

CHAPTER 4

FIELD SURVEYING, IMAGE GEOREFERENCING AND SLOPE MAPPING

4.1 INTRODUCTION
4.2 FIELD SURVEYING
    4.2.1 Introduction
    4.2.2 The Principles of Surveying
        4.2.2.1 Control Survey
        4.2.2.2 Global Positioning System (GPS)
    4.2.3 Surveying in Study Area
        4.2.3.1 Altitude Calculations of The Control Stations
        4.2.3.2 Ground Control Points (GCPs)
        4.2.3.3 Red and Grey Soil Transects.
4.3 TOPOGRAPHIC MAPPING OF THE SLOPE
    4.3.1 Introduction
    4.3.2 Digital Photogrammetry And The DEMs Creation
    4.3.3 The Principles of Photogrammetry:
        4.3.3.1 The principle of collinearity
        4.3.3.2 The principle of Coplanarity
        4.3.3.3 Analytical Aerotriangulation.
4.4 DEM EXTRACTION USING DIGITAL PHOTOGRAMMETRIC TECHNIQUES.
    4.4.1 Block Tool processes
        4.4.1.1 Camera Editor
        4.4.1.2 Frame Editor
        4.4.1.3 Ground Control Editor.
        4.4.1.4 Aerotriangulation.
    4.4.2 DEM Tool processes
4.5 SLOPE CALCULATION FROM THE DEM
4.6 SUMMARY AND CONCLUSION

4.1 INTRODUCTION

It has been discussed in chapter three that a soil-erosion model of a spatially distributed nature will be implemented to predict soil loss in this study. Remotely sensed data are used to parameterise the selected model because these data not only provide localised information but are capable of covering the entire study area. Some

of the parameters needed to implement the model are directly derived from the remotely sensed data (e.g. topographic slope, soil map and vegetation cover map), whereas other parameters are mapped with the aid of these data (e.g. soil properties of soil texture, soil depth and organic matter maps) using soil samples collected from the field.

The remotely sensed data used in this study consist of a number of aerial photographs that provide a high spatial resolution source of data with a pixel size of 0.55 m. However, these aerial photographs are hardcopy images and they need to be scanned and then registered to a common reference system so that they can be imported and integrated in a GIS system for further analysis. This is done by georeferencing these images to the relevant map system using Ground Control Points (GCPs) where the X, Y, and Z measurements for these GCPs were collected using surveying and the Global Positioning System (GPS). These GCPs are used to perform the two types of geometric corrections of planemetric and orthometric rectifications on the aerial photographs in order to create orthorectified images necessary to map the topographic slope and to locate the soil samples accurately. The surveying data are used, in conjunction with the aerial photographs, to create the topographic map using digital photogrammetry for the calculation of slope map which is needed for the Thornes soil-erosion model.

In this chapter the principles of the surveying are investigated and the processes of collecting the geographical locational information for the GCPs and the soil samples are explained. In addition, the methodologies of the digital photogrammetry are reviewed as they are used to derive the Digital Elevation Model (DEM) and the slope map.

4.2 FIELD SURVEYING

4.2.1 Introduction

Surveying is defined as the science of making measurements of the relative positions of natural and anthrogic features on the Earth's surface, and the presentation of this

information either graphically or numerically (Bannister and Raymond, 1984). Broadly speaking, we can divide surveying into two methods: geodetic and plane surveying. Geodetic surveying is implemented when the area under study is very large and the curvature of the Earth's surface should be taken into consideration. An example of this is the construction of a national grid which covers the whole country where the curvature of the Earth's surface is considered when the measurements are carried out. Plane surveying covers relatively smaller areas and treats the Earth's surface as a horizontal plane where the plotted measurements only represent the projection of the actual field measurements on that horizontal plane. In this study the plane surveying method is implemented because the study area is small and the effect of the Earth's curvature can be neglected (Bannister and Raymond, 1984).

While the measurements in the field are taken by surveying, there is always an element of error in the measured distances and angles that will propagate into the successive products which use these measurements. Surveyors usually pay special attention to the nature and sources of such errors in order to avoid, if possible, or minimise them to achieve the required accuracy. This required accuracy should be defined and worked out according to the final purpose of the surveying work. For example, if the survey is carried out to produce a paper plan with a scale of 1/500, this means that each 1mm on the plan represents 0.5m on the ground. Bearing in mind that the thinnest line we can draw on the paper is 0.25mm, the required accuracy should be 0.125m. Another example is the GCPs co-ordinates that are collected in the field by methods of surveying. In this case the spatial resolution of the digital image covering that study area should be first defined and the required accuracy of the survey to collect these GCPs should be half of that spatial resolution. In the case of this study, this accuracy should therefore be $0.55/2 = 0.275$ m.

4.2.2 The Principles of Surveying

There are different surveying methods for geographical measurements but all of them start by pre-defining the control stations and the baseline, and then measuring the locations of the desired points relatively to those control stations.

4.2.2.1 Control Survey

The aim of the control survey is to determine the relative locations of the reference stations in order to use them as a base to further measure and calculate the locations of the points of interest. Caution should be taken to observe the errors when working on a control survey in order to meet the pre-defined accuracy and specifications. In doing so, the survey of the detail points in the area under consideration can be carried out to a lower accuracy because the errors in these will be contained by reference points. When surveying large areas, a simple control framework (of the control survey) is not enough to cover the whole area under consideration. This leads to the need to construct a composite control framework which consists of series of chains and lines, their shape and number depends on the shape and the size of the study area. Because our study area is small in size (1.8 by 1.9 km), a simple control survey was enough to cover the entire area.

Generally speaking, we can distinguish between two main approaches of control survey: traversing and triangulation. Traversing is a simple method of control survey and consists of a number of control stations, joined by the traversing lines. A prior knowledge of the co-ordinates of the first location and the bearing of the first base line is necessary to be able to calculate the co-ordinates of the other locations which form the traverse. The control stations of the traverses should be located in points of good visibility so they can be clearly seen from the previous and successive stations. The distances between the control stations can be measured either by tape (when the distance is short) or by some optical distance systems and electronic instruments such as the EDM (Electromagnetic Distance measurement) when the distance is long.

Triangulation is another method of control survey. In the simplest form of triangulation the area is divided into a series of standard geometrical figures, such as braced quadrilaterals or polygons with central points, the corners of which form a series of accurately located control stations (Bannister and Raymond 1984). If the angles and the length of the baseline in the triangle are known (by measurement)

then the length of the two other triangle sides can be calculated using basic trigonometric equations. When carrying out the triangulation processes, a minimum number of angles needs to be measured in order to be able to calculate all the distances between the control stations. However, it is a general practice that all (or most) of the angles of the braced quadrilaterals or polygons are measured in order to exceed the minimum number of angles required for triangulation. This excess of angular measurement provides redundant information which can be used for adjustment to increase the accuracy of the final results. In this study the traversing approach was used because it was easier than the triangulation approach due to the fact that the first known location was outside the study area.

4.2.2.2 Global Positioning System (GPS)

The Global Positioning System (GPS) is a geodetic system that utilises ground reference frame to give the user the absolute positioning on the ground from a number of satellites in space. The GPS satellite constellation consists of 21 evenly spaced satellites placed in circular 12-hour orbits inclined 55° to the equatorial plane. This satellite distribution scheme ensures that at least four satellites are always electronically visible at any ground location. The GPS satellites are configured to provide the users with the capability of determining their position, expressed for example by latitude, longitude, and elevation. This is accomplished by a simple resection process using the distances measured from the location to the GPS satellites (Hofmann-Wellenhof *et al.* 1994).

When the GPS was launched the intention was to give the users instantaneous three dimensional X, Y, and Z position with high precision for preferred users and less precision for ordinary users. Geodesists realised that GPS could be used in a differential mode to obtain relative positions with higher accuracies.

To perform a survey in the field using Differential GPS, the work starts by placing a pair of receivers on two trigonometric points where the data are collected from at least four satellites for several minutes. After this phase of initialisation, one of the

two GPS receivers should stay in the same location and the other receiver can be moved to different points, provided that there are always at least four satellites being tracked by both receivers. Remondi (1986) reported a variation of this technique to determine quickly the initial vector (between two well-known stations) for kinematic surveys. This variant has been termed the antenna swap technique since the instruments are swapped (within 1 minute) between two points at the beginning of the survey to determine the initial vector. Another differential GPS positioning technique is used where a continuous tracking receiver is placed on a fixed point that has a well-know location and the second receiver moves to the other locations of interest. By comparing the computed range with the pseudorange, the reference site can transmit corrections to the other receiver to improve its pseudorange (Hofmann-Wellenhof *et al.* 1994). In this study the first technique of Differential GPS was used because the available GPS instruments did not have transmission capabilities.

4.2.3 Surveying in Study Area

As has been mentioned earlier, one of the aims of the surveying was to measure the geographical locations of the GCPs and the soil samples which will be used for the image georeferencing, planemetric and orthometric corrections, the creation of the DEM, and for the geostatistical analysis. The first task we faced in the field is the selection of good GCPs that would be visible in the aerial photographs. Caution was taken to make sure that these GCPs should be carefully chosen and well distributed across the entire study area in order to minimise the errors and increase the accuracy of the mathematical transformation in the georeferencing processes as much as possible.

Extensive work was done trying to carry out the surveying using an EDM (Electromagnetic Distance Measurement). However, due to the topography of the study area, which limited the inter-visibility between the surveying stations, and due to the limitations of the EDM maximum distance measurement of 450 metres, it was not possible to carry out the entire surveying using the EDM solely. The solution was to combine the two surveying techniques of the Differential GPS and EDM in order

to establish the control stations. Thus, the traversing surveying method was used to establish the control survey, which consists of a number of points located on the top of the hills. From these points it was possible to measure the geographical locations of all the sites which are of interest to us in the study area.

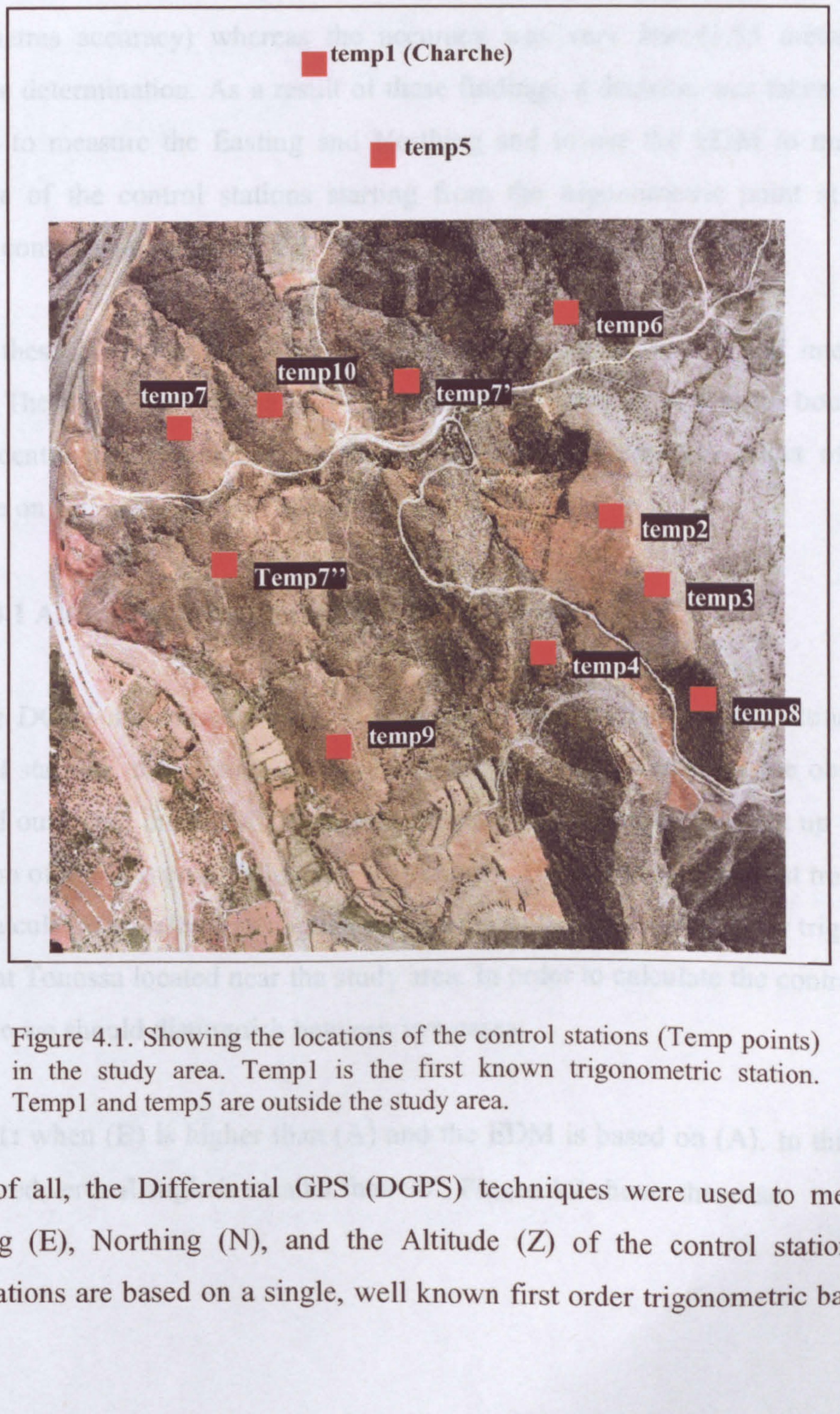

Figure 4.1. Showing the locations of the control stations (Temp points) in the study area. Temp1 is the first known trigonometric station. Temp1 and temp5 are outside the study area.

First of all, the Differential GPS (DGPS) techniques were used to measure the Easting (E), Northing (N), and the Altitude (Z) of the control stations. These calculations are based on a single, well known first order trigonometric base station

located on the top of a hill near the study area called Charche. The geographical co-ordinates of this point were provided on the 1/25,000 map of the study area.

The accuracy of DGPS was tested by measuring the X, Y, and Z of an experimental moving point, starting at the trigonometric point of Charche and closing on the same point, where the differences in X, Y, and Z describe the measurement accuracy. It was clear that it was acceptable to calculate just the Easting and Northing (with 12 centimetres accuracy) whereas the accuracy was very low (1.55 metre) for the altitude determination. As a result of these findings, a decision was taken to use the DGPS to measure the Easting and Northing and to use the EDM to measure the altitude of the control stations starting from the trigonometric point at Charche. These control stations, (called Temp points) are shown in figure (4.1).

From these control stations surveying measurements to the sites of interest were made. These sites include the GCPs and the soil samples, as well as the boundaries of the recently ploughed areas which will be used to assess the effect of land-use change on soil erosion.

4.2.3.1 Altitude Calculations of The Control Stations

As the DGPS did not prove to be accurate enough to measure the altitude of the control stations, the altitude of these stations was calculated from the observations carried out using the EDM. A traverse of the control stations was set up where the location of the first point (Charche) was known. The bearing of the first traverse side was calculated by taking an angular measurement to another first order trigonometric point at Tonossa located near the study area. In order to calculate the control stations altitude we should distinguish between two cases:

Case 1: when (B) is higher than (A) and the EDM is based on (A). In this case the measured vertical angle is smaller than 90°. Figure 4.2 shows this case.

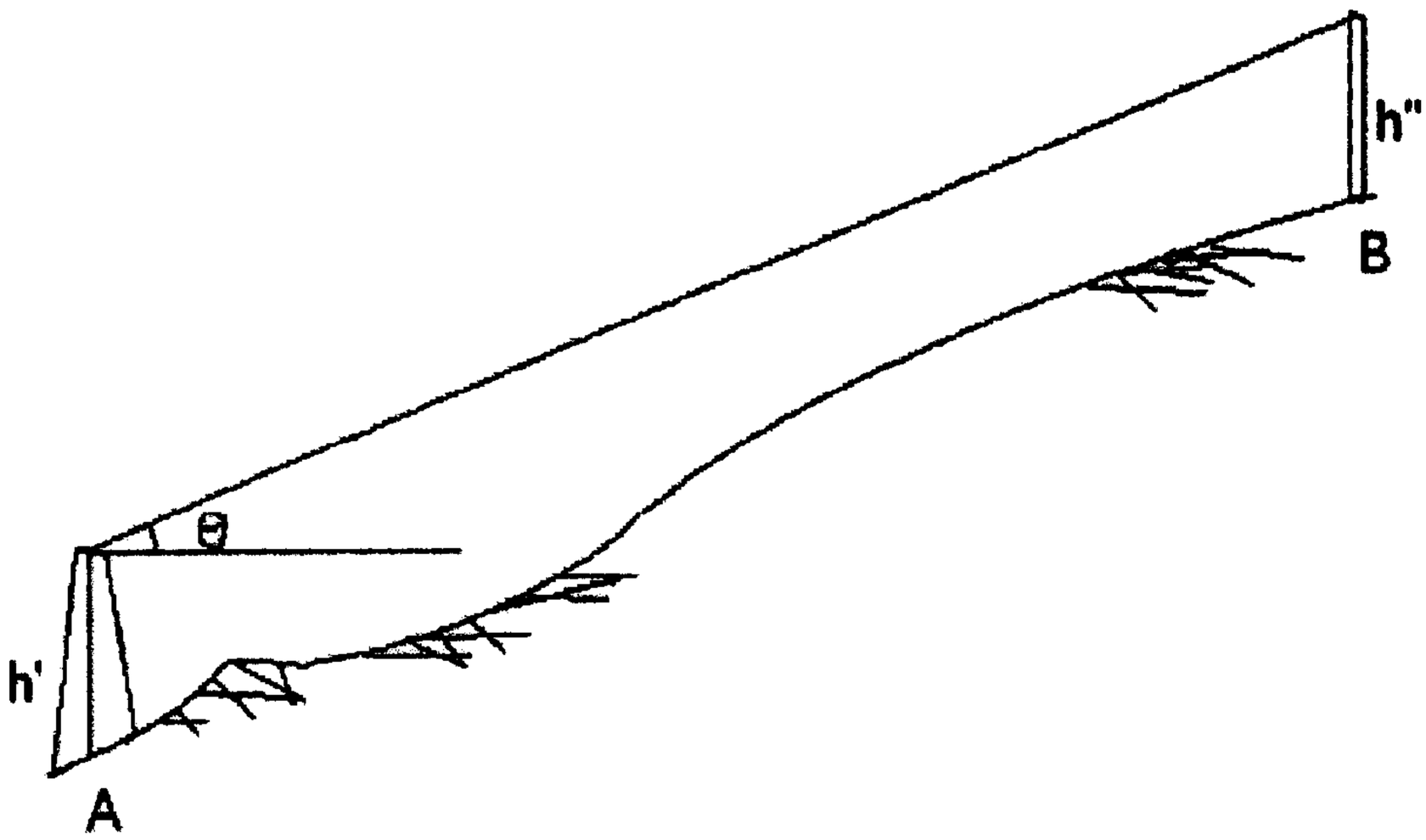

Figure 4.2. A sketch showing the Case A

In this case the following equations apply:

$$\theta = 90\text{-}V \qquad 4.1$$

$$h_B = h_A + D^{*}\sin\theta + h' - h'' \qquad 4.2$$

$$h_A = h_B - D^{*}\sin\theta - h' + h'' \qquad 4.3$$

Where: V is the vertical angle

h' is the EDM height

h" is the reflector height

Case 2: when (B) is lower than (A) and the EDM is based on (A). In this case the vertical angle is greater than 90°. Figure 4.3 shows this case.

$$\theta = V\text{-}90 \qquad 4.4$$

$$h_B = h_A - D^{*}\sin\theta + h' - h'' \qquad 4.5$$

$$h_A = h_B + D^{*}\sin\theta - h' + h'' \qquad 4.6$$

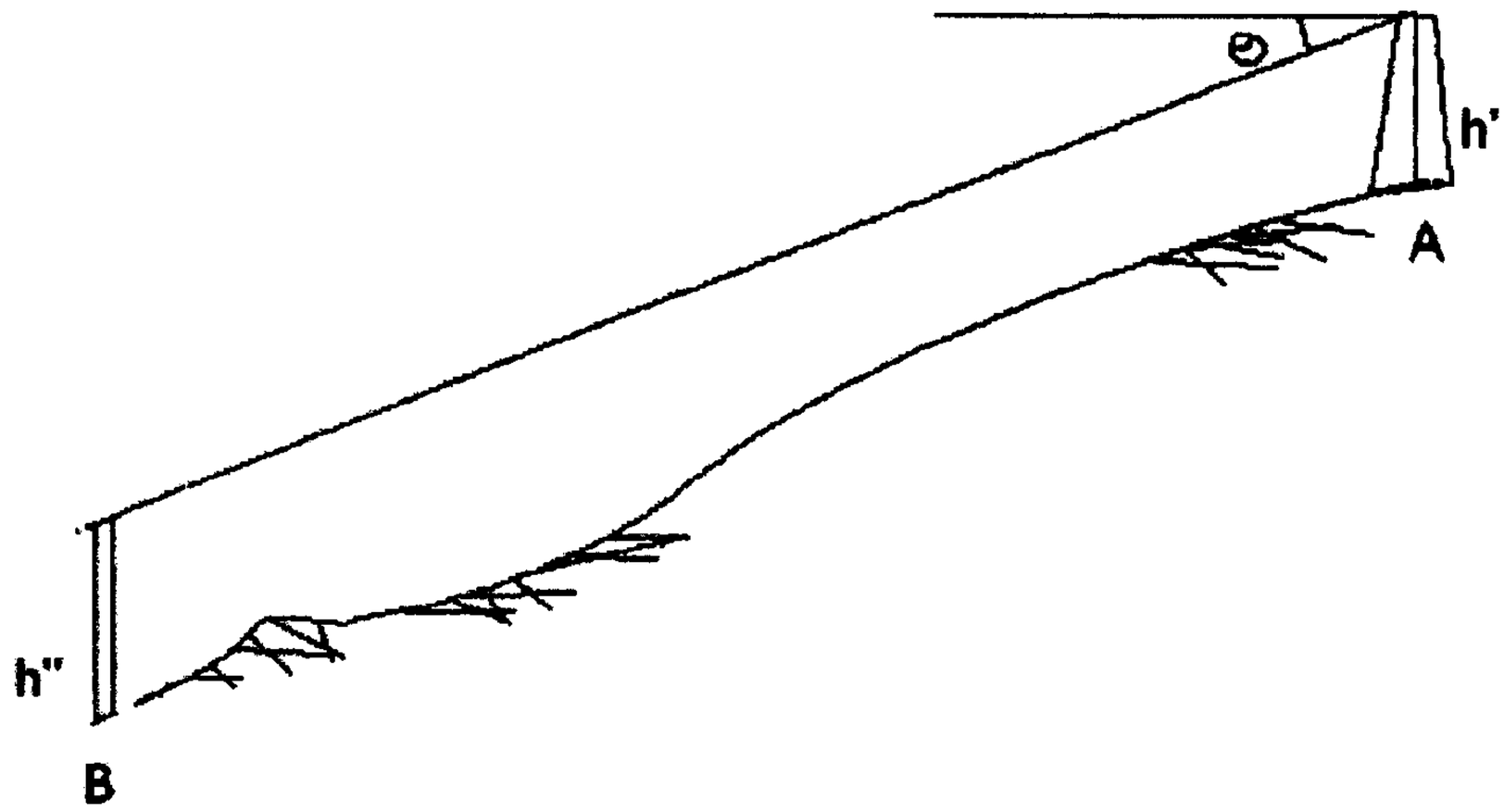

Figure 4.3. A sketch showing the Case B

The table 4.1 shows the altitudes calculation of the control stations of the Temp points where all measurements are in metres.

Station	Looking at X	X height	V	D m	EDM height	Ref. Height	Station Altitude
Temp1	N/A	N/A	N/A	N/A	N/A	N/A	865.41
Temp5	Temp1	865.41	84°58'19"	342.67	1.285	1.235	835.32
Temp6	Temp5	835.32	84°25'55"	446.53	1.310	1.235	878.72
Temp2	Temp6	878.72	94°01'56"	319.98	1.310	1.235	901.15
Temp4	Temp2	901.15	89°51'05"	435.09	1.145	1.235	902.19
Temp7	Temp6	878.72	84°59'20"	717.33	1.320	1.235	815.98
Temp10	Temp7	815.98	92°02'45"	233.54	1.280	1.235	807.69
Temp8	Temp4	902.19	93°11'50"	440.45	1.390	1.235	926.60
Temp3	Temp4	902.19	94°41'50"	324.98	1.295	1.235	928.74
Temp9	Temp4	902.19	80°27'00"	502.69	1.505	1.235	818.51

Table 4.1 showing the Temp points accurate altitude calculations from the EDM observations. V and D stand for vertical angle and distances respectively. Unit is metre for all measurements.

4.2.3.2 Ground Control Points (GCPs)

Station	AZ to	Azimuth	Looking at X	Easting (m)	Northing (m)	Altitude (m)
Temp2	Temp1	74°04'49"	Bridge edge	583437.77	4165756.57	837.61
Temp2	temp1	74°04'49"	Check dam1	583449.50	4165879.59	826.40
Temp2	temp1	74°04'49"	Check dam2	583427.51	4166110.43	807.13
Temp7	temp1	117°15'48"	Check dam3	583406.85	4166293.74	798.92
Temp7	temp1	117°15'48"	Check dam4	583370.22	4166390.34	787.62
Temp2	temp1	74°04'49"	Junction1	583613.81	4165513.66	860.35
Temp2	temp1	74°04'49"	House1	583292.82	4165106.24	868.24
Temp7	temp1	117°15'48"	Gas house	583401.28	4166576.48	793.16
Temp7	temp1	117°15'48"	M.bridge(first-east)	583169.92	4166656.28	765.99
Temp9	temp4	119°11'37"	M.bridge(last-west)	583005.70	4166589.17	767.27
Temp10	temp1	111°46'05"	Check dam5	583793.37	4166365.35	778.68
Temp9	temp4	119°11'37"	House2	582719.34	4166133.24	781.41
Temp9	temp4	119°11'37"	Pigs house	582827.43	4166418.29	777.08
Temp9	temp4	119°11'37"	House3 pool)	582364.07	4166311.72	785.53
Temp9	temp4	119°11'37"	House4(small)	582551.84	4166335.36	781.79
Temp9	temp4	119°11'37"	House5(big)	582413.94	4166341.27	784.76
Temp9	temp4	119°11'37"	Check dam6	582735.83	4165992.41	791.83
Temp9	temp4	119°11'37"	House7	582642.70	4165956.82	819.23
Temp3	temp1	74°44'35"	Junction2	583723.73	4165249.42	850.74
Temp8	temp4	28°34'09"	Check dam7	582616.41	4165445.68	861.66
Temp3	temp1	74°44'35"	house6	583056.18	4165134.74	892.36

Table 4.2. Showing the calculation of the Easting, Northing, and Altitude of the twenty-one selected GCPs.

The GCPs represent locations on the ground, which can be clearly identified in the remotely sensed imagery of that area, and their co-ordinates can be determined accurately. The GCPs are the essential part for any photogrammetric processes, such as georeferencing and orthophoto rectification, and the precision of their determination is reflected in the accuracy of the end product. As a part of the georeferencing process, the GCPs are used to determine the absolute orientation of

the aerial photographs. Theoretically, the plane co-ordinates (E and N) of two GCPs and the altitude co-ordinates (Z) of three GCPs are needed to carry out the absolute orientation, however, more GCPs are used to provide extra information which, in turn, improves the accuracy and prevent mistakes by excluding points of large errors.

An effort has been made to make sure that the GCPs are well distributed as much as possible over the study area. This is very essential for the image georeferencing because it minimises the residuals after the image transformation is carried out. Twenty-one GCPs were selected and the table 4.2 shows the results of the mathematical calculations of their co-ordinates.

4.2.3.3 Red and Grey Soil Transects.

Station	AZ to	Azimuth	Looking at	$\theta°=H-H_{ref.}$	AZ_X	E	N
Temp2	Temp1	74°04'59"	RS 10	217°49'45"	291°54'44"	583447.54	4165506.29
Temp2	Temp1	74°04'59"	RS 20	231°51'46"	305°56'45"	583441.21	4165513.78
Temp2	Temp1	74°04'59"	RS 26	235°47'56"	309°52'55"	583437.75	4165518.37
Temp2	Temp1	74°04'59"	RS 28	236°27'30"	310°32'29"	583436.82	4165519.54
Temp2	Temp1	74°04'59"	RS 43	239°25'50"	313°30'49"	583427.66	4165530.28
Temp2	Temp1	74°04'59"	RS 59	238°43'15"	312°48'14"	583416.20	4165540.03
Temp2	Temp1	74°04'59"	RS 65	238°33'39"	312°38'38"	583411.96	4165543.73
Temp2	Temp1	74°04'59"	RS 95	241°10'45"	315°15'44"	583393.61	4165566.18
Temp2	Temp1	74°04'59"	RS 125	241°26'18"	315°31'17"	583371.22	4165589.56
Temp2	Temp1	74°04'59"	RS 140	240°29'41"	314°34'40"	583359.31	4165598.47
Temp2	Temp1	74°04'59"	RS 145	240°21'38"	314°26'37"	583355.55	4165601.71
Temp2	Temp1	74°04'59"	RS 146	240°21'05"	314°26'04"	583354.75	4165602.47
Temp2	Temp1	74°04'59"	RS 156	239°57'10"	314°02'09"	583347.01	4165608.58
Temp2	Temp1	74°04'59"	RS 186	238°11'49"	312°16'48"	583322.59	4165624.47
Temp2	Temp1	74°04'59"	RS 196	238°12'36"	312°17'35"	583315.26	4165631.19

Table 4.3. Showing the Eastings and Northings calculation of the red soil samples. AZ_x is the azimuth angle.

Station	AZ to	Azimuth	Looking at	$\theta=H-H_{ref}$	AZ_X	E	N
Temp2	Temp1	74°04'59"	GS 2	110°37'05"	184°42'04"	583456.15	4165497.96
Temp2	Temp1	74°04'59"	GS 12	82°28'57"	156°33'56"	583461.65	4165490.89
Temp2	Temp1	74°04'59"	GS 23	73°21'07"	147°26'06"	583468.89	4165483.34
Temp2	Temp1	74°04'59"	GS 28	72°07'32"	146°12'31"	583471.54	4165480.25
Temp2	Temp1	74°04'59"	GS 30	72°06'52"	146°11'51"	583472.48	4165478.85
Temp2	Temp1	74°04'59"	GS 40	70°31'50"	144°36'49"	583478.37	4165471.93
Temp2	Temp1	74°04'59"	GS 50	68°43'55"	142°48'54"	583484.89	4165465.30
Temp2	Temp1	74°04'59"	GS 55	68°34'25"	142°39'24"	583487.81	4165461.69
Temp2	Temp1	74°04'59"	GS 60	67°52'01"	141°57'00"	583491.09	4165458.52
Temp2	Temp1	74°04'59"	GS 70	67°29'22"	141°34'21"	583496.83	4165451.89
Temp2	Temp1	74°04'59"	GS 71	67°32'15"	141°37'14"	583497.59	4165450.85
Temp2	Temp1	74°04'59"	GS 76	66°48'07"	140°53'06"	583500.88	4165448.14
Temp2	Temp1	74°04'59"	GS 86	67°14'37"	141°19'36"	583506.63	4165440.09
Temp2	Temp1	74°04'59"	GS 106	66°28'49"	140°33'48"	583519.99	4165425.51
Temp2	Temp1	74°04'59"	GS 116	66°23'06"	140°28'05"	583526.28	4165418.16
Temp2	Temp1	74°04'59"	GS 146	66°04'22"	140°09'21"	583545.95	4165395.53
Temp2	Temp1	74°04'59"	GS 161	65°42'12"	139°47'11"	583556.06	4165384.96
Temp2	Temp1	74°04'59"	GS 166	65°35'25"	139°40'24"	583559.49	4165381.39
Temp2	Temp1	74°04'59"	GS 167	65°33'45"	139°38'44"	583560.25	4165380.62
Temp2	Temp1	74°04'59"	GS 172	65°33'50"	139°38'49"	583563.39	4165376.92
Temp2	Temp1	74°04'59"	GS 182	65°33'24"	139°38'23"	583569.65	4165369.58
Temp2	Temp1	74°04'59"	GS 187	65°14'20"	139°19'19"	583573.61	4165366.45

Table 4.4. Showing the Eastings and Northings calculation of the grey soil samples.

Fifteen red-soil samples and twenty two grey-soil samples were collected in the field and surveying measurements of distances and vertical angles to calculate the co-ordinates of the soil-sample locations were taken using the EDM which was based on the single control station "Temp2" because both soil transects were best visible from

this control station. The Easting and Northing co-ordinates were then calculated for the soil samples locations and the tables 4.3 and 4.4 show the results.

4.3 TOPOGRAPHIC MAPPING OF THE SLOPE

4.3.1 Introduction

One of the main controlling parameters of the soil loss in Thornes soil-erosion model is the topographic parameter of slope angle where the soil loss increases dramatically as a function of the increasing slope. Slope can be calculated from a Digital Elevation Model (DEM) in a GIS environment and this DEM can be derived from the aerial photographs of the study area using digital photogrammetry.

4.3.2 Digital Photogrammetry and The DEMs Creation

Photogrammetry is defined by the American Society of Photogrammetry as the science and technology of obtaining reliable information about physical objects and the environment through processes of recording, measuring, and interpreting photographic images and patterns of recorded radiant electromagnetic energy and other phenomena (Wolf, 1983). Photogrammetric techniques are based on the geometry of perspective scenes and on the principles of stereovision. There are two kinds of photographs used in photogrammetry: aerial and terrestrial. Aerial photographs are usually acquired from aircraft but can also come from satellites, whereas terrestrial photographs come from cameras based on the ground. There are two distinct areas of photogrammetry: 1-metric photogrammetry and 2- interpretative photogrammetry. Metric photogrammetry consists of making precise measurements from photographs and other information sources to determine the relative locations of points. This enables finding distances, angles, areas, volumes, elevations, and the sizes and shapes of objects. Interpretative photogrammetry deals principally in recognising and identifying objects and judging their significance through careful and systematic analysis.

As hydrological and geomorphological models, such as soil-erosion, overland-flow, and routing models, are becoming more sophisticated, the need for accurate three-dimensional representations of topographic characteristics of land surface is great. In addition, as well as being an important input into various spatially distributed models, Lane (1993) explains that accurate three-dimensional surface data can be an important component when verifying model outputs. This verification process is a very important procedure in the modelling because it acts as an indicative tool for assessing the accuracy and errors of models outputs, as well as minimising the need for field surveys to verify those outputs.

Because of its wide range of advantages, the digital photogrammetric technology is becoming more widespread. For example, it is possible to detect the landform change over a certain period of time by creating two DEMs at two different times for the same location and the resultant DEM is the DEM of difference. Another example of the advantages of digital photogrammetry is its ability to create an infinite number of data points on a three dimensional surface, being limited by the number of points visible on both sets of a stereo-pair of photographs.

4.3.3 The Principles of Photogrammetry

An understanding of the geometric properties of the aerial photographs is of great importance because this leads to an understanding of the various forms of rectifications whereby the effects of any distortion in the aerial photograph, such as tilting, can be corrected. This understanding is important in order to appreciate the limitations of the photogrammetric techniques and their effect on the accuracy of the resultant DEM. The main principles of photogrammetry can be expressed in the collinearity condition, coplanarity condition, and the aerotriangulation.

4.3.3.1 The principle of collinearity

Collinearity is the condition in which the exposure station of any photograph (L), an object point (A), and its photo image (a) all lie on the straight line (Wolf 1983).

Figure 4.4 shows this collinearity condition. The equations expressing this condition are called the collinearity condition equations:

$$x_a = -f\left[\frac{m_{11}(X_A - X_L) + (m_{12}(Y_A - Y_L) + m_{13}(Z_A - Z_L)}{m_{31}(X_A - X_L) + m_{32}(Y_A - Y_L) + m_{33}(Z_A - Z_L)}\right] \quad 4.7$$

$$y_a = -f\left[\frac{m_{21}(X_A - X_L) + (m_{22}(Y_A - Y_L) + m_{23}(Z_A - Z_L)}{m_{31}(X_A - X_L) + m_{32}(Y_A - Y_L) + m_{33}(Z_A - Z_L)}\right] \quad 4.8$$

Where: f is the focal length of the camera

X_A, Y_A, Z_A are ground co-ordinates of a point "A" on the ground

X_L, Y_L, Z_L are ground co-ordinates of the exposure station

x_a, y_a are the photocoordinates of image point a (projection of A)

m_{ij} are the exterior orientation elements.

It is possible to calculate the m_{ij} exterior orientation elements in equations 4.7 and 4.8 from the three rotation angles: ω, ϕ, and κ (the rotation angle around X, Y, and Z respectively) as:

$$m_{11} = \cos\phi \cos\kappa \quad 4.9$$
$$m_{12} = \sin\omega \sin\phi \cos\kappa + \cos\omega \sin\kappa \quad 4.10$$
$$m_{13} = -\cos \sin\phi \cos\kappa + \sin\omega \sin\kappa \quad 4.11$$
$$m_{21} = -\cos\phi \sin\kappa \quad 4.12$$
$$m_{22} = -\sin\omega \sin\phi \sin\kappa + \cos\omega \cos\kappa \quad 4.13$$
$$m_{23} = \cos\omega \sin\phi \sin\kappa + \sin\omega \cos\kappa \quad 4.14$$
$$m_{31} = \sin\phi \quad 4.15$$
$$m_{32} = -\sin\omega \cos\phi \quad 4.16$$
$$m_{33} = \cos\omega \cos\phi \quad 4.17$$

To solve the collinearity equations 4.7 and 4.8, initial approximations for all the nine unknowns (interior orientation parameters, exterior orientation parameters, and ground points locations) are required. These initial approximations are easily obtained by making certain assumptions, such as vertical photography which implies that the initial approximation of the rotation angle κ is 0°. It should be mentioned here that these approximations do not have to be extremely close, but the closer they are to the unknowns, the faster a satisfactory solution will be reached (Wolf 1983).

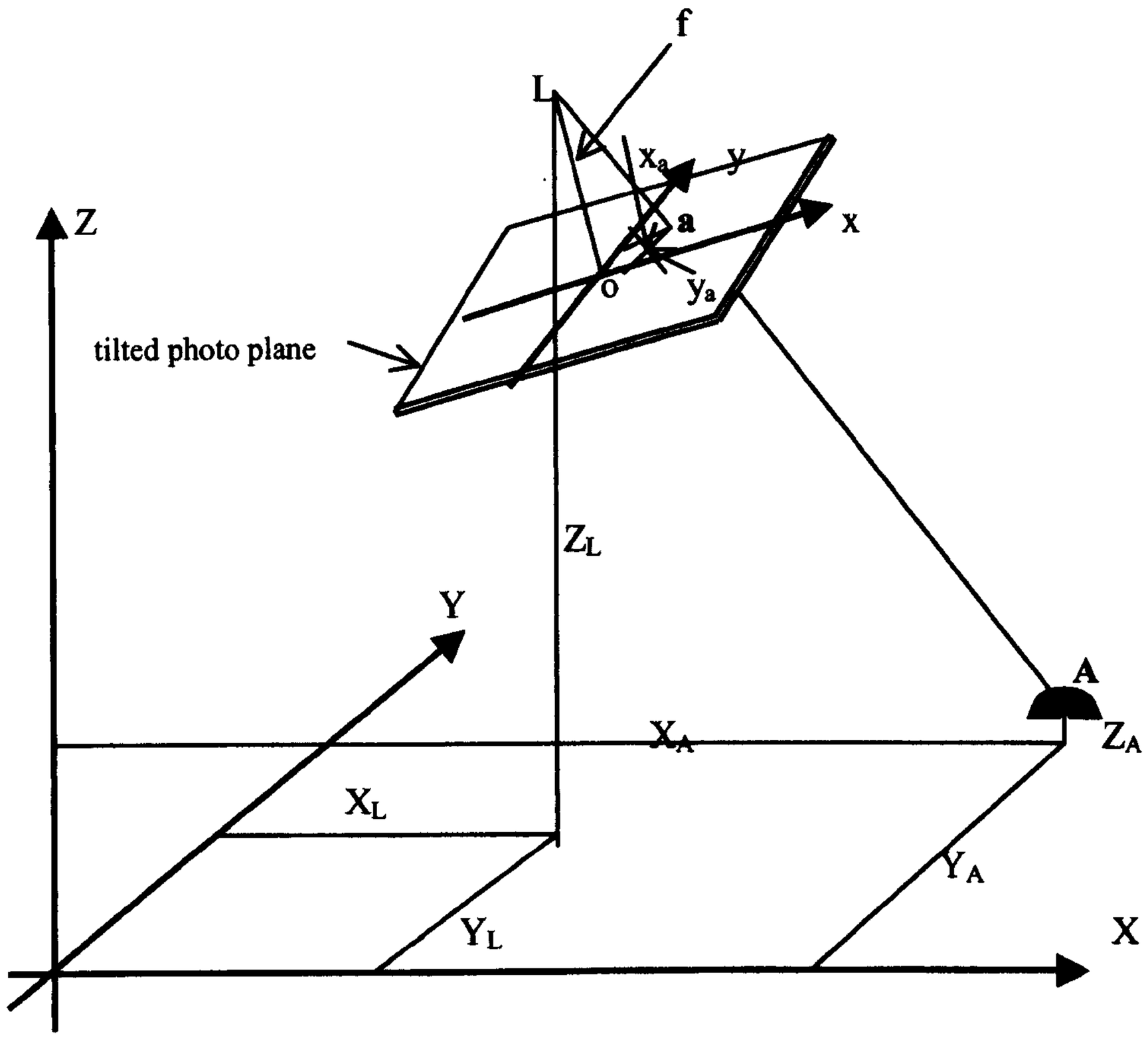

Figure 4.4. The collinearity condition (after Wolf 1983)

4.3.3.1 The Principle of Coplanarity

The coplanarity principle in photogrammetry dictates that the object point on the ground (A), its two corresponding points on the two stereoscopic images (a_1, a_2), and the two exposure stations (L_1, L_2) all fall in one plane (Figure 4.5). We can express the coplanarity condition equation as (Wolf 1983):

$$O = B_X(D_1F_2 - D_2F_1) + B_Y(E_2F_1 - E_1F_2) + B_Z(E_1D_2 - E_2D_1) \qquad 4.18$$

Where: $B_X = X_{L2} - X_{L1}$ 4.19

$B_Y = Y_{L2} - Y_{L1}$ 4.20

$B_Z = Z_{L2} - Z_{L1}$ 4.21

$$D = (m_{12})x + (m_{22})y - (m_{32})f \quad 4.22$$
$$E = (m_{11})x + (m_{21})y - (m_{31})f \quad 4.23$$
$$F = (m_{13})x + (m_{23})y - (m_{33})f \quad 4.24$$

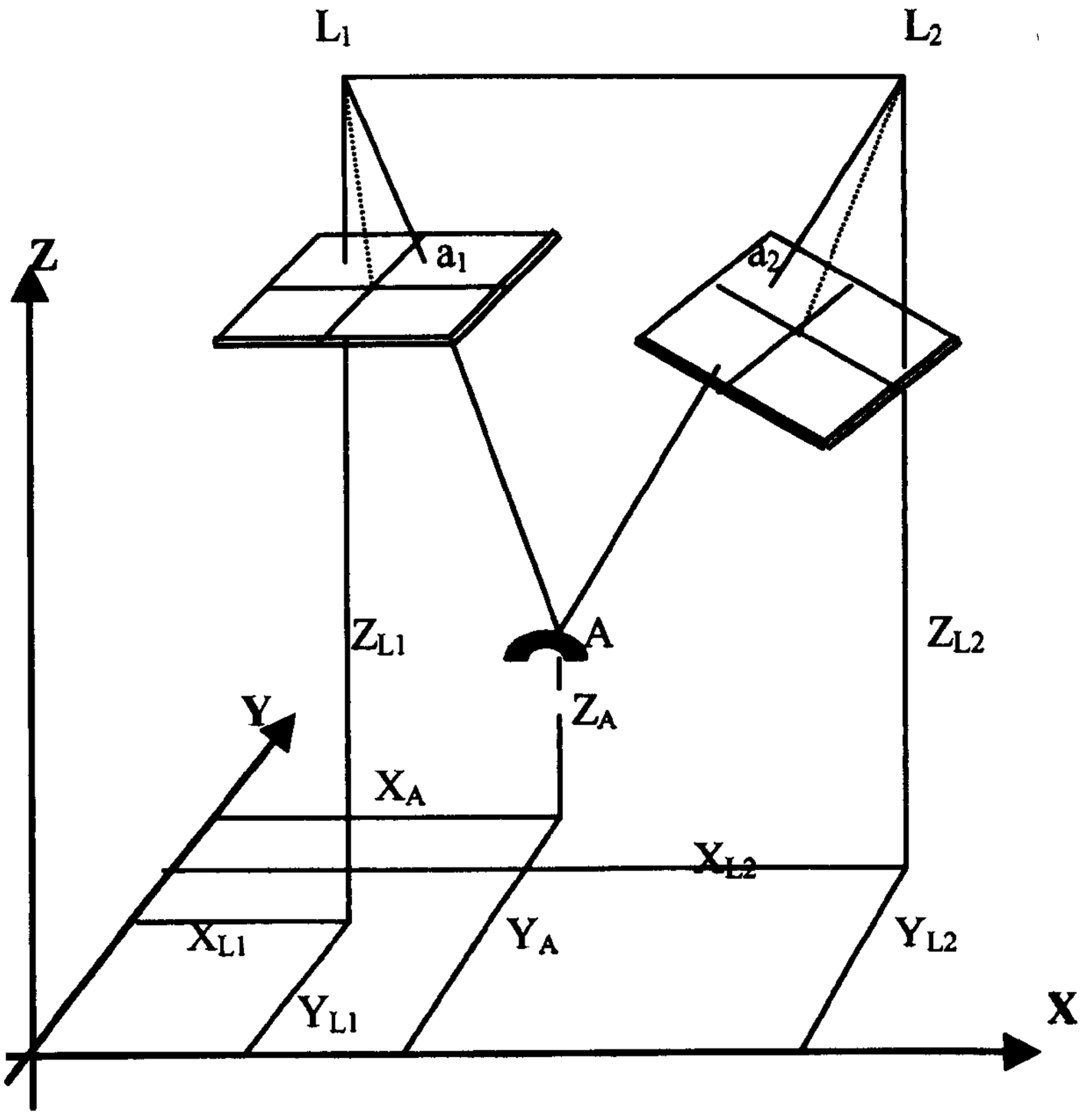

Figure 4.5. The coplanarity condition (after Wolf 1983)

In equation 4.18, subscripts 1 and 2 affixed to terms D, E, and F indicate that the terms apply to either photo 1 or photo 2. The m_{ii} values are, as explained before, functions of the three rotation angles ω, ϕ, and κ. The coplanarity equations, as can be seen above, contain only the elements of the exterior orientation (that is the station location X, Y, & Z and the rotation angles ω, ϕ, and κ) and after a solution for these elements is found, the object point co-ordinates are calculated.

4.3.3.2 Aerotriangulation

Aerotriangulation is the term applied to the process of determining X, Y, and Z ground co-ordinates of individual points based on measurements from photographs

(Wolf 1983). By taking photographs from at least two different locations, so-called "lines of sight" can be developed from each camera to points on the object. These lines of sight are mathematically intersected to produce the 3-dimensional co-ordinates of the points of interest. One of the principle applications of the aerotriangulation is to extend ground control information by creating intermediate control between field-surveyed control. Another application of aerotriangulation is in topographic mapping where Digital Elevation Models (DEMs) are developed by simply computing X, Y, and Z ground co-ordinates of a systematic network of points in an area and this application is the focus of this chapter.

There are different methods of carrying out the aerotriangulation processes and we can classify them into three main approaches: analogue, semi-analytical, and analytical (Wolf 1983). In the analogue approach the relative and absolute orientations are performed manually by using stereoscopic plotting instruments, followed by measurement of model co-ordinates. In the semi-analytical aerotriangulation approach, the relative orientation of stereo-models are carried out manually within a stereoplotter, followed by measurement of model co-ordinates. However, the absolute orientation in this approach is performed numerically. In the analytical approach the photocoordinates are first measured and the relative and absolute orientations are performed numerically and then the model co-ordinates are determined. The third approach is used in this study to derive the DEM.

4.4 DEM EXTRACTION USING DIGITAL PHOTOGRAMMETRIC TECHNIQUES.

In order to extract the DEM, the aerial photograph covering the study area and the two adjacent aerial photographs are needed. These three aerial photographs, which bear the NERC serial numbers 1808, 1809, and 1810, were scanned to 600 dpi optical resolution which corresponds to 0.55 metre spatial resolution. The ERDAS Imagine OrthoMAX photogrammetric module was utilised to extract the DEM. OrthoMAX follows consecutive procedures, utilising different tool types, to produce a DEM. The main two tools in OrthoMAX are the Block tool and the DEM tool.

4.4.1 Block Tool processes

The main functions in the Block Tool are the Camera Editor, Frame Editor, Ground Control Editor, and the Aerotriangulation. Before the Block tool processes are carried out, there are a number of input specifications which the program needs, these can be summarised as:

- The interior orientation parameters for the camera editor.
- The map projection for the Ground Control Points (GCPs) and for the output DEM (whether they are different or the same).
- Initial estimates for the exterior orientation parameters of the exposure stations (X, Y, Z, ω, ϕ, and κ) needed by the Frame Editor.
- The X, Y, and Z co-ordinates for the GCPs.
- GCP measurement, image point measurement and image frame sigmas (standard deviations) of the orientation parameters. These sigmas can be taken as initial approximations.

The map projection in our study was chosen to be the Universal Transverse Mercator (UTM) Zone "30 S" and the Datum is the WGS 84 due to the fact that the X, Y, and Z co-ordinates of the Churche trigonometric point were derived from a map that uses this map projection and Datum.

4.4.1.1 Camera Editor

The camera editor dialogue box requires all the elements of the interior orientation related to the camera (in our case it is the metric camera Universal Aviogon II RC10) to be input into the Block Tool. These elements include the focal length, the principal point offsets, radial lens distortion, and the fiducials supplied by the camera manufacturers. Table 4.5 shows this information.

Radial distortion		Radius (mm)	Distortion (mm)
		20	-0.003
		40	-0.003
		60	0.000
		80	0.002
		100	0.002
		120	-0.001
		140	0.004
Calibrated Focal Length (mm)		153.440	
Co-ordinates of point of symmetry		X (mm)	Y (mm)
		-0.004	0.003
Fiducial Co-ordinates		X	Y
	F_1	105.984	-105.990
	F_2	-106.010	-106.010
	F_3	-105.990	106.012
	F_4	106.009	105.995

Table 4.5. The camera calibration parameters (obtained from the Hunting Aerofilms Certificate of the Camera).

4.4.1.2 Frame Editor

In the frame editor, the choice is to extract the DEM either from two images or three images, depending on the extent and size of the required DEM. In this study the three aerial photographs 1808, 1809, and 1810, which will be implemented in the final triangulation, were imported into the frame editor because a DEM covering the majority of the study area is needed. At this stage the initial estimates for the exterior orientation elements X_L, Y_L, Z_L, ω, ϕ, and κ and their standard deviations (sigma values) are needed. It was difficult to work out these initial estimates because no information was provided about the rotation angles and the locations of the exposure stations (except for the height). As a result of this, the iteration method was implemented where the resultant estimates of the exterior orientation from the first triangulation iteration are considered as the inputs of the initial estimates of the

exterior orientation in the second triangulation iteration and so on. A rough estimates for X_L, Y_L and Z_L for the first iteration were calculated from the co-ordinates of the GCPs and the 1/50000 scale map of the study area, whereas the rotation angles ω, ϕ, and κ were given initial values of zero. Because of the way that the initial estimates in the first iteration were worked out, the standard deviations (sigmas) of these estimates were large and were reduced gradually in the successive iterations.

4.4.1.3 Ground Control Editor.

GCP points	Easting	Northing	Altitude	GCP No.
Bridge edge	583437.77	4165756.57	837.61	1
Check dam1	583449.50	4165879.59	826.4	2
Check dam2	583427.51	4166110.43	807.13	3
Check dam3	583406.85	4166293.74	798.92	4
Check dam4	583370.22	4166390.34	787.62	5
Junction1	583613.81	4165513.66	860.35	6
House1	583292.82	4165106.24	868.24	Not visible
Gas house	583401.28	4166576.48	793.16	7
M.bridge (first from east)	583169.92	4166656.28	765.99	8
M.bridge (last from west)	583005.7	4166589.17	767.27	9
Check dam5	583793.37	4166365.35	778.68	10
House2	582719.34	4166133.24	781.41	11
Pigs house	582827.43	4166418.29	777.08	12
House3(swimming pool)	582364.07	4166101.72	785.53	Not visible
House4(small one)	582551.84	4166335.36	781.79	13
House5(big one)	582413.94	4166341.27	784.76	Not visible
Check dam6	582735.83	4165992.41	791.83	14
House7	582642.70	4165956.82	819.23	15
Junction2	583723.73	4165249.42	850.74	16
Check dam7	582616.41	4165445.68	861.66	17
House6	583056.18	4165134.74	892.36	Not visible

Table 4.6. Showing the ground control points including those which could not been identified on the aerial photograph.

In the ground control editor the surveying measurements of X, Y and Z of the GCPs are imported into the dialogue box along with their estimated accuracy. The interior orientation elements and the camera specifications are also imported into the editor. In this study, twenty-one GCPs were collected from the fieldwork and they were chosen in a way that they are spread fairly evenly over the study area, however, only 17 of these GCPs were clearly visible in the aerial photographs and could be used. Table 4.6 shows the GCPs which have been excluded from the DEM extraction process.

In the GCP editor table, all the X, Y, and Z co-ordinate values in the database should be graphically linked to their geographical locations on the aerial photographs by visually locating and digitising these positions. This is done while all of the three photographs are displayed next to each other so that the GCP locations are shown and the errors are calculated simultaneously. This process was edited until minimum errors were obtained.

4.4.1.4 Aerotriangulation and Georeferencing

The aerotriangulation is the last process in the Block Tool before moving to the DEM Tool. In order to implement the least squares block bundle adjustment in the aerotriangulation, a convergence threshold and a maximum number of iteration should be specified. In our case, the convergence threshold was set to 0.001m and the maximum number of iteration was set to 10.

The aerotriangulation process produces three output reports: 1- Results of Pre-Triangulation Processing report which estimates the co-ordinates of the tie points and shows the GCPs with excessive residuals (bad GCP points), 2- Pre-Triangulation Facts report that shows the co-ordinates corrections and final co-ordinates of GCPs and tie points, 3- Error report which displays the standard deviations of the external orientation elements and the correlation values between X, Y, and Z of GCPs and tie points. Appendices A, B, and C show a summary of these reports and the number of

iterations needed to reach the pre-set convergence. These reports show that three iterations were sufficient to reach the pre-defined convergence of 0.001 where the standard deviation of unit weight for all parameters was 16.55, 0.856, and 0.855 in iteration 1, 2, and 3 respectively.

It should be mentioned here that it is important to read and understand these three report files because they contain all the summary statistics of the aerotriangulation. From these reports a decision can be made whether to keep or remove some of the GCPs that cause errors higher than the others. In our case these reports were used to modify the initial estimates for the external orientation elements and their standard deviations in order to improve the accuracy of the resultant DEM.

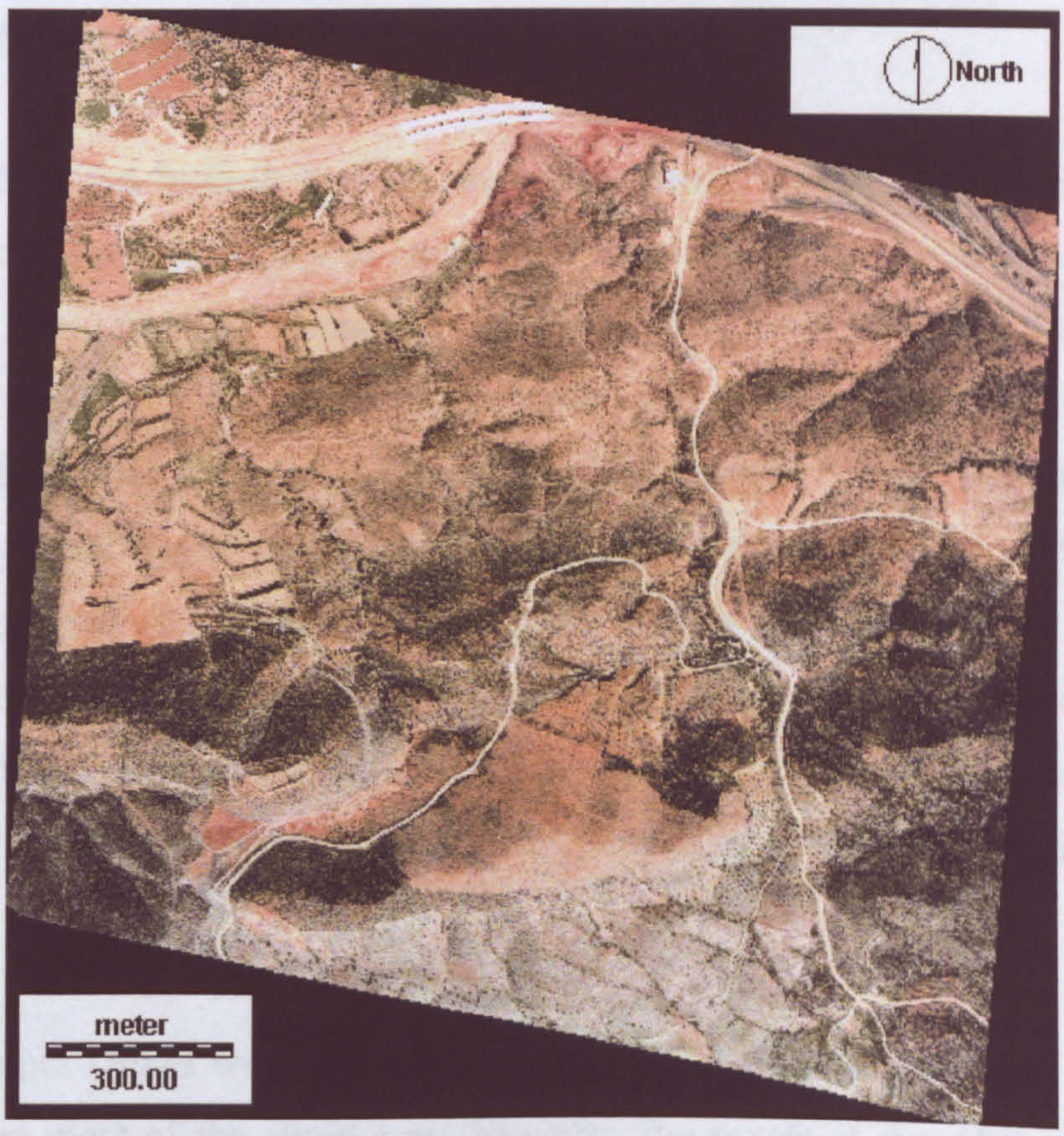

Figure 4.6. The aerial photograph of the study area georeferenced to the UTM-30N projection system.

One of the output results of the Block Tool and the Aerotriangulation processes is the image georeferencing and orthorectification where the GCPs have been used to

resample and transform the aerial photograph of the study area to the UTM-30N projection system. This transformation process was repeated many times before georeferencing the aerial photograph until a minimum RMS error of 0.37 pixel was achieved. This RMS error is considered acceptable because with such high accuracy the soil samples, which were collected in the fieldwork, can be located within the pixels that they belong to. Accurate georeferencing is crucial because all the parameters needed by the soil-erosion model should share a common projection system to enable their integration in a GIS environment. In the resampling processes, the planemetric and orthometric corrections are carried out to rectify the effects of distortions in the aerial photograph. Figure 4.6 shows the georeferenced aerial photograph.

4.4.2 DEM Tool processes

Only one DEM can be built from a stereoscopic pair of images at a time in the DEM Tool, therefore, this process was carried out twice; the first time on the image pair 1808 and 1809, and the second time on the image pair 1809 and 1810. Before extracting the DEM from the stereoscopic images, more than 10 parameters, including the spatial resolution of the output DEM, needed to be set to user-defined values. The DEM spatial resolution was set to 4 times the resolution of the scanned aerial photographs (0.55m $\times$ 4 = 2.20 m) and the rest of the parameters were set to the default values. This spatial resolution was selected according to the recommendation of the OrthoMAX software guidelines and because this software uses a 4 $\times$ 4 moving window in the aerial photographs to create the pixels of the DEM.

The two output DEMs were mosaiced in order to produce the complete DEM. This DEM covers most of the study area, however, the pixels at the edge of the aerial photograph do not contain useful information because the DEM has the highest accuracy at the centre of the images in the area of overlap and this accuracy deteriorates away from the centre. In the mosaic process, the mean pixel value in the

overlapping pixels was chosen to balance the difference in altitude between the first and the second DEM.

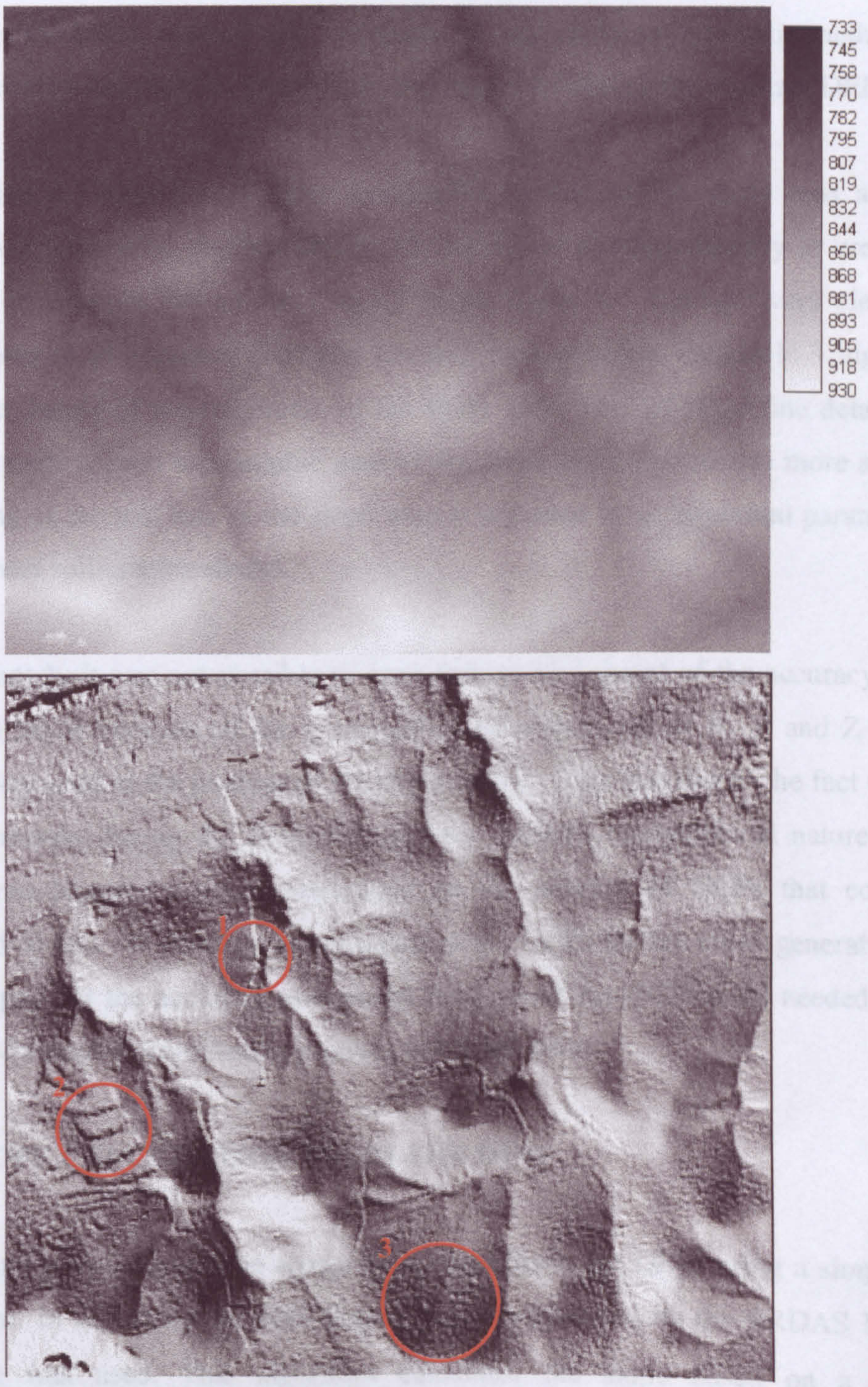

Figure 4.7. The resultant DEM of the study area, along with the shaded relief for visual assessment. For explanation of the red circles refer to text.

It is inevitable to have errors in DEMs generated using digital photogrammetry and these errors are mainly in the form of pits. There are two methods of removing the pits from the DEM, manual and automatic. In this study an automatic method was implemented using Arc/INFO software and figure 4.7 shows the resultant DEM.

The figure 4.7 shows very clear topographic details of the study area and this indicates a successful implementation of the digital photogrammetry to create the DEM. For example, the circles 1 and 2 in the figure 4.7 highlight very clear land cover features of a narrow road and terraced land, whereas the circle 3 highlights very fine details of the roughness of the study area. This DEM of fine details will help to create a good topographic map of the slope and contribute to more accurate modelling of the soil loss as the slope map is regarded as an important parameter in the Thornes soil-erosion model.

Unfortunately it was not possible to carry out an assessment of the accuracy of the resultant DEM because all the geographical measurements of X, Y and Z for the GCPs were used in the process of DEM generation. This was due to the fact that the time limitation during the fieldwork and the difficult topographical nature of the study area imposed certain restrictions on the number of GCPs that could be collected. It was not possible to use a part of the GCPs for the DEM generation and another part for the accuracy assessment because all the GCPs were needed during the transformation procedure to produce low RMS error.

4.5 SLOPE CALCULATION FROM THE DEM

It is possible to calculate the topographic slope from the DEM using a simple GIS algorithm. In this study the GIS slope algorithm provided by the ERDAS Imagine software was used. This algorithm calculates the slope based on a 3×3 neighbourhood around each pixel in the DEM image and this can be mathematically expressed as follows:

	y		
x	a	b	c
	d	e	f
	g	h	i

For the central pixel (x, y), the average changes in elevation in both x and y directions are calculated.

$\Delta x1 = c - a$ $\Delta y1 = a - g$

$\Delta x2 = f - d$ $\Delta y2 = b - h$

$\Delta x3 = I - g$ $\Delta y3 = c - i$

Where a, b, c … and i are elevation values of pixels in a 3 by 3 window as shown above. ΔX and ΔY are then calculated as follows:

$$\Delta X = (\Delta x1 + \Delta x2 + \Delta x3)/(3s_x) \quad 4.25$$

$$\Delta Y = (\Delta y1 + \Delta y2 + \Delta y3)/(3s_y) \quad 4.26$$

Where s_x is the x pixel size

s_y is the y pixel size

The resulting change in elevation is:

$$\Delta Z = \frac{\sqrt{(\Delta X)^2 + (\Delta Y)^2}}{2} \quad 4.27$$

The slope angle can then be calculated as (slope here is calculated in degrees):

$$\text{Slope} = \tan^{-1}(\Delta Z) \quad 4.28$$

Figure 4.8 shows the resultant slope map where the slope values range from 0° to 47°. Although it was not possible to assess the accuracy of the slope map

quantitatively, a qualitative assessment based on knowledge of the study area indicates that the creation of the slope map from the DEM was successful. This is evident, for example, in regions of the river bed and terraced land in the north-west and the west parts of the study area respectively where these regions are characterised by very gentle slopes or flatness. Steepest slopes in figure 4.8 are observed around the edges of terraces, in the embankments of the roads, and around the upslopes and the peaks of the hills and these observations indicate a successful slope mapping.

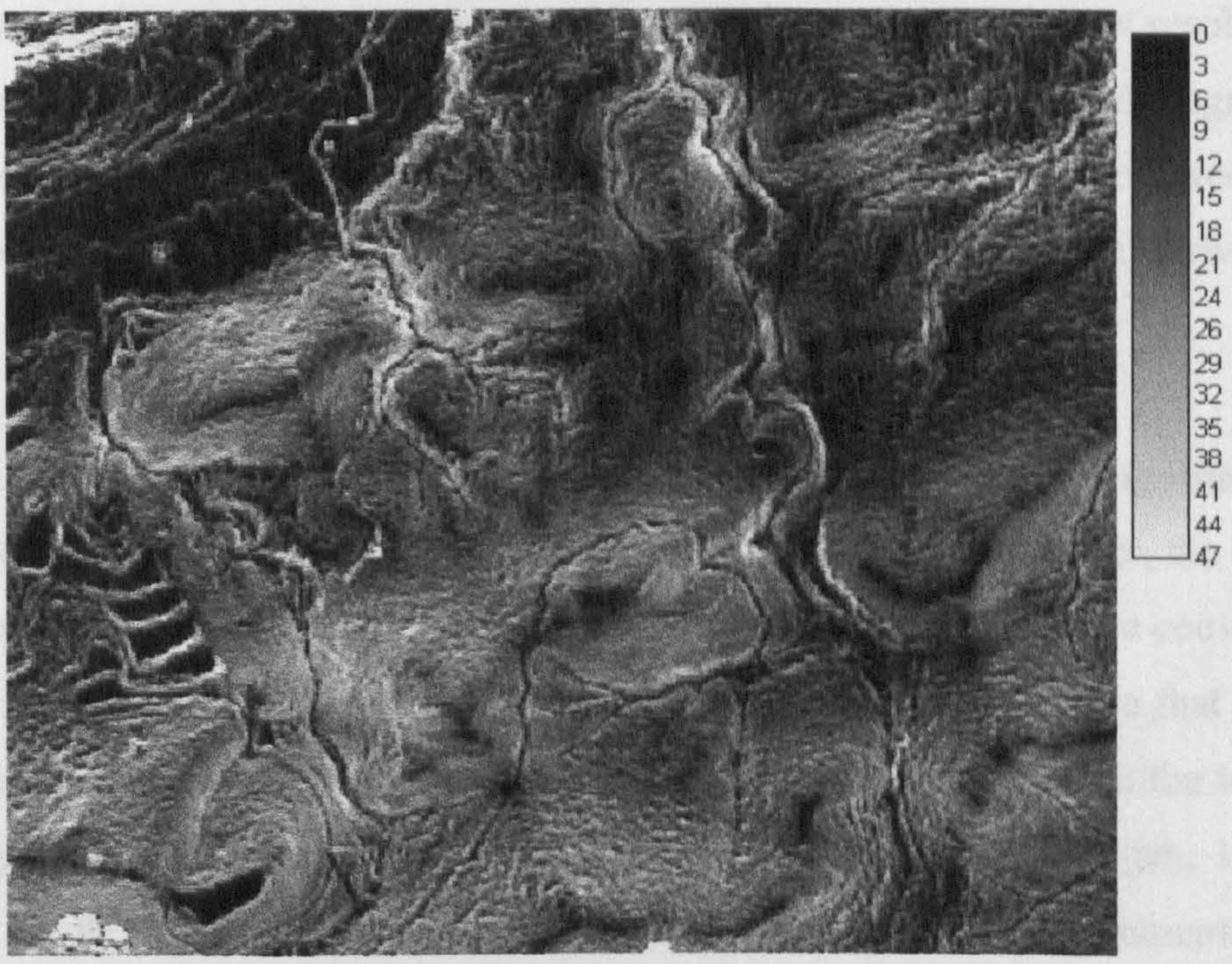

Figure 4.8. The topographic slope image derived from the DEM. The slope values are in degrees.

4.4 SUMMARY AND CONCLUSION

In this chapter the methods of the conventional surveying and the Global Positioning systems (GPS), which have been used in the fieldwork, were reviewed and a combination of these methodologies were implemented in the field surveying. A network of the control stations was initially determined in clearly visible locations

and the geographical co-ordinates of these stations were defined using the GPS and the EDM. GPS techniques proved to be accurate to measure the X and Y co-ordinates but provided poorer accuracy to measure the altitude Z, thus, the EDM was used for this purpose. From these control stations it was possible to carry out the field surveying to collect the locational measurements of the GCPs and the soil samples.

In this study very high spatial resolution data are investigated for soil-erosion modelling and a slope map of a high spatial resolution is required. Thus, it was not possible to use existing 1/50,000 topographic maps because of their low resolution and the slope map of the study area had to be derived from the aerial photography using digital photogrammetry techniques. These techniques have been reviewed and the ERDAS Imagine OrthoMAX photogrammetric module was used to derive the DEM.

From the resultant DEM the slope map was derived using the slope algorithm in ERDAS Imagine software. The unit of this slope map is degrees, however, the slope unit in the Thornes soil-erosion model is percent so the slope map will be converted to the relevant units before implementation. It should be mentioned here that there are other topographic factors that may affect the soil-erosion rate such as the length of the slope and the distance from the ridge (Liu *et al.*, 2000, and Morgan, 1995). However, in this study the Thornes soil-erosion model will be implemented to predict the soil loss and this model incorporates only the slope factor, thus, the other topographic factors are not considered in this study.

CHAPTER 5

VEGETATION COVER AND LAND-USE MAPPING

5.1 INTRODUCTION

5.2 MAPPING THE VEGETATION COVER

5.2.1 Introduction

5.2.2 The Spectroscopy of Vegetation Leaf

5.2.3 VEGETATION INDICES AND GEOMETRICAL OPTICAL MODELS TO MAP VEGETATION COVER

5.2.3.1 Investigating the Correlation between Red Band Reflectance and the Vegetation Cover

5.2.4 VEGETATION COVER MAPPING USING MIXTURE MODELLING

5.2.4.1 Classification Techniques for Vegetation Mapping

5.2.4.2 Fuzzy Classification

5.2.4.3 Mixture Modelling

5.2.4.4 Linear and Non-Linear Mixture Modelling.

5.2.4.5 The Linear Mixture Model

5.2.4.6 Endmembers Extraction for Linear Mixture Modelling.

5.2.4.6.1 Endmembers Derived From Principal Components Analysis

5.2.5 IMPLEMENTATION OF MIXTURE MODELLING

5.2.5.1 Endmembers Extraction from the Aerial Photograph

5.2.5.2 Mixture Modelling Implementation

5.2.6 Re-scaling Vegetation Map to Remove the Shade Effect

5.2.6.1 Implementation of Re-scaling Algorithm

5.2.7 Co-Occurrence Matrix Methods to Rectify Blank Vegetation Pixels

5.3 MAPPING THE LAND USE

5.3.1 The Effect of Land use on Soil erosion

5.3.2 METHODOLOGIES OF LAND-USE MAPPING

5.3.2.1 Image Classification

5.3.2.2 Classification Methods

5.3.3 IMPLEMENTATION OF CLASSIFICATION FOR LAND-USE MAPPING

5.3.3.1 Maximum Likelihood Land-use Classification

5.3.3.2 Accuracy Assessment of Land-use Map

5.3.3.3 Land-use classes collapse for improving classification accuracy

5.3.3.4 Alternative methods for land-use mapping: image interpretation

5.3.3.5 SUMMARY AND CONCLUSION

5.1 INTRODUCTION

In soil conservation it is essential to develop affordable techniques to monitor both where land degradation has occurred and what areas are most at risk for further degradation due to soil erosion. The efficient and accurate measurement of

vegetation cover and the mapping of land use in semi-arid regions are the key to this problem. In chapter 1 and 2 the significance of the natural vegetation cover in controlling the soil-erosion rates in semi-arid environments was discussed. The destruction of this protective vegetation cover by means of changing the land use, such as ploughing the land for almond and olive plantations, was also explained and, thus, the need to map the vegetation and land use for soil-erosion studies is evident and the derivation of these parameters is also essential for implementing the Thornes soil-erosion model.

In this chapter the significance of vegetation cover and land-use information for the soil-erosion and overland-flow modelling in the study area of Vélez Rubio is summarised. In addition, the effectiveness of remote sensing systems for vegetation cover estimation and land-use mapping is investigated. Various approaches to map vegetation cover and land use in the semi-arid study area of Vélez Rubio are analysed and their accuracy is assessed. The vegetation and land-use maps will be implemented in the overland-flow and soil-erosion models, in a later chapter, to create a soil-erosion map of the study area.

5.2 MAPPING THE VEGETATION COVER

5.2.1 Introduction

Vegetation cover is regarded by the geomorphological community as one of the most significant parameters controlling the rate and severity of land degradation and soil erosion. Dregne (1983) emphasises that fact that a significant measure of the land degradation is expressed in the degradation of vegetation, and that a brief assessment reveals that the condition of the vegetation cover is a powerful indicator of where additional degradation is occurring and will occur. According to the literature it is widely recognised and accepted by the majority of scientists that there is an exponential relationship between the vegetation cover and the soil loss due to erosion by water (see Morgan 1982, Thornes 1990).

In semi-arid environments, such as the study area of Vélez Rubio, vegetation is highly adapted to the hot and dry environment in which it lives, and it is remarkably resistant to harsh conditions. Mainguet (1994) states quite clearly that the prominent feature of dryland vegetation (and their soils) is resilience and not fragility. In such a climate the most important property of vegetation in soil-erosion control is the ability to break the flow of erosive agents and prevent energy that would cause erosion from being delivered to the soil. As has been discussed in chapter 2, the impact of raindrops on the soil surface was one of the fundamental causes of soil degradation. As early as 1877, the German scientist Wollny recognised that plant canopies and surface mulch protected soil from water erosion primarily by breaking the fall of raindrops (Mainguet, 1994).

In this study the potential and effectiveness of high spatial resolution remote sensing, namely aerial photography, for vegetation cover estimation is assessed. Different approaches, such as vegetation indices, red band reflectance method, geometrical optical models and mixture modelling, that can be used to derive the vegetation map, are discussed and the appropriate method will be implemented.

In order to obtain reasonable results from the mixture modelling, the principles of constraining the linear mixture modelling equation, based on the least squares fitting technique, is discussed and implemented in this study. Since the determination of endmembers is the most important stage in linear mixture modelling, different methods of extracting endmembers are outlined and the method of Principal Component Analysis (PCA) is implemented. In addition, the problem of shade on the extraction of vegetation information is discussed and an algorithm to remove shade effect from vegetation map is applied. The co-occurrence matrix method is proposed and implemented in this study to correct the errors of zero vegetation in some isolated pixels within the vegetation canopy.

After the vegetation cover map is created, this map is validated by comparing it to the vegetation data collected during a field survey in the study area. This vegetation-

cover map will be used in a later chapter for the implementation of the selected soil-erosion model.

5.2.2 The Spectroscopy of Vegetation Leaf

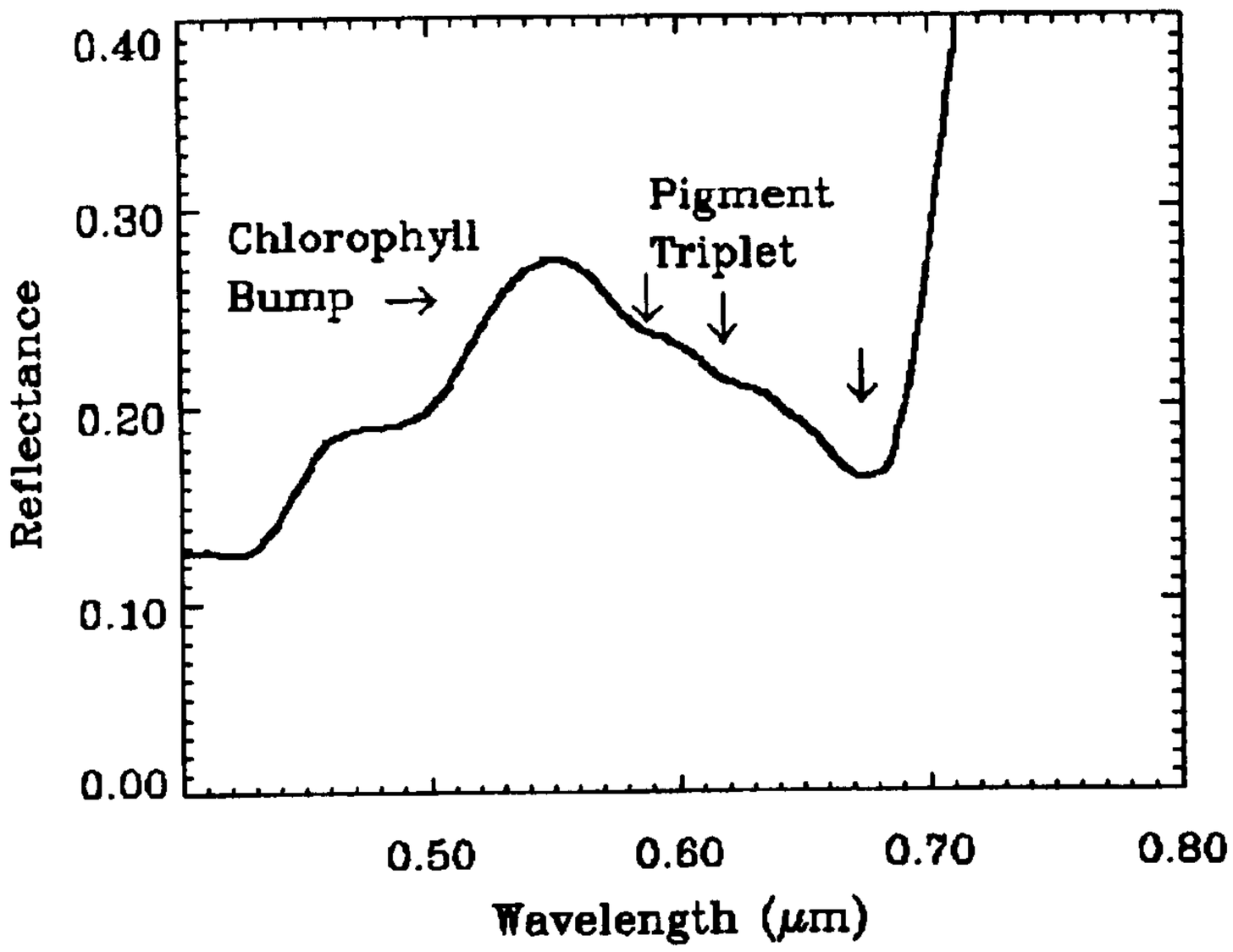

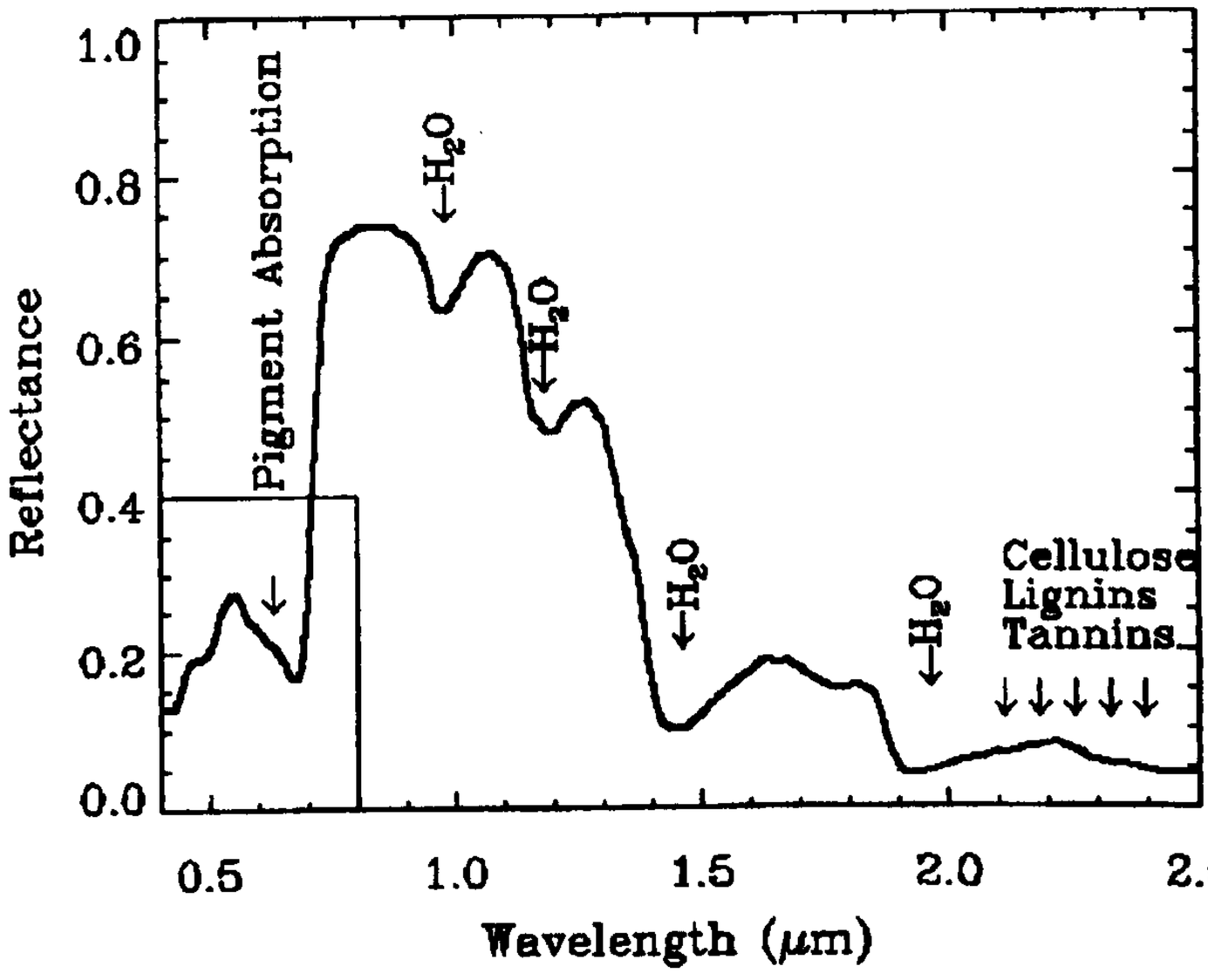

Figure 5.1. Typical green vegetation spectrum of leaf in semiarid environment. Upper plot is an enlargement of the boxed region in the lower plot. The figure shows the pigment absorption in the visible bands. Liquid water in the leaf is the most significant absorber beyond 1.0 μm (adopted from Ray, 1995).

In order to map the vegetation cover of the study area of Vélez Rubio more accurately for the implementation of overland flow and soil erosion, it is important to understand the spectral characteristics of vegetation. This understanding of the vegetation spectrum is crucial, for example, when searching for digital numbers of the vegetation pure endmember to perform the mixture modelling.

Work on the spectral properties of vegetation began as early as 1913 when Willstätter and Stoll proved that light entering leaves is critically reflected internally at the cell walls where the refractive index changes from that of water 1.33 to that of air 1.00 (Ray, 1995). Later on Gates *et al.* (1965) performed some of the earliest work which investigated the spectral properties of plants across the spectrum from the ultraviolet through the thermal infrared in order to acquire a better understanding of vegetation spectrum. Figure 5.1 shows the typical reflectance spectrum of green leaves in the spectral range of visible and near-to-mid-infrared (0.4-2.5 μm) and zoomed in details of the visible spectral range (0.4-0.7μm) because it is of special significance for the aerial photograph data of this study. The figure 5.1 shows that plants pigments, such as chlorophyll, strongly absorb light in the visible and that the liquid water in plant leaves absorbs much of the light at wavelengths longer than 1.4 μm. This contrasts with strong reflectance in the near-infrared in the range from 0.75 μm through about 1.4 μm, wavelengths at which plant materials are relatively transparent.

In the visible part of the spectrum, leaf reflectance and transmittance are low and absorption is high because leaf pigments control leaf reflectance by absorbing light within the photosynthetically active radiation (PAR) region of the electromagnetic spectrum. The main pigments that absorb most of the radiation and control the vegetation reflectance are chlorophyll a and b and carotenoids (Daughtry and Walthall, 1998). In the visible spectrum there are two main absorption bands (figure 5.1): the low reflectance band in the blue wavelength region around 0.4-0.5 μm and the minimum reflectance in the red wavelength region around 0.680 μm, both bands are due to absorption by different types of chlorophyll a and b and carotenoids (Datt,

1999). The vegetation maximum reflectance in the visible spectrum is located around the green wavelength because the radiation that is not absorbed will be reflected.

The vegetation canopies in semiarid environments are characterised by two components: green and dry (non-photosynthetic) vegetation canopy. Although most studies of vegetation reflectance are generally focused on the green vegetation, dry vegetation reflectance cannot be ignored as it affects the reflectances of vegetation canopy and other ground surfaces covered by dry litter (Elvidge, 1990).

Many studies (e.g. Waring *et al.*, 1986, Peterson *et al.*, 1988) suggest that the biochemistry of vegetation canopy can be measured using high spectral resolution remotely sensed data with narrow spectral bands in the order of (~10) *nm* such as the data supplied by AVIRIS (Airborne Visible Infrared Imaging Spectrometer). This biochemistry measurement helps to identify some of the contents of the plant canopy such as lignin and nitrogen contents which serve as an indicator of the green vegetation decay and, consequently, of dry vegetation (Elvidge, 1990). This means that such high spectral resolution remotely sensed data can be used to measure the spectral features of dry vegetation canopy. Figure 5.2 shows the spectral reflectances of some dry vegetation material that can be found in semiarid environments. This figure shows the absence of the chlorophyll and water absorptions which dominate the spectra of green vegetation.

However, the broad spectral bands that are used by most of the remote sensing instruments (e.g. TM, MSS, Spot, and aerial photography camera of this study) cannot measure the distinctive absorption features of dry vegetation (Elvidge, 1990) because these features can be only observed in the narrow spectral bands. In addition, most of these dry vegetation features are present in the near infrared region of the spectrum, whereas the data of this study are aerial photography of visible bands. Furthermore, in this study there is no drive to separate the dry and green vegetation for the purpose of this research. Thus, the vegetation cover that is mapped in this study represents the total vegetation cover.

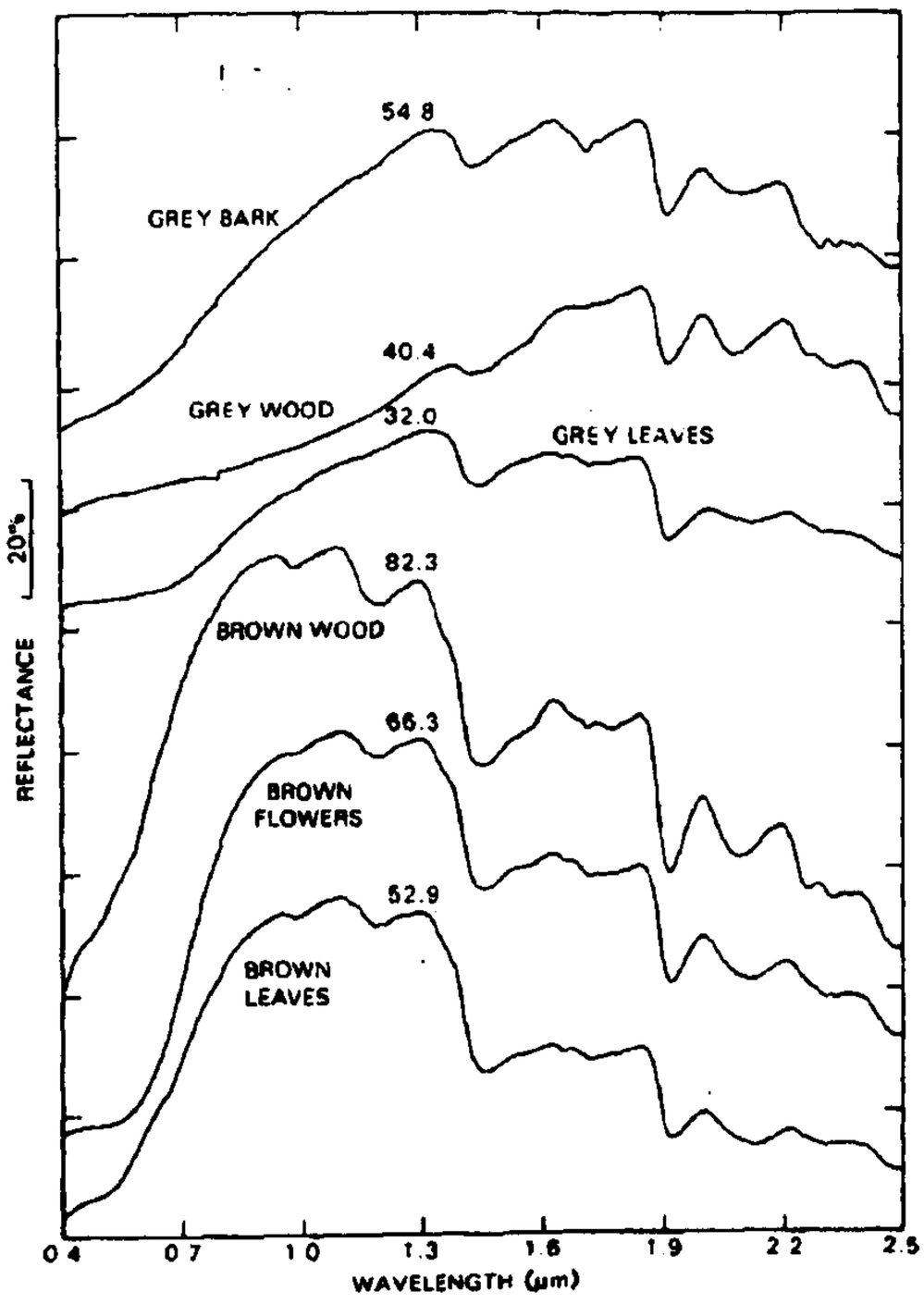

Figure 5.2. Reflectance spectra of some dry vegetation materials in semiarid areas. Spectra are displaced vertically to avoid overlap (after Elvidge, 1990).

5.2.3 GEOMETRICAL OPTICAL MODELS AND VEGETATION INDICES TO MAP VEGETATION COVER

5.2.3.1 Geometrical Optical Models

Geometrical optical models are a vegetation mapping technique which relies on a proposed three-dimensional structure (cylindrical, conical or spherical) of the canopy as the primary factor influencing reflectance from the canopy and are designed to yield estimates of the size and density of trees and bushes from remotely sensed images. In geometrical optical models the determination of the solar zenith angle and the appropriate geometrical shapes which represent the canopy objects is significant and has a substantial effect on the accuracy of vegetation cover mapping (Peddle *et al.*, 1999).

These models have been widely used in remote sensing applications because of their ability to simulate angular variation of remote sensing signals from the Earth's surface and they are generally accurate in the visible part of the solar spectrum, but less accurate in near-infrared part in which multiple scattering in plant canopies is the strongest (Chen and Leblanc, 2001). An example of geometrical optical models is the Li-Strahler model which has been used with some success to simulate the bidirectional and hemispherical reflectance of forest canopies (Peddle *et al.*, 1999). This model estimates the proportion of sunlit and shaded canopy and background of a given tree size and tree density. Although the canopies may have trees of widely varying heights, the underlying terrain has always been represented as level ground in this model. Recently, however, the model has been extended to accommodate sloping terrain in its computation of the forest bidirectional reflectance distribution function and spectral surface albedo. With the model accommodating topography, it has been possible to compute and compare the reflective character of realistic forest canopies on a variety of slopes and aspects (Schaaf *et al.*, 1995).

The geometrical optical models generally assume that the pixel size is much larger than the size of individual tree crowns, but still smaller than the size of forest stands and that the individual trees are randomly distributed within the pixel (Woodcock *et al.*, 1994). In this case the signal received by the sensor is modelled as a combination of reflected light from tree crowns, their shadows, and the background within the field of view of the sensor. Bearing in mind that the pixel size of the aerial photographs in this study is 55 cm, whereas the average size of an almond or olive tree crown is 3-5 meter, the geometrical optical models cannot be used to map the vegetation cover. This is due to the fact that the assumption of a regular geometrical shape for tree crown and bush objects by these models may introduce extreme errors in pixels around these objects where background pixels may be wrongly assigned as canopy and vice versa. Thus, geometrical optical model will not be used to map the vegetation cover and alternative methods will be investigated.

5.2.3.2 Vegetation Indices

Many natural surfaces are about equally bright in the red and near-infrared part of the spectrum, with the notable exception of green vegetation. Red light is strongly absorbed by photosynthetic pigments (such as chlorophyll a) found in green leaves, while near-infrared light either passes through or is reflected by live leaf tissues (Datt, 1999). This means that areas of bare soil having little or no green plant material will appear similar in both the red and near-infrared wavelengths, while areas with much green vegetation will be very bright in the near-infrared and very dark in the red part of the spectrum. These are the underlying principles behind most, but not all, of vegetation indices.

The most commonly used vegetation indices, that utilise the differentiation principles between Red and NIR bands, are the Vegetation Ratio Index (VRI), the Normalised Difference Vegetation Index (NDVI) and the Perpendicular Vegetation Index (PVI) which are expressed in the equations:

$$VRI = \frac{NIR}{Red} \qquad 5.1$$

$$NDVI = \frac{NIR - Red}{NIR + Red} \qquad 5.2$$

$$PVI = (NIR - aRed - b)/(a^2 + 1)^{0.5} \qquad 5.3$$

Where *NIR* is near-infrared reflectance, *Red* is red reflectance, "*a*" is the slope of the soil line and "*b*" is the intercept of soil line.

One of the problems in calculating vegetation indices is the effect of soil background. Huete (1988) suggested a new vegetation index which was designed to minimise the effect of the soil background. This index is called the soil-adjusted vegetation index (SAVI) and expressed in the equation:

$$SAVI = \frac{NIR - Red}{NIR + Red + L}(1 + L) \qquad 5.4$$

Where *L*-factor is related to the differential extinction properties between the red and NIR. *L*-factor ranges between 0 and 1 where L=1, 0.5, and 0.25 for low, intermediate and higher vegetation density respectively (Huete, 1988).

One important difficulty which has been encountered in using vegetation indices that attempt to minimise the effect of a changing soil background is an increase in the sensitivity to variations to atmosphere (Leprieur *et al.*, 1994). There have been several approaches in the development of vegetation indices which are less sensitive to the atmosphere, such as the Atmospherically Resistant Vegetation Index (AVRI) of Kaufman and Tanré (1992) and the Global Environmental Monitoring Index (GEMI) developed by Pinty and Verstraete (1991). Qi *et al.*, (1994) demonstrated that soil noise caused GEMI to break down suddenly at low vegetation covers, and that all of the vegetation indices designed to minimise the effect of the atmosphere have increased sensitivity to the soil, which makes these indices unsuitable to semi-arid regions (Ray, 1995). In addition, a limitation of vegetation indices is that they are only sensitive to the green vegetation and might not recognise nonphotosynthetic vegetation (NPV) (Drake *et al.* 1999). Another limitation of using vegetation indices to estimate the vegetation cover is the problem of shade, cast by either topography or by taller vegetation, which obscures the vegetation partially or totally and creates errors in vegetation cover estimation.

Despite the fact that most of the widely used vegetation greenness indices implement the principles of differentiation between the Red and NIR spectrum, there are some other indices that map the vegetation and canopy cover and utilise the information of the visible bands. These types of the vegetation indices are called brightness indices. There are several brightness indices that have been used by scientists to map vegetation cover such as the red band reflectance, the Kauth-Thomas brightness, and

albedo. The red band reflectance is generally found to have the highest correlation of them (Yang and Prince, 1997).

Moreover, Chavez and Mackinnon (1994) found that if the red is radiometrically corrected, then it becomes more sensitive than the widely used NDVI in detecting vegetation changes in the semi-arid environments. Pickup *et al.*, (1993) investigated various methods, such as calibrated cover-radiance relationships and vegetation indices, to map vegetation cover (green and total vegetation) in arid and semi-arid environment using MSS data. They found that the red visible band "5" of MSS can be a better index of the vegetation cover in such environment than the more traditional near infrared band-based indices, proving a significant correlation at α = 0.05 with a coefficient of determination r^2 of 0.76, 0.83 and 0.84 for dry, green, and total vegetation respectively.

Another example of using the red band reflectance to map vegetation cover in semi-arid areas is the study by Yool *et al.*, (1997) where they implemented time series analysis to create a difference map depicting the change in vegetation cover over a period of time. To do so Yool *et al.*, (1997) used red bands solely, rather than with near infrared NIR bands, of the MSS images because both vegetation and soils in semi-arid areas usually have high reflectance in NIR bands causing the differences in the difference image to be too small (Franklin *et al.*, 1993, Chavez and MacKinnon, 1994). Their results show that red band reflectance successfully mapped the vegetation communities in the semi-arid environment and produced significant correlation.

Due to the fact that the data in this study consist of aerial photographs of the three visible spectral bands: red, green and blue and the absence of the near-infrared and infrared spectral bands, the implementation of red/NIR vegetation indices to map vegetation cover is ruled out. Thus, the red band reflectance, which is based on the visible red band, will be investigated.

5.2.3.3 Investigating the Correlation between Red Band Reflectance and Vegetation Cover

In this study the correlation between the vegetation cover of the semi-arid environment of the study area and the red band reflectance of the aerial photograph has been investigated. To do so ground truth vegetation data were needed. These data were collected by X. Zhang (for full details see Zhang, 1999) at the same time the NERC (Natural Environment Research Council) air campaign took place (the 9th of April 1996) to acquire the aerial photographs of the study area. This research has been restricted throughout to the use of these vegetation ground-truth data for verification purposes because the research started well after aerial photographs were acquired and, in the mean time, the area experienced significant land-use changes.

The collection of ground truth data of vegetation cover was initially carried out at fourteen sample sites. The area of each sample site was composed of a 9×9 metre rectangle, which was divided into twelve sample plots and a photograph was taken in each plot. For determining the location of each sample area, the orientations of plots were measured and more than two landmarks were identified with the distances, orientations and slope angles to the centre of the sample area. The land cover consisted of dense grass, sparse and dense matorral, almond fields, and a burned area that was regenerating back to matorral. Because some slides were under exposed, only some of them were used to calculate vegetation cover in nine sample locations by projecting them to a grid (Zhang, 1999). Figure 5.3 shows the locations of these vegetation plots.

In order to assess the adequacy of using the red band reflectance (band 3 in the aerial photographs) for mapping the vegetation cover in this study, the correlation between this red band and the vegetation fractions measured in the field in the nine vegetation plots was assessed. Figure 5.4 shows a plot of correlation assessment between the red band reflectance of band "3" and the fractions of measured vegetation cover. The following equation expresses their regression:

Figure 5.3. The location of the vegetation plots where vegetation cover has been measured in the field.

$$V = 60.63 - 0.314R \qquad 5.5$$

$$r^2 = 0.8091$$

$$F = 13.34 \, , \, p = 0.0081$$

Where R is the red band reflectance, and V represents vegetation fraction.

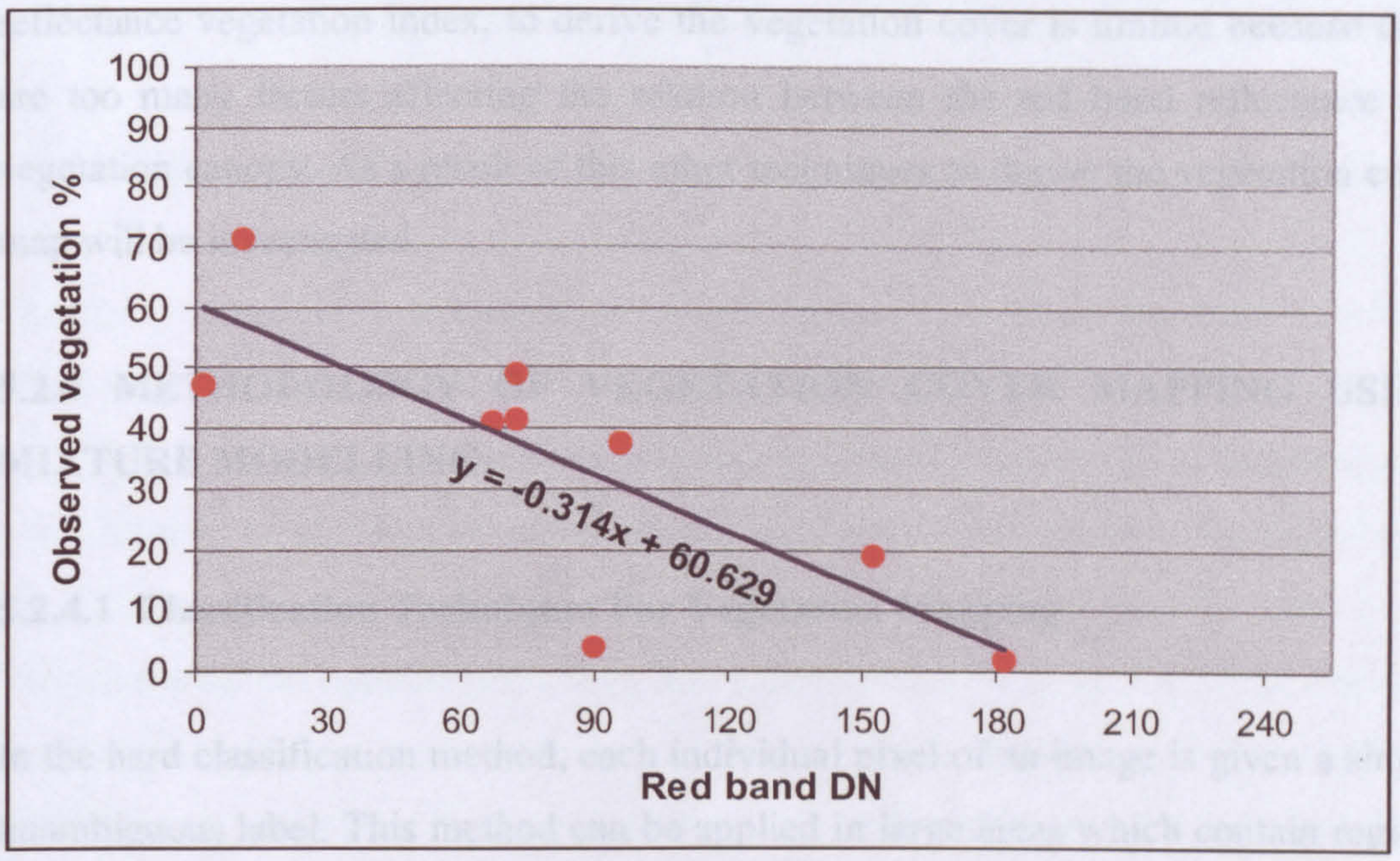

Figure 5.4. Regression of red band reflectance of the aerial photograph that covers the study area against the vegetation fractions measured in the field. Red band reflectance is re-scaled from 0-255 to 0-100 %.

This result of the correlation supports the findings of a large number of studies, some of which were discussed above, that red band reflectance in the visible region of the spectrum could be used as an index of vegetation cover due to the strong correlation that exists between them. Unfortunately 8 out of 9 of the ground truth vegetation samples were collected in plots with a grey soil background and only one vegetation sample with a red soil background. This limited our ability to test the influence of red background soil on the red band reflectance of the vegetation cover.

However, various studies on this correlation found that this relation between red band and vegetation is influenced by different factors such as solar zenith, shadows, background reflectance and topography (Musick, 1986; Franklin *et al.*, 1991). In addition, the red band reflectance method has a disadvantage of not discriminating vegetation because its response to changing greenness is limited (Pickup *et al.*, 1993).

It has been found that the implementation of brightness indices, such as red band reflectance vegetation index, to derive the vegetation cover is limited because there are too many factors affecting the relation between the red band reflectance and vegetation canopy. As a result of this other techniques to derive the vegetation cover map will be investigated.

5.2.4 METHODOLOGY OF VEGETATION COVER MAPPING USING MIXTURE MODELLING

5.2.4.1 Classification Techniques For Vegetation Mapping

In the hard classification method, each individual pixel of an image is given a single, unambiguous label. This method can be applied in large areas which contain regions of a number of pixels of relatively homogenous vegetation cover such as the case of wheat fields in remotely sensed imagery. However, it is unacceptable in some cases to assume that a single pixel is wholly covered by vegetation solely, rather, the spectral reflectance in the pixel represents a mixture of vegetation alongside other land-cover components such as soil background.

A typical example for this case is the vegetation cover in the semi-arid areas, such as the study area of Vélez Rubio, where the natural vegetation, as well as the almond and olive plantations, are discontinuous over short distances of a few metres. Thus, the pixels of any remotely sensed imagery in this case ought to be representing a mixture of vegetation cover and soils. In our study area it was found that matorral is mixed even at the 0.55 m spatial resolution of the aerial photographs. This spectral mixture problem is usually present when the scale of variability of vegetation is less than the size of the pixel of the remotely sensed imagery. Another problem that hard classification methods fail to tackle is capturing the information about the vegetation cover gradients. In such a case the hard classifier labels the pixels as vegetation or non-vegetation disregarding all the wealth of information about the vegetation level and rendering them redundant.

To overcome these hard classification problems, soft classification techniques, such as the mixture modelling method and the fuzzy classification, can be implemented.

5.2.4.2 Fuzzy Classification

The fuzzy classifier is a method of classification which does not reach a definite conclusion in favour of one class or another. Instead, this soft classifier presents the user with a measure of the degree (termed membership grade) to which the given pixel belongs to some or all of the candidate classes, and leaves to the investigator the decision as to the category into which the pixel should be placed (Mather, 1999). This classification method recognises that a pixel may belong to more than one class and each class has a membership grade which ranges between 0 and 1 where the higher values indicates a higher probability that a pixel belongs to the specific class.

The fuzzy classification approach has a wide range of applications especially when users wish to present their results with a degree of uncertainty or fuzziness. For example, when studying semi-natural landscapes it is acceptable to think that different land covers merge gradually in transition zones which do not belong to a specific land cover. Another example of fuzzy classification is the case of studying vegetation patches in semi-arid areas where the land-cover type changes gradually from vegetated to non-vegetated land.

One of the most widespread unsupervised fuzzy classifiers is the fuzzy c-means clustering algorithm. In this algorithm the cluster process represents the distance between each pixel in an image and a set of cluster centres. A user defined factor "m" is used as a weight for this distance and this factor can take any value between 1 and 30. A small value of m indicates that membership function values approach equality where as a value of m equal to 1 means that cluster membership is hard (Mather 1999).

Although fuzzy classification approach for vegetation mapping has recently attracted increasing interest in the land management and the ecological community (Zhang

and Foody, 2001, Maselli *et al.*, 2000), fewer studies have implemented, assessed and verified this approach for vegetation mapping in a semi-arid environment. Rather, most of the established studies of mapping vegetation cover, which is needed for land degradation and soil-erosion modelling, have successfully implemented other approaches and the mixture modelling approach is the best example (see Gillespie *et al.*, 1990, Drake 1991, García-Haro *et al.*, 1996, Foody *et al.*, 1997, Tompkins *et al.*, 1997 Drake *et al.*, 1999, Maas, 2000, Brown *et al.*, 2000)). As a result of this, the fuzzy classification approach will not be used in this study and the alternative approach of mixture modelling is investigated below.

5.2.4.3 Mixture Modelling

The mixture modelling is a soft classification method which assumes that the characteristics of the image pixels of the landscape are combinations (linear or non-linear) of a number of basic ground cover types such as sunlit leaves, shadow, non-photosynthetic vegetation (NPV) and soil. In reality, the pixel size is determined by factors such as the instantaneous field of view (IFOV) and satellite altitude, therefore, the area covered by the pixel is independent of the extent of these ground covers (vegetation cover is one of them) (Foody *et al.*, 1997). As a result of that a pixel in a remotely sensed image can contain different ground features which will be represented in that pixel in a form of spectral mixture. The pure pixels of these cover types are called endmembers.

The mixture modelling approach uses the mathematical principles of least squares fitting techniques (this will be explained later on in this chapter) to produce a set of maps, one for each ground cover type. In these maps each pixel has a fraction value between 0 and 1 for every cover class, so that each cover map contains a continuous range of quantitative fractions. A high fraction value of a pixel in these maps indicates that a large area of that pixel is covered by the relevant cover type while a low fraction value means that a little of the cover type (Bastin 1997). Mixture modelling uses the digital numbers of the pure endmembers in the process of unmixing and, as a result, the cover maps resulting from mixture modelling are

fractions of these endmembers. In contrast, the classification techniques, which have been discussed earlier, are used in remote sensing to derive different type of information about ground cover classes such as land-use and land-cover maps.

The mixture-modelling approach is widely used and more reliable and accurate for vegetation mapping than the vegetation indices approach. Shimabukuro *et al.*, (1998), for example, assessed the two methods of a vegetation index (NDVI) and spectral linear mixing model for monitoring and estimating the vegetation cover. They found that mixture modelling produced higher accuracy results than vegetation index, as well as higher sensitivity of vegetation fraction image to land-cover variation when compared to vegetation index image. Wang (2000) also did an extensive study to compare various vegetation indices and mixture modelling to map vegetation cover and his findings support the finding of Shimabukuro *et al.*, (1998) that mixture modelling produces the highest accuracy. Drake *et al.*, (1999) implemented mixture modelling to map soils, geology, and vegetation in semiarid areas and they found that mixture modelling provides a good tool for vegetation mapping, despite the fact that mixture modelling is sensitive to noise.

The sub-pixel targets on the ground can be detected spectrally under certain conditions of spectral contrast, spectral sampling, and instrumental noise. However, there are factors that limit the spectral detection of these sub-pixel targets. For example, Siegal and Goetz (1977) studied one of these limiting factors, that is the masking effect of vegetation on the detection of rocks and soils. Siegal and Goetz found that the form of a composite spectrum of vegetation and the underlying material depends upon both the fractions and the spectra of the surface components. They reported that some absorption features of soils underlying the vegetation can be obscured by as little as 10 per cent of green vegetation. However, deeper absorption features of soil can still be detected from soil surfaces covered with 60-80 per cent lichen cover (Ager and Milton, 1987).

We can differentiate between two types of the mixture modelling; 1)- the non-linear and 2)- the linear method.

5.2.4.4 Linear and Non-Linear Mixture Modelling.

Most of the mixture modelling methods assume that the spectral mixture at the sub-pixel level occurs in a linear manner in order to facilitate the process of unmixing, however, this spectral mixture is often non-linear. As a result, it is important to understand the linear and non-linear forms of mixing in order to know their advantages and limitations and to implement the appropriate form of mixture modelling in this study.

The relationship between linearity (or non-linearity) and spectral mixing has been investigated by a number of scientists. There is a large number of cases in the literature of remote sensing and spectral studies (Borel and Gerstl. 1994, Fischer 1994) where the spectral response at the sub-pixel level takes the form of non-linear mixture. For example, Singer and McCord (1979) linked the mixture linearity, in general, to the spatial scale and found that the linear spectral mixing can occur at the larger scale (macroscopic) whereas the non-linear mixing occurs for the macroscopic or intimate mixtures. Another very-well known example of that is when one of the ground cover types (such as a bright soil or snow) is proportionally over-represented in a pixel due to its higher contrast characteristics compared to the other ground cover types in that pixel (Kruse *et al.* 1993). The linear model of spectral mixture is generally considered to be valid when the different materials are mixed in a "checkerboard" pattern (see Smith *et al.*, 1990; Boardman, 1994). In the "checkerboard" mixing condition, light reflecting from the surface interacts with one and only one target material before entering the remote sensing instrument. The mixing of the light occurs in the instrument as light from adjoining squares too small to be resolved is focused into a single pixel (Boardman, 1994).

In the case of vegetation, which is the focus of this chapter, the vegetation cover in the semiarid environment, such as the matorral natural vegetation cover in Vélez Rubio, is mostly sparse and the dominant feature in the acquired remotely sensed imagery of such areas is the background soils. In this case the spectral detection of

the vegetation cover is affected by the variability of the reflectance soil background and by the interactions between the plant canopies, their shade, and soil background (Ray and Murray, 1996). This is because light can penetrate the plant leaves and may then be reflected by soil, thus the received reflectance is a non-linear function of vegetation and soil fraction. Figure 5.5 demonstrates the two cases of linear and non-linear interaction of light with ground covers.

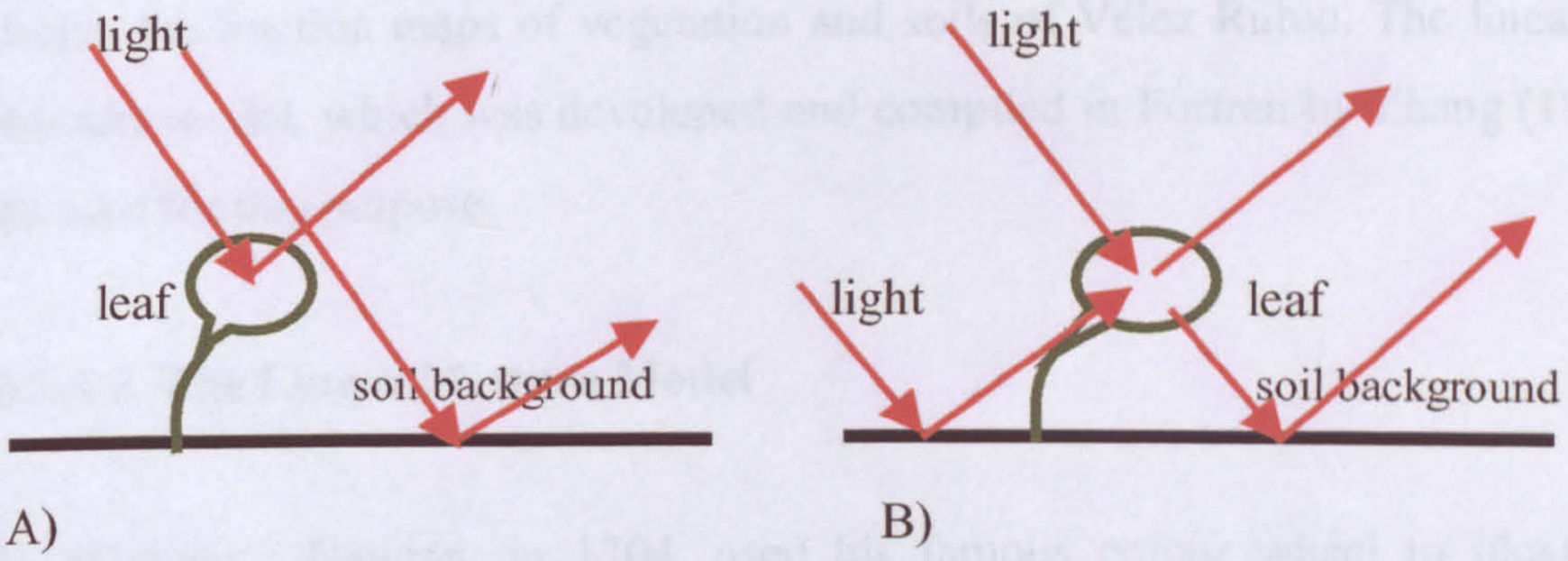

Figure 5.5. A sketch showing the differences between the A) linear and B) non-linear mixture of light reaching the sensor after interacting with ground covers.

In their study on the effect of soil background on vegetation detection, Huete *et al.*, (1985) observed a remarkable change in the cotton-canopy greenness if the soil background is changed and they attributed this change to the non-linear mixture of soil and cotton canopy. Qin and Gerstl (2000) also carried out a study to investigate the linearity of spectral mixture of vegetation, shade, and soil background in the semiarid area of Jornada, New Mexico, using a wide range of data with different spatial resolution between 0.60 *m* to 7 *km*. They found that the dominant characteristic of the natural vegetation cover in semiarid areas is heterogeneity with very complex small-scale details and non-random spatial structures. Qin and Gerstl (2000) concluded that the spectral mixture is related to spatial scale and that it deviates from linearity at the very small scale (where the pixel size is smaller than the size of a shrub) and that the linear mixture hypothesis is more valid at the larger scale due to the low spatial density of plants.

The linear mixture modelling approach is widely applied to multispectral data because it can produce reasonable results and is relatively simple to apply (Tompkins

et al., 1997; Drake *et al.*, 1999; Brown *et al.*, 2000). Examples of this approach can be found in geological, climatological, and vegetation studies (Drake *et al.*, 1991; Drake *et al.*, 1995; Maas, 2000). In the case of vegetation studies, which are of special interest in this chapter, linear mixture modelling provides a remote sensing procedure to assess the compositional distribution of vegetation and its change at a regional scale, and also to estimate accurately its aerial extent over the scene for field or inventory purposes (Garcia-Haro *et al.*, 1996). As a result, the linear mixture modelling, as apposed to non-linear mixing, will be implemented in this study to derive the fraction maps of vegetation and soils of Vélez Rubio. The linear spectral mixture model, which was developed and compiled in Fortran by Zhang (1999), will be used for this purpose.

5.2.4.5 The Linear Mixture Model

In "Opticks", Newton, in 1704, used his famous colour wheel to illustrate how differently coloured light when mixed in various proportions would produce a colour of light different from any of the colours that had been combined. Newton used this colour wheel to predict and demonstrate what colour would be produced by mixtures of individual colours. If Newton's colour wheel could be inverted, then it is possible to find what proportions of given colours would have to be combined to produce the colour of interest. Newton's example is closely related to the concept of the linear mixture modelling. In the case of linear mixture modelling, the spectral reflectance of a pixel is assumed to be a linear combination of various components (Smith *et al.* 1990, White and Drake 1993).

Generally speaking, linear mixture modelling is based on four assumptions (Drake 1991, Settle and Drake 1993). First, there is no significant amount of multiple scattering between the different cover types, and thus each photon that reaches the sensor has interacted with just one cover type. Second, all the components in an image have sufficient spectral contrast to allow their separation. Third, in each pixel of an image, the land cover is defined to be unity. Fourth, each endmember must be known.

The following equation expresses the linear spectral mixture model:

$$y_i = \sum_{j=1}^{n} r_j f_{ji} \qquad 5.6$$

where y_i is the reflectance in the i^{th} pixel, f_{ji} is the fraction of the j^{th} type of land cover in the i^{th} pixel, r_j is the spectral reflectance of the endmember in the j^{th} type of land cover.

When we express the linear mixture in terms of matrix notation (with n pixels, m endmembers and l spectral bands, where $m \leq l$, is considered) the previous equation 5.6 can be expressed as:

$$Y = RF \qquad 5.7$$

Where Y is the spectral reflectance matrix, R is the endmember's reflectance matrix and F is a fraction matrix. These matrices take the following forms:

$$Y = \begin{bmatrix} y_{11} & y_{12} & \cdots & y_{1n} \\ y_{21} & y_{22} & \cdots & y_{2n} \\ .. & .. & .. & .. \\ y_{l1} & y_{l2} & \cdots & y_{ln} \end{bmatrix}, \quad R = \begin{bmatrix} r_{11} & r_{12} & \cdots & r_{1m} \\ r_{21} & r_{22} & \cdots & r_{2m} \\ .. & .. & .. & .. \\ r_{l1} & r_{l2} & \cdots & r_{lm} \end{bmatrix} \text{ and}$$

$$F = \begin{bmatrix} f_{11} & f_{21} & \cdots & f_{1n} \\ f_{21} & f_{22} & \cdots & f_{2n} \\ .. & .. & .. & .. \\ f_{m1} & f_{m2} & \cdots & f_{mn} \end{bmatrix}$$

Most of the remote sensing studies that use linear spectral mixture modelling implement a least squares fitting technique to find the coefficients for each target material spectrum in the linear combination that will produce the observed spectrum, with the resulting coefficient taken to be the relative abundance (or the fraction) of the given material (Smith *et al.*, 1990; Boardman, 1994). In order to find a solution

for the spectral fraction matrix F we apply the least squares method. The fractions of land cover F can be expressed as:

$$F = (R^T R)^{-1} R^T Y \qquad 5.8$$

In the solution of this equation, we can differentiate between two cases: the first case is when the number of endmembers (m) equals to the number of spectral bands (l). In this case the residual vector resulting from the 5.8 equation is zero with the precisely unique solution for $\hat{F}$ ($Y = R\hat{F}$). The second case is when $m<l$ and the solution $\hat{F}$ approximates F ($Y \approx R\hat{F}$) with minimal residuals. In this case the equation 5.7 can be changed to accommodate these resulting errors:

$$Y = RF + \varepsilon \qquad 5.9$$

Where ε is the errors vector.

Under ideal conditions, the equation 5.7 can produce reasonable results. These ideal conditions include the fact that each pixel 1- is linearly mixed, 2- only contains the components of interest, 3- is free of any noise, 4- and the determined endmembers are ideally pure. However, because of the error associated with measurements, it cannot be guaranteed that all the results of the mixture modelling will produce physically acceptable coefficient values in the real world. That is that negative coefficient values or values of more than 100% land cover should be expected to occur (Zhang 1999).

Some researchers such as Roberts *et al.* (1994) and Smith *et al.* (1990) take these negative coefficient values and values greater than 100% to indicate either an incorrect choice of endmembers or non-linear spectral mixing. So it is a very common practice to constrain the mixture modelling so that that sum of coefficient values, and hence the total fractions of materials in a pixel, is equal to one. Other researchers such as Boardman (1993) have constrained the coefficient values to be non-negative, forbidding unphysical negative fractions in the pixel. It is also possible to constrain that the coefficient values to be non-negative and that the sum of the

fractions must not exceed one, which restricts the fractions to physically realistic fractions between zero and one.

In the model, the equation 5.9 can be constrained by applying the linear equality method in order to make it more applicable. That is the fractions of land covers in a pixel should add to unity. This can be expressed as follows:

$$b_i = \sum_{j=1}^{m} f_{ji} = 1 \qquad 5.10$$

or in terms of matrix notation:

$$B = \{1,1,.....1\} \qquad 5.11$$

This equality constraints equation can be regarded as a part of the linear equations and their functions are equal to those of any other linear equations. In this case the maximum number of endmembers can rise up to l+1. This group of equations can be used to solve no more than l+1 variables based on l+1 independent equations. The group of linear equations $Y = RF$ and equality constraints $B=UF$ play an equal role in solving variables in the process of least squares fitting (Zhang 1999).

$$\begin{cases} Y = RF \\ B = UF \end{cases} \Rightarrow \begin{bmatrix} Y \\ B \end{bmatrix} = \begin{bmatrix} R \\ U \end{bmatrix} F \qquad 5.12$$

where $U=\{1, 1,.....1\}$.

Another way of applying the linear equality constraints on the equation 5.9 is to find solutions when the equality $UF = B$ is satisfied. In this case the number of endmembers should be $\leq l$. Therefore the mixture model becomes:

$$/Y - RF/ = min \qquad \text{subject to} \quad UF = B \qquad 5.13$$

When the linear equality constraints mixture modelling solved on the basis of null space, an explicit parametric representation of the members of the linear flat can be used (Lawson and Hanson 1974, Menke 1984). The unique solution vector is:

$$\hat{F} = U'B + K_2(RK_2)'(Y - RU'B) \qquad 5.14$$

Where $K_2 = m\text{-}K_1$, and K_1 is the rank of matrix U.

In this study we are restricted by the fact that the aerial photographs of the study area have only three spectral bands: blue, green, and red bands. However, the number of endmembers that are incorporated in the process of mixture modelling is four representing grey soil, red soil, vegetation, and shade. As a result, the equality constraints equation should be regarded as a part of the linear equations and the equation 5.12 will be implemented in the least squares fitting.

5.2.4.6 Endmember Extraction for Linear Mixture Modelling.

The first stage in spectral mixture modelling is to locate the purest pixels of each ground component within the image, these pure pixels are called endmembers. Tompkins *et al.* (1997) describe the process of selecting spectral endmembers as the most difficult step in linear spectral mixture analysis. Endmembers maybe time-dependent and may have different spectral responses at different times of the same location. The change of image endmembers spectral response over time can be detected when compared against reference endmembers developed in the laboratory or in the field (Adams *et al.* 1995).

Over the years a range of different approaches to select the endmembers for mixture modelling have been developed. One approach is to select endmembers by linking reflectance measured by field and/or laboratory instruments with image relative radiance measurements acquired by satellite images (Jackson 1983, Huete *et al.* 1985, Pech *et al.* 1986). The main problem is that it is difficult to calibrate the atmospheric effects when making the field measurement match the image radiance, and to remove variations in lighting geometry caused by topography and other factors. However, in this research we are limited by the fact that aerial photographs are used which prevents any type of atmospheric correction.

Another approach to select endmembers, described by Bateson and Curtiss (1996), is a manual selection method. This method is a multidimensional visualisation technique for interactively exploring the mixing space in search of spectra to designate as endmembers by looking for extreme pixels. A third approach of endmember selection, which is widely used, is the Principal Components Analysis (PCA) method. In this method it is assumed that the pure endmembers lie at the extremes of the distribution of pixel signatures in the principal components feature space. The number of extremes is equal to the number of spectrally distinct surface components (Wang, 2000). Smith *et al.* (1990) applied PCA analysis interactively with visual analysis of the data clusters to identify the characteristic endmembers in an image, then calibrated them based on laboratory and field measured reflectance of reference endmembers.

Asner and Lobell (2000) describe a completely new approach for endmembers selection using the fuzzy endmember sets and bundles method. In this method a range of endmembers are derived from fieldwork or from image pixels which represent the natural variability of ground cover components, such as soils and vegetation, and then implemented in the process of mixture modelling. This method is proven to produce good results, however, it is laborious and time consuming because it needs a large database of a wide range of endmembers in the study and it also needs atmospheric corrections.

Boardman (1994) has proposed an automatic technique of identifying endmembers through the use of convex geometry. However, in the case of a dataset with a great deal of heterogeneity, no single set of endmembers will be suitable to carry out the mixture modelling on the entire image.

The accuracy of fraction maps resulting from linear mixture modelling greatly depends on the adequate and correct selection of the endmembers, hence, a technique that can produce these fraction maps without the need for endmembers would be desirable. Such a technique has been developed by Boardman (1992), and it is called Spectral Angle Mapping (SAM). This technique measures the similarity between the

spectrum of the pixel, and user-supplied test spectra. The spectra are considered to be vectors in *n*-space, where *n* is the number of bands in both spectra. The angle between these spectra can be found by taking their dot product and the results plotted as an image. When the vectors are parallel, the spectrum of the pixel is the same as the test spectrum, and the pixel could then be considered to be entirely covered by the material whose spectrum was being tested, and if the angle between the vectors is 90° then the pixel does not contain any of the tested material (Ray, 1995).

In this study the principal component analysis method is used to select the endmembers for the mixture modelling. This is because of the simplicity of this method, which derives the endmembers directly from the image, and that the aerial photographs of the study area do not need atmospheric corrections before selecting endmembers from image data.

5.2.4.6.1 Endmembers Derived From Principal Components Analysis

In a multispectral remote sensing image the adjacent spectral bands are generally correlated. Mather (1999) demonstrates an example of multiband visible/near-infrared images of vegetated areas where negative correlations exist among the near-infrared and visible red, as well as positive correlations among the visible bands. This occurs because the spectral characteristics of vegetation are such that as the greenness of the vegetation increases the red reflectance diminishes and the near-infrared reflectance increases. This type of correlation that exists among spectral bands indicates that some information (contained in some image bands) is repeated, hence, spectral bands can be mathematically transformed into a more efficient and independent form to minimise redundant information and reduce data dimensionality.

Principal Components Analysis (PCA) is a method of data transformation performed to determine the dimensionality of a dataset, as well as the main axes of variability of the dataset. The new axes created by the PCA transformation have the advantage of being uncorrelated. There are many advantages of carrying out a PCA transformation

on an image dataset. One of the advantages is the fact that the size of the data can be dramatically reduced by reducing the data dimensionality (or the number of image bands). This speeds the image handling and processing. Another advantage, which is more essential in remote sensing techniques, is that the transformed image may reveal different sorts of relationships between groups of pixels representing some ground features when the data is visualised in terms of PCA axes.

PCA transformation is one of the most commonly used method for identifying candidate image endmembers. Smith *et al.* (1985) and Johnson *et al.* (1985) used this technique to determine the type of mixing, define the potential endmembers of the mixture, and estimate the relative fractions of endmembers in mixtures. When you plot principal components against each other, the pixels representing the endmember for each material should be located at the vertices of the polygon that bounds the data space of the principal components which contain information (Murphy and Wadge 1994). The PCA technique has an advantage in that it makes no assumptions about the interdependence of the set of variables (bands). In this technique the variance/covariance matrix is first calculated, then the new coordinates system is found by maximising the variance/covariance matrix of the data. Mathematically this is shown as:

$$A_{ij} = \sum_{l=1}^{n} [(R_{il} - \overline{R}_l)(R_{jl} - \overline{R}_l)] \qquad 5.15$$

where A_{ij} is the covariance matrix element, $R_{i,l}$ is the scaled reflectance of the i^{th} pixel at wavelength l and is the average scaled reflectance over all pixels at wavelength l. Minimisation of the matrix A derives the eigenvalue/eigenvector equations:

$$|A - \lambda I| = 0 \ and \ (A - \lambda I)\hat{e} = 0 \qquad 5.16$$

where I is the identity matrix, λ is the eigenvalue of the matrix A and $\hat{e}$ is the eigenvector. The eigenvectors are the new coordinate axes and the eigenvalues are representative of the amount of the variance covered by the corresponding eigenvector.

After the PCA transformation is carried out, the multispectral image bands are represented in new axes that are orthogonal to each other. If there is significant correlation between the original images, most of the image information will be contained in the first few components (Canas and Barnett 1985).

5.2.5 IMPLEMENTATION OF MIXTURE MODELLING

5.2.5.1 Endmembers Extraction from The Aerial Photograph

The PCA transformation was carried out using the PCA algorithm in the IDRISI package. This transformation was applied to the multispectral aerial photograph of the study area of Vélez Rubio which consists of three visible bands; band1 (blue), band2 (green) and band3 (red). Before the image transformation is performed, the variance-covariance matrix is calculated and the eigenvalue and eigenvectors are extracted from the image calculation. Table 5.1 shows the transformation results of the correlation matrix, eigenvalues, and eigenvectors. These results reveal that the correlations between all bands, especially between the green and red bands, in this aerial photograph are high. This comes in line with the finding of Galvao *et al.* (1999) that visible bands in remotely sensed imagery are highly correlated. In addition, table 5.1 shows that the first principal component PC1 expresses 93% of the image variance after transformation whereas PC2 and PC3 express 5.5% and 1.5% respectively, which means that most of the endmembers can be found in the feature space of PC1 and PC2.

In table 5.1 the rows of the variance-covariance matrix specify the reverse transformation from PCA components back to the original bands. The variance-covariance matrix, eigenvalue and eigencectors are then implemented by the PCA algorithm to perform the transformation and produce three component bands that are uncorrelated and orthogonal to one another. Figure 5.6 shows these three principal components, where the first component PC1 contains the most of the image information and that the image information is degraded in PC2 and the least information is contained in PC3.

Variance/Covariance	Red band	Green band	Blue band
Red band	4628.11	3418.30	2764.68
Green band	3418.30	2845.31	2352.57
Blue band	2764.68	2352.57	2418.45
Correlation Matrix	**Red band**	**Green band**	**Blue band**
Red band	1.000000	0.941983	0.826369
Green band	0.941983	1.000000	0.896828
Blue band	0.826369	0.896828	1.000000
Component	**C 1**	**C 2**	**C 3**
% var.	93.08	5.54	1.39
Eigenvalue	9207.11	547.64	137.12
Eigenvector1	0.471072	-0.806146	0.358078
Eigenvector2	0.546111	-0.052254	-0.836081
Eigenvector3	0.692715	0.589405	0.415630

Table 5.1. The statistical results of the PCA transformation applied to the bands of the aerial photograph.

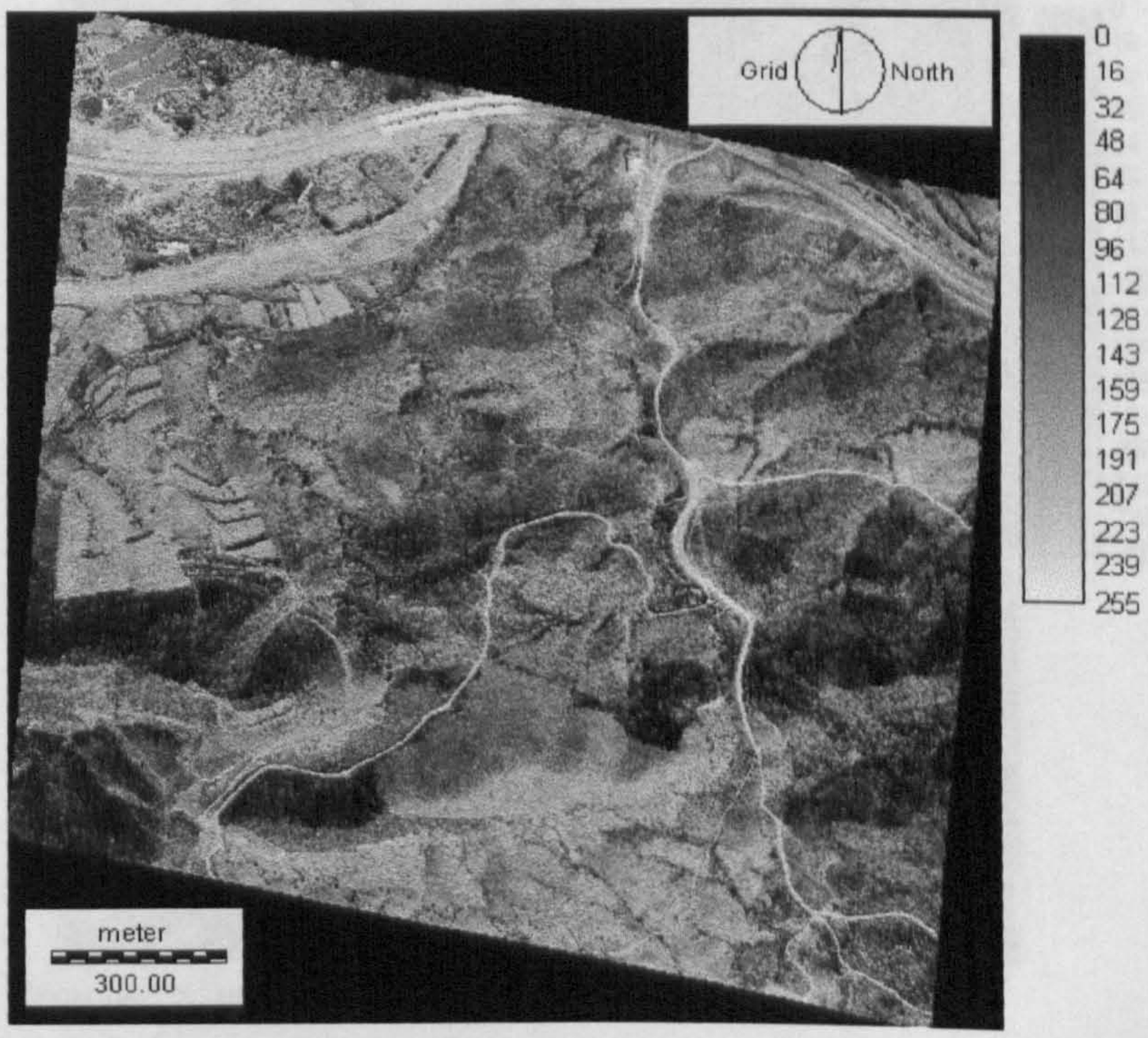

Principal Component 1.

Figure 5.6. Three new images (principal components) resulted from the PCA transformation.

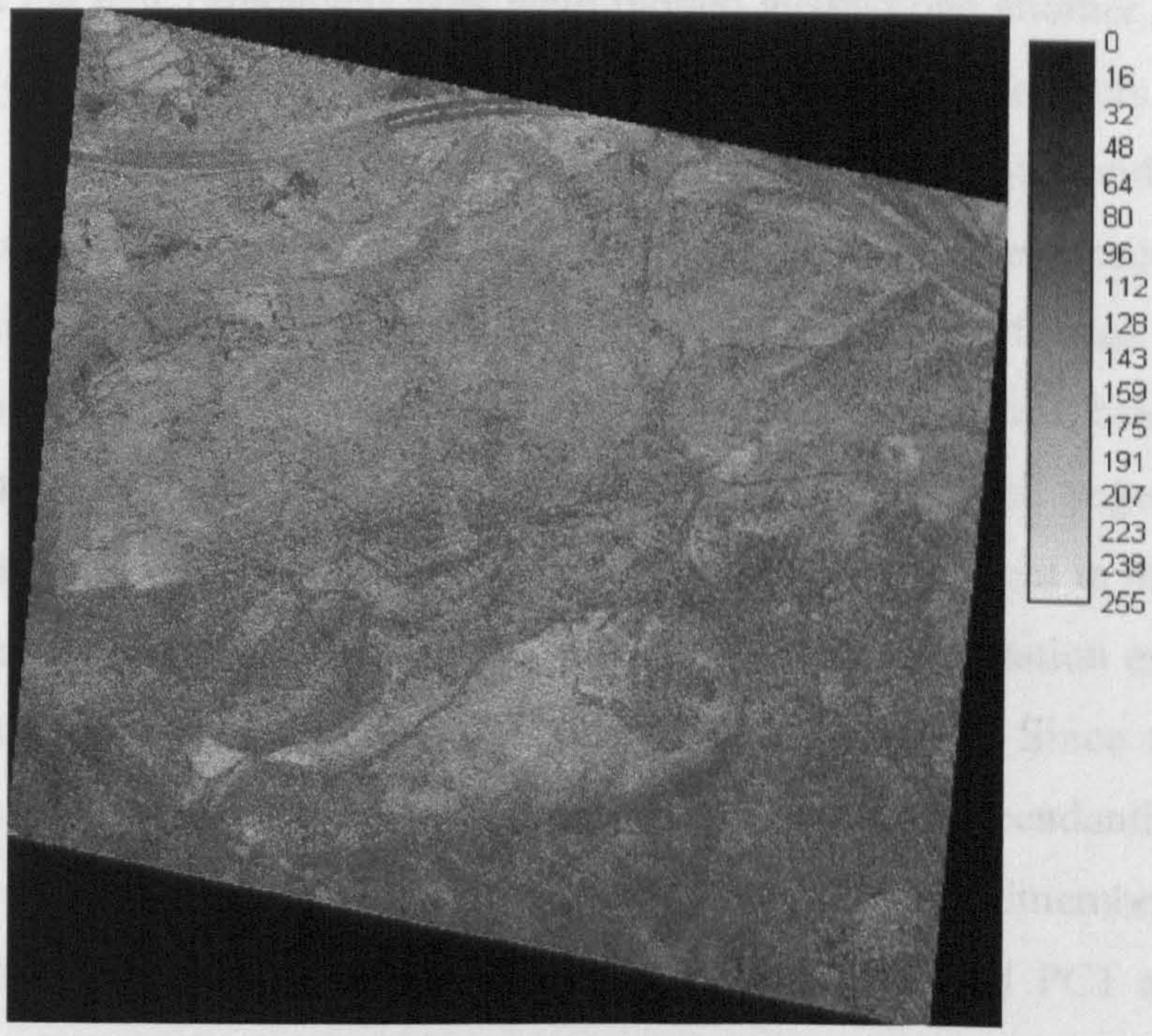

Principal Component 2.

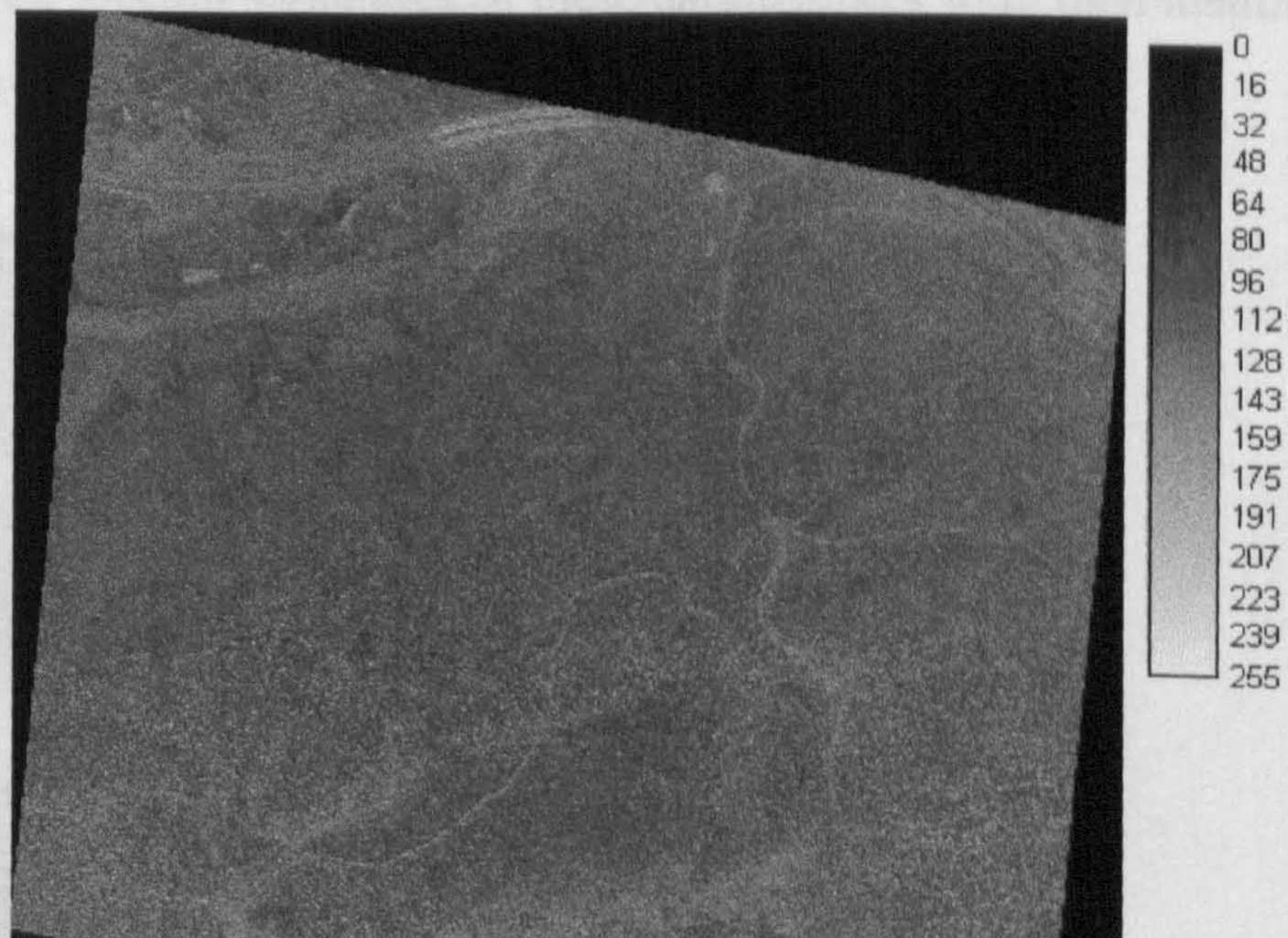

Principal Component 3.

Figure 5.6. *Continued ....*

In order to determine the spectral signatures of endmembers of the ground cover components the new orthogonal axes were plotted against one another. The vertices of the polygons represent potential endmembers. Seven endmembers are defined, some more than once at slightly different locations (i.e. red soil and vegetation). However, as only four endmembers can be used with only three spectral bands of imagery, some endmembers need to be ignored. We chose to discard endmembers that were anthropic and only covered small areas (i.e. unpaved road, bridge concrete, and tarmac). Thus, endmembers representing grey soil, red soil, vegetation cover, and shade (Figure 5.7) are selected. These endmembers are present in more than one scatterplot as figure 5.7 shows, for example, the potential vegetation endmember is present in the scatterplots PC1 and PC3 and PC2 and PC3. Since the principal components resulted from PCA transformation are ranked, descendantly, from PC1 to PC3 in terms of image information they contain, the endmember present in scatterplot PC1 and PC2 has priority over PC1 and PC3, and PC1 and PC2 has priority over PC2 and PC3 and the endmembers were selected according to these priorities. The spectral signatures of these endmembers were then identified from the original three visible bands (table 5.2).

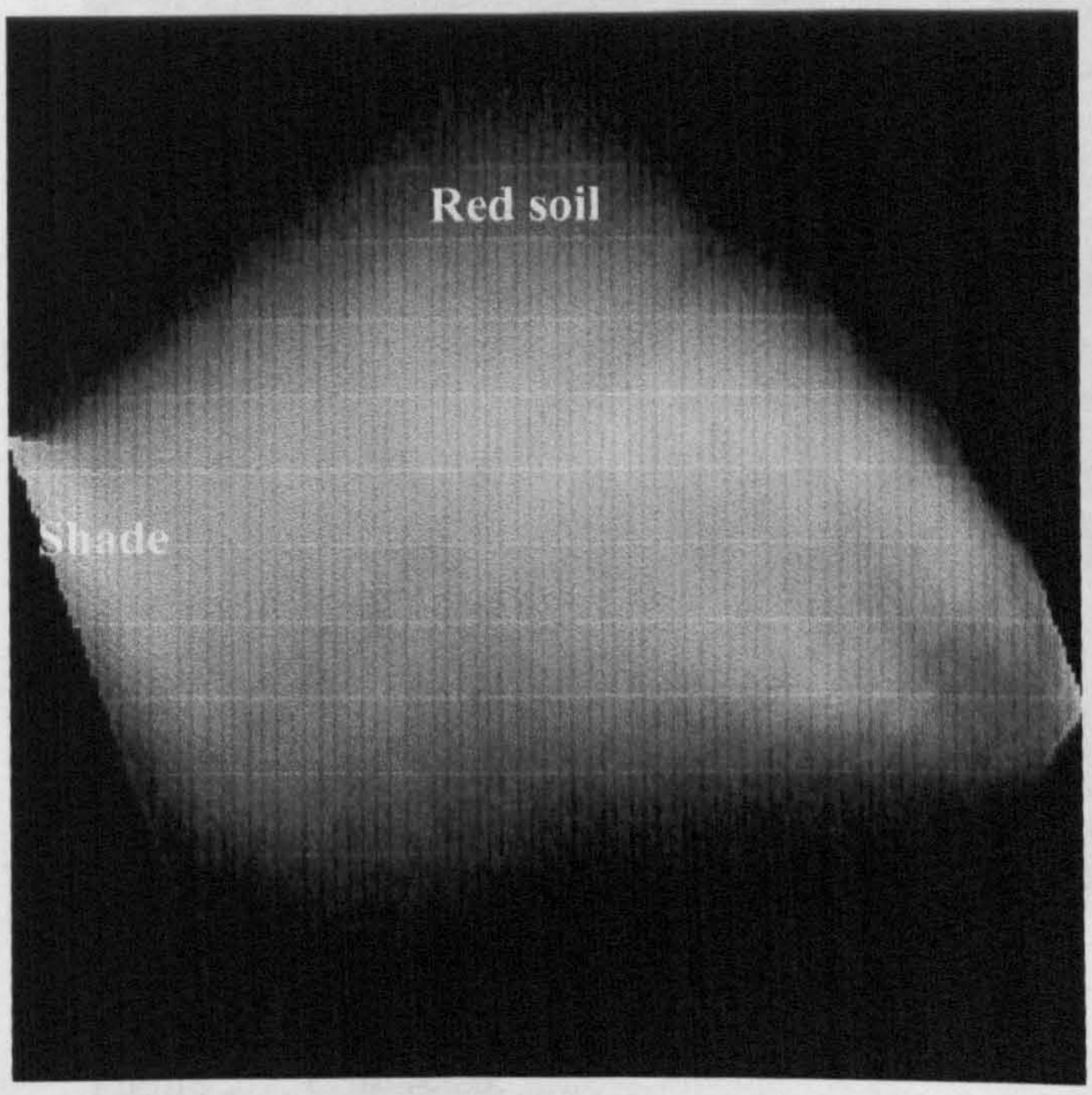

Figure 5.7. scatterplots of PCA components against one another showing the selected endmembers. Scatterplot of PC1 and PC2

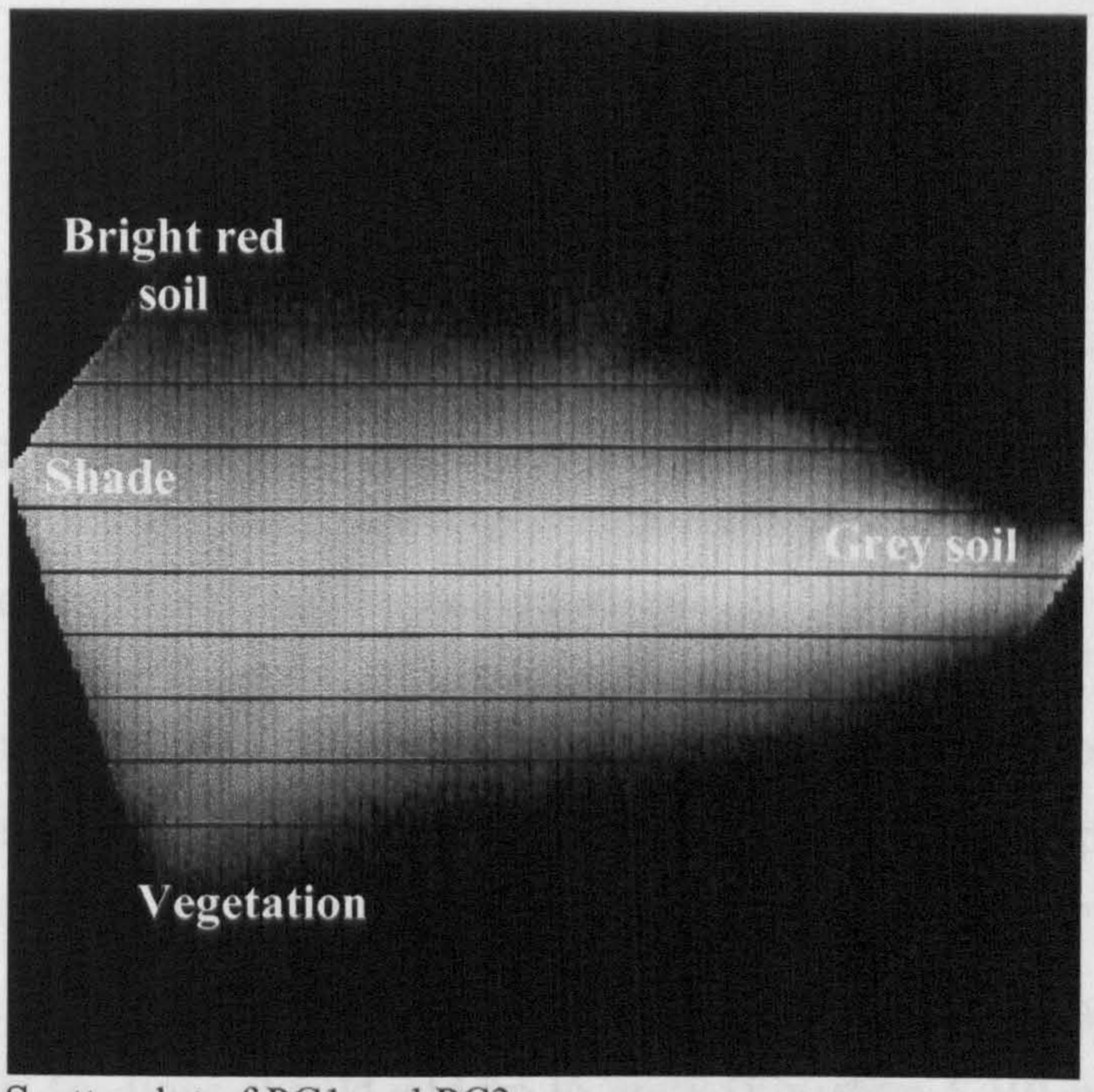

Scatterplot of PC1 and PC3

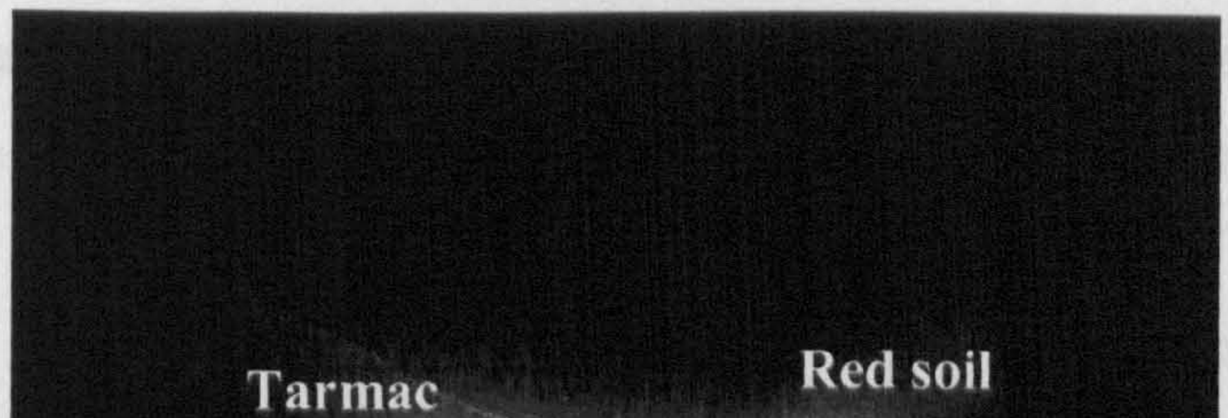

Scatterplot of PC2 and PC3

Figure 5.7. *Continued.* ....

	Blue (mean)	Green (mean)	Red (mean)
Grey soil	189	200	182
Shade	8	4	0
Red soil	46	132	183
Vegetation	26	110	3

Table 5.2. The four endmembers digital numbers.

5.2.5.2 Mixture Modelling Implementation

According to the equation 5.8, linear mixture modelling can be applied to extract the cover fractions (expressed in the matrix "F") provided that a prior knowledge is available for the digital numbers of the image pixels (the vector "Y") and the digital numbers of the endmembers (the matrix "R"). In addition, the constraining condition that the cover fractions should add up to unity (Equation 5.10) was incorporated in the linear mixture modelling equations. This provides an additional equation in the least squares fitting process to overcome the problem that the number of endmembers ($m=4$) is larger than the number of spectral bands ($l=3$) of the aerial photographs used in this study.

The output results of the linear mixture modelling were four maps of grey soil, red soil, vegetation cover, and shade (figures 5.8). Figures (5.8 A and B) reveal, at the first glance, that red soil dominates the north and north-west regions of the study area, whereas the areas of grey soil are concentrated mainly in the south which reflects the lithological characteristics of the underlying phyllite and quartz mica-schist geological structure. These soil maps will be analysed and further discussed in the following chapter on soil mapping. Figure 5.8 D shows the vegetation map which reveals the ploughed fields in the north-west part of the study area, whereas the east, west, and north-east parts of the area are dominated by the natural vegetation of matorral with some ploughed almond fields scattered in the central and east parts.

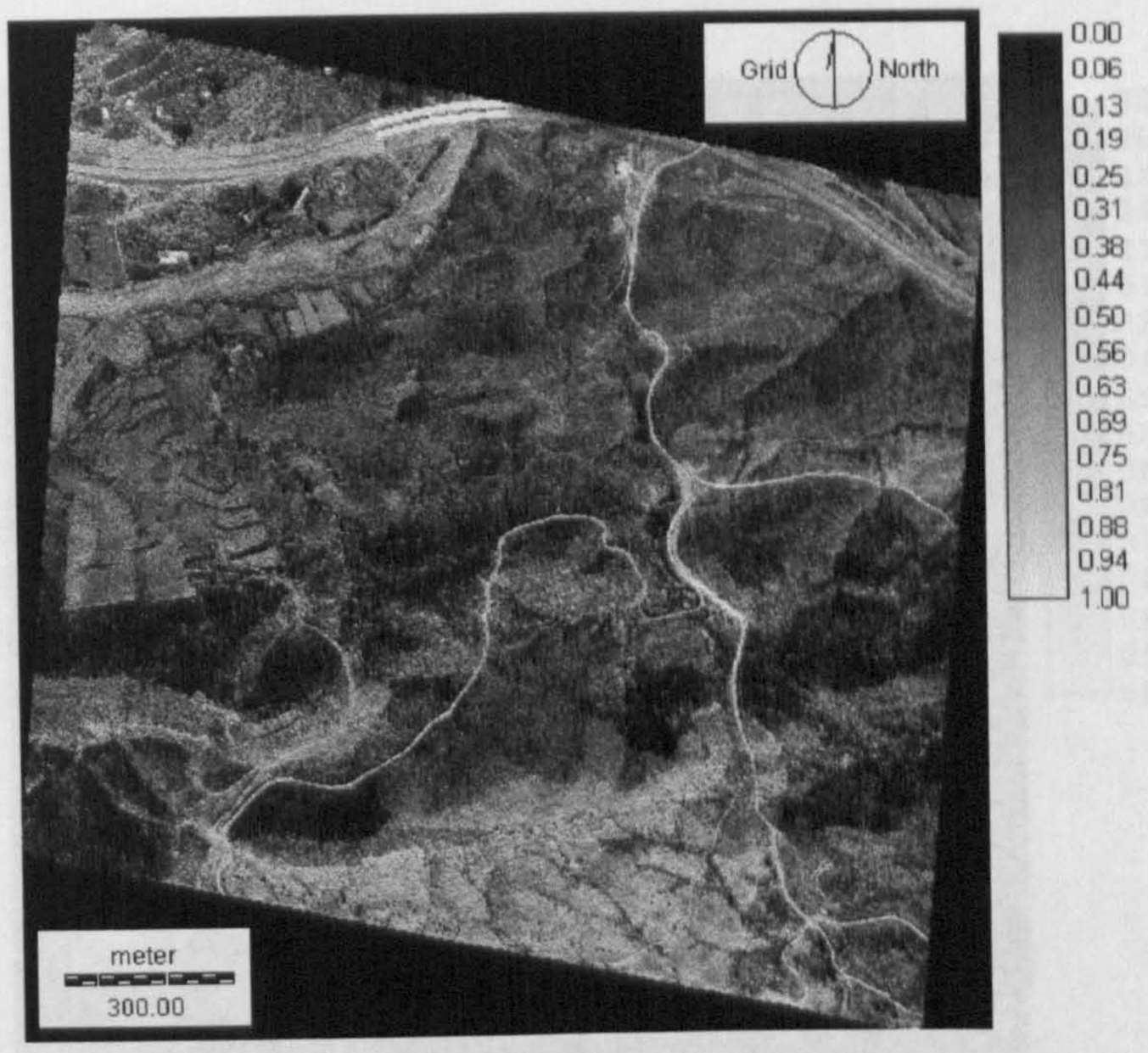

A) Grey soil map

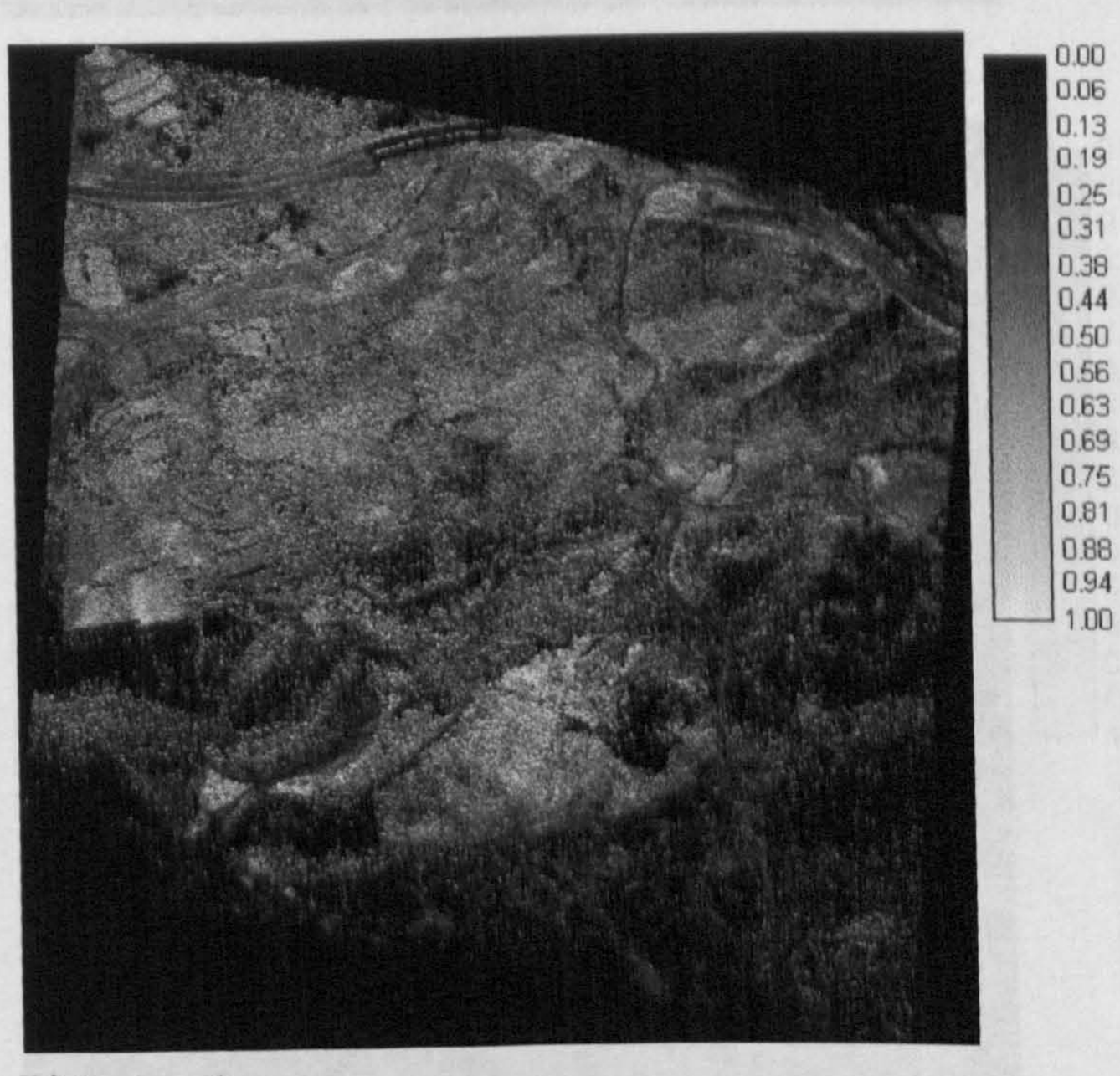

B) Red soil map

Figure 5.8. The cover fraction maps resulted from the linear mixture modelling before re-scaling to remove the shade effect from vegetation map and to remove the vegetation effect from soil maps.

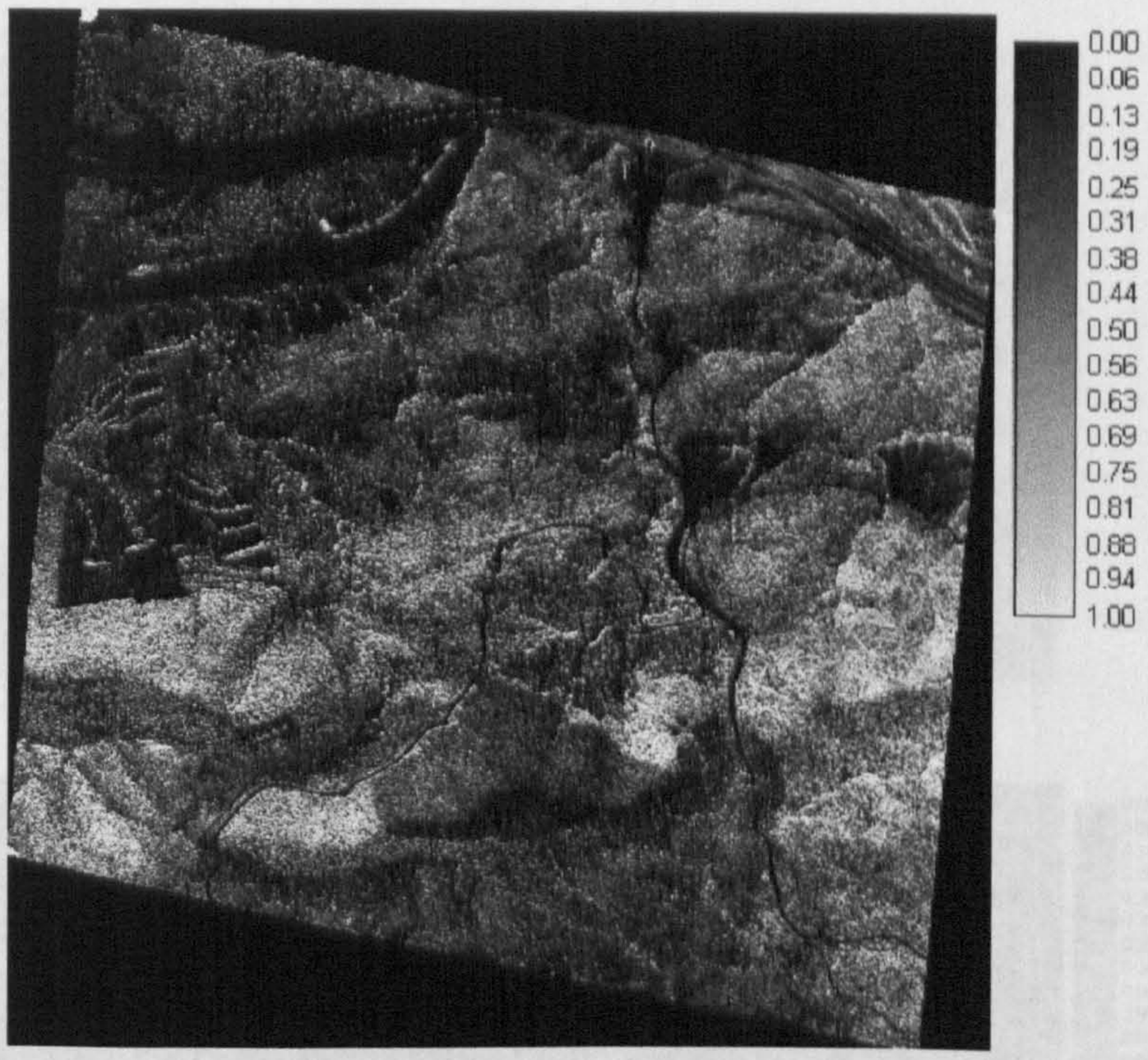

C) Shade

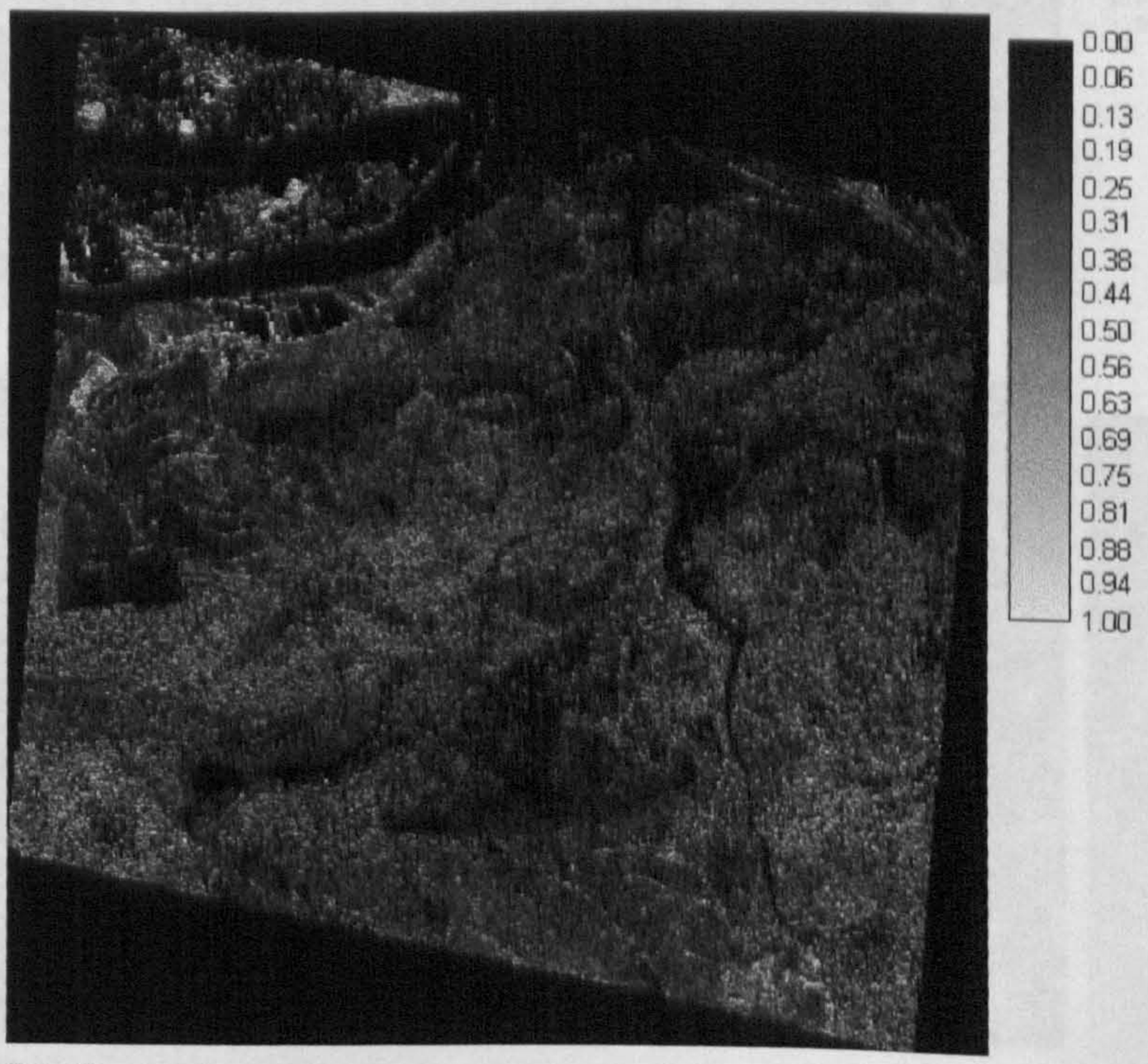

D) Vegetation.

Figure 5.8 *continued* ...

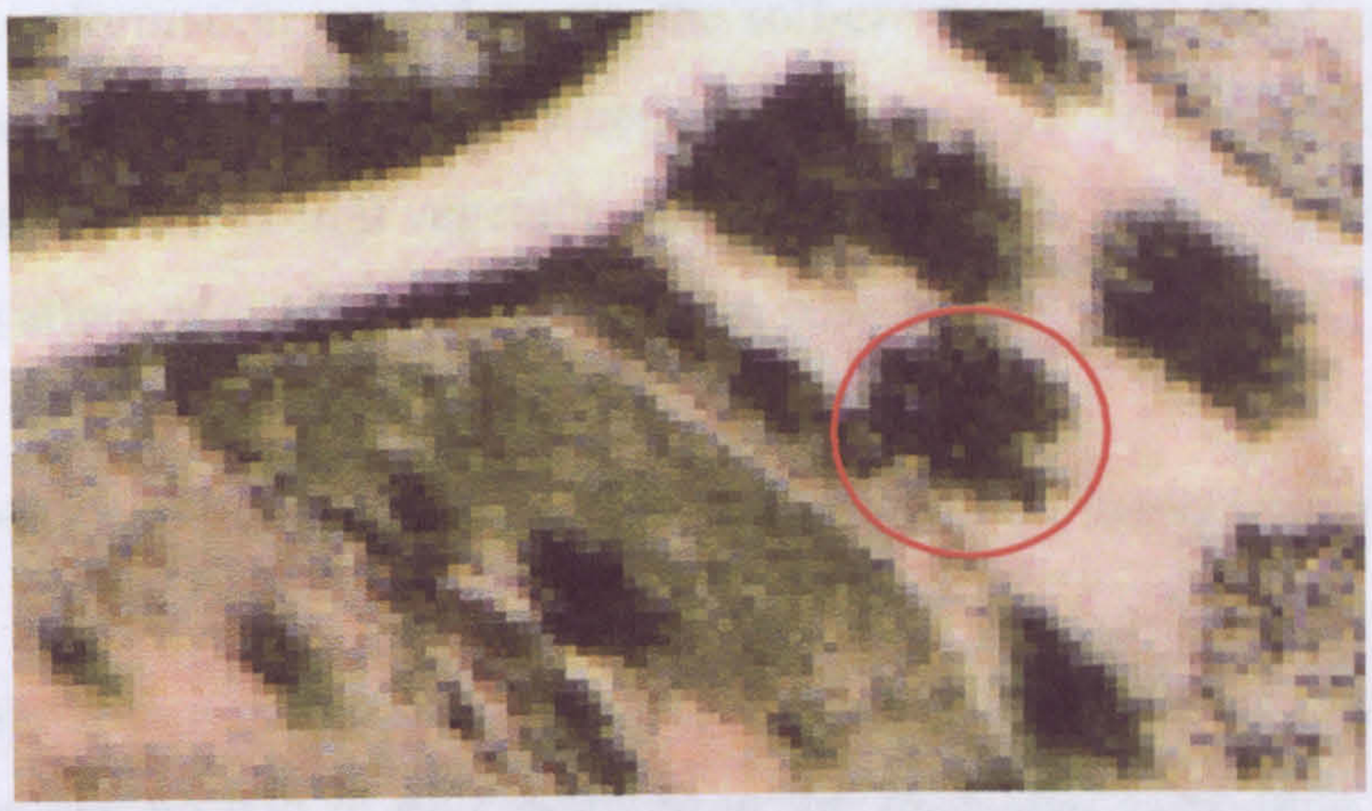

A) True colour image

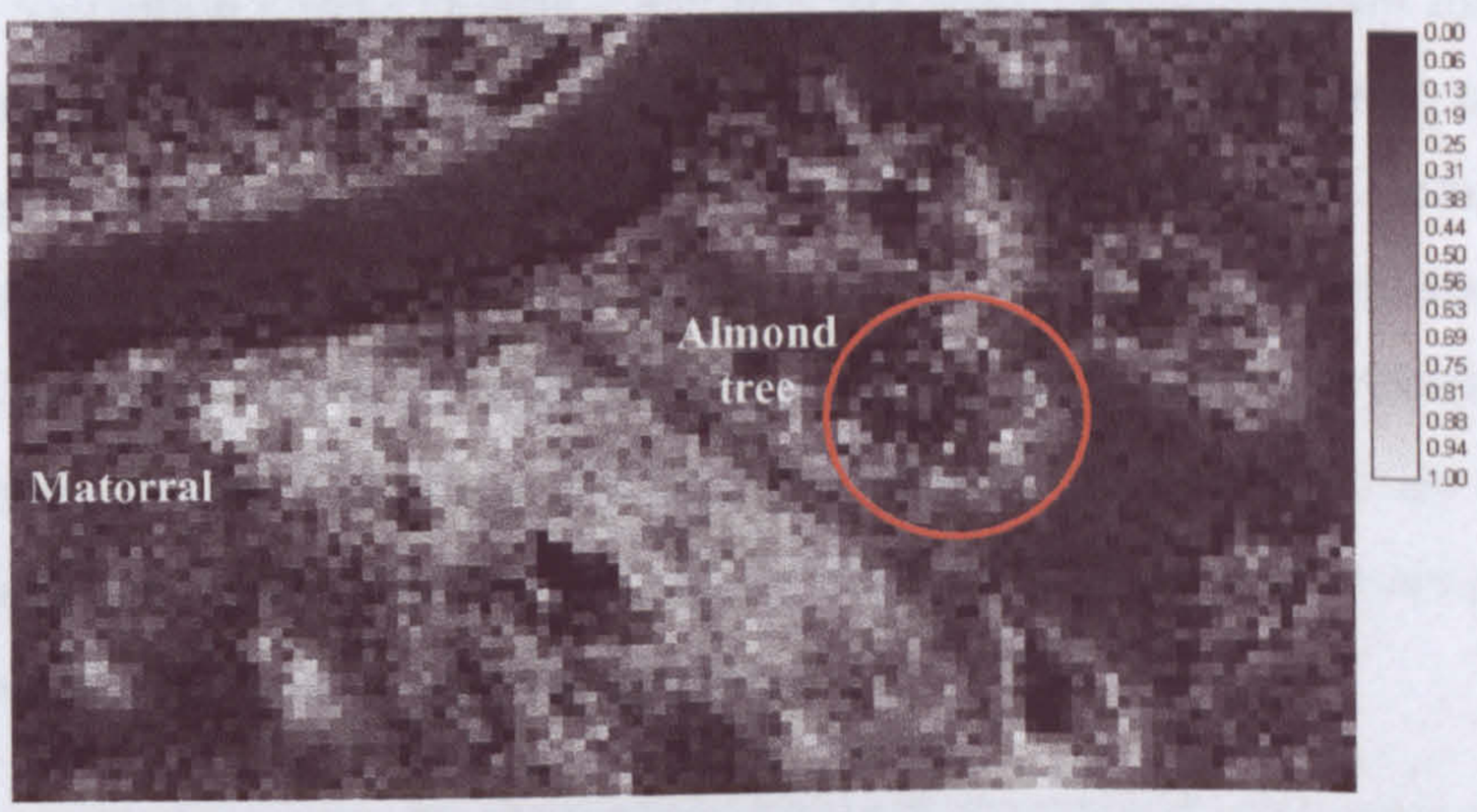

B) Vegetation cover

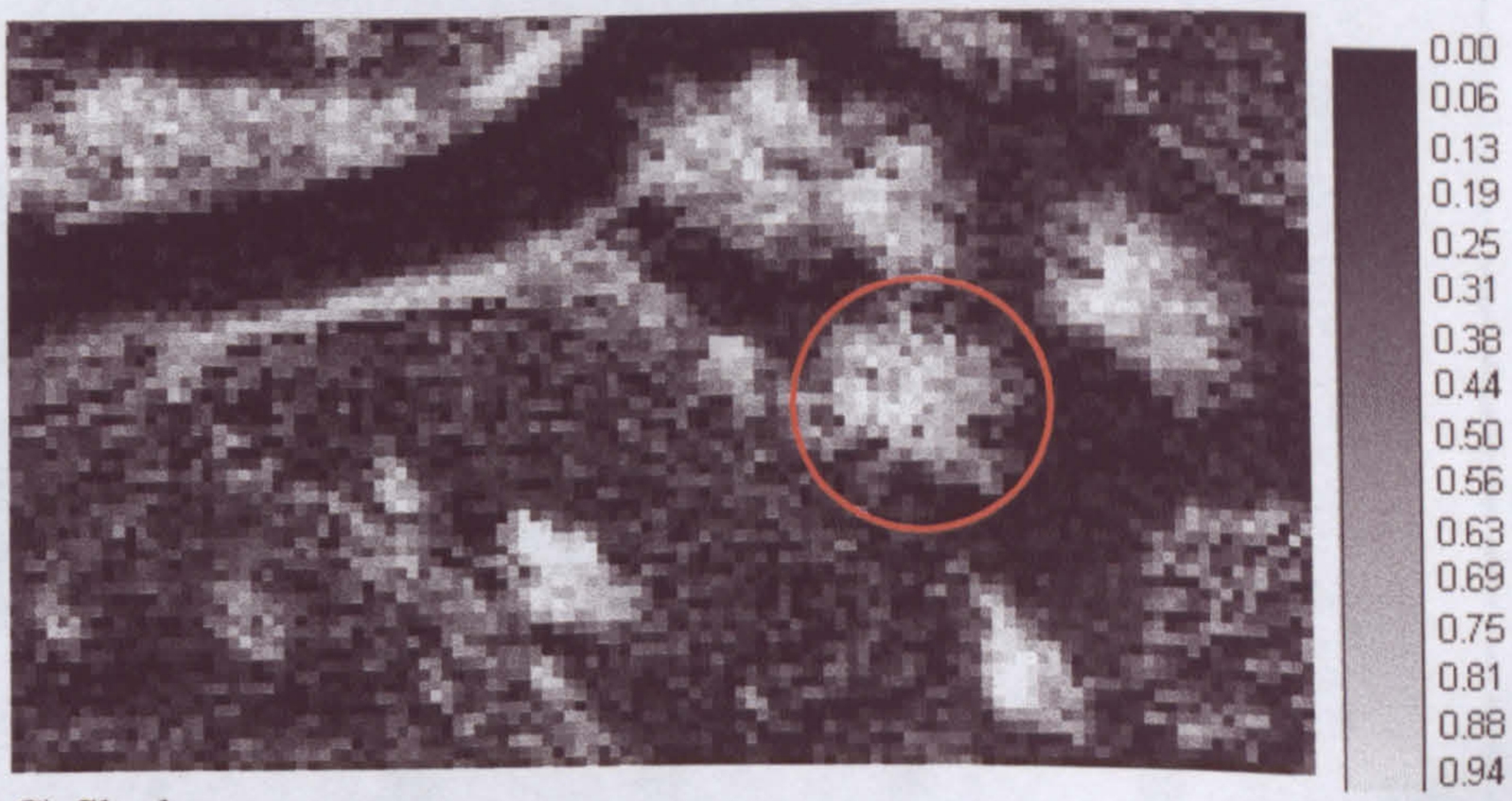

C) Shade

Figure 5.9. A zoomed-in area of almond field and matorral showing the effect of shade on vegetation cover. The red circle surrounds an almond tree which is mostly obscured by shade that is cast by the vegetation canopy.

In addition, figure 5.8 C reveals the extend and the spatial distribution of the shade, which is mostly cast by the higher shrubs and trees. This shade greatly obscures the vegetation information needed to run the soil-erosion model and figure 5.9 shows a zoomed-in area of Vélez Rubio where the shade is partially obscuring the almond trees, as well as the natural vegetation cover of matorral. Thus, a method is needed to rectify the effect of shade on the vegetation cover.

5.2.6 Re-scaling the Vegetation Map to Remove the Shade Effect

To validate the vegetation-cover map, the vegetation fractions calculated using mixture modelling had to be compared to the measured vegetation fractions in the field. The validation shows (figure 5.10) that the calculated vegetation fractions are underestimated in areas of high vegetation density and overestimated in areas of lower vegetation density (see figures 5.9, 5.11 and 5.12). The main reason for the underestimation can be the fact that shrubs and trees in the high vegetation density areas cast a shadow which partially obscures the vegetation optical spectral response in these areas. Figure 5.11 shows the high fractions of shade which exist in areas of almond field (on the non-illuminated side of the tree crowns) and in areas of dense matorral where one bush is shading another.

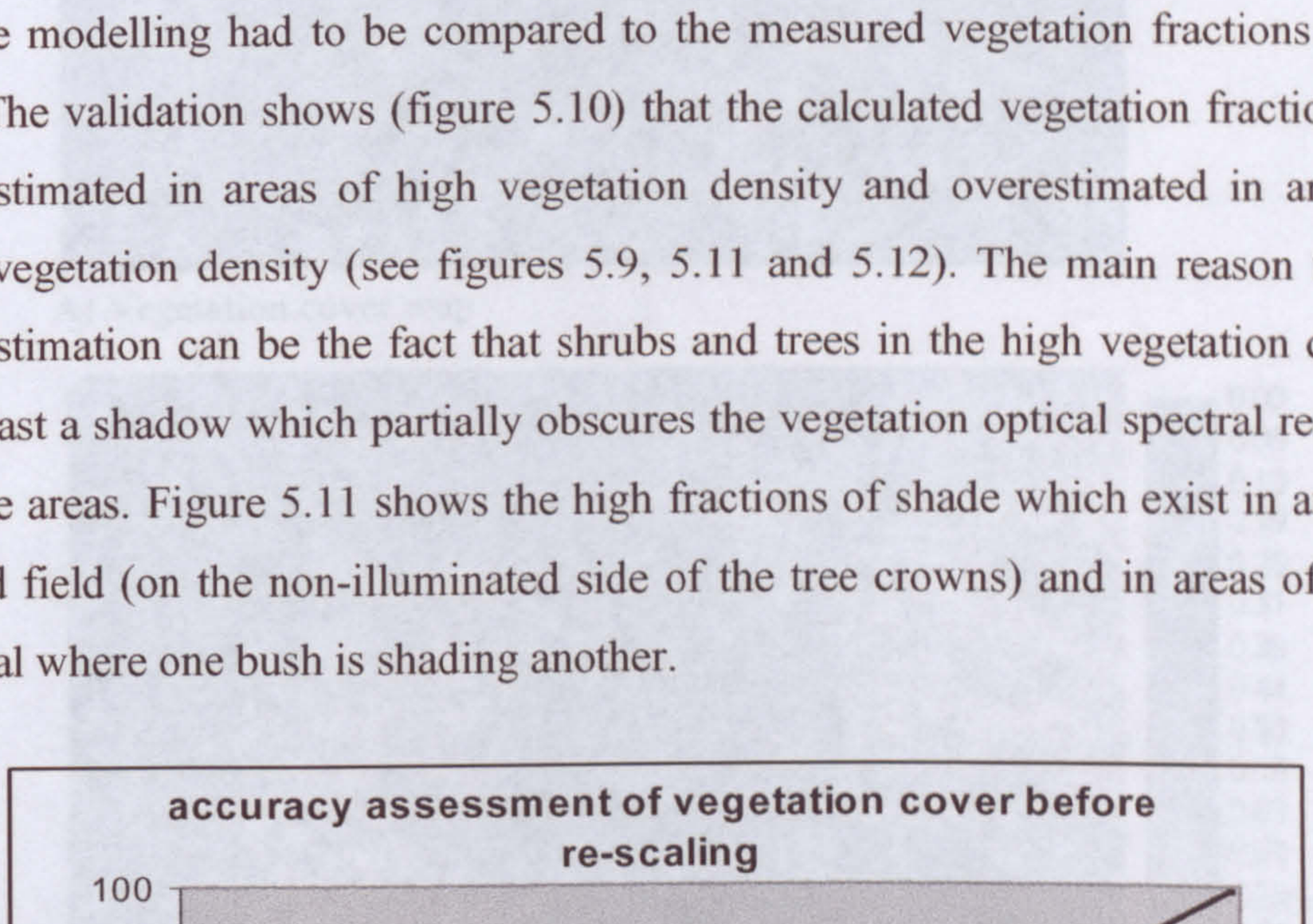

Figure 5.10. The relationship between observed and estimated vegetation cover before re-scaling to remove the shade effect.

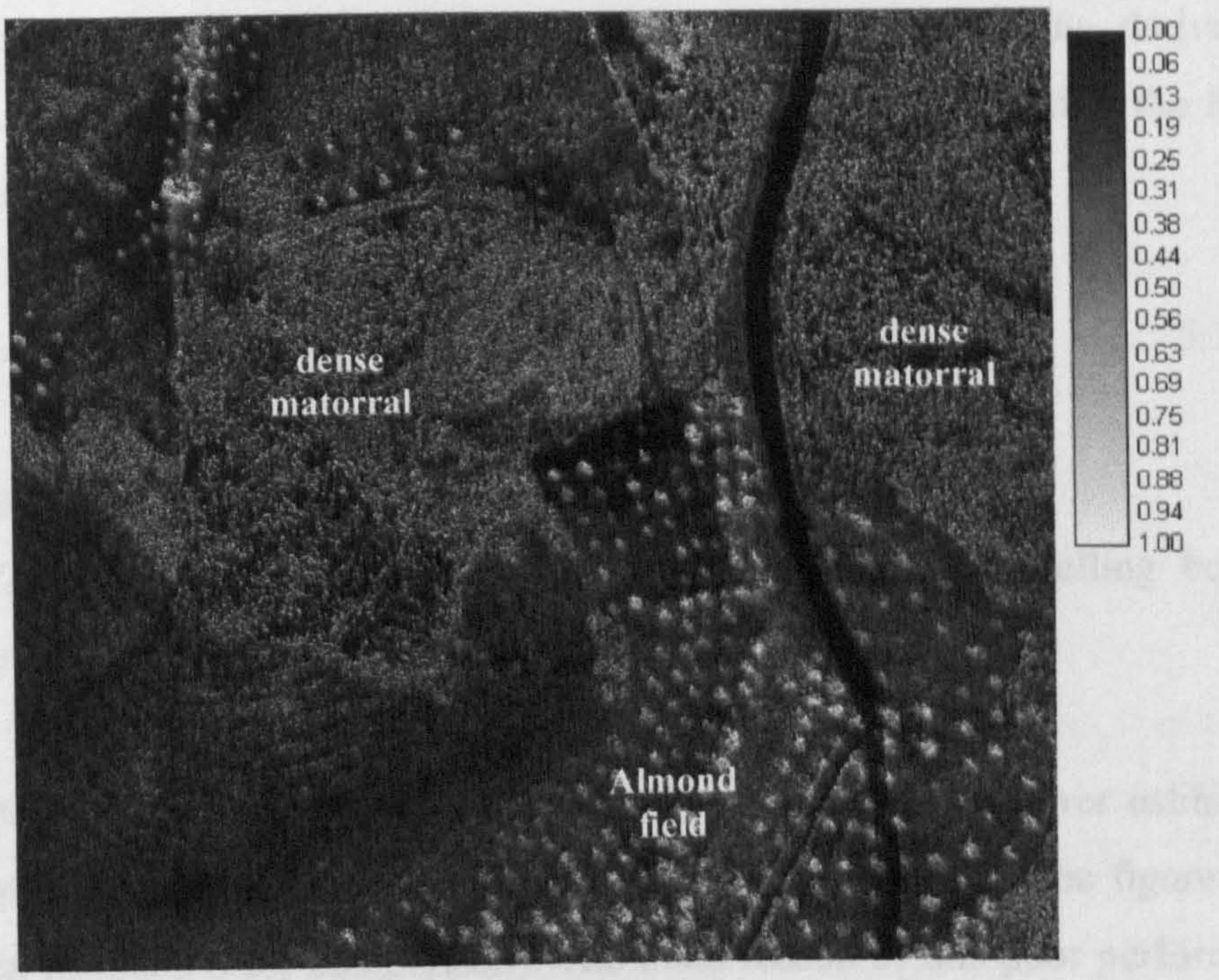

A) Vegetation cover map

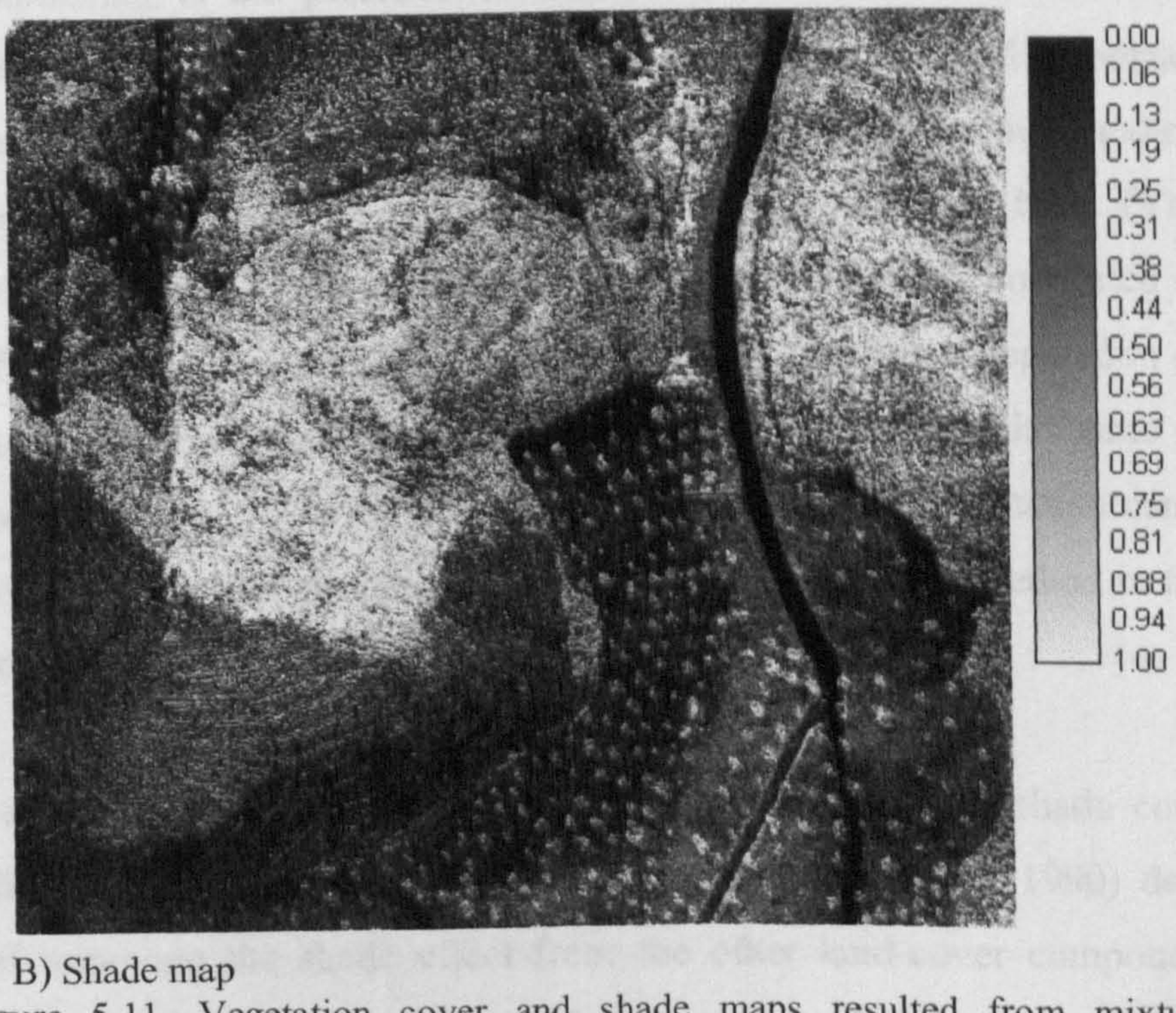

B) Shade map

Figure 5.11. Vegetation cover and shade maps resulted from mixture modelling. The association of shade fraction to the underestimation of vegetation cover in areas of high vegetation density is demonstrated. The figure shows the presence of high fractions of shade in areas of high density matorral and around the tree crowns of almond plantation.

When a regression was applied between the vegetation fractions derived from mixture modelling before re-scaling and vegetation cover measured in the field, the relationship was:

$$V_{calc1} = 4.92 + 0.496V_{obs} \qquad 5.17$$

r^2 =0.79, F=12.16 , p=0.0101,

$RMSE$ = 18.34%

Where V_{calc1} is vegetation fractions derived from mixture modelling before re-scaling, and V_{obs} is vegetation fractions measured in the field.

At this stage the linear mixture modelling seems to produce poorer estimation of vegetation cover compared to the red band reflectance method (see figure 5.4 and correlation results 5.6 for comparison). The main reason of this poor performance of mixture modelling is the presence of shade which seems to obscure a sizeable amount of vegetation information by reducing the optical spectral response of the vegetation cover. However, in the case of the red band reflectance method, both vegetation canopy and shade have lower reflectance in the red band (Yang and Prince, 1997). This means that as the red reflectance is negatively correlated with the density of vegetation canopy (i.e. red reflectance is lower when vegetation cover is higher) the presence of shade also reduces the red reflectance in the same way the vegetation cover does. Thus, the presence of shade within the vegetation canopy did not reduce the correlation coefficient in the red band reflectance method in the same magnitude it did in the case of mixture modelling.

In order to correct the effect of shade on vegetation cover, the shade cover map resulted from the mixture modelling can be used. Smith *et al.* (1990) describe a method of removing the shade effect from the other land-cover components (i.e. vegetation cover and soil maps) derived by mixture modelling. In this method the endmembers corresponding to the material components of the scene are normalised by re-scaling all land-cover fractions, except the shade fraction, so that they sum to

unity, pixel by pixel. To remove the shade effect from the vegetation fraction the following algorithm can be applied:

$$VF_s = F_{veg} /(1-F_{shade}) \quad 5.18$$

Where VF_s is vegetation fraction adjusted by removing the shade effect, F_{veg} and F_{shade} are the fractions of vegetation cover and shade derived from the mixture modelling.

5.2.6.1 Implementation of the Re-scaling Algorithm

To remove the effect of shade from the vegetation cover map, the shade-removal algorithm introduced by Smith *et al.*, (1990) (Equation 5.18) was used. Figure 5.12 shows the effect of removing the shade from the vegetation cover in a ploughed almond field where the oval-shaped objects here represent almond trees. In figure 5.12 A and B it can be noticed that the shade effect was not successfully removed from all pixels within the crowns of trees. This is a major problem in the shade removal process in areas of high vegetation density.

This problem has been further investigated and it was found that it occurs in pixels where 1) high vegetation cover is expected (i.e. almond tree crowns) but 2) more than 95% (in most case 100%) of the pixel is covered by shade and 3) less than 5% fraction (and in most cases 0%) is found to be vegetation. In most of these pixels that have 0% vegetation cover the re-scaling algorithm cannot retrieve any vegetation information and these pixels remain of 0% vegetation fraction. In some other of these pixels, however, traces of grey- or red-soil background (with very low fractions between 0.2-5%) have been found which can be attributed to either errors of the mixture modelling or to micro-spaces in the vegetation canopy where the soil is partially exposed. Although these traces of soil background are very low fractions, they still greatly affect the re-scaling algorithm because they are coupled by high fractions and very low fractions of shade and vegetation cover respectively.

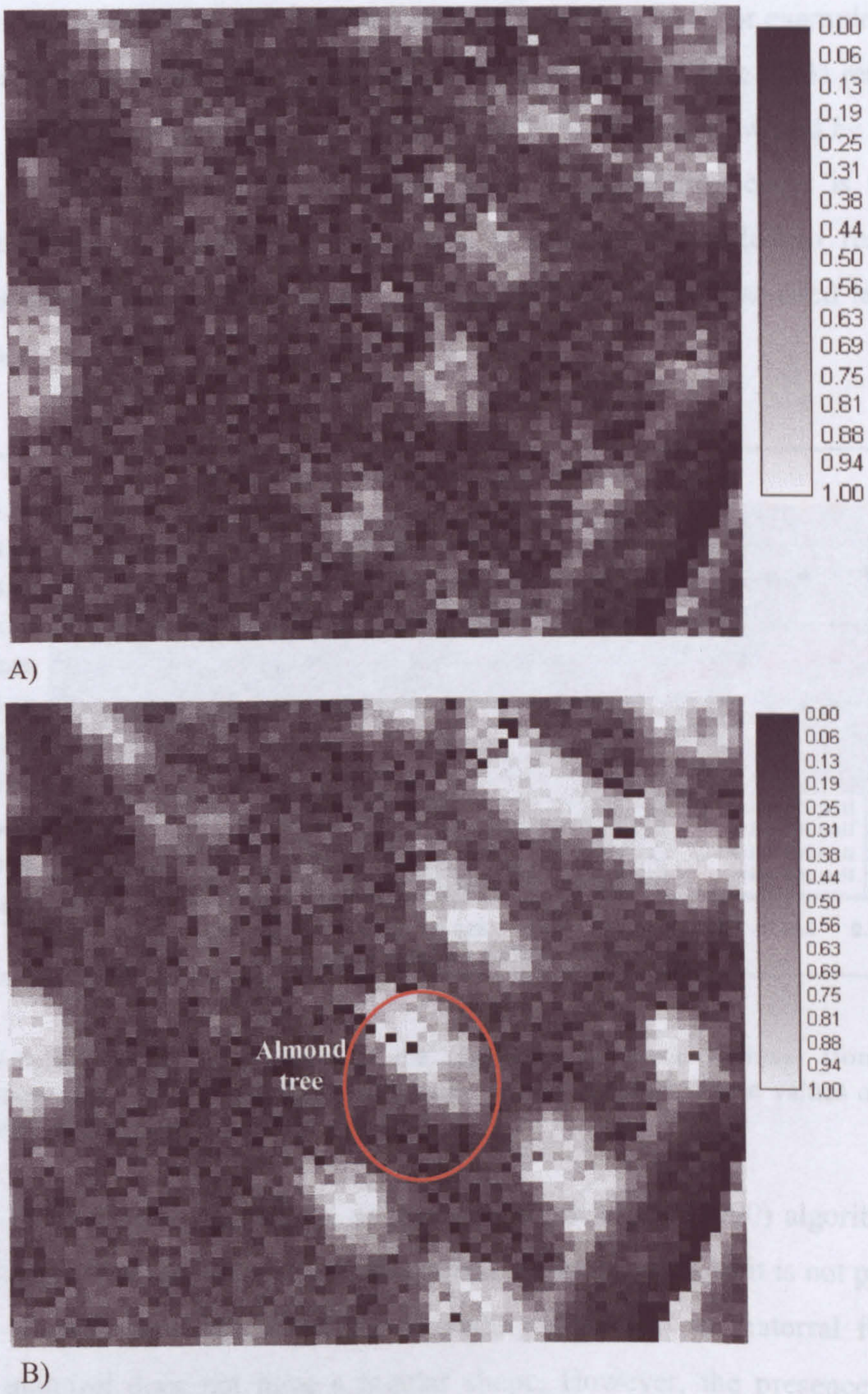

Figure 5.12. Re-scaling the vegetation cover by removing the shade effects in an almond field. A) is before and B) is after re-scaling. The oval-shaped objects are almond trees.

A sensitivity analysis was carried out to evaluate the effect of these traces of soil background on the process of shade removing. Figure 5.13 shows how the re-scaling process is very sensitive to soil fractions present in these pixels. For example, as little as 3% soil in a pixel of 0.1% vegetation (see dotted line in figure 5.13) renders the re-scaled vegetation to 25%, however, the same 0.1% vegetation would be rendered to 100%, if 0% soil exists in that pixel. Since the vegetation cover is the main protection factor in soil-erosion modelling, a solution is needed to restore the vegetation information in these pixels. Such a solution will be discussed later on in this chapter.

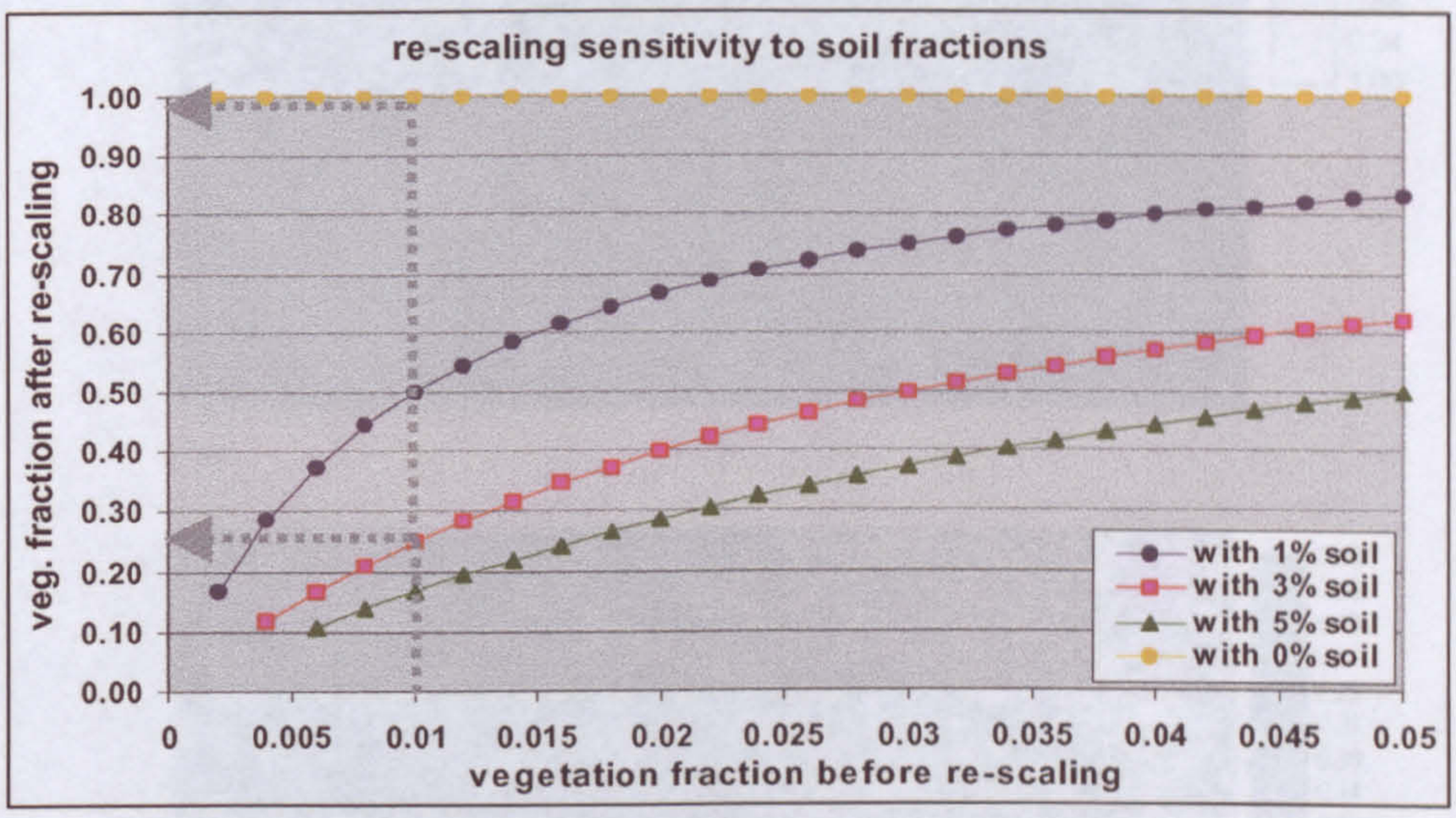

Figure 5.13. Sensitivity analysis of the algorithm of shade removal from the vegetation map to the of soil fractions present in a given pixel. Three values of soil fractions are analysed: 0.01, 0.03, and 0.05.

Figure 5.14 also shows the results of applying Smith *et al.*, (1990) algorithm to re-scale the vegetation cover in a field of matorral. In the figure 5.14 it is not possible to interpret visually how successful the re-scaling algorithm in matorral fields was because matorral does not have a regular shape. However, the presence of black pixels, within matorral clusters, in the shade-free image of figure 5.14 indicates that shade removal was not very successful in areas of high vegetation cover for the reasons outlined above.

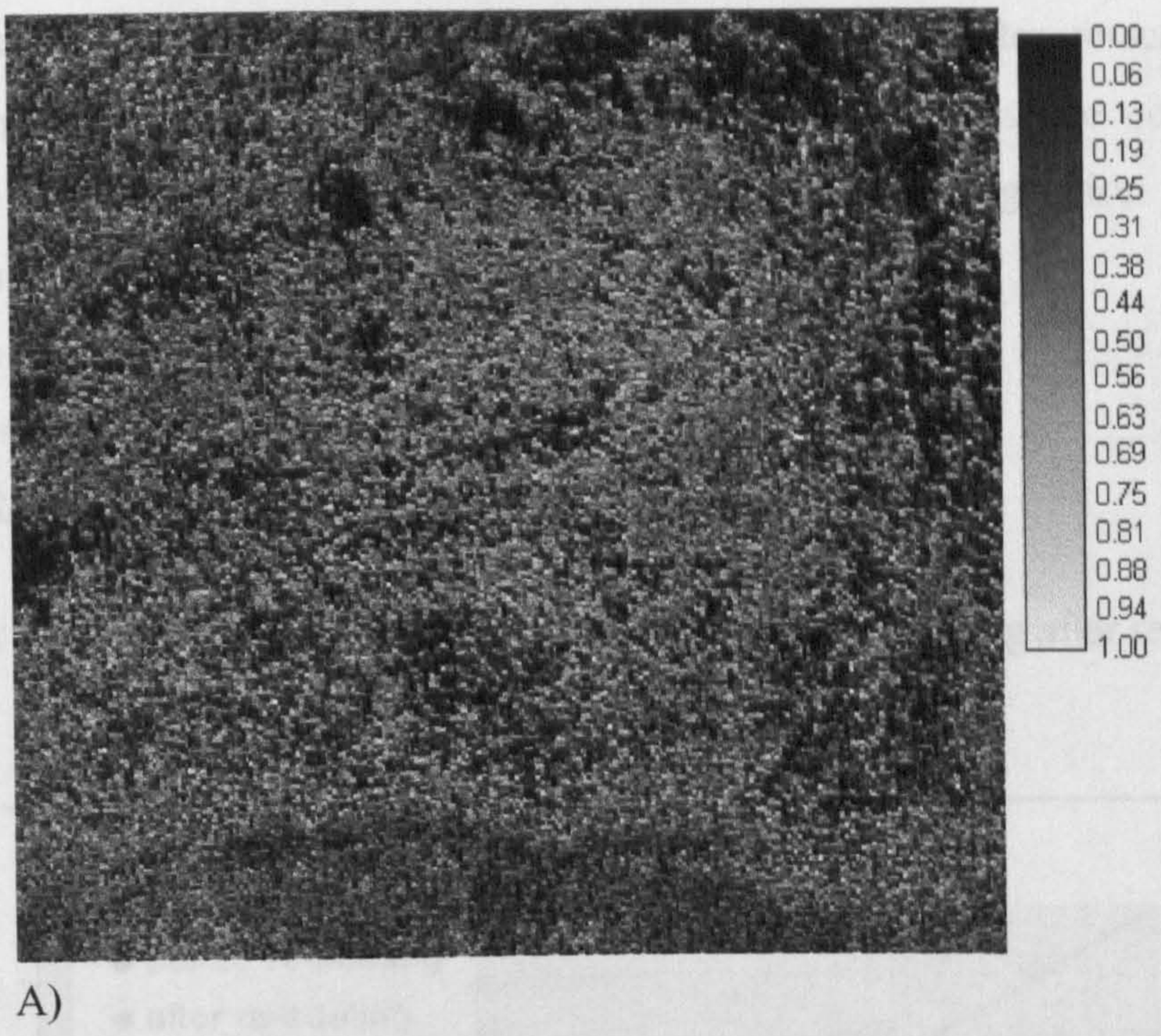

A)

B)

Figure 5.14. Re-scaling the vegetation cover by removing the shade effects in the matorral. A) is before and B) is after re-scaling.

In order to assess the accuracy of re-scaled vegetation cover map, it was compared to the vegetation fractions measured in the field in the nine vegetation plots. Figure 5.15 shows a plot of accuracy assessments of vegetation cover after re-scaling by removing the shade effect. A regression was applied to assess the correlation between the calculated vegetation fractions and the observed vegetation fractions which produced the relationship:

$$V_{calc2} = 4.9 + 1.01V_{obs} \qquad 5.19$$

$$r^2 = 0.918,\ F = 37.35,\ p = 0.0005,$$

$$RMSE = 10.7\%$$

Where V_{calc2} is a vegetation fraction derived from mixture modelling after re-scaling.

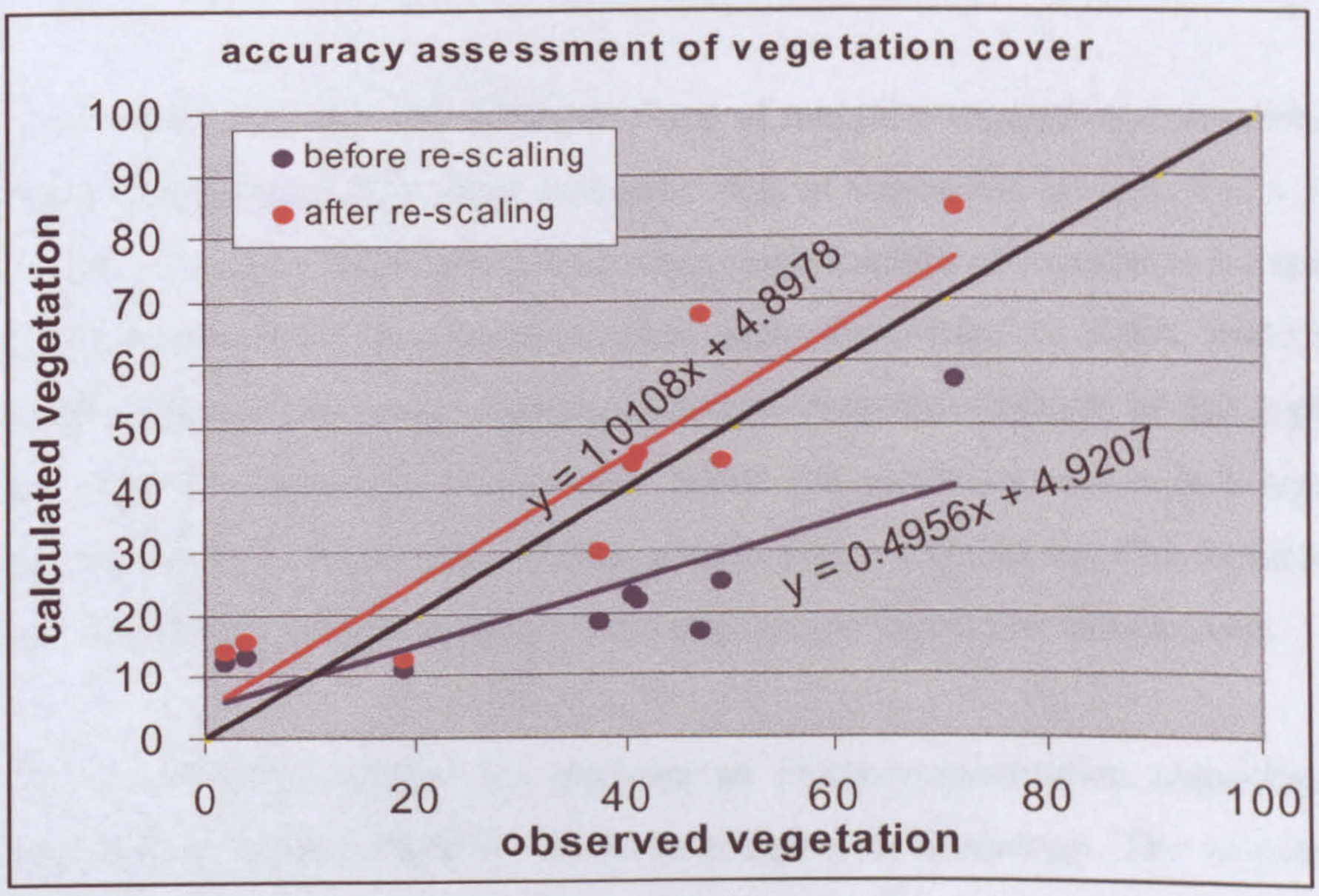

Figure 5.15. The relationship between observed and estimated vegetation cover before and after re-scaling to remove the shade effect.

Equation 5.19 shows a substantial improvement in the accuracy of calculating vegetation cover using mixture modelling techniques when the effect of shade is removed, when compared to mixture modelling results before re-scaling (see regression equation 5.17). Figure 5.15 explains how the slope of the regression line

has changed from 0.49 in the "before re-scaling" case to a value of 1.01, very close to the ideal value of 1, in the "after re-scaling" case.

At this stage the mixture-modelling techniques show a substantial improvement of the accuracy of mapping vegetation cover when compared to the red band reflectance method. The reason for this accuracy improvement is credited to the fact that the effect of shade, which obscured the vegetation canopy by reducing its optical spectral response and to which mixture modelling is sensitive, has been removed. These results of accuracy assessment justify the use of mixture modelling techniques to derive high accuracy vegetation mapping using high spatial resolution remotely sensed data.

5.2.7 Co-Occurrence Matrix Methods to Rectify Blank Vegetation Pixels

It has been shown that one of the problems of mapping vegetation cover using linear mixture modelling is that some isolated pixels of vegetation are assigned a value of zero (or a very low value below 5%) where high fraction of vegetation is expected to exist in those pixels. This happens when such pixels have 95-100% shade fraction because shade obscures the vegetation canopy. A typical example of this is pixels of zero vegetation amongst tree crowns. Since the vegetation cover is a significant parameter controlling the rates of soil-erosion loss, a solution must be found to fill in those individual isolated pixels with the appropriate vegetation information.

Such a solution is offered by applying an image segmentation algorithm which implements a texture-based co-occurrence matrix methodology. The co-occurrence matrix methodology is defined as a second order (moment) statistical measure of image variation and it provides a basis for a number of textural features (Schalkoff, 1989). This textural image segmentation method partitions an image into homogeneous regions on the basis of textural homogeneity. In this method a binary mask depicting the shape of vegetation features (trees, bushes, etc...) in the vegetation cover map is created based on the variation in intensity of the vegetation map texture. This mask can then be intersected with the shade-free vegetation cover

map by applying Boolean algebra in order to identify, and fill in, the pixels of zero (and very low fraction below 5% of vegetation within the tree crowns and bushes with the appropriate vegetation information.

The principles of applying the texture-based co-occurrence matrix to detect land-cover features are not new in remote sensing studies. However, such studies concentrated mainly on the determination of internal image structure and very few studies concentrated on determining the precise pixel classes (Smith *et al.*, 2001), where in this case of vegetation cover the expression "classes" represent different vegetation features based on the variation of their textures.

There are four main steps in this process: 1- the creation of the co-occurrence matrix, 2- the determination of texture classes (representing vegetation features), 3- image segmentation and mask creation, and 4- filling those pixels with appropriate vegetation information.

The process of image segmentation groups pixels to form higher-level regional image structures in order to identify surfaces and objects. Before the image is segmented the co-occurrence matrix has to be created. The co-occurrence matrix (sometimes called grey-tone spatial dependence) evolves from a consideration of the joint probability density function of two pixels (Schalkoff, 1989). The probability function $P((x_1,x_2),f)$ represents the probability that the image function $f(x_1,x_2)$ has an intensity value $\leq f$ at a location (x_1,x_2). If we eliminate the effect of location (x_1,x_2) then the resulting function is $P(f)$, which is recognised as the image intensity probability density function (pdf), and often approximated by a histogram. A second order (joint) probability density function for two pixels is:

$$P((x_1^1, x_2^1), f^1, (x_1^2, x_2^2), f^2) \qquad 5.20$$

which represents the density of the joint occurrence of the events $f^1 = f(x_1^1, x_2^1)$, and $f^2 = f(x_1^2, x_2^2)$. The function 5.20 has four arguments, two of which are spatial locations and two are intensities. However, to simplify this equation and make it

more practical, the location relationships (that is (x_1^1, x_2^1) and (x_1^2, x_2^2)) between pixels are ignored. These results in a local representation characterised by a simpler image intensity pdf which can take the form of a matrix of entries, each entry is of the form of $P(f_1, f_2)$. This matrix is called the co-occurrence matrix (Schalkoff, 1989).

If we consider $\delta = (\delta x_1, \delta x_2)^T$ to be a vector in the (x_1,x_2) plane then we can use this formulation to calculate statistical measures of intensity co-occurrence that do not involve (x_1^2, x_2^2) and (x_1^2, x_2^2), but rather the difference between these quantities. Fixing δ at a specific value (e.g. $\delta = (1,0)^T$) with an intensity resolution of m grey levels (of the image) we form an $m \times m$ matrix H_δ, which indicates the joint probability of occurrence of grey levels occurring in the image at a separation of δ (Mukundan and Ramakrishnan, 1998):

$$H\delta = (h\delta(i, j)) \qquad 5.21$$

Where element $h\delta(i, j)$ is a measure of the co-occurrence of intensities i and j with a pixel separation of δ.

Figure 5.16 explains the process of calculating the co-occurrence matrix using an example of a simple operator. However, different types of operators can be applied on remotely sensed data to calculate the co-occurrence matrix, depending on the vegetation features to be extracted form these images. In this research it has been found that the bow-tie operator (Figure 5.17) is a good operator to extract the vegetation features in our study area because it successfully recognised the main features of the vegetation cover such as bushes and tree crowns of the almond and olive plantations.

Operator →

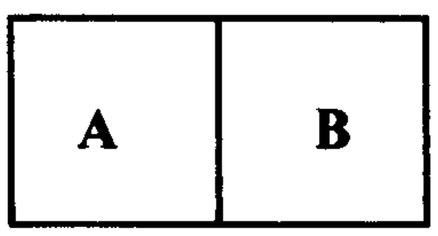

Pixel values →

3	1	1	2
2	2	3	3
3	2	2	3
1	2	1	1

Co-occurrence matrix →

C(1,1)=2	C(1,2)=2	C(1,3)=0
C(2,1)=1	C(2,2)=2	C(2,3)=2
C(3,1)=1	C(3,2)=1	C(3,3)=1

Figure 5.16. The process of extracting the co-occurrence matrix using an example of a simple operator.

0	0	1	0	0	0	1	0	0
0	1	2	1	0	1	2	1	0
0	2	3	2	0	2	3	2	0
0	1	2	1	0	1	2	1	0
0	0	1	0	0	0	1	0	0

Figure 5.17. The bow-tie operator which was used to extract the co-occurrence matrix for the vegetation cover map.

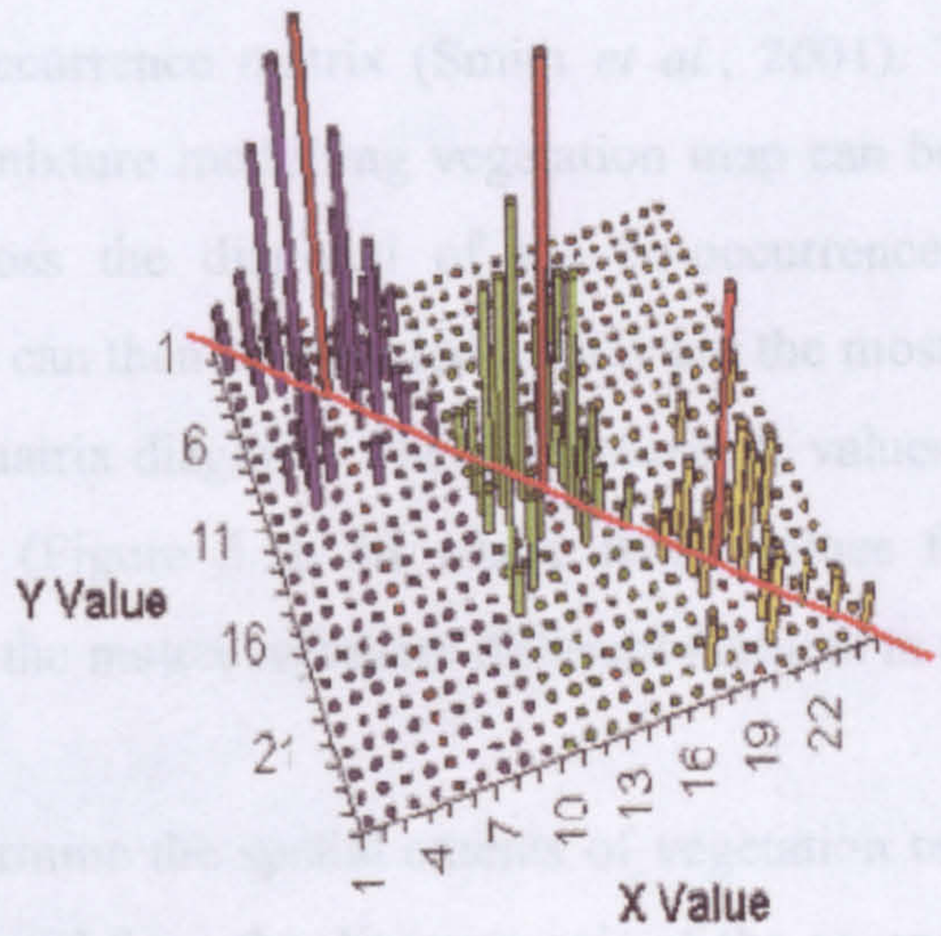

A)

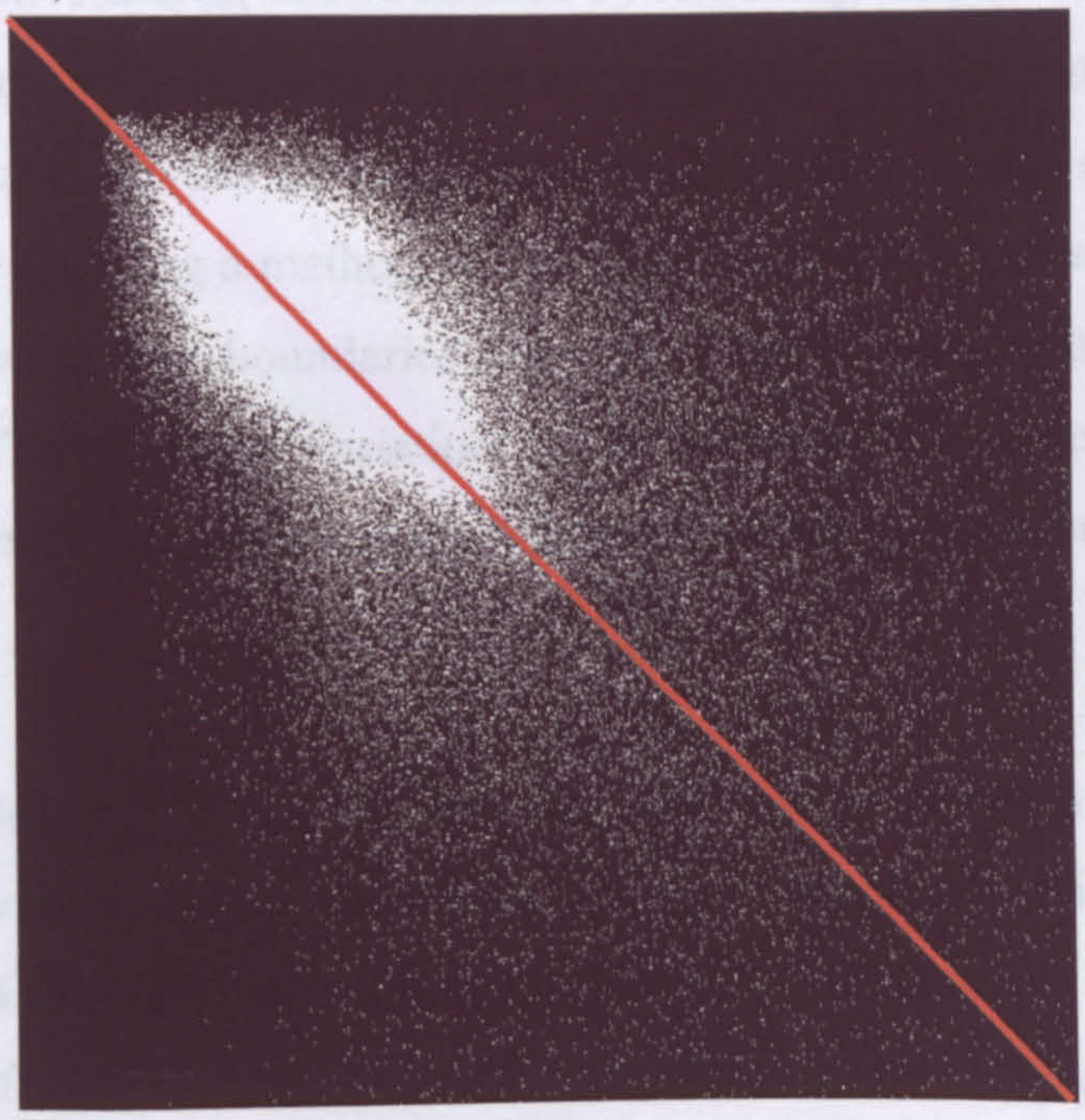

B)

Figure 5.18. A) sketch and B) diagram showing the plot of co-occurrence matrix. A) demonstrates the meaning of peaks along the diagonal and B) is the diagonal axis of the matrix (in red) which shows the peaks representing potential classes. (sketch is after Smith *et al.*, 2001).

In the resultant co-occurrence matrix the significant values of the joint intensities are found to be clustered around the diagonal (Schalkoff, 1989). This is attributed to the fact that entries belonging to the same vegetation feature will have similar values within the co-occurrence matrix (Smith *et al.*, 2001). This means that vegetation features in the mixture modelling vegetation map can be detected because they are represented across the diagonal of the co-occurrence matrix. These vegetation textural features can then be detected as they are the most significant peaks along the co-occurrence matrix diagonal. The co-occurrence values in this matrix were plotted in a scatterplot (Figure 5.18 B) where those values falling at the diagonal axis (marked red) of the matrix represent different features in the vegetation cover map.

In order to determine the spatial extents of vegetation textural features, a histogram should be produced from the diagonal axis of the co-occurrence matrix by applying techniques of projection. From this histogram the main peaks, which represent the main vegetation features, can be defined by removing the smaller textural variations in the histogram using techniques such as Expectation-Maximisation Algorithm, low pass filtering, and wavelet analysis (Smith *et al.*, 2001). In this study the histogram was refined by applying a method of low pass filtering to remove the high frequency variations, representing boundaries between various features, because it produced good results. The remaining variations in the histogram (expressed as peaks in figure 5.18A) represent different vegetation features in the mixture modelling vegetation map.

After the histogram is filtered and the main peaks representing the vegetation features are isolated, a process of thresholding is applied. In this process minimum and maximum threshold values are selected and applied to the histogram, and this selection is reflected in thresholding the vegetation cover. By varying the minimum and maximum threshold values in the histogram and monitor their effect on the vegetation features selected in the vegetation cover, a binary map that depicts the shape of the objects in the vegetation cover image is achieved (figure 5.19). This binary map (or binary mask) is then used for intersection with the mixture modelling shade-free vegetation cover by applying Boolean algebra intersection techniques.

From this intersection the pixels of zero (or very low fractions of) vegetation, where high density of vegetation is expected to occur, are isolated.

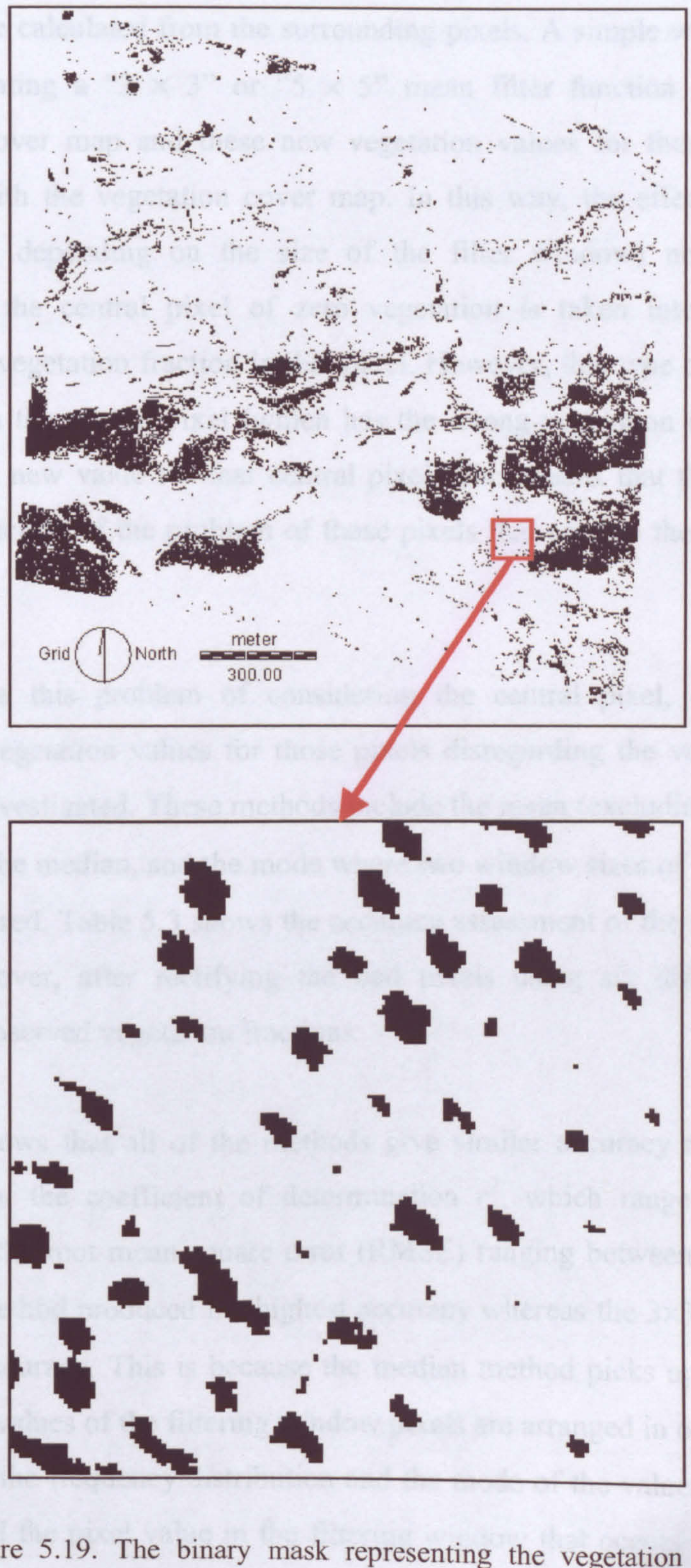

Figure 5.19. The binary mask representing the vegetation objects which was created from the co-occurrence matrix methodology.

After those pixels are identified, new vegetation values for them should be found. Since such vegetation values cannot be extracted from within those pixels, these values can be calculated from the surrounding pixels. A simple way of doing this is by implementing a "3 × 3" or "5 × 5" mean filter function on the shade-free vegetation cover map and these new vegetation values for those pixels are then integrated with the vegetation cover map. In this way, the effect of the eight (or twenty four, depending on the size of the filter window) neighbouring pixels surrounding the central pixel of zero vegetation is taken into consideration to estimate the vegetation fraction in that pixel. However, this type of filters takes into consideration the central pixel (which has the wrong vegetation information) when calculating a new value for that central pixel. This means that this method carries forward a fraction of the problem of those pixels that contain the wrong vegetation information.

To overcome this problem of considering the central pixel, other methods of calculating vegetation values for those pixels disregarding the value of the central pixel were investigated. These methods include the mean (excluding the central pixel of interest), the median, and the mode where two window sizes of "3 × 3" or "5 × 5" were considered. Table 5.3 shows the accuracy assessment of the mixture modelling vegetation cover, after rectifying the bad pixels using six different techniques, against the observed vegetation fractions.

The table shows that all of the methods give similar accuracy results with minor differences in the coefficient of determination r^2, which range between 0.8806-0.9010, and the root mean square error (RMSE) ranging between 12.21-13.96. The 3×3 mode method produced the highest accuracy whereas the 3×3 median produced the lowest accuracy. This is because the median method picks up the middle value when all the values of the filtering window pixels are arranged in order of magnitude, disregarding the frequency distribution and the mode of the values. However, in the mode method the pixel value in the filtering window that occurs most frequently is attributed to the central pixel and this method worked well because the central pixel

is more likely to resemble those neighbouring pixels that share common values between them due to spatial dependency between pixels. Thus, the 3×3 mode method was implemented in this study and figure 5.20 shows the regression of the accuracy assessment of the mixture modelling vegetation cover after applying the co-occurrence analysis and the 3×3 mode method.

Method	r^2	***F***	***P***	**RMSE**
3×3 mean (without central pixel)	0.8823	24.58	0.0016	13.83
5×5 mean (without central pixel)	0.8814	24.39	0.0016	13.92
3×3 median	0.8806	24.18	0.0017	13.96
5×5 median	0.8824	24.63	0.0016	13.82
3×3 mode	0.9010	30.20	0.0009	12.21
5×5 mode	0.9005	30.03	0.0009	12.30

Table 5.3. Comparison of the results of different techniques used to replace the vegetation fraction values of the pixels of zero (or very low value of) vegetation in the shade-free mixture modelling vegetation cover.

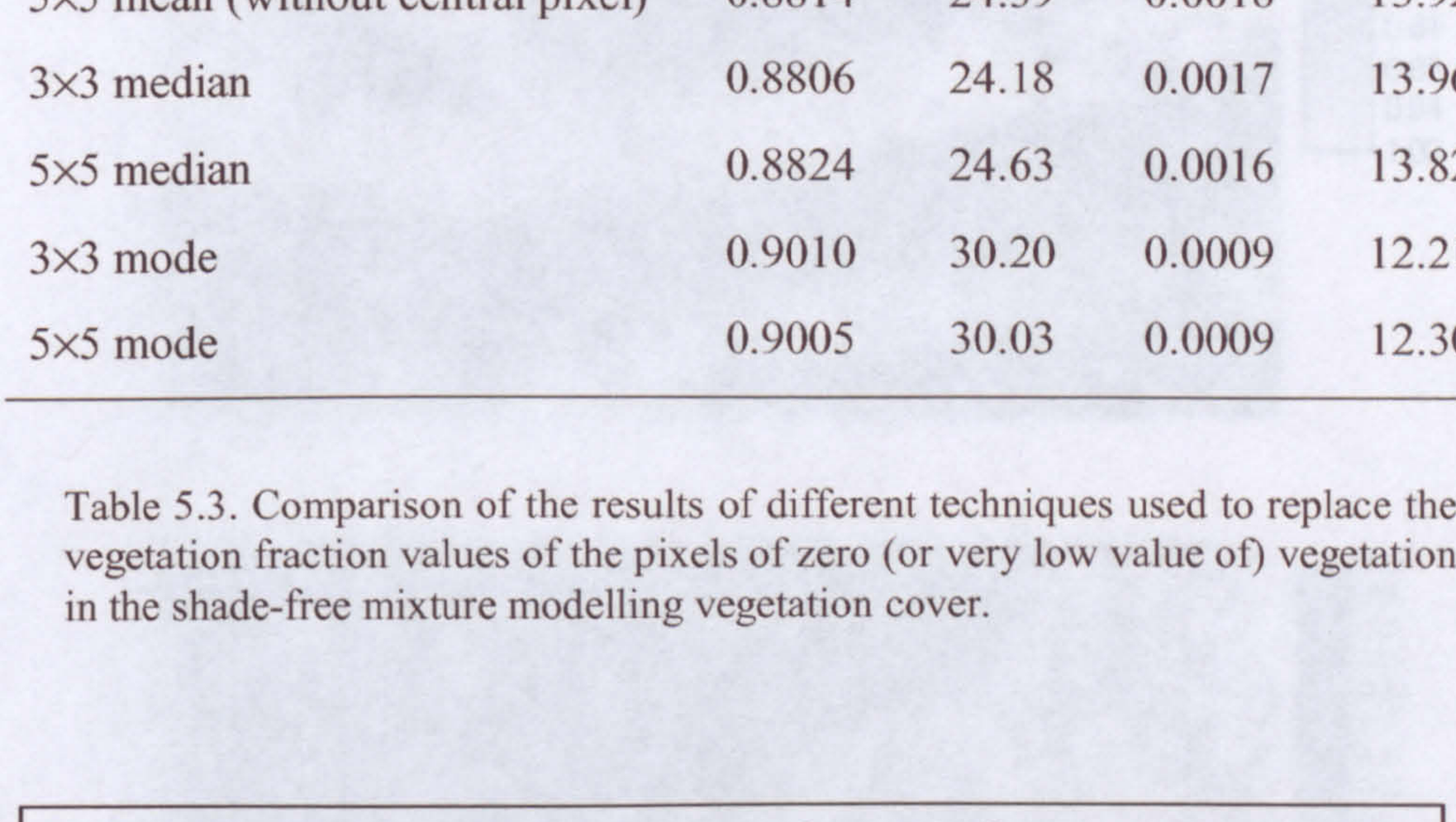

Figure 5.20. The relationship between observed and estimated vegetation cover after applying the co-occurrence matrix analysis and the 3×3 mode window.

A)

B)

Figure 5.21. The effect of applying co-occurrence matrix method on the vegetation cover map in areas of bushes, olive and almond trees. A) is the shade-removed vegetation map and B) is the vegetation map after applying co-occurrence matrix.

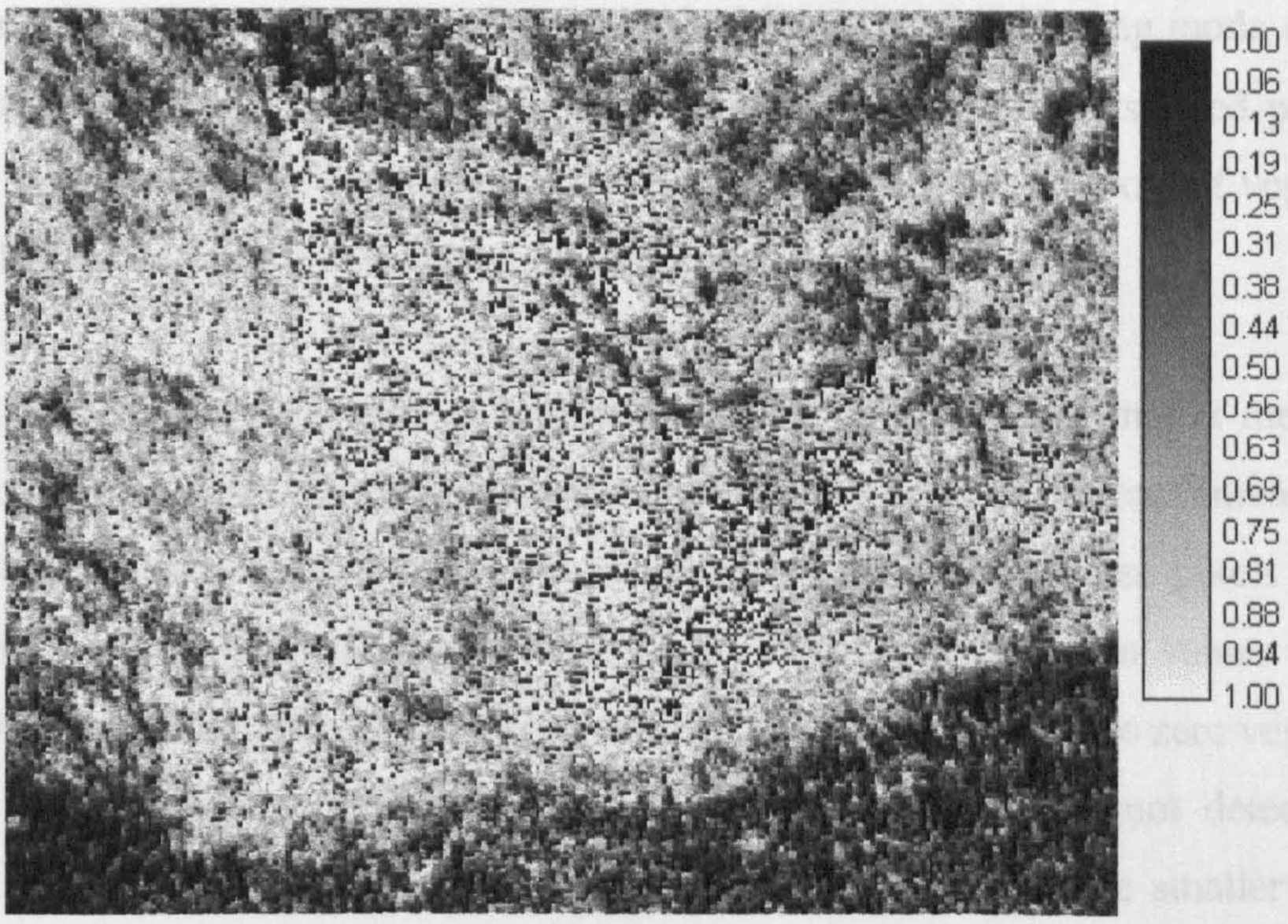

A)

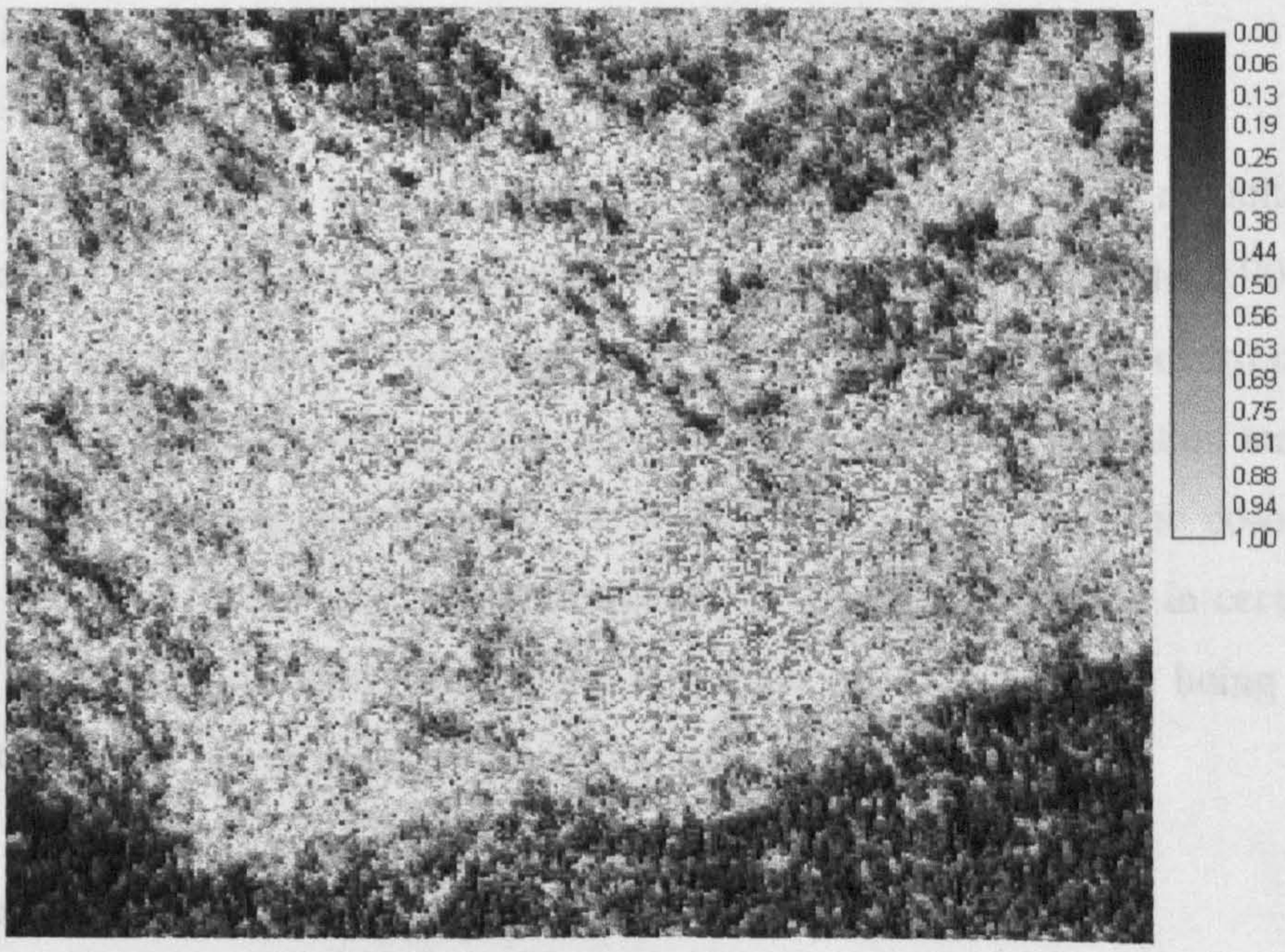

B)

Figure 5.22. The effect of applying co-occurrence matrix method on the vegetation cover map in areas of natural vegetation of matorral. A) is the shade-removed vegetation map and B) is the vegetation map after applying co-occurrence matrix.

Figure 5.21 shows the improvement of the vegetation cover mapping by implementing the co-occurrence matrix analysis and the 3×3 filtering mode method. It should be mentioned here that figure 5.21 B still shows some isolated pixels in darker shade within the vegetation objects but these pixels are not void of vegetation but rather have vegetation information of between 15-25%.

Figure 5.22 shows the results of implementing the co-occurrence matrix method in areas covered by natural vegetation of matorral. A substantial improvement in the vegetation cover is noticed in the first instance where most of those pixels of zero vegetation within matorral bushes have been filled with vegetation values derived from the surrounding pixels. However, some of these pixels still have zero vegetation (black pixels) because the co-occurrence matrix operator could not detect these pixels. This could be attributed to the fact that matorral bushes are smaller objects than the almond and olive trees and that they have irregular shape which makes them difficult to detect.

These results show an overestimation of vegetation and a slight reduction of the accuracy of vegetation cover calculation (r^2 reduced from 0.918 to 0.9010) when compared to the results of vegetation cover before applying the co-occurrence matrix analysis. This seems to be logical because the shade-removed vegetation map already overestimated the vegetation cover (with RMSE of 10.7%) and the co-occurrence matrix approach caused the vegetation cover to have higher values in certain pixels within the vegetation map. Thus, there is a trade off with the gaps being filled but vegetation cover being slightly overestimated.

5.3 MAPPING THE LAND USE

5.3.1 The Effect of Land use on Soil Erosion

Semi-arid areas of the Southern-East of Spain are characterised by the limiting factors of water and natural vegetation which, if combined with intensive agriculture

practices and overgrazing, produce accelerated soil-erosion patterns. Land use has a great effect on the state of the soil properties and vegetation cover and this influences the water infiltration rate and the frequency and intensity of the over-land flow generation (these are discussed below). Hence, land-use mapping is important in the soil-erosion modelling (Auzet *et al.*, 1998).

Agriculture practices in the study area of Vélez Rubio increase the risk of soil erosion through their disturbance of the natural vegetation cover by way of land-use conversion, tilling or overgrazing. Farmers prepare land by tilling or ploughing their fields to increase infiltration and remove the natural vegetation cover. This process is one of the oldest agricultural practices and involves mixing up the nutrients within the soil, loosening the soil particles, incorporating oxygen and removing weeds. These practices have great implications on the hydrological characteristics of the landscape as they significantly alter parameters controlling the overland-flow generation such as soil bulk density (BD), soil depth, surface stone fraction, and initial soil moisture (these parameters were discussed in detail in chapter 3). The process of ploughing deepens the soil depth, which may imply reduction of the overland-flow generation due to higher soil-water-storage capacity. In addition, the ploughing process reduces the soil bulk density and surface stone fraction significantly and increases the initial soil moisture and the soil water storage capacity. These factors, when they are combined, are a good recipe for reducing overland-flow generation. However, there is a trade off as the ploughing process increases the likelihood of soil erosion because it disturbs the natural surface and removes the protective vegetation.

Overgrazing of animals in parts of the study area (see figure 1.6 in chapter 1), where more animals are raised than the land can sustain, is another land-use intensification factor contributing to land degradation by destroying the natural vegetation cover. In addition, animals trampling over the natural vegetation in areas of overgrazing diminish the vegetation species growing in that particular area, and without adequate vegetative cover the land becomes more susceptible to soil erosion.

In their studies about the effect of land use on overland-flow and soil-erosion rates under Mediterranean conditions, Kosmas *et al.* (1997) established a strong link between land-use patterns, overland-flow generation, and soil erosion. They found that greater rates of overland flow and sediment loss are expected in lands cultivated with crops (such as almond, vines and olives) that require frequent removal of natural vegetation from around the trees, leaving soils bare and susceptible to sediment loss all around the year. In addition, using heavy machinery around plantations, such as vines, reduces aggregate stability and organic matter contents and leads to an increase in overland-flow generation and soil-erosion rates (see table 5.4). Martínez-Casasnovas and Sánchez-Bosch (2000) carried out research to assess the impact of change in land use on soil-erosion rates in the North-east of Spain. Their findings were in agreement with the conclusions of Kosmas *et al.* (1997) in that the soil-erosion rate is closely related to the type of land use where soil erosion increase in the area is caused by uncontrolled transformation of land to modern vineyard plantations.

Land use	**Runoff coefficient %** (per year)	**Erosion** (t km^{-2} yr^{-1})
Wheat	1.5-24	15-90
Vines	0.7-31.8	67-460
Eucalyptus	0.6-8.2	1.4-65.6
Shrubland	0.0-10	0.5-21.5
Olives	0.0-2.6	0.0-2.8

Table 5.4. Values of runoff coefficient and soil-erosion rate under different agricultural practices in the Mediterranean region. The table shows the effect of land use on sediment loss (after Kosmas *et al.*, 1997).

In this study the aim of constructing the land-use map of the study area of Vélez Rubio is to use this map to distribute spatially the effects that different land-use practices have on soil properties (e.g. bulk density, soil depth, stone content, ...) because different agricultural practices lead to soil having different characteristics. Since one of the objectives of this study is to evaluate the utility of applying image

processing techniques, that have been developed for lower resolution systems, to high spatial resolution imagery, techniques of image classification are reviewed and implemented. In addition, a method of image interpretation for land use mapping is investigated and implemented and the most appropriate technique will be considered for this study. The soil properties maps which will result from the land use map will be incorporated in the implementation of the selected over-land flow and the soil-erosion models in chapters 6 and 7.

5.3.2 METHODOLOGIES OF LAND-USE MAPPING

5.3.2.1 Image Classification

The process of image classification requires the user to perform two steps (Mather 1999), the first step is to determine a priori the number and nature of the categories in term of which land-cover classes are to be described. An example of these real world object categories is urban areas, woodland, matorral and olive plantations, ploughed fields, etc..... The second step is to assign numerical labels to the pixels on the basis of their properties using a decision-making procedure, usually termed a classification rule. If this labelling operation is carried out for all pixels in the area then the result is a thematic map, showing the geographical distribution of a "theme" such as vegetation type rather than a wide variety of details associated with each place.

Land-use/land-cover changes over the space and time which makes it difficult to measure it in the field, especially over large areas. In this context, remote sensing is regarded as a powerful tool because it provides a wide range of sensors which enable the user to collect the desired data in an appropriate spatial and temporal resolution.

5.3.2.2 Classification Methods

Classification techniques produce a single qualitative map where each pixel in the image is allocated exclusively to one class. A mathematical decision rule is used here to assign image pixels to clusters representing land-cover categories, in the feature space delimited by the spectral bands of the image. There are two main methods of

classification: unsupervised and supervised classification. Unsupervised classification is implemented when insufficient observational or documentary evidence of the nature of the land-cover types is available for the geographical area covered by a remotely sensed image (Mather 1999) or for image exploration. In these circumstances, it is not possible to estimate the means of the classes. The supervised classification methods are based on a prior knowledge of the area, such as the signatures of some land-cover types, and this knowledge is implemented as an input before the classification is carried out. Unsupervised classification is not used in this study as we have a considerable amount of ground reference data.

Figure 5.23. A sub-image of the high resolution aerial photograph study area showing different vegetation types.

Classification methods are appropriate for areas where the number of boundary pixels is small and the scene is nicely partitioned into regions of homogeneous cover. This may be satisfied in many agricultural scenes (Settle and Drake 1993). For instance, the characteristics of the high spatial resolution aerial photographs of our study area aided us in the interpretation of the landscape into meaningful land-cover

classes. In this area, it was easy to distinguish between trees, bare ground and matorral (Figure 5.23). Nevertheless, these methods are not suitable to the regions where land cover varies continuously because most pixels are usually mixtures.

One of the conventional problems in mapping land cover/land use at regional and national scales has been the fact that the data are restricted to low spatial resolution imagery such as MSS, TM, and SPOT imagery of 80 m, 30 m, and 20 m resolution respectively (Townshend, 1992; Harris and Ventura, 1995, Aplin *et al.*, 1999). In such imagery it is difficult to distinguish between distinctive land-cover classes, especially in areas where the spatial extent of the objects in a land-cover class is smaller than the pixel size, such as the case of almond trees and matorral bushes in the study area, where a large amount of details is obscured. This limitation can be overcome through the availability (and future supply) of high spatial resolution satellite sensors such as IKONOS, QuickBird, and OrbView-3 which provides panchromatic and multispectral imagery of 1 *m* and 4 *m* spatial resolution. The aerial photographs, which are used in this study, are a representation of data provided by this generation of satellite sensors because they have similar spatial resolution and similar spectral characteristics in the visible region.

The data provided by this new generation of satellite sensors have greater use in land-cover/land-use mapping because of their ability to reveal various land-cover classes more appropriately by reducing the size of the land-cover objects that can be identified in this imagery. Thus, the ability to map land cover/land use at the local scale will be increased (Aplin *et al.*, 1999). However, this increase in the spatial resolution of remotely sensed imagery is associated with the inevitable increase of the internal variability (or called spectral heterogeneity) within land-cover classes that are present in such imagery (Townshend, 1992). This increase in internal variability can lead to misclassification and, consequently, may result in the decrease of the classification accuracy, despite the fact that the information content in the image is increased (Aplin *et al.*, 1999). In the lower spatial resolution imagery this internal variability is usually averaged out, producing land-cover classes of less spectral overlap and higher classification accuracy.

Markham and Townshend (1981) carried out a study to investigate the relationship between classification accuracy and spatial scale using simulated high spatial resolution imagery. They found that the internal variation varies considerably between different land-cover types and between spectral bands when the spatial resolution is changed. They also found that the classification accuracy does not only change as a function of spatial resolution, but it also changes as a function of the relative location of the land-cover types in the feature space which makes it impossible to predict the effect of resolution on classification accuracy.

Woodcock and Strahler (1987) carried out a study to investigate the effect of spatial scale (or resolution) on the amount of information contained in the remotely sensed imagery, on the selection of a suitable method to extract this information, and on the spatial structure of the scene itself. They did so by calculating the relationship between the spatial scale and the local image variance of a high resolution remotely sensed image as this resolution collapses to coarser resolutions by applying averaging techniques. This spatial scale/local image variance relationship revealed that the spatial structure of the scene is a function of the sizes and the spatial relationships of the objects in the scene and that the local variance is maximum when the resolution of the image is slightly smaller than the size of the objects in the scene. This local image variance becomes smaller as the image resolution becomes either smaller or larger than the size of these objects.

These findings are significant when extracting information from remotely sensed imagery by means of classification so that the right type of classifier is implemented. This means that when the local image variance is high, information extracting techniques that utilise the texture and context of an image are more appropriate. However, the traditional per-pixel classifiers, such as in the Maximum Likelihood Classification, can produce better results and higher accuracy when the local image variance is low. In this study the resolution of the aerial photographs is 0.55 *m* which is far smaller than the size of most objects in the scene such as the ploughed fields, bare ground area, and almond and olive trees, with the exception of matorral bushes

where their size, on average, is similar to the aerial photographs spatial resolution. This type of scene produces a very low local image variance in most of the image, thus, the per-pixel classification techniques are more appropriate here to produce the land-use map from the aerial photograph.

We can distinguish between a wide range of commonly used supervised hard classifiers such as parallelpiped, minimum distance to mean, Maximum Set Basic Probability, and maximum likelihood classification method. Maximum likelihood classifier is generally considered to be the most accurate and most widely used per pixel hard classifier. This classification method is based on the probability density function associated with a particular class signature. Pixels are assigned to the most likely class based on a comparison of the posterior probability that it belongs to each of the signatures being considered. This classifier is also known as a Bayesian classifier since it has the ability to incorporate prior knowledge using Bayes' Theorem. Prior knowledge is expressed as a prior probability that each class exists. It can be specified as a single value applicable to all pixels, or as various values in an image expressing different prior probabilities for each pixel (Strahler, 1980). In the maximum likelihood classification method the distance from the mean of the training data is not the only criterion to include or exclude a point to a specific class. The relative dimensions of the axes, the shape, and the orientation of the probability ellipse are taken into account during the classification. This probability distribution function can be expressed in the following equation:

$$P(x) = 2\pi^{-0.5p} \, /S_i/^{-0.5} \, exp[\,-0.5(y^T S_i^{-1} y)] \qquad 5.22$$

Where: S_i is the sample variance-covariance matrix for the class i, y is the residual $(x-x_{i(mean)})$, the $x_{i(mean)}$ is the multivariate mean of the class i, p is number of classes, and y^T is the transpose of $(x-x_{i(mean)})$.

The maximum likelihood classification method was selected in this study to derive the land-use map of the study area for two reasons. First, this method is relatively simple to implement, yet it is robust and produces reasonably good results which

make it a very widely used classification method amongst scientists. Secondly, it has been shown to be more accurate than the other three methods.

5.3.3 IMPLEMENTATION OF CLASSIFICATION FOR LAND-USE MAPPING

5.3.3.1 Maximum Likelihood Land-use Classification

In order to classify the aerial photograph of the study area, the distinctive land-use classes in this aerial photograph will be considered and the signatures of their training sites will be developed using the signature development tools in the IDRISI package. The distinctive land-use classes that have been initially chosen are matorral, ploughed fields, road, river, and bare ground (these classes are explained below) where bare ground class represents the areas of overgrazing and the fire scar (figure 5.23b). These classes have been selected because they represent all of the land-use types and practices in the study area.

However, if the maximum likelihood classification method is to be used for land-use mapping, then the selected classes to perform this classification should fulfil certain criteria that 1) these classes should have different distinctive spectral reflectances which is essential to minimise any spectral overlap. 2) They represent the different types of land use of the area where land is either ploughed, kept covered with natural vegetation, or overgrazed. 3) The spectral reflectance of training data in each of these classes, and in each spectral band, should be as close as possible to the normal distribution which is essential to perform this type of classification. 4) Consequently, these classes should then represent the two different types of soils prevailed in the study area: grey and red soil, as well as representing the different soil backgrounds in other classes because these soils have different spectral reflectances.

To fulfil all the above conditions, eleven new distinctive classes have been chosen for land-use mapping. These classes are: grey soil matorral, ploughed grey soil, grey soil river, red soil river, bare ground, ploughed red soil, red soil matorral, shade, trees, and unpaved white road and the figure 5.23b shows the relationship between

these classes (termed class types 1) and the initial five land use classes. The classes of grey and red soil matorral represent the unploughed fields covered with natural vegetation with grey and red background soils respectively. The ploughed grey and red soils are areas of cultivation where the natural vegetation cover is removed for the purpose of almond and olive plantation. Classes of red and grey soil river represent the red and grey soils in a seasonal river which runs through the study area. These two classes are considered as separate classes from unploughed red and grey soil classes, despite having relatively close spectral reflectances, because their soils are more compacted and have higher bulk density values. The bare ground class represents an area where vegetation cover is destroyed and soil is compacted in the act of goats overgrazing as well as the area of fire scar.

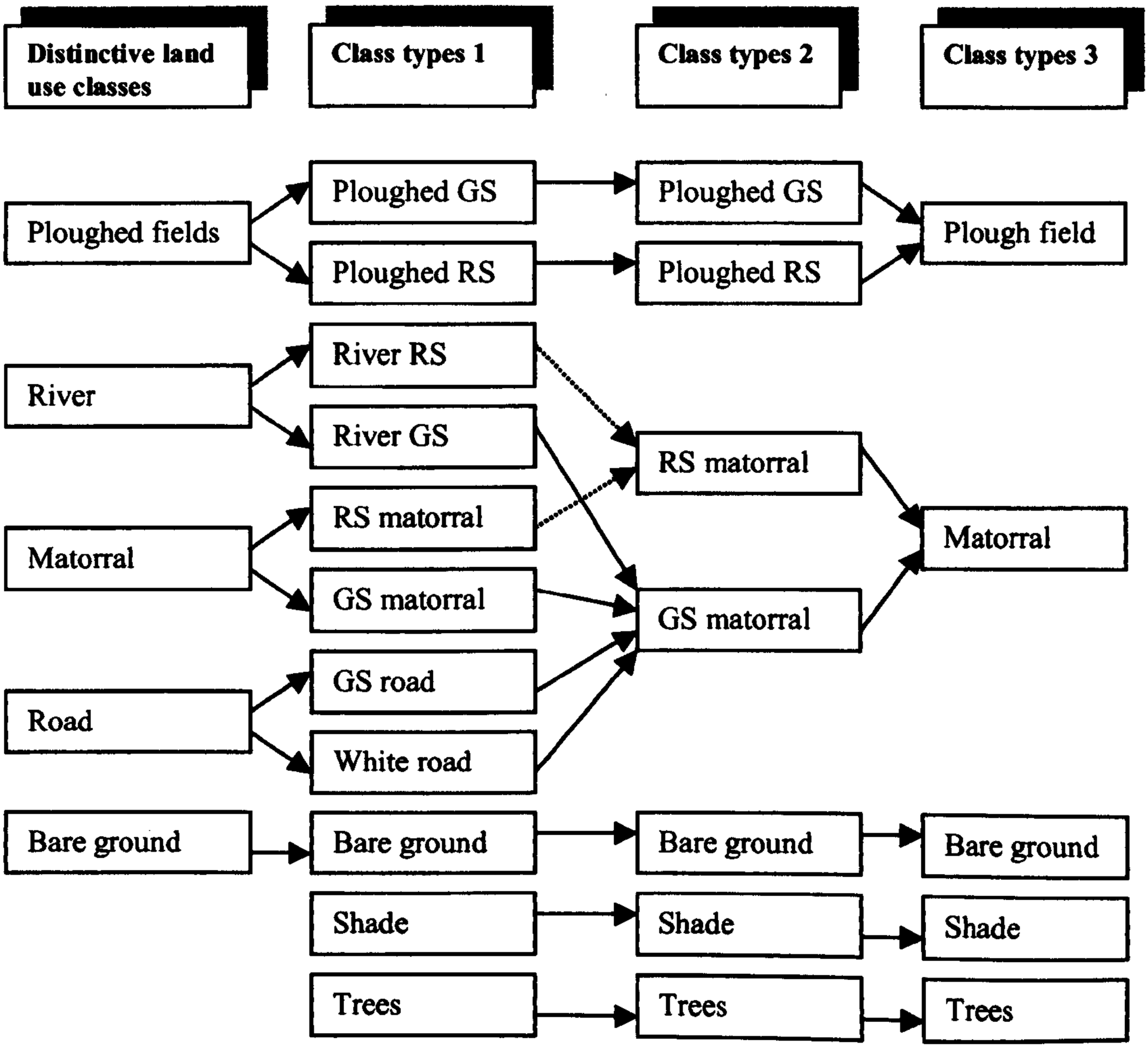

Figure 5.23b. Showing the land use/land cover classes at various stages of classification and amalgamation where class types 1, 2 and 3 are classes that will be explained later on in this chapter in figures 5.26, 5.27 and 5.28 respectively.

The trees class is the almond and olive trees that exist in the ploughed fields of both grey and red soils. The shade class describes the shadow cast by trees and matorral bushes and as a result of this the shade is spatially associated with the vegetation cover across the area. Although the spectral reflectance of the shade does not follow the normal distribution, it has to be treated as a separate class from the trees class because considering shade and trees as one class will cause the spectral reflectance of this class to be bimodal which will lead to classification errors. When developing the spectral signatures of these classes in the 0.55m spatial resolution aerial photograph, each pixel was assumed to be a pure pixel in the training areas.

These chosen classes for maximum likelihood image classification represent a combination of land-cover and land-use classes, though land-cover classes are much more dominant across the study area. This is due to the fact that spectral reflectance in remotely sensed imagery is related to land-cover and not the land-use types (Aplin *et al.*, 1999). For example, the red soil matorral and grey soil matorral are two different land-cover classes and they have different distinctive spectral reflectances but they are regarded as a one land-use type of unploughed natural vegetation in terms of land utility. Aplin *et al.*, (1997) used land-use classes to classify high spatial resolution imagery directly and found that the accuracy of classification was low. This accuracy was greatly improved when land-cover classes, as opposed to land-use classes, were used in the classification.

However, despite the fact that most of the chosen classes represent land-cover types, some of these classes represent land-use types. For example, the bare ground class has been merely selected according to its land-use type because, despite relative spectral similarity with ploughed red soil, it has different hydrological characteristics such as soil depth and bulk density. The same scenario applies to the red and grey soil river classes when compared to ploughed red and grey soil classes respectively. For simplicity reasons, all these classes will be called land-cover classes from now onwards.

Before the image classification can be carried out, the training signatures for the classification classes were created by choosing representative training sites across the study area for each class which cover the variation in that class. As it has been mentioned earlier in this chapter, the maximum likelihood classification method assumes that histograms of the spectral signatures of training sites in all three bands in any given class are normally distributed. As a result of this, after the training signatures of the selected classes are created and their statistics (e.g. mean and standard deviation) are calculated, these signatures had to be edited in order to simulate the normal distribution as much as possible before classification and their statistics were re-calculated. This editing process was performed in the IDRISI package by subjectively trimming the ends of the frequency distribution histograms. This editing process can be a source of error by excluding parts of a certain class which will then be assigned to another class wrongly and this potential error should be taken in consideration when assessing the accuracy of the resultant maps.

Figure 5.24 A and B shows the spectral signature distribution of two of the 11 classes, the grey soil matorral and shade. In this figure the histograms of the three visible bands representing grey soil matorral are quite normally distributed, however, the histograms of the shade clearly deviate from a normal distribution which is the main assumption that the maximum likelihood classification is based on. The spectral signature distributions of training sites for the rest of the classes are included in appendix "C" and demonstrate that some classes, such as grey soil road and ploughed red soil, have bimodal distribution in one or all of the spectral bands and that the other classes, such as the trees class, are also not normally distributed. These bimodal distributions and the other deviations from the normal distribution, despite efforts to avoid them, will be a source of errors in the classification processes and it is difficult to rectify their effects.

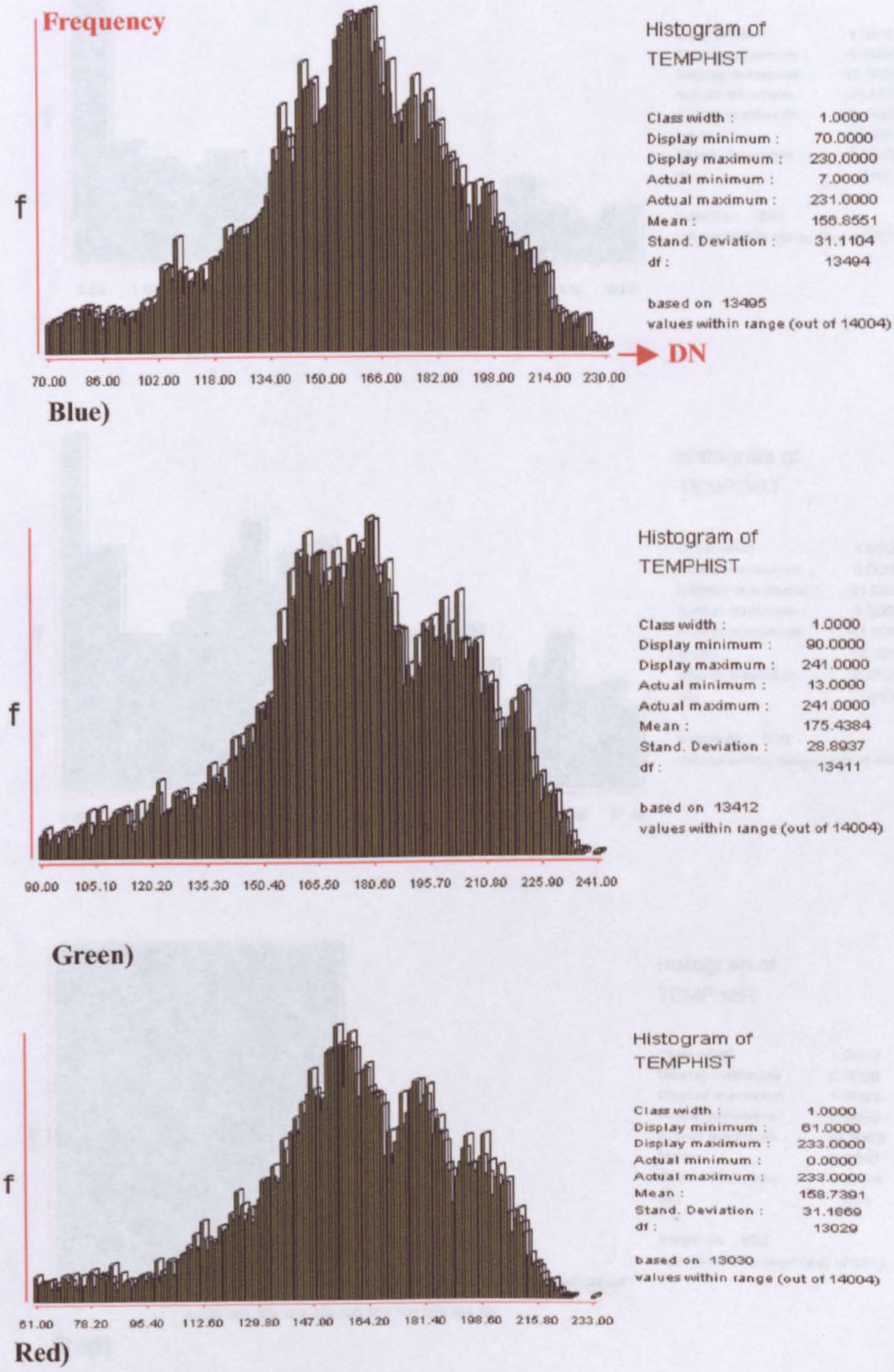

Figure 5.24 A. Histograms and statistics of the spectral signature of the training site of grey soil matorral in the blue, green, and red bands. X and Y axis represents DN and frequency respectively.

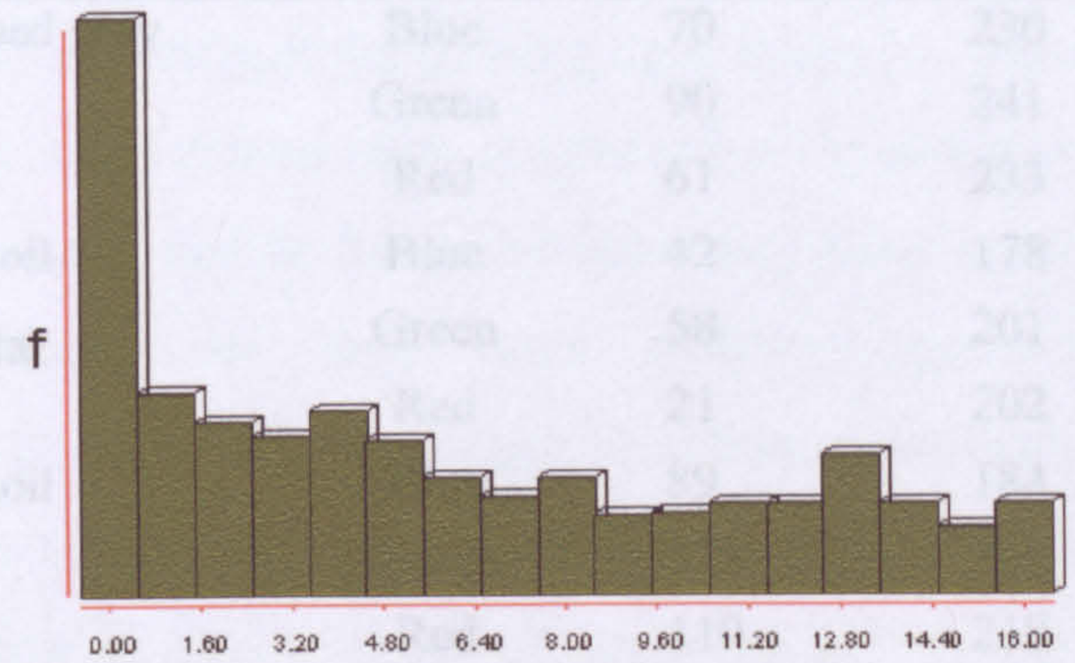

Histogram of
TEMPHIST

Class width :	1.0000
Display minimum :	0.0000
Display maximum :	16.0000
Actual minimum :	0.0000
Actual maximum :	42.0000
Mean :	5.5154
Stand. Deviation :	5.1093
df :	649

based on 650
values within range (out of 857)

Blue)

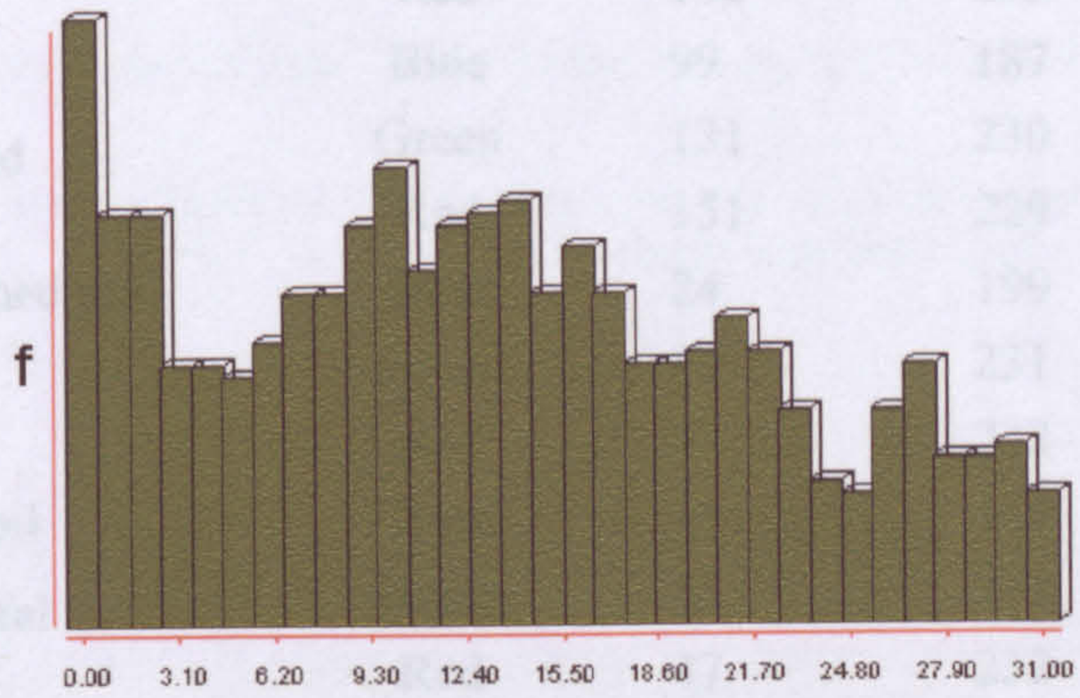

Histogram of
TEMPHIST

Class width :	1.0000
Display minimum :	0.0000
Display maximum :	31.0000
Actual minimum :	0.0000
Actual maximum :	41.0000
Mean :	13.1241
Stand. Deviation :	8.6629
df :	813

based on 814
values within range (out of 857)

Green)

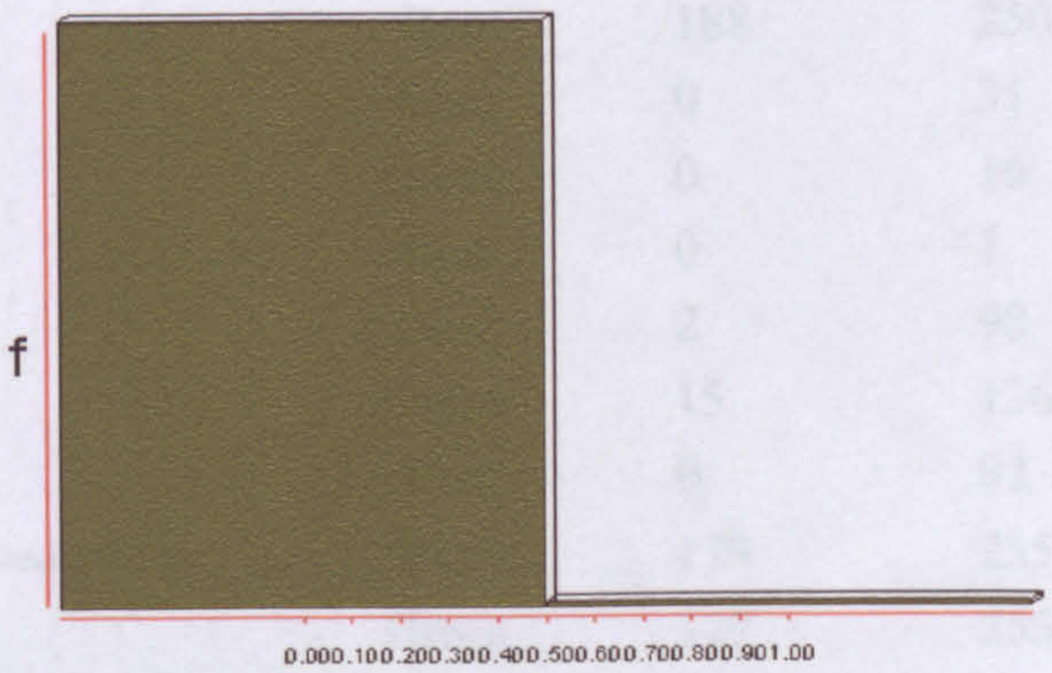

Histogram of
TEMPHIST

Class width :	1.0000
Display minimum :	0.0000
Display maximum :	1.0000
Actual minimum :	0.0000
Actual maximum :	10.0000
Mean :	0.0047
Stand. Deviation :	0.0684
df :	851

based on 852
values within range (out of 857)

Red)

Figure 5.24 B. Histograms and statistics of the spectral signature of the training site of shade.

Land cover	Spectral band	Minimum	Maximum	Mean	St.dv.
Ploughed grey soil	Blue	70	230	153	30.7
	Green	90	241	170.9	28.6
	Red	61	233	149.5	31.4
Grey soil	Blue	42	178	111.3	31.1
Matorral	Green	58	201	131.7	32.3
	Red	21	202	111.5	38.5
Grey soil	Blue	89	184	136.1	16.7
River	Green	128	209	168	14.8
	Red	119	218	165	14.3
Grey soil	Blue	102	215	155.5	22.6
Road	Green	114	244	180.5	26.9
	Red	102	253	182.7	32.4
Bare	Blue	99	187	144.1	17.1
Ground	Green	131	230	179.4	16.8
	Red	151	229	190.8	16.7
Ploughed red soil	Blue	24	199	114.4	39.3
	Green	89	231	160.4	29.6
	Red	47	232	183.2	33.3
Red soil	Blue	11	169	87.8	30.2
Matorral	Green	45	211	126.9	32.2
	Red	47	232	133.3	39.1
Red soil	Blue	110	210	147.6	17.6
River	Green	163	231	190.6	14.0
	Red	188	250	220.3	12.5
Shade	Blue	0	31	14.3	8.5
	Green	0	16	10.4	6.2
	Red	0	1	0.03	0.07
Trees	Blue	2	98	47.2	22.8
	Green	15	136	78.8	29
	Red	0	82	31.4	31.4
Unpaved white	Blue	179	255	227.3	22.0
Road	Green	127	255	244.1	11.7
	Red	213	255	244.1	11.9

Table 5.5 the spectral signatures of the classes used by the supervised maximum likelihood classification.

Table 5.5 shows the means and standard deviations of spectral signatures of the chosen training data representing the 11 classes and the figure 5.25 is the signature comparison chart of the training data. It can be noticed in figure 5.25 that the training data of some classes such as grey soil river and grey soil road are quite similar in all of the three visible bands because they have similar characteristics of the surface reflectance, yet they have different geomorphological and hydrological characteristics. The maximum likelihood classification is very sensitive to this kind of spectral overlap problem which may generate errors in the output maps, thus, problems of errors should be expected in the output classification results. Despite this, classes with spectral overlap problems are kept separate in order to maintain a normal distribution, where possible. Classes of similar characteristics (i.e. classes that have similar land use) can be amalgamated in a later stage.

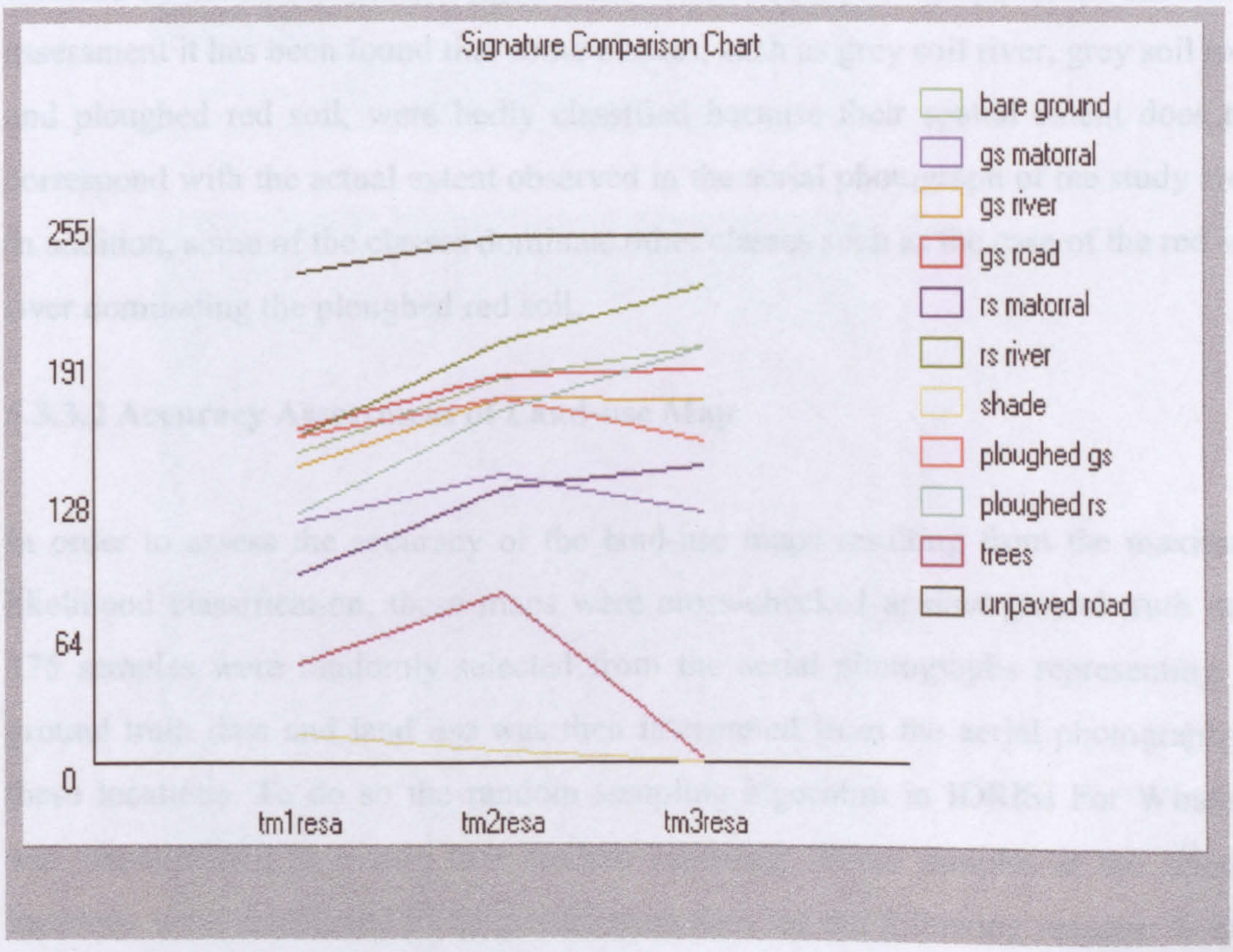

Figure 5.25. The signature comparison chart of the 11 training sites in the study area. "tm1resa" is the blue band, "tm2resa" is the green band, and "tm3resa" is the red band. RS and GS are red soil and grey soil respectively.

The maximum likelihood classification is also known as a Bayesian classifier since it has the ability to incorporate prior knowledge using Bayes' Theorem. Prior knowledge is expressed as a prior probability that each class exists. Consequently, there are two types of the maximum likelihood classification carried out in this study, these are equal prior probability and defined prior probability for each spectral signature. The prior probabilities were defined by roughly digitising each class in the aerial photograph and working out the fractions of each class as a percentage of the whole area. The figures 5.26 A and B show the output results of this maximum likelihood classification with the equal prior probability and the defined prior probability respectively.

The maps resulting from the maximum likelihood classification were initially assessed by visual comparison against the colour aerial photograph. From this initial assessment it has been found that some classes, such as grey soil river, grey soil road and ploughed red soil, were badly classified because their spatial extent does not correspond with the actual extent observed in the aerial photograph of the study area. In addition, some of the classes dominate other classes such as the case of the red soil river dominating the ploughed red soil.

5.3.3.2 Accuracy Assessment of Land-use Map

In order to assess the accuracy of the land-use maps resulting from the maximum likelihood classification, these maps were cross-checked against ground truth data. 175 samples were randomly selected from the aerial photographs representing the ground truth data and land use was then interpreted from the aerial photographs at these locations. To do so the random sampling algorithm in IDRISI For Windows was implemented to ensure true random sampling. These samples at the selected locations were considered to be ground truth data for the following reasons: 1- each sample location is contained within one pixel. 2- Because the aerial photographs were of a very high spatial resolution (55 cm), it was decided to accept that each pixel in these aerial photographs contains one ground object and, consequently, represents one type of land use. 3- this was the only way to collect the ground truth data about

the study area because aerial photographs of the study area were taken on the 9th of April 1996 and by the time this research was conducted it would be impossible to say which areas had experienced changes in land use.

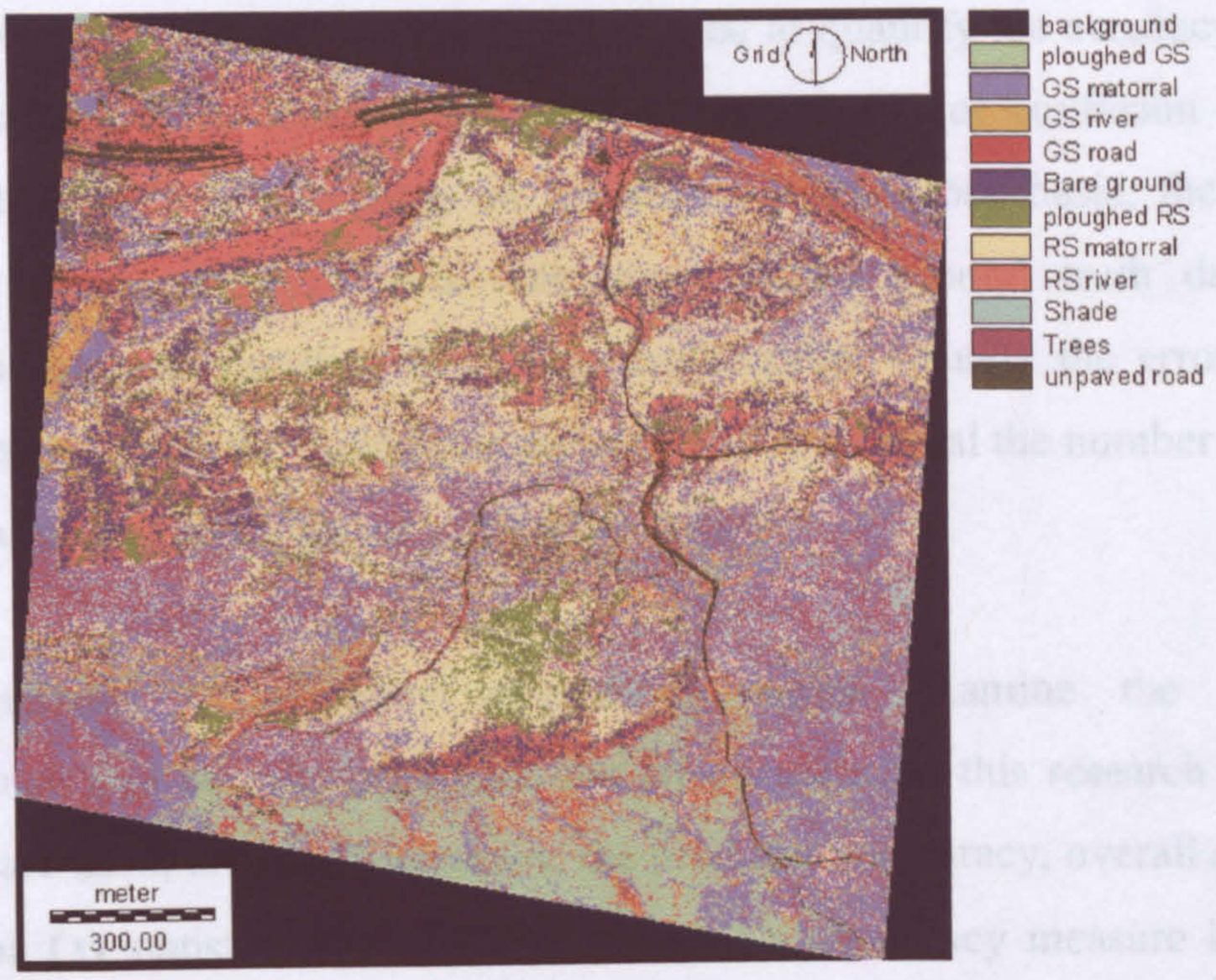

A)

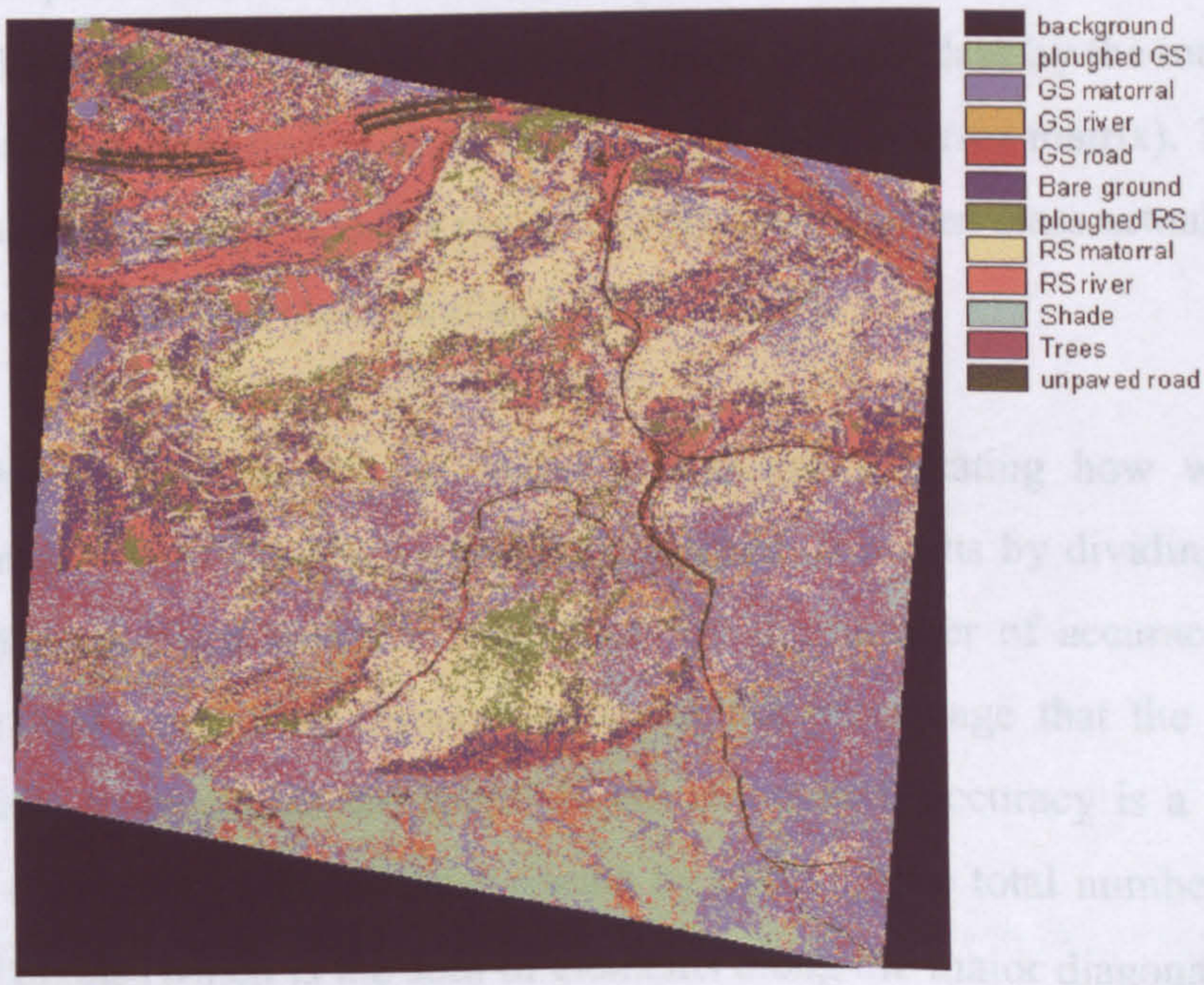

B)

Figure 5.26. The maximum likelihood supervised classification result of the 11 classes with A) equal prior probability and B) defined prior probability. RS and GS are red soil and grey soil respectively.

The process of image classification is incomplete until the accuracy associated with these maps is assessed. According to Lillesand and Kiefer (2000), the ability of remote sensing techniques to produce land-use/land-cover maps, by means of classification, far exceeds the ability to meaningfully quantify their accuracy. One of the most common remote sensing methods used to quantify the accuracy of land-use maps, resulting from classification, is the error matrix (or confusion matrix). The error matrix method compares, on a category-by-category basis, the relationship between known reference data (sometimes called ground truth data) and the corresponding map resulting from the classification. Usually the error matrix is a square matrix where the number of columns and rows equal the number of categories in the resulting map (Lillesand and Kiefer, 2000).

Many methods of accuracy assessment, which examine the classification performance, can be calculated from the error matrix. In this research four of these methods are used, the user's accuracy, the producer's accuracy, overall accuracy, and the Kappa (κ) statistic. The user's accuracy is an accuracy measure indicating the fraction of pixels that were correctly classified in each class. It is calculated by dividing the number of correctly classified pixels in each class by the total number of pixels that were classified in that class (the row total in error matrix). This measure indicates the percentage % that a pixel classified into a given class actually represents that class on the ground (Lillesand and Kiefer, 2000).

The producer's accuracy is an accuracy measure indicating how well accuracy assessment pixels of the given class are classified. It results by dividing the number of correctly classified pixels in each class by the number of accuracy assessment pixels for that class. This measure indicates the percentage that the classification method fails to recognise the actual class. The overall accuracy is a more general accuracy assessment indicator and results by dividing the total number of correctly classified pixels (which is the sum of elements along the major diagonal) by the total number of accuracy assessment pixels (Lillesand and Kiefer, 2000).

Accuracy methods, such as the overall accuracy, give no insight into how well the classifier is performing for each of the different classes. In particular, a classifier might perform well for a class which accounts for a large proportion of the test data and this will bias the overall accuracy, despite low class accuracies for other classes. In addition, If pixels in an image are randomly assigned to classes, the error matrix still produces percent correct values due to chance. Thus, the effect of this chance agreement should be corrected for during accuracy assessment. The κ statistic is a measure of the difference between the actual agreement between reference data and the classifier and the chance agreement between the reference data and a random classifier:

$$\kappa = \frac{overall\ accuracy - chance\ agreement}{1 - chance\ agreement} \qquad 5.23$$

The chance agreement in equation 5.23 is calculated from the error matrix as follows: if each entry in the error matrix is labelled as p_{ij} , where i denotes the row number and j denotes the column number. Then the class accuracies are calculated by taking the row totals p_{io} and dividing by the number of test sites, N. The column totals is denoted by p_{oj}. Thus the error matrix and totals are denoted as:

$$\begin{vmatrix} P_{1,1} & P_{1,2} & \dots & P_{1,j} & P_{1,o} \\ P_{2,1} & P_{2,2} & \dots & P_{2,j} & P_{2,o} \\ \dots & \dots & \dots & \dots & \dots \\ P_{i,1} & P_{i,2} & \dots & P_{i,j} & P_{i,o} \\ P_{o,1} & P_{o,2} & \dots & P_{o,j} & N \end{vmatrix} \qquad 5.24$$

The chance agreement in this case is expressed in the following equation:

$$\text{Chance agreement} = \sum_{i,j=1,N} PioPoj \qquad 5.25$$

κ statistic can be treated as an indicator of the extent to which the percentage correct values of an error matrix are due to true agreement versus chance agreement (Lillesand and Kiefer, 2000). κ value ranges between 0 and 1, in the ideal situation κ =1 when true agreement approaches 1 and chance agreement approaches 0.

Error Matrix Analysis of ground truth (columns) against maximum likelihood classification image with equal prior probability (rows). No. of classes 11. Numbers in table represent No. of samples

	Ploughed GS	GS mato.	GS road	Bare ground	Ploughed RS	RS mato.	RS river	shade	Trees	Unpaved white road	Total No.	User Accuracy
Ploughed GS	4	6	0	0	1	0	0	0	0	0	11	0.364
GS matorral	0	13	1	0	1	10	0	0	5	0	30	0.433
GS river	0	0	1	0	0	2	1	0	0	0	4	0
GS road	1	1	0	0	2	0	1	0	0	1	6	0
Bare ground	2	1	0	1	8	8	0	0	0	0	20	0.05
Ploughed RS	0	1	0	0	5	3	0	0	0	0	9	0.556
RS matorral	0	4	0	0	3	24	0	0	4	0	35	0.686
RS river	0	0	0	0	4	1	4	0	0	0	9	0.445
Shade	0	1	0	0	0	0	0	5	0	0	6	0.833
Trees	0	0	0	0	0	2	0	0	2	0	4	0.5
Unpaved white road	0	0	0	0	0	0	2	0	0	1	3	0.333
Total No. of samples	7	27	2	1	24	50	8	5	11	2	137	
Producer's Accuracy	0.571	0.482	0	1	0.208	0.48	0.5	1	0.182	0.5		

Overall accuracy is 0.431

KAPPA INDEX OF AGREEMENT (KIA)

Category	Using MAXLIKE as the reference image (user's)	Using ground truth as the reference image (producer's)
Ploughed GS	0.3294	0.5340
GS matorral	0.2942	0.3361
GS river	0.0000	N/A
GS road	-0.0148	-0.0458
Bare ground	0.0430	1.0000
Ploughed RS	0.4612	0.1527
RS matorral	0.5051	0.3016
RS river	0.4100	0.4648
Shade	0.8270	1.0000
Trees	0.4563	0.1572
Unpaved white road	0.3235	0.4888

Overall Kappa = 0.3207

A)

Table 5.6. The error matrix analysis to assess the accuracy of the landuse maps. GS represents grey soil and RS is red soil. MAKLIKE and MAXLIKE2 are the results of maximum likelihood classifications using the equal and defined prior probability approaches respectively. For explanation of cases (A and B) see text.

Error Matrix Analysis of ground truth (columns) against maximum likelihood classification image with defined prior probability (rows). No. of classes 11.

	Ploughed GS	GS mato.	GS road	Bare ground	Ploughed RS	RS mato.	RS river	shade	Trees	Unpaved white road	Total No.	User's Accuracy
Ploughed GS	4	5	0	0	1	0	0	0	0	0	10	0.4
GS matorral	0	13	1	0	1	10	0	0	5	0	30	0.433
GS river	0	0	1	0	0	2	0	0	0	0	3	0
GS road	1	2	0	0	2	0	1	0	0	1	7	0
Bare ground	2	1	0	1	8	10	1	0	0	0	23	0.044
Ploughed RS	0	1	0	0	5	2	0	0	0	0	8	0.625
RS matorral	0	4	0	0	3	23	0	0	4	0	34	0.677
RS river	0	0	0	0	4	1	4	0	0	0	9	0.444
Shade	0	1	0	0	0	0	0	5	0	0	6	0.833
Trees	0	0	0	0	0	2	0	0	2	0	4	0.5
Unpaved white road	0	0	0	0	0	0	2	0	0	1	3	0.333
Total No. of samples	7	27	2	1	24	50	8	5	11	2	137	
Producer's Accuracy	0.571	0.482	0	1	0.208	0.46	0.5	1	0.182	0.5		

Overall accuracy is 0.423

KAPPA INDEX OF AGREEMENT (KIA)

Category	Using MAXLIKE2 as the reference image (user's)	Using ground truth as the reference image (producer's)
Ploughed GS	0.3677	0.5377
GS matorral	0.2942	0.3361
GS river	0.0000	N/A
GS road	-0.0148	-0.0538
Bare ground	0.0364	1.0000
Ploughed RS	0.5454	0.1592
RS matorral	0.4905	0.2817
RS river	0.4100	0.4648
Shade	0.8270	1.0000
Trees	0.4563	0.1572
Unpaved white road	0.3235	0.4888

Overall Kappa = 0.3153

B)

Table 5.6 *continued* ....

Table 5.6 shows the error matrix results of the accuracy assessment where tables 5.6 A and 5.6 B are the error matrices of the equal and defined prior probability respectively when 11 classes are used to derive the land-use map. The results from tables 5.6 A and 5.6 B show similar overall accuracy of 0.43. This overall accuracy is regarded to be very low in most of the land-use mapping applications from remotely sensed data. When the error matrix is investigated thoroughly it can be noticed that grey soil road and grey soil river classes give the lowest user's and producer's accuracies 0.00 respectively and the worst κ statistic values 0.00 in the classification process. This lowest accuracy for these two classes could be attributed to the fact that these classes are very small and there was a small number of ground truth samples for these classes during the accuracy assessment process, as well as the possibility of these classes being confused with another class.

The grey soil river class does not have a producer's accuracy value in the error matrix because none of the ground truth samples fall within this class. The error matrix also shows that there are nine ground truth samples representing the ploughed red soil, however, there are twenty four of the samples that fall in this class bringing down the producer's accuracy to 0.21, compared to a user's accuracy of 0.56. This indicates that the classified land cover of ploughed red soil spatially extends beyond the true boundaries of this land-cover type and this justifies the low κ statistic (producer's) value of 0.15 for that class.

In addition, the accuracy assessment of the bare ground class produced a very low user's accuracy of 0.05 because this class has been greatly dominated by ploughed red soil and red soil matorral classes. Although the bare ground class represents a different land-use type from the ploughed and matorral red soil classes, it has, to some extent, similar surface reflectance characteristics to the other two classes (see figure 5.25) and caused large errors in the classification. Producer's accuracy for the bare ground class is very high 1.00 because only one sample, which is rightly classified, falls within this class. This caused the κ statistic for this class to appear very high for the producer's and very low for the user's accuracies.

Shade, however, has the highest user's and producer's accuracies which can be justified by the distinctive spectral signature of shade. κ statistic produces similar overall reasonable results of 0.32 in tables 5.6 A and 5.6 B for both equal and defined prior probability classifications. κ statistic values in these tables indicate that some classes, such as bare ground and shade, are ideally classified due to true agreement between the ground truth data and the classifier and that the chance agreement is minimal. Some other classes such as grey soil road, ploughed red soil and trees have very low κ statistic indicating a very high element of the chance agreement in the classification process.

5.3.3.3 Land-use Class Merging for Improving Classification Accuracy

Some land-cover classes can be amalgamated into one class for three main reasons: 1- these classes have similar soil and land-use characteristics (e.g. Bulk density), 2- the available soil and hydrological data do not cover such land-cover classes, 3- they are spectrally different so they had to be treated as separate classes during classification. For example, it is possible to amalgamate unpaved white road, grey soil road, grey soil river, and grey soil matorral into one class because these classes share similar characteristics such as soil being unploughed which means that the soil depth and bulk density measurements are very similar in these classes. In addition, for the same reasons, red soil river and red soil matorral classes could be amalgamated into one class. Figure 5.23b explains the relationship between these classes (termed class types 2) and the initial eleven classes. Figures 5.27 A and 5.27 B show the new land-use maps both with equal and defined prior probability respectively.

Tables 5.7 A and 5.7 B show the accuracy assessment of the land-use maps after amalgamation. The results from these tables prove a slight improvement of overall classification accuracy from 0.43 to 0.47 because some classes have been merged. This is due to the fact that the producer's accuracy of grey soil matorral has risen from 0.48 to 0.58 and of red soil matorral from 0.48 to 0.50. However, this rise in producer's accuracy is accompanied with a slight drop of the user's accuracy for both

classes. This means that in the new two classes less proportional number of the ground truth samples fall in the relevant land-cover class of these two classes (worse user's accuracy) and that less number of the ground truth samples which belong to other classes actually fall in these classes (better producer's accuracy).

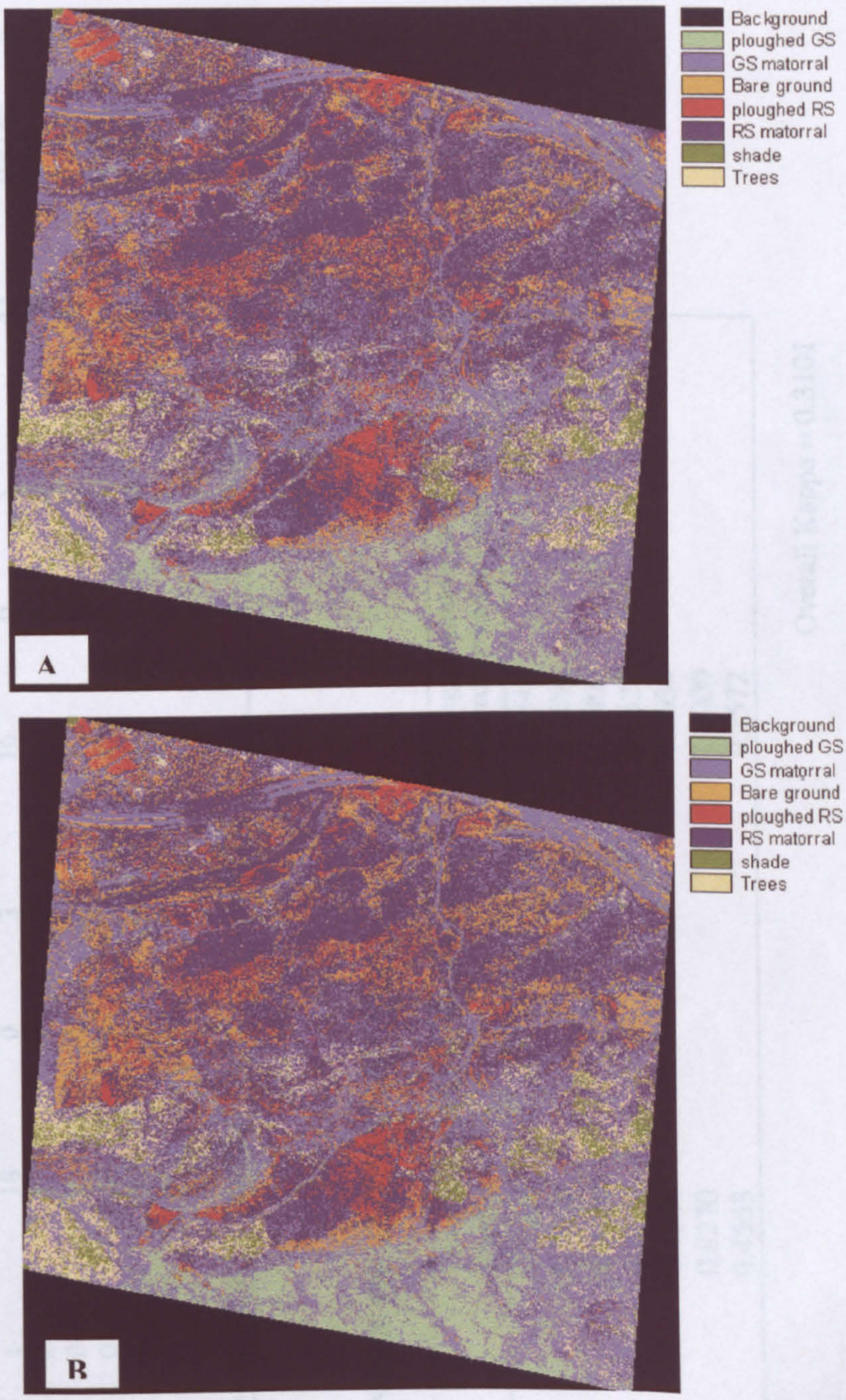

Figure 5.27. The A) equal prior probability and B) the defined prior probability maximum likelihood classifications. The classes unpaved road, grey soil road and grey soil river are amalgamated into grey soil matorral, and red river class is amalgamated into red soil matorral.

Error Matrix Analysis of ground truth (columns) against maximum likelihood classification image with equal prior probability (rows). No. of classes 7

	Ploughed GS	GS matorral	Bare ground	Ploughed RS	RS matorral	Shade	Trees	Total No.	User's Accuracy
Ploughed GS	4	6	0	1	0	0	0	11	0.3636
GS matorral	1	18	0	3	16	0	5	43	0.4186
Bare ground	2	1	1	8	8	0	0	20	0.05
Ploughed RS	0	1	0	5	3	0	0	9	0.5556
RS matorral	0	4	0	7	29	0	4	44	0.6591
Shade	0	1	0	0	0	5	0	6	0.8333
Trees	0	0	0	0	2	0	2	4	0.5
Total No. of samples	7	31	1	24	58	5	11	137	
Producer's Accuracy	0.5714	0.5806	1	0.2083	0.5	1	0.1818		

Overall accuracy is 0.467

KAPPA INDEX OF AGREEMENT (KIA)

Category	Using MAXLIKE as the reference image (user's)	Using ground truth as the reference image (producer's)
Ploughed GS	0.3294	0.5340
GS matorral	0.2486	0.3888
Bare ground	0.0430	1.0000
Ploughed RS	0.4612	0.1527
RS matorral	0.4088	0.2634
Shade	0.8270	1.0000
Trees	0.4563	0.1572

Overall Kappa = 0.3101

A)

Table 5.7. The error matrix analysis to assess the accuracy of the landuse maps. GS represents grey soil and RS is red soil. MAKLIKE and MAXLIKE2 are the results of maximum likelihood classifications using the equal and defined prior probability approaches respectively. For explanation of cases (A-D) see text

Error Matrix Analysis of ground truth (columns) against maximum likelihood classification image with defined prior probability (rows). No. of classes 7

	Ploughed GS	GS matorral	Bare ground	Ploughed RS	RS matorral	Shade	Trees	Total No.	User's Accuracy
Ploughed GS	4	5	0	1	0	0	0	10	0.4
GS matorral	1	19	0	3	15	0	5	43	0.4419
Bare ground	2	1	1	8	11	0	0	23	0.0435
Ploughed RS	0	1	0	5	2	0	0	8	0.625
RS matorral	0	4	0	7	28	0	4	43	0.6512
Shade	0	1	0	0	0	5	0	6	0.8333
Trees	0	0	0	0	2	0	2	4	0.5
Total No. of samples	7	31	1	24	58	5	11	137	
Producer's Accuracy	0.5714	0.6129	1	0.2083	0.4828	1	0.1818		

Overall accuracy is 0.467

KAPPA INDEX OF AGREEMENT (KIA)

Category	Using MAXLIKE2 as the reference image (user's)	Using ground truth as the reference image (producer's)
Ploughed GS	0.3677	0.5377
GS matorral	0.2786	0.4358
Bare ground	0.0364	1.0000
Ploughed RS	0.5454	0.1592
RS matorral	0.3951	0.2461
Shade	0.8270	1.0000
Trees	0.4563	0.1572

Overall Kappa = 0.3142

B)

Table 5.7 *continued ...*

Error Matrix Analysis of ground truth (columns) against maximum likelihood classification image with equal prior probability (rows). No. of classes 5

	Bare ground	Ploughed field	Matorral	Shade	Trees	Total No.	User's Accuracy
Bare ground	1	10	9	0	0	20	0.05
Ploughed field	0	10	10	0	0	20	0.5
Matorral	0	11	67	0	9	87	0.7701
Shade	0	0	1	5	0	6	0.8333
Trees	0	0	2	0	2	4	0.5
Total No. of samples	1	31	89	5	11	137	
Producer's Accuracy	1	0.3226	0.7528	1	0.1818		

Overall accuracy is 0.6204

KAPPA INDEX OF AGREEMENT (KIA)

Category	Using MAXLIKE as the reference image (user's)	Using ground truth as the reference image (producer's)
Bare ground	0.0430	1.0000
Ploughed field	0.3538	0.2068
Matorral	0.3439	0.3227
Shade	0.8270	1.0000
Trees	0.4563	0.1572

Overall Kappa = 0.3092

C)

Table 5.7 *continued ...*

Error Matrix Analysis of ground truth (columns) against maximum likelihood classification image with defined prior probability (rows). No. of classes 5

	Bare ground	Ploughed field	Matorral	Shade	Trees	Total No.	User's Accuracy
Bare ground	1	10	12	0	0	23	0.0435
Ploughed field	0	10	8	0	0	18	0.5556
Matorral	0	11	66	0	9	86	0.7674
Shade	0	0	1	5	0	6	0.8333
Trees	0	0	2	0	2	4	0.5
Total No. of samples	1	31	89	5	11	137	
Producer's Accuracy	1	0.3226	0.7416	1	0.1818		

Overall accuracy is 0.6131

KAPPA INDEX OF AGREEMENT (KIA)

Category	Using MAXLIKE2 as the reference image (user's)	Using ground truth as the reference image (producer's)
Bare ground	0.0364	1.0000
Ploughed field	0.4256	0.2201
Matorral	0.3362	0.3058
Shade	0.8270	1.0000
Trees	0.4563	0.1572

Overall Kappa = 0.3058

D)

Table 5.7 *continued ...*

The overall value of κ statistic has fallen by a negligible amount from 0.32 to 0.31 but κ value went up from 0.33 to 0.39 for grey soil matorral indicating that classification accuracy is more associated with true agreement, whereas κ went down from 0.30 to 0.26 for red soil matorral which associate classification for this class more with chance agreement. In tables 5.7 A and 5.7 B the differences between the equal and defined prior probability maximum classifications became clearer where ploughed grey soil, grey soil matorral and ploughed red soil classes show higher user's, producer's, and overall accuracies in the defined prior probability classification method.

It has been seen in figures 5.26 A and B and 5.27 A and B of the land-use maps and has been demonstrated in tables 5.6 A and B and 5.7 A and B that we cannot expect to map soil types using hard classification tools such as the maximum likelihood classification. These land-use maps show that a large misclassification problem exists in trying to classify red soil matorral and grey soil matorral into separate classes, as well as classifying ploughed red soil and ploughed grey soil into separate classes. However, it will be shown in the following chapter that mixture modelling can map these soil types more accurately. As a result of this, the soil information in the land-use map, derived from maximum likelihood classification, can be amalgamated into the same class.

This can be done by amalgamating ploughed red soil and ploughed grey soil classes into one class called ploughed field, and the grey soil matorral and red soil matorral classes into one class called matorral (class types 3 in figure 5.23b). This amalgamation process is in agreement, anyway, with the fact that red and grey soils are land-cover classes and not land-use types. The figures 5.28 A and 5.28 B show the resulting land-use maps both with equal and defined prior probability respectively.

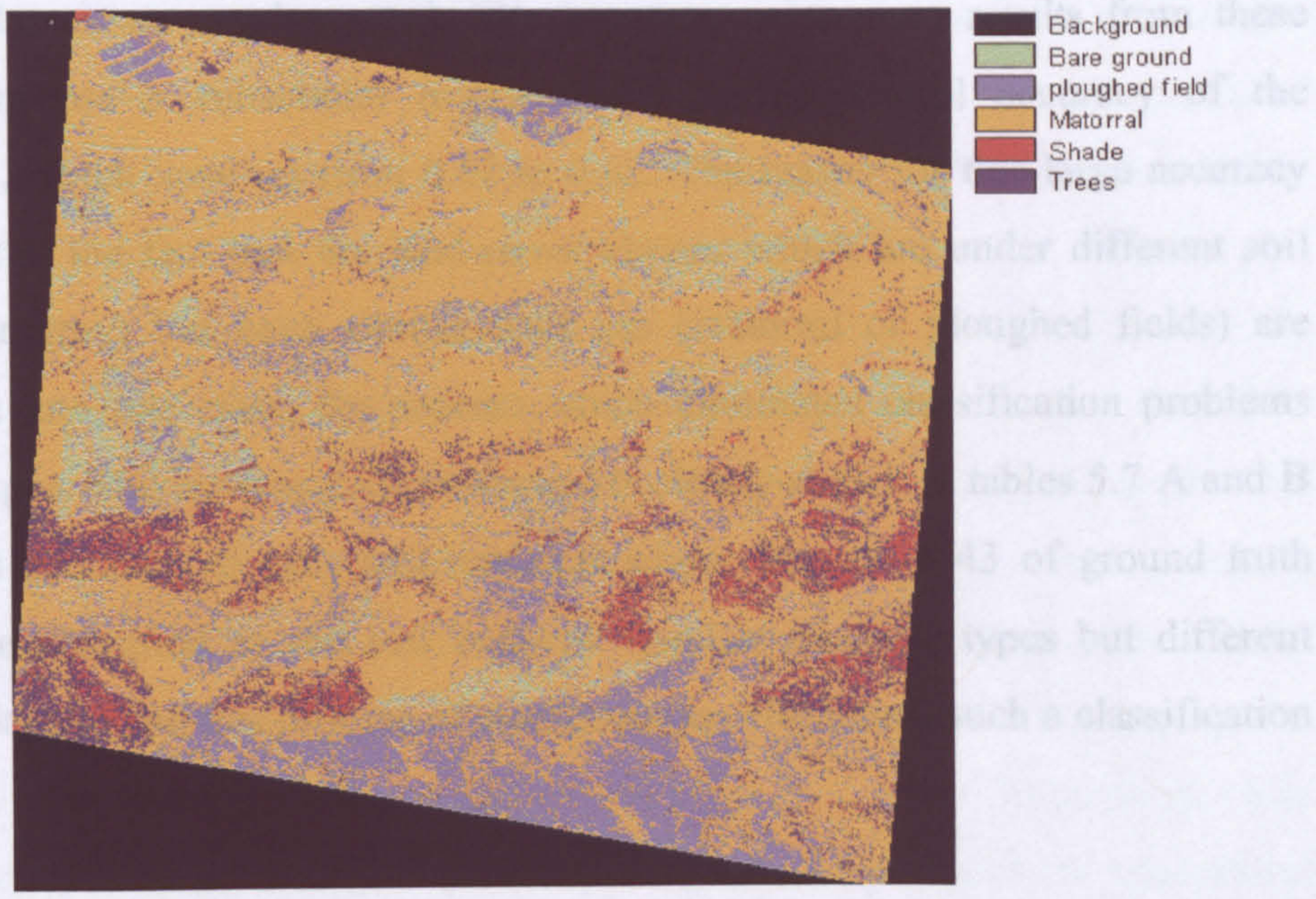

A)

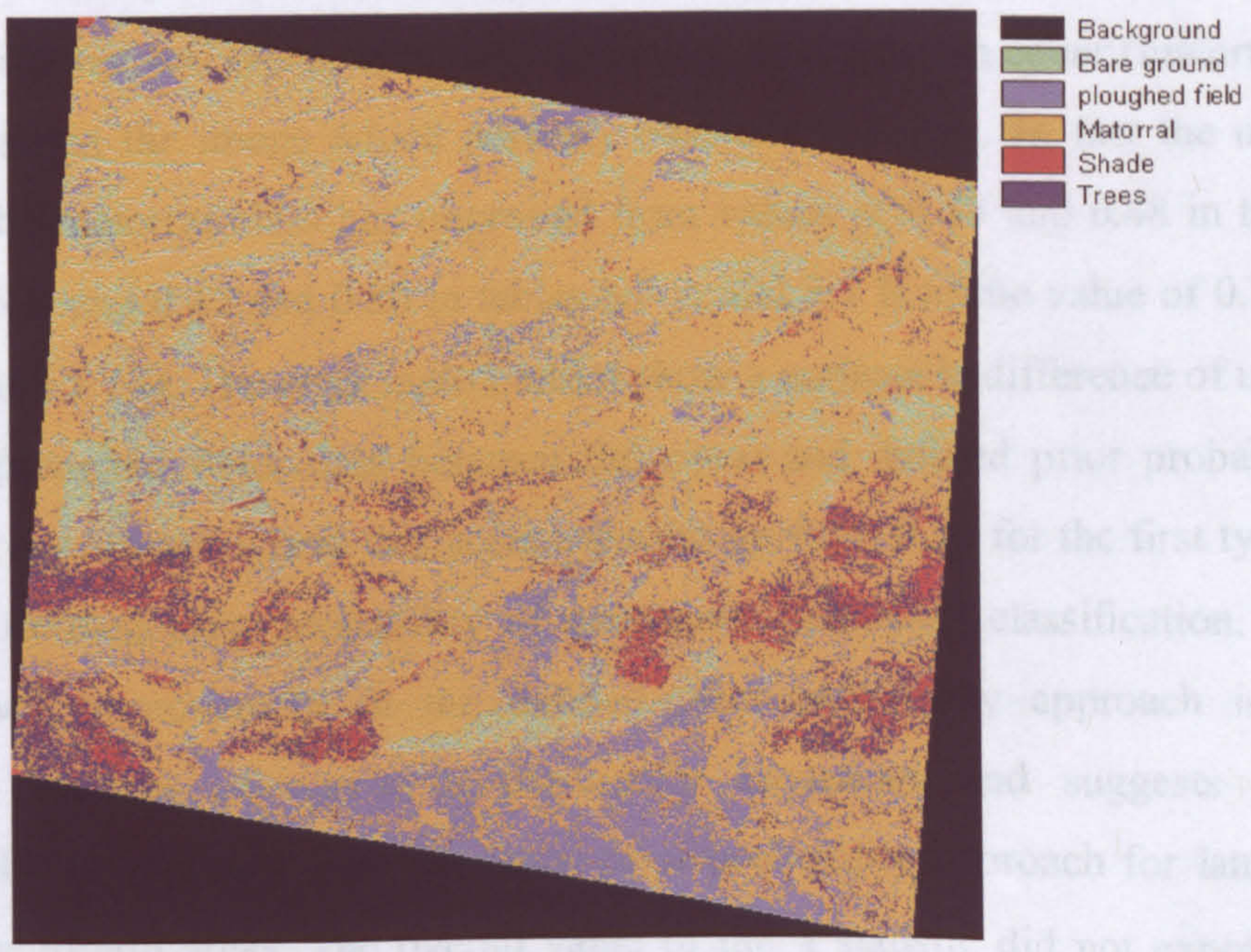

B)

Figure 5.28. The A) equal prior probability and B) defined prior probability maximum likelihood classification. The classes unpaved road, grey soil road and grey soil river are amalgamated into grey soil matorral, and red river class is amalgamated into red soil matorral. In addition, the ploughed grey soil and red soil are amalgamated into one class (ploughed field) and grey soil and red soil matorral are amalgamated into one class (matorral).

Tables 5.7 C and 5.7 D show the error matrix analysis for land-use maps after these land-cover classes are amalgamated. The accuracy assessment results from these tables demonstrate a substantial improvement of the overall accuracy of the classification, which went up from 0.47 to 0.62. The reason for this large accuracy improvement is the fact that the land-cover classes which are under different soil types (red or grey) but have similar land use (matorral or ploughed fields) are amalgamated into one class, the process which eliminated classification problems across soil types. This accuracy improvement is clearly shown in tables 5.7 A and B in the user's accuracy of grey soil matorral where 16 out of 43 of ground truth samples were classified as red soil matorral (similar land-use types but different land-cover classes) and this process of amalgamation eliminated such a classification error.

The results in tables 5.7 C and 5.7 D suggests that hard classifiers are not successful in mapping different soil types especially when natural vegetation cover (matorral in our case) exists in the image which partially obscures the soils. In fact the user's accuracy of the matorral class has improved from values of 0.43 and 0.48 in tables 5.6 A and 5.6 B and 0.42 and 0.50 in tables 5.7 A and 5.7 B to the value of 0.77 in tables 5.7 C and 5.7 D. The error matrix tables show a noticeable difference of user's accuracy of ploughed field class between the equal and defined prior probability classification approaches where this accuracy went up from 0.50 for the first type to 0.56 for the defined prior probability of maximum likelihood classification. This slight accuracy improvement in the defined prior probability approach is not accompanied by loss of user's or producer's accuracies and suggests some advantages of this approach over the equal prior probability approach for land-use mapping of semi-arid areas. The overall value of the κ statistic did not experience any noticeable change and the κ value did not drop down as classes become larger. This means that the accuracy improvement is not due to the chance agreement between the classifier and the ground truth data but it is due to the true agreement between them.

The maximum overall accuracy of the final land-cover map that has been achieved using the maximum likelihood classification is 0.62. This accuracy is regarded as unacceptable in this study because it is too low and that, as will be seen in the following chapter, the soil map which will be integrated with this land-use map is of much higher accuracy. This high accuracy of the soil map will be degraded if that soil map is integrated with a land-use map of much lower accuracy.

Another problem that hinders the usability of this land-use map is the fact that there are some land-cover classes (i.e. shade and trees classes) which are meaningless for this study if they are treated as separate classes. Shade, for example, is mostly cast by the almond and olive trees and the matorral bushes, or by topography to some extent, over the soil background or over the vegetation cover. Thus, there is a strong spatial correlation that exists between the shade and the vegetation cover. In addition, olive and almond trees exist on the slopes that are ploughed and prepared for agricultural activities so this type of plantation has a strong spatial correlation with the surrounding fields that have been ploughed to remove the natural vegetation cover and so that the top soil is exposed.

The traditional per-pixel hard classification tools, such as the maximum likelihood classification that has been investigated in this chapter, unfortunately fail to recognise such spatial correlation because each pixel of the image being classified is treated separately regardless of the nature of pixels surrounding it. Thus, for all of the above mentioned reasons this final land-use map will not be adopted and implemented to derive soil characteristics maps that are needed for models implementation. Thus, other alternative methods, which can overcome the classification problems mentioned above, should be investigated to derive the land-use map.

5.3.3.4 Alternative Methods for Land-use Mapping: Image Interpretation

There are two types of alternative methods that have been used in remote sensing to overcome such problems of land-use and land-cover mapping. The first is to

implement a more robust classification systems that can recognise, and take into account during classification, the complex spatial nature of different objects and land-cover types in the scene. The second is to implement the much widely used approach of image interpretation, especially in our case where the data consist of aerial photographs of very high spatial resolution.

Many studies have been carried out by different scientists to develop expert classification systems which can be used for land-use/land-cover mapping from high spatial resolution imagery. One of these expert classification systems is per-field (or sometimes called per-parcel) classification method. In this method, the per-pixel classification is first applied on the remotely sensed imagery to produce the initial land-cover map. The errors associated with this type of classification are then overcome by applying the per-field classification (Aplin *et al.*, 1999). This is done by integrating digital vector data, which describe the spatial extent and attributes of the various fields in the area, into the initially classified land-use map and the process of re-classification is applied. This classification method is more accurate than the per-pixel classification because it overcomes the problem of internal variability that is associated with high spatial resolution imagery such as the case of our aerial photographs.

Another advanced expert classification system is proposed by Barnsley and Barr (1996) and called Kernel-Based Spatial Reclassification. In this method the remotely sensed imagery is first classified into the main land-cover types by implementing some conventional classification techniques. In the second stage, which is called the spatial reclassification, the pixels in the pre-classified imagery are grouped into discrete land use classes on the basis of both the frequency and the spatial arrangement of the land-cover labels within a square kernel (Barnsley and Barr, 1996). This method of classification can be very successful, if applied in this study, to recognise the spatial correlation between different objects and fields in the study area such as the relationship between the shade and the vegetation cover and between the almond trees and the ploughed fields surrounding them. However, one of the weaknesses of this classification method is that its accuracy is strongly dependent on

the accuracy of the initial land-use map which has been produced by the conventional classification process.

Another expert classification system, which can improve the classification accuracy of land-use map, integrates the remotely sensed imagery with other sources of geo-referenced information such as the spatial texture of the scene and the digital elevation model (DEM) (Stefanov *et al.*, 2001). The first step of land-use mapping in this system is to use a per-pixel classification algorithm for the initial classification and then logical decision rules are applied utilising the extra spatial data sets of the geo-referenced information for post-classification processes.

As has been mentioned above, the other type of alternative methods for land-use mapping is the image-interpretation method. In this method an interpretation is made as to the physical nature of objects and phenomena appearing in the image. The image interpretation can be carried out at different levels of complexity ranging from the simple recognition of objects on the Earth's surface to the extraction of detailed information about the complex interaction of different features (Lillesand and Kiefer, 2000).

The accuracy of the land-use map resulting from image interpretation depends on a wide range of factors such as the experience and training of the interpreter, the nature of objects on the land surface, and the quality of the image being interpreted. Although image interpretation seems to be a very widely used method for land-use/land-cover mapping, it has some weaknesses and disadvantages. Some of the weaknesses of this method relate to the subjectivity of the interpreter during the process of interpretation. This means that different interpreters may derive different land-use maps from the same remotely sensed imagery, depending on their training, experience, and judgement. The other weakness of image interpretation is the fact that it is time consuming especially when a large number of remotely sensed images are needed to be interpreted in the study.

Due to the complexity of some of the methods discussed above or the lack of input data (e.g. digital vector data of fields) for the other methods, the image-interpretation method has been selected to derive the land-use map of the study area. Since there is only one aerial photograph to be interpreted for land use in this study, the image interpretation method is regarded as a faster method than the other methods mentioned above.

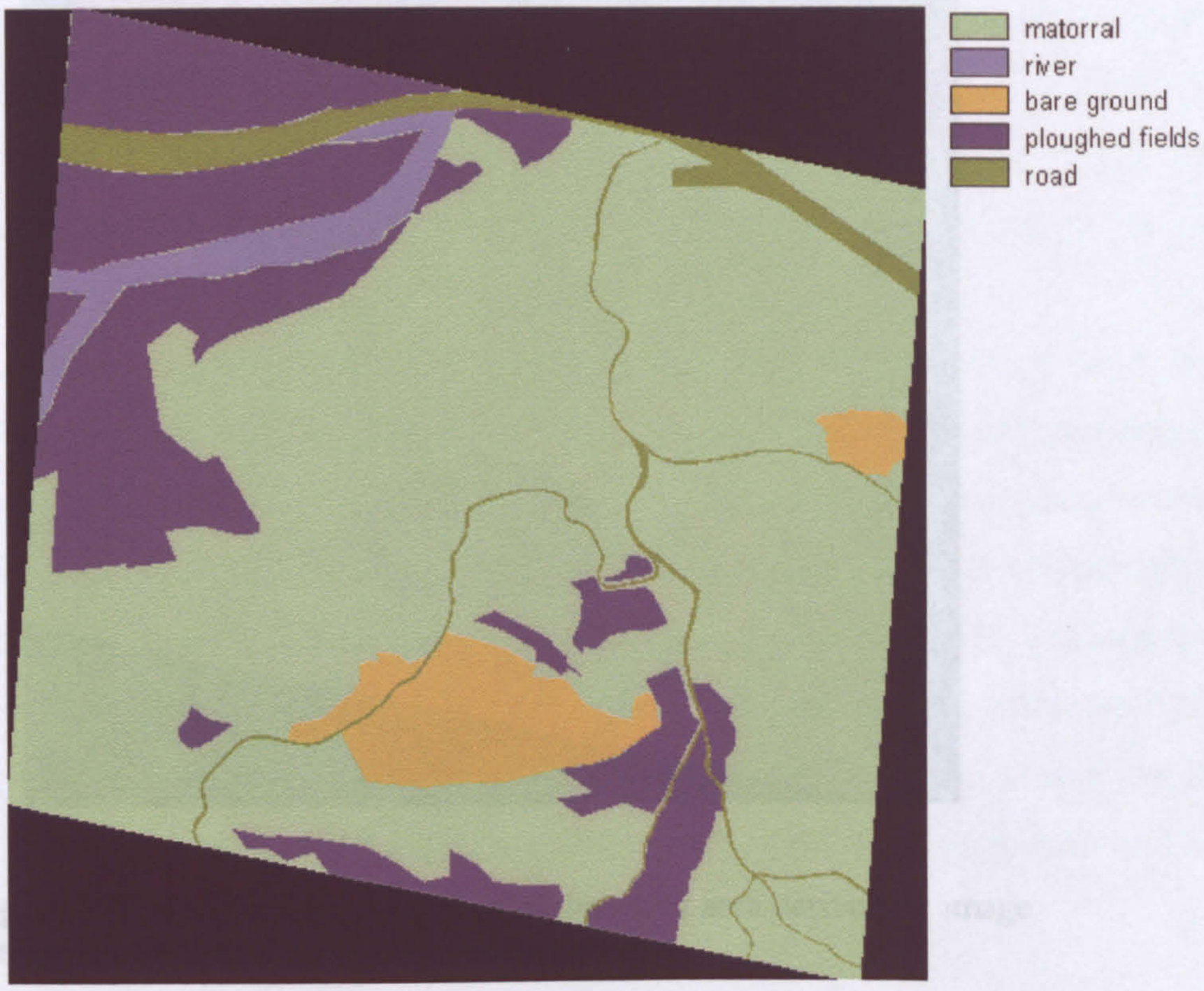

Figure 5.29. The initial land-use map of the study area derived by image interpretation.

To derive the land-use map from the aerial photograph, the same five land-use classes which were initially considered for maximum likelihood classification are selected. These classes are matorral, ploughed fields, road, river, and bare ground, where the bare ground class consists of the overgrazing and the fire scar areas. These classes have been selected because they have distinctive land-use types and different physical meanings in the study area. It can be noticed here that the process of land-use classes selection is much more straightforward in comparison to the maximum likelihood classification where there were many strict conditions to observe. These

land-use classes were then digitised over the colour aerial photograph of the study area using the digitising module in the IDRISI For Windows package and the figure 5.29 shows the result of this land-use map.

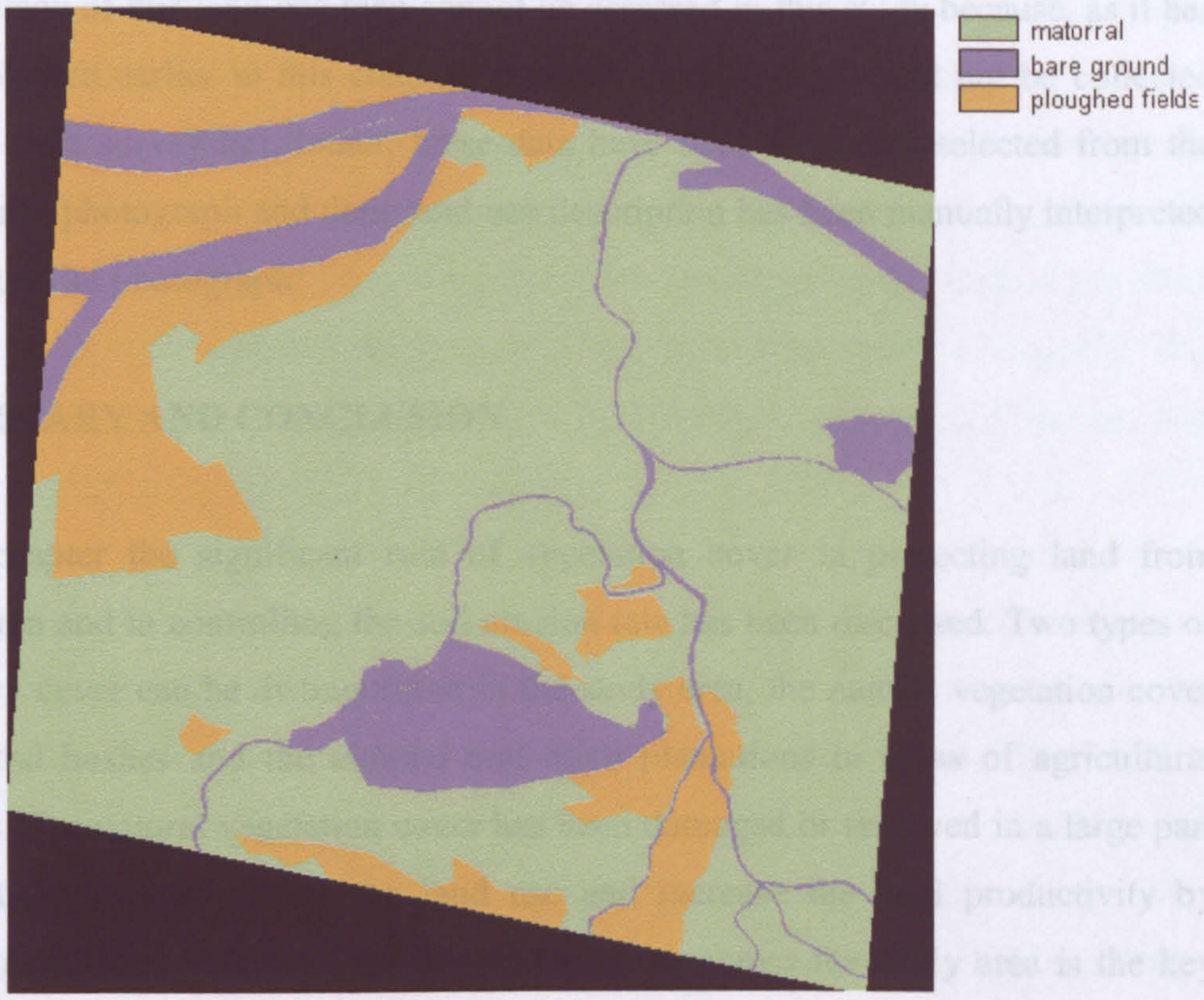

Figure 5.30. The final land-use map of the study area derived by image interpretation and land-use class amalgamation.

As it has been explained earlier in this chapter, some of these land-use types can be amalgamated into one land-use class because they share similar soil characteristics and hydrological properties and because of the lack of soil and hydrological information about some of these classes in the data collected from the field survey. As a result, the land-use classes of river, fire scar, overgrazing, and road can be amalgamated into one land-use class called bare ground. This amalgamation process can be justified by the fact that these land-use classes have small coverages, are not covered by vegetation and have similar properties for the bulk density and the soil depth. This is due to the fact that the land represented by these land-use types has not been prepared for agricultural activities and the soil in this land is compacted due to

various reasons of overgrazing and natural vegetation cover. Figure 5.30 shows the final land-use map with the three land-use classes of matorral, bare ground, and ploughed fields.

The accuracy of this land-use map cannot be assessed in this study because, as it has been explained earlier in this chapter, the ground truth data could not be collected from the field survey but, rather, these data have been randomly selected from the actual aerial photograph and their land-use description has been manually interpreted from that aerial photograph.

5.4 SUMMARY AND CONCLUSION

In this chapter the significant role of vegetation cover in protecting land from degradation and in controlling the soil-erosion rate has been discussed. Two types of vegetation cover can be distinguished in the study area, the natural vegetation cover of matorral bushes and the almond and olive plantations in areas of agricultural activities. The natural vegetation cover has been damaged or removed in a large part of the study area to change the land use and increase the land productivity by planting cash crops. Mapping the vegetation cover across the study area is the key element in understanding the soil state and assessing the land degradation and soil erosion.

Different methods of mapping the vegetation cover, such as vegetation indices and fuzzy classification, have been discussed. Due to the limitation of our data of aerial photographs to the three visible bands: red, green, and blue, most of the vegetation indices cannot be implemented in this study to map the vegetation cover. Red band reflectance, as a vegetation index, has been especially investigated because it depends solely on the red band reflectance and it has been found that the relationship between the red band and the vegetation cover produced a high coefficient of determination of 0.81.

Other vegetation mapping techniques have been reviewed such as the fuzzy classification, non-linear mixture modelling and the linear mixture modelling method. The linear mixture modelling has been implemented because of its simplicity to use due to the assumption of linearity in the mixed pixels, and because it is reported to produce results of high accuracy. Since the process of selecting endmembers for implementing mixture modelling is the most critical phase, different approaches to extract endmembers were reviewed and the Principal Component Analysis (PCA) was implemented. It was found after applying PCA transformation that 93%, 5.5% and 1.5% of the variance between the three visible bands of the aerial photograph are represented by the PC1, PC2 and PC3 components respectively. This explains the fact that three out of four endmembers were found in the first component of PC1.

The power of using linear mixture modelling to map vegetation cover in semi-arid areas was demonstrated in this chapter. It was shown that one of the most powerful characteristics of mixture modelling, as a soft classification technique, is its ability to create a fractional vegetation map where the fraction of vegetation covering each individual pixel is calculated. In addition, by using mixture modelling it was possible to extract shade as a ground cover component, which was then used to create a shade-free vegetation map using a shade removal algorithm proposed by Smith *et al.*, (1990). The vegetation cover map was well underestimated before it was re-scaled using the shade map, however, re-scaling increased the coefficient of determination from 0.79 to 0.91 and the RMS Error decreased from 18.3% to 10.7%.

After the shade effect has been removed from the vegetation cover, some isolated pixels that fall within the crowns of almond trees and the matorral bushes still had no vegetation information, or very low fractions of vegetation, where the vegetation fractions are expected to be very high. Thus, it was necessary to isolate those pixels within the vegetation trees and bushes and fill them with the appropriate vegetation information. A methodology of using a co-occurrence matrix of image segmentation was analysed and applied to correct the errors in these pixels. In this method a texture-based image segmentation algorithm was applied to the aerial photograph of

the study area and the spatial extents of various types of ground objects were defined. An image depicting the vegetation objects of almond and olive trees and matorral bushes was created and a GIS intersection was applied between this image and the vegetation cover map to isolate those error pixels and fill them with the appropriate vegetation information.

The accuracy assessment of the vegetation-cover map after applying the co-occurrence matrix method shows that this accuracy did not improve, in fact the coefficient of determination has dropped by 1% from 91% to 90% and the RMS Error increased from 10.7% to 12.2%. This slight reduction in the accuracy could be attributed to two factors. The first factor is the fact that our vegetation validation sites did not have very high shade and the problem of these error pixels manifests itself under these conditions. Second, the shade-removed vegetation map already overestimated the vegetation cover and the co-occurrence matrix approach caused further overestimation, because the vegetation fractions in certain pixels within the vegetation map have been upgraded, resulting in lower accuracy.

Although the co-occurrence matrix method did not improve the accuracy of the vegetation cover map, it showed some other advantages. This process is significant due to the fact that vegetation cover is one of the most significant factors controlling the soil-erosion rate and its absence (due to error factors) will cause very high soil-erosion estimation when implementing soil-erosion modelling. In addition, it was demonstrated in this chapter the possibility of using co-occurrence matrix method to extract the vegetation objects from high spatial resolution imagery, based on the texture and intensity of that image.

Land use is an important factor in soil-erosion modelling because of its effect on the conditions of soils and natural vegetation, thus, land-use mapping is crucial for this study. In this chapter the use of the maximum likelihood classification for land-use mapping, using high spatial resolution remotely sensed data, was investigated. It has been demonstrated that the classification of high spatial resolution imagery leads to some problems of misclassifications and higher errors. This problem is attributed to

the fact the land-cover/land-use classes have high level of internal variability in this type of imagery. This high internal variability caused multi-modal populations. The central assumption in maximum likelihood classification method is that the spectral reflectances of the training data of each class, in each of the spectral band, should be normally distributed. However, because some of the training data in some classes in this study did not meet this condition, classification errors were relatively high in those classes and in the other classes that are spectrally adjacent to them. This coupled with spectral overlap between some of the training data such as between red soil matorral and grey soil matorral, as well as between grey soil river, grey soil road, and bare ground. Classes that have distinctive spectral reflectances, such as the case of shade, were better classified with a higher accuracy level.

In addition, it should be mentioned here that maximum likelihood classification is very sensitive to the selection of training sites. This means that training sites should be as representative as much as possible of the land-cover classes which can be a difficult task when using high spatial resolution remotely sensed data. This difficulty is due to high internal variability within land-cover classes which is associated with high spatial resolution data.

It has been demonstrated that maximum likelihood classification performs poorly when used in semi-arid areas to classify different types of land cover with different underlying soil types because of the high level of heterogeneity in such landscapes. This performance improved substantially when we disregarded the soil type because the errors associated with classification problems across soil was eliminated. Some differences of classification results were noticeable when using two different methods of maximum likelihood classifier: equal prior and defined prior probabilities. Although the first method produced better results in mapping the matorral, the second method was better in mapping ploughed fields and mapping the two types of soil, however, both methods produced a relatively similar overall accuracy.

Another problem was faced when implementing the maximum likelihood classification method. This problem is summarised by the fact that the shade had to be treated as a land-cover class because its presence was a common feature in the study area. However, in reality the areas that are covered by shade belong to other land-cover types such as grey and red soil or vegetation cover. During the classification process, shade can not be dropped as a land-cover class because information in pixels covered with shade can not be extracted using standard classification techniques.

The question to be asked here whether the maximum likelihood classification is a good enough method compared to the efforts and time it needs to carry out the classification for such a small area. Thus, a decision was taken to drop the maximum likelihood method as a tool to map the land use and an alternative method of image interpretation was adopted. Although it has some disadvantages such as the interpreter's subjectivity and the time needed for the interpretation, this method is widely used for land-use/land-cover mapping because it is proven to be a more accurate mapping method.

One of the objectives of this study was to attempt to automate the extraction of all (or most) of the parameters that are needed for the implementation of overland-flow and soil-erosion models. The image interpretation method for land-use mapping is a manual method, however, the poor performance and low accuracy of the map resulted from the automated maximum likelihood classifier limited us to the use of image interpretation.

The land-use map resulted from image interpretation will be used, in conjunction with the soil map in the following chapter, to construct the maps of different soil characteristics (e.g. soil bulk density, soil depth, soil texture, ...etc.) as hydrological response units. These maps are needed to parameterise the Carson and Kirkby overland-flow and the Thornes soil-erosion models.

CHAPTER 6

SOIL ANALYSIS AND SOIL MAPPING

6.1 INTRODUCTION
- 6.1.1 Published Versus Remote Sensing-Derived Soil Maps
- 6.1.2 Spectroscopic Characteristics of Soils and The Soil Colour

6.2 MAPPING SOIL TYPES USING LINEAR MIXTURE MODELLING
- 6.2.1 Re-scaling The Mixture Modelling Soil Maps To Remove The Shade and Vegetation Effect
- 6.2.2 Results of The Re-scaling Process and The Soil Map Generation

6.3 SOIL SAMPLING AND ANALYSIS
- 6.3.1 Soil Sampling
- 6.3.2 Field Methods
- 6.3.3 Soil Analysis
  - 6.3.3.1 Pre-treatment and Organic Matter Removal
  - 6.3.3.2 Particle-size Analysis - Sieving
  - 6.3.3.3 Particle-size Analysis - Sedimentation
  - 6.3.3.4 Bulk Density Measurement
- 6.3.4 Results of Soil Analysis

6.4 STATISTICAL METHODS FOR MAPPING SOIL PROPERTIES
- 6.4.1 Investigating The Probability Distributions of Soil Properties
- 6.4.2 Investigating the Correlation Between Soil Properties and Soil Fractions to Spatially Map the Soil Properties
- 6.4.3 Geostatistical Analysis of Soil Properties
  - 6.4.3.1 Results of Mapping Soil Properties Using Geostatistical Techniques
- 6.4.4 Mapping Soil Properties Based on The Principles of Hydrological Response Units

6.5 THE CONSTRUCTION OF THE SOIL PROPERTIES MAPS

6.6 SUMMARY AND CONCLUSION

6.1 INTRODUCTION

A soil map is one of the most significant data sources needed for the development and implementation of robust overland-flow and soil-erosion models. This requirement is because soil physical properties of soil texture, soil structure, soil depth, and organic matter content, have great effects and control over the overland-flow generation and the soil-erosion rates. These effects are manifested in the soil infiltration capacity, soil moisture content, runoff generation, and in the extent to which soil particles can be detached, transported and deposited.

Soil erosion by water is mainly dominated by three factors: energy, protection and resistance. The energy factor is controlled by the amount of overland flow and the topographic slope, which dominate the potential amount of soil which can be detached and transported. The protection factor is dominated by coefficients relating to the vegetation cover, which can protect the soil from erosion by intercepting rainfall, reducing the velocity of runoff and increasing the cohesiveness of soil. The third factor dominating the soil-erosion rate, which is of special interest to us in this chapter, is resistance to erosion. This resistance to erosion is mainly controlled by the soil erodibility which depends upon the soil physical and chemical properties. Thus, the need for mapping different types of soil is evident for proper understanding and modelling of the soil erosion in this study.

The aim of this chapter is to investigate the potential of using the high spatial resolution 0.55 m aerial photographs, to map accurately the soil types of grey and red soil and their soil properties in the study area of Vélez Rubio. Before soils are mapped, their spectroscopic characteristics were reviewed in order to acquire understanding of the differences in soil spectral responses resulting from their mineral and clay contents.

To investigate the properties of grey and red soils in this study, soil samples were collected from the field and analysed in the laboratory. Various statistical analyses were then carried out in order to evaluate the variability of the physical properties of these soil types and to investigate whether these physical properties of the two soil types are significantly different from each other. This statistical analysis is needed to investigate the potential of remote sensing techniques for automated soil mapping in soil-erosion studies.

Linear mixture modelling, which was discussed in detail in chapter 5, has been implemented to derive maps of grey and red soil. In this chapter these soil maps are then manipulated to remove the shade the vegetation effects and then hardened to produce a map of grey and red soils and the accuracy of this map is then assessed. This final soil map will be used, in conjunction with the land-use map produced in

chapter 5, to derive the final soil properties maps that are needed to implement the overland-flow model and to calculate the soil erodibility needed by the Thornes soil-erosion model. These soil properties maps are bulk density, organic matter content, soil depth, sand percent, very fine sand percent, silt percent, and clay percent. Two different approaches will be investigated to spatially map these soil properties. The first approach is the implementation of the geostatistical and correlation techniques to create spatially continuous maps. The second approach is based on the implementation of the hydrological response units to create discontinuous and discrete regions of similar hydrological properties. These two approaches will be discussed in detail later on in this chapter.

6.1.1 Published Versus Remote Sensing-Derived Soil Maps

There are several ways of acquiring information about soil types and soil properties of the study area. One method is to map soil types and collect the necessary soil information by visiting the field site. A second method is to use published soil maps which are usually available from governmental agencies such as the environment management or agriculture agencies. The third method is to map soil types from remotely sensed data by applying image-processing techniques such as classification or linear mixture modelling, in conjunction with the soil information about soil properties collected by fieldwork. Although the first method is accurate, it is time consuming and needs large financial and labour resources to carry out the task which makes it not feasible for most studies.

The second method, of using published soil maps, which has been adopted in soil-erosion and land-degradation studies that are carried out at smaller (such as regional) scales rather than the field scale. The available published soil map of the study area in our case is the soil map of Vélez Rubio (series number 974) which was published by the Ministry of Agriculture in Spain in 1992 (Proyecto Lucademe, 1992). Figure 6.1 shows a subset of this soil map which has been cut to size to bound the extent of the study area. The scale of this soil map is 1:100,000 which means that 1 mm on the map represents 100 metres on the ground. The soil information in this soil map can

be digitised, however, if the precision of the digitising process is taken as 0.5 mm, as considered by most GIS textbooks, then the error generated by digitising this soil map is 50 metres which is not acceptable for our scale of study.

An initial cross checking between the digitised soil map and the geocoded aerial photograph of the study area (as shown in figure 6.1) shows that the published soil map does not correspond well to the spatial distribution of the red and grey soils identified by remote sensing. For example, this cross checking reveals differences of the spatial representation of the calcareous soil types between the published soil map and the aerial photograph which is over-represented in the soil map. In addition, this published soil map is accompanied by qualitative and quantitative descriptions of various soil properties. When these quantitative soil descriptions were compared against the calculated values derived from the fieldwork samples (this calculation will be explained in details later on in this chapter), the errors were very large in most cases (e.g. for sand, clay, and very fine sand) (table 6.1). This soil map is designed to assess agriculture potential of land at the regional scale and is not designed to provide detailed soil information that is required by hydrological and soil-erosion modelling at the local scale (Band and Moore, 1995, Nielsen *et al.*, 1996, Zhu and Mackay, 2001).

For the reasons mentioned above, the published soil map, and the accompanied descriptive data, will not be used in this study.

	Clay%	Sand%	Silt%	VFS%	Stone%
From published map	8.3	33.7	24.1	32.0	54.9
Measured (mean)	14.3	65.4	21.7	8.1	59.3
Relative error	72 %	94 %	10 %	75 %	8 %

Table 6.1. A comparison of soil properties between the published (see Proyecto Lucademe, 1992) and measured (average) values from the fieldwork. VFS represents very fine sand content.

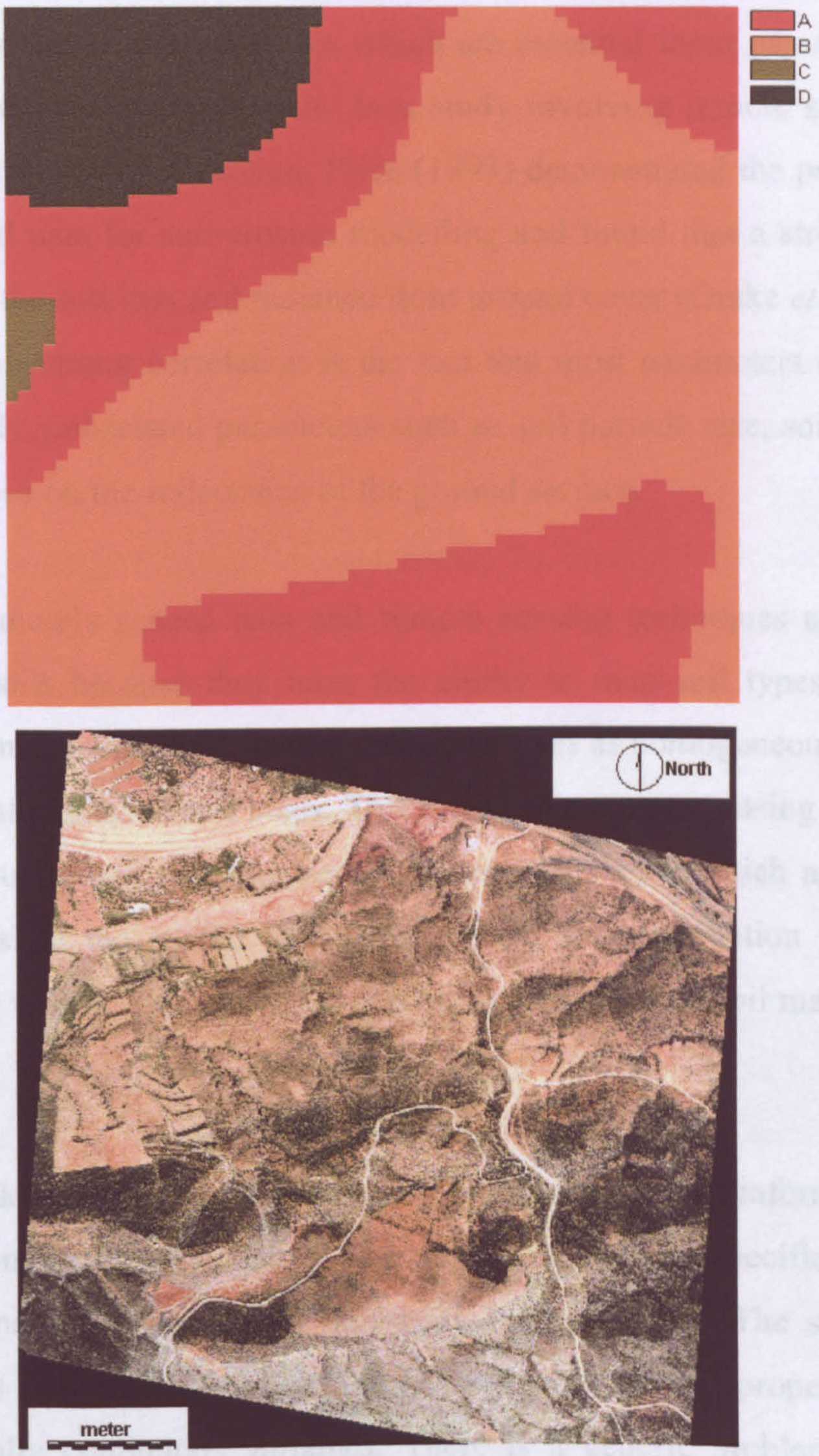

Figure 6.1. A digitised soil map of the study area as a subset from the published soil map of Vélez Rubio, Ministry of Agriculture, Spain with a scale of 1:100000. The soil map is compared to the aerial photograph. Class A represents lithosols, class B is calcareous regosols, lithosolic regosols, and eutric regosols, class C is calcic cambisols and calcareous regosols, and class D is calcic cambisols and calcareous fluvisols.

There is a growing trend amongst geomorphologists and land-management communities to use remote sensing techniques for monitoring and mapping a wide range of ground cover characteristics which are essential input parameters for land degradation and soil-erosion studies. In a study involving remote sensing for soil mapping and soil-erosion detection, Price (1993) demonstrated the potential uses of remotely sensed data for soil-erosion modelling and found that a strong correlation exists between the soil loss and radiance from ground cover (Drake *et al.*, 1997). The logic behind this strong correlation is the fact that most parameters controlling soil loss (particularly soil-related parameters such as soil particle size, soil type, ... etc.) have an influence on the reflectance of the ground surface.

In addition, remotely sensed data and remote sensing techniques are increasingly used to map soils because they have the ability to map soil types in a spatially distributed manner rather than treating these soil types as homogeneous units, such as the case of most published soil maps. This means that remote sensing can potentially provide an accurate and realistic method for mapping soils which approximates as closely as possible the spatial complexity of the soil distribution patterns. Thus, remote sensing will be investigated in this study to derive the soil maps of the study area.

Generally speaking, there are two methods of representing soil information in a soil map. The first method treats the soil map as discrete units of specific soil types and the soil information is distributed uniformly in those units. The second method, however, takes into account the spatial variability of the soil properties and treats these as spatially continuous variables. There is a generic problem in soil maps (whether they are published or derived from remotely sensed data) in that these soil maps lack information on the variability of soil properties within polygons. Such information is significant for hydrological modelling and is increasingly needed for land degradation and soil-erosion modelling using geographical information systems (GIS). In their study on the effects of spatial detail of soil information on hydrological modelling, Zhu and Mackay (2001) investigated the different impacts of

implementing two types of soil map on the watershed hydrology. To do so they used a detailed and spatially continuous soil map of spatially continuous soil properties and a conventional soil map derived from soil survey published maps. They found that the implementation of the detailed and spatially continuous soil map had positive impacts on the watershed hydrological modelling by reducing the peak runoff and producing more realistic hydrographs for the watershed (Zhu and Mackay, 2001).

Thus, a better soil mapping approach for this study may be to combine spatially interpolated distributions of measured soil properties, using geostatistical techniques, with soil map unit delineations of an appropriate scale within a GIS framework. Using this approach, data analysis would provide insights into the potential continuity of soil properties within and between the map units (Rogowski and Wolf, 1994). The outcome of such an approach is a soil map that preserves the map unit boundaries but incorporates spatial variability of attribute data into map unit delineations.

6.1.2 Spectroscopic Characteristics of Soils and the Soil Colour

Because remotely sensed data are used to map soil types, the first question that needs to be asked in this chapter is what is the significance of soil colour (grey and red soil colours in our case) in mapping the soils and how may different soil colours indicate different soil properties. The answer to this question comes from an understanding and review of the spectroscopic characteristics of soils and soil mineralogy.

Soil can be defined in this context as a complex material that is extremely variable in physical and chemical compositions. Five environmental factors greatly influence the generation of soils: parent materials, topography, vegetation, living organisms, and climate (Ben-Dor *et al.*, 1999) and the parent materials factor is of special interest to this analysis because it strongly influences the soil colour of the study area. Baumgardner *et al.* (1985) state that "ever since soil science evolved into an important discipline for study and research, colour has been one of the most useful soil variables in characterising and describing a particular soil". Soil colour can be

attributed to the pigments of soil which absorb the visible light in different intensities and wavelengths.

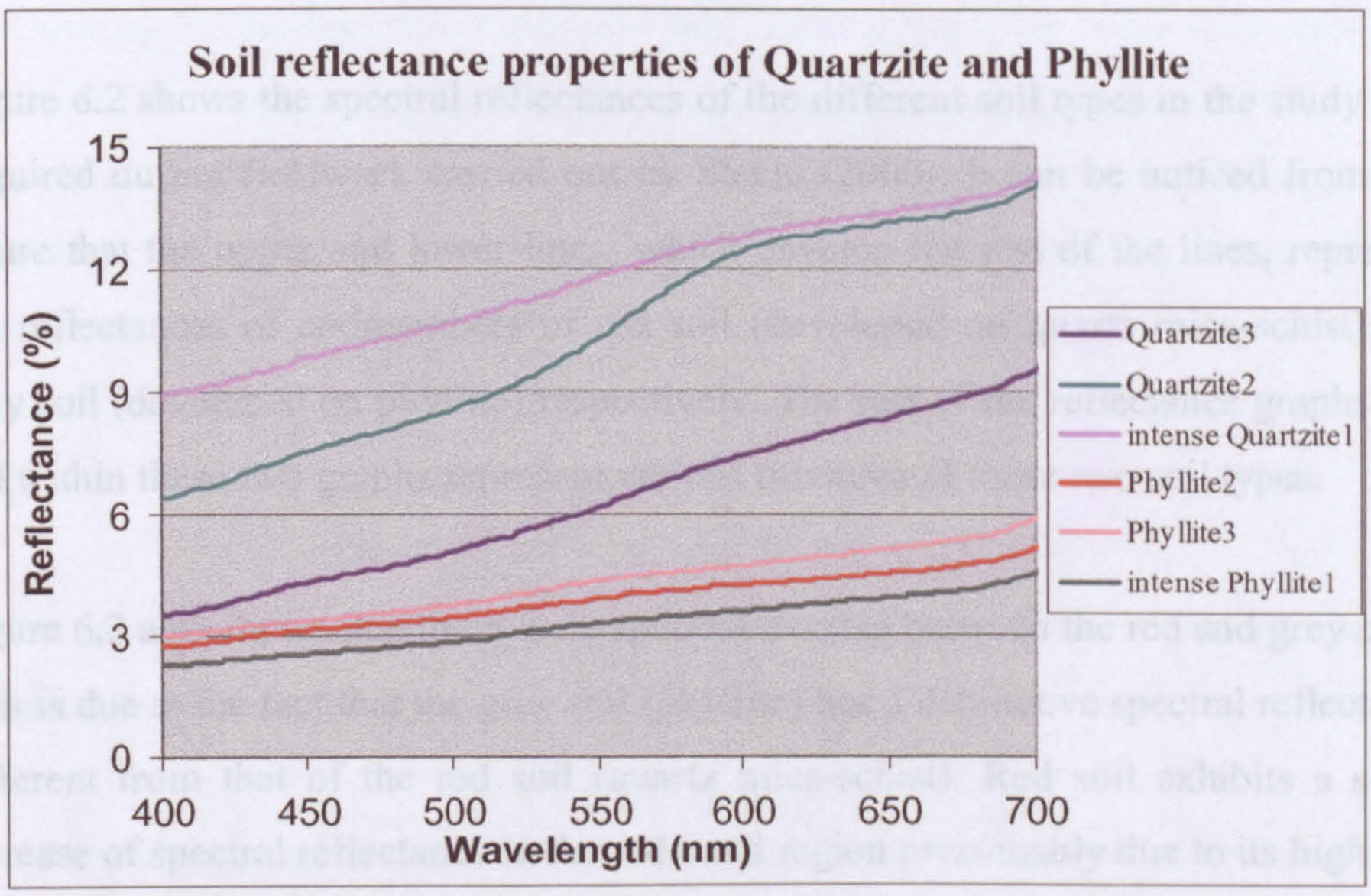

Figure 6.2. Spectroscopic analysis of the soil reflectance for grey (Phyllite) and red (Quartzite/Quartz Mica-Schist) soils in the study area. The "intense" graph represents the spectral reflectance of pure soils and the rest represent mixtures of soils (modified from Steele, 2000).

Various studies have investigated the relationship between soil properties and soil colour where soil colour has been used for years for qualitative assessment of many soil components such as organic matter content, iron oxides, and carbonates in both the remote sensing and soil science fields (Escadafal, 1993). These studies found that the major components that determine the soil colour are organic matter, water, iron oxides, and chemical composition of transition metals in clay minerals (Kondratyev and Fedchenko, 1983). As a result of these studies there is a common agreement by soil scientists that a strong qualitative correlation exists between soil colour and soil properties due to the interaction between visible light and soil material (Ben-Dor *et al.*, 1999). Da Costa (1979) studied various relationships between soil properties and soil colour and found that clay, organic carbon, and water content are important properties related to soil colour and that silt and sand components are the least important properties in determining soil colour. Sand is positively correlated with the

soil colour but only for certain moisture conditions. Da Costa also concluded that climatic variations in terms of moisture, which affect soil properties, are expressed by variations in the soil colour.

Figure 6.2 shows the spectral reflectances of the different soil types in the study area acquired during fieldwork carried out by Steele (2000). It can be noticed from this figure that the upper and lower lines, which envelop the rest of the lines, represent the reflectances of endmembers of red soil (developed on quartz mica-schist) and grey soil (developed on phyllite) respectively. The rest of the reflectance graphs that fall within these two graphs represent various mixtures of these two soil types.

Figure 6.2 also shows that there is no spectral overlap between the red and grey soils. This is due to the fact that the grey soil (phyllite) has a distinctive spectral reflectance different from that of the red soil (quartz mica-schist). Red soil exhibits a slight increase of spectral reflectance in the red band region presumably due to its high iron oxide concentration. Thus, the soils of the study area are mapped on the basis of their colour. Whether soil properties in the grey and red soils are significantly different or not is discussed and analysed later on in this chapter.

6.2 MAPPING SOIL TYPES USING LINEAR MIXTURE MODELLING

The principles and implementation of the linear mixture modelling has been discussed in detail in chapter five and it has been shown that two of the mixture modelling output results were the grey soil and red soil maps (figure 6.3). The initial visual assessment of these soil maps reveals the spatial distribution patterns of both grey and red soil types in the study area are similar to the soil colour variations in the aerial photograph. In these soil maps the red soil type dominates the north, central, and northwest regions, and the grey soil is concentrated mainly in the south and northeast. These spatial distribution patterns reflect the lithological characteristics of the underlying phyllite and quartz mica-schist geological structures.

Although these mixture modelling soil maps depict the spatial extent and distributions of soils, they do not reflect the actual fractions of grey and red soils in the study area. This is due to the fact that a large amount of the soil information is obscured by the presence of vegetation (both almond trees and matorral bushes) and by the shade which is cast by vegetation and topography. Figures 6.4 and 6.5 show this and reveal the association of shade intensity with the presence of the vegetation so that the shade fraction is high adjacent to locations where the vegetation fraction is also high and this causes a reduction in the soil fraction. Thus, a method is needed to rectify the effects of the shade and the vegetation cover on the grey and red soil maps.

6.2.1 Re-scaling The Mixture Modelling Soil Maps To Remove The Shade and Vegetation Effect

The methodology of Smith *et al.* (1990), which has been discussed in chapter 5, describes a way of removing the shade effect from the vegetation maps that were derived by linear mixture modelling. In this method the vegetation cover is normalised by re-scaling. This method can be extended to re-scale the soil maps resulting from linear mixture modelling by removing the effect of both vegetation and shade. This is done by first adding up the fractions of shade and vegetation:

$$SUM = F_{shade} + F_{veg} \qquad 6.1$$

Where F_{shade} is the shade fraction, and F_{veg} represents the vegetation fraction resulting from mixture modelling.

Using equation 6.1, the equations for re-scaling the grey and red soil maps become:

$$GSF_s = F_{greysoil}/(1-SUM) \qquad 6.2$$

$$RSF_s = F_{redsoil}/(1-SUM) \qquad 6.3$$

Where GSF_s and RSF_s are respectively grey and red soil fractions adjusted by removing the vegetation and shade effects, $F_{greysoil}$ and $F_{redsoil}$ are grey and red soil fractions resulted from mixture modelling Smith *et al.* (1990).

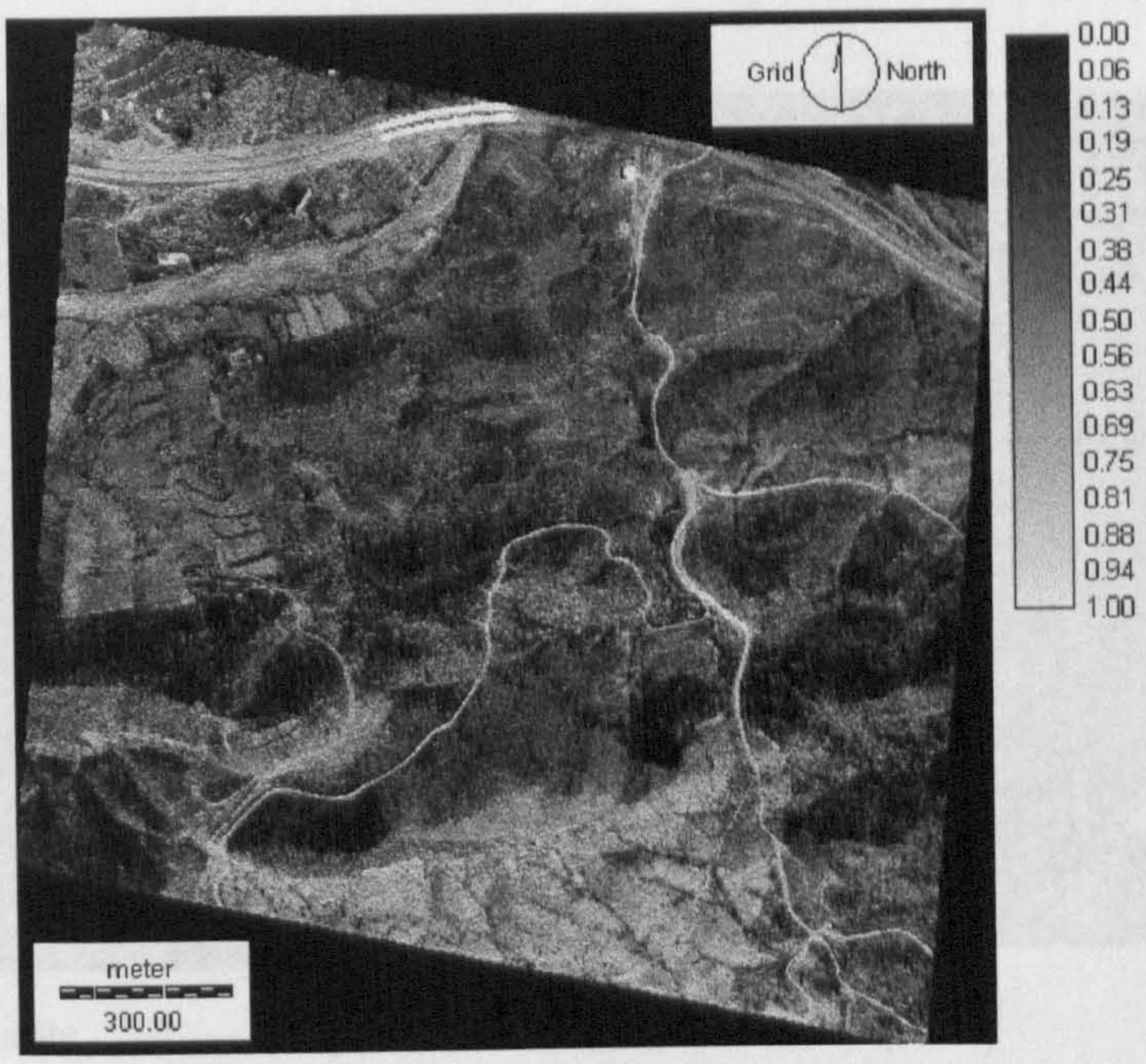

A) Grey soil map

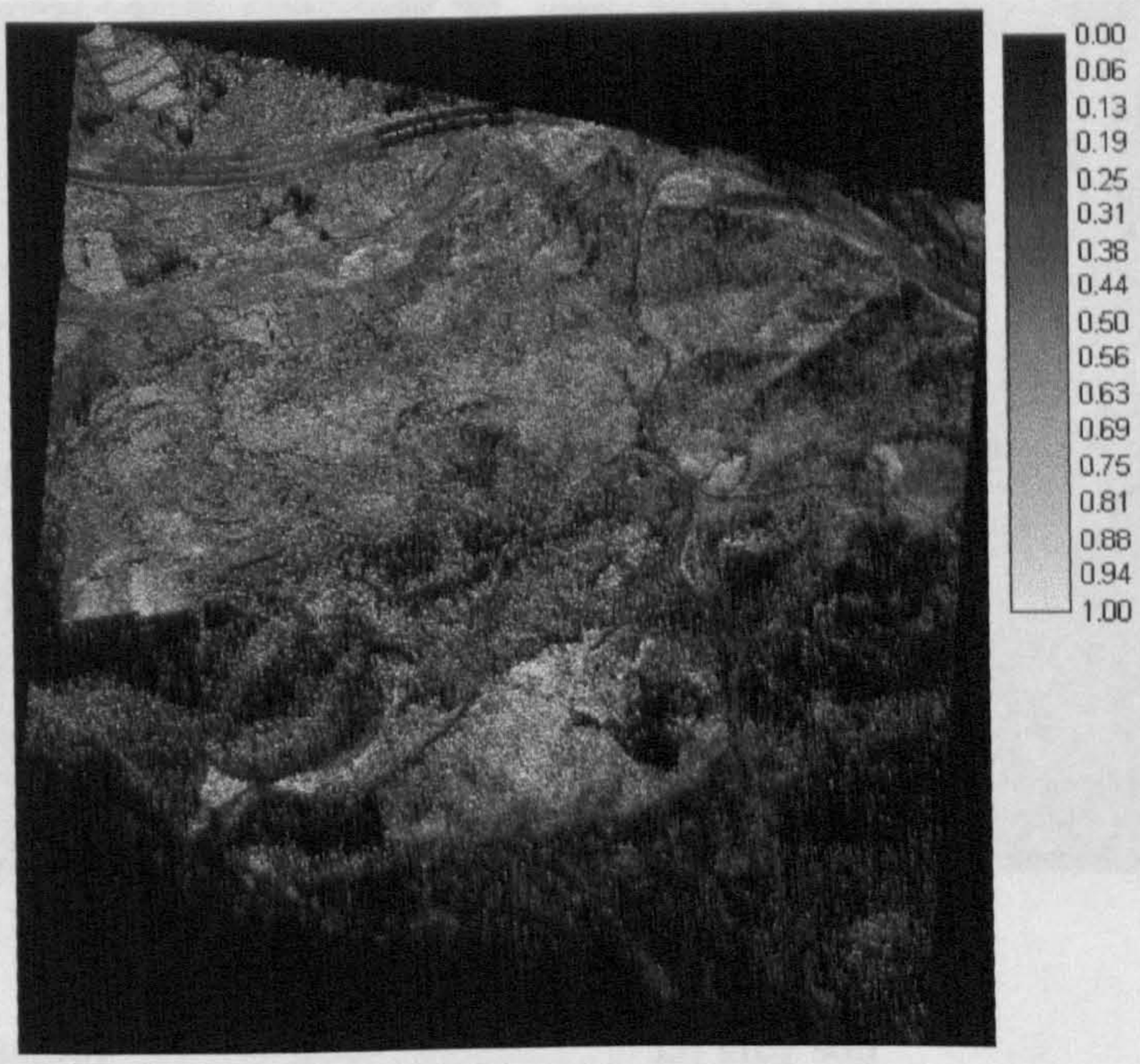

B) Red soil map

Figure 6.3. The soil fraction maps resulted from the linear mixture modelling before re-scaling to remove the shade and vegetation effects from the grey and red soil maps.

A) colour image

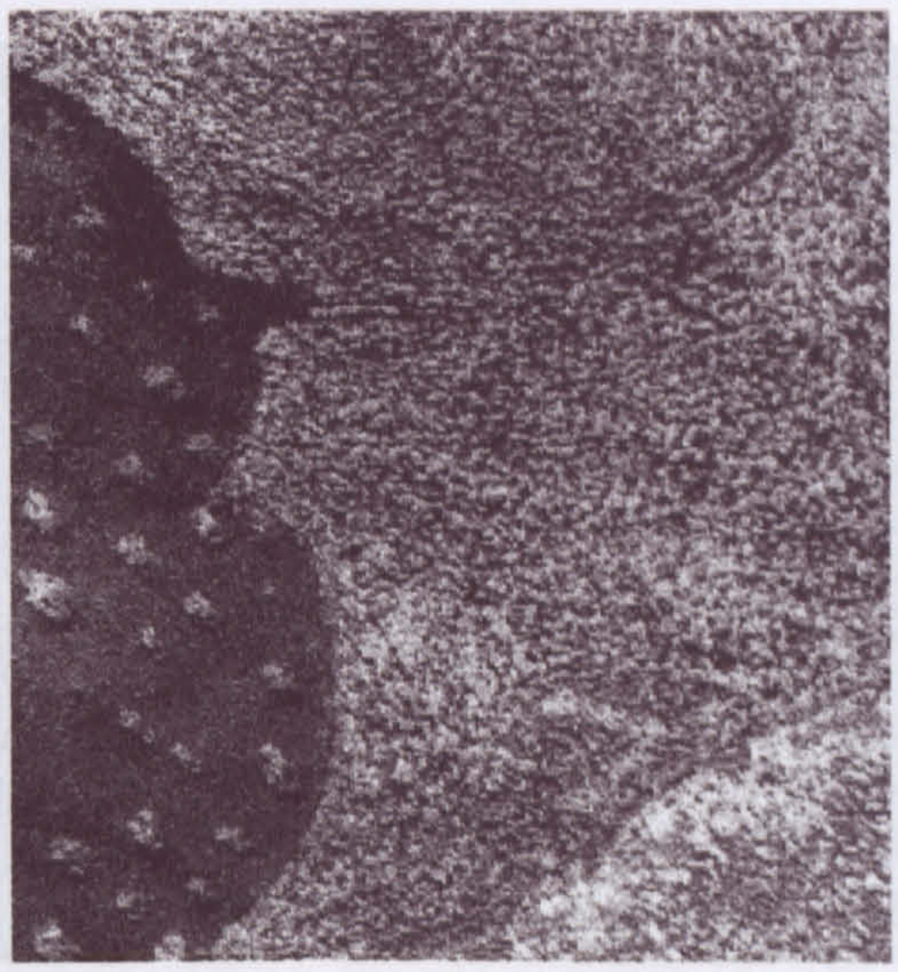

B) shade

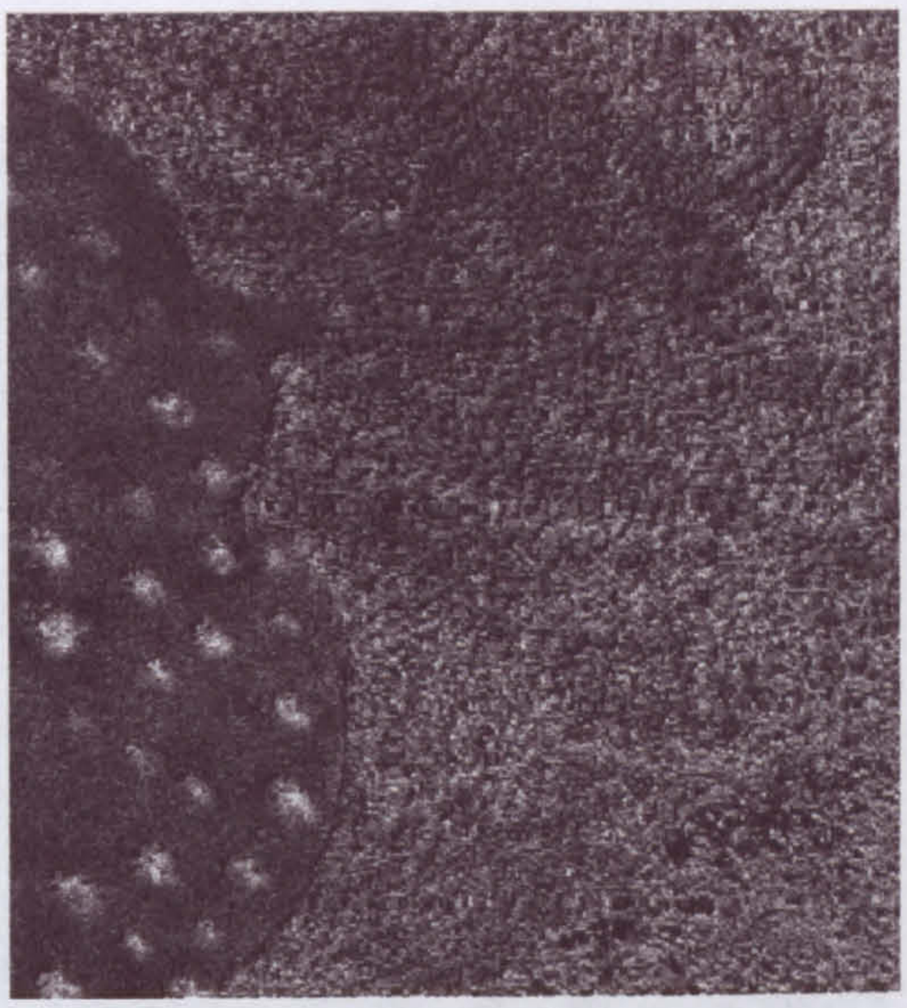

C) vegetation

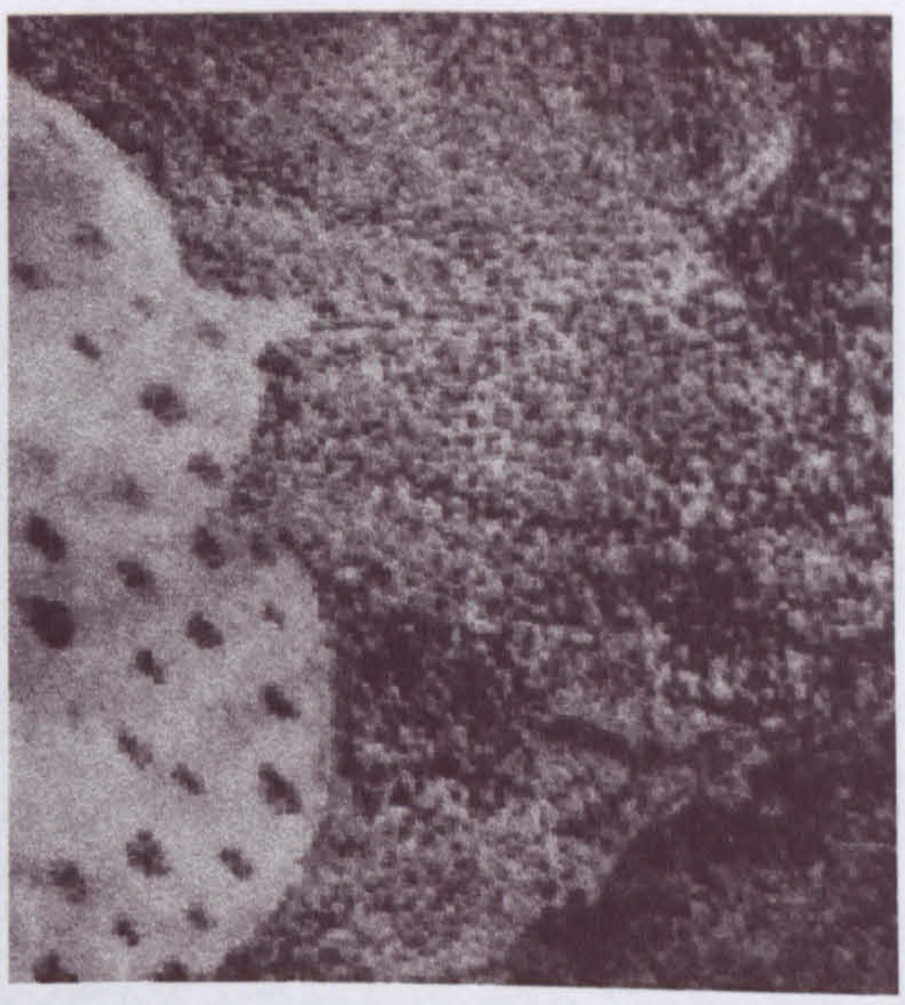

D) grey soil

Figure 6.4. The effect of vegetation and shade presence on the grey soil map resulted from the mixture modelling.

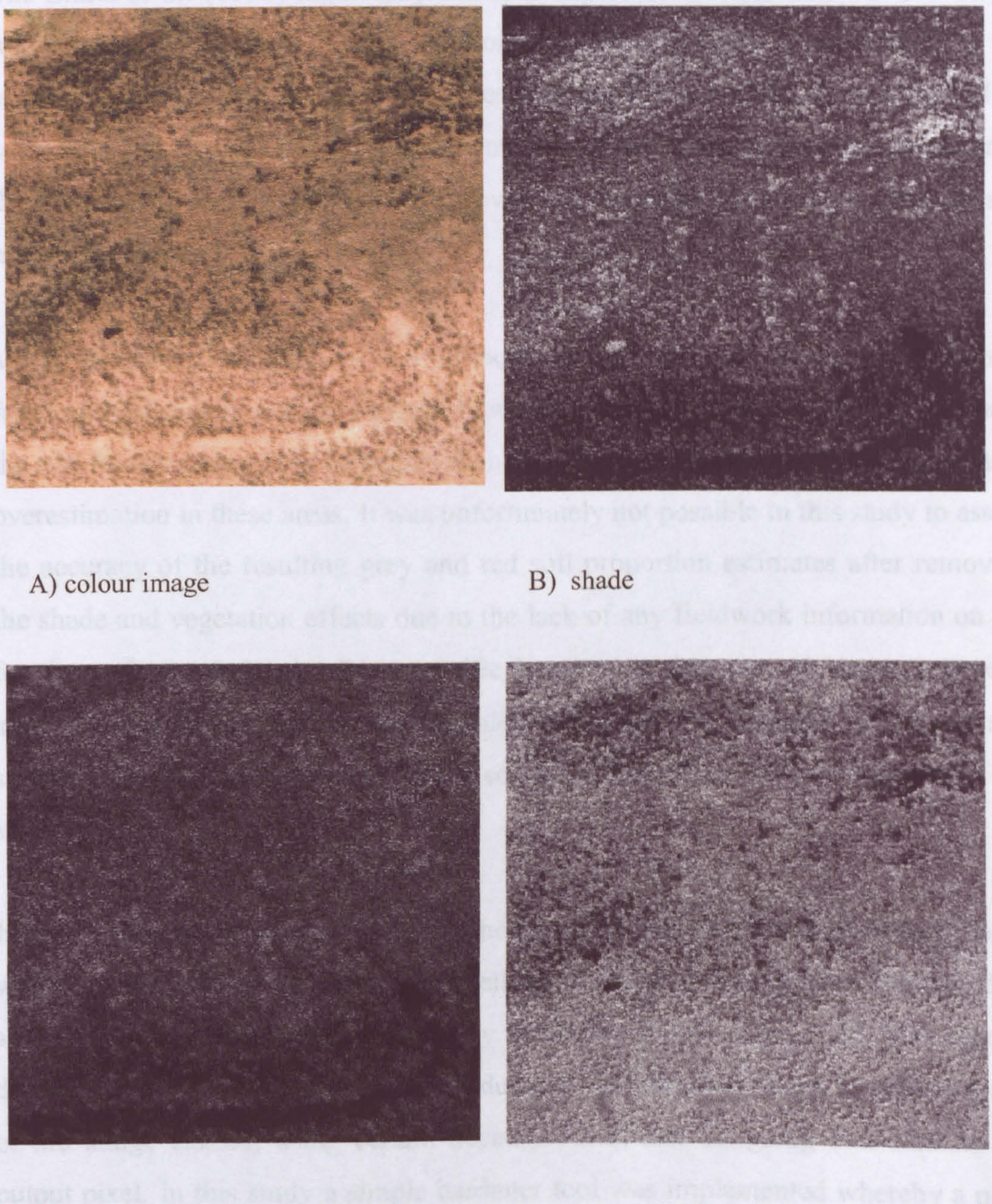

A) colour image

B) shade

C) vegetation

D) red soil

Figure 6.5. The effect of vegetation and shade presence on the red soil map resulted from the mixture modelling.

6.2.2 Results of The Re-scaling Process and The Soil Map Generation

The Smith *et al.* (1990) algorithm, which is expressed in equations 6.2 and 6.3, is implemented to recover the loss of soil information which is obscured by the vegetation objects and the shade. Figures 6.6 and 6.7 show the mixture modelling soil maps before and after the implementation of the algorithm which demonstrate the effects of removing the vegetation cover and the shade from the grey and red soil maps respectively.

Visual interpretation indicates that although the re-scaled soil maps depict the soil fractions realistically in most regions, however, in areas of high vegetation and shade the soil fractions appear to be higher than those in the immediate vicinity suggesting overestimation in these areas. It was unfortunately not possible in this study to assess the accuracy of the resulting grey and red soil proportion estimates after removing the shade and vegetation effects due to the lack of any fieldwork information on the fractions of grey and red soils at specific locations in that area. However, a general accuracy assessment will be implemented using the soil descriptions of our soil samples after hardening these fractional soil maps to produce a binary soil map of the study area.

In order to construct the soil map from the re-scaled grey and red soil fractional maps which resulted from the mixture modelling, a decision tool was implemented to assign each pixel in the map exclusively to either red soil or grey soil. This type of decision tool is called a hardener. It produces a hard decision image by selecting one of the image classes, using certain decision rules, and assigning that class to the output pixel. In this study a simple hardener tool was implemented whereby a pixel that contains 50% or more of grey or red soil is assigned to that soil type. This hardening can be explained as follows:

IF a pixel contains > 50% grey soil = grey soil class

IF a pixel contains > 50% red soil = red soil class

A) zoomed-in colour image in a grey soil area

B) grey soil map before re-scaling

C) grey soil map after re-scaling

Figure 6.6. Re-scaling the grey soil map by removing the shade and vegetation effects.

A) zoomed-in colour image in a red soil area

B) red soil map before re-scaling

C) red soil map after re-scaling

Figure 6.7. Re-scaling the red soil map by removing the shade and vegetation effects.

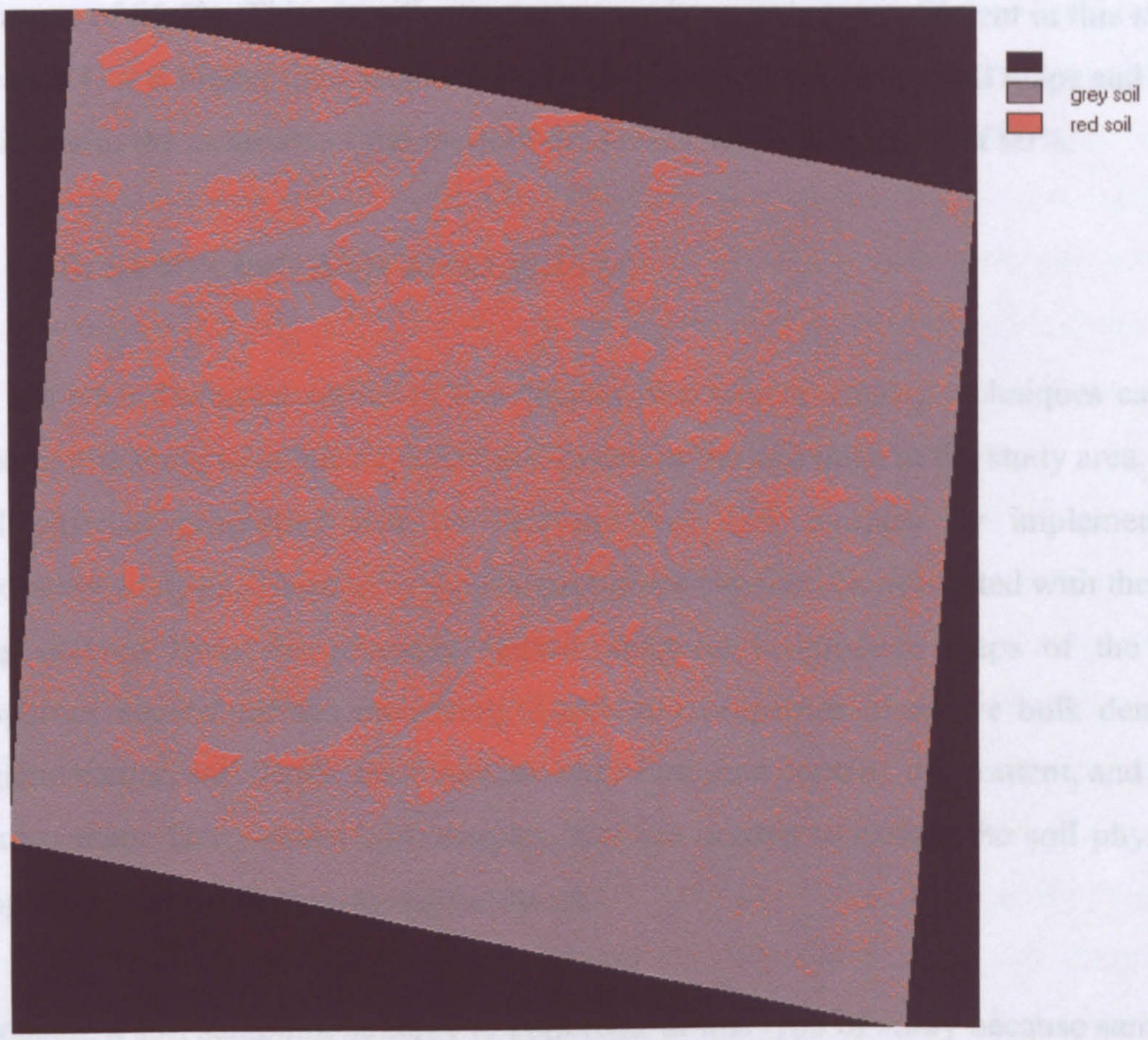

Figure 6.8. The geo-referenced soil map showing the spatial distribution of red and grey soil in the study area.

This hardening process produced two sets of binary maps. By applying the simple GIS function of overlaying on these two binary maps the final hardened soil map was produced (Figure 6.8).

When the resultant hardened soil map was visually cross-checked against the colour aerial photographs of the study area, it seemed to depict well the spatial distribution patterns of the soil types in the study area. To investigate the accuracy of the hardened soil map quantitatively, the locations of soil samples, which were collected in the field and have soil descriptions, were checked against their corresponding locations in the hardened soil map. This accuracy assessment showed that a

misclassification occurred in two grey soil samples out of the twenty-two samples and in three red soil samples out of fifteen samples, giving an overall classification accuracy of 86.5%. This classification accuracy is regarded as sufficient in this study because 1) it is higher than accuracies provided by most published soil maps and 2) it is similar to the accuracy of the mixture modelling vegetation cover of 90%.

6.3 SOIL SAMPLING AND ANALYSIS

As has been discussed earlier in this chapter, the remote sensing techniques can be used in this study to delineate the spatial extent of the soil units in the study area. The soil physical properties will be derived from soil samples by implementing laboratory analysis. These soil physical properties can then be integrated with the soil map derived from the remotely sensed imagery, to produce maps of the soil properties needed for the modelling. These soil properties maps are bulk density, organic matter, soil depth, sand content, very fine sand content, silt content, and clay content map. Thirty-seven soil samples, that are needed to extract the soil physical properties, were collected during fieldwork.

Choosing a soil sampling strategy is important in this type of study because samples should represent the complex nature of the soils. A range of soil sampling methodologies are discussed and the advantages and disadvantages of their implementation are explained. Following this, the processes of soil analysis, such as sample manipulation, pre-treatment, and particle analysis, are then discussed. Statistical tests and techniques, such as the t test, analysis of variance and regression, are applied to investigate the variability of soil properties and to test whether the differences between soil properties of different soils mapped by remote sensing under various land-use types are significant.

6.3.1 Soil Sampling

The results of overland flow and soil-erosion modelling depend on the availability, accuracy and completeness of the data used to implement the models. Generally

speaking, we can differentiate between two types of data used in soil-erosion modelling. First, is the continuous data that have spatial distribution patterns (e.g. images of vegetation cover and soil maps), and second is point pattern data such as the samples of vegetation cover and soil physical characteristics which are collected at specific locations in the field. According to Curran *et al.* (1986), one of the strengths of remotely sensed data is that they are samples that represent a complete spatial population of the phenomenon under study. By contrast, one of the weaknesses of the data used to calibrate or determine the accuracy of the products derived from remotely sensed data is that they are usually localised point samples which are regarded as a general representation of the whole population.

Thus, the issue of sampling is important because it is rarely the case that we have sufficient time and resources to conduct research on all those individuals who could potentially be included in the study (Brayman and Cramer 1999). Sampling can be defined as a process where a population of a large number of locations (or events) can be represented, within specified limits of statistical probability, by a sample of a smaller group of items. According to Daugherty (1978), before going to the field for sampling, several questions should be answered. First, what exactly is the parent population? This step involves the description of the population which should be precisely and carefully specified according to the research objectives. Second, which method of sampling is most appropriate? Sampling methods include random, systematic, stratified and convenience (methods are further explained below). Third, what is the minimum size of sample necessary to give what we could accept as a reliable picture of the parent population?

However, there are other aspects of the sampling process that should be taken into consideration when collecting a sample. One of these is to ensure that the sample is unbiased (i.e. it is a good representation of the population from which it has been drawn) (Burt and Barber 1996). Spatz (1997) defines a biased sample as one that is obtained by a method that systematically underselects or overselects from certain groups within the population.

The size of a sample is also vital. Kalton (1983) argues that to determine an appropriate sample size, it is first necessary to specify the degree of precision required where the larger the sample, the greater the accuracy. Sampling errors, differences between the sample and the population that are due to sampling, can be reduced by increasing the sample size (Brayman and Cramer 1999).

There are a wide range of sampling methods but the most widely used methods are random, systematic, stratified, and along transect sampling. In the random method all the elements of the population have an equal probability of being selected for sampling. This method ensures that the process of collecting the sample is unbiased. However, in reality it is difficult to maintain a random selection throughout the process of sampling and the partial loss of the randomness seems inevitable. This randomness can be more readily achieved in cases where the process of sampling is more mechanical, such as the selection from random number tables, and has minimum personal choices.

The second method of sampling is the systematic sampling. In this method different forms of regular patterns can be used in order to extract the individuals from the population to form a sample. These regular patterns include selecting, for example, each fifth or tenth individual in a population, using a grid, and sampling at the grid point intersections (Daugherty, 1978). Systematic sampling has some advantages over the random sampling such as saving time and effort needed to collect samples. However, the disadvantage of this method is that this regularity in the sample selection pattern can be coupled by a similar regularity in the population leading to some phenomena being overestimated or underestimated.

Stratified sampling is the third sampling method. This method can be implemented in incidences where the population contains major subpopulations that have distinctive characteristics. In this method the population is subdivided into different subpopulations (or strata) that share the same characteristics so samples can be drawn from each stratum according to a desired sampling method such as random or systematic sampling. In this case the implementation of stratified sampling ensures

that these subpopulations are fairly represented in the overall sample. The transect method is the fourth method of sampling and is usually implemented to collect samples with the subjective knowledge of areas where these samples present a representative picture of the population (Peterson and Calvin, 1985). In the transect sampling method the samples are usually collected at various sampling distances in order to enable the analysis of the spatial variation and patterns of the population under investigation.

In this study the transect sampling method was implemented and the soil samples were collected along two transects, the red and grey soil transect. The transect placement and the sampling intervals along these transects were determined subjectively so that the full range of soil spatial variability within the various land-use types could be captured. One of the reasons for sampling the soils along a transect is the fact that we were interested in collecting soil samples from areas where the dominant soil is either red or grey soil. This was important for the statistical test of whether grey and red soils are significantly different to justify soil mapping from remotely sensed data. Another reason was the need to collect soil samples at various, pre-defined lag distances along grey and red soils which is necessary to investigate the spatial variability. These samples were analysed to extract bulk density, organic matter content, sand percent, very fine sand percent, silt percent, and clay percent. The soil depth was also measured at each sampling location using an auger and the land-use type was noted. The descriptions and geographical locations of these sampling sites are explained and shown later on in this chapter.

6.3.2 Field Methods

As discussed above, a decision was taken to sample the red and grey soils along two different transects, these transects run across areas dominated by the red soil and grey soil respectively. Along the red soil transect, 15 samples were collected with different lags between them ranging between 1 to 30 metre. In addition, 22 samples were collected along the grey soil transect with lags ranging between 1 to 20 metres. These

two transects were chosen so that they cover different land-use types such as matorral, almond plantations and abandoned land (Figure 6.9).

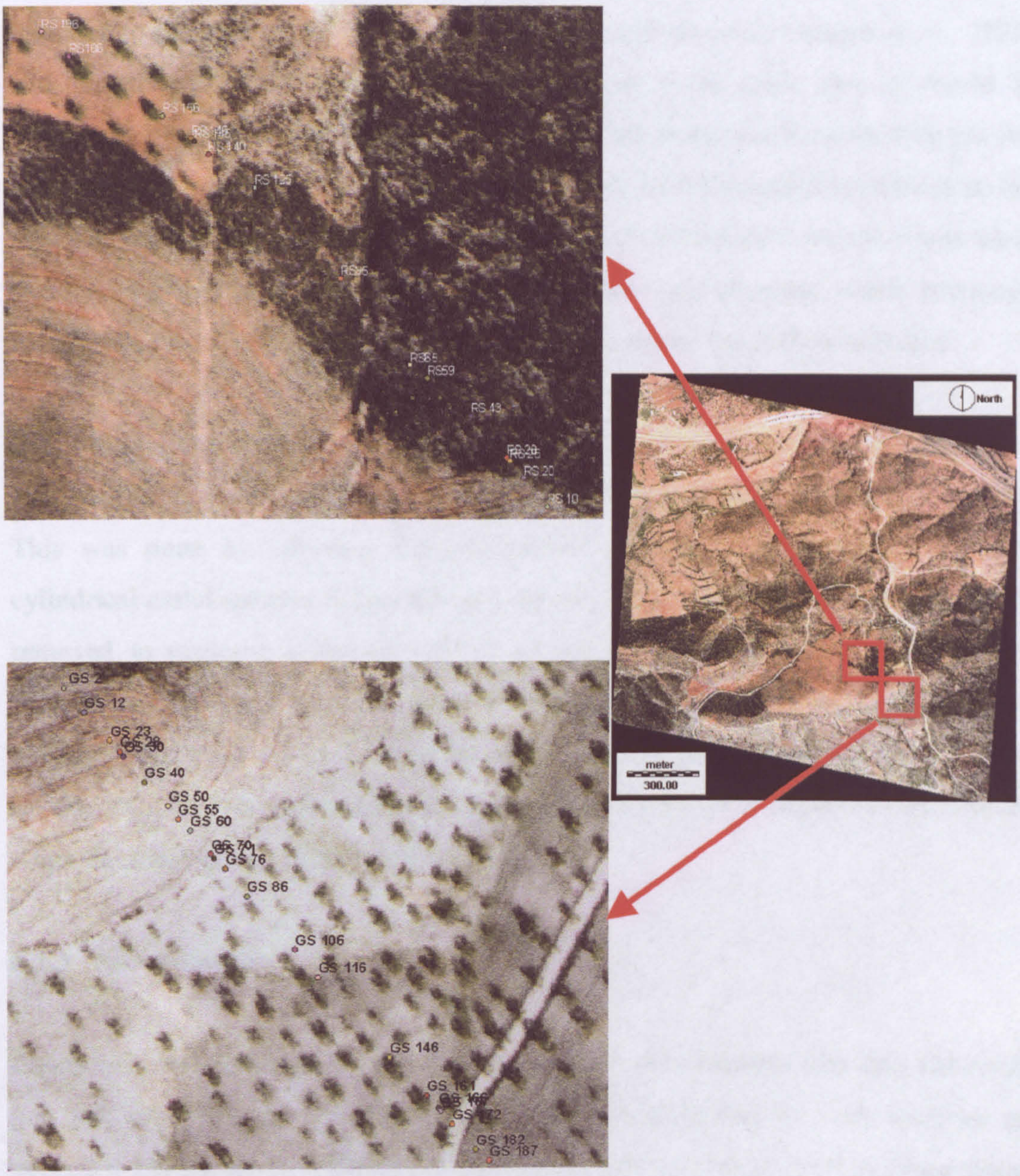

Figure 6.9. The locations of grey soil (top) and red soil (lower) samples in the study area of Velez Rubio.

Due to the limitations in time, labour, and resources, the soil sampling process was restricted to samples from the topsoils rather than across various horizons in the soil profile at the sampling locations. This is due to the fact that these topsoils are most sensitive to the changes in land use and conservation practices (Brejda *et al.*, 2000) and that the soils show little horizon development in the study area. It should be mentioned here that lower soils may have different properties because they are not affected by ploughing and thus they have different hydrological properties from the topsoils and this may cause errors in the overland-flow results. A decision was taken that the weight of each soil sample should be around one kilogram, which is enough for laboratory analysis to measure organic matter content and soil particle size.

In addition to the soil samples collected at the 37 sampling locations, an extra set of soil samples was collected at each location for the measurement of the bulk density. This was done by adopting the pre-defined volume of core method where a cylindrical metal sampler is pressed into the soil to the desired depth and is carefully removed to preserve a known volume of soil sample as it existed in the field. Samples for bulk density measurement were collected and kept at their field moisture conditions for later soil analysis in the soil laboratory. The soil depth at each of the sample location was also measured using an auger where the depth was determined when the auger hit the underlying bedrock.

6.3.3 Soil Analysis

Characterisation and, hence, our understanding of soils requires that they should be precisely analysed and described. The parameters generated by such analyses are needed to generalise hypotheses for differences among soils as well as observations on the same soil under different circumstances of time and manipulation (Klute, 1986). The aim of soil analysis in this study is to extract the physical properties of soils which are essential to understand the hydrological properties and to assess soil susceptibility to soil erosion. In addition, these physical properties of soils may reveal the geological characteristics of the materials underlying the soils and the processes which formed the topsoils which may contribute to better understanding of

the study area. The analysis of the soil samples was carried out in the departmental soil laboratory using a variety of techniques outlined below.

6.3.3.1 Pre-treatment and Organic Matter Removal

Soil pre-treatments are intended to prepare the soil samples for further treatments such as for particle-size and sedimentation analysis. Kunze and Dixon (1986) explain how the use of pre-treatments involves the risk of altering or destroying fractions of the soil other than those for which the treatments are intended. Nevertheless, the process of soil pre-treatment is essential prior to any soil analysis and ignoring this process limits the data that can be obtained from the soil samples and may introduce large errors to the results of the soil analysis.

The first process of soil pre-treatment in our study involves the removal of organic matter prior to the particle-size analysis and sedimentation. Organic matter, which includes dead plant litter and partially decomposed plant material, has an aggregating effect and its removal is necessary if the soil analysis requires dispersion of the samples. The most widely used chemical substance to remove the organic matter is hydrogen peroxide H_2O_2. In this method water is first added to the air-dried soil and then the hydrogen peroxide can then be mixed with the soil in a volumetric proportion of two parts soil to one part hydrogen peroxide. After the chemical reaction is complete, the soil is dried and the loss of weight indicates the organic matter weight, hence, the soil sample is ready for the particle-size analysis.

Before soil is pre-treated, a small quantity of it is taken for organic matter content measurement which is needed to calculate the soil erodibility. The method used in this study to measure the organic matter content was to heat soil to 550 C° for three hours so that the organic matter is burnt off, and the loss of weight represents the organic matter content in the soil. This method of organic matter measurement is preferred over the hydrogen peroxide method because it produces more accurate results.

6.3.3.2 Particle-size Analysis - Sieving

Figure 6.10. The sieving processor to separate stones (larger than 2000 μm), sand (2000-125 μm), very fine sand (125-63 μm), and silt & clay (below 63 μm)

Particle-size analysis (PSA) is a measurement of the size distribution of individual particles in a soil sample. The major features of PSA are the destruction or dispersion of soil aggregates into discrete units by chemical, mechanical, or ultrasonic means and the separation of particles according to size limits by sieving and sedimentation (Gee *et al.*, 1986). There is a wide range of particle-size classification systems which define the limits of soil particle size such as the U. S. Department of Agriculture (USDA), the American Society for Testing and Materials (ASTM), and the International Soil Science Society (ISSS). In this study the USDA classification system was selected because it defines the very fine sand class which is necessary for

calculating soil erodibility (see Wischmeier *et al.*, 1971). In the USDA system soil particles smaller than 2 mm are classified into three major groups; sand (2000-63 μm), silt (63-2 μm), and clay (smaller than 2 μm). The "very fine sand" group is defined as a sub-class of sand which ranges between 63-125 μm.

After the organic matter has been removed, the soil has to be dispersed before the process of sieving. Dispersion of soils can be accomplished by a combination of chemical and physical methods. The chemical dispersion was carried out by adding the Sodium Hexametaphosphate (HMP) to soil in a weight proportion of two parts HMP to one part soil. This mixture of soil and HMP was then physically dispersed using an electric mixer which has specially designed stirring paddles. In order to separate the sand from the other particles, the soil was washed through a 63 μm sieve using a mixture of distilled water and HMP, and the retained sand was weighed (Figure 6.10).

6.3.3.3 Particle-size Analysis - Sedimentation

It is possible to use sieving techniques to separate particles down to the size of 63μm, however, the remaining particles are still a mixture of two groups: silt and clay. The fundamental principle of sedimentation analysis relies on the relationship between the particle diameter and the settling velocity in a liquid. There are different approaches to the measurement of the soil particle distribution for silt and clay by sedimentation and the most widely used are the Pipette sedimentation and x-ray scanning sedimentation approaches. In this study the x-ray based Micromeretics Sedigraph 5100 was used for sedimentation analysis. In this method, the sample is mixed with a fluid of known viscosity which allows the particles to go into solution while being stirred with a magnetic stirrer. The x-ray intensity is used to determine the settling rate and to calculate the particle size distribution. This sedigraph can be used for particle-size distribution analysis of spherical particles between 100 and 0.3 μm in size (Figure 6.11).

Figure 6.11. The Micromeretics Sedigraph 5100 which was used for X-ray sedimentation for particle-size analysis.

6.3.3.4 Bulk Density Measurement

The soil bulk density (BD) can be defined as the ratio of the mass of dry soil to the bulk volume of that soil. The soil bulk volume includes the volume of all the solids in the soil as well as the pore space. The bulk density of a soil depends on the porosity of the soil and on how tightly the pores in the soil are packed, and also the composition of the solid material. For example, soils made of minerals will have a different bulk density from soils made of organic material, even if they have the same amount of pore space.

Another factor that greatly influences the soil bulk density is the content of sand, silt, and clay because different combinations of these three materials affect pores in the soil. Sandy soils have large pore spaces, but because sand grains are large, there are fewer pore spaces than in a soil with smaller particles. Silty soils have smaller particles with smaller pore spaces, but there is more total empty space in a silty soil

than in a sandy soil. In general, clay soils, which have good soil structure, have a greater amount of pore space because the size of the particles is very small, and many small pore spaces fit between them. Table 6.2 shows the effect of sand, silt, and clay contents on the soil bulk density and on the soil porosity.

Soil description	Bulk density Mg m^{-1}	Porosity
Surface soil of wet clay	1.12	0.58
Surface soil of loam texture	1.28	0.52
Subsoil of sandy texture	1.61	0.39
Compacted sandy loam soil	1.90	0.28
Sandstone	2.12	0.20

Table 6.2. A range of bulk density and porosity values for a variety of soils (after Marshall *et al.*, 1996).

Two quantities are needed to measure the bulk density of a soil sample: soil mass and soil bulk volume. The soil mass should be determined after drying the soil to constant weight at 105°C, and the volume is that of the sample as taken in the field (Blake *et al.*, 1986). There are different methods to determine the soil volume for bulk density calculation, and these methods depend on the way the soil has been sampled in the field. The main two methods are the pre-defined volume (such as the core method) and the volume measurement in the field (such as clod and excavation methods). The core method has been implemented in this study to measure the bulk density where BD unit is expressed in g cm^{-3}.

6.3.4 Results of Soil Analysis

Tables 6.3-1 and 6.3-2 show the values of the soil properties for both red and grey soils which resulted from the laboratory soil analysis. An initial assessment of the results shows that both red and grey soils are very stony with stone percent as high as 69 % at some sampling locations. This is due to the stony nature of soils in general in the study area as explained in the Spanish published soil map of the Vélez Rubio (see

Proyecto Lucdeme, 1992). This stoniness could be caused by the past soil erosion of fine particles where coarser materials are left un-eroded. Stone presence in the soils of study area is a significant factor in controlling the hydrological properties of the slopes because it affects the rates of infiltration, overland-flow generation and reduces the soil-erosion rate. However, in this study the stone presence is not used because both the selected overland-flow and soil-erosion models do not incorporate the stone as a parameter in their algorithms, thus, some errors should be expected in the model implementation.

	BD g/cm^3	**OM%**	**Sand%**	**VFS%**	**Silt%**	**clay%**	**Stone%**	**Depth (cm)**
RS 10	1.248	4.91	57.9	8.5	29.2	4.4	65.4	17
RS 20	1.379	3.75	55.5	9.5	27.1	8.0	48.1	47
RS 26	1.573	2.31	56.2	8.3	18.7	16.8	47.3	11
RS 28	1.625	2.05	62.6	10.9	20.5	6.0	61.6	15
RS 43	1.497	2.41	67.4	6.3	17.2	9.0	53.1	13
RS 59	1.366	2.5	47.4	8.5	28.4	15.7	39.8	11
RS 65	1.321	3.63	55.7	8.6	26.8	8.9	42.3	20
RS 95	1.766	2.84	64.4	6.8	16.6	12.2	53.9	19
RS 125	1.528	3.43	48.1	7.8	18.6	25.5	34.8	14
RS 140	1.277	3.15	48.9	8.1	14.8	28.3	40.3	25
RS 145	1.343	3.91	45.2	6.2	16.0	32.7	40.5	59
RS 146	1.304	3.76	43.3	6.5	16.8	33.4	33.9	78
RS 156	1.352	3.61	44.3	5.0	16.7	34.1	48.4	45
RS 186	1.392	2.57	52.3	7.3	14.9	25.5	51.4	22
RS 196	1.409	2.29	46.3	6.4	13.5	33.8	41.2	17

Table 6.3-1. Soil analysis results for the red soil samples. The sand is classified >0.10 mm. Very fine sand (VFS) is classified between 0.05-0.10 mm. The numbers next to the sample name (such as RS 145) represent distances along the red transect.

	BD g cm^{-3}	OM%	Sand%	VFS%	Silt%	Clay %	Stone%	Depth (cm)
GS 2	1.421	5.47	60.1	10.5	22.1	7.4	61.9	19
GS 12	1.486	3.94	63.4	9.0	15.5	12.0	51.0	35
GS 23	1.459	2.54	57.3	9.3	26.5	6.9	54.7	28
GS 28	1.434	2.95	60.1	9.8	24.4	5.8	54.2	12
GS 30	1.589	2.93	60.3	6.9	22.3	10.5	53.8	31
GS 40	1.652	1.3	57.1	8.6	25.7	8.5	50.7	54
GS 50	1.801	1.44	49.5	10.6	30.1	9.9	53.4	33
GS 55	1.62	1.28	56.4	9.6	25.8	8.1	55.9	64
GS 60	1.68	1.08	57.6	8.3	24.9	9.2	50.7	38
GS 70	1.617	1.17	60.6	7.7	19.2	12.6	59.8	42
GS 71	1.6	1.18	62.4	8.0	22.6	7.0	55.7	40
GS 76	1.56	0.76	64.0	8.6	21.6	5.9	58.7	71
GS 86	1.312	4.38	54.6	7.1	16.8	21.6	52.2	36
GS 106	1.398	3.57	55.1	7.5	22.2	15.2	54.7	65
GS 116	1.439	1.45	55.2	7.3	22.3	15.2	50.1	56
GS 146	1.588	1.11	66.2	8.0	20.6	5.2	67.1	37
GS 161	1.771	1.87	53.3	6.1	16.2	24.4	60.6	35
GS 166	1.757	2.23	62.3	13.5	9.4	14.8	69.4	57
GS 167	1.661	1.82	60.5	7.9	12.9	18.7	53.2	48
GS 172	1.659	2.05	56.7	9.4	12.1	21.8	62.3	49
GS 182	1.621	2.37	56.4	6.7	25.8	11.2	56.9	30
GS 187	1.727	1.8	55.9	7.6	27.1	9.5	63.3	37

Table 6.3-2. Soil analysis results for the grey soil samples. The sand is classified >0.10 mm. Very fine sand (VFS) is classified between 0.05-0.10 mm. The numbers next to the sample name (such as GS 146) represent distances along the grey transect.

6.4 STATISTICAL METHODS FOR MAPPING SOIL PROPERTIES

After the various soil physical properties are extracted from the soil samples in the laboratory, they can be used to make the soil properties maps. A range of

statistical approaches can be implemented to spatially distribute these soil properties and these approaches are investigated.

6.4.1 Investigating The Probability Distributions of Soil Properties

Generally speaking, there are two different groups of technique that can be carried out for the statistical analysis of the soil properties: the parametric and non-parametric techniques. The choice of the appropriate technique depends on the probability distributions of these soil properties. The parametric technique can be applied if the sub-samples of the relevant soil property are normally distributed, whereas the non-parametric technique should be applied if the probability distributions of these sub-samples deviate significantly from normality.

As a result of this, the underlying distributions of the sub-samples, which describe the soil properties, should be first analysed and tested for normality. To do so various statistical techniques can be applied such as the descriptive statistics, histograms and normal probability plots, and the chi-square test. The descriptive statistics for testing normality consist of mean, median, mode, skewness, and kurtosis measures where the median and mode tend to have close values to the value of the mean if the distribution is normal. The skewness is a measure of the asymmetry of the distribution where a skewness value of zero (or near zero) indicates potential normality in the distribution. A distribution with a significant positive or negative skewness value has a long right or left tail respectively. The kurtosis is a measure which expresses the extent to which observations in a sample cluster around a central point. In a distribution that is regarded as normal, the value of the kurtosis statistic is zero (or near zero). A significant positive value of kurtosis means that the observations in a sample cluster more and have longer tails than those in the normal distribution, whereas a significant negative kurtosis value indicates the observations cluster less and have shorter tails.

Another test for the normality of a distribution is the graphical approach which is expressed by the histogram and the normal probability plot (a plot of the sample's

cumulative proportions against the normal cumulative proportions). The histogram represents graphically the frequency distribution of the sample values and indicates that this distribution is normal if it is bell-shaped. In the case of the normal probability plot, if the distribution of the selected sample matches the normal distribution, then the plot points cluster around a straight diagonal line. The chi-square test is another test which can be implemented to check whether the distribution of a sample differ significantly from the normal distribution. In this test, a calculation of the goodness of fit test is carried out for comparison of observed data of a sample with data expected based on the assumption of a normal distribution.

No matter which normality test is used, all may fail to detect the actual non-normality of the population distribution if the sample size is too small (less than 15). The histogram and the normal probability plot, for example, may be unable to provide much information in such situations. The chi-square test also needs a minimum of three sub-groups (defined from the same sample under investigation), and each group of them should have a minimum of five observations (15 observations in total) in order the chi-square test to be a success.

In this study the thirty-seven soil samples representing each of the soil properties were split up into two sub-samples, fifteen samples derived from areas of red soil and twenty-two samples from areas of grey soil. The distributions of these sub-samples were first graphically investigated to test whether they can be initially regarded as normal distributions. Figure 6.12 shows the histograms and the normal probability plots of all the sub-samples representing the soil properties of bulk density, clay percent, organic matter (OM), sand percent, silt percent, soil depth, and very fine sand percent (VFS).

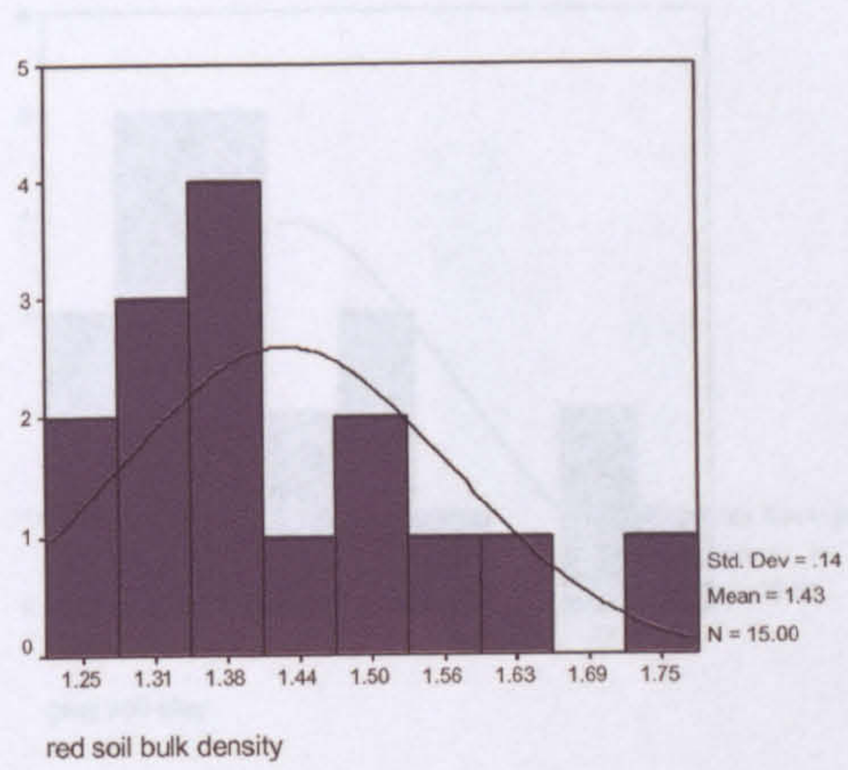

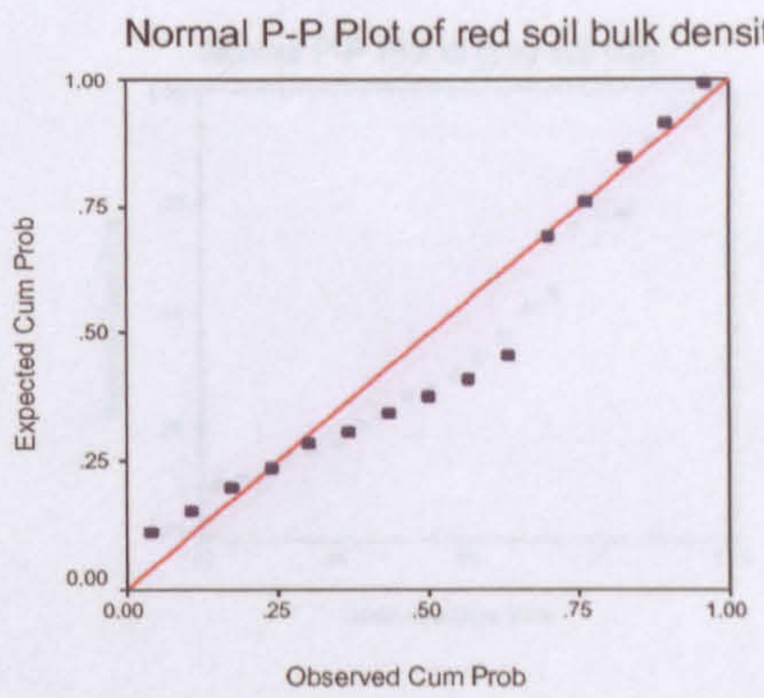

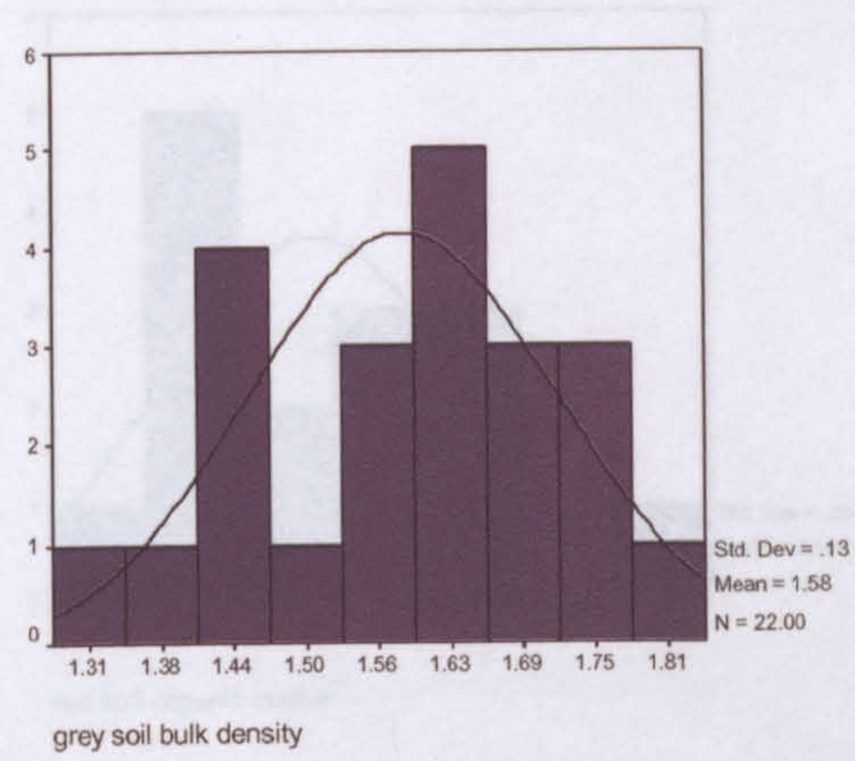

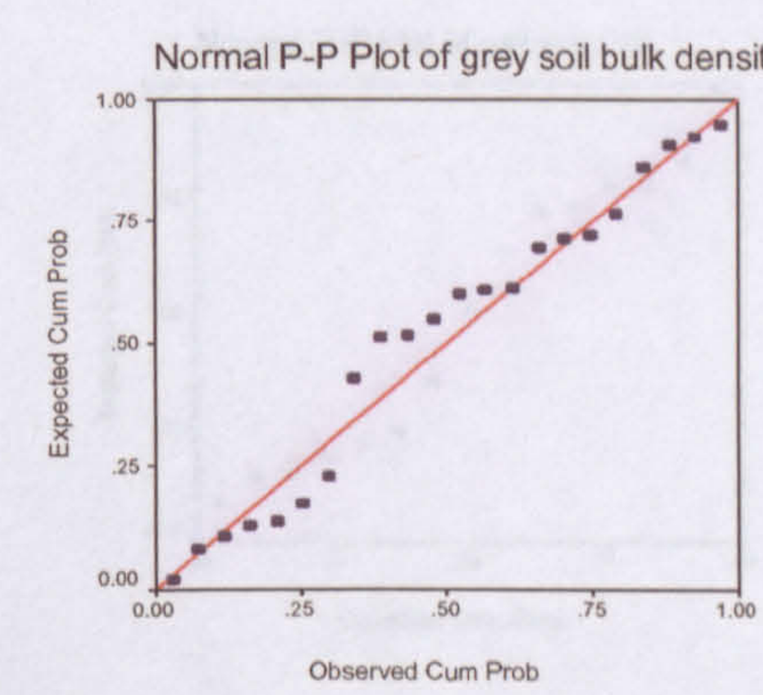

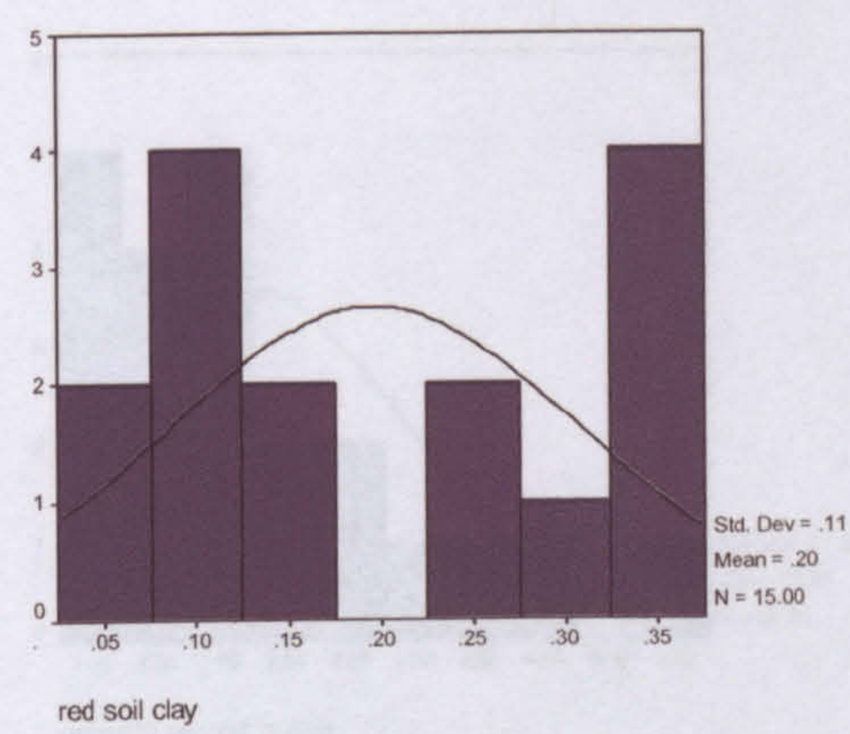

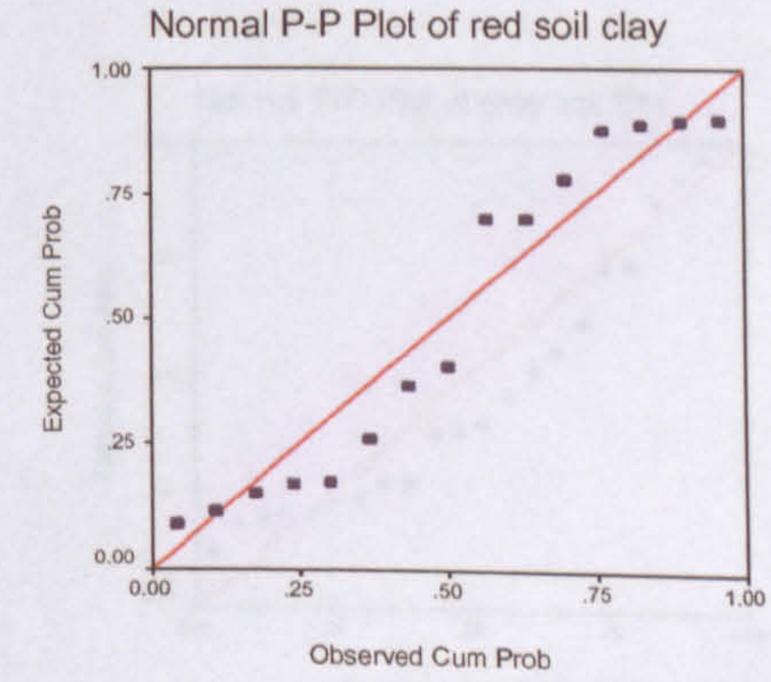

Figure 6.12. Showing the histograms, with the normal distribution curve, of the soil properties samples in both red and grey soil types. The figure also shows the probability plots of the cumulative proportions against the cumulative proportions of the normal distribution curve.

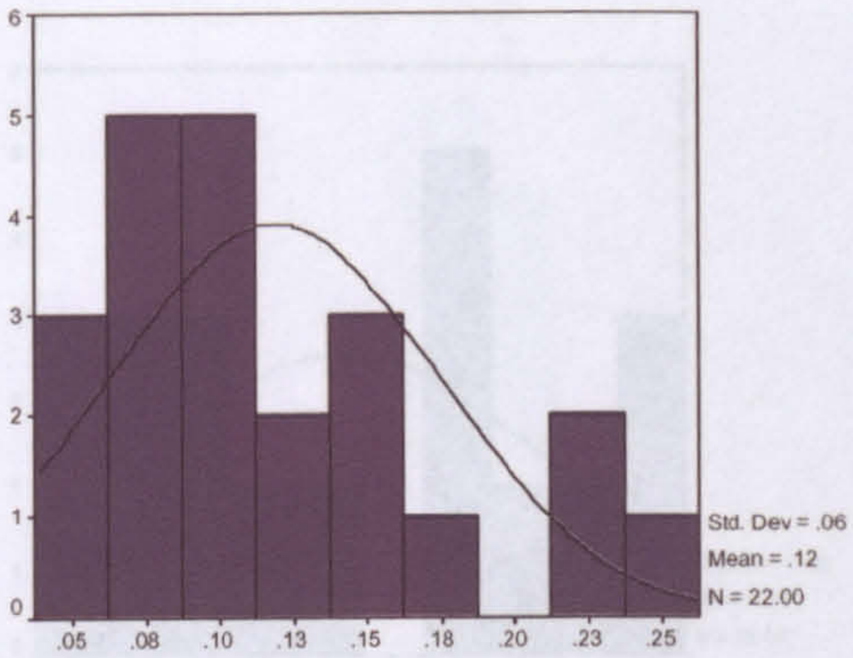

grey soil clay

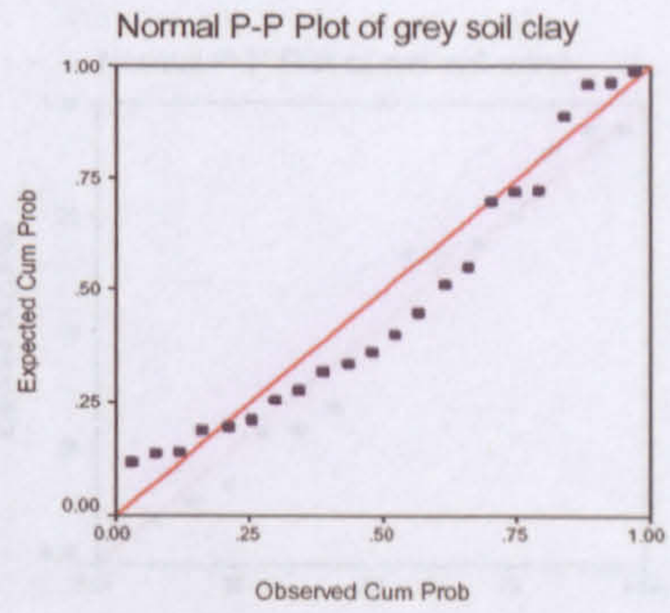

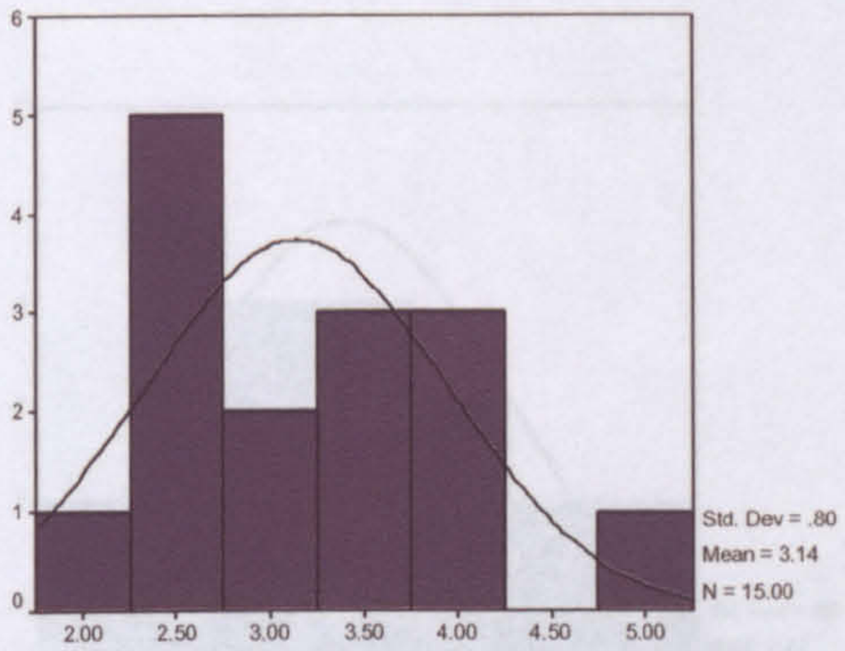

red soil organic matter

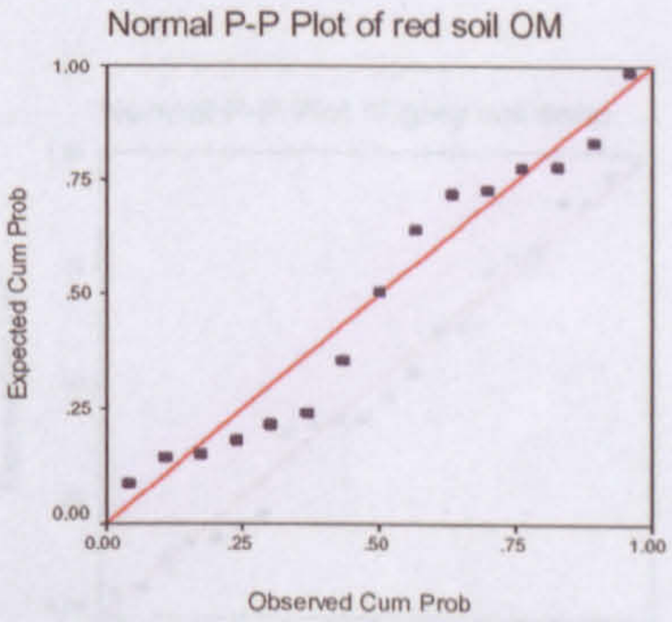

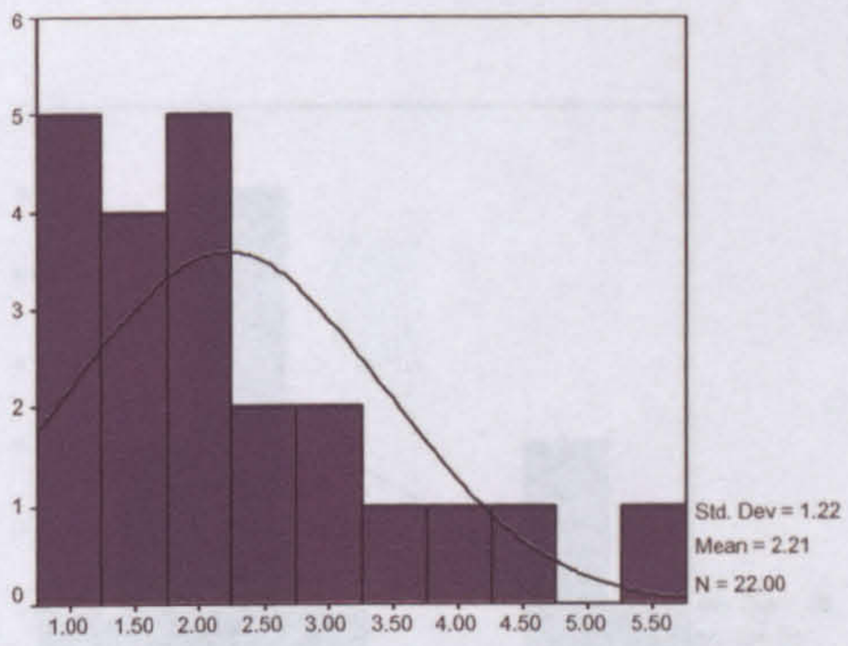

grey soil organic matter

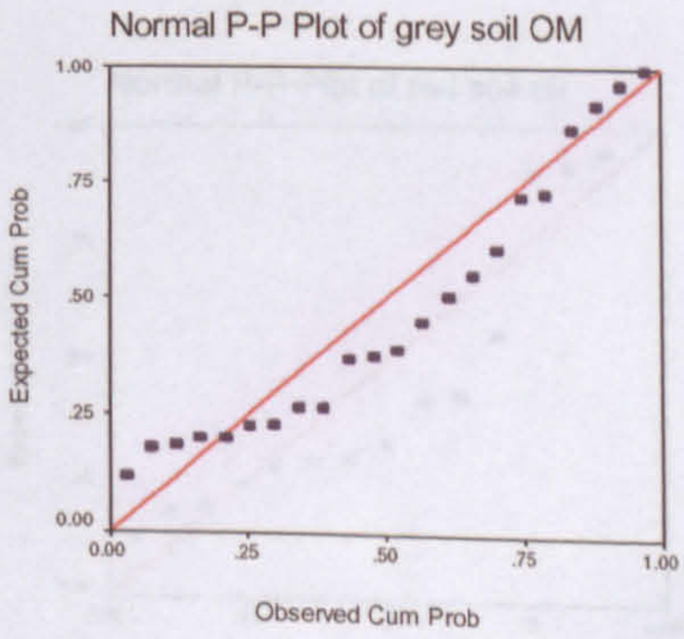

Figure 6.12 *continued ...*

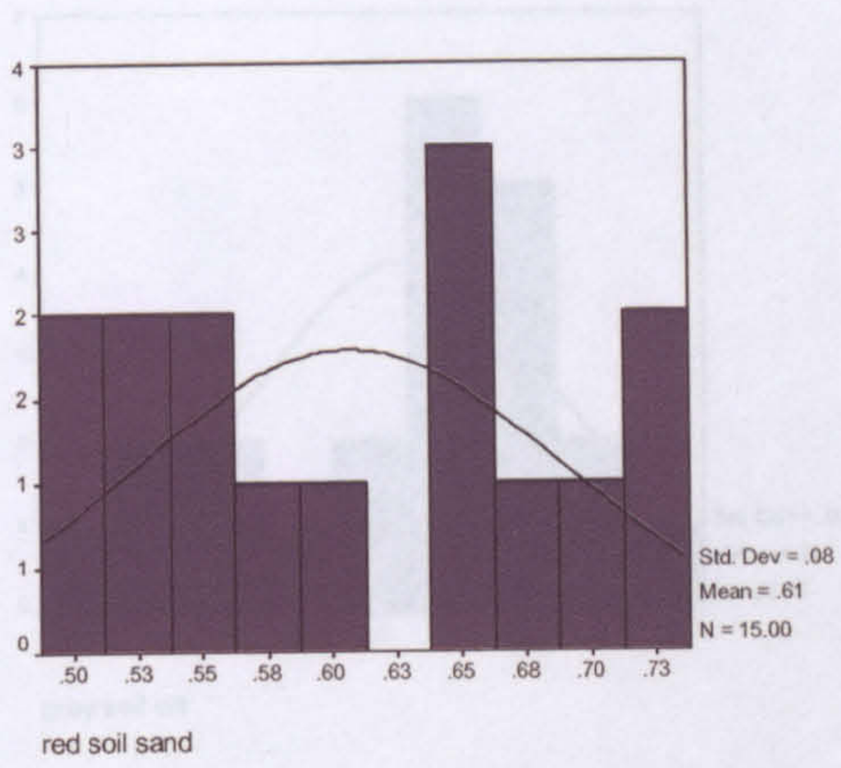

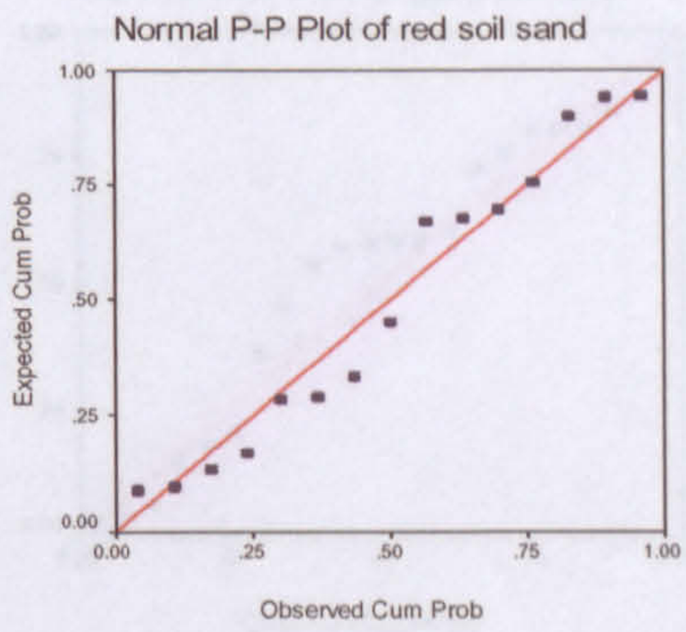

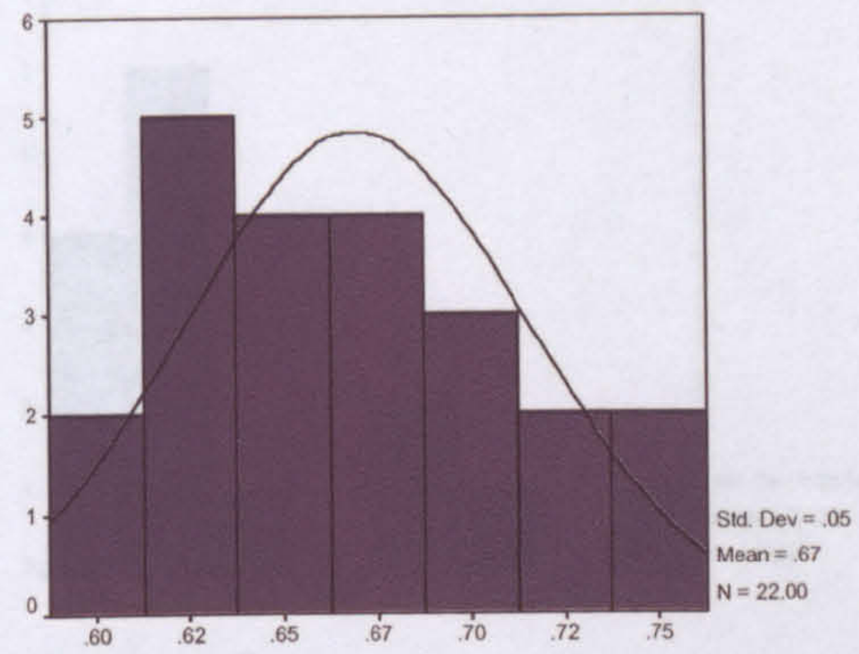

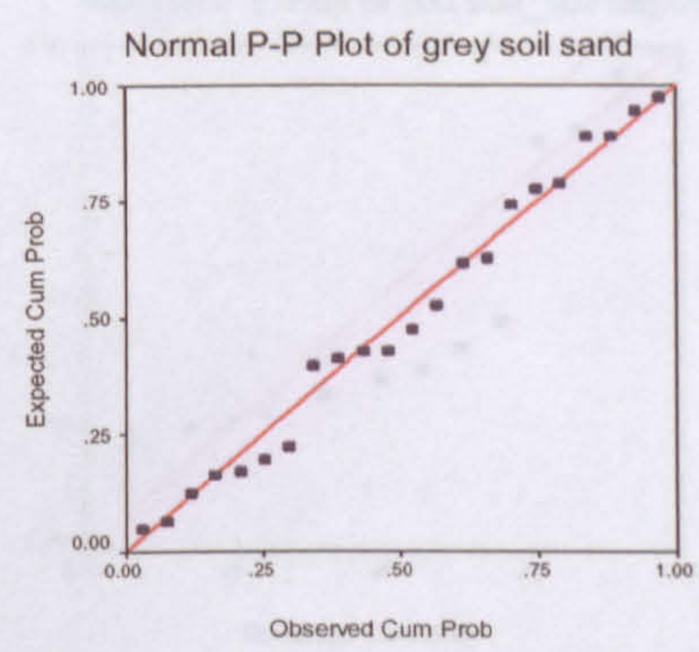

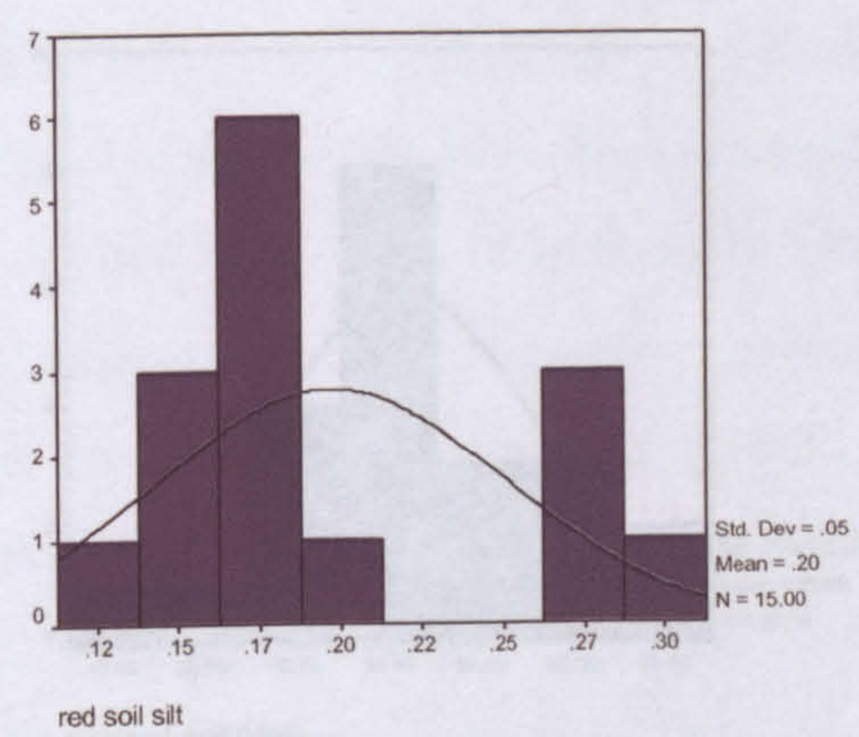

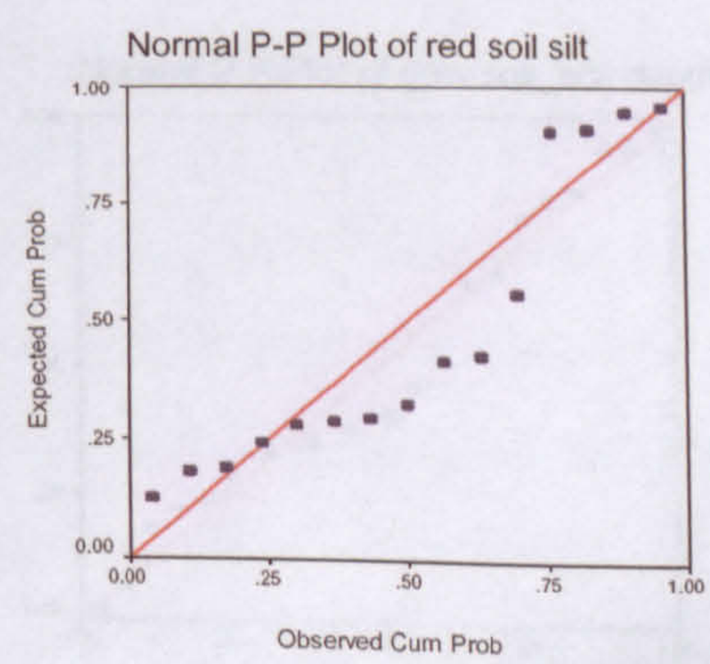

Figure 6.12 *continued ...*

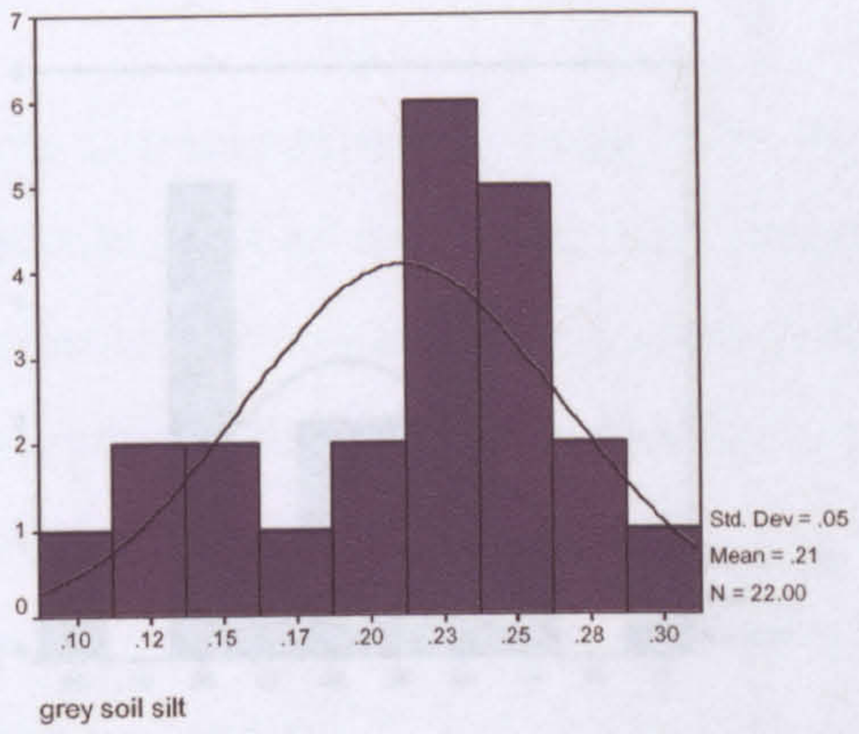

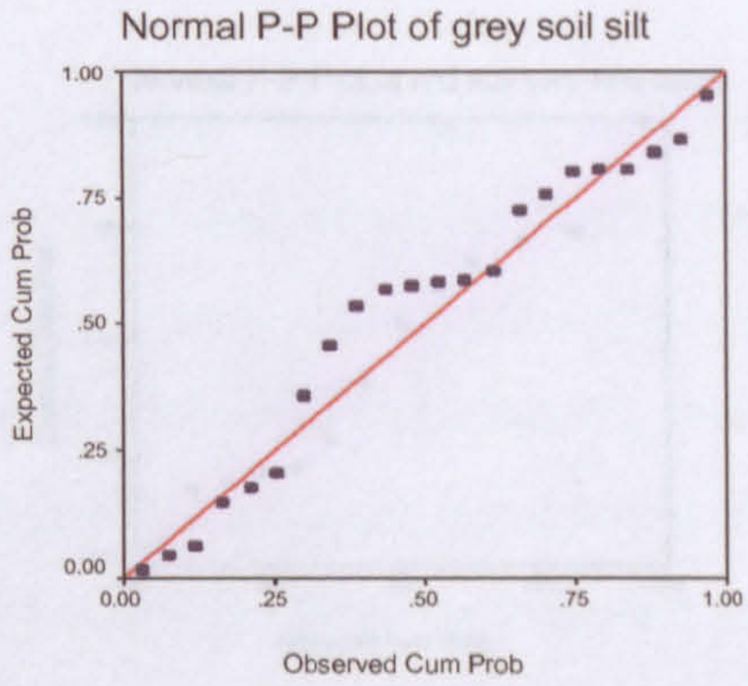

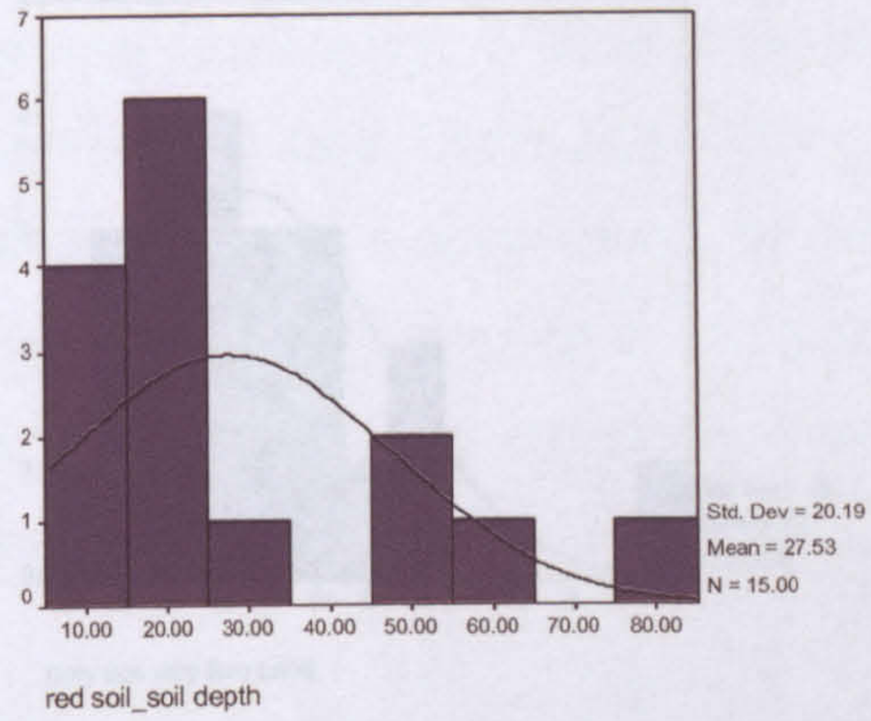

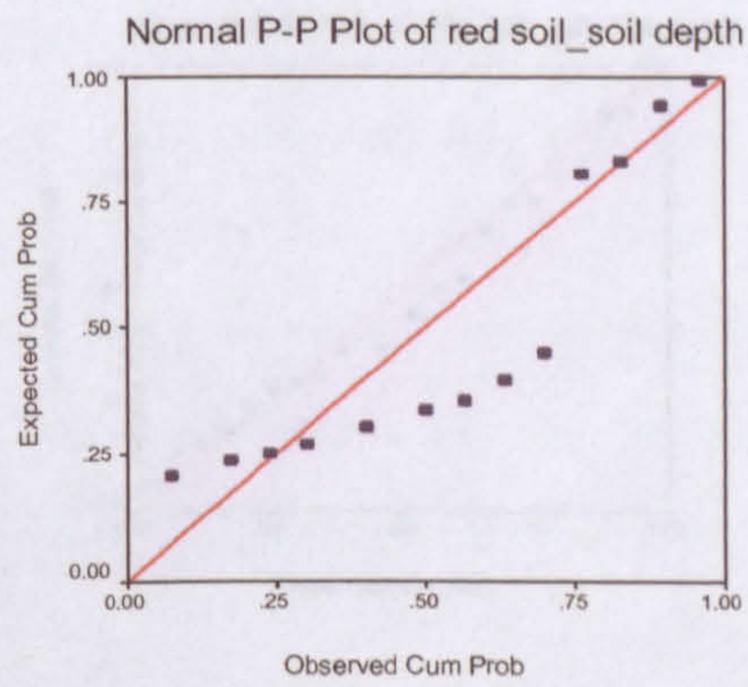

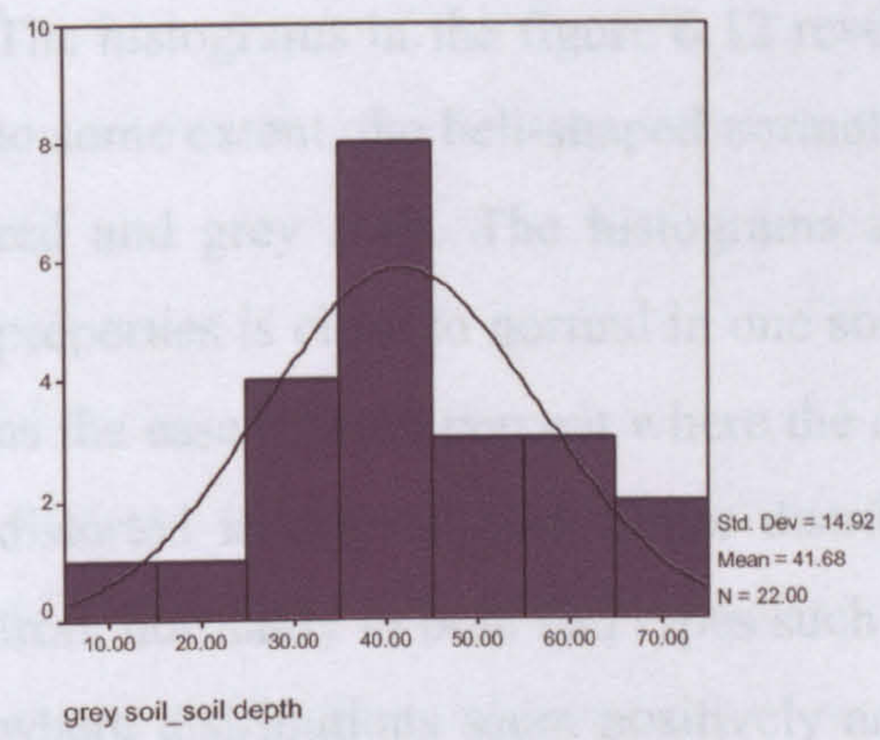

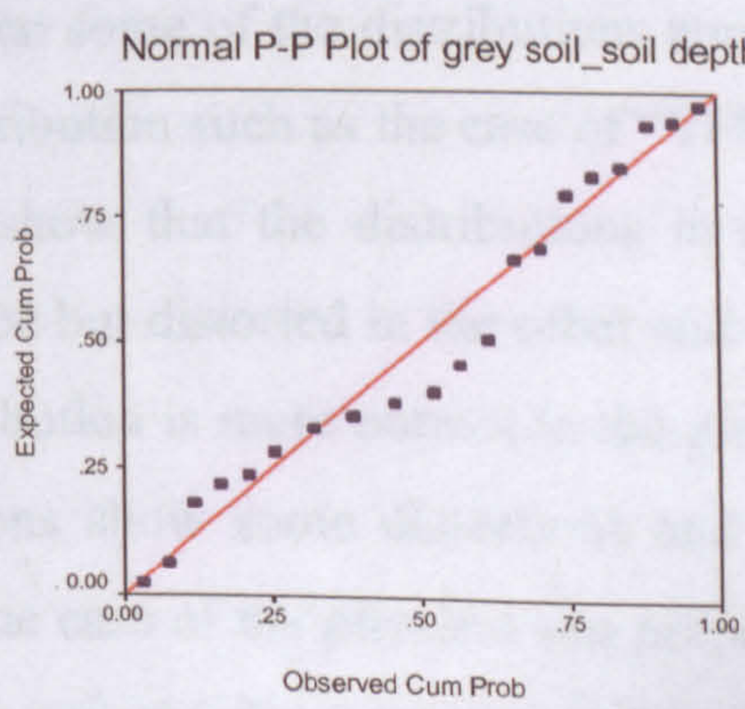

Figure 6.12 *continued ...*

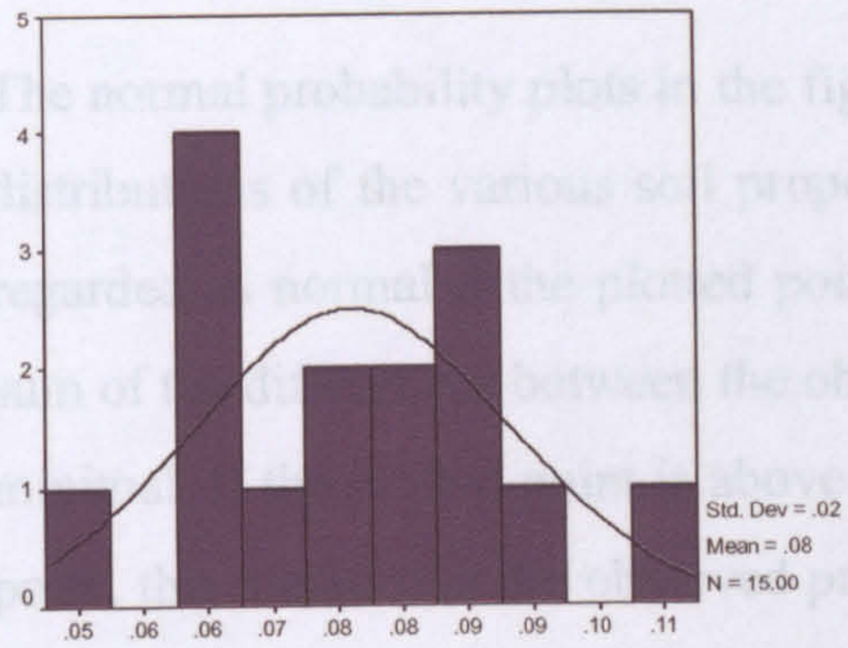

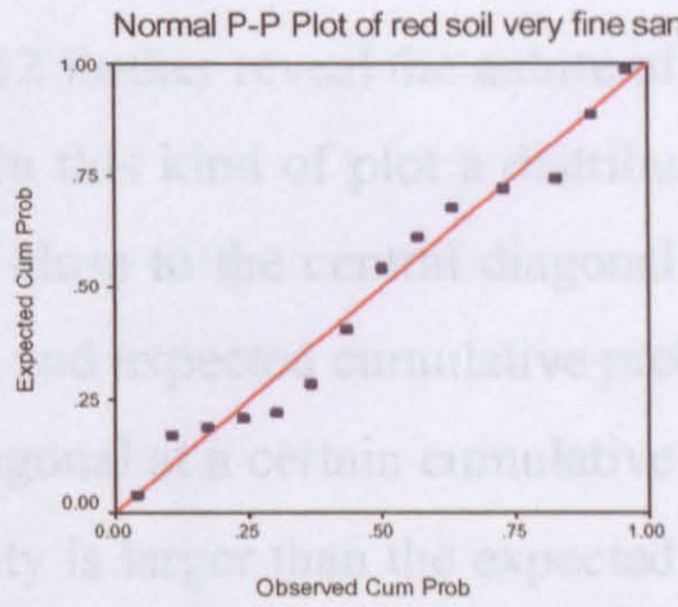

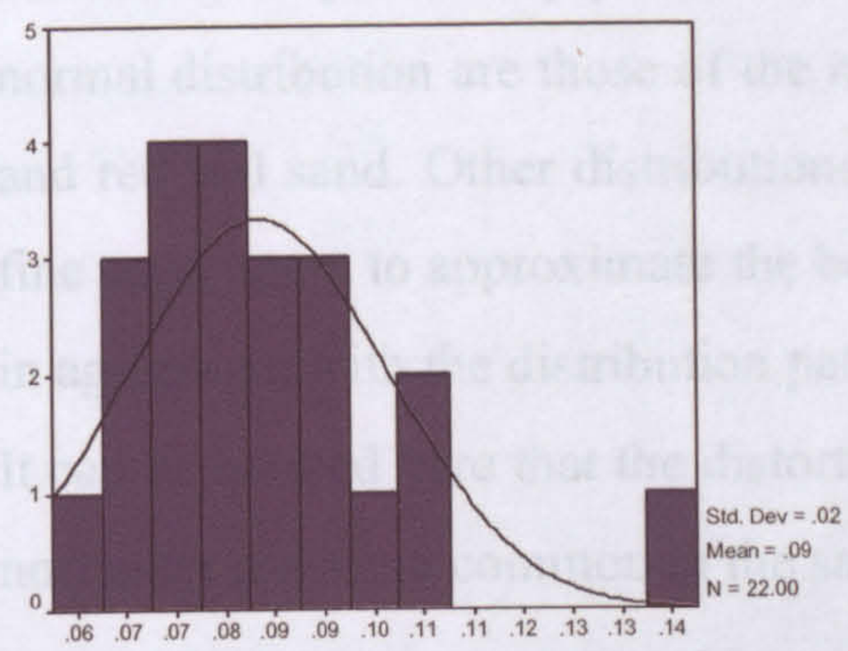

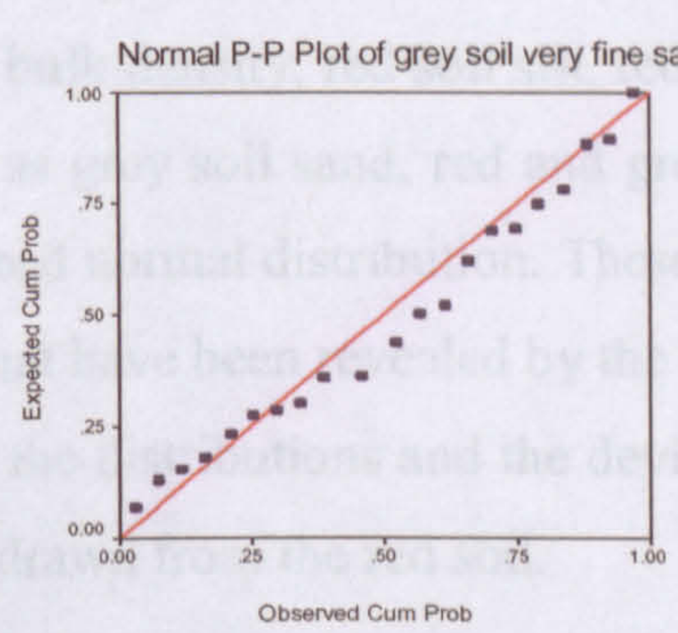

Figure 6.12 *continued ...*

The histograms in the figure 6.12 reveal that some of the distributions approximate, to some extent, the bell-shaped normal distribution such as the case of "VFS" in both red and grey soils. The histograms also show that the distributions in some soil properties is close to normal in one soil type but distorted in the other soil type such as the case of sand percent where the distribution is more normal in the grey soil but distorted in the red soil. Other distributions show some distortions and deviation from normality in both soil types such as the case of the physical soil property of silt where distributions seem positively and negatively skewed in the red and grey soil types respectively. These distortions in some of the distributions could be attributed to the potential existence of two or more distinctive sub-groups in the sand samples

representing the red soil type which have different means and distributions and causing the distribution of the overall sample to be distorted.

The normal probability plots in the figure 6.12 further reveal the nature of the sample distributions of the various soil properties. In this kind of plot a distribution can be regarded as normal if the plotted points are close to the central diagonal so that the sum of the differences between the observed and expected cumulative probabilities is minimal. If the plotted point is above the diagonal at a certain cumulative probability point, this means that the observed probability is larger than the expected probability and vice versa.

These normal probability plots show that the distributions that most deviate from the normal distribution are those of the red soil bulk density, red soil silt, red soil depth, and red soil sand. Other distributions, such as grey soil sand, red and grey soil very fine sand, seem to approximate the bell-shaped normal distribution. These results are in agreement with the distribution patterns that have been revealed by the histograms. It can be noticed here that the distortions in the distributions and the deviations from normality are more common in the samples drawn from the red soil.

To evaluate statistically if the samples come from normally distributed populations, the chi-square test was applied and the skewness and kurtosis measures were calculated. Table 6.4 shows the results of this test and reveals that in only two sub-samples out of fourteen (red soil silt and grey soil depth) the test proved to be significant at $\alpha = 0.05$ (i.e. samples are not normally distributed). The skewness and kurtosis measures take values around zero in some cases but they are significantly different from zero in some other distributions suggesting a possible departure from normality. It should be noted that high values for the skewness and kurtosis measures are not accompanied by high and significant values for chi-square test and vice versa. This means that an overall assessment of all these statistics, as well as of the central tendency indices, histograms, and normal probability plots, should be carried out before a decision is taken about the nature of a distribution under investigation.

Soil property	Soil type	Mean	Median	chi-square	Skewness	Kurtosis
BD	RS	1.425	1.379	0.31	1.07	0.68
	GS	1.584	1.608	1.63	-0.30	-0.65
Clay%	RS	0.196	0.168	2.56	0.07	-1.76
	GS	0.119	0.102	2.25	0.91	-0.10
OM%	RS	3.14	3.15	1.67	0.53	-0.16
	GS	2.21	1.85	1.61	1.21	1.03
Sand%	RS	0.606	0.596	0.28	0.21	-1.23
	GS	0.669	0.663	0.86	0.19	-0.70
Silt%	RS	0.197	0.172	4.43 *	0.86	-0.85
	GS	0.212	0.222	3.32	-0.64	-0.25
Soil depth	RS	27.5	19	2.32	2.52	1.51
	GS	41.7	37.5	6.21 *	0.20	-0.25
VFS%	RS	0.076	0.078	1.26	0.33	0.23
	GS	0.085	0.081	2.30	1.29	2.69

Table 6.4. The results of testing the normality (chi-square, central tendency, skewness, and the kurtosis) of the two groups of red and grey soil samples. The (*) indicates that the chi-square test is significant at alpha=0.05 probability level (and the sample is not normally distributed) but the test is not significant at alpha=0.01 probability level.

Such a general assessment was carried out on the soil properties. In addition, the results of other studies were taken into consideration in understanding and determining the frequency distributions of the soil properties. For example, Young *et al.* (1999) evaluated the frequency distributions of sixty soil properties in the Missouri Watershed and found that only five soil properties approximated the normal distribution. In addition, they found that nearly three-quarters of these distributions have large skewness measure and more than 80% of them have a large kurtosis measure. Some of these distributions were improved to better approximate the normal distribution when a $\log_e$ transformation was applied. Brejda *et al.* (2000) investigated the distributions of seventeen soil properties in the USA and found that most of these soil properties are non-normally distributed. They also found that

applying different transformations, mainly the $\log_e$ transformation, resulted in distributions that approximate the normal distribution.

Soil property	Soil type	Mean	Median	Chi-square	Skewness	Kurtosis
Transformed Clay%	RS	0.423	0.41	2.05	-0.16	-1.61
	GS	0.336	0.319	0.66	0.59	-0.60
Transformed OM%	RS	1.76	1.77	1.98	0.31	-0.66
	GS	1.44	1.36	0.82	0.75	-0.09
Transformed Sand%	RS	0.777	0.772	0.31	0.13	-1.27
	GS	0.818	0.818	1.43	0.13	-0.72
Transformed Silt%	RS	0.44	0.415	2.11	0.77	-0.93
	GS	0.456	0.472	1.46	-0.91	0.21
Transformed Soil depth	RS	4.98	4.36	1.78	1.18	0.31
	GS	6.35	6.13	2.10	-0.34	0.39
Transformed VFS%	RS	0.275	0.279	0.74	0.06	0.08
	GS	0.291	0.285	1.42	0.97	1.67

Table 6.5. The results of testing the normality, skewness, and the kurtosis of the two groups of red and grey soil samples after transformation by applying the square-root. All the chi-square tests became not significant at alpha=0.05 probability level (and the samples are normally distributed).

In the case of this study, it has been found that applying transformations to some of the soil properties causes these distributions to better approximate the normal distribution, whereas some other distributions do not need any transformations as they are normally distributed. However, unlike the conclusions of Young *et al.* (1999) and Brejda *et al.* (2000) studies, the $\log_e$ transformation did not improve the distributions of the data sets. Instead the square-root transformation was found to be more suitable for the data sets that need transformation. This square-root transformation was applied to clay, organic matter, sand, silt, soil depth, and very fine sand and the table 6.5 shows the results of the normality tests after transformation is applied.

Soil property	Soil type	Mean-median difference	Chi-square	Skewness	Kurtosis
Transformed Clay%	RS	+	+	-	+
	GS	+	+	+	-
Transformed OM%	RS	-	-	+	-
	GS	+	+	+	+
Transformed Silt%	RS	+	+	+	-
	GS	-	+	-	+
Transformed Sand%	RS	+	-	+	-
	GS	+	-	+	+
Transformed Soil depth	RS	+	+	+	+
	GS	+	+	-	-
Transformed VFS%	RS	+	+	+	+
	GS	+	+	+	+

Table 6.6. Showing the improvement of the normality indicators (mean-median differences and chi-square tests), skewness, and kurtosis of the distributions of the samples representing the red and grey soil types after applying the transformation. The sign (+) represents improvement and (-) represents degradation.

The table 6.5 reveals that all the chi-square tests became not significant for all sample distributions at the $\alpha = 0.05$ probability level which suggests normality. The table 6.6 compares the normality test indicators (including the difference between the mean and the median) between the samples before and after the transformation was applied and indicates an overall improvement of distribution normality when the transformation is applied.

6.4.2 Investigating the Correlation Between Soil Properties and Soil Fractions to Spatially Map the Soil Properties

One of the statistical methods to create spatially continuous soil properties maps is to investigate whether significant correlations exist between the values of the soil properties and a spatially continuous map. In this study the correlation between the

soil properties derived from the field samples and the mixture modelling soil fractions has been investigated in order to derive the soil properties maps. If significant relationships are found to exist between the mixture maps and soil properties, then the grey and red soil information provided by these mixture modelling soil maps can be implemented to interpolate and extrapolate spatially the soil properties in all locations of the study area.

Soil property	Soil type	R^2	Significance value
BD	GS	0.16	0.47
	RS	0.11	0.70
OM	GS	0.52	0.013*
	RS	0.32	0.24
Soil depth	GS	0.57	0.005*
	RS	0.46	0.08
Silt percent	GS	0.015	0.95
	RS	0.48	0.07
Sand percent	GS	0.24	0.29
	RS	0.53	0.04*
VFS percent	GS	0.23	0.30
	RS	0.64	0.010*
Clay percent	GS	0.40	0.08
	RS	0.63	0.011*

Table 6.7. The results of the regression between soil properties and the mixture modelling soil fractions. The sign "*" means that the regression is significant at 95% level.

To investigate this correlation, the soil samples representing the various soil properties were subdivided into two groups, one group for the red soil and the other group for the grey soil so that regressions can be applied between these groups and the mixture maps. These regressions were carried out after the necessary transformations on some soil properties (see table 6.5 and 6.6) to approximate normality because the coefficient of determination assumes normality in this correlation test.

Table 6.7 shows the results and the significance of these correlations at the 95% confidence level. The results reveal that most of these soil properties are not significantly correlated to the soil information in the mixture maps. This weak correlation can be explained by the fact that there are other factors, other than the soil colour, which influence these soil properties such as the agricultural practices, topography of slope and aspect, and vegetation cover. The analysis also shows that some of these soil properties are significantly correlated to one soil type but are not correlated to the other soil type. Examples of this are the organic matter content and the soil depth which are shown to be only correlated with the grey soil fractions and not to the red soil fractions.

To investigate whether the consideration of the effect of land use and agricultural practices will improves the correlation between the soil properties and the mixture maps, the samples were further subdivided into two groups according to whether they had been ploughed or not. However, it was not possible to statistically investigate the normality of the frequency distributions of the sub-groups resulting from this subdivision because the sample size was too small (the size for 50% of these sub-samples is between 6-9 and for the other 50% is 11) and the implementation of any normality test (i.e. histogram, chi-square, skewness and kurtosis) will not be reliable. However, due to the fact that the earlier normality tests which was implemented in table 6.7, showed that all the sample distributions approximate normality, the distributions of these sub-samples will be assumed to be normal because these sub-samples resulted by subdividing the original normally populated samples.

The correlations between the soil information and the subdivided soil properties have been statistically investigated and table 6.8 shows the coefficient of determination and the significance values at the 95% confidence level. It can be noticed in table 6.8 that the number of significant correlations is less than in table 6.7 and that some soil properties, which were significantly correlated to soil information, became uncorrelated (e.g. organic matter content and soil depth for grey soil). This suggests

that regression equations between mixture maps and soil properties cannot be used to spatially distribute the soil properties.

Soil property	Soil type	Land use	R^2	Significance value
BD	GS	Matorral	0.78	0.004*
	GS	Agricultural	0.52	0.10
	RS	Matorral	0.33	0.39
	RS	Agricultural	0.32	0.53
OM	GS	Matorral	0.56	0.07
	GS	Agricultural	0.15	0.66
	RS	Matorral	0.30	0.43
	RS	Agricultural	0.45	0.37
Soil depth	GS	Matorral	0.52	0.10
	GS	Agricultural	0.08	0.81
	RS	Matorral	0.45	0.22
	RS	Agricultural	0.45	0.37
Silt percent	GS	Matorral	0.38	0.25
	GS	Agricultural	0.74	0.009*
	RS	Matorral	0.28	0.49
	RS	Agricultural	0.27	0.59
Sand percent	GS	Matorral	0.47	0.15
	GS	Agricultural	0.45	0.16
	RS	Matorral	0.03	0.94
	RS	Agricultural	0.86	0.029*
VFS percent	GS	Matorral	0.09	0.79
	GS	Agricultural	0.69	0.02*
	RS	Matorral	0.44	0.23
	RS	Agricultural	0.48	0.33
Clay percent	GS	Matorral	0.74	0.009*
	GS	Agricultural	0.48	0.13
	RS	Matorral	0.46	0.21
	RS	Agricultural	0.90	0.013*

Table 6.8. The results of the regression between soil properties and the mixture modelling soil fractions after taking the land-use type into consideration. The sign "*" means that the regression is significant at 95% level.

Thus, the mixture modelling soil maps will not be used for this purpose and other methods of mapping will be investigated. It should be mentioned here that the subdivision of the soil properties according to the land use created very small sub-samples and this limitation in sample size undermined the power of the statistical tests, thus, the results should be interpreted with a degree of caution.

6.4.3 Geostatistical Analysis of Soil Properties

It is a difficult, expensive, and sometimes not possible in practice to collect field measurements that comprehensively describe the nature, pattern and extent of natural phenomena. One way of trying to achieve this is to use a relatively small number of field observations to describe natural phenomena using statistical interpolation and extrapolation techniques called geostatistical analysis. A typical example is precipitation data, which is crucial for the implementation of over-land flow and soil-erosion modelling, where precipitation is gauged in scattered, point-based stations and then geostatistical techniques are applied to derive continuous precipitation information over the area under study. Another example is in soil mapping where soils are characterised by heterogeneity and by complex spatial distribution patterns. In this case soil samples are collected at specific locations and a continuous form of soil mapping is interpolated by applying the geostatistical analysis to these soil samples.

In this study, the methodology of geostatistics is investigated for application on soil properties, which have been derived from the soil samples, to produce continuous maps of the various soil properties. These maps will be used later on for the estimation of soil erodibility and for the implementation of over-land flow and soil-erosion model.

Geostatistics is described by Kitanidis (1997) as "the guide to the unknown; it is an approach for utilising observations to make inferences about an unmeasured quantity". In statistical terms, geostatistics is a collection of statistical methods that

describe spatial autocorrelation among sample data, and can be implemented in various types of spatial models. Geostatistics changes the entire methodology of sampling because traditional sampling methods do not work with autocorrelated data and therefore, the main purpose of sampling plans is to avoid spatial correlations. In geostatistics, however, there is no need in avoiding autocorrelations and sampling becomes less restrictive. Also, geostatistics changes the emphasis from estimation of averages to mapping of spatially distributed populations.

The spatial autocorrelation can be analysed using correlograms, covariance functions and variograms (sometimes called semivariograms). In this study, the semivariogram is used as a measure of the spatial autocorrelation because it is more widely used and proven to produce good results. Generally speaking, geostatistical analysis usually has the following steps: 1)- estimation of the spatial autocorrelation (semivariogram), 2)- estimation of parameters of the semivariogram model, and 3)- estimation of the interpolated surface using interpolation techniques such as ordinary kriging or cokriging.

Ordinary kriging can be expressed in the following equation:

$$Z'_0 = \sum_{i=1}^{n} W_i Z_i \qquad 6.4$$

Where Z'_0 is the value at unsampled location "0" which is estimated as a weighted average of sample values Z_i at locations i around it. Weights W_i depend on the degree of correlations among sample points and estimated point. The sum of weights is equal to 1 (this value is specific to ordinary kriging). Weights are estimated individually for each point in a regular spatial grid using the correlations between points estimated from the semivariogram model.

However, if only a limited number of observations are available for a particular parameter and these observations are not well distributed over the area of interest, such as the case of this study, ordinary kriging method tends to produce poor results (Rosenbaum and Soderstorm, 1996). As a result, the ordinary kriging interpolation

method will not be used in this study and the alternative method of cokriging will be investigated to create the interpolated continuous soil properties maps.

The cokriging interpolation method is based on the knowledge of the experimental variogram behaviour of a similar parameter with which it can be correlated so it can be used to assist the fitting of a more realistic model. The concept of cokriging achieves this for a parameter whose estimation is primarily required and which is cross-correlated with a secondary parameter (Stein *et al.*, 1988). The estimation error in this method is reduced substantially because more information is being used for the estimation of the primary parameter and a two-fold reduction in error of estimation would be typical (Rosenbaum and Soderstorm, 1996). The cokriging estimation is done by minimising the variance of the estimation error using the cross-correlation between the primary and the secondary variables.

In order for the semivariogram calculations and the geostatistical analysis to be successful for the soil mapping, the number of samples should not be too small. Webster and Oliver (1992) studied the relationship between the sample size and the confidence in the semivariogram resulting from this sample and found that semivariograms computed from samples of size smaller than 50 are not reliable and that at least 100 data points are needed for more reliable semivariograms. However, Tsegaye and Hill (1998) investigated the spatial variability of various soil properties including particle size, bulk density, soil strength, and saturated hydraulic conductivity and found that particle size and bulk density (needed for this study) are more weakly spatially dependent producing a lower coefficient of variation. They concluded that due to this weak spatial dependence, the number of samples needed to estimate these soil properties spatially is lower.

In this study the number of samples is only 37 and well below the sample size recommended by Webster and Oliver (1992). However, according to Tsegaye and Hill (1998), a smaller sample size is needed to calculate the semivariograms for the soil properties evaluated in this study. Thus, the semivariograms will be calculated for the soil properties but poor results of these semivariograms should still be

expected during the geostatistical analysis because sample size for some soil properties is too small.

6.4.3.1 Results of Mapping Soil Properties Using Geostatistical Techniques

Cokriging is usually applied when the primary variable is difficult or expensive to measure. It can greatly improve interpolation estimates without having to more intensely sample the primary variable. In this study the secondary variable that can be used for cokriging interpolation are the mixture modelling soil maps of grey and red soil which have been re-scaled to remove the vegetation and shade effects. This is because such a map is spatially distributed and provides continuous information across the study area. Thus, the clay content map, because the soil property of clay has the highest correlation with mixture maps, will be created using the grey soil map as a secondary variable.

There are five stages in implementing the cokriging method: 1) the derivation of the clay percent semivariogram, 2) the derivation of the grey soil semivariogram, 3) the cross-variogram for the two variables, 4) fitting the semivariograms and the cross-variogram with the appropriate mathematical models, and 5) applying the cokriging interpolation algorithm to calculate the clay prediction and variance. Figure 6.13 shows the mathematical models representing the semivariograms of clay percent and grey soil variables and the mathematical model of their cross-variogram.

The resultant clay prediction map indicated large errors in the interpolation process where error-prone extreme values, both negative and greater than 100%, are common in that map. The resultant variance map also indicated very large negative values which could be attributed to the fact that a weak correlation exists between the clay soil property and the mixture modelling grey soil map where the existence of a strong correlation is essential for a successful cokriging interpolation. The cokriging interpolation techniques were also applied to the rest of the soil properties and similar results to the clay content were obtained due to weak correlations.

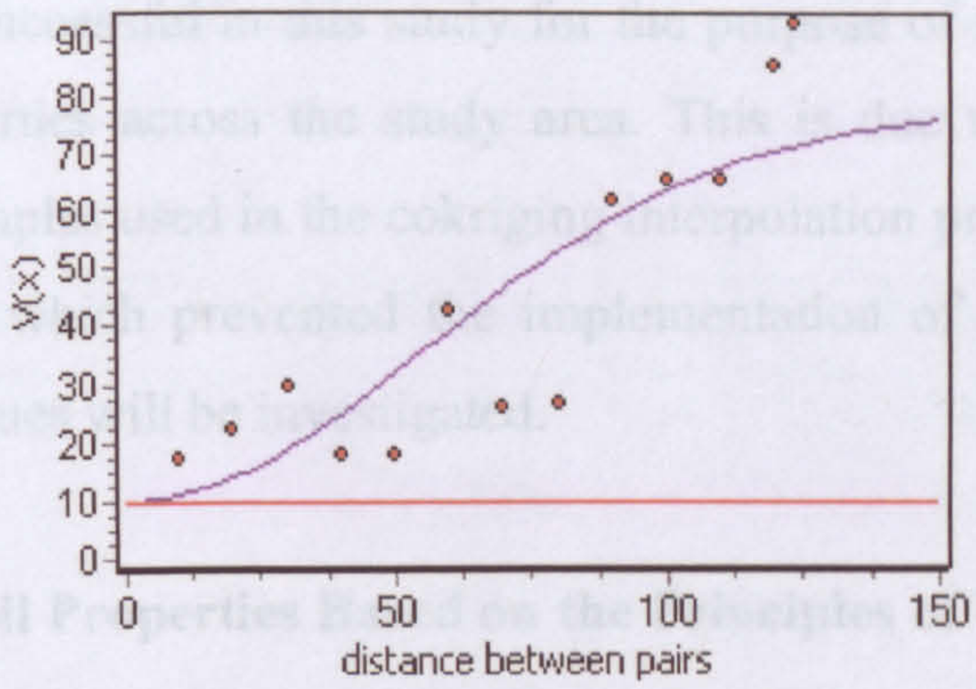

Combined mathematical model for the clay

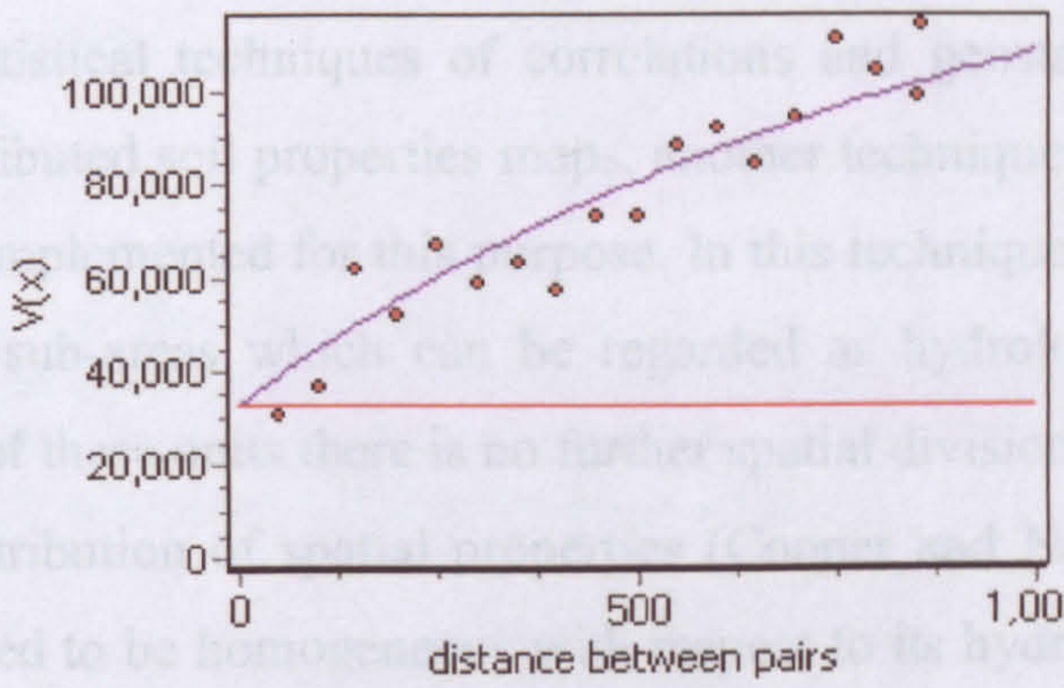

Combined mathematical model for the grey soil

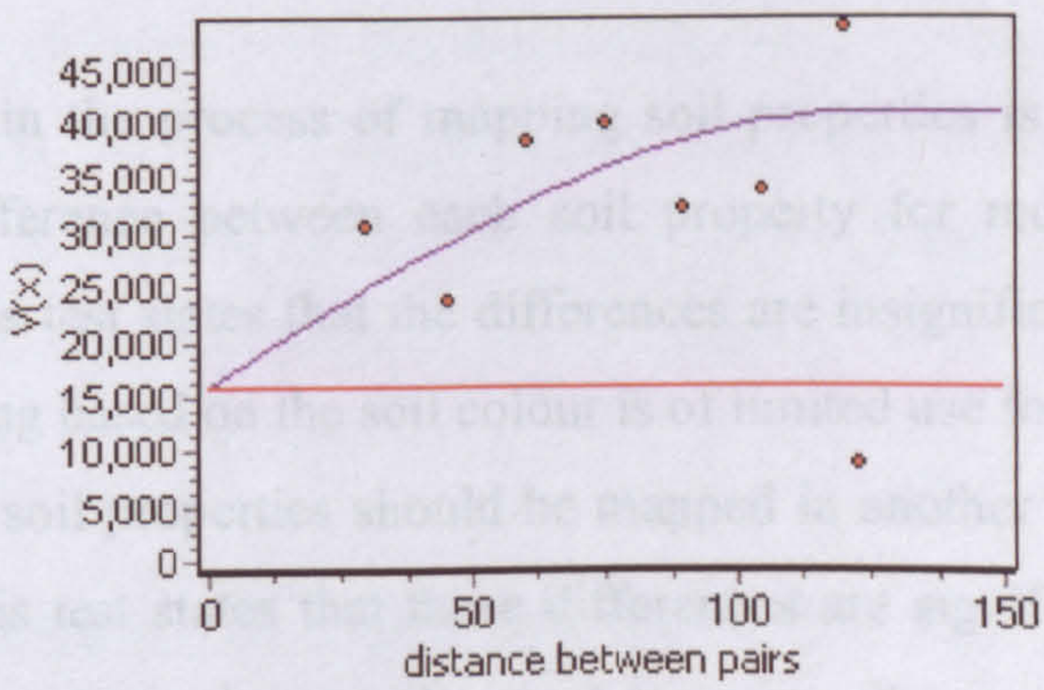

Model for the cross-variogram

Figure 6.13. The models of the clay semivariogram, grey soil semivariogram, and their cross-variogram needed for the interpolation process.

It has been shown here that geostatistical techniques did not produce good results and that they are not successful in this study for the purpose of spatially distributing the various soil properties across the study area. This is due to the limitations in the number of soil samples used in the cokriging interpolation process and the method of transect sampling which prevented the implementation of ordinary kriging. Thus, alternative techniques will be investigated.

6.4.4 Mapping Soil Properties Based on the Principles of Hydrological Response Units

Since the statistical techniques of correlations and geostatistics failed to produce spatially distributed soil properties maps, another technique of hydrological response units can be implemented for this purpose. In this technique the study area is divided into discrete sub-areas which can be regarded as hydrologically distinctive units. Within each of these units there is no further spatial division according to the internal statistical distribution of spatial properties (Cooper and Naden, 1998) so that each unit is assumed to be homogeneous with respect to its hydrological response. In this study hydrological response units were delineated using the soil type and land-use maps.

The first step in the process of mapping soil properties is to evaluate if there is a significant difference between each soil property for red and grey soils. If the outcome of this test states that the differences are insignificant, then this means that the soil mapping based on the soil colour is of limited use for mapping soil properties and that these soil properties should be mapped in another manner. However, if the outcome of this test states that these differences are significant, then the soil types defined by remote sensing can be used to map soil properties and implement the hydrological response units approach.

Once the normality of the distributions has been established and the necessary data transformations are carried out, the two-samples t test was applied to the different

soil properties to investigate if there was a significant difference in these properties between the two soil types. The table 6.9 shows that all of the soil properties apart from silt are significantly different from each other in the two of soil types.

Soil property	Significance value	H_0 hypothesis
Bulk Density	0.001	Rejected
Clay %	0.018	Rejected
OM %	0.007	Rejected
Sand %	0.006	Rejected
Silt %	0.425	Accepted
Soil Depth	0.007	Rejected
V.F.S	0.048	Rejected

Table 6.9. Summary statistics of the two-samples t test. The two samples come from different populations when the significance value is greater than (0.05) so the hypothesis H_0 is rejected. Significance value is calculated at 95% confidence level.

These findings suggest that most soil properties are significantly related to the soil types. This is important because it shows that soil mapping using remote sensing can be used to discriminate soils that have different properties. The two-samples t test also shows that silt is not significantly different between the soil types. This conforms with the finding of Da Costa (1979) who stated that silt component in the soil is the least important property in determining soil colour and, consequently, the least correlated to the soil type.

However, in addition to the soil type, the agricultural practices and the land-use types in the study area have an important influence on some of the soil properties due to the fact that ploughing increases soil depth and reduces soil bulk density. Young *et al.* (1999) studied the effect of land-use change on the frequency distributions of soil properties by subdividing the soil samples according to the land-use type. They

found that this sample subdivision normalised substantially the frequency distributions of 40% of soil properties under investigation.

To investigate the effect of this subdivision, the samples were subdivided into four sub-samples of grey soil matorral, red soil matorral, agriculture grey soil, and agriculture red soil. The matorral land-use type represents areas which are not ploughed and the agriculture land-use type represents areas where the land has been ploughed and the vegetation cover is removed for almond and olive plantations.

Soil property	Significance value *P*	H_0 hypothesis
Bulk Density	0.003	Rejected
Clay %	0.000	Rejected
OM %	0.012	Rejected
Sand %	0.095	Accepted
Silt %	0.019	Rejected
Soil Depth	0.001	Rejected
V.F.S	0.047	Rejected

Table 6.10. The results of analysis of variance (ANOVA). The four sub-samples come from different populations when the significance value P is smaller than (0.05) and the H_0 hypothesis is rejected.

The two-samples t test cannot be applied to test differences between more than two samples and, thus, analysis of variance statistical technique was applied to test whether the four sub-samples of each soil property are significantly different from one another and thus come from different populations. Assuming a value for "α" of 0.05 the table 6.10 lists the results of the ANOVA test which show that all of the soil properties (apart from the sand percent) are significantly different in the four sub-samples of different soils and land-use types.

One of the important observations from table 6.10 is that ANOVA showed a significant difference between sub-samples in the case of silt, whereas the two-samples t test table 6.9 suggested that it was not significant. This could be attributed to the presence of distinctive sub-populations in the original samples. However, the results also reveal that sand is not significantly different and that these sub-samples can be regarded as originating from the same population. Thus, changing the land-use practice does not appear to have a significant influence on the sand content of the red and grey soils. This could be attributed to the fact that loosening of the soil by ploughing does not make the sand particles more susceptible to erosion due to the fact that they are the heaviest particles.

In conclusion, ANOVA suggests that most of the soil properties (six out of seven) are significantly different between the different soil and land-use types, thus, they can be used to spatially distribute these soil properties over the entire study area and create maps of soil properties based on the principles of the hydrological response unit. These maps will be used to spatially estimate the soil erodibility and overland flow for the implementation of the Thornes soil-erosion model.

6.5 The Construction Of The Soil Properties Maps

In order to distribute the soil properties spatially over the study area, a map which describes the hydrological response units should be created first. The units of such a map will then be used as a base map for the creation of soil properties maps where the mean value of a soil property for each of the soil and land-use types will be assigned to the corresponding unit. This map was derived by applying a GIS intersection technique between the digitised land-use map which was created in chapter 5 (see figure 5.30) and the soil map which was created by hardening of the mixture maps of grey and red soils (figure 6.8).

Before the GIS intersection was carried out, the land-use map was modified by amalgamating the two land-use classes of matorral and bare ground into one class. There are two reasons for this amalgamation process. The first reason is the lack of

any soil data that can provide information about the soil properties in the bare ground area which is too small. The second reason is that the matorral and bare ground land-use types are likely to have some similar physical properties due to that fact that they have not been ploughed, despite the fact that they have different infiltration rates due to the presence of vegetation in matorral areas. Figure 6.14 shows the map of the four hydrological response units that was used as a base map to spatially distribute the bulk density, organic matter content, clay percent, sand percent, silt percent, very fine sand percent, and soil depth.

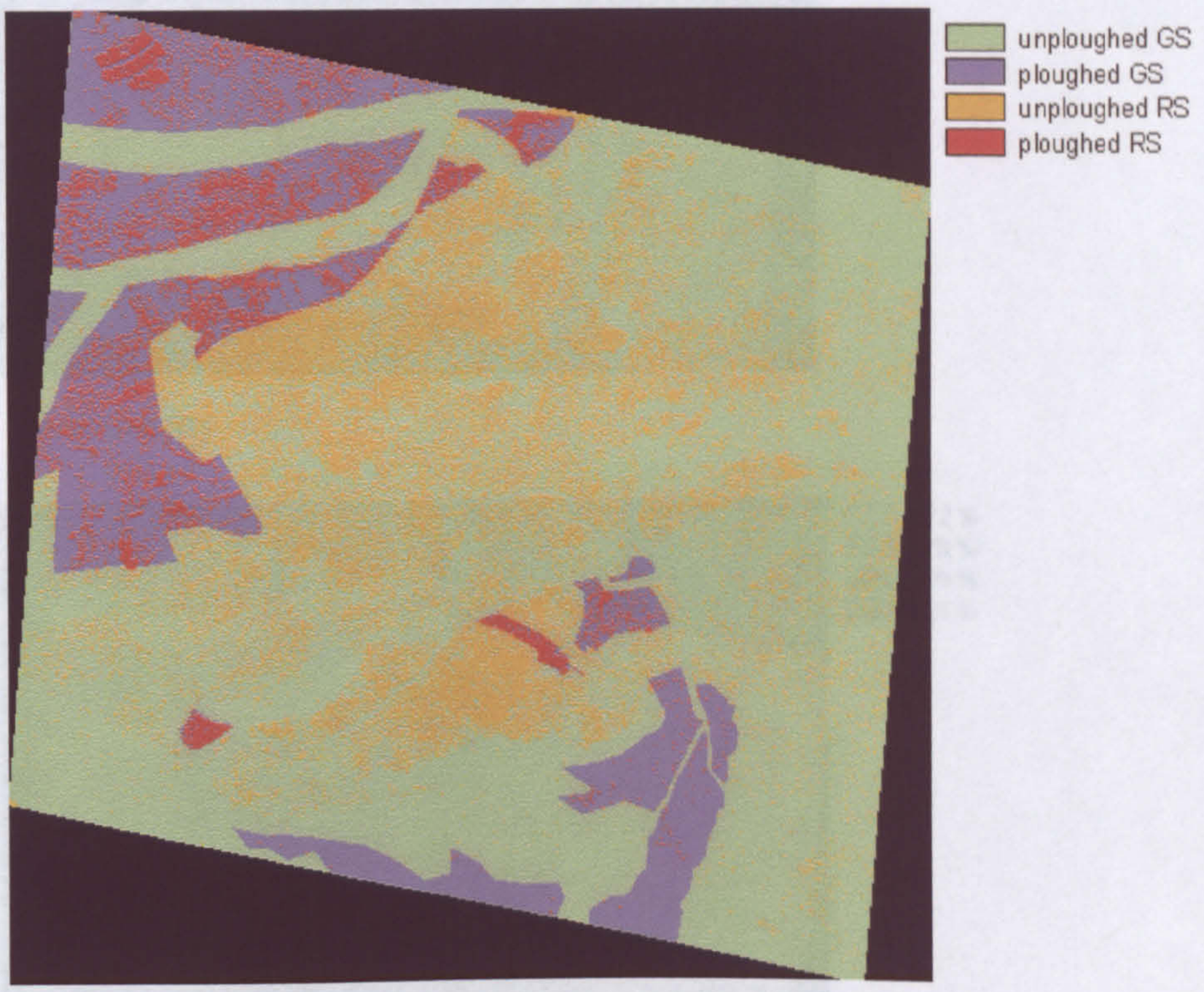

Figure 6.14. The hydrological response units map which will be used as a base map to spatially distribute the soil properties. GS and RS stand for grey soil and red soil respectively.

In order to derive the soil property maps the mean values for these groups were used to distribute the relevant soil property to the corresponding hydrological response unit (figure 6.15). These maps will be used to estimate the soil erodibility and to parameterise the overland-flow and Thornes soil-erosion models in the following chapter.

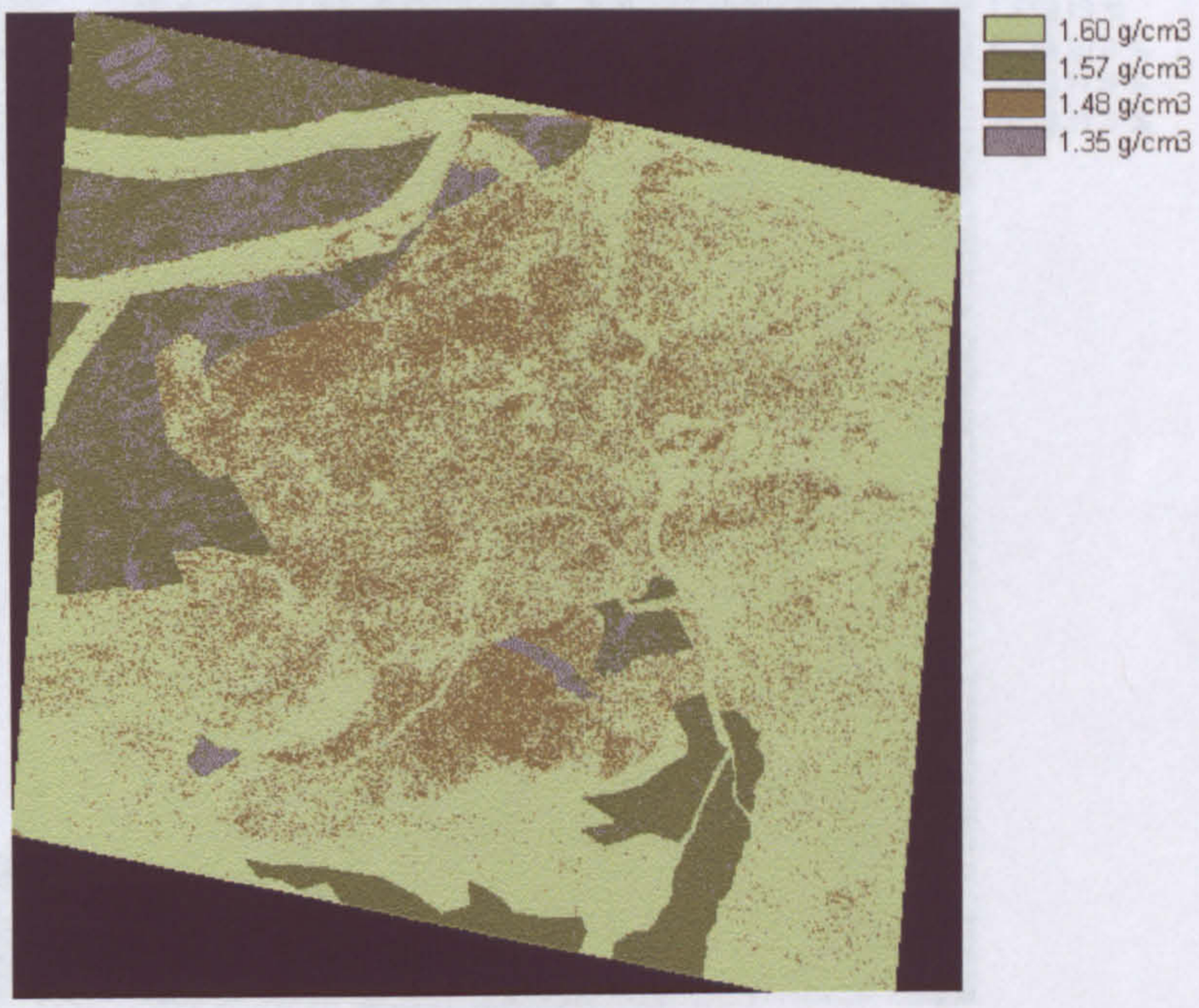

Bulk density

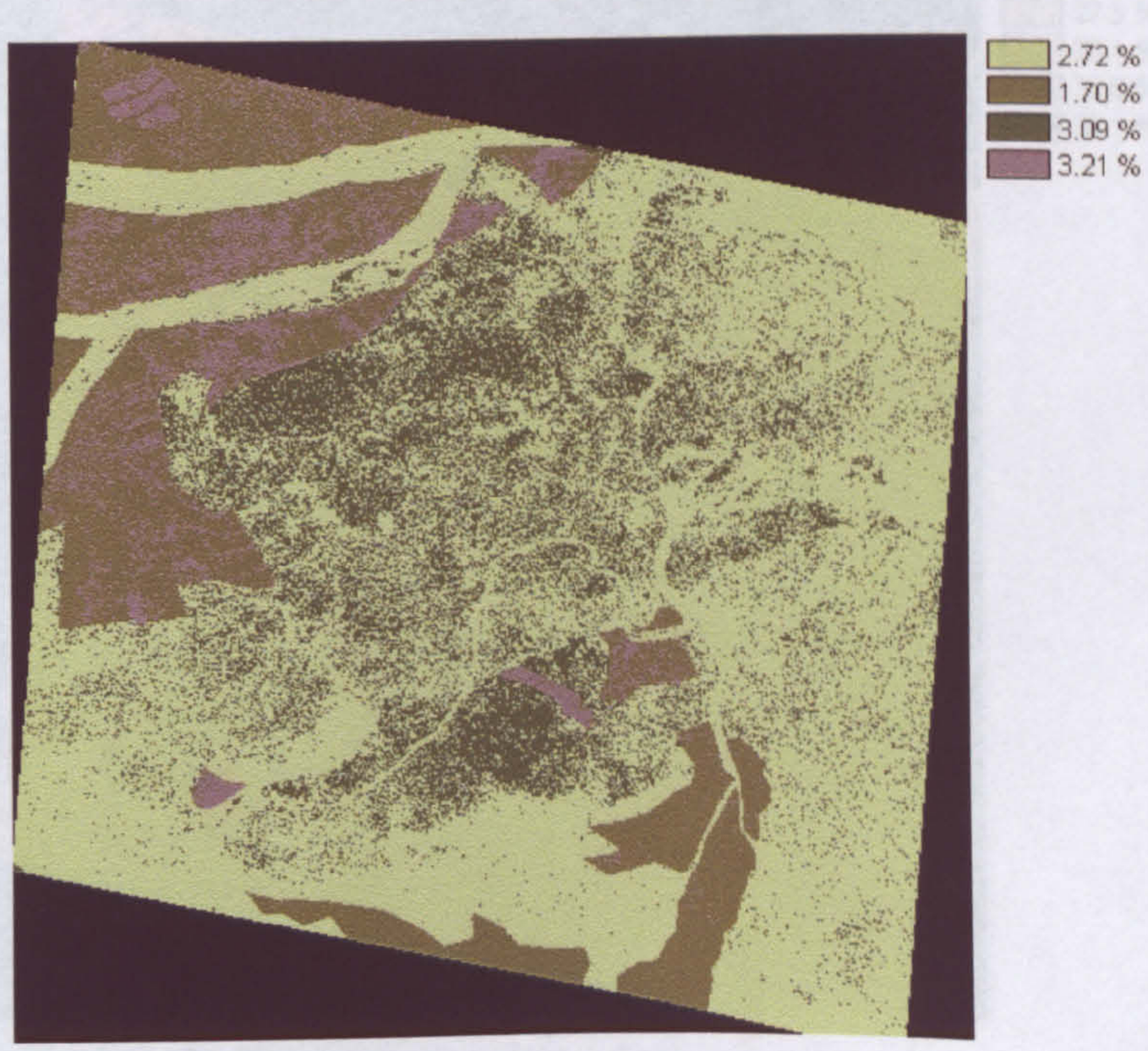

Organic matter

Figure 6.15. Spatially distributed soil properties maps generated using the principle of the hydrological response units.

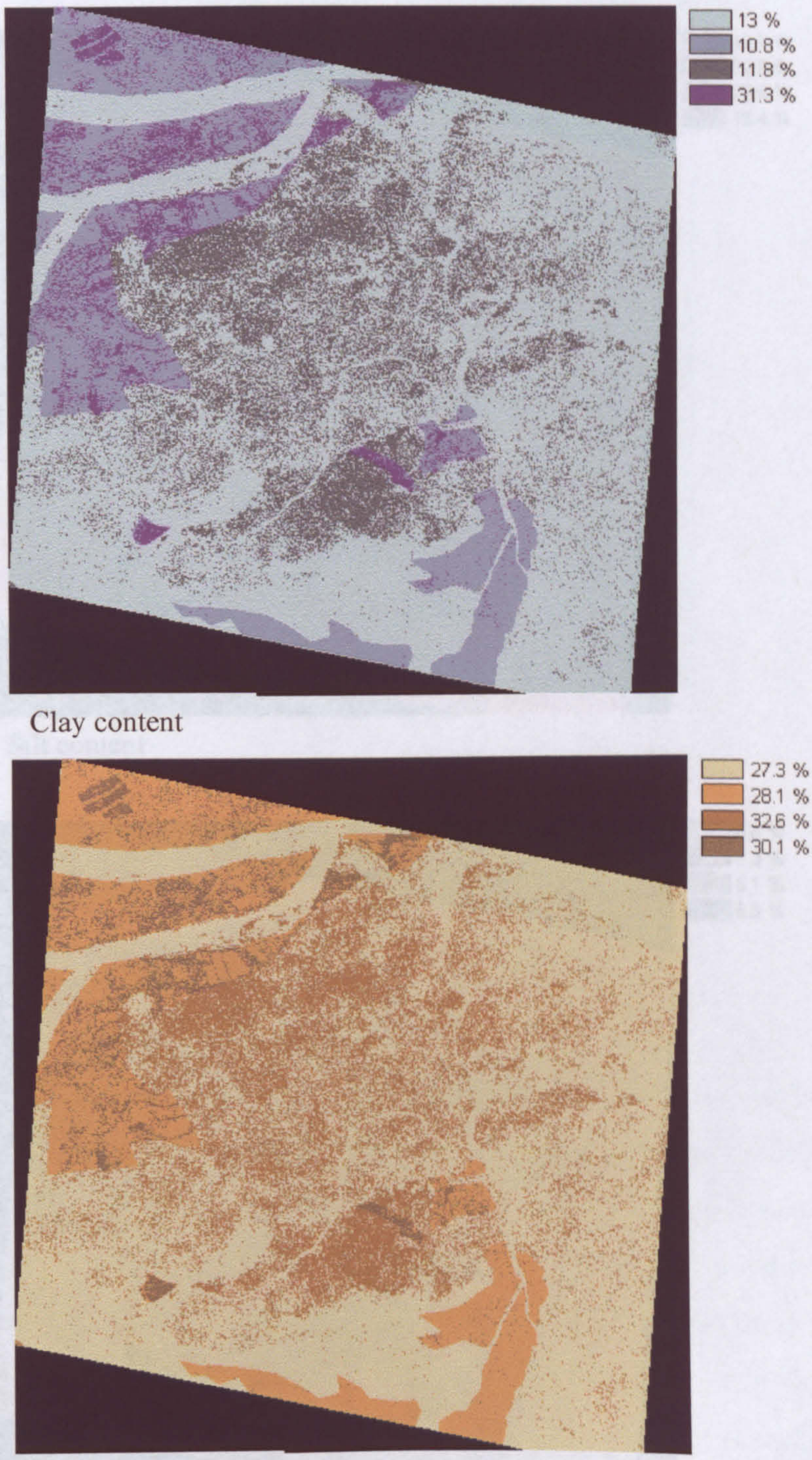

Clay content

Sand content

Figure 6.15. *continued ...*

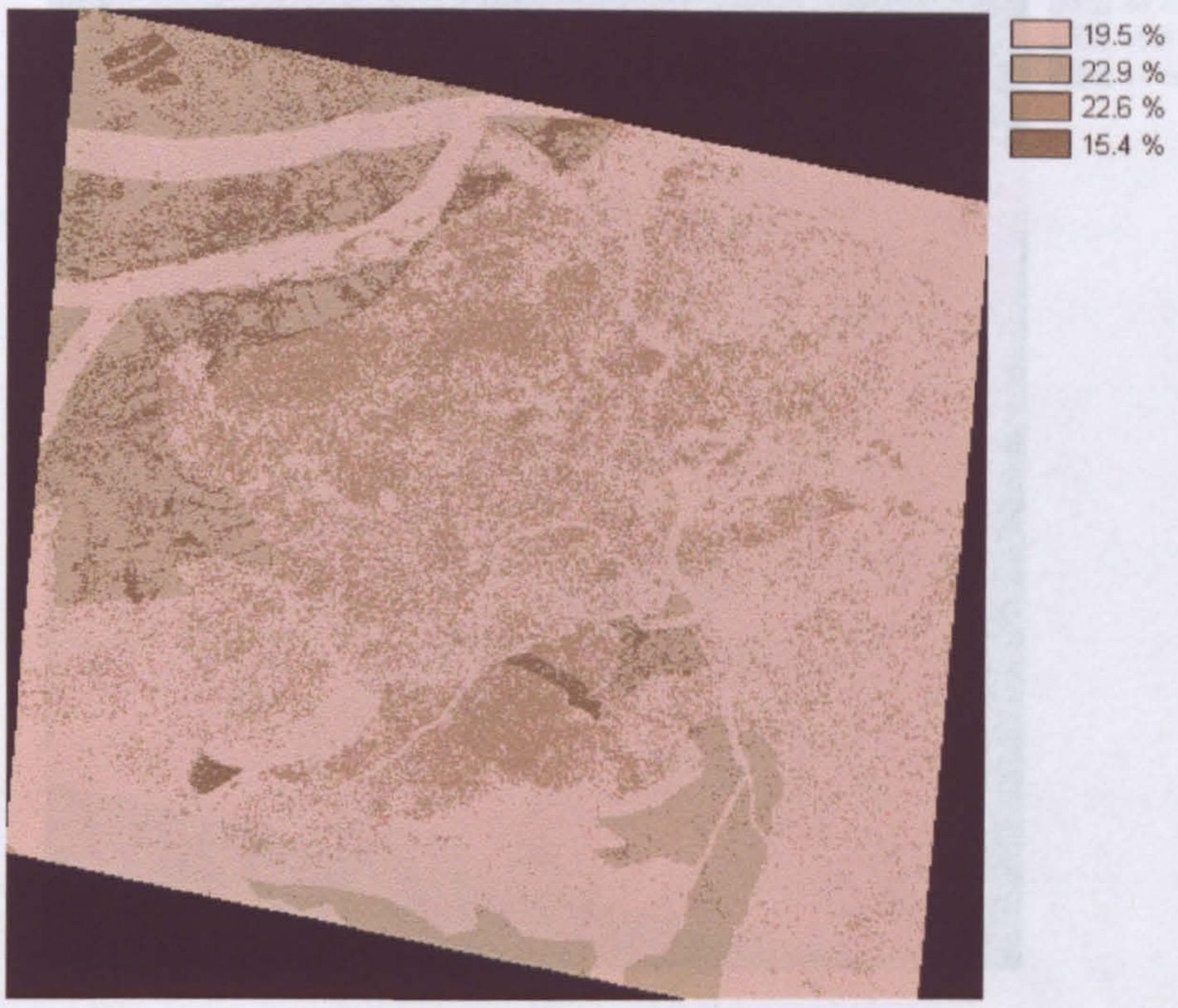

Silt content

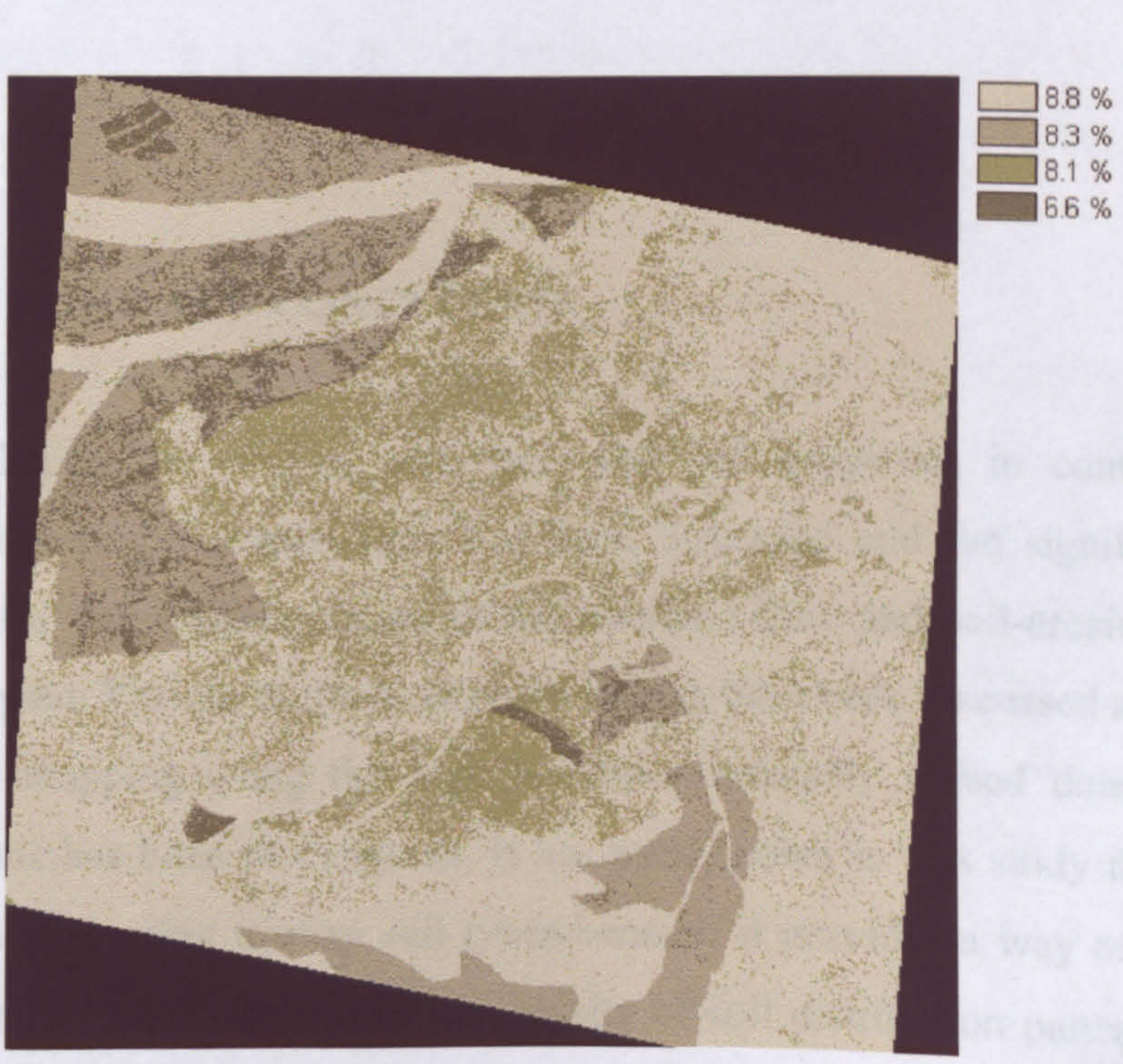

Very fine sand content

Figure 6.15. *continued* ...

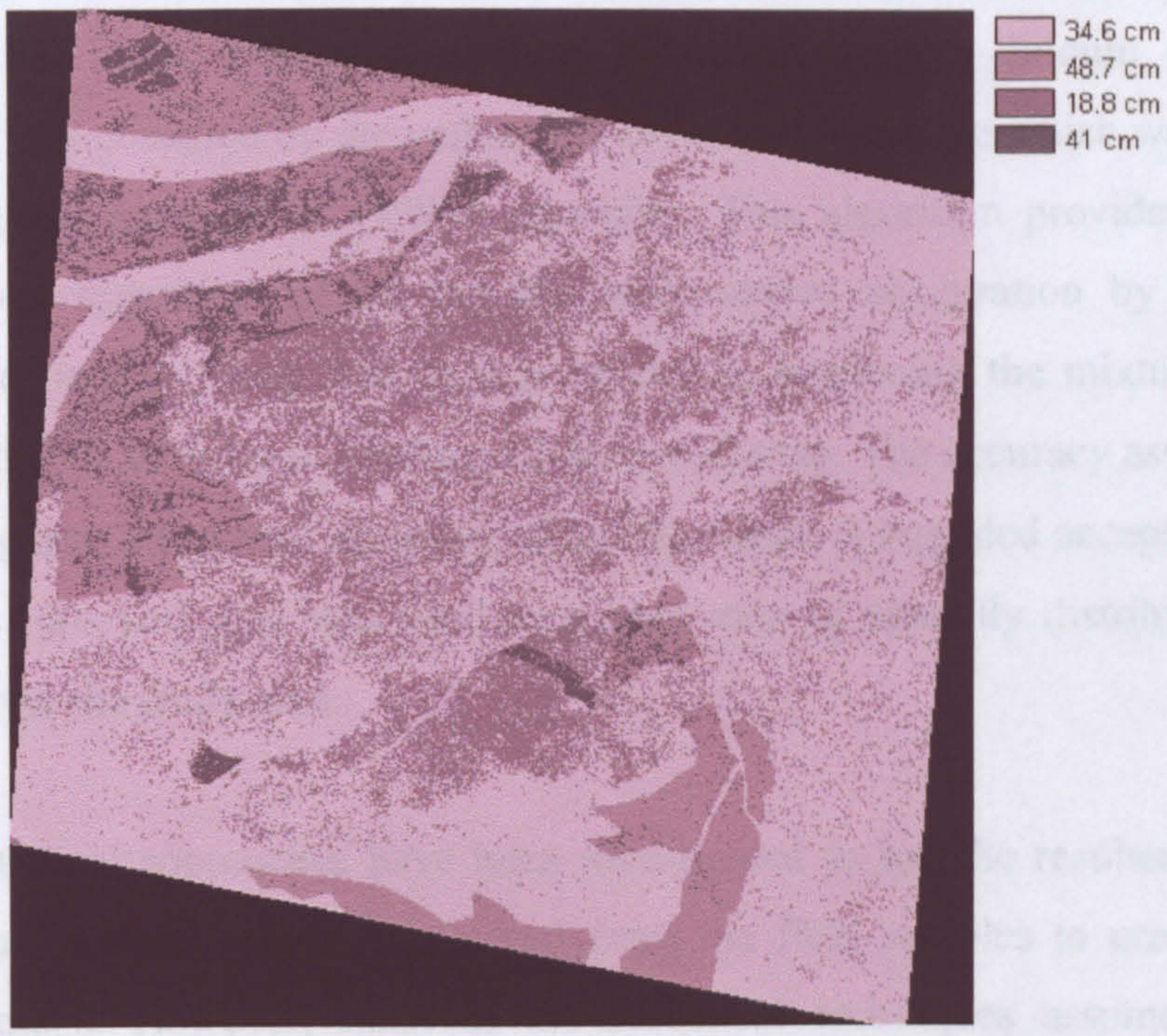

Soil depth (cm)

Figure 6.15 *continued* ...

6.6 SUMMARY AND CONCLUSION

In this chapter the role of soil types and soil properties in controlling runoff generation and soil-erosion rates has been discussed and the significance of soil mapping for the implementation of the overland-flow and soil-erosion models has been analysed. Various methods of soil mapping have been discussed and the method of spatial mapping using the high resolution remotely sensed data of the aerial photographs has been investigated. It has been shown in this study the potential of using remote sensing to map soil types because it provides a way of mapping that approximates closely the spatial complexity of soil distribution patterns at the local scale better than the existing soil maps which are at the regional scale. In addition, this type of remote sensing-derived maps has the ability to incorporate information on the variability of soil properties across that area.

The first step was the derivation of grey and red soil maps from the remotely sensed data using the linear mixture modelling. However, a large amount of the soil information was obscured by the vegetation cover and the shade which was removed by applying the Smith *et al.* (1990) algorithm. This algorithm provides a way of mapping soils regardless of all but the most severe obscuration by overlaying method. The final soil map was then produced by hardening the mixture maps of grey and red soils in order to produce a binary soil map. The accuracy assessment of this map suggests an overall accuracy of 86.5% which is regarded acceptable in this study. Thus, this soil map was used as a base map to spatially distribute the soil properties over the study area.

Various statistical approaches have been investigated to use the resultant hardened soil map and the soil properties derived from the field samples to create the soil properties maps. However, most of the statistical techniques assume a normal distribution pattern for the data under investigation, thus, the soil properties data were tested for normality. A transformation was necessary for some of the soil properties data to approximate normality as they belong to a square-root normal distribution.

Various statistical methods have then been investigated and implemented to create the soil properties maps. One of these statistical methods was testing the significance of the correlations between the soil properties and the soil information provided by the mixture maps. The basis for this statistical method is to investigate whether the presence of a certain soil type has a significant influence on these soil properties so that this soil information can be used to spatially distribute the soil properties. The statistical test of correlation shows that the great majority of these soil properties are not significantly correlated to soil information and the introduction of the land-use types did not improve this correlation. Thus, these soil fractional and land-use maps cannot be used for mapping the soil properties. The lack of significant correlations between the soil information and the soil properties suggests that there are other

parameters which greatly influence the soil properties such as the agricultural practices, the topography factors of slope and aspect, and vegetation cover.

The geostatistical method of cokriging was also investigated to map the soil properties. However, cokriging was not successfully implemented for this purpose and it did not produce acceptable soil properties maps. One of the main reasons for this was the fact that the number of samples used for the interpolation process was too small (Webster and Oliver, 1992). The other reason for the bad results was the fact that the spatial distribution of the soil samples, used for cokriging, over the study area covered only a very small region of that area and a more comprehensive spatial cover was needed for proper geostatistical interpolation.

The third statistical method that has been investigated to map the soil properties was the method of the hydrological response units. Although this method does not produce a spatially continuous surface of the interpolated soil property parameter, it is still a widely used method because it sub-divides the area into regions of distinctive and meaningful hydrological properties. The central assumption in the hydrological response units approach is that the soil properties that influence the hydrology should be significantly different in the various hydrological units, thus, the soil samples representing the various soil properties should be first statistically tested for the significance of difference. Two-samples t test was carried out for this purpose and showed that the great majority of the soil properties are significantly different between red and grey soils. These findings provide a clear evidence of the potential of using remote sensing to map soils due to the existence of a strong correlation between the soil type and soil properties.

The land use also has an influence on soil properties. To test the statistical validity of considering land use in mapping soil properties, the analysis of variance (ANAOV) test was applied. This test shows that the majority of soil properties are significantly different across the different soil and land-use types. These findings provide a strong argument for the implementation of the hydrological response units as a basis for soil properties mapping.

The resultant soil properties maps will be used in chapter 7 for the derivation of the soil erodibility and for the implementation of the overland-flow and soil-erosion models. However, one of the problems of spatially mapping soil properties on the basis of the hydrological response units is that this method discards the internal variability of the soil properties within each of the hydrological units because they are regarded to be homogenous. This can affect hydrological modelling as it can produce less realistic hydrographs for the watershed (Zhu and Mackay, 2001). Thus, some errors as a result of using the hydrological response units should be expected during the implementation of overland-flow and soil-erosion models.

CHAPTER 7

IMPLEMENTATION AND VERIFICATION OF SOIL-EROSION AND OVERLAND-FLOW MODELS IN THE STUDY AREA OF VELEZ RUBIO

7.1 INTRODUCTION

7.2 IMPLEMENTATION OF CARSON AND KIRKBY MODEL TO PREDICT OVERLAND FLOW

7.2.1 Precipitation and Validation of Overland-flow Model Using Rainfall Simulation

7.2.2 Water Storage Capacity (r_c) Parameter

7.2.3 Initial Soil Moisture Parameter

7.2.4 Implementation of Carson and Kirkby Model

7.2.4.1 The Deterministic Approach

7.2.4.2 The Stochastic Approach

7.2.5 Discussion of The Results of Carson and Kirkby Model

7.2.6 Assessing The Overland-flow Errors Introduced by Using The Hydrological Response Units Method

7.2.7 Sensitivity Analysis of Carson and Kirkby Model

7.3 SOIL ERODIBILITY ESTIMATION

7.4 MODELLING SOIL EROSION

7.4.1 Implementation of The Thornes Soil-Erosion Model

7.4.2 Discussion of Results

7.4.3 Investigating The Effect of Land-use Change on Soil Erosion

7.4.4 Sensitivity Analysis of The Thornes Soil-Erosion Model

7.5 SUMMARY AND CONCLUSION

7.1 INTRODUCTION

In chapter three various empirical and process-based models to predict the soil loss were reviewed and the Thornes soil-erosion model has been selected to predict the soil loss in the study area. Four parameters control the soil erosion in the Thornes model: overland flow, soil erodibility, slope, and the vegetation cover. The slope and vegetation-cover map have been previously derived in chapters four and five. Maps of the overland-flow and soil erodibility parameters are needed to distribute the Thornes model spatially. These maps are developed and evaluated in this chapter.

Various overland-flow models have also been described in chapter three and the Carson and Kirkby model was selected to predict the overland flow which is needed by the soil-erosion model. In chapters five and six various parameters of the Carson and Kirkby model have been derived including land-use and soil property maps. In this chapter the model is implemented by integrating its controlling parameters into a GIS using different deterministic and stochastic approaches to derive a spatially distributed prediction of the overland-flow map. The accuracy of the resultant overland-flow map is assessed by cross checking against the measured overland-flow data collected in the field and a sensitivity analysis for the Carson and Kirkby model is performed.

In addition, the soil physical properties, soil permeability, and organic matter maps are used to calculate the soil erodibility map using the Wischmeier equation. This equation is used instead of the Wischmeier nomograph (figure 2.7) as both are derived from the same data. Once all the parameters of Thornes model are mapped, this model is implemented by integrating the relevant parameters in a GIS environment and the predicted soil-loss map is created. Accuracy assessment of the predicted soil loss map is carried out and sensitivity analysis is performed to evaluate the soil loss response to changes in the controlling parameters.

7.2 IMPLEMENTATION OF CARSON AND KIRKBY MODEL TO PREDICT OVERLAND FLOW

According to equation 3.18 in chapter three there are three parameters controlling the initiation conditions and the rate of the overland flow in the Carson and Kirkby model. These controlling parameters are the rainfall precipitation (P), the water storage capacity (r_c), and the initial soil moisture (Q_{iT}). A proportion of the rainfall precipitation is infiltrated into the soil layers and this infiltration process is limited by the water storage capacity and by the initial soil moisture conditions prior to the rainfall precipitation. After the soil layers reach a stage of saturation, the excess of the rainfall precipitation, which has not infiltrated into the soil, is generated as a runoff causing the occurrence of the overland flow.

7.2.1 Precipitation and Validation of Overland-flow Model Using Rainfall Simulation

Since the overland-flow generation and soil loss will be modelled at an event time scale in this study, no comprehensive meteorological data sets of monthly or yearly rainfall precipitation are needed for this purpose. Instead, a uniform distribution of the precipitation across the study area is considered. The rate of this precipitation is equal to the mean of the field rainfall simulations applied in the nine plots (124 mm during 30 minutes of simulation) which was carried out by Zhang (1999). The reason for using this precipitation rate, though it seems excessive, is to validate the overland-flow results predicted from the Carson and Kirkby model against the measured overland flow resulting from the rainfall simulation as this is the only validation data available for this study.

The rainfall simulation was undertaken in April 1996 by Zhang (1999) where nine rainfall-simulation plots were constructed at locations with a range of soil types, vegetation covers and slopes (figure 7.1) and table 7.1 shows their land use types. These plots included areas of almond and olive plantation, a newly ploughed hillslope, an overgrazed area of matorral, and an area of burnt matorral. In each of the rainfall simulation sites, a 61 x 61 cm plot was surrounded by boards in the upslope, right and left sides and with a collector sealed with soil on the downslope edge. The land surface was kept undisturbed in each plot and a drop-former simulator was installed about 1.65 m high over the plot. Samples of rainfall excess and eroded soil were collected for total rainfall duration of 30 minutes (Zhang, 1999). Rainfall rate was determined by putting a collector on the plot for 1 minute at the beginning, middle and end of the experiment in order to determine the average rainfall intensity.

It should be mentioned here that the applied rainfall simulations in various plots in the field varied between 114-138 mm, having a mean of 124 mm. As a result of this,

errors will be introduced to the predicted overland-flow values using the Carson and Kirkby model because we did not incorporate this variation in the precipitation map.

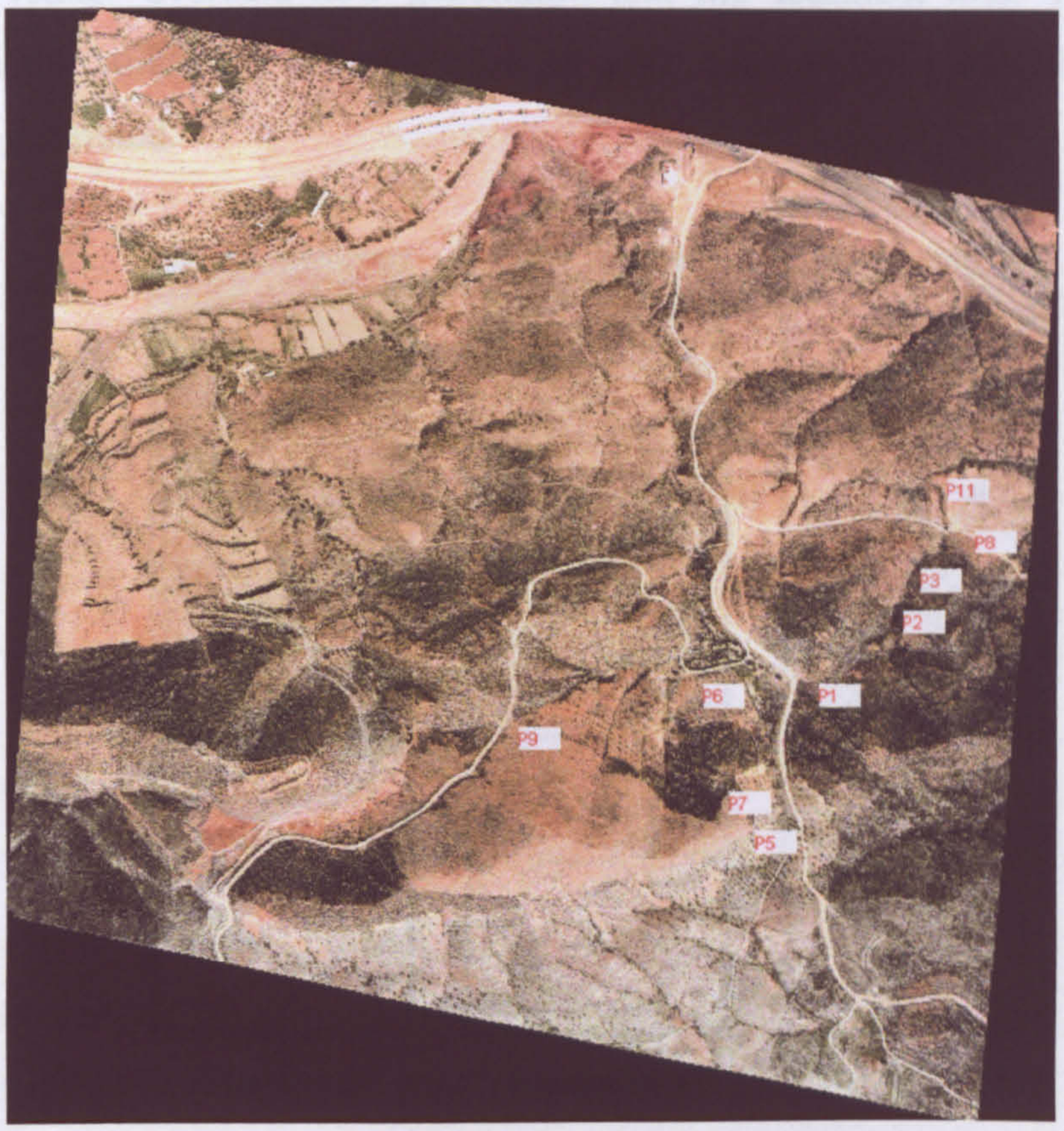

Figure 7.1. The locations of the rainfall-simulation plots in the study area.

Plot	P1	P2	P3	P5	P6	P7	P8	P9	P11
Land use	3	3	2	1	1	4	3	4	4

Table 7.1. The land use types for the rainfall simulation plots. The numbers 1, 2, 3 and 4 represent ploughed grey soil, ploughed red soil, unploughed grey soil and unploughed red soil respectively.

7.2.2 Water Storage Capacity (r_c) Parameter

Water storage capacity (r_c) is an important parameter in the overland-flow model. It reflects not only infiltration in various soils, but also the effects of water subtraction for irrigation, evaporation and vegetation cover (Francis 1985). The particle size

determines water storage capacity of soil to a large extent with clay soils having the smallest water storage capacity (figure 7.2). Ploughing is often applied to land in order to reduce overland-flow generation and the sediment loss. This ploughing increases the soil water storage capacity and, consequently, the time before the runoff is generated.

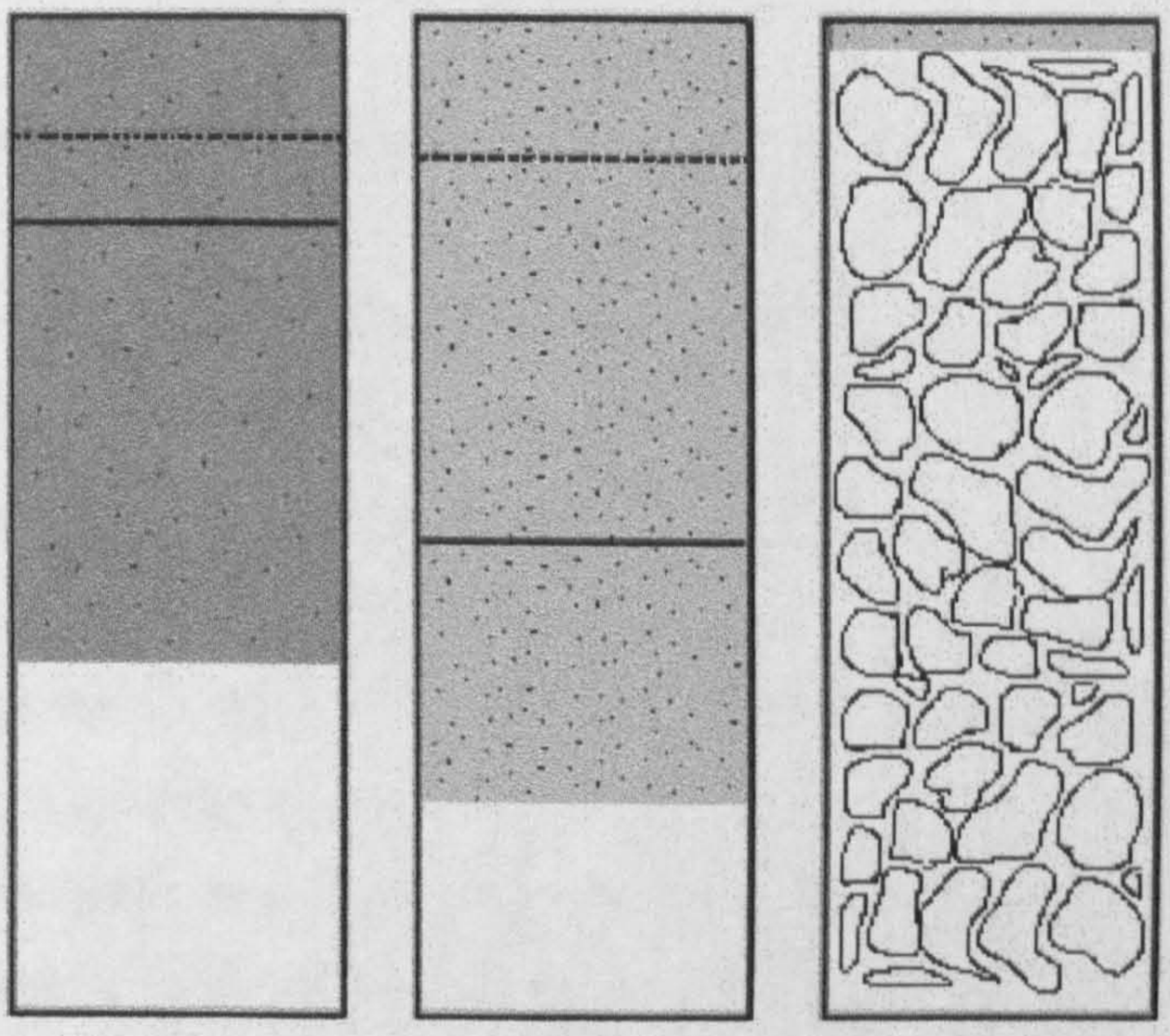

Figure 7.2. The effect of soil type and soil particle size on the water storage capacity.

There are various methods that can be used to estimate the water storage capacity. These methods depend on factors such as the vegetation cover, soil depth, bulk density, and stone fraction. For example, Carson and Kirkby (1972) propose a method to link the (r_c) to the vegetation cover where (r_c) can be considered = 10 mm for bare ground, r_c = 40 mm for a good grass cover and r_c = 100 mm for a forest. Alternatively, if more information about the soil physical properties is available then the (r_c) value can be calculated according to the following equation:

$$r_c = 10 \ \phi \ h \qquad 7.1$$

Where the water storage capacity r_c is estimated in mm, ϕ is the soil porosity (percentage), h is the soil depth (in cm), and the number "10" in the equation is for

unit transfer from cm (for soil depth) to mm (for r_c). The soil porosity ϕ in equation 7.1 can be calculated according to the equation:

$$\phi = (1 - \frac{BD}{PD})(1 - fs) \qquad 7.2$$

Where *BD* is the soil bulk density (g cm^{-3}), *PD* is the particle density (g cm^{-3}), and *fs* is the stone fraction in the soil (percentage).

7.2.3 Initial Soil Moisture Parameter

The initial soil moisture (Q_{iT}) parameter in equation 3.18 controls the initiation and the rate of overland flow because it limits the amount of rainfall precipitation infiltrating through the soil. The higher the initial soil moisture value is, the less is the amount of water permitted to infiltrate into the soil and this causes higher rates of overland-flow generation. In a study to investigate the hydrological conditions of runoff generation and its sensitivity to various factors, Sardo *et al.* (1994) carried out a hydrological investigation to develop and validate the EUROSEM soil erosion model using a rainfall simulator in Sicily. This hydrological investigation showed that overland flow is influenced significantly by the antecedent condition of the soil moisture. Thus, it is important to consider the initial soil moisture in the overland-flow model as accurately as possible, however, the initial soil moisture changes spatially and temporally in a complex way so it should be measured in a distributed manner. This initial soil moisture (Q_{iT}) can be calculated from the following equation:

$$Q_{iT} = 10\ Qi\ h \qquad 7.3$$

Where Q_{iT} is estimated in mm, *Qi* is the volume water content ($cm^3\ cm^{-3}$), *h* is the soil depth (cm), and the number "10" in the equation is for unit transfer from (cm) to (mm). In this study no data or field measurements are available for the volume water content *Qi* so an average value of 4% was assumed uniformly across the study area. This value for *Qi* is considered to be a standard starting condition following drought in a dryland setting such as the conditions of the study area in the Southern-east of Spain. It has been explained earlier the significance of the antecedent soil moisture

on the overland-flow generation, thus, assuming a uniform average value for *Qi* can be a source of errors and such errors should be expected when implementing Carson and Kirkby overland-flow model.

7.2.4 Implementation of Carson and Kirkby Model

Now that maps of all the parameters controlling the Carson & Kirkby overland-flow model (i.e. soil depth, soil bulk density, soil moisture, and stone percent) have been estimated, the model can be implemented using the equations 3.18, 7.1, and 7.3 to predict the overland-flow generation. This implementation was carried out by integrating the parameters in the IDRISI GIS environment. Two different approaches are followed in the implementation of the Carson & Kirkby overland-flow model, these are the deterministic and the stochastic approaches.

7.2.4.1 The Deterministic Approach

In the deterministic approach the mean values of different soil properties, derived from those soil samples located in a specific hydrological response unit, are assigned to that unit according to the land use and soil type (see figure 6.15 in chapter 6). In this approach the internal variability of the various soil properties in the hydrological response units are not considered. This method has been termed OF1. Figure 7.3 shows the resultant overland-flow map with the overland-flow rate ranging from 0 to 77 mm/event using a simulated rainfall rate of 124 mm/event (where the event lasted 30 minutes).

The Figure 7.3 reveals that the overland-flow generation is lowest in the ploughed areas and highest in unploughed areas covered with matorral. This can be explained by the fact that the act of ploughing the land to prepare it for agricultural activities led to deepening of the soil layer and a reduction in the soil bulk density. The combination of these factors means that the soil can take a larger amount of the rainfall precipitation, in the form of infiltration, before the soil becomes saturated and overland flow is generated.

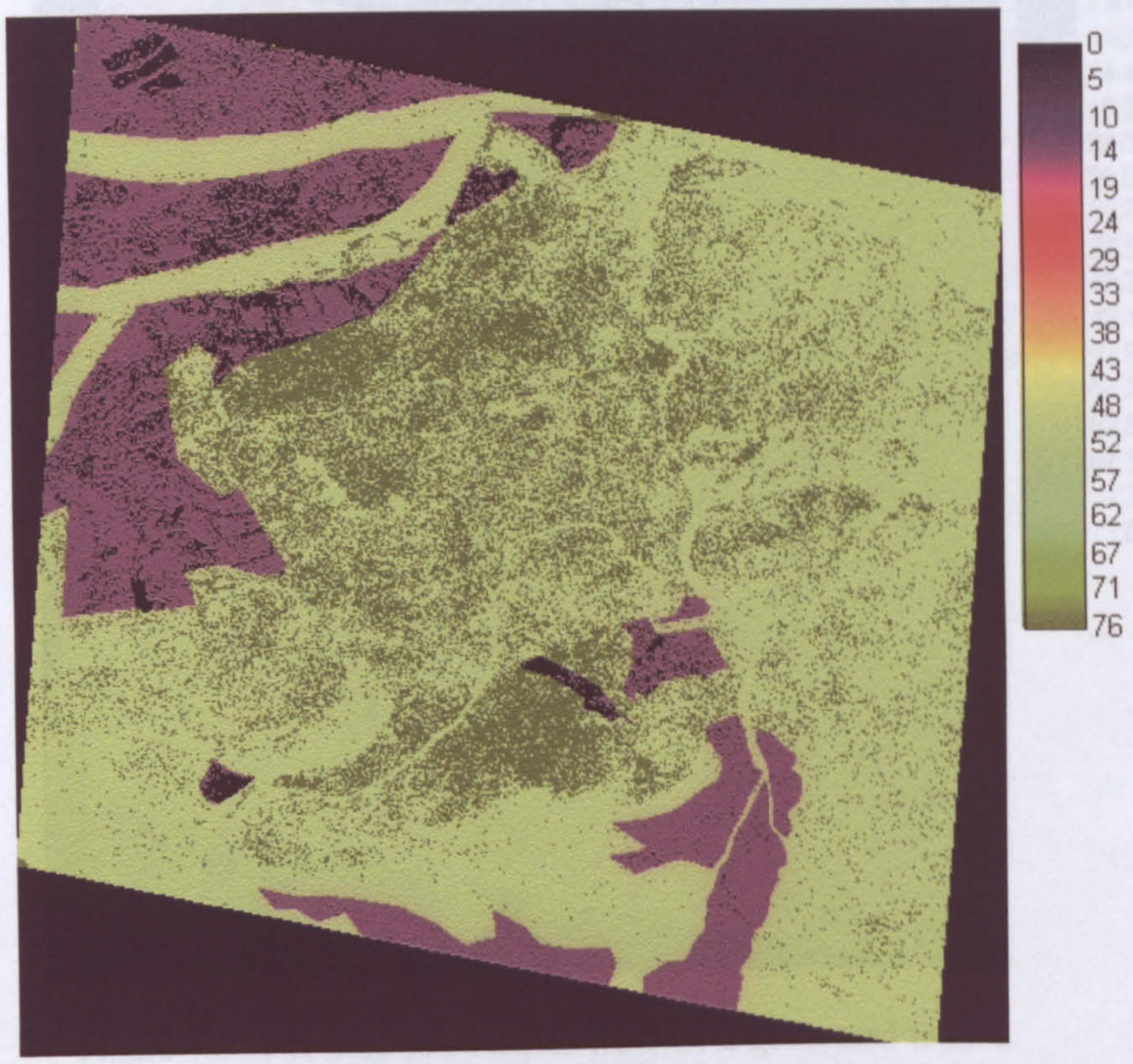

Figure 7.3. The map of overland flow OF1 generated from a 124 mm rainstorm. The unit is mm per event of 30 minutes.

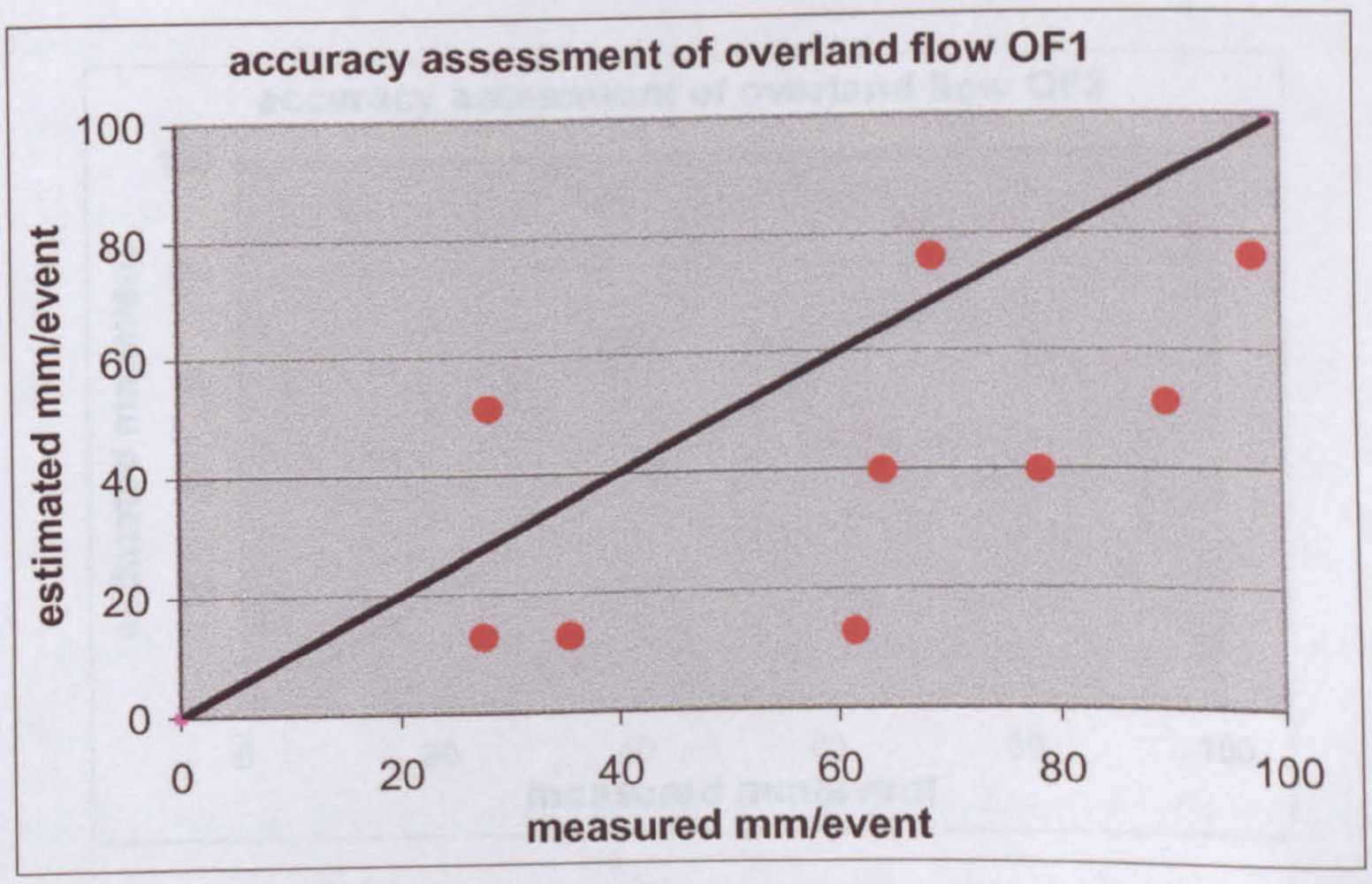

Figure 7.4. The accuracy assessment of the results of Carson and Kirkby overland-flow model.

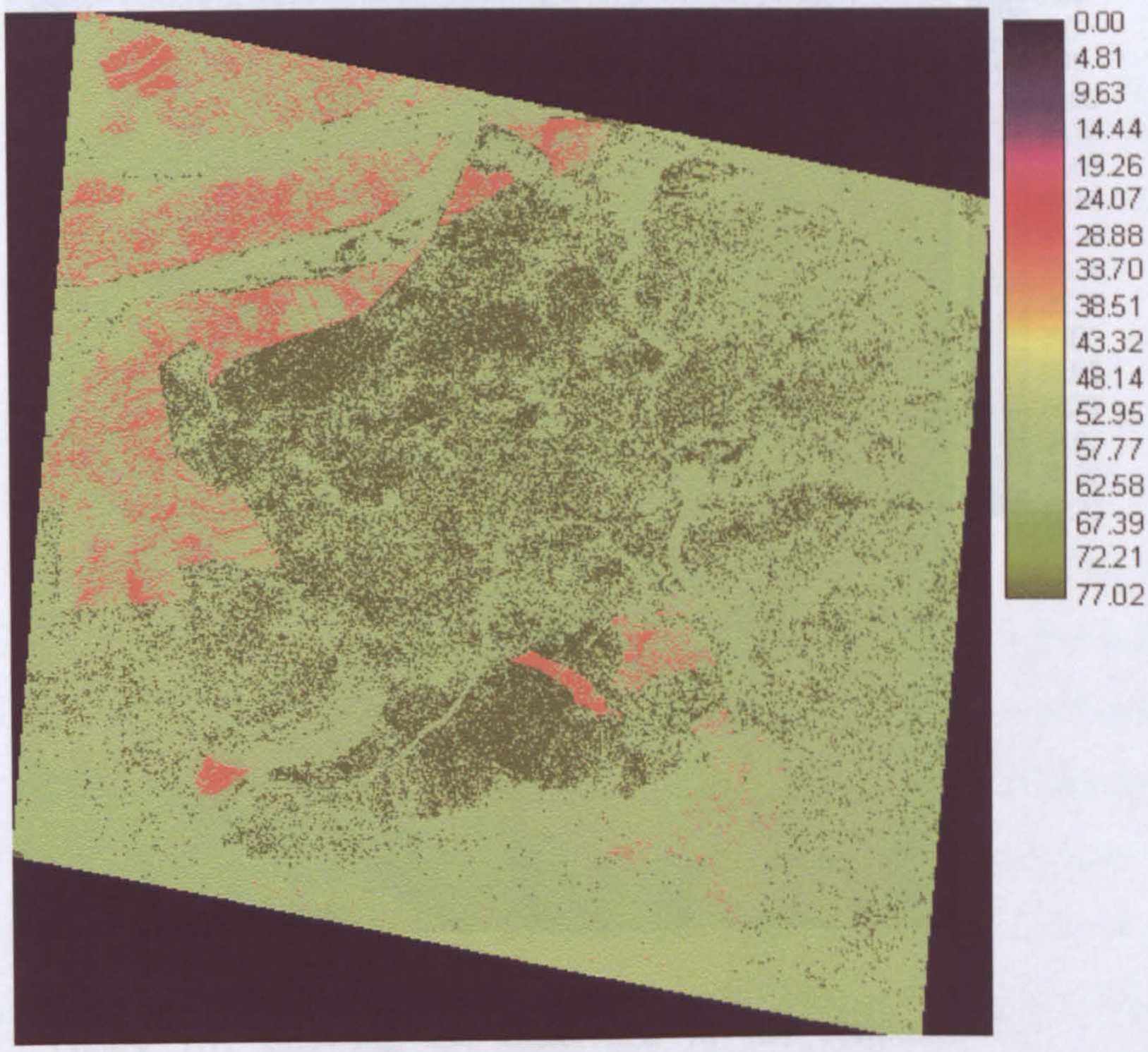

Figure 7.5. The map of overland flow OF2 generated from a 124 mm rainstorm with the soil depth constrained to 30 cm. The unit is mm per event of 30 minutes.

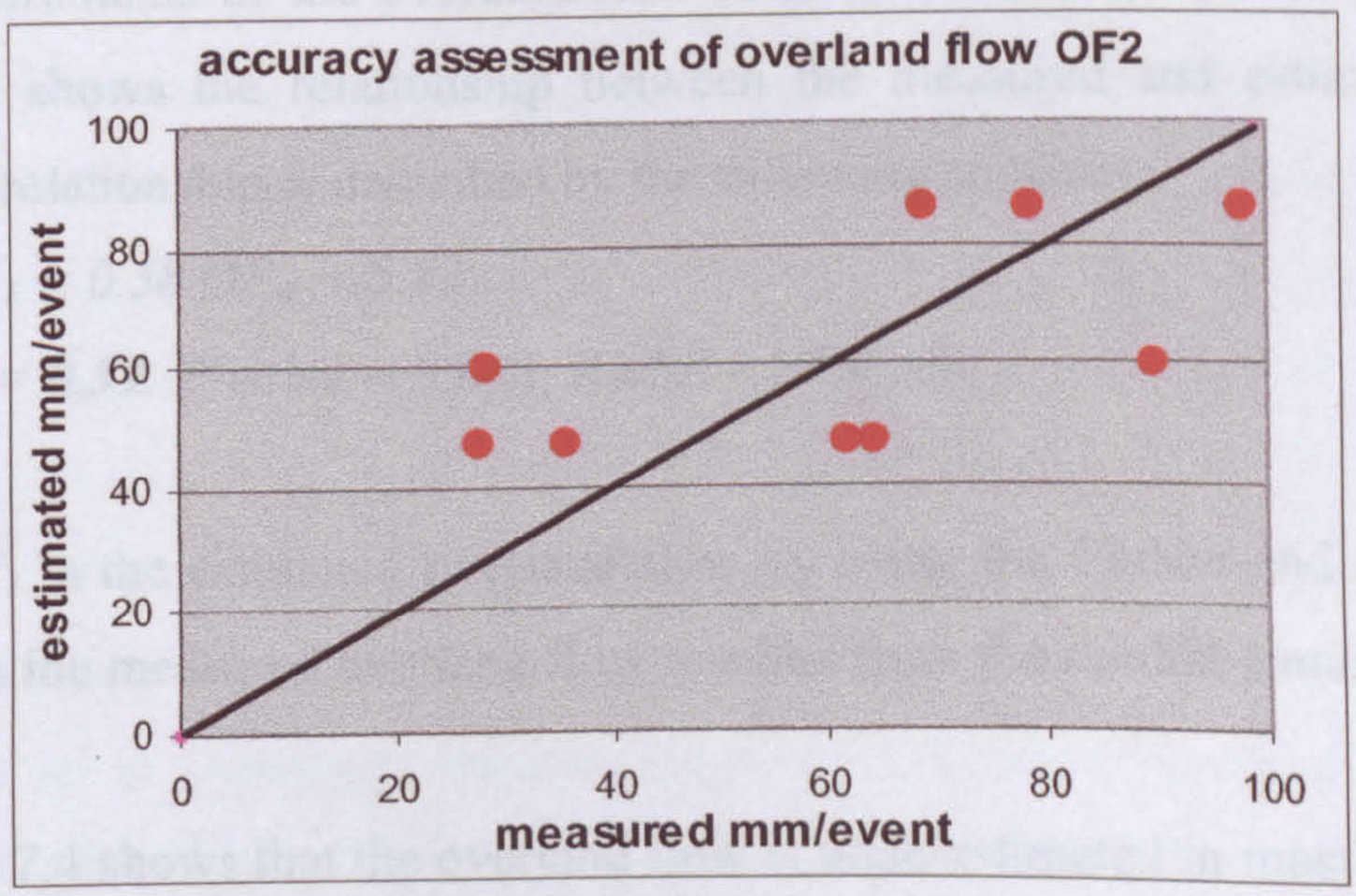

Figure 7.6. The accuracy assessment of the results of Carson and Kirkby overland-flow model after soil depth is constrained to maximum 300 mm.

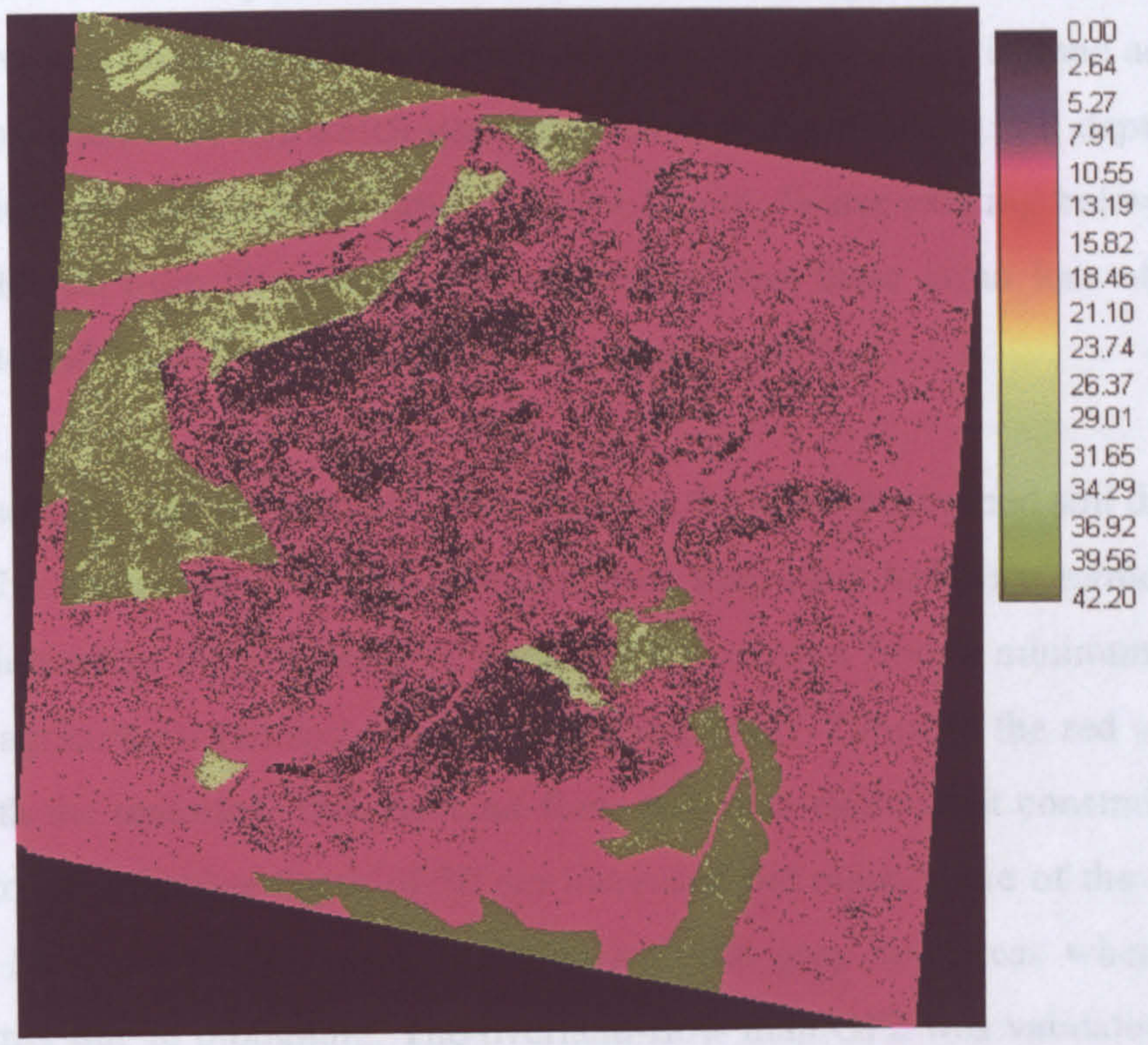

Figure 7.7. Showing the difference in the resultant overland-flow maps as a result of constraining the soil depth to a maximum of 300 mm.

In order to assess the accuracy of the overland-flow map, it was validated against the field measurements of the overland-flow rates in the nine rainfall-simulation plots. Figure 7.4 shows the relationship between the measured and estimated overland flow. This relationship is described by the following statistics:

$$OF_1 = 0.58\ OF_m + 5.73 \qquad 7.4$$

$$R^2 = 0.59,\ P\text{-}value = 0.085,\ RMSE = 37.4\ mm.$$

Where OF_1 is the estimated overland flow by using the Carson and Kirkby model, and OF_m is the measured overland flow resulted from the rainfall simulation.

The figure 7.4 shows that the overland flow is underestimated in most of the rainfall-simulation plots. In addition, the statistics in equation 7.4 suggest that the coefficient of determination R^2 is not significant at 95% confidence level and the value of 37.4 mm for the RMSE is high. In order to improve the correlation 7.4 and to reduce the

RMSE of *OF1* the soil depth, which affects the water storage capacity and the initial soil moisture, was constrained to a maximum value of 30cm. This is done according to a study by Hanks (1992) which demonstrates that the effective soil depth where the infiltration takes place has a limit of about 30 cm. Water existing below this 30 cm threshold has little likelihood of being lost so that there is no loss of rainfall infiltration to soil layers below this threshold (Hanks 1992).

The overland flow was re-calculated according to the new constrained soil depth and the figure 7.5 shows the resultant overland-flow map (this has been termed OF2). This map shows that the re-calculated overland flow ranges from a minimum of 29.5 mm in the agricultural red soil areas to a maximum of 77 mm in the red soil areas covered with the matorral. The overland-flow map also shows that constraining the soil depth to the effective depth of 30 cm increased the mean value of the overland flow from 14.9 mm to 56.2 mm in the agricultural grey soil areas where soil is usually deeper due to ploughing. The overland-flow map OF2 was validated against the field measurements of overland flow and the resulting relationship (figure 7.6) yielded the following statistics:

$$OF_2 = 0.49\ OF_m + 29.7 \qquad 7.5$$

$$R^2 = 0.66,\ P\text{-}value = 0.048,\ RMSE = 26.3\ mm.$$

This correlation shows a substantial improvement when compared to the correlation 7.4 of OF1. The P-value is smaller than 0.05 and the relationship between the estimated and the measured overland flow is significant at the 95% confidence level. In addition, improvement in the accuracy of the relationship between the predicted and measured overland flow can be noticed where the value of the *RMSE* has dropped by 31% from 37.4 mm to 26.3 mm.

The effect of constraining the soil depth to the effective depth of 30 cm is demonstrated in figure 7.7 which represents the difference of the overland-flow generation between OF1 and OF2, and this difference can be as large as 42.2 mm in some locations.

7.2.4.2 The Stochastic Approach

The second method of implementing the Carson & Kirkby overland-flow model is the stochastic approach. In this approach the soil properties in all hydrological response units are allowed to take any value between the maximum and minimum values of that class, which are defined from the soil samples, according to a normal distribution or a square-root normal distribution. This approach depicts the internal variability of the soil properties and the hydrological processes better than the deterministic approach and is expected to produce more realistic results because it allows interaction of the soil properties in a random manner.

In order to implement the stochastic approach, 500 runs are used to generate random values for the soil depth, stone content, and the soil bulk density. This large number of runs is chosen in order to generate enough values to depict the shape of the relevant frequency distribution as accurately as possible. The random values are generated using ranges, defined from the soil samples of the relevant hydrological response unit, according to the square-root normal distribution for the stone content and soil depth and according to the normal distribution for the soil bulk density. These frequency distribution types are in accordance with those defined previously in chapter 6.

If the stochastic approach is to be implemented in a spatially distributed manner to derive an overland-flow map, this implies the generation of 500 maps for each of the soil properties where huge work and disk space is needed. Instead, to test the validity of the approach it was tested at the locations of the nine plots (see table 7.1 and figure 7.1) where the rainfall simulations took place and this allows accuracy assessment of the stochastic approach. Figures 7.8, 7.9, 7.10, and 7.11 represent the frequency distributions of the generated values for the soil depth, bulk density, and stone content in the nine field plots of rainfall simulations. The figures illustrate a successful replication of normal distribution for the bulk density and square-root normal distribution for the soil depth and the stone content.

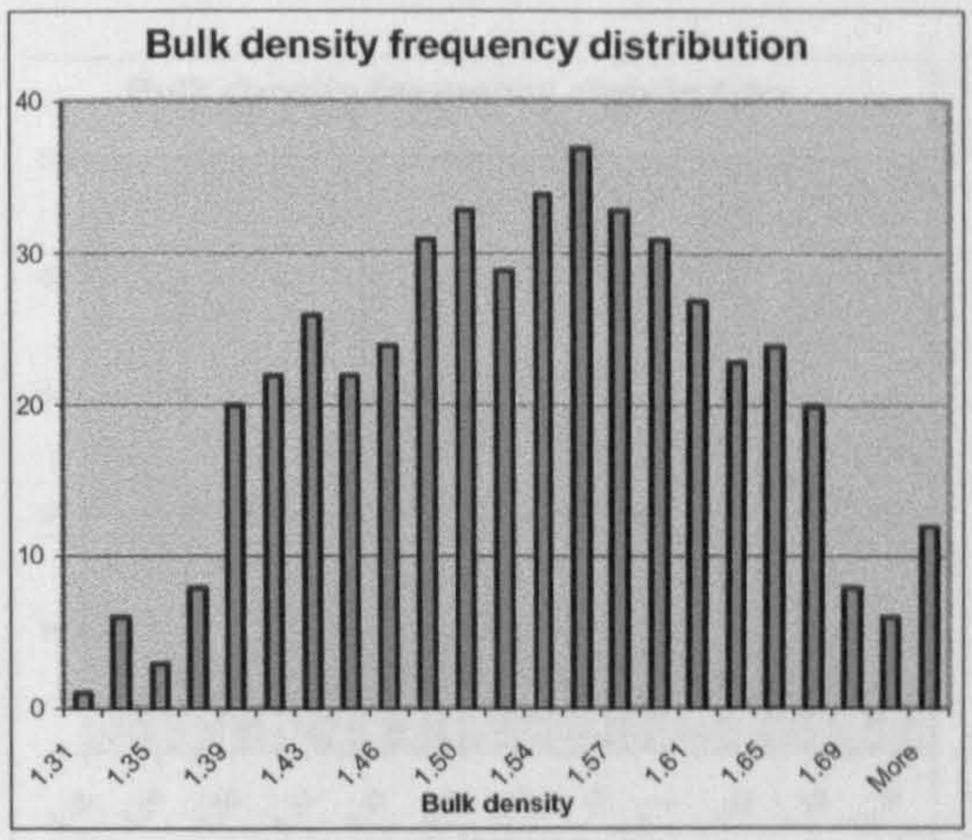

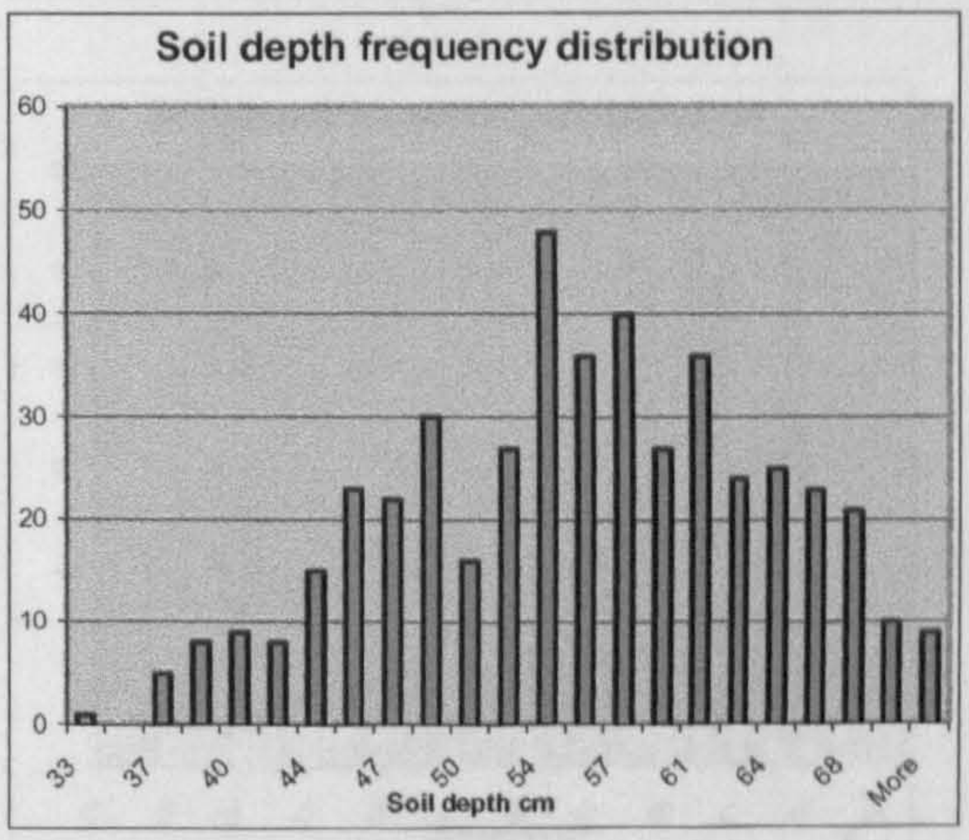

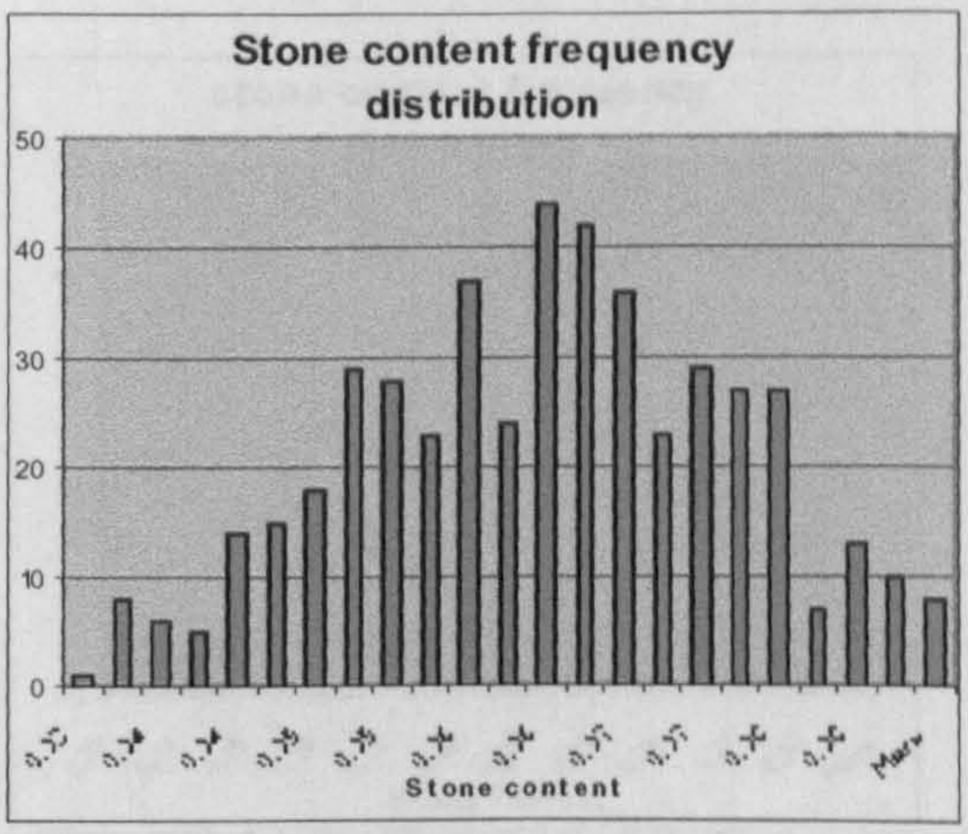

Figure 7.8. The randomly generated frequency distributions of soil properties for the plots P5 and P6.

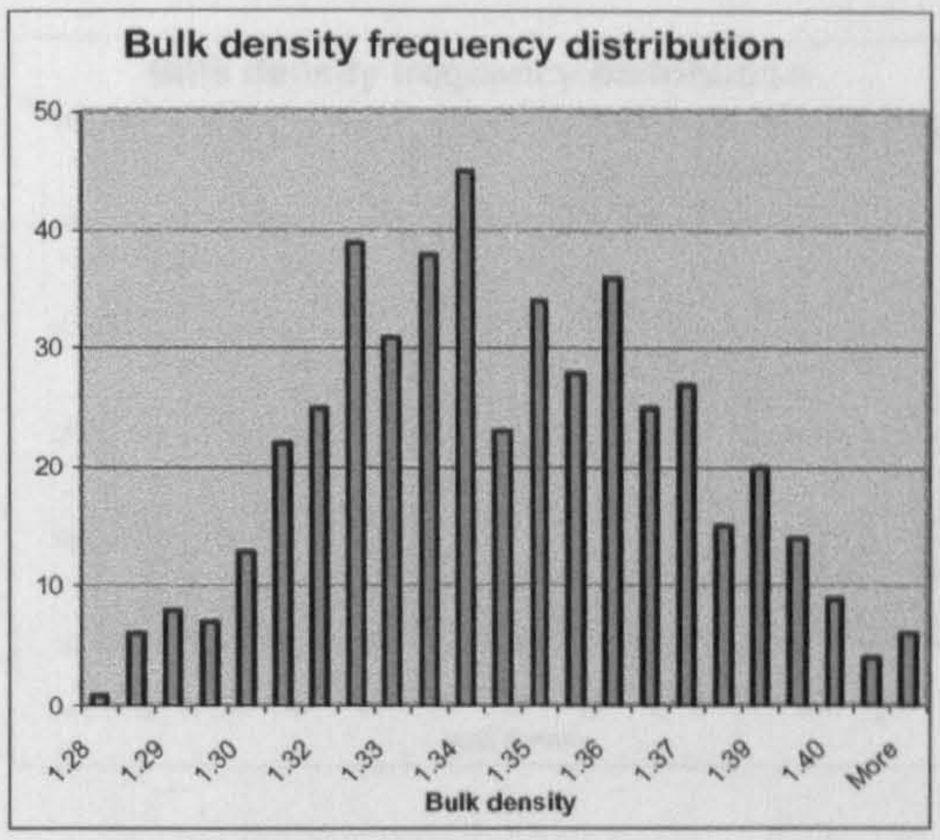

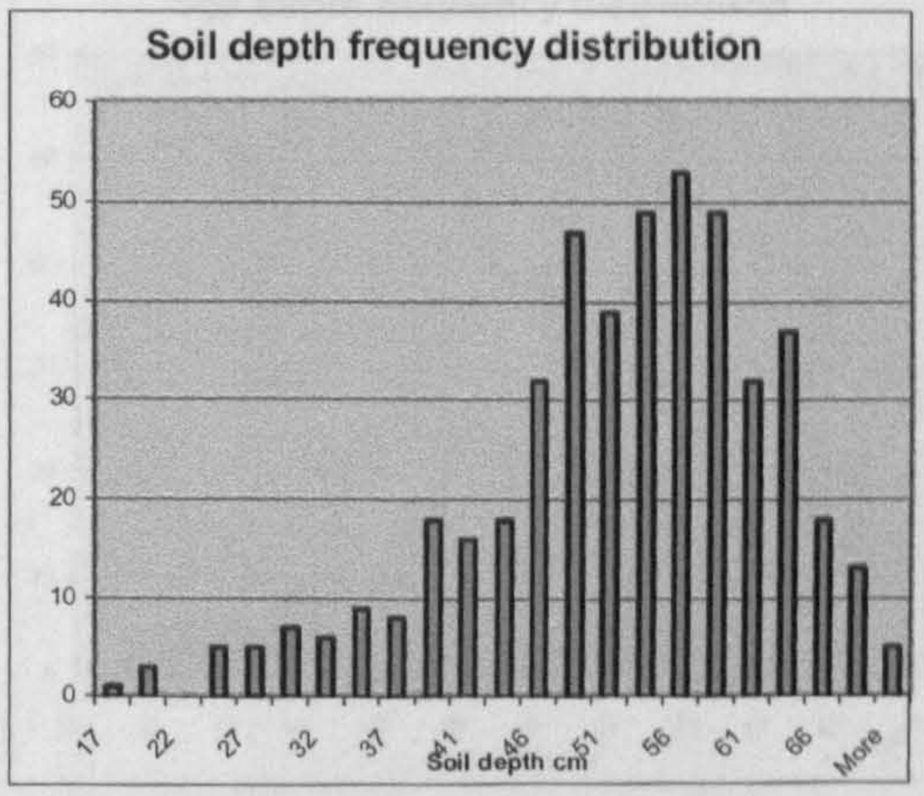

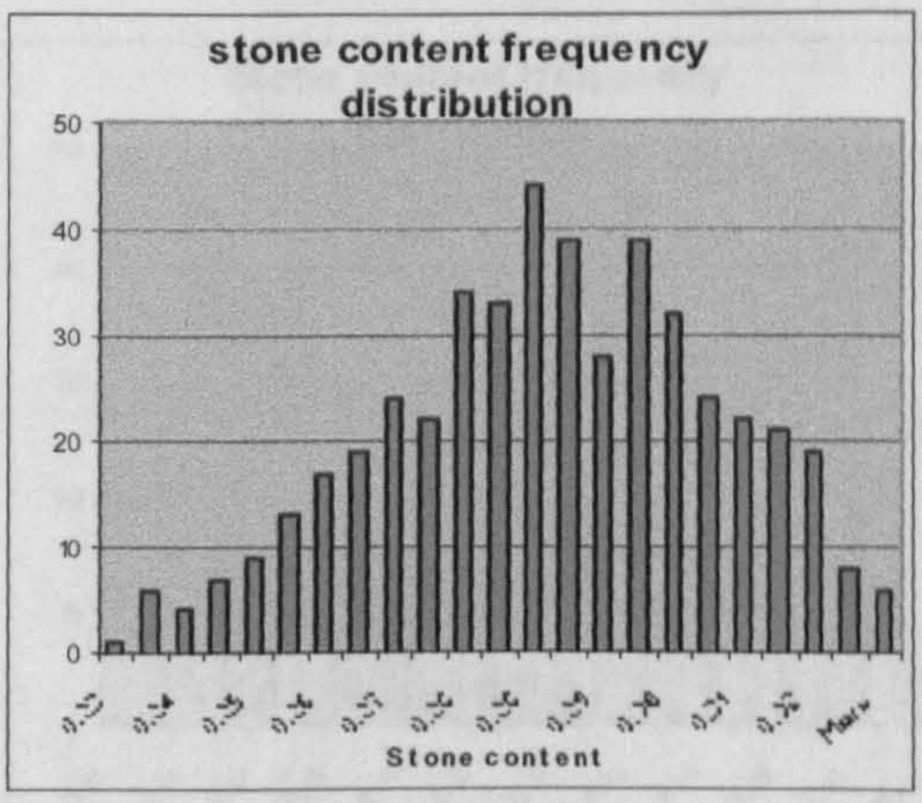

Figure 7.9. The randomly generated frequency distributions of soil properties for the plot P3.

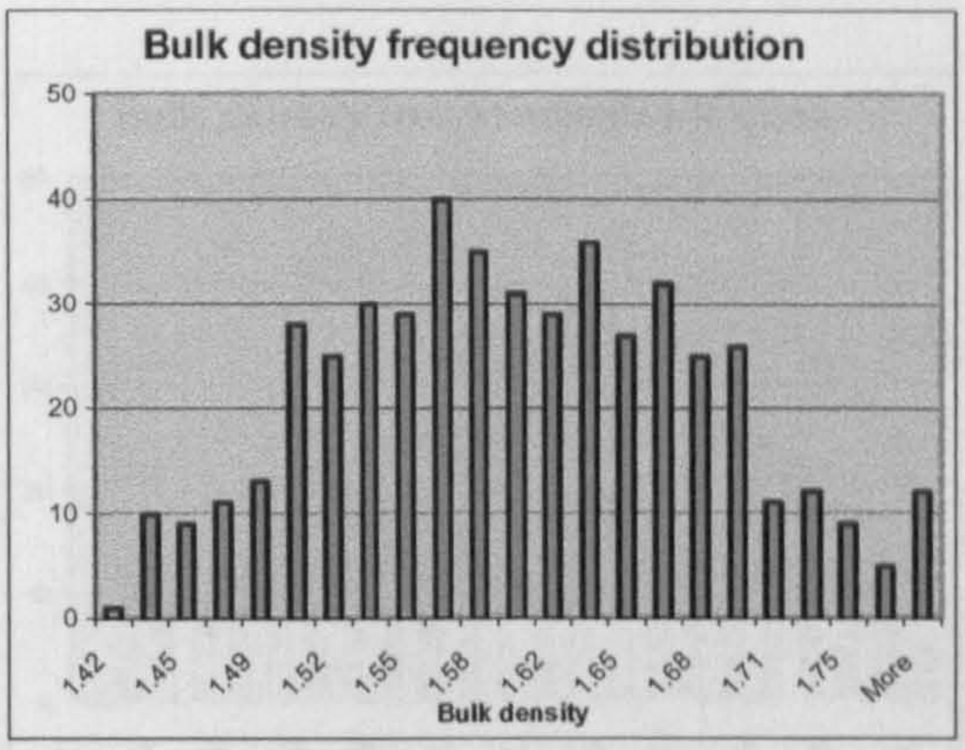

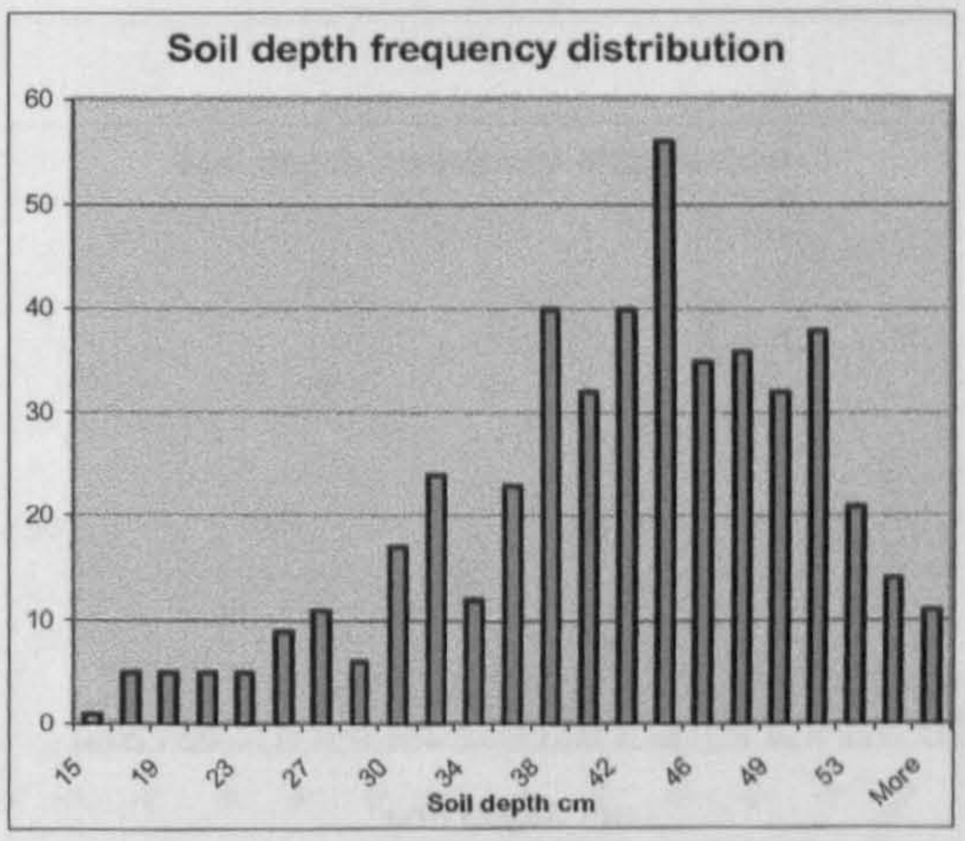

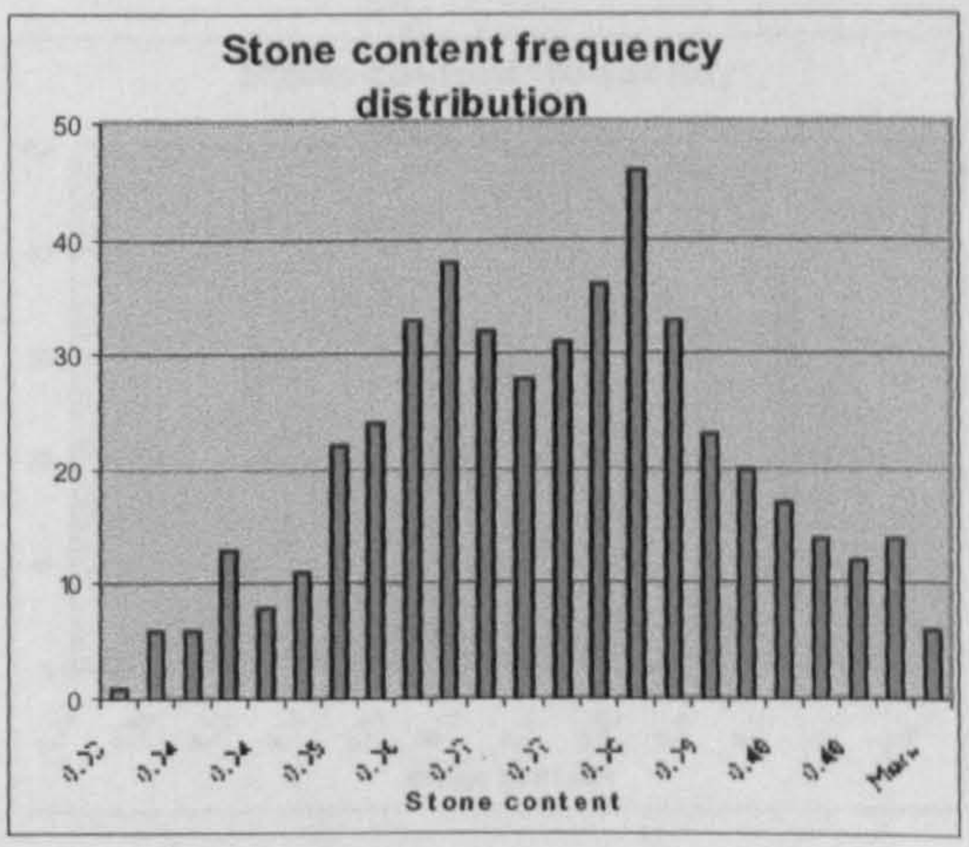

Figure 7.10. The randomly generated frequency distributions of soil properties for the plots P1, P2, and P8.

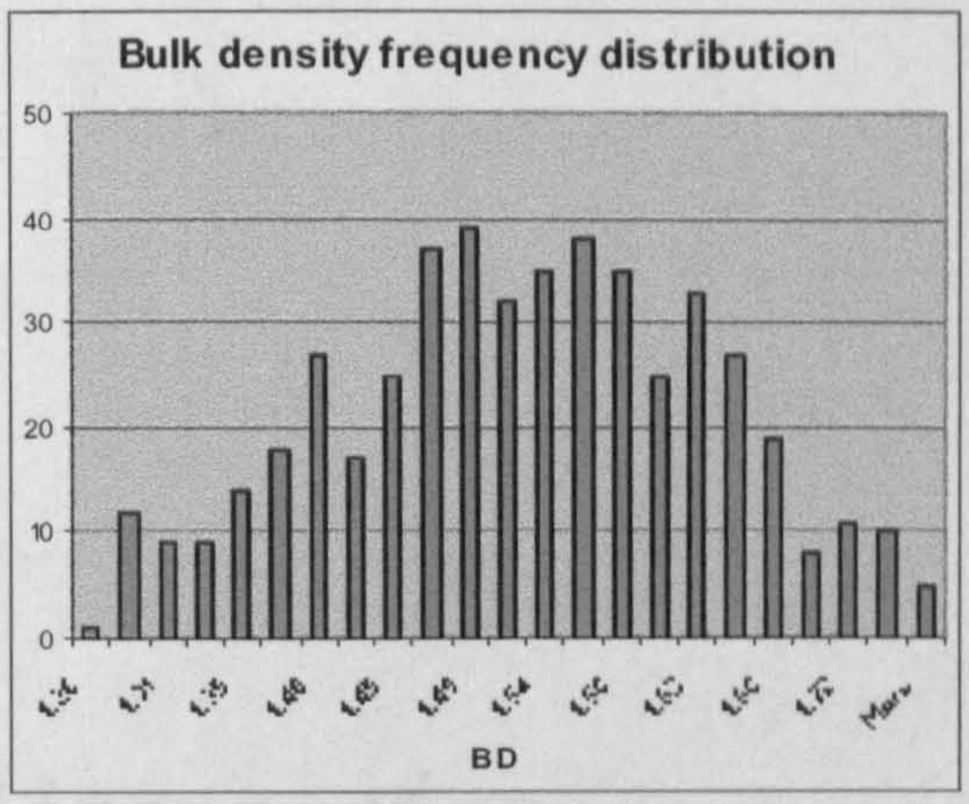

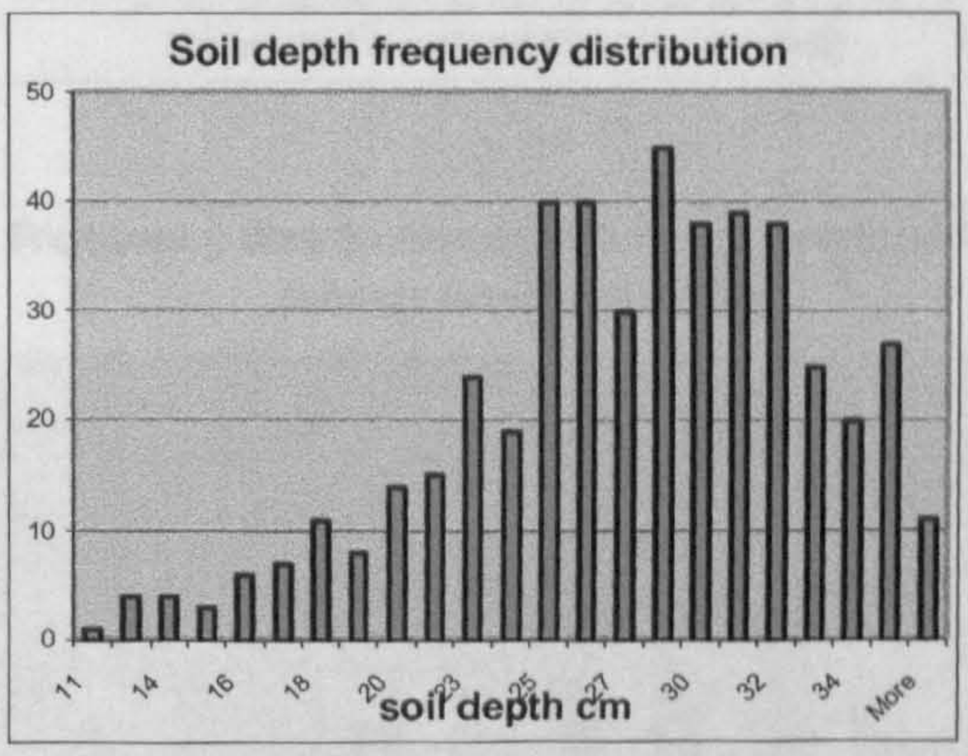

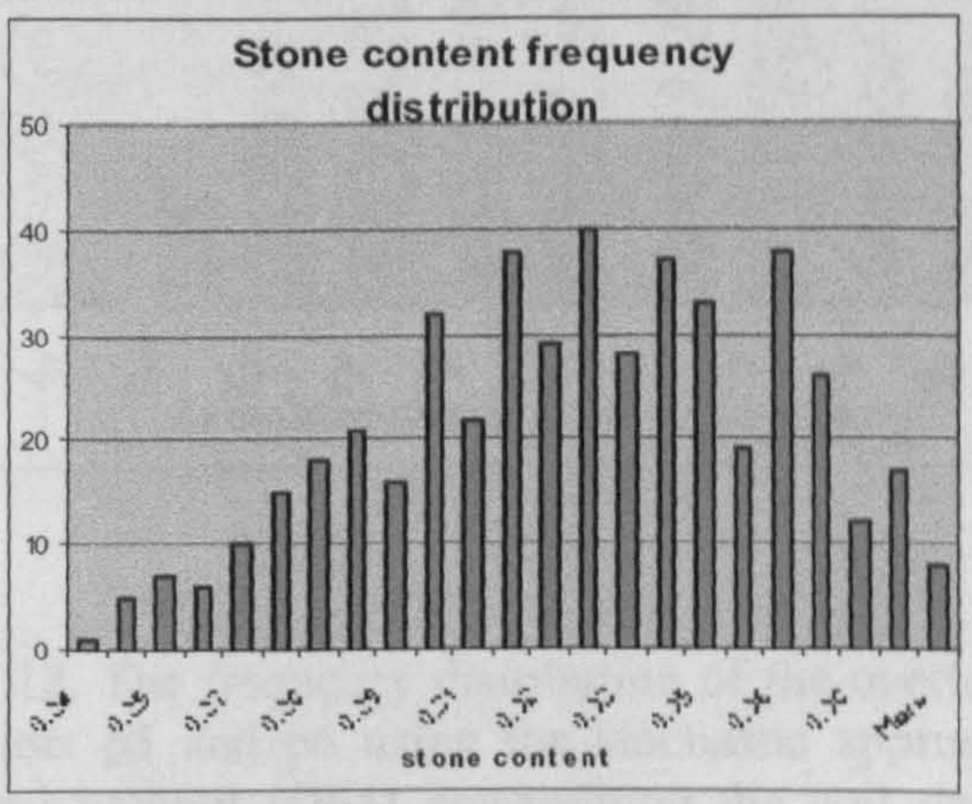

Figure 7.11. The randomly generated frequency distributions of soil properties for the plots P7, P9, and P11.

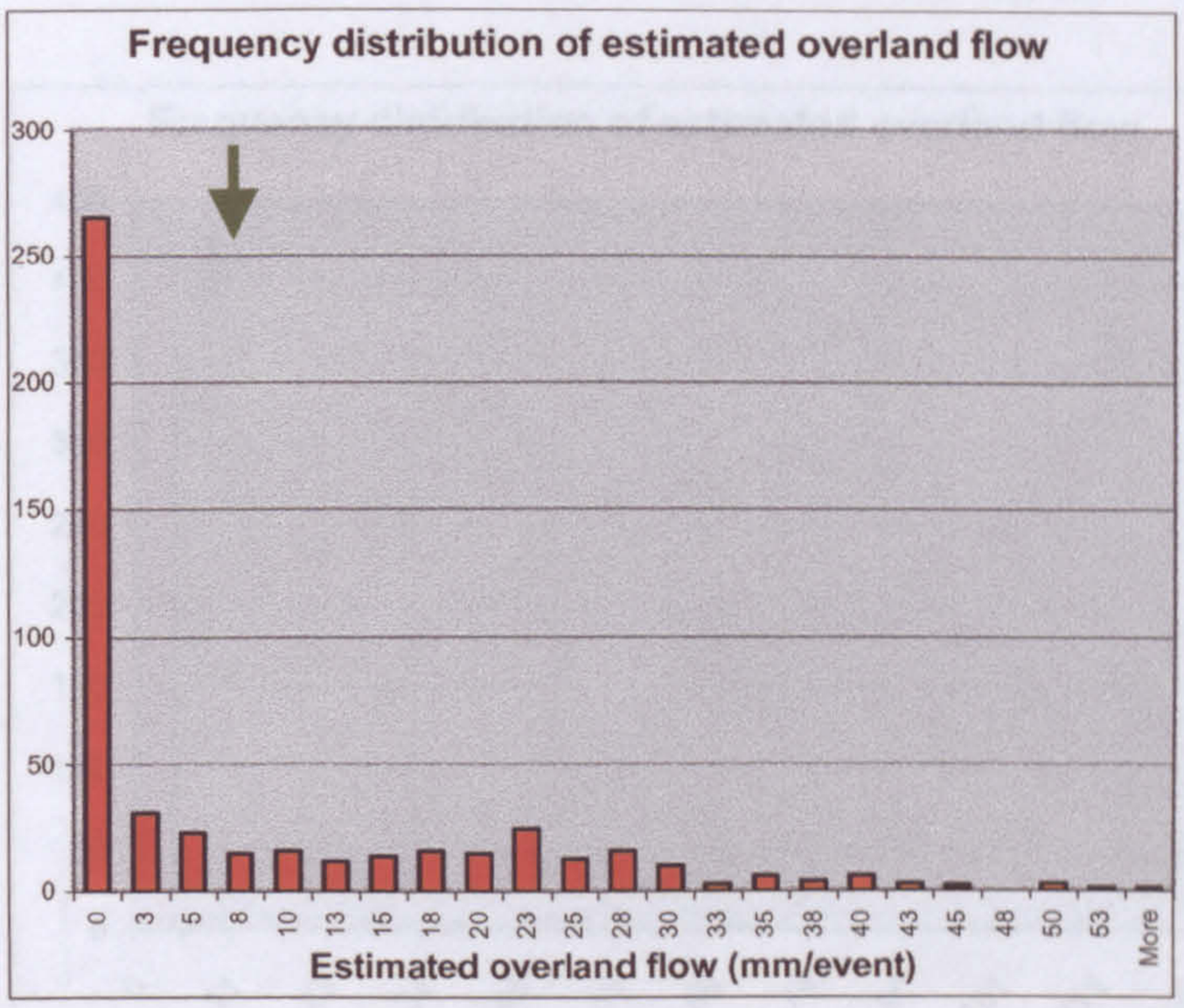

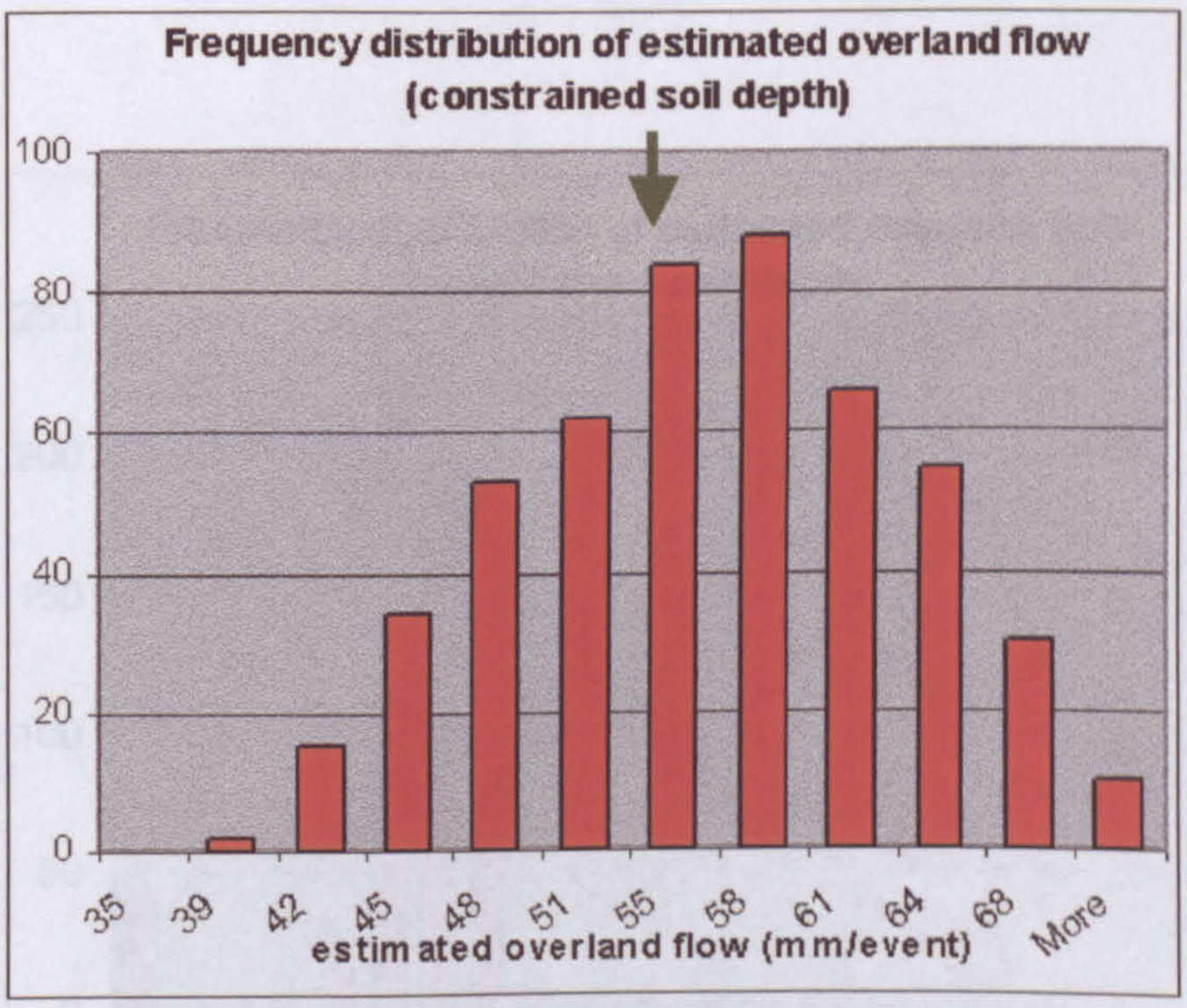

Figure 7.12. The frequency distribution of the overland flow in the plots p5 and p6 using the stochastic approach with (OF3) and without (OF4) constraining the soil depth to a maximum value of 300 mm. The green arrow indicates the mean value

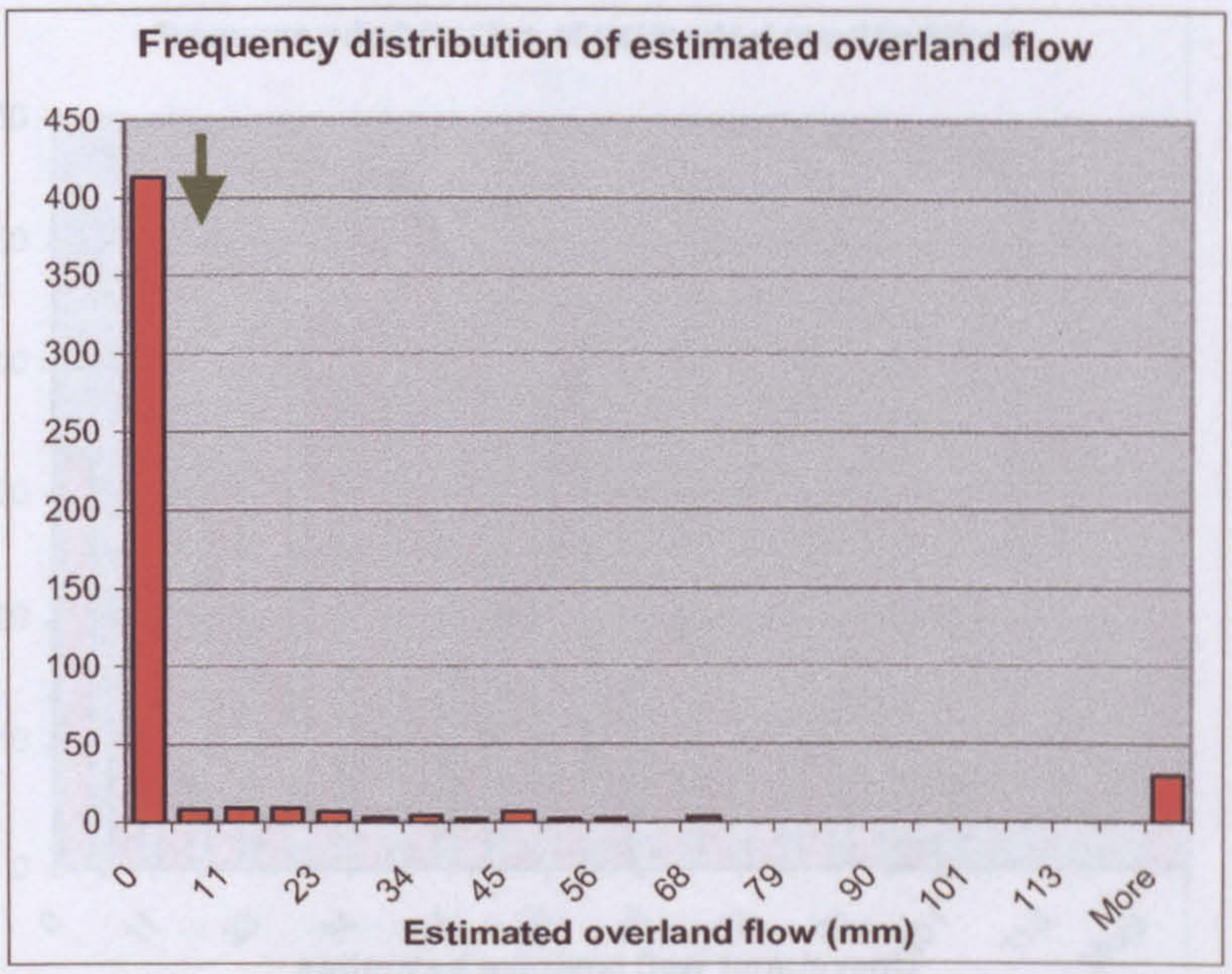

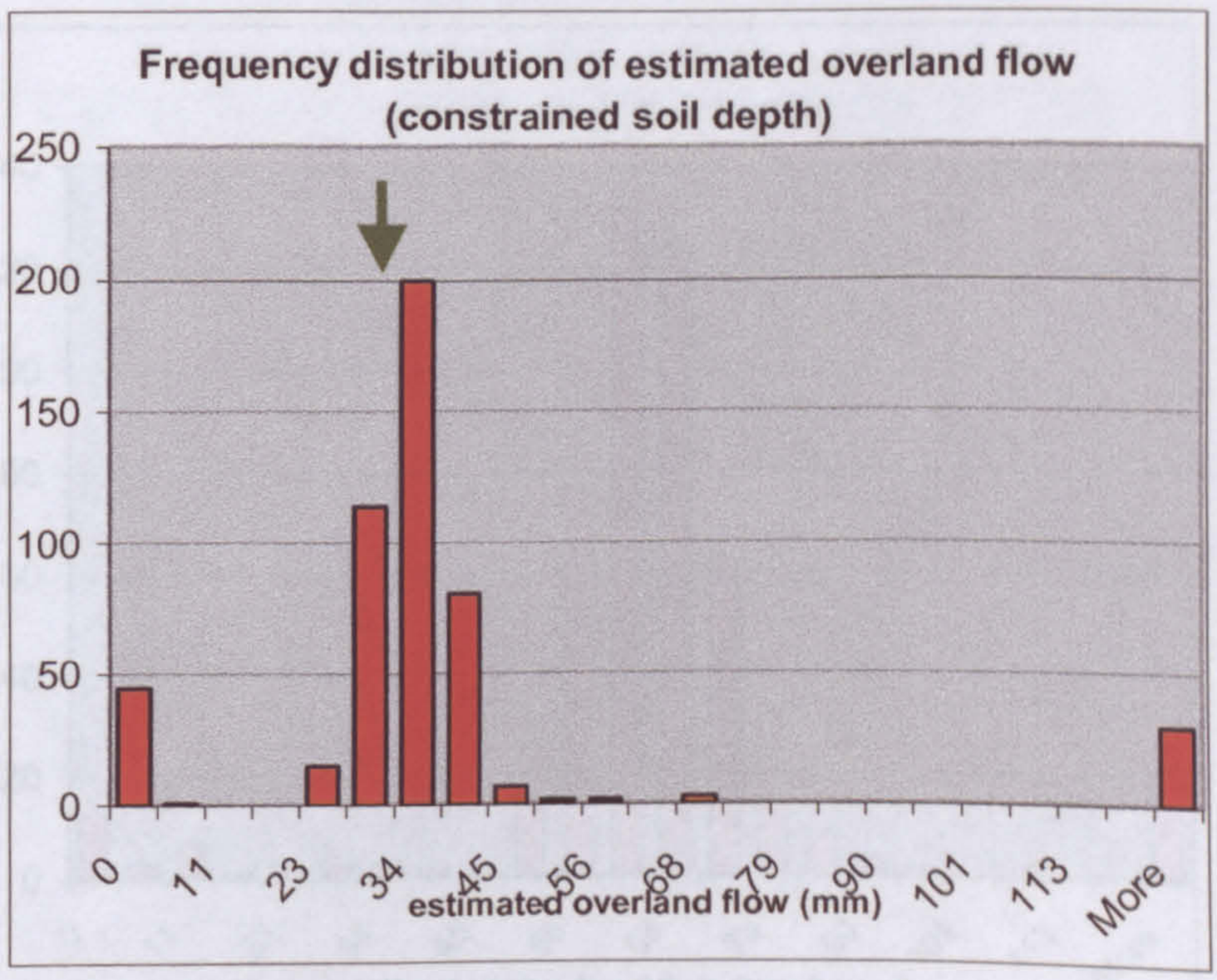

Figure 7.13. The frequency distribution of the resultant overland flow in the plot p3 using the stochastic approach with (OF3) and without (OF4) constraining the soil depth to a maximum value of 300 mm.

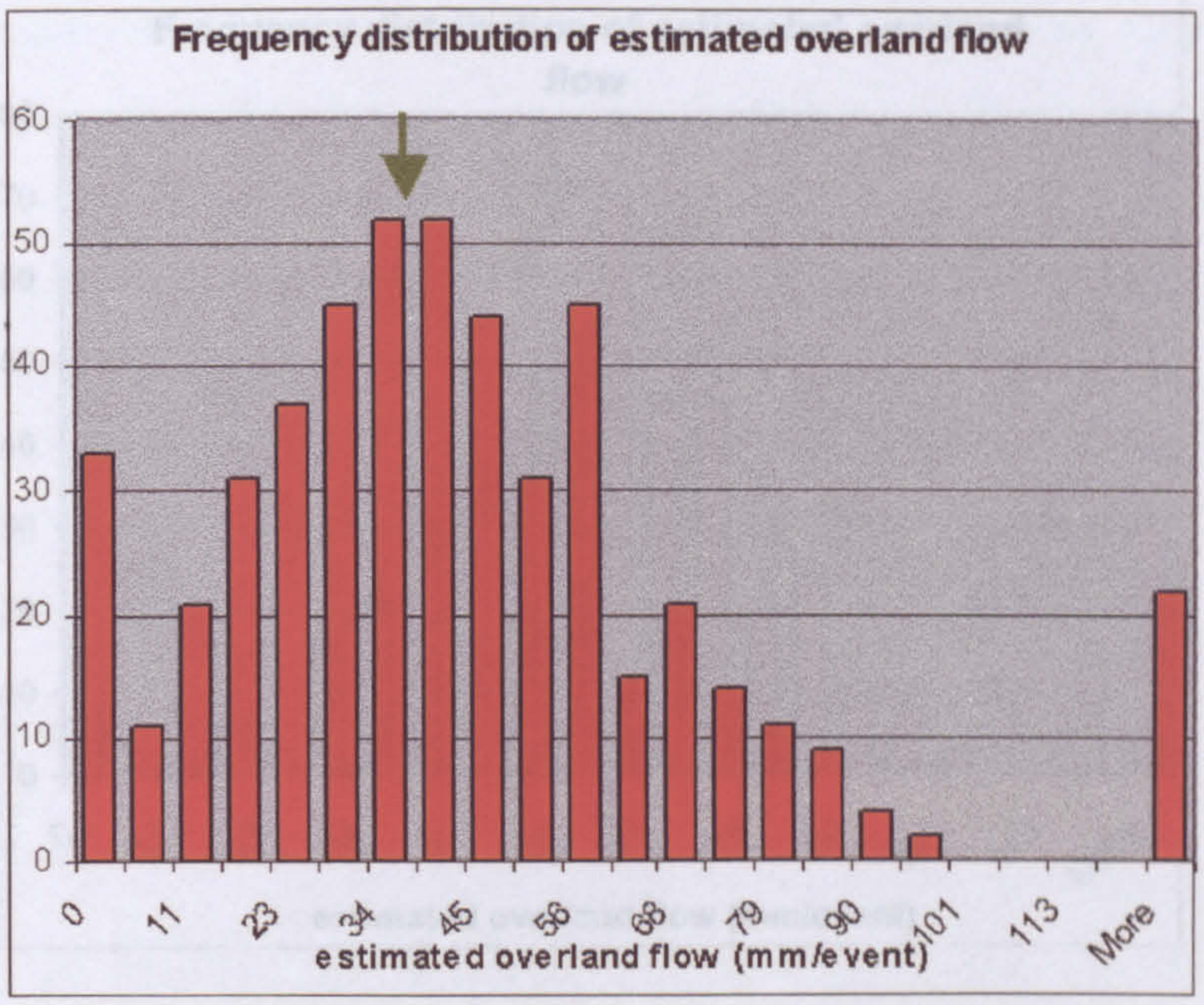

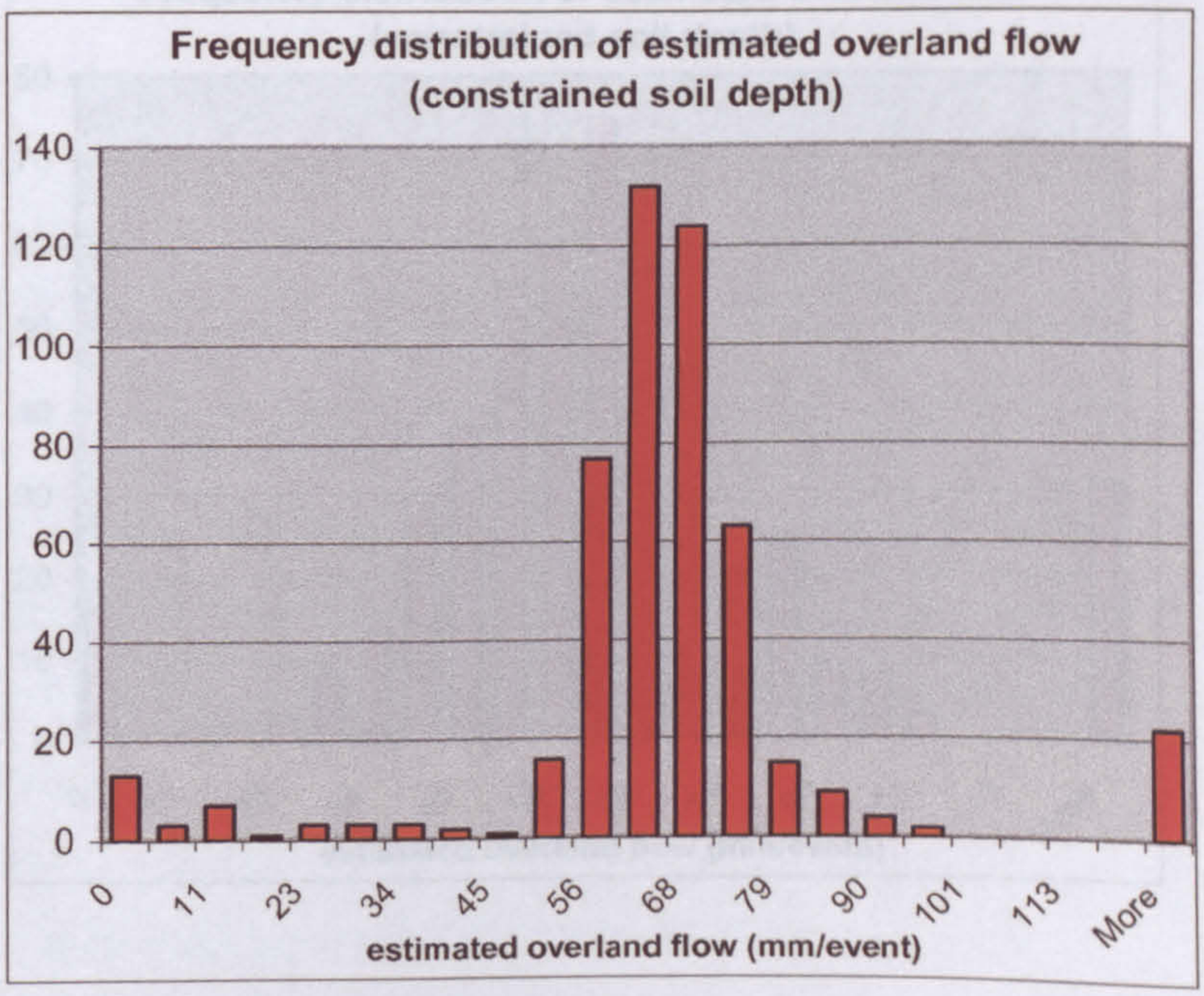

Figure 7.14. The frequency distribution of the resultant overland flow in the plots p1, p2, and p8 using the stochastic approach with (OF3) and without (OF4) constraining the soil depth to a maximum value of 300 mm.

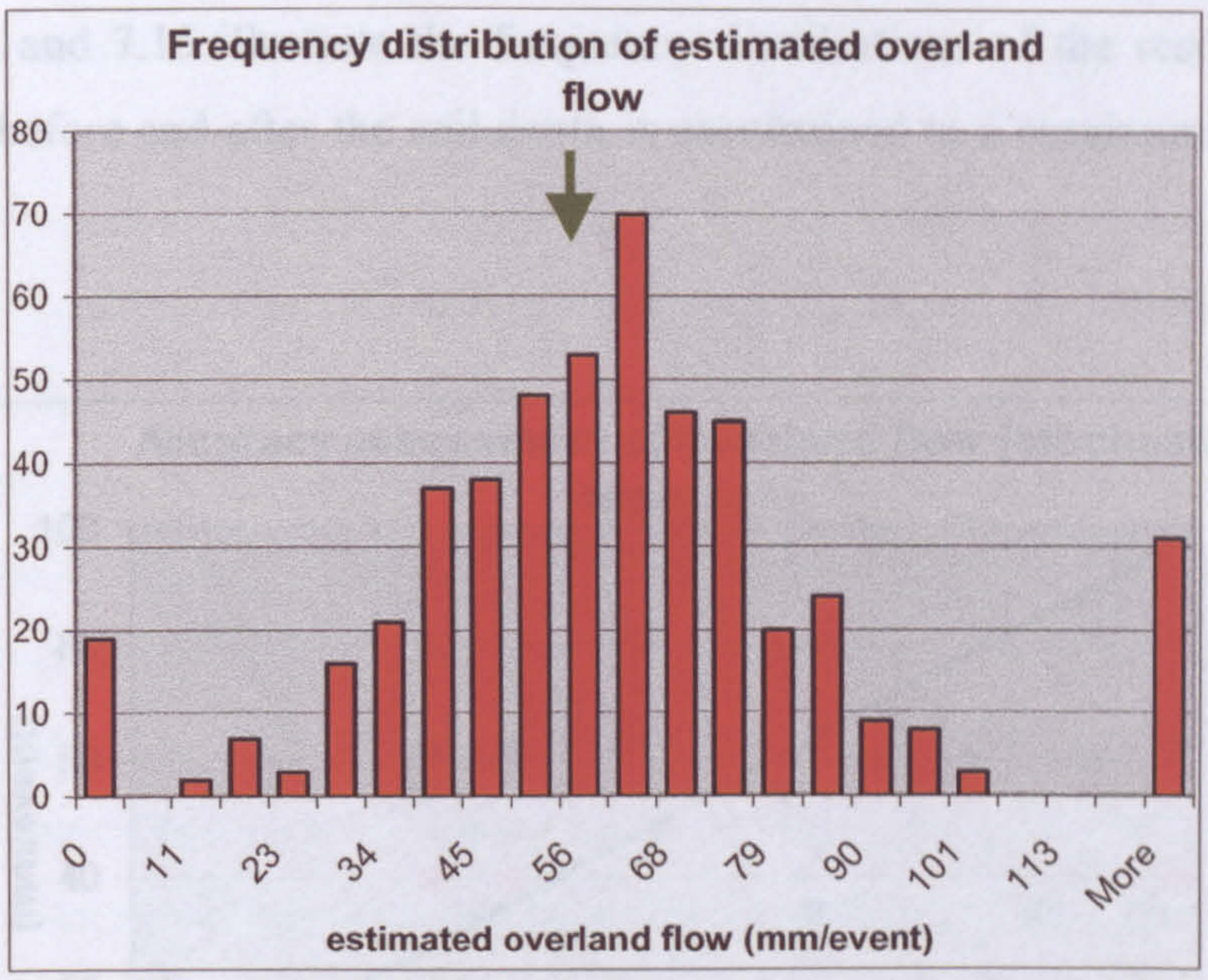

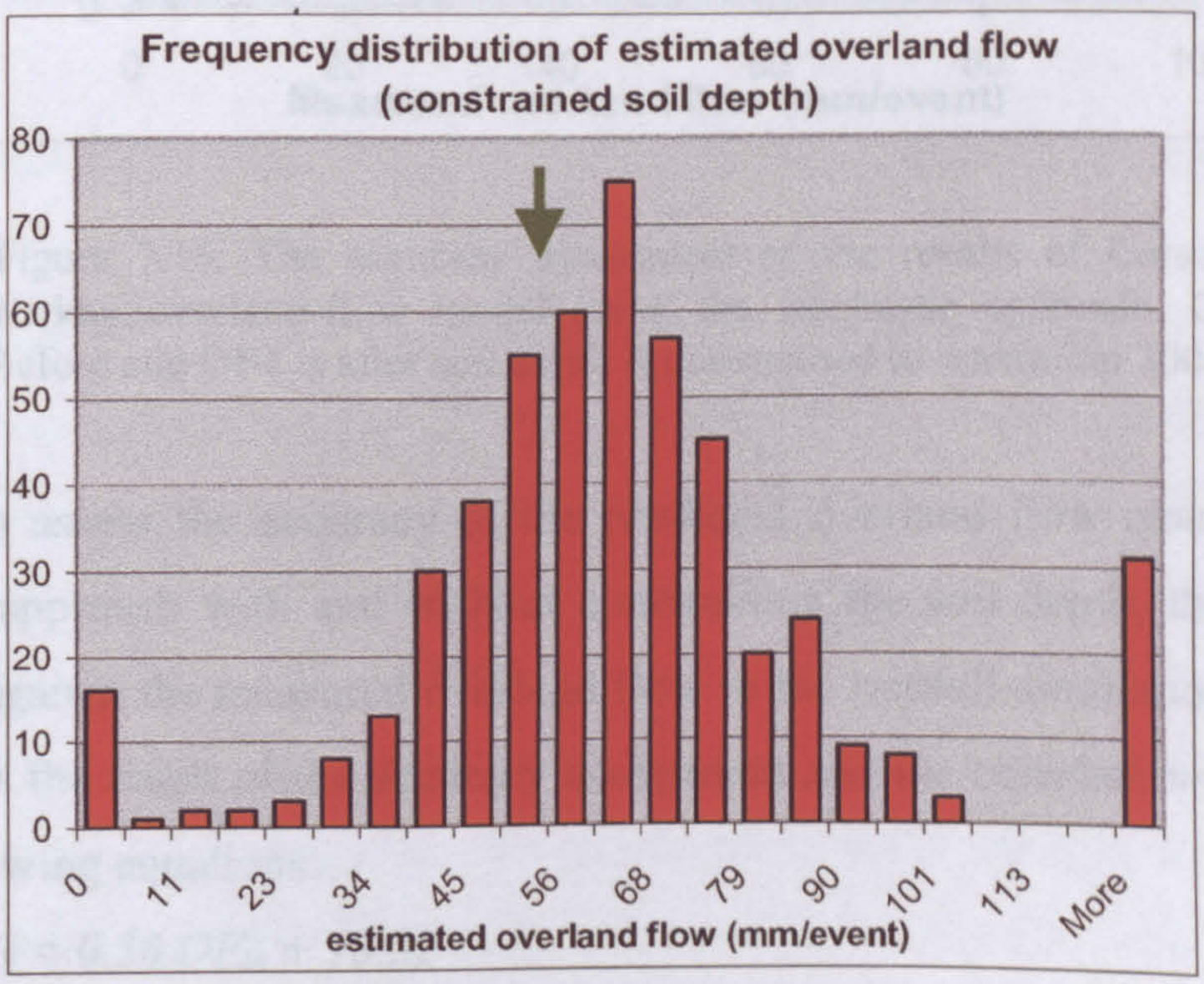

Figure 7.15. The frequency distribution of the resultant overland flow in the plots p7, p9, and p11 using the stochastic approach with (OF3) and without (OF4) constraining the soil depth to a maximum value of 300 mm.

These random values of the soil properties were generated in an EXCEL spreadsheet and then were incorporated randomly into the overland-flow equations 3.18, 7.1, and

7.3. The outputs resulting from the stochastic approach are 500 values for each of the rainfall-simulation plots which describe the predicted overland flow. Figures 7.12, 7.13, 7.14, and 7.15 illustrate the frequency distributions of the results in the nine plots both before and after the soil depth is constrained to a maximum values of 300 mm.

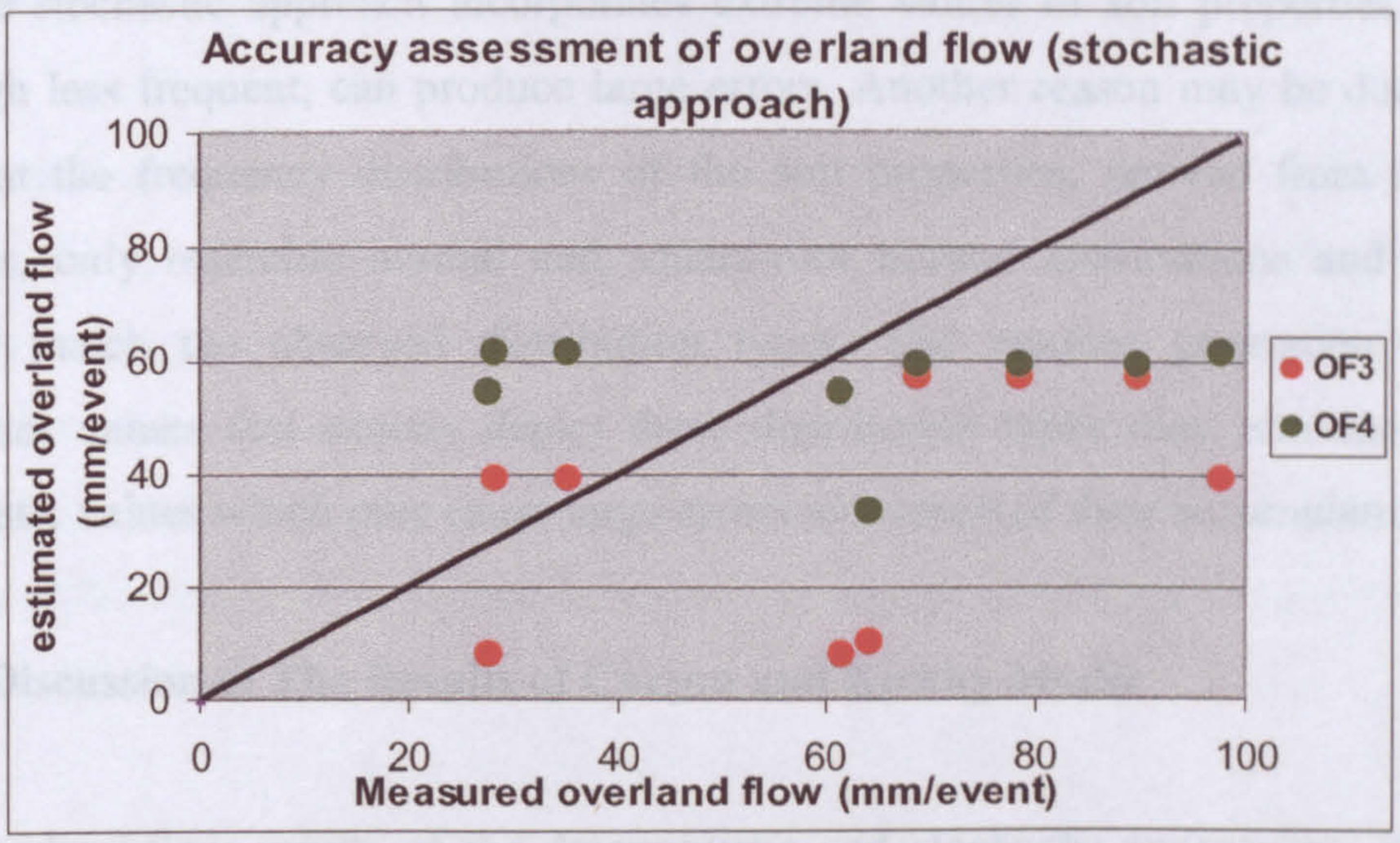

Figure 7.16. The accuracy assessment of the results of Carson and Kirkby overland-flow model using the stochastic approach. OF3 is before and OF4 is after soil depth is constrained to maximum 300 mm.

In order to assess the accuracy of the predicted overland flow resulting from the stochastic approach with and without constraining the soil depth, these results are validated against the measured overland flow in the rainfall-simulation plots. Figure 7.16 shows the result of the accuracy assessment and the correlations are expressed in the following equations:

$$OF_3 = 0.36\ OF_m + 13.32 \qquad 7.6$$

$R^2 = 0.49$, *P-value* $= 0.18$, *RMSE* $= 42.7$ *mm.*

$$OF_4 = 0.009\ OF_m + 55.59 \qquad 7.7$$

$R^2 = 0.025$, *P-value* $= 0.94$, *RMSE* $= 35.2$ *mm.*

Where OF_3 and OF_4 are the overland flow resulted from implementing the stochastic approach without and with constraining the soil depth respectively. OF_m is the measured overland flow.

These results demonstrate that the stochastic approach did not improve the prediction accuracy of overland-flow model. The reason for this may be attributed to the fact that the stochastic approach incorporates extreme values of soil properties which, although less frequent, can produce large errors. Another reason may be due to the fact that the frequency distributions of the soil properties, derived from the soil samples, only resemble normal and square-root normal distributions and do not exactly match the observed distribution types. The random generation of soil properties values that exactly depict these distribution types may introduce some unrealistic values which may cause large errors as a result of their accumulation.

7.2.5 Discussion of The Results of Carson and Kirkby Model

The overland-flow results of the deterministic and stochastic approaches, with the two cases of with and without constraining the soil depth to a maximum of 300 mm, shows that the deterministic approach with the constrained soil depth (OF_2) was the most accurate method to model the overland flow. This method produced the lowest RMSE and the best correlation for the relationship between predicted and measured overland flow in the rainfall-simulation plots. The stochastic approach was expected to produce better results because this approach compensates for the variability of the soil properties within a hydrological response unit and simulates the natural processes more accurately than the deterministic approach which assumes fixed values for soil properties within each unit. In addition, a quick comparison between *OF1* and *OF2* results indicates that constraining the soil depth to the a maximum value of 300 mm dramatically improved the accuracy of the overland-flow mapping. As a result of this, the overland-flow map resulted from this method will be implemented in the Thornes soil-erosion model.

The best overland-flow map (OF_2) has an RMSE was 26.3 mm (equivalent to 21% of the simulated rainfall during the 30 minute event). Although the accuracy of the overland-flow map (OF_2) may not seem particularly high in the first instance, such results can be regarded as acceptable in hydrological modelling. This is due to the lack of a comprehensive understanding of the inherent complexity of the hydrological processes and the interactions of various hydrological parameters in both a linear and non-linear sophisticated manners.

An example of the complexity of overland-flow prediction is noticed by Sardo *et al.* (1994) who carried out a hydrological study to investigate the overland-flow generation on four plots that are similar in topography and soil properties by applying rainfall simulations of the same intensity and duration. The results of this investigation show high variability in the resultant runoff generation between the various plots, despite their similarity, where the runoff coefficient ranged from 0.22 to 0.38.

Another example of the problems to predict the overland flow is demonstrated by Scoging and Moore (1992) who carried out a rainfall simulation on a semi-arid slope in Walnut Gulch, Arizona to measure the overland flow. They implemented various infiltration and runoff models to predict the overland flow in that area and when they validated the predicted overland flow they found that the models under-predicted the overland-flow generation by up to 60%. A third example is a study by Grayson *et al.* (1992) who investigated the catchment hydrology in a number of plots in the Wagga catchment in New Wales, Australia and found that the difference between the predicted and measured overland flow ranges from 8% to 63%.

Perrin *et al.* (2001) also carried out a comprehensive hydrological study on 429 different catchments of various characteristics using a wide range of hydrological models in order to investigate how reliable and robust such models can be. They found that the differences between the outcomes of these hydrological models can be as little as 2% and increase up to 60% for the same catchments. These three examples of hydrological modelling demonstrate the prediction problems in most of

the models as a result of the inherent complexity of the hydrological processes. Thus, the overland-flow results obtained from Carson and Kirkby model may be regarded acceptable when compared to the results obtained by these hydrological investigations.

Despite the fact that the overland-flow results are regarded as acceptable, a number of error sources can be identified which may affect the accuracy of the modelling. One source of such errors can be attributed to the simplification of the infiltration behaviour in the Carson and Kirkby overland-flow model. According to Scoging (1992) there are three phases that can be recognised from the beginning of a storm. First is the pre-ponding phase where the infiltration capacity is greater than the rainfall intensity and the soil does not become saturated at this stage. Second is the ponding phase which occurs at the time of the storm where the rainfall intensity and the infiltration are equal. Third is the profile control stage where the infiltration capacity decreases as a result of the hydraulic changes and the rainfall intensity exceeds the infiltration rate the runoff is generated. In the simplification of the infiltration parameter in the Carson and Kirkby model, however, the phase of ponding is not recognised and this may cause error in the runoff generation.

However, the error sources are not only associated with the conceptual modelling of the hydrological process and some errors may arise from the rainfall-simulation field data that have been used to validate the predicted overland-flow map. There are many potential problems in implementing such field experiments to assess the accuracy of the results of the overland-flow model. One of these potential problems arises from the measurement of the simulated rainfall intensity in each of the experimental field plots and keeping a constant rainfall intensity rate throughout the experiment which is proven in the literature to be difficult to measure accurately. The rates of the simulated rainfall intensity directly influence the overland-flow generation rates and errors in their measurement are strongly manifested in the results of the overland-flow modelling.

Another problem is regarding the conditions prior to the rainfall-simulation experiment such as crusting and soil moisture which are difficult to take into account. A third problem is inherent in the experimental field data is that the ability of such data to replicate the real processes of the infiltration and overland-flow generation because they do not include the effects of inflow and they cannot reproduce the influence of the spatial position in the hillslope hydrological cascade (Scoging *et al.*, 1992).

7.2.6 Assessing the Overland-flow Errors Introduced by Using The Hydrological Response Units Method

In chapter six the soil properties were spatially mapped across the study area on the basis of the hydrological response units. In this method the mean values of the various soil properties, which were derived from the relevant field soil samples, were used to represent each of the soil properties in the corresponding hydrological response unit. This means that the soil properties in each pixel of the image of the study area are average values and this may introduce errors to the resultant overland-flow map.

One way of assessing these errors is to compare the overland flow that is predicted using the soil-property maps of the hydrological response units to that is predicted using soil properties data that are measured in the field. Such measurements of the soil properties are available at the locations of the validation sites of rainfall-simulation plots which were measured by Zhang (1999). The overland flow was re-calculated using Zhang's soil properties data at the specific nine rainfall-simulation plots. These overland-flow results were then validated against the measured overland flow in these plots and the figure 7.17 shows the result of the accuracy assessment where the correlation between the measured and predicted values is expressed in the following equation:

$$OF_5 = 0.66\ OF_m + 26.4 \qquad 7.8$$

$$R^2 = 0.74,\ P\text{-}value = 0.026,\ RMSE = 18.1\ mm$$

where OF_5 is the predicted overland flow using soil properties measured at the validation sites.

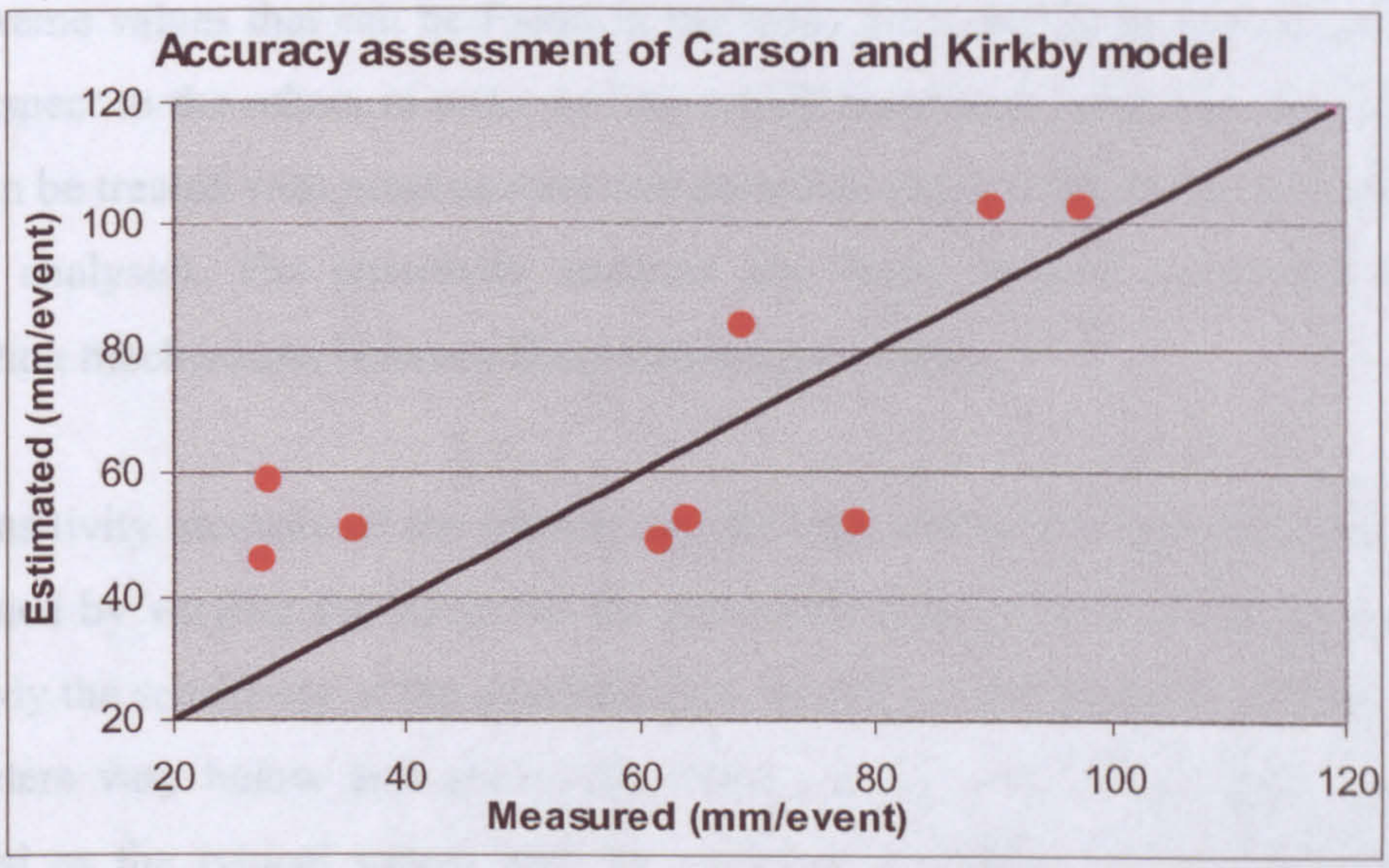

Figure 7.17. Assessment of the prediction accuracy of Carson and Kirkby overland-flow model using soil properties data collected at the nine verification plots.

When the results of this accuracy assessment are compared to those in equation 7.5 and figure 7.6, it seems that small errors are introduced to the prediction of overland flow as a result of implementing the hydrological response units. These errors are manifested by an increase of the value of RMSE by 8.2 mm from 18.1 mm to 26.3 mm of OF2. This increase of the RMSE is smaller in magnitude than that increase which resulted from considering the actual soil depth (in OF1) or from the stochastic approach (in OF3 and OF4). This means that the hydrological response units approach can be successfully used for hydrological modelling at the local scale as it minimises the potential errors.

7.2.7 Sensitivity Analysis of Carson and Kirkby Model

It has been shown in equations 3.18, 7.1, 7.2, and 7.3 that parameters of porosity, initial soil moisture, soil depth, stone content, and bulk density affect the overland-flow generation rates in Carson and Kirkby model. However, these parameters affect

the overland flow in different ways with different magnitudes, thus, sensitivity analysis should be carried out to reveal those parameters that the model is most or least sensitive to. This sensitivity analysis is used to 1) test the model response for the extreme values that can be found in the study area, and 2) to test one parameter with respect to the others in order to find which parameter needs the most attention so it can be treated with most caution and precision when collected in the field (cost-benefit analysis). The sensitivity analysis also helps to give an insight into the interaction mechanisms between these various parameters.

The sensitivity analysis of the Carson and Kirkby model to a specific parameter is performed by varying the values of the parameter around its most typical value. In this study the sensitivity of the overland-flow model is investigated by letting the soil parameters vary below and above the mean values, where the means values are regarded as the typical values and the variation is chosen to keep the generated parameter values within their natural variations (figure 7.18). The variations in the parameters values are standardised to the range between -50% and +50% to visualise the effect of their relative changes on the model outcomes.

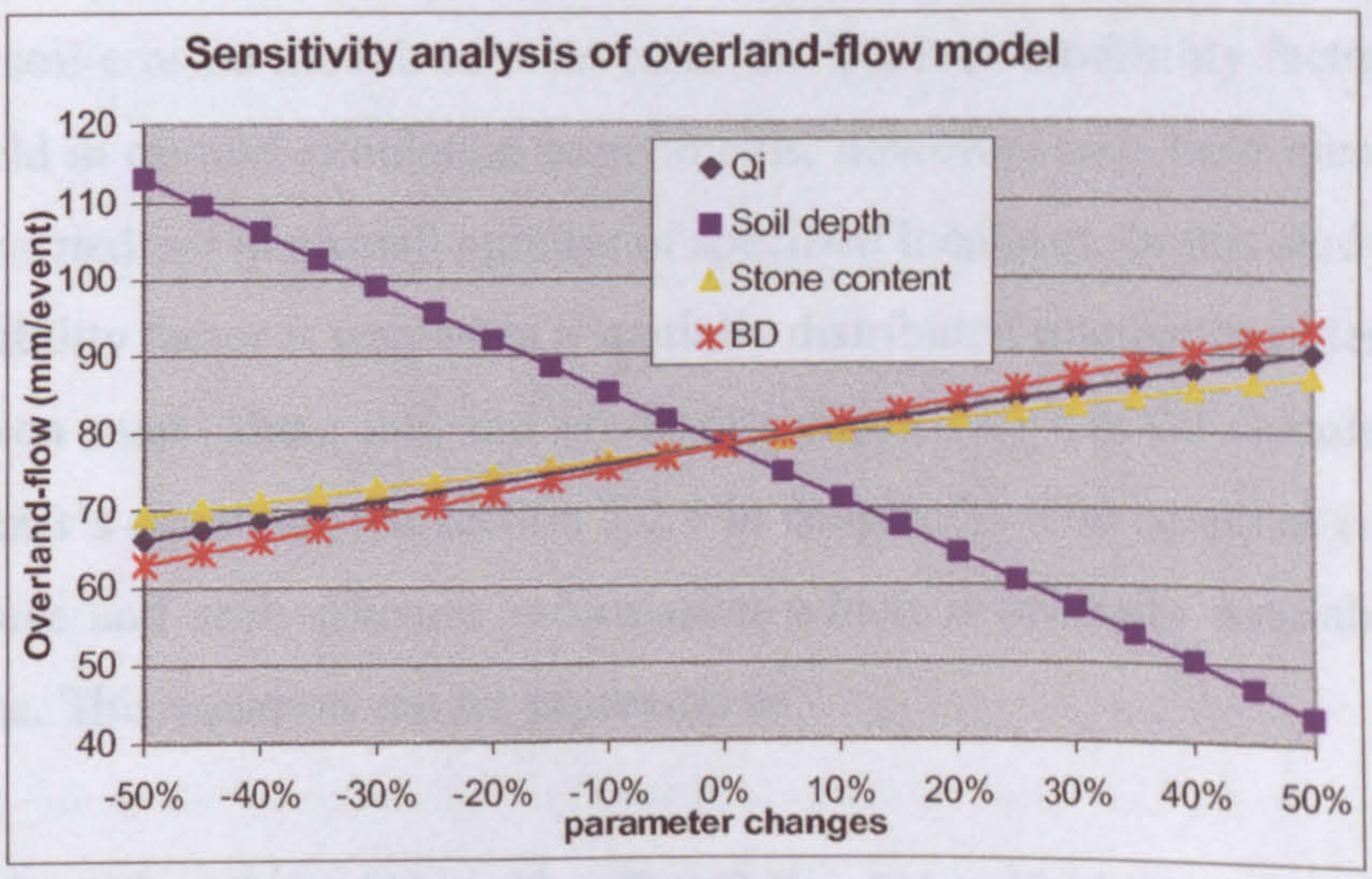

Figure 7.18. Sensitivity analysis of the Carson and Kirkby overland-flow model where Qi is the initial soil moisture and BD is the bulk density.

The results in figure 7.18 show that the initial soil moisture (Q_i), bulk density (BD), and the stone content parameters have similar effects, to some extent, on the

overland-flow model. The model is most sensitive to variations in soil depth where the overland-flow rate decreases strongly as the soil depth increases in a linear relationship. The reason for this high sensitivity of the model to the soil depth is the fact that the soil depth is the main controlling parameter on the water storage capacity (r_c) and the total initial soil moisture (Q_iT) where a larger soil depth greatly increases the infiltration capacity and decreases the runoff.

7.3 SOIL ERODIBILITY ESTIMATION

The only parameter that now needs to be calculated before the soil-erosion model can be implemented is soil erodibility *K*. Soil erodibility is a measure of the soil susceptibility to erosion by the act of the erosive power of the rainfall. The main factors that determine soil erodibility are soil physical properties (*e.g.* Bryan, 1968). The most widely applied soil erodibility factor for soil-erosion modelling is the USLE erodibility (Wischmeier *et al.* 1971), which has been satisfactorily described for many agricultural soils in the USA (Wischmeier and Smith 1978).

No clear methodology is available on the calculation of the soil erodibility for the Thornes soil-erosion model. In most cases the Thornes erodibility factor is measured in the field in rainfall-simulation experiments, however, such field measurement can only be carried out in a small number of specified locations. In this study the Thornes soil erodibility factor is needed in a spatially distributed manner in order to create the soil-erosion map. Thus, this soil erodibility factor (K) will be calculated from the Wischmeier's equation (see section 2.2.5 in chapter 2). The equation is based on the soil texture and soil structure information which is spatially available across the study area. This equation can be expressed as:

$$K = [2.77 \cdot 10^{-6} \cdot M^{1.14} \cdot (12 - a)] + [0.043\,(b - 2)] + [0.033\,(c - 3)] \qquad 7.9$$

where K is the soil erodibility factor (tonne hectare hour/hectare megajoule millimetre), a is the organic matter (percentage), b is the soil structure code used in

the soil classification, c is the profile permeability class, and M is expressed in the following equation:

$$M = [silt + VFS] \cdot [(silt + VFS) + sand] \qquad 7.10$$

where *VFS* is very fine sand percent, and *silt* and *sand* are percentages of soil.

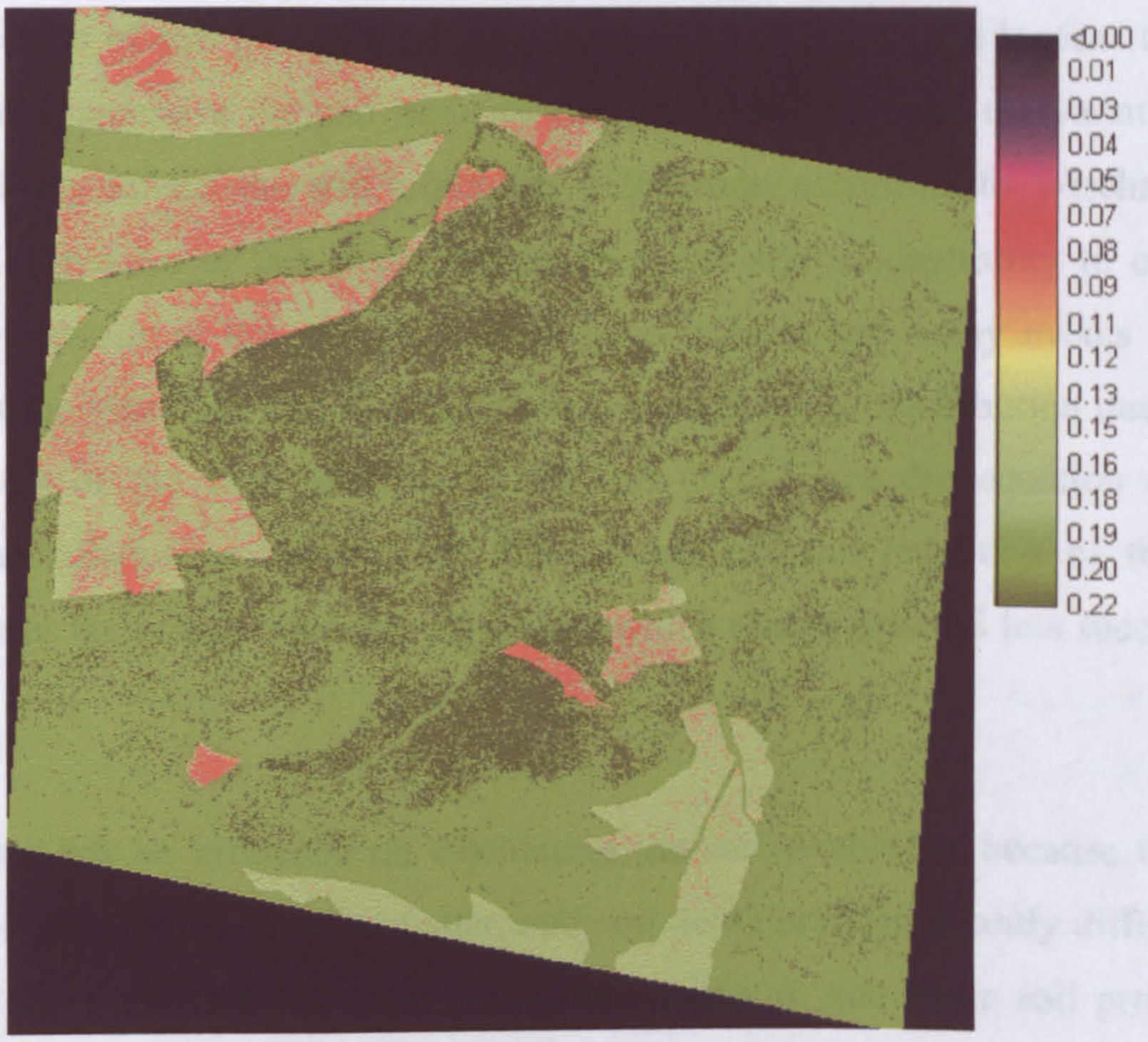

Figure 7.19. The map of the soil erodibility factor calculated from Wischmeier's equation. The erodibility values range from 0.08-0.22.

Using the soil samples collected in the study area it was found that the value of soil structure parameter in the erodibility equation for the study area ranges between 1-4 (Proyecto Lucademe, 1992) where 1 indicates very fine granular, 2 is fine granular, 3 is medium to coarse granular, and 4 is blocky or massive. The soil permeability parameter in the erodibility equation was defined from Proyecto Lucademe (1992) and for this study it ranges from 1 for rapid, 2 is medium to rapid, 3 is medium, 4 is

slow to medium, 5 is slow, and 6 is very slow. Figure 7.19 shows the soil erodibility map where the value of erodibility factor rages from 0.08 to 0.22.

The soil erodibility map in figure 7.19 reveals that the soil susceptibility to erosion is at its maximum in the unploughed areas covered by matorral, whereas it is lowest in the agricultural areas that have been ploughed. This suggests an influence of land-use type on the soil susceptibility to erosion and there are two main reasons for that. First, the process of soil ploughing destroys the soil aggregates and loosens the soil particles which increases the soil porosity and permeability. Since the variations in soil permeability affects the soil erodibility calculation according to Wischmeier's equation, the increase in this permeability decreases soil susceptibility to erosion. Second, the topsoils in the ploughed areas have experienced many events of soil erosion over the years and this changed their soil particle size distribution due to the washing away of the fine particles of silt and clay. Since the equation of soil erodibility calculation is sensitive to the soil texture, the reduction of the fine particles leaves the coarser particles of the soil which makes that soil less susceptible to erosion.

Soil type also has an influence on calculating the soil erodibility because the soil properties of soil texture, organic matter, and soil depth are significantly different in the red and grey soils, as has been shown in chapter 6, and these soil properties control the soil erodibility. In a study to evaluate the soil erodibility in relation to the soil physical properties, Schjonning (1994) carried out rainfall simulations on eleven different soils in Denmark where all soil physical properties of texture, porosity, and the organic matter were measured, as well as the topography, soil moisture content, shear strength, surface roughness, runoff and sediment loss. By varying the soil type in the rainfall simulation, Schjonning found that soil physical properties are the most dominant factor influencing the soil erodibility and these findings are in agreement with the result of soil erodibility map.

Before the Thornes soil-erosion model is implemented to predict the soil loss in the study area, the soil erodibility factor in this model had to be adjusted in order to

balance the units of all parameters that control the Thornes model. This is due to the fact that the soil erodibility in this study was calculated from the Wischmeier's equation which was originally developed for the Universal Soil Loss Equation (USLE) due to the lack of a clear recognised method to calculate Thornes soil erodibility parameter in a spatial manner. Soil erodibility in Thornes model needs further investigation and development in order to simplify its calculation and to make it fit well within the model. However, for the purpose of this study a simple, dimensionless conversion factor of 2.49×10^{-5}, which was developed by Mokrech (2001), can be used in order to balance the units in Thornes model. This conversion factor is adequate for the rainfall intensity and the time scale of a rainfall event specified in the rainfall simulation of this study.

7.4 MODELLING SOIL EROSION

7.4.1 Implementation of the Thornes Soil-Erosion Model

According to the equation 3.6 there are four parameters governing the soil-erosion rates in the Thornes model, these are soil erodibility (soil factor), overland flow (hydrological factor), slope (topography factor) and the vegetation cover. The map describing the slope parameter was derived in chapter four using the aerial photograph of the study area and the two adjacent aerial photographs by implementing the digital photogrammetric techniques of the ERDAS OrthoMAX. The vegetation-cover map was derived in chapter five by implementing the linear mixture modelling techniques where the errors in the resultant vegetation cover were removed using the shade removal algorithm and the co-occurrence matrix analysis. The overland flow and the soil erodibility parameters in the Thornes model were calculated in this chapter using the Carson and Kirkby overland-flow model and the Wischmeier's equation respectively.

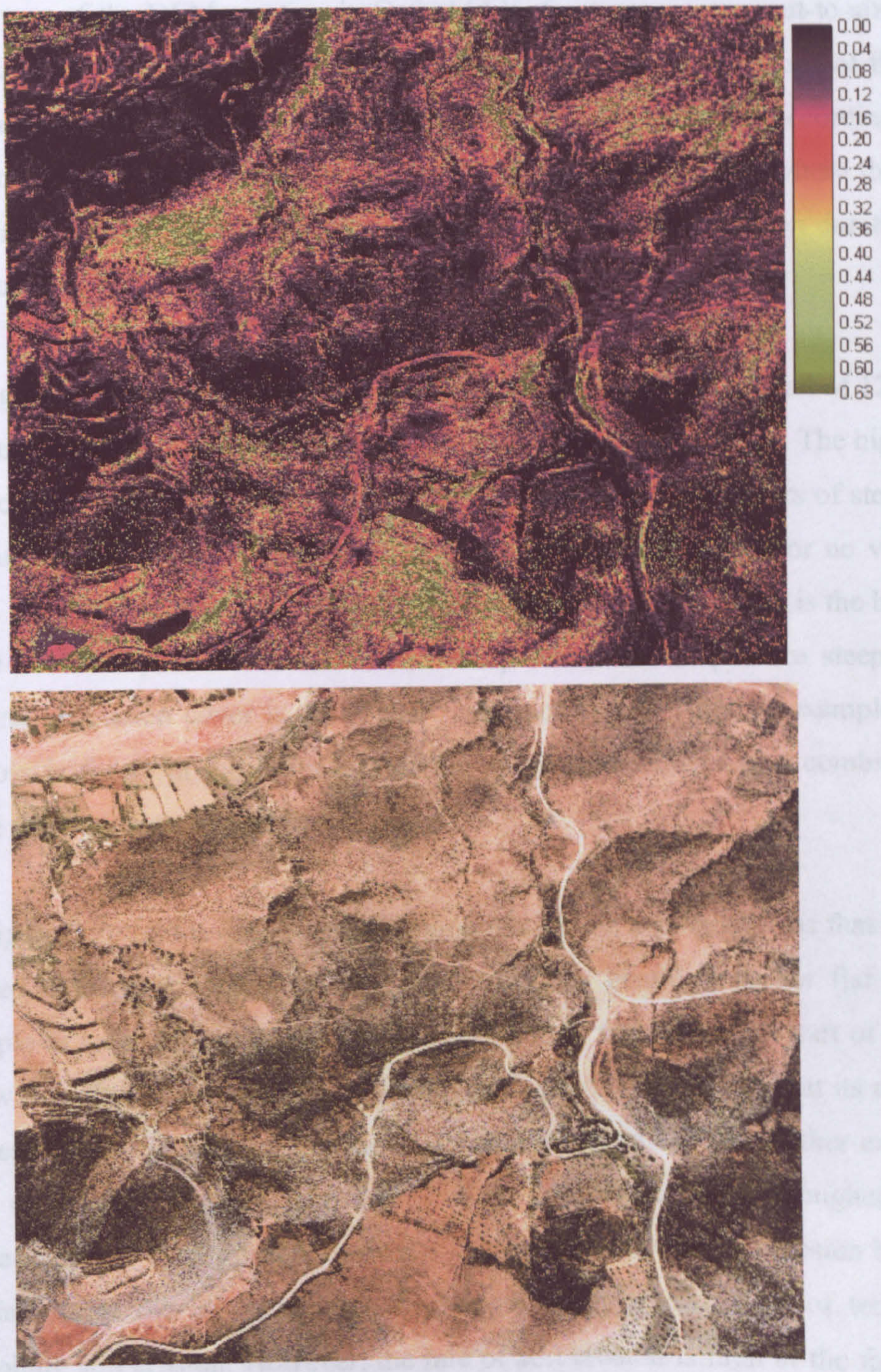

Figure 7.20. The predicted soil-erosion map using Thornes model. The units are (mm/event) where the rainfall is 124 mm and the event is 30 minutes in this case. The aerial photograph is shown here to illustrate areas of high and low soil-erosion rates.

Since the map of slope was smaller than the rest of the maps due to the technical limitations of the DEM creation in OrthoMAX, these maps were cut-to-size so that they have the same geographic properties as the slope map. The maps of these four parameters were then combined in IDRISI GIS environment according to the equation 3.6 and the soil-erosion map was created (Figure 7.20) where the unit of this map is mm/event and the event is equal to the rainfall simulation duration of 30 minutes.

The figure 7.20 reveals that the soil loss rates, under a uniform rainfall of 124 mm of 30 minutes duration, range from nil soil loss to as much as 0.63 mm. The highest soil loss occurs in areas that have combinations of some or all the factors of steep slope, unploughed soil which is associated with higher runoff, and little or no vegetation cover. An example of areas that are characterised by a high soil loss is the burnt area in the southern part of the soil-erosion map where the slopes are steep and the matorral vegetation cover is destroyed by the act of fire. Another example of high soil loss is found in the north-east of the study area which has a combination of scarce vegetation cover and steep slopes.

The figure 7.20 also reveals that the minimum soil loss occurs in areas that are either covered with dense vegetation or characterised by gentle slopes or flat land. An example of areas of low soil loss is the river bed in the north-west part of the study area where, despite the absence of the vegetation cover, the slope is at its minimum. The terraces in the west part of the study area in figure 7.20 is another example of areas of low soil loss. Despite the fact that these terraces are ploughed and the vegetation cover is reduced, they are not threatened by severe soil erosion because of the flatness of the land providing a good example of the effect of terracing on controlling soil erosion. However, the rate of soil erosion is high at the faces of the terraces, as can be seen in figure 7.20, due to a combination of a steep slope and a lack of vegetation cover and this high rate of soil erosion can be slightly reduced by a protective vegetation cover. Another example of low soil loss is the areas of dense matorral in the centre of the study area which is accompanied with gentle slopes.

In order to assess the accuracy of the predicted soil-erosion map, it should be validated against measured soil-erosion rates from the rainfall-simulation experiments in the nine field plots. However, two of the validation plots fall outside the spatial extent of the soil-erosion map due to the fact that the maps of the model parameters were re-sized to match the extent of the slope map. Thus, only the remaining seven plots can be used for the accuracy assessment of the soil-erosion map. Figure 7.21 shows the correlation between the predicted and measured soil loss rates that are described in the following statistics:

$$E_p = 0.015 + 0.53\, E_m \qquad 7.11$$

$$R^2 = 0.82,\ P\text{-}value = 0.022,\ RMSE = 0.058\ mm\ (65\%).$$

where E_p is the predicted soil-erosion rate and E_m is the measured soil-erosion rate from the rainfall simulation.

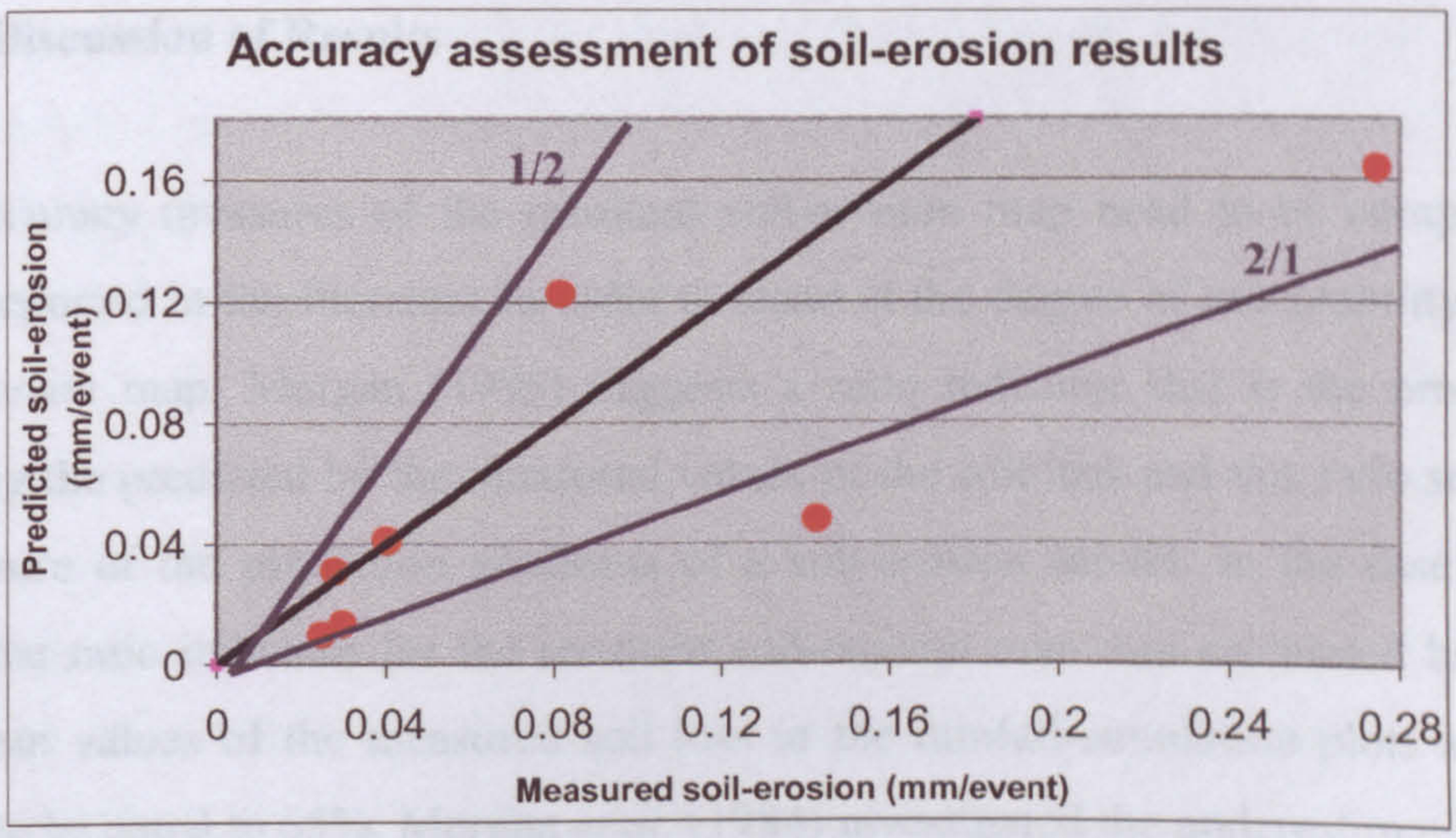

Figure 7.21. The accuracy assessment of the results of Thornes soil-erosion model. The rate of the soil loss is calculated in mm/event where the event equals to 30 minutes period of the rainfall simulation. The 1/2 and 2/1 lines indicate the envelop of an RMSE of 100%.

These results demonstrate that predicted soil erosion is significantly correlated with the validation data (p-value <0.05 at 95% significance level) and this is a first indication of successful modelling of the soil erosion by Thornes model. The RMSE

of 0.058 mm is transformed to a relative RMSE for better understanding of the results and it is equivalent to a relative RMSE of 65% of the average measured soil loss in all the rainfall-simulation plots. This indicates that the resultant soil-erosion map is acceptable in comparison with results reported in the literature as will be discussed later on in this chapter.

Figure 7.21 shows that the soil-erosion rate is largely underestimated in one of the rainfall-simulation plots and this could be attributed to errors in the rainfall-simulation experiment which can lead to excess in the yielded soil loss. If this plot is excluded from the accuracy assessment then the RMSE is greatly improved to 0.043 mm (equivalent to a relative RMSE of 49% of the average measured soil loss). However, these statistics should be interpreted with some cautions due to the lack of power of the test as a result of the limitations of the number of rainfall-simulation plots used for validation.

7.4.2 Discussion of Results

The accuracy measures of the resultant soil-erosion map need to be compared to those reported in the literature in order to stand at the degree of acceptability of this soil-erosion map. Morgan (1995) suggests a ratio indicator that is the product of dividing the predicted by the measured values of the soil loss and this ratio serves as a measure of the prediction goodness of a soil-erosion model. In the case of this study the ratio indicator for the resultant soil-erosion map was calculated based on the mean values of the measured soil loss in the rainfall-simulation plots and was found to be equal to 65%. Morgan *et al.* (1984) investigated the underestimations and overestimations of soil-erosion models of an individual rainstorm and suggested that a soil-erosion model may be considered successful if the ratio of the predicted to measured value is between 0.5 and 2 (equivalent to a relative RMSE of 100%).

Walling (1996) investigated the accuracy of modelling the soil erosion in different types of catchments in Africa and found that the estimates of soil-erosion rates are different from the measurements of the soil loss by up to two orders of magnitude. In

addition, as a part of the activities of the International Geosphere-Biosphere Programme-Global Change and Terrestrial Ecosystems (IGBP-GCTE) Soil Erosion Network, Jetten *et al.* (1999) evaluated the performance of a large number of field scale soil-erosion models on various land-use and soil types using soil-loss measurements of 73 site-years. The evaluation was based on a comparison between the measured and predicted soil loss and showed that the predicted soil loss values can differ from the measured values by up to one order of magnitude (this is equivalent to a relative RMSE of 1000%). According to the findings of all these studies, the accuracy of the soil-erosion map that resulted from Thornes model can be regarded as acceptable.

It should be mentioned here that one of the important discussions amongst geomorphologists and erosion modellers is whether soil-erosion models should be used to predict absolute amounts of soil or for relative erosion prediction. When soil-erosion models are used to produce quantitative maps of soil loss, as is the case in this study, the weaknesses, strengths, and limitations of these models should be borne in mind when conclusions are drawn from the model results (Garen *et al.*, 1999). This is due to the fact that errors resulting from modelling the soil loss are inevitable because of the inherent complexity of the processes.

This accuracy assessment demonstrates that errors in the resultant soil-erosion map exist and many possible sources for these errors can be identified. One of the error sources could be attributed to errors in the field measurements of the different soil properties, as well as errors is the laboratory analysis where soil samples have been analysed for bulk density, organic matter and soil texture. Errors may also arise from the measured overland-flow and soil-erosion rates in the rainfall-simulation experiments. This is because measuring soil-erosion rates is fraught with methodological and practical uncertainty and experimental results of erosion rates are difficult to interpret and subject to exaggeration (Stocking 1996). Another source of errors can be attributed to the fact that small plots (where the rainfall simulations took place) might underestimate the soil loss due to the boundary effects (Wainwright *et al.*, 2000).

A fourth source of errors may arise from the fact that Wischmeier's equation was used to calculate the erodibility factor in the Thornes model. Wischmeier's equation is an empirical equation that was developed to calculate the soil erodibility for the types of soils that exist in the US and errors may arise from using the equation on soils of the semi-arid south-east of Spain. In addition, the assumption that the study area is divided into different hydrological response units to map the land use and the soil physical properties contributed to errors generation in soil-erosion map and this will be evaluated later on in this chapter.

One of the factors that exerts control over the overland-flow generation and the soil loss, yet is ignored in modelling the soil erosion in this study, is crusting. Soil crusting often occurs on agricultural lands in semi-arid environment as a result of rapid drying of soils after an intense event of rainfall. This soil crusting partially seals the thin topmost layer of the soil and causes a decrease of the amount of rainfall infiltrating into the soil layers and an increase of the overland-flow generation which results in higher soil loss (Le Bissonnais, 1990). Stone cover is another factor which has a control over the overland flow and soil erosion and also has been ignored in this study due the lack of data that can spatially describe the stone cover. The Thornes and Carson and Kirkby models, which were used in this study, do not take these factors into account in the modelling process and this may result in errors of the estimation of the overland flow and the soil loss.

Unlike the case of the overland-flow modelling, the stochastic approach was not implemented to model the soil erosion in this study due to the fact that it produced poor results in modelling the overland flow.

7.4.3 Investigating The Effect of Land-use Change on Soil Erosion

As has been mentioned earlier in chapter 1, the aerial photographs of the study area were taken on the 9th of April 1996. However, during August 1998 more than two years after the campaign, the fieldwork of this study was undertaken to collect the

soil samples, soil depth, and the Ground Control Points (GCPs). During this fieldwork a change in the land use in some regions of the study area was noticed, where these regions had been ploughed and the matorral was removed to prepare the land for almond and olive plantations. These regions were surveyed using the control points and the techniques of Differential GPS and Electromagnetic Distance Measurement described in chapter 4 in order to delineate the spatial extent of the change in the land use. Figure 7.22 shows the geographical locations of these land-use changes where the polygons of the green colour delineate these regions.

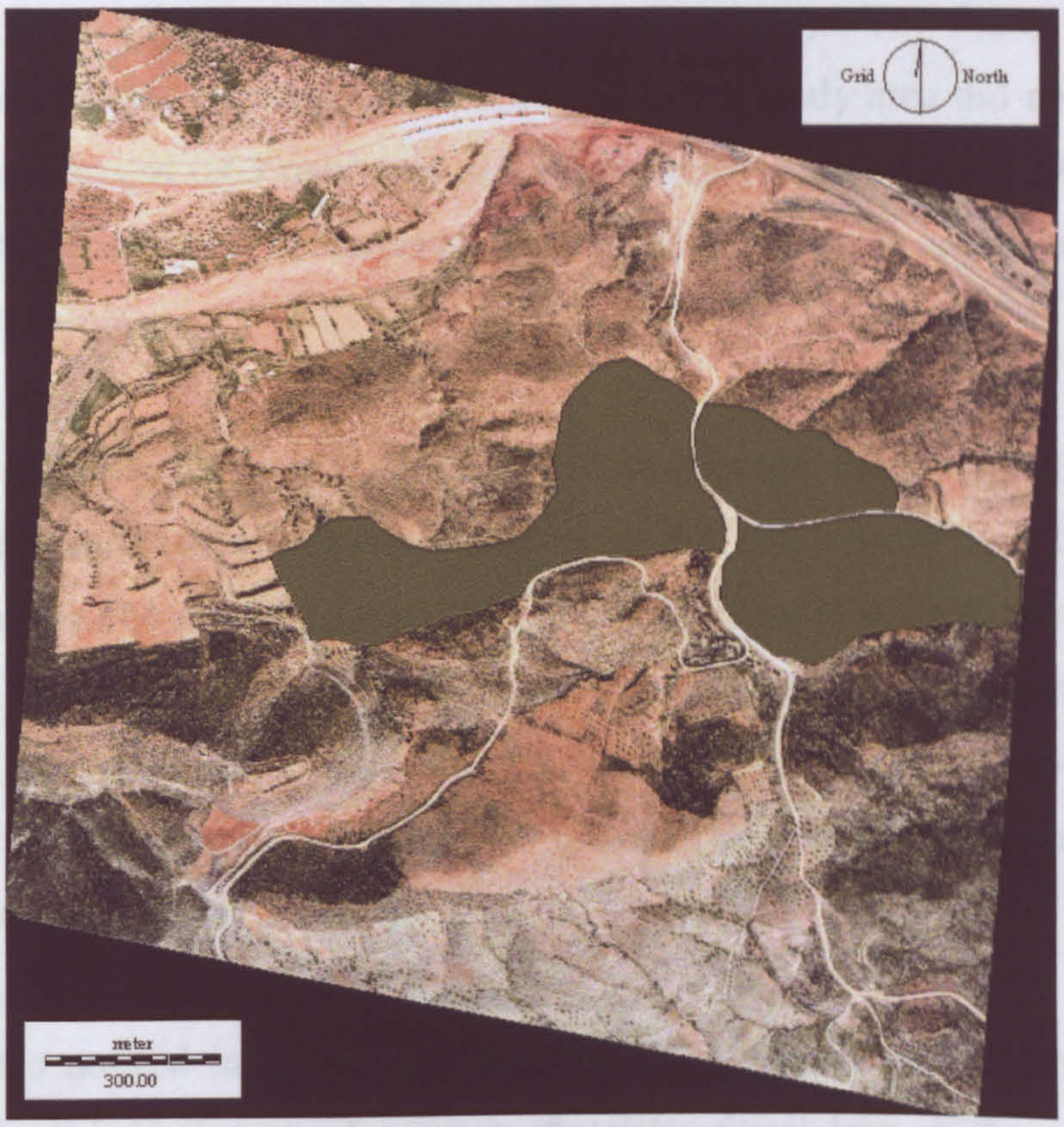

Figure 7.22. Showing the location of the regions which have been recently ploughed. The green polygons delineate these regions.

These changes in the land use provided this study with a unique opportunity to assess the impact of the agricultural activities on the acceleration of the soil erosion. To do so the boundaries of the regions where land-use change has taken place were measured in the field and the hydrological response units, which were defined in

chapter 6, were updated to reflect the current land use of the study area. The soil-property maps were also re-calculated for the same purpose. Since the ploughing process caused the removal of the vegetation cover in these regions, the vegetation-cover map was also updated by re-setting the vegetation cover in the ploughed regions to zero. The Carson and Kirkby model was implemented in order to derive the overland-flow map. This was then integrated with the Thornes soil-erosion model, along with the vegetation and slope maps, to derive the soil-erosion map which reflects the effect of land-use change. Figure 7.23 shows this soil-erosion map along with a change of soil loss map which represents the difference between the soil-erosion maps of before and after the land-use change. The figure 7.23 reveals that the land-use change effect on the soil loss in the study area did not exceed the maximum soil loss of 0.63 mm/event which was reported in figure 7.20. This is due to the fact that this change in the land use occurred in areas that are not at the highest risk of soil erosion.

The difference soil-erosion map in figure 7.23 also reveals that ploughing the land to prepare it for agricultural activities may raise the risk of soil loss by up to 21 mm/event under 124 mm of rainfall. To put this increase in the risk of soil loss into perspective, the difference soil-erosion map was re-produced in proportional terms, relative to the soil loss before the land-use change. Figure 7.24 shows the proportional difference map where the soil loss rose up to 500% in some locations as a result of the agricultural activities.

It can be also noticed in figure 7.24 that the difference values in some pixels are negative which indicates a reduction in the risk of soil loss in these pixels. The causes of this reduction were investigated and it was found that it occurs in pixels that are characterised by very gentle slopes (or flat area), very low vegetation cover (or zero vegetation cover), or a combination of these both factors. Pixels in such areas are minimally affected by the removal of the vegetation cover, on the contrary, the ploughing process loosens the soils and destroys the soil aggregates in these areas which leads to higher infiltration rates and lower overland flow and this, consequently, leads to lower soil loss.

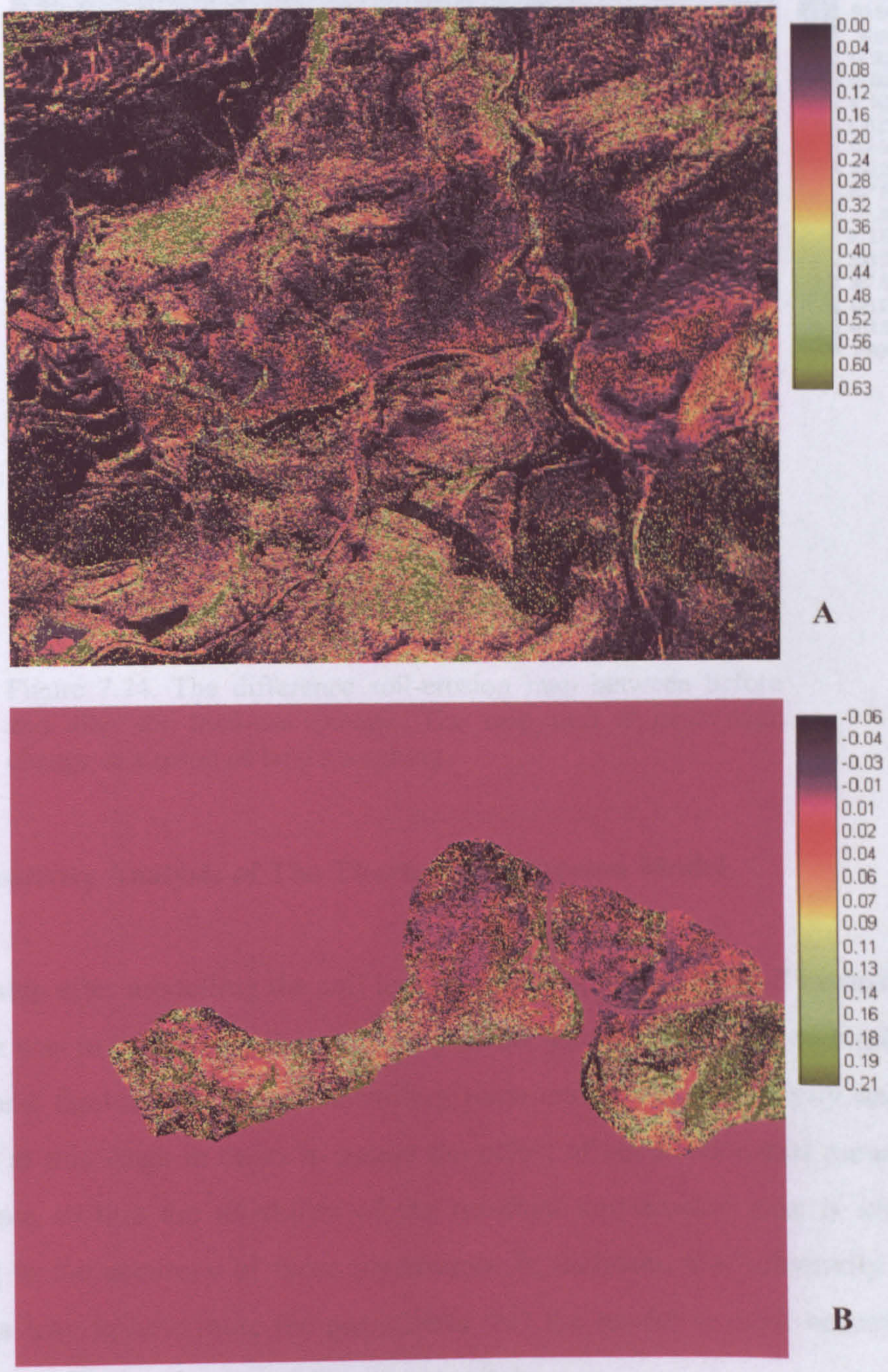

Figure 7.23. Soil-erosion map after the consideration of the ploughed area (mm/event). A) is the predicted soil-erosion map, and B) is the difference map between soil-erosions before and after considering the ploughed area.

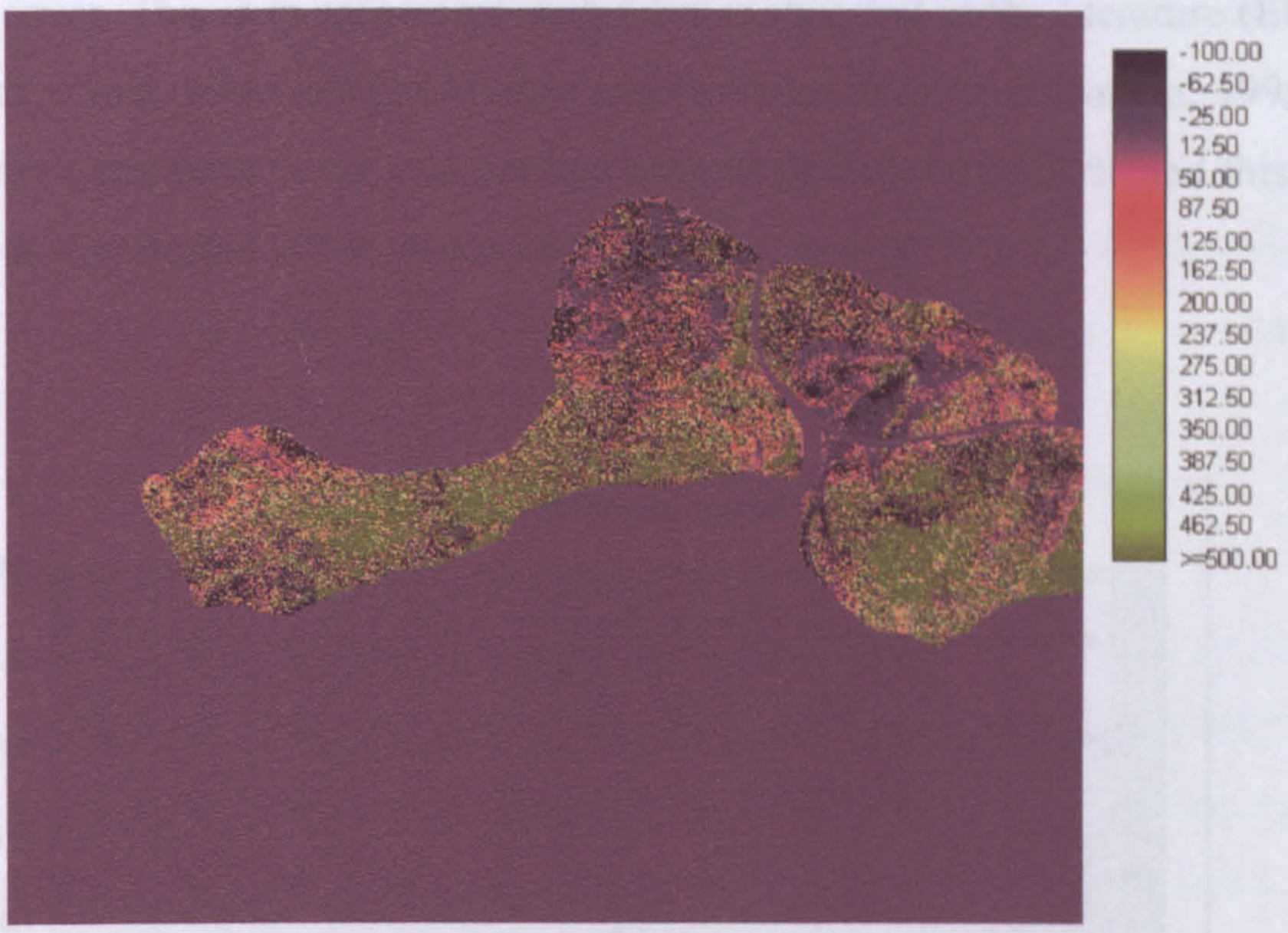

Figure 7.24. The difference soil-erosion map between before and after the land-use change. The map unit is percentage change as a result of land ploughing.

7.4.4 Sensitivity Analysis of The Thornes Soil-Erosion Model

The next step after modelling the soil loss under the specified rainfall intensity in the study area was to investigate the sensitivity of the Thornes soil-erosion model to the changes and fluctuations in its controlling parameters. This sensitivity analysis is important at this stage in order to assess the effect of each individual parameter on the soil loss so that the reliability of the resultant soil-erosion map is interpreted according to the accuracy of these parameters. In addition, this sensitivity analysis provides a way to determine the parameters that the model is most sensitive to so they can be defined and measured more accurately.

To do so the soil-erosion model parameters are varied around their average values within the range found in the study area. These variations are also standardised between -50% and 50% of change, relative to the average values, so that their effects on the soil loss can be determined. Figure 7.25 displays the results of this sensitivity

analysis and reveals that the soil loss is most sensitive to the presence of the vegetation cover. This is in agreement with what is reported in the literature (Elwell, 1981; Foster, 1982; Johns 1983; Eldridge and Rothon, 1992; and Morgan, 1995). In this study the vegetation cover was derived with an RMSE of 12.21% and this high accuracy was manifested in the results of the model.

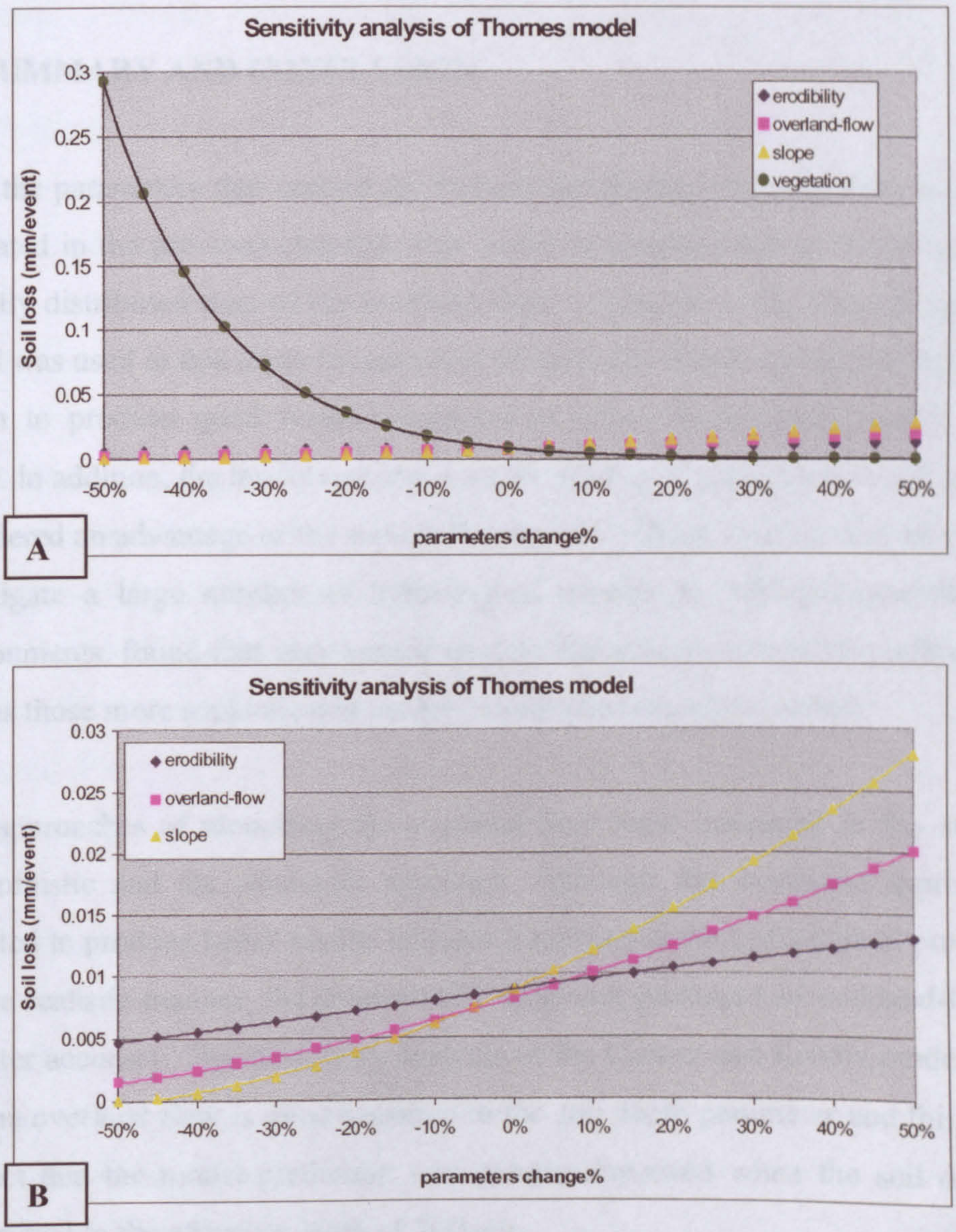

Figure 7.25. The sensitivity analysis of the Thornes soil-erosion model. A) is for all model parameters and B) is for parameters excluding the vegetation cover for illustration purposes.

The figure 7.25-A was re-produced after excluding the vegetation cover so that the effect of the other parameters on the soil loss can be analysed. The figure 7.25-B shows that the slope also has a significant effect on the rates of soil erosion. The combination of a steep slope and the absence of vegetation has a devastating effect on the soil resources and this explains the problem of ploughing steep slopes and the advantage of terracing the lands of agricultural activities.

7.5 SUMMARY AND CONCLUSION

After the parameters that control the Carson and Kirkby overland-flow model were generated in the previous chapters, this model is implemented in this chapter and a spatially distributed map of the overland flow is generated. The Carson and Kirkby model was used in this study because it is of spatially distributed nature and has been shown to produce good results compared to other hydrological models (Zhang, 1999). In addition, the model requires a small number of parameters to run and this is considered an advantage of the model. Perrin *et al.* (2001), who carried out a study to investigate a large number of hydrological models in different catchments and environments, found that very simple models can achieve a level of performance as high as those more sophisticated models which need more parameters.

Two approaches of modelling the overland flow were compared in this study, the deterministic and the stochastic approach. Although the stochastic approach was expected to produce better results because it represents the hydrological processes in a more realistic manner, the deterministic approach produced an overland-flow map of better accuracy. The sensitivity analysis of the Carson and Kirkby model showed that the overland flow is most sensitive to the soil depth parameter and this explains the fact that the model prediction was greatly improved when the soil depth was constrained to the effective depth of 300 mm.

The maps of the various soil properties were constructed in this study based on the principle of the hydrological response units due to the fact that the other continuous

methods of correlations and geostatistical analysis were not successful in mapping soil properties. This method of mapping introduces interpolation errors and these errors were assessed. It was found that the hydrological response units introduced a small error in the overland-flow mapping equivalent to an RMSE of 8.2 mm out of the 124 mm of the simulated rainfall. This means that the hydrological response units provide a successful tool in hydrological modelling. The usefulness of the approach could be due to the fact that the map was so detailed it incorporated a large degree of the spatial variability.

Despite the presence of various sources of errors in the parameters that control the soil-erosion model, it produced quite accurate predictions of soil loss in comparison to other soil-erosion results reported in the literature. Despite their acceptable accuracy, these quantitative results should be interpreted with cautions. This is due to the fact that the quantitative estimates of soil loss are problematic to model because of the complexity of the hydrological processes governing soil erosion (Mitasova *et al.*, 1998). For example, Bjorneberg *et al.*, (1997) implemented the WEPP soil-erosion model to predict the soil loss and they reported soil loss predictions of 2 tonne/hectare when measured soil loss was less than 0.05 tonne/hectare. Such studies indicate that closer correspondence between experiments and soil-erosion models is needed to further the understanding of the inherent complexity of the hydrological processes of soil erosion and to improve the quantitative prediction of soil-erosion models.

The sensitivity analysis of the soil-erosion model revealed that the soil loss prediction in this model is most sensitive to the vegetation cover and an exponential relationship exists between the vegetation cover and the soil loss where the soil loss increases dramatically as the vegetation cover decreases. This exponential relationship becomes steeper as the vegetation cover becomes sparse. This finding is supported by a large number of soil-erosion studies which show the importance of the vegetation cover to combat the soil erosion. The sensitivity analysis also stressed the significance of the slope factor on the soil loss where the soil loss increases in a non-linear relationship with the increase of the topographic factor of slope. The role

of slope in increasing soil erosion highlights the usefulness of terracing in agricultural areas as a means of reducing the risk of soil erosion.

The effect of ploughing on increasing the risk of soil erosion in the study area has been assessed in this study. Although the ploughing deepens the soil and loosens the soil particles which increases the infiltration and decreases the overland-flow generation, ploughing causes the destruction of the vegetation cover which has a greater impact on the soil loss. This assessment shows that ploughing the land to prepare it for almond and olive plantations may increases the soil loss rapidly which may mount to an increase of as much as 500%.

In summary GIS is shown to be an effective tool to implement spatially distributed Carson and Kirkby overland flow and Thornes soil-erosion models. The overland-flow and soil-erosion maps produced using GIS tools give a comprehensive picture of the hydrological processes and conditions in the study area as well as the capacity to analyse the between-site variations and effects of hydrological properties. In addition, the successful use of remote sensing to parameterise the soil-erosion model has been demonstrated in this chapter where the accuracy of the resultant soil-erosion map was high. The implementation of remote sensing has an advantage over the traditional data collection systems in providing a spatially distributed map of the risk of soil erosion which can be a great benefit for the decision makers to tackle areas that are most in need for preservation.

CHAPTER 8

CONCLUSIONS AND FURTHER WORK

8.1 INTRODUCTION
8.2 DISCUSSION OF THE OUTCOMES OF THIS STUDY
8.3 SUGGESTIONS FOR FURTHER WORK

8.1 INTRODUCTION

This chapter summarises the potential and applicability of the high spatial resolution remote sensing and Geographical Information Systems (GIS) for automating, as much as possible, the parameterisation of soil-erosion modelling at the field scale. The automation of modelling soil erosion is important because it speeds up the modelling of the soil loss at lower cost and time as it requires less labour. The results of this study are discussed within the scope of the aims and objectives set at the beginning of this study and conclusive remarks are drawn. Then the work that is needed to further the aims and objectives of this study is discussed and suggestions are made for the improvement of soil-erosion modelling.

8.2 DISCUSSION OF THE OUTCOMES OF THIS STUDY

Soil erosion is a complex phenomenon and is controlled by a number of natural and human-induced processes such as rainfall regime, soil physical properties, vegetation cover, topographic characteristics of the landscape, and the land use (De Jong, 1994). When these processes are accelerated, the soil erosion becomes a serious problem and conservation measures are required to be implemented for sustainable land-use before the soil condition reaches an irreversible stage. The need to maintain sustainable land use requires that soil conditions are monitored so that the soil-erosion problem may be addressed in the early stages. In addition, another benefit of the soil-erosion modelling is that it helps in assessing the effectiveness of the conservation measures taken to control this problem. However, the large degree of

spatial and temporal variability of the factors controlling the soil-erosion processes (e.g. vegetation cover and soil type) makes it unfeasible and impractical to collect field samples to represent the attributes of these factors. Thus, the alternative method of remote sensing, as a data collection system, was investigated for this purpose and the focus was on the high spatial resolution data.

The aim of this study was to investigate the potential of using aerial photography and Geographical Information Systems (GIS) to parameterise spatially-distributed soil-erosion models at the field scale. In this study we investigated the potential use of Natural Environment Research Council (NERC) true colour aerial photographs, which are characterised by a spatial resolution of 0.55 metre, as a data collection system for the automation of extracting soil-erosion parameters and for the implementation of a spatial soil-erosion model. The launch of the new generation of high spatial resolution satellites, such as IKONOS of Space Imaging and PAN/MS of Quickbird with 1 metre spatial resolution, means that the methodology developed in this study can be used anywhere on the globe.

A wide range of soil-erosion models, including models of an empirical nature, process-based models, and models that are characterised by a combination of both types, have been reviewed and analysed in chapter 3. Amongst these models Thornes (1985) soil-erosion model was selected to estimate the soil loss because it is relatively easy to parameterise, it needs a limited number of parameters, and it can be implemented in a GIS environment which facilitates the integration of all the parameters controlling the soil erosion. One of the significant inputs in Thornes model is overland flow and this also needed to be modelled, thus, it is necessary to select a suitable overland-flow model for this purpose. A range of the available hydrological overland-flow models, both empirical and process-based, were reviewed and analysed in chapter 3, with a special emphasis on their spatial distribution capabilities. The Carson and Kirkby overland-flow model was selected because this model produced the best average estimate of overland flow and the lowest average relative error amongst a number of models used in a comparative study carried out by Zhang (1999) in the study area. In addition, the Carson and

Kirkby model has another advantage that satisfies the prior conditions of this study such as the temporal scale of a rainfall event and the possibility of implementing it in a GIS environment.

In chapter 4 the methodologies of surveying and the Global Positioning Systems (GPS), which were used in the fieldwork, were reviewed. The co-ordinates of the soil samples locations and the Ground Control Points (GCPs), that are needed to geometrically correct the imagery and to extract the Digital Elevation Model (DEM), were calculated from these data. Slope is one of the main controlling parameters of the soil loss in Thornes soil-erosion model, where the soil loss increases dramatically as a function of the increasing slope. This is because topography defines the effects of gravity on the movement of water and sediments in a catchment. Thus, slope needs to be calculated in a spatially distributed manner. To do so the DEM was first created from the aerial photographs by implementing the digital photogrammetry techniques using the ERDAS Imagine OrthoMAX. From this resultant DEM the slope map was derived using the slope algorithm in ERDAS Imagine.

It has been shown in chapter 5 that vegetation cover plays an important protective role in soil-erosion processes. This includes the interception of raindrops to protect the underlying soils against rainsplash, as well as the improvement of soil structure and increasing the soil infiltration capacity and water storage capacity of the soils (De Jong, 1994). Due to the important role of the vegetation cover, various methods have been investigated to map it from remotely sensed data. Potential methods include (but are not restricted to) the vegetation indices, the red band reflectance, and the mixture modelling method. Since the majority of the vegetation indices are based on the relationship between the reflectance in the red and the near infrared parts of the spectrum, they could not be implemented in this study because the aerial photographs consist only of the three visible bands. The investigation of the red band reflectance method to map the vegetation cover showed that a significant linear relationship, of a negative nature, exists between the red band digital numbers of the aerial photograph and the abundance of vegetation cover ($r^2 = 0.81$). However, due

the fact that 88% of the field verification data fall in areas of grey soil, the influence of the red soil on this relationship could not be assessed.

The other method that was investigated to map the vegetation cover was the mixture modelling. However, the most difficult step in mixture modelling lies in the selection of spectral endmembers because they may be time-dependent and may have different spectral responses at different times of the same location. Various methodologies of endmember selection were reviewed in this study and the method of Principal Component Analysis (PCA) was selected because of it is simple to use and it does not need atmospheric and radiometric corrections. The implementation of the mixture modelling method resulted in four fraction maps representing grey soil, red soil, vegetation cover, and shade.

The strength of linear mixture modelling to map vegetation cover has been demonstrated in this study. It was possible to overcome the problem of shade cast by the vegetation bushes and trees on other vegetation (but not shade cast by topography which was not addressed in this study). This was done by extracting shade as a separate component, which was then used to create a shade-free vegetation map using a shade removal algorithm proposed by Smith *et al.*, (1990). The vegetation cover map was underestimated before it was re-scaled using the shade map, however, re-scaling increased the coefficient of determination from 0.79 to 0.91 and the RMS Error declined from 18.3% to 10.7%. The mixture modelling and shade-removal processes resulted in a few isolated pixels of zero vegetation values where the vegetation cover is expected to be high. Correcting the vegetation information in these pixels is critical because the soil-erosion model is very sensitive to vegetation abundance and zero vegetation value will wrongfully result in high prediction of soil loss in these pixels. To overcome this problem a co-occurrence matrix image segmentation method was implemented and those pixels were isolated and filled with the appropriate vegetation information.

The important effect of the land-use type on the conditions of soils and natural vegetation, and consequently on the soil erosion, has also been reviewed in chapter 5.

Thus, mapping the land use was necessary. Since the aim of this study was to automate the processes of soil-erosion modelling, the potential of maximum likelihood classification to map the land use was investigated. Two different approaches were investigated: the equal prior probability and defined prior probability. Although the first approach proved to produce slightly more accurate results, it has been shown that both approaches lead to problems of misclassifications and a high level errors as a result of the high level of internal variability in the land-use classes at the 0.55 metre spatial resolution. This internal variability led to a problem of multimodal populations in most of the land-use classes and this violated the central assumption of normality in the maximum likelihood classifier.

In the classification of the land use, shade was treated as a land-cover type due to its common presence in a large number of pixels in the aerial photograph. However, in reality the areas that are covered by shade belong to a land-cover type that is obscured by shade. This was another source of errors in the land-use mapping. As a result of these errors and the low accuracy of the resultant land-use map, this automated method of the land-use mapping was dropped and the method of image interpretation was implemented. This method proved to be more accurate, however, the drawback is the fact that it is a manual method and is both labour intensive and time consuming.

The importance of soil mapping in soil-erosion modelling was discussed in chapter 6. Soil texture, structure, depth, bulk density and organic matter content, have great effects and control over the overland-flow generation and the soil resistance to erosion. Since the scale of the published soil maps of the study area is too coarse for the purpose of this study and the accuracy of soil properties in these maps is low, mixture modelling was implemented to map grey and red soils from the aerial photographs. The aerial photographs have the ability to map soil types in a spatially distributed manner at high spatial resolution. A binary soil map was produced from the mixture modelling soil maps so that it can be used to spatially distribute the soil properties. The resultant soil map was validated against the soil field data giving a satisfactory accuracy of 85.6%.

In order to distribute the soil properties spatially over the study area, the underlying distributions of these properties in the sub-samples that correspond to various soil and land-use types were statistically analysed and tested for normality so that parametric statistical techniques can be applied. It was found that some of the soil properties are normally distributed, whereas others departed from normality and the square-root transformation was applied so that they approximated normality.

Three methods of soil-property mapping were then investigated. The first method was to investigate the correlation between the soil properties and the soil fractions derived from the mixture modelling so that these fractions can be used to spatially distribute the soil properties using regression. This method showed that no significant correlation exists between the great majority of soil properties and the soil fractions, whether the land-use effect was considered or neglected. The second method was the implementation of the geostatistical techniques of cokriging where the fractional soil maps resulted from the mixture modelling were used as the secondary variable. The resultant interpolated soil property maps indicated large errors in the interpolation process where extreme negative and greater than 100% values were common in these maps. This could be attributed to the very small size of soil samples which was well below the recommended size and resulted in a poor semivariogram.

The third method of soil properties mapping was the implementation of the hydrological response units approach. Four hydrologically distinctive classes were observed in the study area, these are grey soil matorral, red soil matorral, agriculture grey soil, and agriculture red soil. The ANOVA test showed that soil properties, with the exception of sand, are significantly different in the four classes. Thus, the hydrological response units map was used to spatially distribute the soil properties over the study area.

In order to validate the results of the overland-flow and soil-erosion models, a rainfall simulation was carried out in the study area by Zhang (1999) in nine different

plots at locations with a range of soil types, vegetation covers and slopes. These plots included areas of almond and olive plantation, a newly ploughed hillslope, an overgrazed area of matorral, and an area of burnt matorral. Samples of rainfall excess and eroded soil were collected for total rainfall duration of 30 minutes and these samples are used for the purpose of validation.

In order to calculate the hydrological parameter in the Thornes soil-erosion model, the rainfall, water storage capacity (r_c), and initial soil moisture (Q_{iT}) were integrated in chapter 8 using the Carson and Kirkby overland-flow equation in an IDRISI GIS environment. Two approaches were considered in the overland-flow modelling: deterministic and stochastic. The internal variability of the soil properties is ignored in the first approach and taken into account in the second approach. The stochastic approach produced poorer estimation of the overland flow than the deterministic approach and, thus, the latter results were used in the soil-erosion model.

In addition, it was shown in this study that constraining the soil depth, which greatly affects the water storage capacity and the initial soil moisture, to an effective depth of 300 mm improved the calculation of the overland flow substantially from $r^2 = 0.59$ and RMSE = 37.4 mm to $r^2 = 0.66$ and RMSE = 26.3 mm. These results are regarded as satisfactory in comparison to the results reported in the literature of hydrological modelling (Scoging *et al.*, 1992; Grayson *et al.*, 1992; Sardo *et al.*, 1994; and Perrin *et al.*, 2001).

The soil loss in the Thornes model is controlled by four parameters: soil erodibility, overland flow, slope, and the vegetation cover. Due to the lack of a clear method to calculate the soil erodibility in this model, Wischmeier's equation was implemented for this purpose and then the erodibility factor was adjusted to accommodate the imbalance of the units in the Thornes soil loss equation. The parameters of the Thornes model were then integrated in an IDRISI GIS environment and the soil loss map was produced. The qualitative visual assessment of this map revealed a successful result where the highest soil loss occurs in areas that have combinations of some or all the factors of steep slope, unploughed soil which is associated with

higher runoff, and little or no vegetation cover. However, the minimum soil loss occurs in areas that are either covered with dense vegetation cover or characterised by gentle slopes or flat land. The quantitative assessment of the accuracy of the soil-erosion map showed an accuracy of 0.058 mm RMSE (equal to 65% in relative terms) when it was compared to the results reported in the literature of soil-erosion modelling (Morgan *et al.*, 1984; Morgan, 1995; Walling, 1996; and Jetten *et al.*, 1999)

The effect of the land-use change, as a result of ploughing the land for almond plantation, on the acceleration of soil-erosion rates was also assessed. This assessment revealed that ploughing the land to prepare it for agricultural activities might raise the risk of soil loss by up to 500%. However, it was also shown that ploughing might reduce the soil loss under certain circumstances in areas that are characterised by very gentle slopes and very low vegetation cover. Such areas are minimally affected by the removal of the vegetation cover and the ploughing process leads to higher infiltration rates and lower overland flow and this, consequently, leads to lower soil loss.

An overall assessment of the results and findings of this study is necessary in order to arrive at the facts whether the study fulfilled the aim and objectives set at the initial stage of the work. It was shown in this study that very high spatial resolution imagery is a valuable source of data at the field scale for soil-erosion study in semiarid environment. This is due the ability of such imagery to map topography at finer resolution and to express the heterogeneity nature of vegetation and soils which change at very short distances. This heterogeneity is largely suppressed in semiarid environment by lower resolution remotely sensed data. In addition, the automation of soil-erosion modelling was successful to a large extent where models were parameterised using remotely sensed data and a limited field data set. The exception for this automation was land use/land cover mapping where image classification techniques investigated in this study did not produce acceptable results and the map was created manually.

Mapping the soil properties in this study revealed that producing more accurate and continuous maps is more data demanding and, although produced errors, the use of a discrete units method was acceptable for the purpose of this study. However, automating soil properties mapping was not fulfilled and, thus, further work is needed. Furthermore, the use of GIS to create, collate and integrate various data sets and to implement the overland-flow and soil-erosion models was successful and facilitate spatially-distributed modelling.

8.3 SUGGESTIONS FOR FURTHER WORK

The potential of using the high spatial resolution remotely sensed data and GIS has been demonstrated in this study for implementing a spatially a distributed soil-erosion model at the local scale. A number of parameters, that control the soil erosion, can be derived and mapped from the high spatial resolution imagery. However, a number of limitations were faced in this study and further work is needed to improve the accuracy of the model results and to refine some of the automation procedures.

The linear mixture modelling methodology was applied to the remotely sensed imagery and produced vegetation cover and a soil maps of satisfactory accuracy, proving to be an effective way of mapping land-cover components. However, it has been shown in this study that one of the problems of the implementation of linear mixture modelling is determining the number of end members, alongside their spectral responses, in a remotely-sensed image under investigation that will be included in the process of spectral unmixing. Roberts *et al.* (1994) found that with a fewer number of endmembers the process of mixture modelling is better performed and that a maximum of two or three endmembers produce the best results and larger number of endmembers can produce instability and less accuracy of ground-cover estimation.

To overcome the problem of including large number of endmembers to find a best solution of mixture modelling, Roberts *et al.* (1998) proposed a new method. In this

method not all endmembers are considered to find the best fit solution for all pixels, rather, the best fit solution starts by considering two endmembers for the mixture modelling. Pixels that result in large residuals are re-modelled by considering a combination of three endmembers and the same procedures continue until all endmembers are used and best fit is found for all pixels (Ustin *et al.*, 1999). With the availability of infrared bands in the new remote sensing sensors such as IKONOS and Quickbird, which is advantageous over the aerial photographs of the visible bands in this study, the proposed method of Roberts *et al.* (1998) may produce more accurate mapping of vegetation cover and soils.

In this study the hydrological response units approach was implemented in order to spatially distribute the soil properties over the study area due to the fact that the geostatistical approach of cokriging produced poor results. However, it has been shown that these poor results are mainly a consequence of the limited number of the soil samples (37 samples) whereas the minimum number of the data points that is recommended by Webster and Oliver (1992) to produce acceptable results is 100 samples. The limitation of the number of soil samples collected in the study area was due to financial and time constraints where these 37 samples took two weeks to collect and one month to analyse in the laboratory. Thus, more fieldwork is recommended as a follow-up in this study in order to collect more soil data so that the cokriging method can be applied to produce spatially continuous maps of the various soil properties. Since the overland-flow generation and soil loss are sensitive to spatial variability, spatially distributed soil properties have potential to produce a more accurate soil-loss map.

The process of soil erosion has been regarded in this study as a discrete process that occurs in each pixel in isolation from the surrounding pixels. In addition, only interrill soil erosion was taken into consideration. However, in reality the process of soil erosion should be regarded as a continuous hydrological process across all the hillslope from the top to the bottom, as well as from interrill, rill, to gully where an interaction between the erosion, transport and sediment deposition exits in all these processes. Thus, the routing of sediment and overland flow should be considered and

further study should be carried out to evaluate the effect of routing on the results of the soil-erosion modelling.

One of the factors that has an effect on the overland-flow generation and soil loss and yet ignored in this study is the stone cover. In the Mediterranean region, soils are rich in stone cover which dominates more than 60% of the land surface (Poesen *et al.* 1990). Stone cover was not regarded in the process of mapping the soil erosion due to the lack of data that describe this factor and due to the fact that selected soil-erosion model does not incorporate the stone cover in its mathematical equation. Thus, it is important to consider the effects of stone cover on the overland flow and soil loss in a further study by investigating various methodologies to map the stone cover and to include its effect in mapping the soil loss.

In this study an attempt was made to investigate the rates of soil loss under various land-use types. However, it was not possible to assess the effect of overgrazing on the soil-erosion rates because the overgrazing region was excluded from the study area due to limitations in the spatial extent of the DEM and, consequently, in the slope map as was explained in chapter 7. In order to investigate this effect, further topographic data describing the slope of the overgrazed region is needed so that soil erosion can be predicted in this region using Thornes model and the results can then be compared to the measured soil loss in the rainfall-simulation plots located in that overgrazed area.

One of the limitations of the Thornes soil-erosion model that has been realised in this study is the calculation of the soil erodibility K which proved to be not straightforward in this model. This could be attributed to the fact that little fieldwork has been done on the determination of soil erodibility factor in the model (Zhang, 1999). However, many different factors control the soil erodibility with different magnitude such as soil texture, soil structure and organic matter which makes it more difficult to measure accurately. In order to improve the accuracy of the soil loss results in Thornes model, further studies should be carried out to investigate alternative techniques for the calculation of soil erodibility in this model.

BIBLIOGRAPHY

Abrahams, A. D., Parsons, A. J. and Hirsch, P. J. 1992. Field and laboratory studies of resistance to interrill overland flow on semi-arid hillslopes, southern arizona. In: Anthony J. Parsons & Athol D. Abraham (eds.). Overland flow, hydraulics and erosion mechanics. University College London Press Limited. London.

Adams, J. B., Sabol, D. E., Kapos, V., Almeida, R., Roberts, D. A., Smith, M. O., and Gillespie, A. R. 1995. Classification of multispectral images based on fractions of endmembers - application to land-cover change in the brazilian amazon. Remote Sensing of Environment, 52 (2): 137-154.

Ager, C. M. and Milton, N. M. 1987. Spectral reflectance of lichens and their effects on the reflectance of rock substrates. Geophysics, 52, 898-906.

Anderson, M. G. and Burt, T. P. 1985. Modelling strategies. In: Anderson, M. G. and Burt, T. P. (eds.), Hydrological forecasting, John Wiley and Sons. Chichester.

Anthony J. Parsons & Athol D. Abraham 1992. Overland flow, hydraulics and erosion mechanics. University College London Press Limited. London.

Aplin, P., Atkinson, P. M., and Curran, P. J. 1999. Fine spatial resolution simulated satellite sensor imagery for land cover mapping in the UK. Remote Sensing of Environment, 68: 206-216.

Asner, G. P., and Lobell, D. B. 2000. A biogeophysical approach for automated SWIR unmixing of soils and vegetation. Remote Sensing of Environment, 74: 99-112.

Auberville, A. 1949. Climats, Forêts et Dédertification de l'Afrique Tropicale. Soc d' É ditions Géographiques et Coloniales, Paris, Pp 352.

Auzet, A, V., Boiffin, J., Ludwig, B. and Guerif, J. 1998. Effects of agriculture land use on spatial and tempo. distribution of soil erosion in small catchments: implications for modelling. In: Boardman, J. and Favis-Mortlock, D. (eds.). Modelling soil erosion by water. Springer-Verlag, Berlin.

Band, L. E. 1986. Topographic partition of watersheds with digital elevation models. Water Resources Research, 22:15-24.

Band, L. E., and Moore, I. D. 1995. Scale: landscape attributes and geographic information systems. Hydrological processes: 9, 401-422.

Bannister, A. and Raymond, S. 1984. Surveying (5th edition). Longman Scientific & Technical, Harlow.

Bannister, A. and Baker, R. 1991. Solving problems in surveying. Longman Scientific & Technical, Harlow. 70-134.

Barnsley, M. J., and Barr, S. L. 1996. Inferring urban landuse from satellite sensor images using kernel-based spatial reclassification. Photogram. Eng. and Remote Sensing, 62(8): 949-58.

Barrow, C. J. 1991. Land degradation. development and breakdown of terrestrial environments. Cambridge, Cambridge University Press.

Bastin, L. 1997. Comparison of fuzzy c-means classification, linear mixture modelling and mlc probabilities as tools for unmixing coarse pixels. International Journal of Remote Sensing, 18(17): 3629-3648.

Bateson, A. and Curtiss, B. 1996. A method for manual endmember selection and spectral unmixing. Remote Sensing of Environment, 55 (3): 229-243.

Bateson, C. A., Asner, G. P., and Wessman, C. A. 2000. Endmember bundles: a new approach to incorporating endmembers variability in spectral mixture analysis. IEEE Trans. Geosci. Remote Sensing, 38: 1083-1094.

Baumgardner, M. F., Silva, L. F., Biehl, L. L. and Stoner, E. R. 1985. Reflectance properties of soils. Adv. Agron., 38, 1-44.

Beasley, D. B., Huggins, L. F. and Monke, E. J. 1980. ANSWERS: a model for watershed planning. Transactions of the American Society of Agricultural Enginners, 23: 938-944.

Ben-Dor, E., Irons, J. R. and Epema, G. F. 1999. Soil reflectance. In: Rencz, A. N (ed.), Remote sensing for the earth sciences, manual of remote sensing (3rd ed.). John Wiley & Sons, Inc, New York, pp 112.

Bennett, H. H. 1939. Soil conservation. McGraw-Hill, New York.

Beven, K. J. and Kirkby, M. J. 1979. A physically based, variable contributing area model of basin hydrology. Hydrological Sciences Bulletin, 24(1):43-69.

Bjorneberg, D. L., Aase, J.K., and Trout, T.J. 1997. WEPP model erosion evaluation under furrow irrigation. Paper no. 972115, 1997 ASAE Ann. Int. Meeting, Minneapolis, MI.

Bingner, R. L., Murphee, C. E., and Mutcher, C. K. 1989. comparison of sediment yield models on watersheds in Mississippi. Trans. of the American Society of Agricultural Engineers, 32, 529-534.

Binley, A. and Beven, K. 1993. Three dimensional modelling of hillslope hydrology. In: Moor, I. D., and Beven, K. J. (eds.) ' Terrain analysis and distributed modelling in hydrology, John Wiley & Sons, England. P 107-119.

Blake, G. R. and Hartge, K. H. 1986. The Bulk density. In: Klute, A. (ed.). Methods of soil analysis (part 1), physical and mineralogical methods. American Society of Agronomy, Inc and Soil Science Society of America, Inc. Madison, Wisconsin USA.

Boardman, J. W. 1992. Spectral Angle Mapping. Unpublished manuscript.

Boardman, J. W. 1993. Automating linear mixture analysis of imaging spectrometry data. Proceedings International Symposium on Spectral Sensing Research, 94. 302-309.

Boardman, J. W. 1994. Geometric mixture analysis of imaging spectrometry data. In: Proc. IEEE Int. Geosci. And Remote Sensing Symp, 1994. IEEE, New York, 2369-2371.

Bock, Y. 1998. Reference systems. In: Teunissen, P. J. G., and Kleusberg, A. (eds.). GPS for geodesy. Springer-Verlag Berlin Heideleberg. Germany.

Bolle, H. 1999. Impact of climate variability on desertification processes. In: Balabanis, P., Peter, D. and Ghazi, M. (eds.). Mediterranean desertification research results and policy implications, Proceedings of The International Conference 29 Oct-1 Nov 1999, Greece. European Commission.

Borel, C. C., and Gerstl, S. W. A. 1994. Non-linear spectral mixing models for vegetative and soil surfaces. Remote Sensing of Environment, 47, 403-416.

Brady, N. C. 1990. The nature and the properties of soils. Macmillan Company, London.

Bridges, E. M. and Oldeman, L. R. 1999. Global assessment of human-induced soil degradation. Arid Soil Research And Rehabilitation, 13: (4) 319-325.

Brayman, A. and Cramer, C. 1999. Quantitative data analysis with SPSS release 8 for windows: a guide for social scientists. London and New York: Routledge. Pp 99-103.

Brejda, J. J., Moorman, T. B., Smith, J. L., Karlen, D. L., and Dao, T. H. 2000. Distribution and variability of surface soil properties at a regional scale. Soil Sci. Soc. Am. J. 64:974-982.

Bridges, E. M. and Oldeman, L. R. 1999. Global assessment of human-induced soil degradation. Arid Soil Research and Rehabilitation, 13:319-325.

Brown, M., Lewis, H. G. and Gunn, S. R. 2000. Linear spectral mixture models and support vector machines for remote sensing. IEEE Transactions on Geoscience and Remo. Sens.. 38:(5) 2346-60.

Bryan, R .B. 1968. The development, use and efficiency of indices of soil erodibility. Geoderma, 2:5-26.

Bryan, R. and Yair, A. 1982. Perspectives on studies of badland geomorphology. In: Bryan, R. and Yair, A (eds.). Badland geomorphology and piping. Norwich, Geo Books: 1-12.

Bryan, R. B. ed. 1987. Rill erosion: processes and significance. Catena Supplement. 8.

Buckman, H. O. & Brady, N. C. 1971. The nature and properties of soil. McMillan Company. London.

Burrough, P. A., 1990. Principles of geographical information systems for land resources assessment. Oxford, Clarendon.

Burt, J. E. and Barber, G. M. 1996. Elementary statistics for geographers (2nd edition). London and New York. Guilford Press. Pp 215-219.

Byers, B. A., 1997. Environmental threats and opportunities in Namibia: A comprehensive assessment. Department of Environmental Affairs, Windhoek, Namibia.

Carson, M. A. and Kirkby, M. J. 1972. Hillslope form and process. Cambridge, Cambridge Uni. Press.

Caulfield, F., Britz, S. J., and Bunce, H. A. 1992. Shade spectral quality and the photosynthetic capacity of soybean leaves. Photosynthetica, 26: 555-568.

Chandler, J. H. and Moore, R. 1989. Analytical photogrammetry: a method for monitoring slope instability. Quarterly Journal of Engineering Geology, 22. Pp. 97-110.

Chappell, N. and Ternan, L. 1993. Flow path dimensionality and hydrological modelling. In: Moor, I. D., and Beven, K. J. (eds.) Terrain analysis and distributed modelling in hydrology. John Wiley & Sons, England. 121-139.

Chavez, P. S. Jr., and MacKinnon, D. J. 1994. Automatic detection of vegetation change in the south western United States using remotely sensed images. Photogram. Eng. & Remote Sens. 60:571-83.

Chen, J.M., and Leblanc, S. G. 2001. Multiple-scattering scheme useful for geometric optical modeling. IEEE Transactions on Geoscience and Remote Sensing, 39 (5): 1061-1071.

Cherchali, S., Amram, O., and Flouzat, G. 2000. Retrieval of temporal profiles of reflectances from simulated and real NOAA-AVHRR data over heterogeneous landscapes, Int. J. Remote Sensing, 21:753-775.

Chorley, R .J. 1959. The geomorphic significance of some Oxford soils. American Journal of Science, 257:503-515.

Clark, R. N. 1999. Spectroscopy of rocks and minerals, and principles of spectroscopy. In: Rencz, A. N (ed.), remote sensing for the earth sciences, manual of remote sensing (3rd ed.). John Wiley & Sons, Inc, New York, pp 7.

Conacher, A. J. and Sala, M. 1998. The cause of land degradation 2. In: Conacher, A. J. and Sala, M. (eds.). Land degradation in Mediterranean environments of the world.: nature and extent, causes and solutions. John Wiley and Sons, Ltd, Chechester, UK. Pp. 285-307.

Cooper, D. M., and Naden, P. S. 1998. Approaches to delivery modelling in LOIS. Science of The Total Environment, 210 (1-6): 483-498.

Costa-Cabral, M. C., and Burges, S. J. 1994. Digital elevation model networks (DEMON): A model of flow over hillslopes for computation of contributing and dispersal areas. Water Resources Research, 30(6), 1681-1692.

Curran, P. J., and Hay, A. M. 1986. The importance of measurement error for certain procedures in remote-sensing at optical wavelengths. Photogrammetric Engineering and Remote Sensing, 52 (2): 229-241.

Da Costa. 1979. Surface soil color and reflectance as related to physio-chemical and mineralogical soil properties. PhD dissertation, University of Missouri, Colombia.

Datt, B. 1999. Visible/near infrared reflectance and chlorophyll content in Eucalyptus leaves. Int. J. Remote Sensing, 20 (14): 2741-59.

Daugherty, R. 1978. Science in geography, data collection. Oxford University Press.

Daughtry, C. S. T., and Walthall, C. L. 1998. Spectral discrimination of cannabis sativa L. leaves and canopies. Remote Sensing Environment, 33:55-64.

Davies, J. C. 1986. Statistics and data analysis in geology. 2nd edition. John Wiley & Sons, Canada.

De Jong, S.M, 1994. Application of reflective remote sensing for land degradation studies in a mediterranean environment. Utrecht University, Netherlands.

De Lima, J. L. M. P. 1992. Model KININF for overland flow on pervious surfaces. In: Anthony J. Parsons & Athol D. Abraham (eds.). Overland flow, hydraulics and erosion mechanics. University College London Press Limited. London.

Del Valle, H. F., Elissalde, N. O., Gagliardini, D. A., and Milovich. J. 1998. Status of desertification in the Patagonian region: Assessment and mapping from satellite imagery. Arid Soil Research and Rehabilitation, 12: (2) 95-121 APR-JUN 1998

De Ploey, J. 1989. A model for headcut retreat in rills and gullies. Catena Supplement 14: 81-86.

De Roo, A. P. J., Hazelhoff, L. and Burrough, P. A. 1989. Soil erosion modelling using ANSWERS and GIS. Earth Surface Processes and Landforms, 14, 517-532.

De Roo, A. P. J. 1993. Modelling surface runoff and soil erosion in catchments using GIS. Validity and applicability of ANSWERS model in two catchments in the Loess area of South Limburg (The Netherlands) and one in Devon (UK). Nederlandse Geografische Studies No. 157.

Dietrich, W. E., Wilson, C. J., Montgomery, D. R. and McKean, J. 1993. Analyses of erosion thresholds, channel networks and landscape morphology using a digital terrain model. Journal of Geology, 101, 259-278.

Douglas, T., Kirkby, S. J., Critchley, R. W. and Park, G. J. 1994. Agricultural terrace abandonment in the Alpujarra, Andalucia, Spain. Land Degradation and Rehabilitation 5: 280-291.

Drake, N.A., 1991. Mapping rocks, soil, vegetation communities and vegetation density with the GERIS using linear mixture modelling and post-processing techniques. Earsel Advances in Remote Sensing, 1(1): 48-57.

Drake, N.A., Vafeidis, A., Wainwright, J. and Zhang, X. 1995. Modelling soil erosion using remote sensing and GIS techniques. In proceedings of the 21st Annual Conference of the Remote Sensing Society: RSS'95 Remote Sensing in Action, Southampton, p217-224.

Drake, N. A., Zhang, X., Berkhout, E., Bonifacio, R., Grimes, D., Wainwright, J., and Mulligan, M. 1997. Modelling Soil Erosion at Global and Regional Scales Using Remote Sensing and GIS Techniques. In: Atkinson, P. (ed.), Spatial Analysis for Remote Sensing and GIS, Wiley & Sons, Chechester.

Drake, N., Mackin, S., and Settle, J. J. 1999. Mapping vegetation, soils, and geology in semiarid shrublands using spectral matching and mixture modelling of SWIR AVIRIS imagery. Remote Sensing of Environment 68: 12-25.

Dregne, H. E. 1983. Desertification of Arid Lands, Harwood Academic Publishers, Chur, London, Paris, New York. Pp 242.

Dregne. H. E. and Tucker, C. J. 1988. Desert encroachment. Desertification Control Bulletin, Nairobi, Kenya, 16:16-19.

D'Souza, V. P. C. and Morgan, R. P. C. 1976. A laboratory study of the effect of slope steepness and curvature on soil erosion. Journal of Agricultural Engineering Research 21: 21-31.

Dudal, R. 1981. An evaluation of conservation needs. In: Morgan, R.P.C. (ed.), Soil conservation: Problem and prospects. John Wiley & Sons, Chichester.

Dunne, T. and Aubry, B. F. 1986. Evaluation for Horton's theory of sheetwash and rill erosion on the basis of field experiments. In: Abrahams, A. D (ed.), Hillslope Processes. London, Allen and Unwin: 31-55.

Dwivedi, R. S., Ravi Sankar, T., Venkataratam, L., Karle, R. L., Gawande, S. P., Seshagiri Rao, K. V., Senchaudhary, S. and Bhaumik, K. R. 1997. The inventory and monitoring of eroded lands using remote sensing data. International Journal of Remote Sensing. Vol. 18, No. 1, 107-119.

Eastman, J. R, 1997. IDRISI for Windows User's Guide, Version 2. Clarks Labs for Cartographic Technology and Geographic Analysis. Clark University. USA.

Ekwue, E. I. 1990. Effect of organic matter on splash detachment and the processes involved. Earth Surface Processes and Landforms 15: 175-81.

Eldridge, D, J. and Rothon, J. 1992. Runoff and sediment yield from a semi-arid woodland in eastern Australia.1. The effect of pasture type. The Rangeland Journal, 14, 26-39.

Elvidge, C. D. 1990. Visible and near infrared reflectance characteristics of dry plant materials. International Journal of Remote Sensing. Vol. 11, No. 10:1775-1795.

Elwell, H. A. and Stocking, M. A. 1976. Vegetal cover to estimate soil erosion hazard in Rhodesia. Geoderma, 15: 61-70.

Elwell, H. A. 1981. A soil loss estimation technique for southern Africa. In: Morgan, R. P. C (ed.), Soil Conservation: Problems and Prospects. Chichester, Wiley: 281-292.

Epstein, E. and Grant, W. J. 1973. Soil crust formation as affected by raindrop impact. In: Hadas, A., Swartzendruber, D., Rijtima, P. E., Fuchs, M and Yaron, B (Eds.)., Physical Aspect of Soil Water and Salts in ecosystems. Springer-Verlag, Berlin, pp. 195-201.

Escadafal, R. 1993. Remote sensing of soil colour: principles and applications. Remote Sensing Reviews, 7, 261-279.

Evans, R. 1980. Mechanics of water erosion and their spatial and temporal controls: an empirical viewpoint. In: M. J. Kirkby & Morgan, R. P. C (eds.), soil erosion. Chichester, Wiley. Pp. 109-128.

FAO. 2000. Sustainable land use and management needed to prevent soil degradation. FAO Press.

Farres, P. 1980. Some observations on the stability of soil aggregates to raindrop impact. Catena Vol.7. 211-224.

Faulkner, H. 1995. Gully erosion associated with the expansion of unterraced almond cultivation in the coastal Sierra de Lujar, Southern Spain. Land Degradation and Rehabilitation 6: 179:200.

Fenton, T. E. 1982. Estimating soil erosion by remote sensing techniques. In: Johnnsen, C. J. and Sanders, J. L. (eds.). Remote Sensing for Resource Management. Soil Conservation Society of America, p665.

Fischer, A. 1994. Model for the seasonal variations of vegetation indices in coarse resolution data and its inversion to extract crop parameters. Remote Sensing for Environment, 48, 220-230.

Folly, A., Quinton, J. N., and Smith, R. E. 1999. Evaluation of the EUROSEM model using data from Catsop Watershed, the Netherlands. Catena, 37, 507-519.

Foody, G. M., Lucas, R. M., Curran, P. J. and Honzak, M. 1997. Non-linear mixture modelling without endmembers using an artificial neural network. International Journal of Remote Sensing, Vol. 18, No. 4: 937-953.

Foster, G. R. 1982. Modelling the erosion process. In: Haan, C. T., Johnson, H. P. and Brakenseik, D. L (eds.), Hydrologic modelling of small watersheds. American Society of Agricultural Engineers Monograph 5: 297-380.

Franklin, J., Davies, F. W., and Lefebvre, P. 1991. Thematic Mapper analysis of tree cover in semi-arid woodlands using a model of canopy shadowing. Remote Sens. Environ. 36:189-202.

Franklin, J., Duncan, J., and Turner, D. L. 1993. Reflectance of vegetation and soil in Chihuahuan Desert plant communities from ground radiometry using SPOT wavebands. Remote Sensing of Environ., 46:291-304.

Francis, C. F. 1985. The role and significance of surface and subsurface hydrology on gully head growth in south east Spain. PhD thesis. Bedford College, University of London.

Freeze, R. A. 1972. Role of subsurface flow in generating surface runoff, 2. Upstream source area. Water Resources Research, Vol. 8, No. 5: 1272-83.

Gabriels, D., Pauwels, J. M., and De Boodt, M. 1975. The slope gradient as it affects the amounts and size distribution of soil loss material from runoff on silt loam aggregates. Medelingen Fakulteit Landbouw-wetenschappen. Rijksuniversiteit Gent 40: 1333-8.

Galvao, L. S., Vitorello, I., and Almeida, R. 1999. Effects of band positioning and bandwidth NDVI measurements of tropical savannas. Remote Sensing of Environment, 67 (2): 181-193.

García-Haro, F. J., Gilabert M. A. and Meliá, J. 1996. Linear spectral mixture modelling to estimate vegetation amount from optical spectral data. International Journal of Remote Sensing, 17(17):3373-3400.

Garen, D., Woodward, D., and Geter, F. 1999. A user agency's view of hydrologic, soil erosion and water quality modelling. Catena, 37: 277-289.

Garg, P. K. and Harrison, A. R. 1992. Land degradation and erosion risk analysis in south east Spain: a geographic system approach. Catena, Vol, 19, pp. 411-425.

Gates, D. M., Keegan, H. J., Schleter, J. C., and Weidner, V. R. 1965. Spectral properties of plants. Applied Optics, 4:11-20.

Gee, G. W. and Bauder, J. W. 1986. Particle-size analysis. In: Klute, A. (ed.). Methods of soil analysis (Part 1), physical and mineralogical methods. American Society of Agronomy, Inc and Soil Science Society of America, Inc. Madison, Wisconsin USA.

Gillespie, A. R., Smith, M. O., Adams, J. B., Willis, S. C., Fischer, A. F. and Sabol, D. E. 1990. Interpretation of residual images: spectral mixture analysis of AVIRIS images, Owens Valley, California, Proceedings of 2nd AVIRIS Workshop, Jet Propulsion Lab., Pasadena, CA. 4-5 June, JPL Publications. 90-54, pp 28.

Gilman, A. and Thornes, J. B. 1985. Land-use and prehistory in South-East Spain. The London research series in Geography & Allen and Unwin, London.

Giordano, A., ed. 1992. CORINE. Soil erosion risk and important land resources in the southern regions of the european community. Report EUR 13233, Brussels, pp97.

Govers, G. and Rauws, G. 1986. Transporting capacity of overland flow on plane and on irregular beds. Earth Surface Processes and Landforms 11:515-524.

Govers, G. and Poesen, J. 1988. Assessment of the interrill and rill contributions to total soil loss from an upland field plot. Geomorphology 1: 343-354.

Graetz, R.D. 1994. Empirical and practical approaches to land surface characterisation and change detection. In: Hill, J., and Peter, D. The use of remote sensing for land degradation and

desertification monitoring in the Mediterranean basin, State of the art and future research. European Commission.

Grayson, R. B. and Moore, I. D. 1992. Effect of land surface configuration on catchment hydrology. In: Anthony, J., Parsons & Athol D. Abrahams. Overland Flow, Hydraulics and Erosion Mechanics. UCL Press Limited. 147-175.

Grenon, M. and Matisse, M. 1989. Futures of the Mediterranean basin: the blue plan. Oxford University Press, Oxford.

Grissinger, E. H and Asmussen, L.E. 1963. Discussion of channel stability in undisturbed cohesive soils by E. M. Flaxman. Journal of Hydraulics Division ASCE 89:529-64.

Guy, B. T., Rudra, R. P. and Dickinson, W. T. 1992. Process-oriented research on soil erosion and overland flow. In: Anthony J. Parsons & Athol D. Abraham (eds.) Overland flow, hydraulics and erosion mechanics. 1992. University College London Press Limited. London.

Hanks, R.J. 1992. Applied soil physics--soil water and temperature applications (2nd ed.), Springer-Verlag, New York.

Harris, P. M., and Ventura, S. J. 1995. The integration of geographic data with remotely sensed imagery to improve classification in an urban area. Phtogramm. Eng. Remote Sens. 61: 993-98.

Hawkes, C. 1998. Mediterranean shrub mortality: a field and modelling investigation. Ph.D. thesis, King's College London.

Heede, B. H. 1975. Watershed indicators of landform development. In: hydrology and water resources in Arizona and the Southwest, Volume 5. Proceedings, 1975 meeting, Arizona Section, American Water Resources Association and Hydrology Section, Arizona Academy of Science:43-46.

Hill, J. and Peter, D. 1994. The use of remote sensing for land degradation and desertification monitoring in the Mediterranean basin, state of the art and future research. European Commission.

Hill, J. (ed.). 1996. Integrated approaches to desertification mapping and monitoring in the Mediterranean Basin, final report of the DEMON-1 project. Joint Research Centre Euro. Commi..

Hillel, D. 1980. Fundamentals of soil physics. Academic Press. New York.

Hillel, D. 1982. Introduction to Soil Physics, Academic Press, San Diego, New York, Boston, London, Sydney, Tokyo, Toronto. Pp 364.

Hofmann-Wellenhof, B., Lichtenegger, H. and Collins, J. 1994. Global Positioning System, theory and practice. Springer-Verlag Wien. New York.

Holý, M. 1980. Erosion and Environment. Pergamon Press, Oxford.

Horvath, V. and Erodi, B. 1962. Determination of natural slope category limits by functional identity of erosion intensity. International Association of Scientific Hydrology Publication 59: 131-43.

Horvath, E. H., Klingebiel, A. A., Moore, D. G. and Fosnight, E. G. 1983. Alternate data source for soil survey on rangeland. U.S. Geological Survey Open File Report, 83-880, Washington,DC, p27.

Hudson, N. W. 1957. Erosion control research: progress report on experiments at Henderson research station, 1953-56. Rhodesia. Agric. J., 54:297-323.

Hudson, N. 1981. Soil conservation. Batsford Academic, London. Pp 321.

Hudson, N. 1995. Soil Conservation (third edition), BT Batsford Ltd, London.

Huete, A. R., Jackson, R. D., and Post, D. F. 1985. Spectral response of plant canopy with different soil backgrounds. Remote Sensing of Environment, 17:37-53.

Huete, A.R. 1988. A soil adjusted vegetation index (SAVI), Rem. Sens. of the Envir., 25:295-309.

IDRISI online. 1997. Clark Labs, The Idrisi Project, Clark University Graduate School of Geography.

Imeson, A. C. 1996. Desertification research-thematic issues and spatial and temporal scaling. In: Hill, J., and Peter, D. The use of remote sensing for land degradation and desertification monitoring in the Mediterranean basin, state of the art and future research. European Commission.

Iyer, H. S., Singh, A. N. and Ram Kumar. 1975. Problem area inventory of parts of Hoshiarpur district through photointerpretation. Journal Indian Society of Photo Interpretation 11, 79-85.

Jacks, G. V. 1939. Soil erosion, the rape of the earth, a survey of soil erosion. In: Jacks, G. V. and Whyte, R. O. (eds.), Soil erosion and its control. Faber, London, Pp 313.

Jackson, R.D. 1983. Spectral indices in n-space. *Remote Sensing of Environment*, **14**:409-421.

Jacquemound, S., Baret. F., and Hanocq, J. F. 1992. Modelling spectral and bidirectional soil reflectance. Remote Sensing of Environment, 41:123-132.

Jenson, S. K., 1993. Applications of hydrologic information automatically extracted from digital elevation models. In: Moor, I. D., and Beven, K. J. Terrain analysis and distributed modelling in hydrology. John Wiley & Sons, England. 35-47.

Jetten, V., de Roo, Ad., Favis-Mortlock, D. 1999. Evaluation of field-scale and catchment-scale soil erosion models. Catena, 37: 521-541.

Johns, G. G. 1983. Runoff of soil loss in a semi-arid shrub invaded polar box (Eucalyptus Populnea) woodland. Australian Rangeland Journal, 5, 3-12.

Johnson, P. E., Smith, M. O. and Adams, J. B. 1985. Quantitative analysis of planetary reflectance spectra with principal components analysis. Journal of Geophysical Research, 90, C805-810.

Jurgens, C. and Fander, M. 1993. Soil erosion assessment and simulation by means of SGEOS and ancillary digital data. International Journal of Remote Sensing, Vol. 14, No. 15, 2847-2855.

Kalton, G. 1983. Introduction to survey sampling. California: Sage. Pp 83.

Kaufman. Y. J, and Tanre, D. 1992. Atmospherically resistant vegetation index (Arvi) for Eos-Modis. IEEE Transactions on Geoscience and Remote Sensing, 30 (2): 261-270.

Kirkby, M. J., 1971. Hillslope process-response models based on the continuity eqaution. In: Brunsden, D (ed.). Slopes form and process. Institute of British Geog. Special Publi. 3: 15-30.

Kirkby, M. J. 1976. Hydrological slope model: The influence of climate. In: Derbyshire, E. (ed.). Geomorphology and climate. John Wiley and Sons, Chichester. p246-267.

Kirkby, M. J. and Neale, R. H. 1987. A soil erosion model incorporating seasonal factors. In: Gardiner, V. (ed.), Interna. Geomorphology. John Wiley & Sons, Chichester. Vol II, p189-210

Kirkby, M. J. and Cox, N. J. 1995. A climatic index for soil erosion potential (CSEP) including seasonal and vegetation factors. Catena, 25:333-352.

Kitanidis, P.K. 1997. Introduction to geostatistics: applications to hydrogeology. Cambridge University Press, pp 2.

Klute, A. 1986. Methods of soil analysis (Part 1), physical and mineralogical methods. American Society of Agronomy, Inc and Soil Science Society of America, Inc. Madison, Wisconsin USA.

Kondratyev, K. Y. and Fedchenko, P. P. 1983. Investigation of humus in soil from their colours. Sov. Soil Sci. 15, 108-111.

Kosmas, C., Danalatos, N., Cammeraat, L. H., Chabart, M., and Diamantopoulos, J. 1997. The effect of land use on runoff and soil rates under Mediterranean conditions. Catena (29), 45-59.

Krenkel, P. A. and Novotny, V. 1979. River water quality model constructure. In: Sten, H. W. (ed.), modelling of rivers. Wiley-Interscience, New York, chapter 17.

Kruse, F. A. 1999. Visible-infrared sensors and case studies. In: Rencz, A. N (ed.), remote sensing for the earth sciences, manual of remote sensing (3rd ed.). John Wiley & Sons, Inc, New York, pp 568.

Kruse, F. A., Lefkoff, A. B., and Dietz, J. B. 1993. Expert system-based mineral mapping in Northern Death valley, California/Nevada, using the Airborne Visible/Infrared Imaging Spectrometer (AVIRIS). Remote Sensing Environment, 44:309-336.

Kunze, G. W. and Dixon, J. B. 1986. Pre-treatment for mineralogical analysis. In: Klute, A. (ed.). Methods of soil analysis (Part 1), physical and mineralogical methods. American Society of Agronomy, Inc and Soil Science Society of America, Inc. Madison, Wisconsin USA.

Laflen, J. M. and Colvin, T. S. 1981. Effect of crop residue on soil loss from continuous row cropping. Transactions of the American Society of Agricultural Engineers, 24: 605-609.

Laflen, J. M., Lane, L. J. and Foster, G. R. 1991. WEPP- a new generation of erosion prediction technology. Journal of Soil and Water Conservation, 46(1): 34-38.

Lambin, E. F. 1999. Monitoring forest degradation in tropical regions by remote sensing: some methodological issues. Global Ecology and Biogeography, 8: (3-4) 191-198

Lane, L. J. 1993. Transmission losses. National Engineering Handbook 4- Hydrology. Soil Conservation Service, US. Dept. of Agriculture., Washington, D. C. pp.1-21.

Lantieri, D., Dallemand, J. F., Biscaia, R., Sohn, S. and Potter, R.O. 1990. Erosion mapping using high resolution satellite data and geographic information system. FAO Remote Sensing Centre Series, No. 56, FAO, Rome, 150 p.

Lea, N. J., 1992. An Aspect-Driven Kinematic Routing Algorithm. In: Anthony, J., Parsons & Athol D. Abrahams. Overland Flow, Hydraulics and Erosion Mechanics. UCL Press Limited. 393-408.

Le Bissonais, Y. 1990. Experimental study and modelling of soil surface crusting processes. Catena Supplement. 17, pp.13-28.

Le Houerou, H. N. 1981. Impact of man and his animals on Mediterranean vegetation. In: Di Castri, F., Goodall, D. W. and Specht, R. L. (eds.). Mediterranean-type shrublands. Elsevier, Amsterdam, Oxford, New York. Pp. 479-522.

Leprieur, C., M., Verstraete, M., and Pinty, B. 1994. Evaluation of the performance of various vegetation indices to retrieve vegetation cover from AVHRR data. Remote Sensing Reviews, 10, 265-284.

Levy, G. j., Agassi, M., Smith, H. J. C. and Stern, R. 1993. Microaggregate stability of kaolinitic and illitic soils determined by ultrasonic energy. Journal of Soil Science Soci. of Amer., 57, pp. 803-8.

Leymarie, P. and Fairfield, J. 1991. Drainage networks from grid digital elevation models. Water Resources Research, 27(5), 709-717.

Lillesand, T. M. and Kiefer, R. W. 2000. Remote sensing and image interpretation. John Wiley and Sons, New York. P 436-38.

Liu, B. Y., Nearing, M. A., Shi, P. J., and Jia, Z. W. 2000. Slope length effects on soil loss for steep slopes. Soil Science Society of America Journal, 64 (5): 1759-1763

Lopez-Bermudez, F. 1997. Environmentally sensitive areas. In: Second annual report of MEDALUS III: Project 2, target areas. MEDALUS Office, Thatcham, Berkshire, UK. Pp. 65-76.

Lopez-Bermudez, F., Barbera, G. G., Alonso-Sarria, F. and Romero-Diaz, M. A. 1999. Guadalentin basin (Murcia, Spain): an area threatened by desertification. In: Balabanis, P., Peter, D., Ghazi, M. and Tsogas, M. (eds.). Mediterranean Desertification Research results and policy implications, Proceedings of the International Conference 29 Oct-1 Nov 1999, Greece. European Commission.

Lowdermilk, W. C. 1935. "Man-Made Desert," Pacific Affairs, University of British Colombia, 8: 409-419. In: Morgan, R. P. C (ed.), Soil Erosion and Its Control. Van Nostrand Reinhold, New York, Pp 311.

Lucas, L. F., Janssen and Frans, J.M., 1994. Accuracy assessment of satellite derived land cover data: a review. Photogrammetric Engineering & Remote Sensing, Vol. 60, No. 4, pp. 419-426.

Maas, S. J. 2000. Linear spectral mixture modeling approach for estimating cotton canopy ground cover using satellite multispectral imagery. Remote Sensing of Environment, 72:(3) 304-308.

Maidment, D. R., 1996. Environmental modelling within GIS. In: Goodchild, M. F., Steyaert, L. T., and Parks, B. O. (eds.), GIS and Environmental Modelling: Progress and Research Issues, GIS World, Inc., pp. 315-324.

Mainguet, M. 1994. Desertification: natural background and human mismanagement, 2nd ed., Springer-Verlag, Berlin, Heidelberg, New York, London, Paris, Pp 314.

Markham, B. L., and Townshend, J. R. G. 1981. Land cover classification accuracy as a function of sensor spatial resolution. The Fifteenth International Symposium on Remote Sensing of Environment, Ann Arbor, MI, May 1981.

Marshall, T. J., Rose, C. W., and Holmes, J. W. 1996. Soil physics, 3rd edition. Cambridge University Press, Cambridge. P 9, 199-204.

Martínez-Casasnovas, J. A. and Sánchez-Bosch, I. 2000. Impact assessment of changes in landuse/ conservation practices on soil-erosion in the Penedès-Anoia vineyard region (NE Spain). Soil & Tillage Research, 57: 101-106.

Maselli, F., Rodolfi, A, Bottai. L., Romanelli, S., and Conese, C. 2000. Classification of Mediterranean vegetation by TM and ancillary data for the evaluation of fire risk. International Journal of Remote Sensing, 21 (17): 3303-3313.

Mather, P. M. 1999. Computer processing of remotely-sensed images. John Wiley & Sons, England.

Mattikalli, N, M., Devereux, B. J. and Richards, K. S. 1996. Prediction of river discharge and surface water quality using an integrated Geographical Information System approach. International Journal of Remote Sensing, 1996, Vol. 17, No. 4: 683-701.

Metternicht, G. I. and Zinck, J. A. 1998. Evaluating the information content of JERS-1 SAR and Landsat TM data for discrimination of soil erosion features. ISPRS Journal of Photogrammetry and Remote Sensing, 53: (3) 143-153.

Meyer, L. D. and Wischmeier, W. H. 1969. Mathematical simulation of the process of soil erosion by water. Transactions of American Society of Agricultural Engineers, 18: 905-911.

Mitasova, H., Mitas, L., Brown, W. M., and Johnston, D., 1998. GIS tools for erosion/deposition modeling and multidimensional visualization. Part IV: Process-based erosion simulation for spatially complex conditions and its applications to installations. Report for USA CERL. University of Illinois, Urbana-Champaign, IL.

Mokrech. M. 2001. The management of uncertainty in geographic information systems : a case study using a soil-erosion model. Ph.D. thesis, King's College London.

Molnar, D. K. and Julien, P. Y. 1998. Estimation of upland erosion using GIS. Computers & Geosciences Vol. 24, No. 2, Pp 183-192.

Montas, H. J., and Madramootoo, C. A. 1991. using the ANSWERS model to predict runoff and soil loss in South-western Quebec. Trans. of the American Soci. of Agri. eng., 34,1754-1762.

Moore, I. D., Grayson, R. B. and Ladson, A. R. 1991. Digital terrain modelling: a review of hydrological, geomorphological and biological applications. Hydrological Processes, 5, 3-30.

Morgan, R. P. C. 1982. Splash detachment under plant covers: results and implications of a field study. Transaction of the American Society of Agricultural Engineers, 25: 987-991.

Morgan, R. P. C., Morgan, D. D. V. and Finney, H. J. 1984. A predictive model for the assessment of soil erosion risk. Journal of Agricultural Engineering Research 30:245-53.

Morgan, R. P.C. 1995. Soil Erosion and Conservation. Longman Group Limited, Essex.

Morris, D.G. and Heerdegen, G. 1988. Automatically derived catchment boundaries and channel networks and their hydrological applications. Geomorphology, 1:131-141.

Mukundan, R. and Ramakrishnan, K. R. 1998. Moment functions in image analysis. World Scientific, Singapore, New Jersey, London. Pp 115.

Murphy, R. J. and Wadge, G. 1994. The effects of vegetation on the ability to map soils using imaging spectrometer data. International Journal of Remote Sensing, 15:63-86.

Musgrave, G. W. 1947. The quantitative evaluation of factors in water erosion: a first approximation. Journal of soil and water conservation, 2: 133-138.

Musick, H. B. 1986. Temporal change in Landsat MSS albedo estimates in arid rangeland. Remote Sensing of Environment, 20:107-20.

Myneni, R. B., Ross, J., and Asrar, G. 1989. A review on the theory of photon transport in leaf canopies. Agric. For. Meteor. 45: 1-153.

Navas, A. and Machin, J. 1991. A Preliminary Research of the Use of Cesium-137 to Investigate Soil Erosion in the Semiarid Landscape of the Central Ebro River Valley. In M. Sala, J. L. Ruibo & J. M. Garcia-Ruiz (eds): Soil Erosion in Spain. Geoforma Ediciones Logrono. 191-202.

Naveh, Z. and Vernet, J.-L. 1991. The palaehistory of the Mediterranean biota. In: Groves, R. H. and Castri, F. D. (eds.). biogeography of the Mediterranean invations. Cambridge University Press, Cambridge. Pp. 19-32.

Nielsen, R. D., Bigler, R. J., Sobecki. T., Lytle, D. L. 1996. Applications of soil survey attribute data to GIS pollution assessment models. In: Corwin, D. L., Laogue, K. (eds.). applications of GIS to the modelling of non-point source pollutants in the Vadose Zone. SSSA Special Publication No. 48SSSA, Madison WI, pp. 175-183.

Obando, J. 1996. Modelling the impact of land abandonment on runoff and soil erosion in a semi-arid catchment. PhD thesis, King's College London, University of London.

Oldeman, L. R. 1994. The global extent of soil degradation. In: Greenland, D. J. and Szabolcs, I. (eds.). Soil Resilience and Sustainable Land Use. CAB International, Wallingford, p98-118.

Parsons, A. J., and Abraham, A. D. 1992. Overland flow, Hydraulics and Erosion Mechanics. University College London Press Limited. London.

PCRaster User's Manuals. 1996. PCRaster Environ. Software V.O.F. Utrecht Uni.. The Netherlands.

Pech, R. P., Graetz, R. D. and Davis, A. W. 1986. Reflectance modelling and the derivation of vegetation indices for an Australian semi-arid shrubland. International Journal of Remote Sensing, 7:389-403.

Peddle, D. R., Hall, F. G., LeDrew, E. F. 1999. Spectral mixture analysis and geometric-optical reflectance modeling of Boreal Forest biophysical structure. Remote Sensing of Environment, 67:288-297.

Perrin, C., Michel, C., and Andreassian, V. 2001. does a large number of parameters enhance model performance? Comparative assessment of commom catchment model structures on 429 catchments. Journal of Hydrology, 242: 275-301.

Peterson, D. L., Aber, J. D., Matson, P. A., Card, D. C., Swanberg, N., Wessman, C., and Spanner, M. 1988. Remote sensing of forest canopy and leaf biochemical constituents. Remote Sensing of Environment, 24: 85-108.

Peterson, R. G., and Calvin, L. D. 1985. soil sampling. In: Black, C. A., Evans, D. D., Ensminger, L. E., White, J. L., and Clark, F. E. (eds.), methods of soil analysis, part 1, physical and mineralogical properties, including statistics of measurement and sampling. Pp56.

Philip, J. R. 1957. The theory of infiltration: 4. Sorptivity and algebraic infiltration equations. Soil Science, 84:257-267.

Philip, J. R. 1987. The infiltration joining problem. Water Resources Research, 23: 2239-2245.

Pickup, G. and Chewings, V. H. 1988. Forecasting patterns of soil erosion in arid lands from landsat MSS data. International Journal of Remote Sensing, 9, 69-84.

Pickup, G., Chewings, V. H., and Nelson, D. J. 1993. Estimating changes in vegetation cover over time in arid rangelands using Landsat MSS data. Remote Sens. Environ., 43:243-63.

Pickup, G. and Chewings, Y. H. 1996. Correlations between DEM-derived topographic indices and remotely-sensed vegetation cover rangelands. Earth Processes and Landforms, Vol. 21, 517-529.

Pilesjo, P. 1992. GIS and remote sensing for soil erosion studies in semi-arid environments - estimation of soil erosion parameters at different scales. Lund University Press, Lund, p 203.

Pilgrim, D. H. and Cordery, I. 1993. Flood runoff. In: Maidment, D.R. (ed.), Handbook of Hydrology, McGraw-Hill, New York, p9.1-9.41.

Pinty, B., and Verstraete, M. M. 1992. GEMI - a nonlinear index to monitor global vegetation from satellites. Vegetatio, 101 (1): 15-20 Jul 1992.

Poesen, J., Ingelmosanchez, F., and Mucher, H. 1990. The hydrological response of soil surfaces to rainfall as affected by cover and position of rock fragments in the top layer. Earth Surface Processes and Landforms, 15 (7): 653-671.

Price, K. P. 1993. Detection of soil erosion within pinyon-juniper woodlands using Thematic Mapper (TM) data. Remote Sensing of Environment, 45: 233-248.

Proyecto Lucademe. 1992. Mapa De Suelos, Velez Rubio 974. Ministerio De Agricultura, Pesca Y Alimentacion, Icona.

Qi, J., Kerr, Y., and Chehbouni, A. 1994. External Factor Consideration in Vegetation Index Development. In Proceedings of Physical Measurements and Signatures in Remote Sensin. ISPRS, 723-730.

Qin, W., and Gerstl, S. A. W. 2000. 3-D scene modelling of semiarid vegetation cover and its radiation regime. Remote Sensing of Environment, 74:145-162.

Quansah, C. 1982. Laboratory experimentation for the statistical derivation of equations for soil erosion modelling and soil conservation design. Ph.D. thesis, Cranfield Institute of Technology.

Quine, T. A., Navas, A., Walling, D. E. and Machin, J. 1994. Soil erosion and redistribution on cultivated and uncultivated land near Las Bardenas in the central Ebro river basin, Spain. Land Degradation and Rehabilitation, 5(1), 41-55.

Quinn, P., Beven, K., Chevallier, P. and Planchon, O. 1993. The prediction of hillslope flow paths for distributed hydrological modelling using digital terrain models. In: Moor, I. D., and Beven, K. J. Terrain Analysis and Distributed Modelling in Hydrology. John Wiley & Sons, England. 63-83.

Rawls, W.J., Ahuja, L.R., Brakensiek, D.L. and Shirmohammadi, A. 1993. Infiltration and soil water movement. In: Maidment, D.R. (ed.), Handbook of Hydrology, 5.1-5.51, McGraw-Hill, New York.

Ray, T. W. 1995. Remote monitoring of land degradation in arid/semi-arid regions. Ph.D. thesis, California Institute of Technology, Pasadena, California.

Ray, T. W., and Murray, B. C. 1996. Nonlinear spectral mixing in desert vegetation. Remote Sensing of Environment: 55: 59-64.

Remondi, B. W. 1986. Performing centimetre-level surveys in seconds with GPS carrier phase: initial results. In Proceedings of the Fourth International Geodetic Symposium on Satellite Positioning, Austin, Texas, April 28- May 2, Vol 2: 1229-1249.

Ringrose, S., Vanderpost, C., and Matheson, W. 1997. Use of image processing and GIS techniques to determine the extent and possible causes of land management fenceline induced degradation problems in the Okavango, northern Botswana. Intern. Journal of Remote Sens., 18: (11) 2337-64

Robinson, A. H., Morrison, J. L., Muehrcke, P. C., Kimerling, A. J. and Guptill, S. C. 1995. Elements of Cartography. 6th ed. John Wiley & Sons, Inc, Toronto, Canada. 127 pp.

Roberts, D. A., Smith, M. O., and Adams, J. B. 1993. Green vegetation, nonphotosynthetic vegetation, and soils in AVIRIS data. Remote Sensing of Environment, 44:117-126.

Roberts, D. A., Green, R. O., Adams, J. B., Cothern, J. S., Sabol. D. E. and Smith, M. O. 1994. Temporal and spatial relationships between topography, atmospheric water vapour, liquid water and vegetation endmember fractions determined using AVIRIS. Proc. IGARSS 94, IEEE 2366-68.

Roberts, D. A., Gardner, M., Church, R., Ustin, S., Scheer, G., and Green, R. O. 1998. Mapping chaparral in the Santa Monica Mountains using multiple endmember spectral mixture models. Remote Sensing of Environment, 65 (3): 267-279.

Rogowski, A. S. and Wolf, J. K. 1994. Incorporating variability into soil map unit delineations. Soil Science Society of America Journal, 1994, vol.58, no.1, pp.163 174.

Rosenbaum, M., and Soderstorm, M. 1996. Geostatistics as an Aid to Mapping. The ESRI 1996 European User Conference Proceedings, ESRI, UK.

Ruecker, G., Schad, P., Alcubilla, M. M. and Ferrer, C. 1998. Natural regeneration of degraded soils and site changes on abandoned terraces in Mediterranean Spain. Land Degradation and Development 9: 179-188.

Rydgren, B. environmental impacts of soil erosion and soil conservation, a Lesotho case study. Uppsala University, Institute of Earth Science, Physical Geography. Ph.D. Thesis.

Sabins, F. F. 1987. Remote Sensing: Principles and Interpretation. Freeman, New York. P 449.

Sardo, V., Vella, P., and Zimbone, S. M. 1994. Preliminary investigation of runoff using a rainfall simulator. In: Rickson, R. J (ed.). Conserving soil resources, European perspectives. CAB International. Pp 136.

Savat, J. 1979. Laboratory experiments on erosion and deposition of loess by laminar sheet flow and turbulent rill flow. In: Vogt, H. and Vogt, Th. (eds.). colloque sur l'erosion agricole des sols en milieu tempere non Mediterraneen. Strasbourg, l'Universite Louis Pasteur: 139-143.

Savat, J. 1982. Common and uncommon selectivity in the process of fluid transportation: field observations and laboratory experiments on bare surfaces. Catena Supplement 1: 139-160.

Schaaf, C. B., Li, X., and Strahler, A. H. 1995. Using a geometric-optical model to calculate the bidirectional and hemispherical reflectance of forested slopes. In Proceedings of SPIE (Multispectral and Microwave Sensing of Forestry, Hydrology, and Natural Resources) (Vol. 2314, 21-26). Palos Verdes Estates, CA: SPIE.

Schalkoff, R. J. 1989. Digital image processing and computer vision. John Wiley & Sons, New York, Chichester. Pp 263, 273.

Schjonning, P. 1994. Soil erodibility in relation to soil physical properties. In: Rickson, R. J. (ed.). Conserving Soil Resources, European Perspectives. CAB International. Pp 78.

Schultz, G. A. 1993. Application of GIS and remote sensing in hydrology. In: K. Kovar., and H. P. Nachtnebel Wallingford (eds.), Application of geographic information systems in hydrology and

water resources management. International Conference Application of Geographic Information Systems in Hydrology and Water Resources Management (1993, Vienna). pp. 127 - 140

Scoging, H. 1992. Modelling overland-flow hydrology for dynamic hydraulics. In: Anthony J. Parsons & Athol D. Abraham (eds.) Overland flow, Hydraulics and erosion mechanics. University College London Press Limited. London.

Scoging, H., Parson, A. J., and Abrahams, A. D. 1992. Application of a dynamic overland-flow hydraulic model to a semi-arid hillslope, Walnut Gulch, Arizona. In: Anthony J. Parsons & Athol D. Abraham (eds.) Overland flow, Hydraulics and erosion mechanics. University College London Press Limited. London.

Serrano, L., Ustin, S. L., Roberts, D. A., Gamon, J. A., and Penuelas, J. 2000. Deriving water content of chaparral vegetation from AVIRIS data. REMOTE SENSING OF ENVIRONMENT, 74 (3): 570-581.

Settle, J.J. and Drake, N. A. 1993. Linear mixing and the estimation of ground cover proportions. International Journal of remote sensing, 14(6): 1159-1177.

Sharma, P. P., Gupta, S. C. and Foster, G. R. 1993. Predicting soil detachment by raindrop. Journal of Soil Science Society of America. 57, pp.674-680.

Sharma, P.P., and Singh K.D. 1995. satellite remote sensing for soil erosion modelling using the ANSWERS model. Hydrological Sciences- Journal de Sciences Hydrologiques, 40, 2, 259-272.

Shimabukuro, Y. E., Novo, E. M., and Ponzoni, F. J. 1998. Vegetation index and spectral linear mixing model for monitoring the Pantanal region. Pesquisa Agropecuaria Brasileira, 33: 1729-1737.

Siegal, B. S. and Goetz, F. H. 1977. Effect of vegetation on rock and soil type discrimination. Photogrammetric Engineering and Remote Sensing, 43, 191-196.

Singer, R. B. and McCord, T. B. 1979. Mars: large scale mixing of bright and dark surface materials and implications for analysis of spectral reflectance, in proceedings Lunar and Planetary Science Conference, 10th, pp. 1835-1848.

Smith, A. M. S., Wooster, M. J., Powell, A. K., and Usher, D. 2001. Texture based feature extraction algorithm: application to burn scar detection in Earth observation imagery. IJRS (submitted).

Smith, M. O., Adams, J. B., and Sabol, D. E. 1994. Spectral mixture analysis-new strategies for the analysis of multispectral data. In: imaging spectrometry- a tool for environmental observations (Hill, J. and Megier, J., Eds.), Kluwer Academic, Dordrecht, the Netherlands, pp. 125-144.

Smith, M. O., Ustin, S. L., Adams, J. B. and Gillespie, A. R. 1990. Vegetation in deserts: I. A regional measure of abundance from multispectral images. Remote Sensing of Environment, 31:1-26.

Smith, M. O., Jonson, P. E. and Adams, J. B. 1985. Quantitative determination of mineral types and abundances from reflectance spectra using principle components analysis. Journal of Geophysical Research, 80:797-804.

Soil Conservation Service 1972. SCS National Engineering Handbook, Sec. 4, Hydrology, USDA.

Spatz, C. 1997. Basic statistics: Tales of Distributions (6th ed.). California: Brooks & Cole. Pp-148.

Stafford Smith, M. and Pickup, G. 1993. Out of Africa, looking in: Understanding veg. change. In: Behnke, R. H., Scoone, I. And Kerven, C. (Eds.) Range ecology at disequilibrium. Overseas Develop. Institute and Interna. Institute for Environment and Development, London, pp 196-226.

Stallings, J. H. 1957. Soil conservation. Prentice-Hall, Pp 575.

Steele, C. 2000. Empirical evidence of the relationship between spectral reflectance and vegetation canopy physiology. Ph.D. thesis. King's College London.

Stefanov, W. L., Ramsey, M. S., and Christensen, P. R. 2001. Monitoring urban land cover change: an expert system approach to land cover classification of semi-arid to arid urban centres. Remote Sensing of Environment. 77: 173-185.

Stein, A., van Dooremolen, W., Bouma, J., and Begt, A. K. 1988. Cokriging point data on moisture deficit. Soil Science Society of America Journal, 52: 1418-1423.

Steyaert, l. 1993. A perspective on the state of environmental simulation modelling, in Environmental Modelling with GIS. Oxford University press. Pp 16-30.

Stocking, M. A. 1996. Soil erosion. In: Adams, W. M., Goudie, A. S., and Orme, A.R. (ed.), The Physical Geography of Africa, Oxford University Press, Oxford, p326-341.

Stojic, M. and Shannon, J. 1997. Digital Cameras and Their Application to Digital Photogrammetry for Landform Modelling. King's College London.

Story, M. and Congalton, R. G. 1986. Accuracy Assessment: A User's Perspective. Photogrammetric Engineering and Remote Sensing, Vol. 52, No. 3. American Society for Photogrammetry and Remote Sensing, pp. 397-399.

Strahler, A. H. 1980. The use of prior probabilities in maximum likelihood classification of remotely sensed data. Remote Sensing of Environment, 10: 135-163.

Styczen, M. E. and Morgan, R. P. C. 1995. Engineering properties of vegetation. In: Morgan, R. P. C. and Rickson, R. J. (eds.). Slope stabilisation and erosion control: a bioengineering approach, E & FN SPON, London, p5-58.

Summer, W., Klaghofer, E. and Zhang, W. 1998. Modelling soil erosion, sediment transport and closely related hydrological processes. Proceedings of an international symposium held at Vienna between 13-17 July 1998. International Association of Hydrological Sciences.

Thornes, J.B. 1976. Semi-Arid Erosional Systems. Geographical Paper No. 7. London School of Economics and Political Science.

Thornes, J .B. 1985. The ecology of erosion. Geography, 68(3): 225-235.

Thornes, J.B. 1990. The interaction of erosional and vegetational dynamics in land degradation: spatial outcomes. In: Thornes, J. B (ed.). Vegetation and erosion: processes and environments. Wiley, Chichester, pp. 41-53.

Tomaselli, R. 1977. The degradation of the Mediterranean maquis. Ambio, 6: 356-362.

Tompkins, S., Mustard, J. F., Pieters, C. M, and Forsyth, D. W. 1997. Optimization of endmembers for spectral mixture analysis. Remote Sensing Of Environment, 59: (3) 472-489.

Torboton, D. G., Bras, R. L. and Rodriguez-Iturbe, I. 1993. On the extraction of channel networks form digital elevation data. In: Moor, I. D., and Beven, K. J. Terrain Analysis and Distributed Modelling in Hydrology. John Wiley & Sons, England. 85-104.

Torboton, D. G. 1997. A new method for the determination of flow directions and upslope areas in grid digital elevation models, Water Resources Research, 33(2), 309-319.

Townshend, J. R. G. 1992. Land cover. International Journal of Remote Sensing, 13: 1319-28.

Truman, C. C., Bradford, J. M. and Ferris, J.E. 1990. Antecedent water content and rainfall energy influence on soil aggregate breakdown. Journal of Soil Science Society of America 54: 1385-92.

Tsegaye, T., and Hill, R. L. 1998. Intensive tillage effects on spatial variability of soil physical properties. Soil Science, 163(2): 143-154

UNEP (United Nations Environment Programme). 1978. United Nations Conference on Desertification: Roundup, Plan of Action and Resolutions. United Nations, New York.

UNEP (United Nations Envir. Prog.). 1992. Status of desertification and implementation of the United Nations plan of action to combat desertification, particularly in Africa., Fourth session: 21-31.

United Nations. 1994. Elaboration of an interna. convention to combat desertifi. in those countries experiencing serious droughts and/or desertification, particularly in Africa. Fourth session: 21-30.

USDA (United States Department of Agriculture). 1993. Soil survey manual, USDA Handbook No. 18, U. S. Government Printing Office, Pp 437.

Ustin, S. L., Roberts, D. A., Green, R. O., Zomer, R. J., and Garcia, M. 1999. Remote sensing methods monitor natural resources. Photonics Spectra, 33 (10): 108.

Valentin, C. and Bresson, L. M. 1992. Morphology, genisis and classification of surface crusts in loamy and sandy soils. Geoderma 55, pp. 225-245.

Van Lynden, G. W. J. 1995. European soil resources: current status of soil degradation, cause, impacts and needs for action. Nature and Environment, 71, Council of Europe, Strasbourg.

Vieux, B. E. 1993. Geographic information systems and non-point source water quality and quantity modelling. In: Moor, I. D., and Beven, K. J. Terrain Analysis and Distributed Modelling in Hydrology. John Wiley & Sons, England. 169-181.

Voroney, R. P., Van Veen, J. A. and Paul, E. A. 1981. Organic carbon dynamics in grassland soils. II. Model validation and simulation of the long-term effects of cultivation and rainfall erosion. Canadian Journal of Soil Sience 61: 211-24.

Wainwright, J., Parsons, A. J., and Abrahams, A. D. 2000. Plot-scale studies of vegetation, overland flow and erosion interactions: case studies from Arizona and New Mexico. Hydrological Processes, 14 (16-17): 2921-2943.

Wainwright, J. 1994. Anthropogenic factors in the degradation of semi-arid regions: A prehistoric case study in southern France. In: Millington, A. C. and Pye, K. (eds.), Environmental change in drylands: biogeographical and geomorphological perspectives, p285-304.

Walling, D. E. 1996. Hydrology and Rivers. In: Adams, W. M., Goudie, A. S., and Orme, A. R. (eds.), The Physical Geography of Africa, Oxford University Press, Oxford, pp103-121.

Walling, D.E., and Webb, B.W. 1996. Erosion and sediment yield: a global overview. In: Walling, D.E., and Webb, B.W. (eds.), Erosion and Sediment Yield: Global and Regional Perspectives. International Association of Hydrological Sciences, Wallingford, p3-19.

Wang, M. C. J. 2000. Mapping and monitoring land degradation in Southern New Mexico using Landsat data. Unpublished Ph.D. thesis. King's College London.

Waring, R. H., Aber, J. D., Melillo, J. M., and Moore, B., III. 1986. Precursors of change in terrestrial ecosystems. Bioscience, 36, 433-438.

Warner, T. A., Evans, C. S., and Heirtzler, J. R. 1989. Remote sensing of geo-botanical trends in East Africa. In proceedings of IGARSS' 89/12, Canadian symposium on remote sensing: an economic tool for the nineties, July 10-14, Vancouver, British Colombia, Canada, Vol. 3, pp 1331-34.

Warren, A. and Agnew, C. 1988. An assessment of desertification and land degradation in arid and semi-arid areas. International Institute for Environment, Drylands Programme, University College, London. Pp 72.

Webster, R., and Oliver, M. A. 1992. sample adequately to estimate variograms of soil properties. Journal of Soil Science, 43:177-192.

White, K. and Drake, N. A. 1993. Mapping the distribution and abundance of gypsum in south-central Tunisia from Landsat Thematic Mapper data. Zeitschrift für Geomorphologie, N.F., 37(3):309-25.

Wischmeier, W. H., Johnson, C. B. and Cross, B. V. 1971. A soil erodibility nomograph for farmland and construction sites. Journal of Soil and Water Conservation 26: 189-93.

Wischmeier, W. H. and Smith, D. D. 1978. Predicting soil erosion losses, a guide to conservation planning. Agricultural Handbook No. 282, United States Department of Agriculture, Washington.

Wolf, P. R., 1983. Elements of Photogrammetry: With Airphoto Interpretation and Remote Sensing. 2nd Edition. McGraw-Hill. Singapore.

Woodcock, C. E. and Strahler, A. H. 1987. The factor of scale in remote sensing. Remote Sensing of Environment 21:311-332.

Woodcock, C. E., Collins, J. B., Jakabhazy, V. D., Li, X., Malcomer, S., Ryherd, S., Harward, V., Levitan, J., Wu, Y., and Warbingtom. 1994. Mapping forest vegetation using Landsat TM imagery and a canopy reflectance model. Remote Sensing of Environment, 50:240-254.

World Resources Institute. 1992. World Resources 1992-1993. Oxford Uni. Press, Oxford, Pp385.

Yair, A. 1992. The control of headwater area on channel runoff in a small arid watershed. In: Anthony J. Parsons & Athol D. Abraham (eds.). Overland flow, Hydraulics and Erosion Mechanics. University College London Press Limited. London.

Yang, J. and Prince, S. D. 1997. A theoretical assessment of the relation between woody canopy cover and red reflectance. Remote Sensing of Environment 59: 428-439.

Yassoglou, N. 1999. Land, desertification vulnerability and management in Mediterranean landscapes. In: Balabanis, P., Peter, D., Ghazi, M. and Tsogas, M. (eds.). Mediterranean Desertification Research results and policy implications, proceedings of the International Conference 29 Oct-1 Nov 1999, Greece. European Commission.

Yool. S. R., Makaio. M. J., and Watts. J. M. 1997. Techniques for computer-assisted mapping of rangeland change. Journal of Range Management, 50 (3): 307-314.

Young, F. J., Hammer, R. D., and Larsen, D. 1999. frequency distributions of soil properties on a loess-mantled Missouri Watershed. Soil Sci. Soc. Am. J. 63: 178-185.

Zhang, J., and Foody, G. M. 2001. Fully-fuzzy supervised classification of sub-urban land cover from remotely sensed imagery: statistical and artificial neural network approaches. International Journal Of Remote Sensing: 22 (4): 615-628.

Zhang, X. 1999. Soil erosion modelling at the global scale using Remote Sensing and Geographical Information Systems. Ph.D. Thesis, King's College London.

Zhu, A. X., and Mackay, D. S. 2001. Effects of spatial details of soil information on watershed modelling. Journal of Hydrology: 248: 54-77.

Zingg, A. W., 1940. Degree and length of land slope as it affects soil loss in runoff. Agricultural Engineering 21:59-64.

APPENDICES

Appendix A: the DEM triangulation iterations results

Pre-Triangulation Facts:

Total Number of Frames:	5
Total Number of Active Frames:	3
Total Number of Points:	39
Total Number of Active Points:	26
Total Number of Elements:	3
Maximum Number of Correlations:	2
Unsorted Element Bandwidth:	3

Frame Parameter Residuals (Unit is Meter and degrees)

Frame	Description	Cam	X	Y	Z	Omega	Phi	Kappa
3	comp1808	1	0.000	0.000	0.000	0.000000	0.000000	0.000000
4	comp1809	1	0.000	0.000	0.000	0.000000	0.000000	0.000000
5	comp1810	1	0.000	0.000	0.000	0.000000	0.000000	0.000000

		Point Residuals (Meter)			Image Residuals			
Point ID	Type	X	Y	Z	Frame ID	Sample	Line	Image X	Image Y
1	C	0.000	0.000	0.000					
					comp1808	-4.39	-1.99	83.4	186.1
					comp1809	-3.02	-0.39	15.9	128.2
					comp1810	-6.49	-4.25	178.7	275.6
2	C	0.000	0.000	0.000					
					comp1808	-2.72	0.75	-32.2	115.2
					comp1809	-2.52	2.38	-101.4	106.7
					comp1810	-5.82	-1.53	63.5	246.8
3	C	0.000	0.000	0.000					
					comp1808	-4.29	-1.47	61.7	182.0
					comp1809	-5.08	1.29	-55.4	215.3
					comp1810	-4.76	-1.30	54.1	202.1
4	C	0.000	0.000	0.000					
					comp1808	6.66	4.38	-184.2	-282.8
					comp1809	5.65	5.75	-242.4	-240.0
					comp1810	8.47	0.17	-5.3	-359.4

5	C	0.000	0.000	0.000				
				comp1808	5.20	11.63	-491.3	-221.2
				comp1809	3.12	12.36	-522.8	-133.1
				comp1810	6.86	3.13	-130.9	-291.3
6	C	0.000	0.000	0.000				
				comp1809	-2.88	-1.49	62.4	122.2
				comp1810	-5.01	-4.25	178.9	212.9
7	C	0.000	0.000	0.000				
				comp1808	0.15	-38.99	1650.2	-3.6
				comp1809	-1.79	-38.70	1638.4	78.6
				comp1810	9.60	-43.46	1842.2	-403.2
8	C	0.000	0.000	0.000				
				comp1808	11.96	13.72	-578.9	-507.9
				comp1809	10.43	17.01	-718.1	-443.8
				comp1810	24.55	8.35	-348.1	-1042.2
9	C	0.000	0.000	0.000				
				comp1809	-14.01	6.33	-271.0	594.2
				comp1810	0.14	-0.07	3.1	-6.0
10	C	0.000	0.000	0.000				
				comp1809	-4.19	4.28	-182.1	177.4
				comp1810	-1.44	10.02	-424.6	60.4
12	C	0.000	0.000	0.000				
				comp1808	-3.37	-3.45	145.7	143.3
				comp1809	-4.44	-0.88	36.4	188.5
13	C	0.000	0.000	0.000				
				comp1808	0.20	-0.22	9.3	-8.3
				comp1809	-0.30	-3.25	137.7	12.9
14	C	0.000	0.000	0.000				
				comp1808	-1.44	3.50	-148.4	60.7
				comp1809	-2.72	-8.02	339.2	115.7
15	C	0.000	0.000	0.000				
				comp1808	-2.90	3.06	-130.1	122.7
				comp1809	-2.45	-2.99	126.3	104.4
17	C	0.000	0.000	0.000				
				comp1808	-4.80	2.29	-97.8	203.4
				comp1809	-3.65	-9.76	412.7	155.3
16	C	0.000	0.000	0.000				
				comp1809	-2.47	-6.99	295.3	105.3
				comp1810	1.06	-13.11	555.3	-43.6
TP1	T							
				comp1809	0.61	0.09	-3.7	-25.7

					comp1810	-2.84	-6.29	265.8	121.0
TP2	T								
					comp1809	0.24	0.12	-4.9	-10.1
					comp1810	-3.97	-2.64	110.8	168.6
TP3	T								
					comp1809	0.06	0.13	-5.5	-2.6
					comp1810	0.06	0.03	-1.1	-2.5
TP4	T								
					comp1808	0.36	0.02	-0.7	-15.2
					comp1809	1.28	-0.07	3.2	-54.5
					comp1810	11.36	-6.49	277.2	-481.5
TP5	T								
					comp1809	0.13	0.24	-10.3	-5.7
					comp1810	-0.00	-2.88	121.8	0.3
TP6	T								
					comp1808	-0.67	0.04	-1.8	28.6
					comp1809	0.28	0.20	-8.2	-12.0
TP7	T								
					comp1808	0.67	0.35	-14.8	-28.5
					comp1809	-0.55	-0.61	25.7	23.4
					comp1810	-2.03	-6.22	262.9	86.7
TP8	T								
					comp1808	-0.04	0.36	-15.3	1.8
					comp1809	-0.08	-0.03	1.0	3.2
					comp1810	-0.10	-0.11	4.8	4.1
TP9	T								
					comp1808	0.34	-1.22	51.8	-14.5
					comp1809	0.10	-0.12	5.1	-4.4
TP10	T								
					comp1808	0.20	-0.33	13.9	-8.4
					comp1809	-0.44	0.10	-4.3	18.6
Averages:		0.000	0.000	0.000					
RMS:		0.000	0.000	0.000					
					Averages:	3.51	5.25	222.1	148.8
					RMS:	5.50	10.32	436.6	233.4

----- Results for Iteration 1 -----

Statistics Summary

Number of Equations: 220
Number of Unknowns: 96
Degrees of Freedom: 124

Standard Deviation of Unit Weight: 16.544967

Category	VTPV Sum	Ratio	Sigma0
a priori photo	0.000	0.000	0.000
a priori point	0.000	0.000	0.000
collinearity equations	33943.255	1.774	16.545

Frame Parameters (Unit is Meter and degrees)

Frame	Description	Cam	X	Y	Z	Omega	Phi	Kappa
3	comp1808	1	582593.886	4165913.066	1925.961	2.120454	-2.101938	-3.439362
4	comp1809	1	583138.654	4165880.135	1932.188	-0.030645	-3.149888	-3.318554
5	comp1810	1	583674.838	4165862.481	1946.742	1.681713	-1.366331	-1.645383

Point Results for Iteration 1

Point ID	Type	Description	Current Correction X	Y	Z	Current Position X	Y	Z
1	C		0.287	1.388	1.392	583438.057	4165757.958	839.002
2	C		-0.666	1.114	1.096	583448.834	4165880.704	827.496
3	C		-0.762	1.284	1.638	583426.748	4166111.715	808.768
4	C		-1.957	-1.817	-0.355	583404.893	4166291.924	798.565
5	C		-3.629	-0.443	-1.811	583366.591	4166389.897	785.809
6	C		0.427	1.365	2.007	583614.237	4165515.025	862.357
7	C		11.912	-0.829	0.024	583413.192	4166575.651	793.184
8	C		-5.990	-4.681	0.204	583163.930	4166651.600	766.194
9	C		-1.069	-0.056	5.821	583004.631	4166589.114	773.091
10	C		-4.408	-0.742	4.183	583788.962	4166364.608	782.863
12	C		0.674	0.588	0.543	582828.104	4166418.878	777.623
13	C		-0.332	0.878	-3.109	582551.508	4166336.239	778.681
14	C		-0.169	1.207	-7.314	582735.661	4165993.617	784.516
15	C		-0.779	1.000	-3.596	582641.921	4165957.820	815.634

17	C	-0.258	-1.722	-4.928	582616.152	4165443.958	856.732
16	C	2.610	0.763	1.889	583726.340	4165250.184	852.629
TP1	T	0.048	0.477	1.253	584007.061	4165555.841	836.268
TP2	T	-0.057	0.358	-0.034	584000.394	4166007.956	805.630
TP3	T	-0.142	0.251	-1.116	584098.531	4166373.224	771.632
TP4	T	-0.149	0.092	-1.781	583435.222	4166674.525	772.849
TP5	T	0.118	0.499	2.109	583543.875	4165322.098	862.498
TP6	T	0.023	0.371	0.465	583363.892	4165908.176	852.022
TP7	T	0.007	0.256	0.138	583256.136	4166030.714	824.171
TP8	T	0.200	0.476	2.605	583079.517	4165201.264	877.672
TP9	T	-0.064	-0.025	-1.529	582615.611	4166678.704	793.778
TP10	T	-0.024	0.072	-0.402	583005.620	4166250.182	786.243

Frame Parameter Residuals (Unit is Meter and degrees)

Frame	Description	Cam	X	Y	Z	Omega	Phi	Kappa
3	comp1808	1	-2.606	-0.489	-0.977	0.139111	-0.030215	-0.025821
4	comp1809	1	-3.171	-0.419	-0.458	0.155894	-0.016017	-0.017204
5	comp1810	1	5.076	-3.199	-0.879	-0.219329	-0.213206	0.027418

Point ID	Type	Point Residuals (Meter) X	Y	Z	Image Residuals Frame ID	Sample	Line	Image X	Image Y
1	C	-0.287	-1.388	-1.392					
					comp1808	-1.07	-0.22	9.3	45.2
					comp1809	0.45	0.47	-20.0	-19.0
					comp1810	0.62	-0.22	9.3	-26.4
2	C	0.666	-1.114	-1.096					
					comp1808	-0.27	-0.21	8.8	11.5
					comp1809	0.20	0.41	-17.4	-8.5
					comp1810	0.06	-0.19	7.9	-2.7
3	C	0.762	-1.284	-1.638					
					comp1808	-0.16	-0.02	1.0	6.7
					comp1809	-0.38	0.06	-2.6	16.0
					comp1810	0.51	-0.00	0.1	-21.5
4	C	1.957	1.817	0.355					
					comp1808	0.19	-0.18	7.7	-8.0
					comp1809	-0.29	0.31	-13.1	12.5
					comp1810	0.09	-0.10	4.4	-3.9

5	C	3.629	0.443	1.811					
					comp1808	1.21	-0.47	20.3	-51.5
					comp1809	-0.08	0.92	-39.0	3.5
					comp1810	-1.11	-0.38	15.9	47.1
6	C	-0.427	-1.365	-2.007					
					comp1809	-0.29	0.00	-0.2	12.1
					comp1810	0.33	-0.01	0.7	-13.8
7	C	-11.912	0.829	-0.024					
					comp1808	0.43	0.12	-5.2	-18.4
					comp1809	-0.96	-0.18	7.4	40.7
					comp1810	0.61	-0.08	3.5	-26.0
8	C	5.990	4.681	-0.204					
					comp1808	0.13	0.17	-7.3	-5.4
					comp1809	-0.51	-0.47	19.9	21.7
					comp1810	0.34	0.36	-15.0	-14.6
9	C	1.069	0.056	-5.821					
					comp1809	-0.25	-0.06	2.6	10.5
					comp1810	0.29	0.05	-2.0	-12.2
10	C	4.408	0.742	-4.183					
					comp1809	-0.50	-0.05	2.0	21.3
					comp1810	0.47	-0.01	0.6	-19.9
12	C	-0.674	-0.588	-0.543					
					comp1808	0.08	0.00	-0.0	-3.3
					comp1809	-0.08	0.00	-0.1	3.5
13	C	0.332	-0.878	3.109					
					comp1808	0.07	0.02	-0.9	-2.9
					comp1809	-0.02	-0.02	0.8	0.8
14	C	0.169	-1.207	7.314					
					comp1808	0.71	0.07	-3.0	-30.2
					comp1809	-0.60	-0.09	3.6	25.3
15	C	0.779	-1.000	3.596					
					comp1808	-0.15	0.04	-1.5	6.2
					comp1809	0.19	-0.02	0.8	-8.2
17	C	0.258	1.722	4.928					
					comp1808	-0.22	0.04	-1.9	9.3
					comp1809	0.31	-0.07	3.0	-13.2
16	C	-2.610	-0.763	-1.889					
					comp1809	-0.39	0.01	-0.3	16.5
					comp1810	0.41	-0.01	0.3	-17.6
TP1	T								
					comp1809	0.60	-0.03	1.6	-25.5

TP2	T				comp1810	-0.55	-0.03	1.0	23.3
					comp1809	0.30	-0.02	0.8	-12.9
					comp1810	-0.32	-0.00	0.1	13.5
TP3	T								
					comp1809	0.02	-0.01	0.4	-0.8
					comp1810	-0.07	0.02	-0.8	2.9
TP4	T								
					comp1808	-0.81	0.02	-1.2	34.4
					comp1809	1.34	-0.07	3.3	-56.8
					comp1810	-0.59	0.09	-4.0	24.9
TP5	T								
					comp1809	0.15	-0.01	0.5	-6.4
					comp1810	-0.09	-0.03	1.1	3.7
TP6	T								
					comp1808	-0.58	-0.01	0.2	24.7
					comp1809	0.58	0.00	-0.0	-24.6
TP7	T								
					comp1808	0.70	0.38	-15.8	-29.6
					comp1809	-0.23	-0.77	32.5	10.0
					comp1810	-0.48	0.40	-17.2	20.3
TP8	T								
					comp1808	0.35	0.25	-10.3	-15.0
					comp1809	0.00	-0.52	22.2	0.0
					comp1810	-0.29	0.25	-10.6	12.1
TP9	T								
					comp1808	-0.51	-0.01	0.3	21.8
					comp1809	0.48	0.02	-0.9	-20.5
TP10	T								
					comp1808	0.08	-0.00	0.1	-3.4
					comp1809	-0.07	0.00	-0.0	3.1
Averages:		2.246	1.242	2.494					
RMS:		3.748	1.590	3.249					
					Averages:	0.39	0.15	6.2	16.6
					RMS:	0.49	0.24	10.3	20.9

----- Results for Iteration 2 -----

Statistics Summary

Number of Equations: 220
Number of Unknowns: 96
Degrees of Freedom: 124

Standard Deviation of Unit Weight: 0.857244

Category	VTPV Sum	Ratio	Sigma0
a priori photo	3.771	0.506	0.458
a priori point	12.058	0.373	0.393
collinearity equations	75.294	1.466	0.779

Frame Parameters (Unit is Meter and degrees)

Frame	Description	Cam	X	Y	Z	Omega	Phi	Kappa
3	comp1808	1	582593.920	4165913.087	1925.913	2.119938	-2.101928	-3.439246
4	comp1809	1	583138.649	4165880.157	1932.141	-0.031123	-3.150137	-3.318519
5	comp1810	1	583674.820	4165862.481	1946.676	1.682449	-1.365769	-1.645994

Point Results for Iteration 2

Point ID	Type	Description	Current Correction X	Y	Z	Current Position X	Y	Z
1	C		-0.015	0.020	0.011	583438.043	4165757.978	839.013
2	C		-0.017	0.015	0.017	583448.817	4165880.719	827.513
3	C		-0.016	0.003	0.013	583426.733	4166111.718	808.781
4	C		-0.019	-0.013	0.032	583404.874	4166291.910	798.597
5	C		-0.028	-0.028	0.046	583366.563	4166389.869	785.855
6	C		-0.021	0.025	0.002	583614.216	4165515.050	862.359
7	C		0.016	0.014	-0.062	583413.209	4166575.666	793.121
8	C		-0.003	-0.056	0.065	583163.927	4166651.544	766.259
9	C		0.022	-0.044	0.039	583004.653	4166589.071	773.131
10	C		-0.014	-0.001	-0.007	583788.948	4166364.607	782.856
12	C		0.017	-0.018	0.016	582828.122	4166418.860	777.639
13	C		0.033	-0.021	0.010	582551.541	4166336.218	778.691
14	C		0.019	-0.006	-0.035	582735.680	4165993.611	784.482

15	C	0.024	0.001	0.003	582641.946	4165957.820	815.637
17	C	0.027	0.012	-0.015	582616.179	4165443.970	856.717
16	C	-0.037	0.054	0.027	583726.303	4165250.238	852.656
TP1	T	-0.061	0.036	0.044	584007.000	4165555.877	836.312
TP2	T	-0.056	0.004	0.034	584000.338	4166007.960	805.664
TP3	T	-0.066	-0.020	0.037	584098.465	4166373.205	771.669
TP4	T	-0.020	-0.038	0.022	583435.202	4166674.487	772.871
TP5	T	-0.018	0.040	0.011	583543.857	4165322.137	862.509
TP6	T	-0.013	0.012	0.018	583363.879	4165908.187	852.040
TP7	T	-0.007	0.007	0.021	583256.129	4166030.720	824.192
TP8	T	0.008	0.049	0.013	583079.525	4165201.313	877.685
TP9	T	0.030	-0.038	0.015	582615.641	4166678.666	793.793
TP10	T	0.007	-0.011	0.019	583005.628	4166250.172	786.263

Frame Parameter Residuals (Unit is Meter and degrees)

Frame	Description	Cam	X	Y	Z	Omega	Phi	Kappa
3	comp1808	1	-2.626	-0.522	-0.929	0.139627	-0.030225	-0.025937
4	comp1809	1	-3.193	-0.414	-0.411	0.156372	-0.015768	-0.017239
5	comp1810	1	5.076	-3.182	-0.814	-0.220065	-0.213768	0.028028

Point ID	Type	Point Residuals (Meter) X	Y	Z	Image Residuals Frame ID	Sample	Line	Image X	Image Y
1	C	-0.273	-1.408	-1.403					
					comp1808	-1.07	-0.23	9.7	45.3
					comp1809	0.45	0.48	-20.0	-19.2
					comp1810	0.61	-0.22	9.4	-25.9
2	C	0.683	-1.129	-1.113					
					comp1808	-0.27	-0.21	8.8	11.5
					comp1809	0.21	0.41	-17.4	-8.8
					comp1810	0.06	-0.20	8.4	-2.6
3	C	0.777	-1.288	-1.651					
					comp1808	-0.15	-0.03	1.2	6.4
					comp1809	-0.36	0.06	-2.5	15.5
					comp1810	0.51	-0.02	0.8	-21.8
4	C	1.976	1.830	0.323					
					comp1808	0.20	-0.16	6.6	-8.4
					comp1809	-0.28	0.31	-13.1	11.9

				comp1810	0.10	-0.15	6.4	-4.1
5	C	3.657	0.471	1.765				
				comp1808	1.22	-0.45	19.4	-51.6
				comp1809	-0.08	0.89	-37.9	3.2
				comp1810	-1.11	-0.48	20.0	47.2
6	C	-0.406	-1.390	-2.009				
				comp1809	-0.30	-0.00	0.0	12.5
				comp1810	0.28	0.01	-0.5	-12.0
7	C	-11.929	0.815	0.039				
				comp1808	0.42	0.06	-2.6	-18.0
				comp1809	-0.97	-0.13	5.5	41.2
				comp1810	0.59	0.05	-1.9	-24.9
8	C	5.993	4.736	-0.269				
				comp1808	0.16	0.24	-10.3	-6.7
				comp1809	-0.48	-0.47	20.0	20.2
				comp1810	0.34	0.26	-10.9	-14.6
9	C	1.047	0.100	-5.861				
				comp1809	-0.24	-0.02	1.0	10.3
				comp1810	0.25	0.03	-1.2	-10.7
10	C	4.422	0.743	-4.176				
				comp1809	-0.49	-0.02	0.8	20.7
				comp1810	0.49	0.04	-1.5	-20.9
12	C	-0.692	-0.569	-0.559				
				comp1808	0.08	-0.00	0.1	-3.4
				comp1809	-0.08	-0.00	0.0	3.3
13	C	0.299	-0.857	3.099				
				comp1808	0.04	0.02	-0.7	-1.8
				comp1809	-0.04	-0.02	0.7	1.8
14	C	0.150	-1.201	7.348				
				comp1808	0.66	0.04	-1.5	-28.0
				comp1809	-0.65	-0.04	1.5	27.5
15	C	0.754	-1.000	3.593				
				comp1808	-0.17	0.02	-0.7	7.4
				comp1809	0.17	-0.01	0.6	-7.2
17	C	0.231	1.710	4.943				
				comp1808	-0.26	0.02	-1.1	11.1
				comp1809	0.27	-0.03	1.1	-11.4
16	C	-2.573	-0.818	-1.916				
				comp1809	-0.38	0.00	-0.2	16.1
				comp1810	0.36	0.01	-0.3	-15.3
TP1	T							

				comp1809		0.60	-0.02	0.8	-25.3
				comp1810		-0.57	-0.01	0.1	24.3
TP2	T								
				comp1809		0.30	-0.01	0.3	-12.9
				comp1810		-0.30	-0.00	0.0	12.8
TP3	T								
				comp1809		0.03	-0.00	0.0	-1.3
				comp1810	-0.03	-0.00	0.0	1.3	
TP4	T								
				comp1808		-0.81	0.04	-1.7	34.2
				comp1809		1.34	-0.07	3.4	-57.0
				comp1810		-0.60	0.05	-2.2	25.5
TP5	T								
				comp1809		0.15	-0.01	0.3	-6.4
				comp1810		-0.15	-0.00	0.0	6.2
TP6	T								
				comp1808		-0.59	-0.00	-0.0	24.9
				comp1809		0.58	0.01	-0.1	-24.7
TP7	T								
				comp1808		0.71	0.38	-16.1	-29.9
				comp1809		-0.22	-0.77	32.4	9.4
				comp1810		-0.48	0.37	-15.9	20.3
TP8	T								
				comp1808		0.35	0.24	-10.2	-14.9
				comp1809		0.01	-0.51	21.5	-0.2
				comp1810		-0.36	0.24	-10.4	15.4
TP9	T								
				comp1808		-0.52	-0.01	0.3	22.0
				comp1809		0.48	0.02	-0.7	-20.5
TP10	T								
				comp1808		0.08	0.00	-0.0	-3.2
				comp1809		-0.07	-0.00	0.1	3.1
Averages:		2.241	1.254	2.504					
RMS:		3.752	1.604	3.259					
					Averages:	0.39	0.14	5.9	16.6
					RMS:	0.49	0.24	10.2	20.9

----- Results for Iteration 3 -----

Statistics Summary

Number of Equations: 220
Number of Unknowns: 96
Degrees of Freedom: 124

Standard Deviation of Unit Weight: 0.855308

Category	VTPV Sum	Ratio	Sigma0
a priori photo	3.783	0.510	0.458
a priori point	12.123	0.377	0.394
collinearity equations	74.807	1.463	0.777

Frame Parameters (Unit is Meter and degrees)

Frame	Description	Cam	X	Y	Z	Omega	Phi	Kappa
3	comp1808	1	582593.920	4165913.087	1925.913	2.119936	-2.101924	-3.439244
4	comp1809	1	583138.649	4165880.157	1932.141	-0.031128	-3.150130	-3.318516
5	comp1810	1	583674.820	4165862.481	1946.676	1.682452	-1.365765	-1.645989

Point Results for Iteration 3

Point ID	Type	Description	Current Correction X	Y	Z	Current Position X	Y	Z
1	C		-0.000	0.000	-0.000	583438.043	4165757.978	839.013
2	C		-0.000	0.000	-0.000	583448.817	4165880.719	827.513
3	C		-0.000	0.000	-0.000	583426.733	4166111.718	808.781
4	C		-0.000	-0.000	0.000	583404.874	4166291.910	798.597
5	C		-0.000	-0.000	0.000	583366.563	4166389.869	785.855
6	C		-0.000	0.000	-0.000	583614.216	4165515.050	862.359
7	C		-0.000	-0.000	0.000	583413.208	4166575.665	793.121
8	C		-0.000	-0.000	0.000	583163.927	4166651.544	766.259
9	C		-0.000	-0.000	0.000	583004.653	4166589.070	773.131
10	C		-0.000	0.000	-0.000	583788.948	4166364.608	782.856
12	C		0.000	-0.000	0.000	582828.122	4166418.859	777.639
13	C		0.000	-0.000	0.000	582551.541	4166336.217	778.691
14	C		0.000	-0.000	0.000	582735.680	4165993.611	784.482

15	C	0.000	-0.000	0.000	582641.946	4165957.820	815.637
17	C	0.000	0.000	0.000	582616.179	4165443.970	856.717
16	C	-0.000	0.000	-0.000	583726.303	4165250.238	852.656
TP1	T	-0.000	0.000	-0.000	584006.999	4165555.877	836.312
TP2	T	-0.000	0.000	-0.000	584000.338	4166007.960	805.664
TP3	T	-0.000	0.000	-0.000	584098.465	4166373.205	771.669
TP4	T	-0.000	-0.000	0.000	583435.202	4166674.487	772.871
TP5	T	0.000	0.000	-0.000	583543.857	4165322.138	862.509
TP6	T	-0.000	0.000	-0.000	583363.879	4165908.187	852.040
TP7	T	-0.000	0.000	0.000	583256.129	4166030.720	824.192
TP8	T	0.000	0.000	-0.000	583079.525	4165201.313	877.685
TP9	TïÿÇ^	0.000	-0.000	0.000	582615.641	4166678.666	793.793
TP10	T	-0.000	-0.000	0.000	583005.628	4166250.171	786.263

Timing Information (in minutes):

Time in Pre-Triangulation:	0.00
Time in Estimation:	0.00
Time in Initialization:	0.00
Time in Solution:	0.00
Average Time Per Iteration:	0.00
Time in Error Propagation:	0.00
Total Triangulation Time:	0.00

Appendix B: The Estimated X, Y, and Z Co-ordinates of GCPs

Results of Pre-Triangulation Processing:

Frame Description	Control Points	Tie Points
comp1808	18	0
comp1809	26	0
comp1810	18	0

Estimated Frame Parameters (Units are Meter and degrees)

E = estimated U = previously updated I = imported from external

Frame	Description	Status	Pass	X	Y	Z	Omega	Phi	Kappa	RMSE(pixels)
3	comp1808	U	1	582593.397	4165910.460	1924.984	2.259565	-2.132153	-3.465183	0.0
4	comp1809	U	1	583138.235	4165876.964	1931.729	0.125249	-3.165904	-3.335758	0.0
5	comp1810	U	1	583671.639	4165867.557	1945.862	1.462384	-1.579537	-1.617965	0.0

Estimated Point Positions (Unit is Meter)

E = estimated U = previously updated

Point ID	Description	Status	Type	Pass	X	Y	Z
TP1		U		0	584007.013	4165555.364	835.015
TP2		U		0	584000.451	4166007.598	805.664
TP3		U		0	584098.673	4166372.973	772.748
TP4		U		0	583435.371	4166674.432	774.630
TP5		U		0	583543.757	4165321.599	860.389
TP6		U		0	583363.869	4165907.805	851.557

TP7	U	0	583256.129	4166030.458	824.033
TP8	U	0	583079.317	4165200.788	875.067
TP9	U	0	582615.675	4166678.728	795.307
TP10	U	0	583005.644	4166250.110	786.645

Appendix C: The Errors and Correlation for GCPs and Tie Points

----- Results After 3 Iterations -----

Statistics Summary

Number of Equations:	220
Number of Unknowns:	96
Degrees of Freedom:	124

Standard Deviation of Unit Weight: 0.855308

Category	VTPV Sum	Ratio	Sigma0
a priori photo	3.783	0.510	0.458
a priori point	12.123	0.377	0.394
collinearity equations	74.807	1.463	0.777

Frame Parameter Standard Deviations (Unit is Meter and degrees)

Frame	Description	Cam	X	Y	Z	Omega	Phi	Kappa
3	comp1808	1	2.108	2.069	2.181	0.086191	0.085984	0.089644
4	comp1809	1	1.855	1.877	2.003	0.085972	0.085503	0.089319
5	comp1810	1	2.057	2.059	2.149	0.085988	0.086286	0.089647

Point Standard Deviations and Correlations (Unit is Meter)

Point ID	Description	X	Y	Z	XY	XZ	YZ
1		1.363	1.360	1.351	-0.0153	-0.0096	0.0269
2		1.316	1.304	1.311	-0.0078	-0.0163	0.0201
3		1.275	1.266	1.285	0.0098	-0.0230	-0.0017
4		1.310	1.316	1.327	0.0204	-0.0218	-0.0204
5		1.345	1.366	1.366	0.0220	-0.0169	-0.0311
6		1.642	1.650	1.616	-0.0366	-0.0042	0.0493
7		1.492	1.536	1.503	0.0312	-0.0165	-0.0393
8		1.516	1.585	1.536	0.0030	0.0133	-0.0492

9	1.498	1.569	1.566	-0.0332	0.0569	-0.0866
10	1.652	1.624	1.644	0.0467	-0.0571	-0.0223
12	1.463	1.486	1.491	-0.0280	0.0404	-0.0423
13	1.677	1.651	1.646	-0.0376	0.0597	-0.0105
14	1.443	1.417	1.457	-0.0014	0.0348	0.0086
15	1.530	1.492	1.517	0.0027	0.0351	0.0169
17	1.823	1.828	1.791	0.0439	0.0168	0.0420
16	1.976	2.011	1.912	-0.0505	0.0022	0.0597
TP1	2.014	1.949	1.916	-0.0476	-0.0305	0.0661
TP2	1.846	1.749	1.777	0.0064	-0.0615	0.0303
TP3	2.043	1.953	1.976	0.0592	-0.0850	-0.0131
TP4	1.593	1.653	1.605	0.0364	-0.0179	-0.0482
TP5	1.775	1.825	1.755	-0.0370	0.0046	0.0580
TP6	1.272	1.255	1.308	-0.0046	-0.0479	0.0121
TP7	1.211	1.210	1.232	0.0017	-0.0074	-0.0005
TP8	1.810	1.894	1.785	0.0092	0.0107	0.0312
TP9	1.816	1.861	1.796	-0.0555	0.0634	-0.0439
TP10	1.286	1.299	1.352	-0.0053	0.0078	-0.0424

Appendix C

The spectral signatures of the training sites used for the Maximum Likelihood Classification

Ploughed grey soil

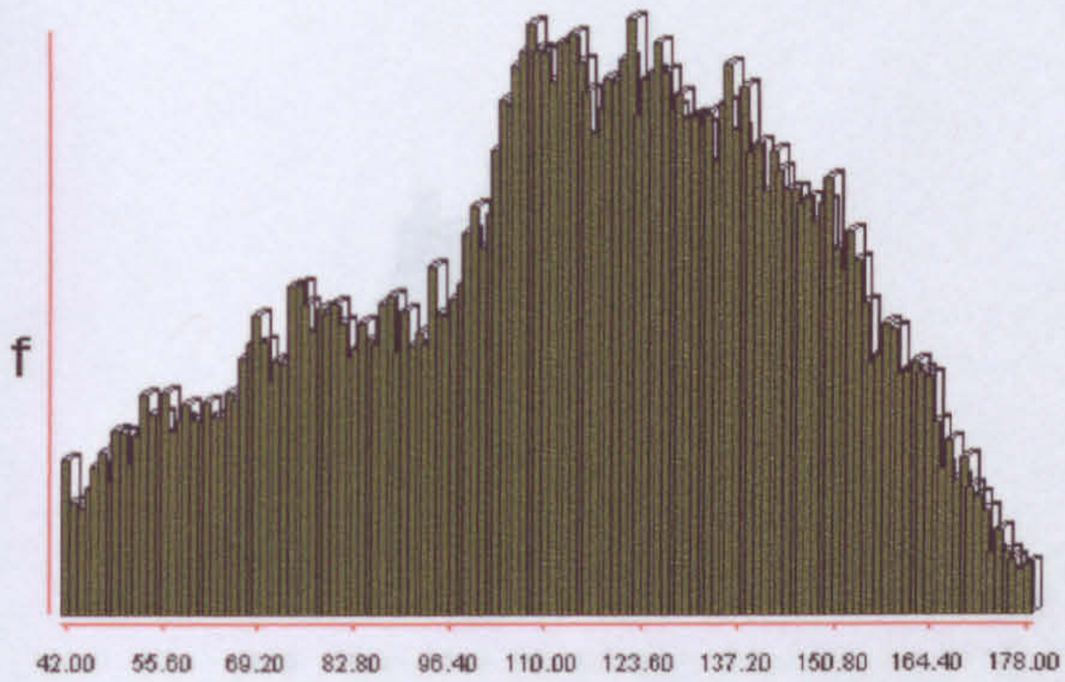

Histogram of
TEMPHIST

Class width :	1.0000
Display minimum :	42.0000
Display maximum :	178.0000
Actual minimum :	5.0000
Actual maximum :	203.0000
Mean :	113.2352
Stand. Deviation :	31.7138
df :	23298

based on 23299
values within range (out of 24226)

A)

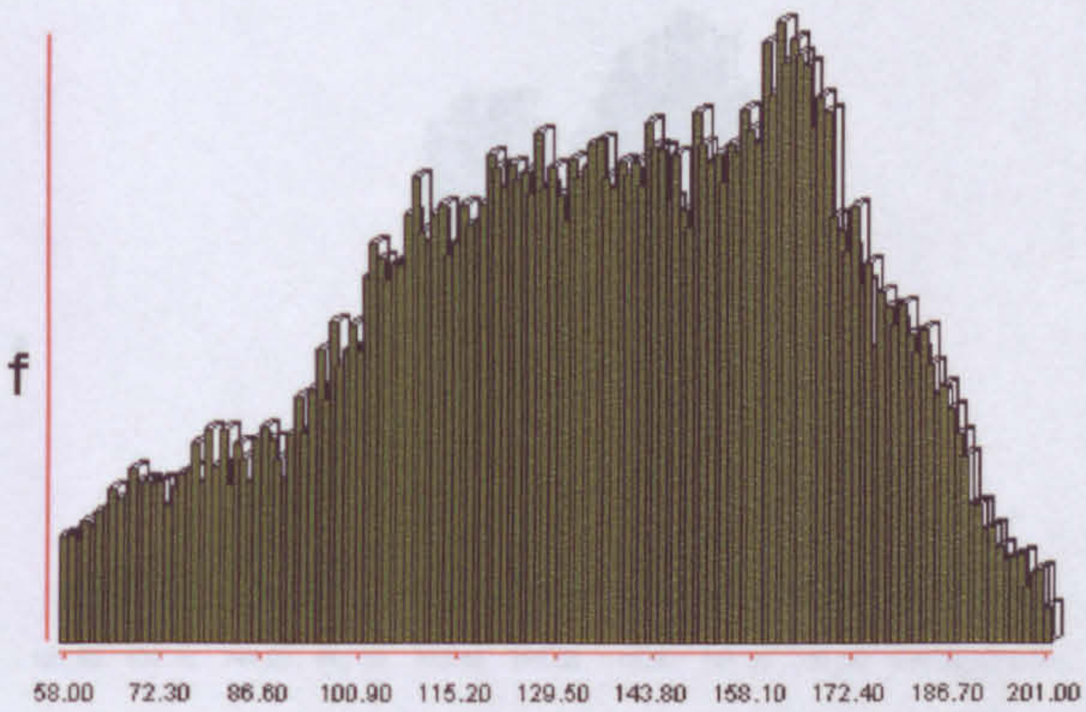

Histogram of
TEMPHIST

Class width :	1.0000
Display minimum :	58.0000
Display maximum :	201.0000
Actual minimum :	3.0000
Actual maximum :	216.0000
Mean :	134.8068
Stand. Deviation :	32.9145
df :	23133

based on 23134
values within range (out of 24226)

B)

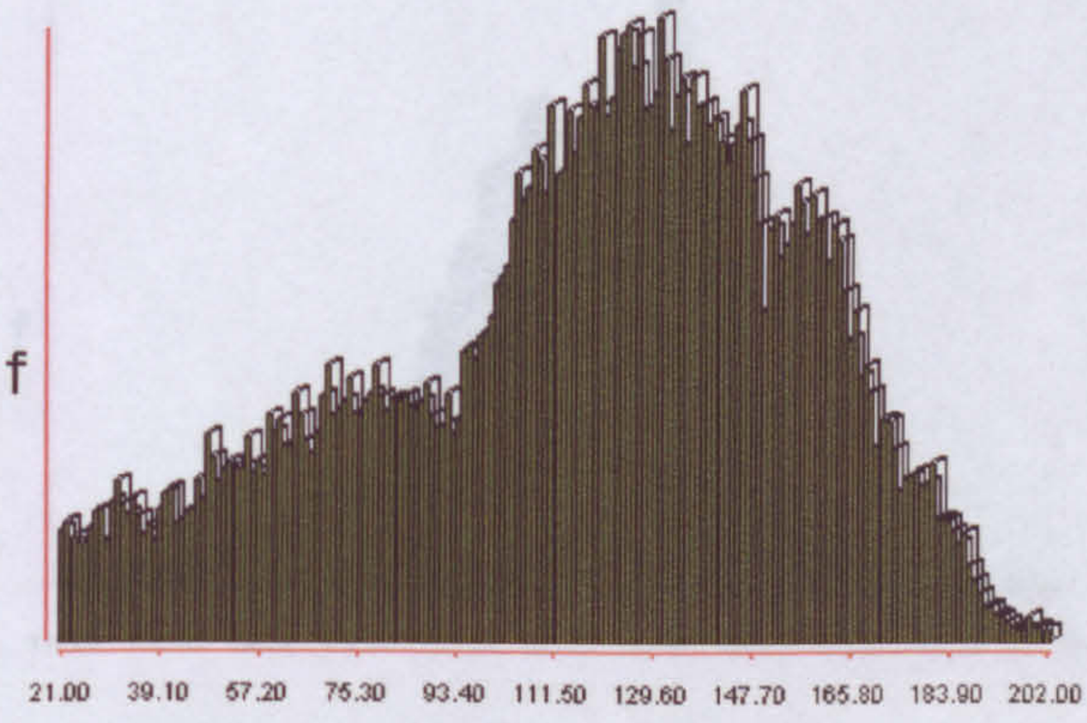

Histogram of
TEMPHIST

Class width :	1.0000
Display minimum :	21.0000
Display maximum :	202.0000
Actual minimum :	0.0000
Actual maximum :	208.0000
Mean :	116.5910
Stand. Deviation :	39.0978
df :	23072

based on 23073
values within range (out of 24226)

C)

Figure C-1 Spectral signature of ploughed grey soil in A) blue, B) green, and C) red band

Grey soil river

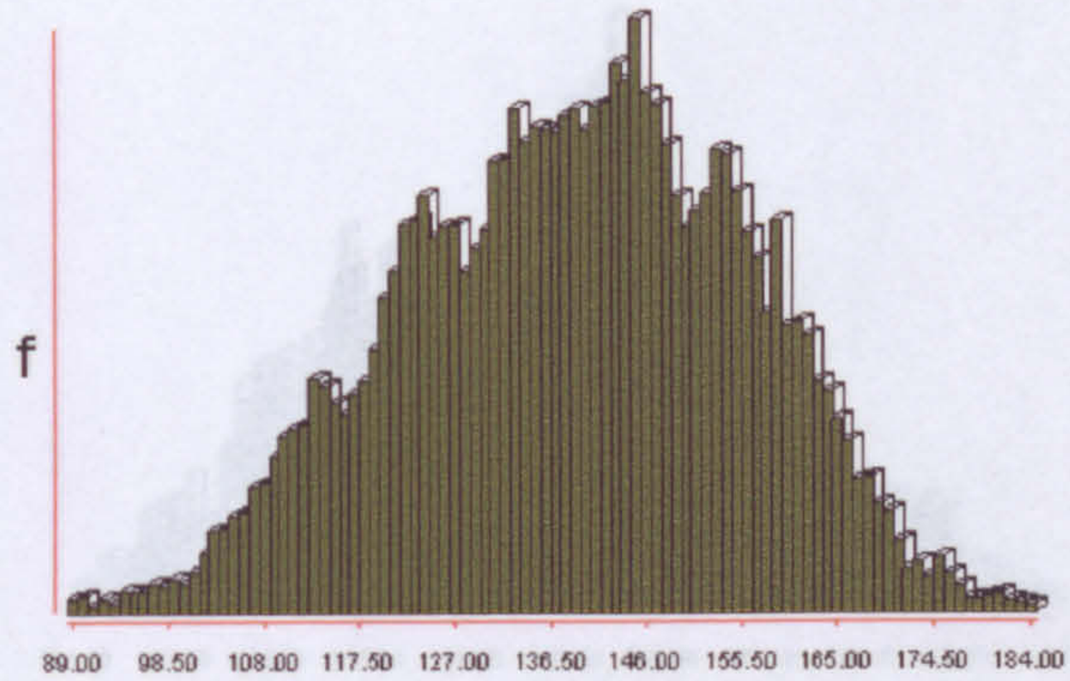

Histogram of
TEMPHIST

Class width :	1.0000
Display minimum :	89.0000
Display maximum :	184.0000
Actual minimum :	2.0000
Actual maximum :	193.0000
Mean :	138.6702
Stand. Deviation :	16.7599
df :	18673

based on 18674
values within range (out of 19248)

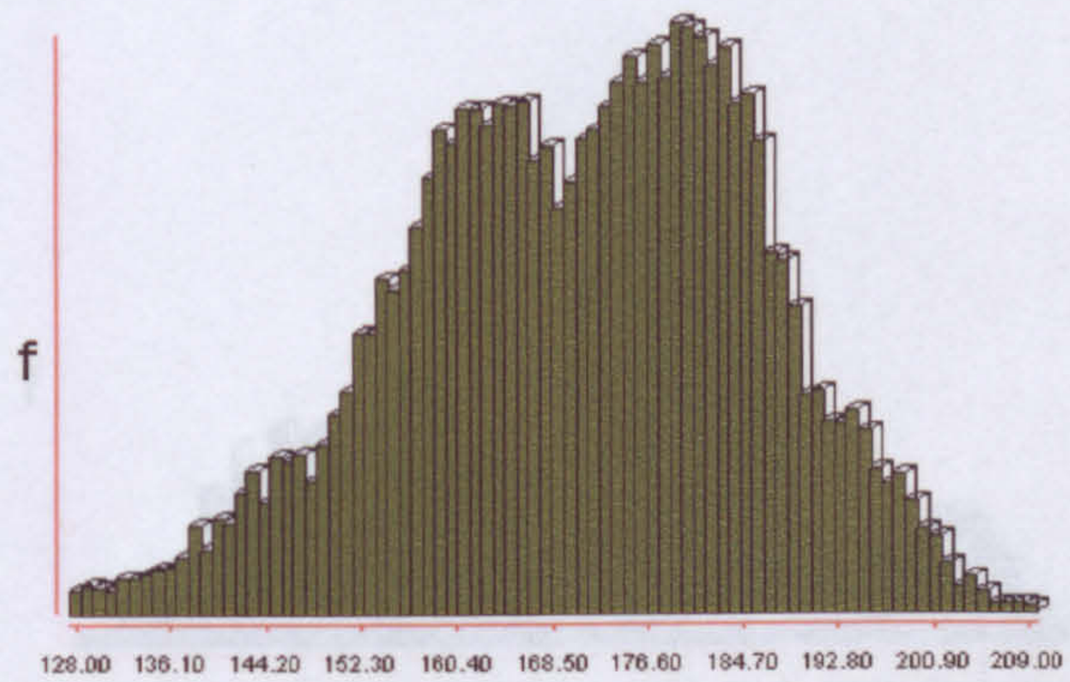

Histogram of
TEMPHIST

Class width :	1.0000
Display minimum :	128.0000
Display maximum :	209.0000
Actual minimum :	32.0000
Actual maximum :	222.0000
Mean :	170.7541
Stand. Deviation :	14.7931
df :	18657

based on 18658
values within range (out of 19248)

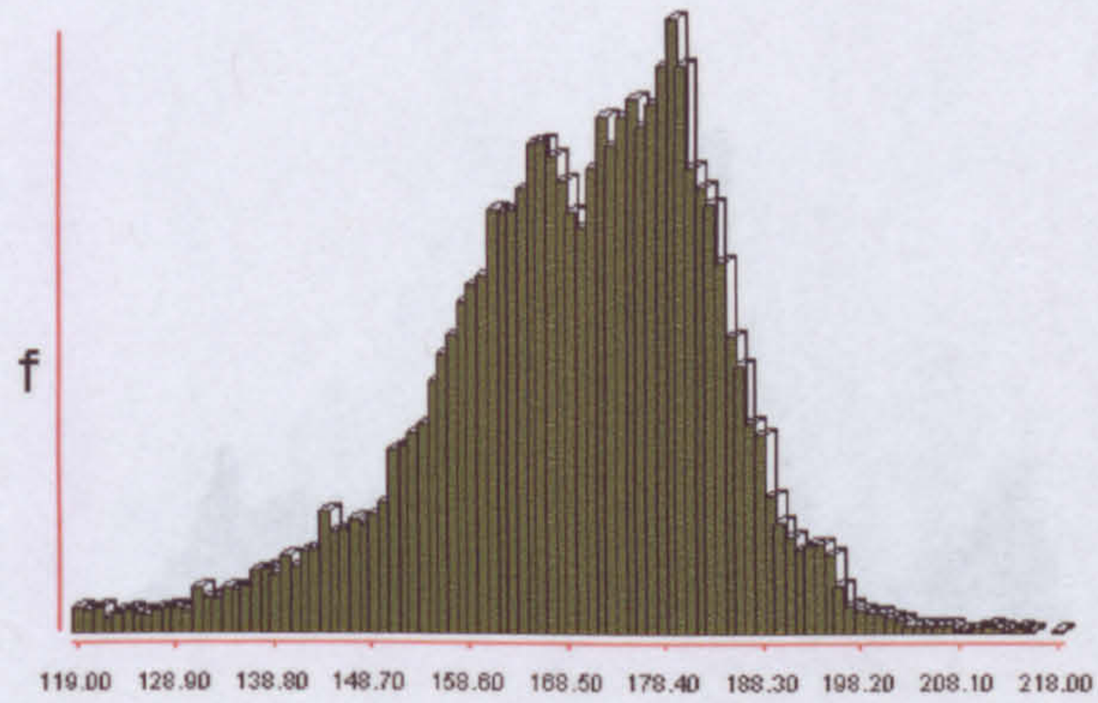

Histogram of
TEMPHIST

Class width :	1.0000
Display minimum :	119.0000
Display maximum :	218.0000
Actual minimum :	0.0000
Actual maximum :	220.0000
Mean :	168.8515
Stand. Deviation :	14.0537
df :	18606

based on 18607
values within range (out of 19248)

Figure C-2 Spectral signature of grey soil river

Grey soil road

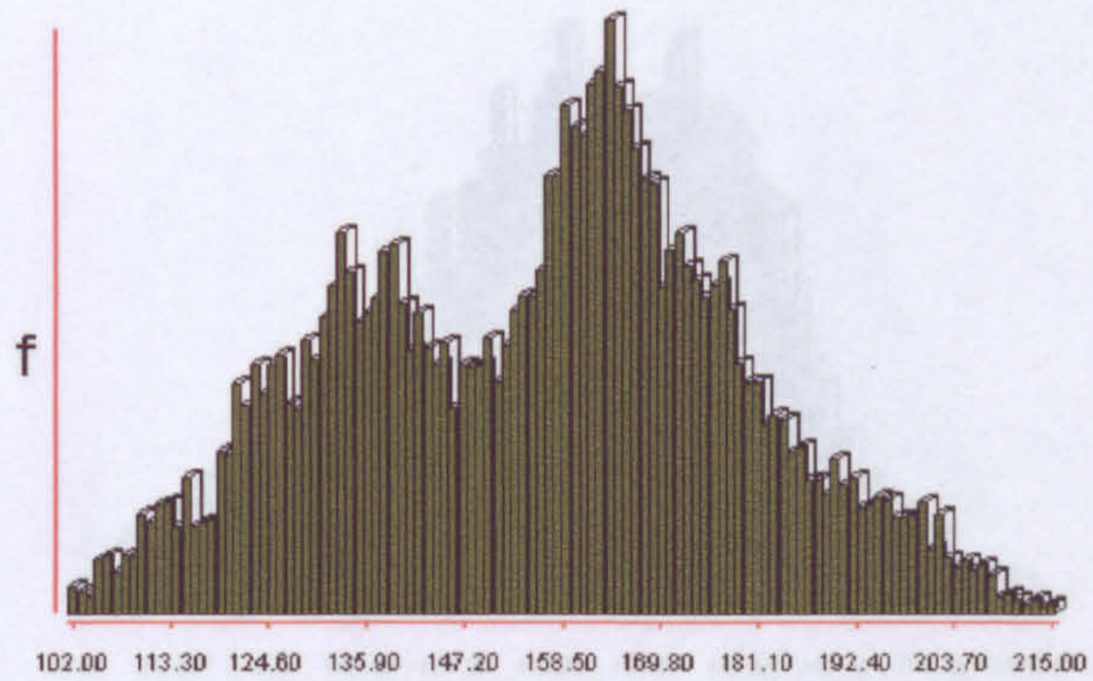

Histogram of
TEMPHIST

Class width :	1.0000
Display minimum :	102.0000
Display maximum :	215.0000
Actual minimum :	75.0000
Actual maximum :	220.0000
Mean :	155.7068
Stand. Deviation :	22.6467
df :	13043

based on 13044
values within range (out of 13100)

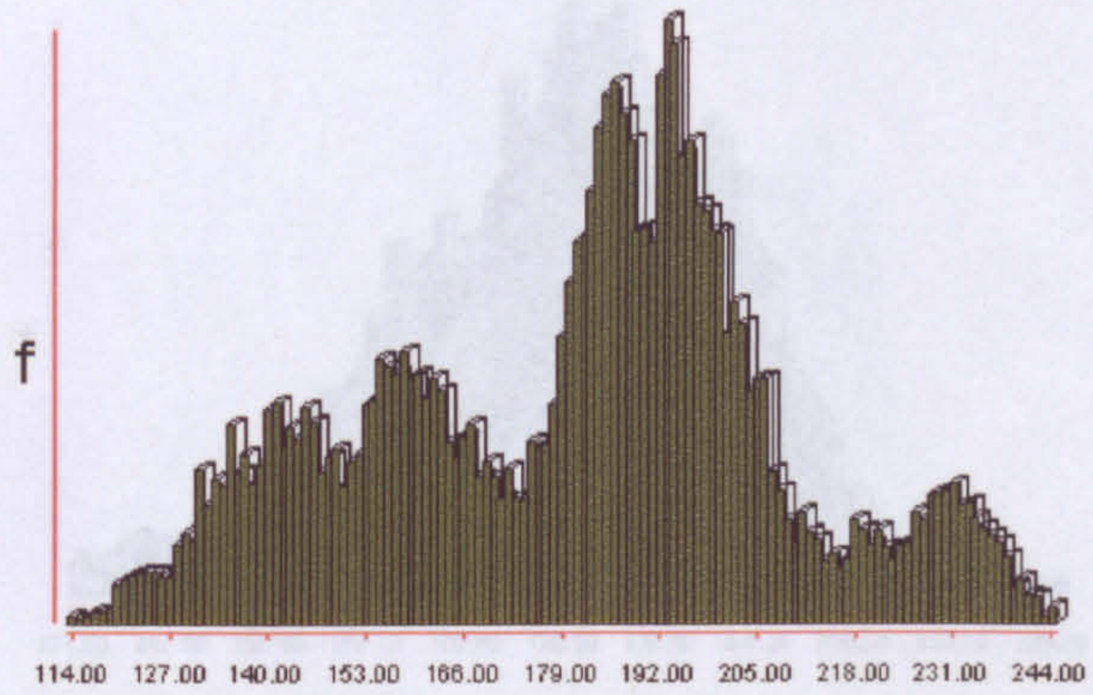

Histogram of
TEMPHIST

Class width :	1.0000
Display minimum :	114.0000
Display maximum :	244.0000
Actual minimum :	99.0000
Actual maximum :	247.0000
Mean :	180.6241
Stand. Deviation :	26.9445
df :	13077

based on 13078
values within range (out of 13100)

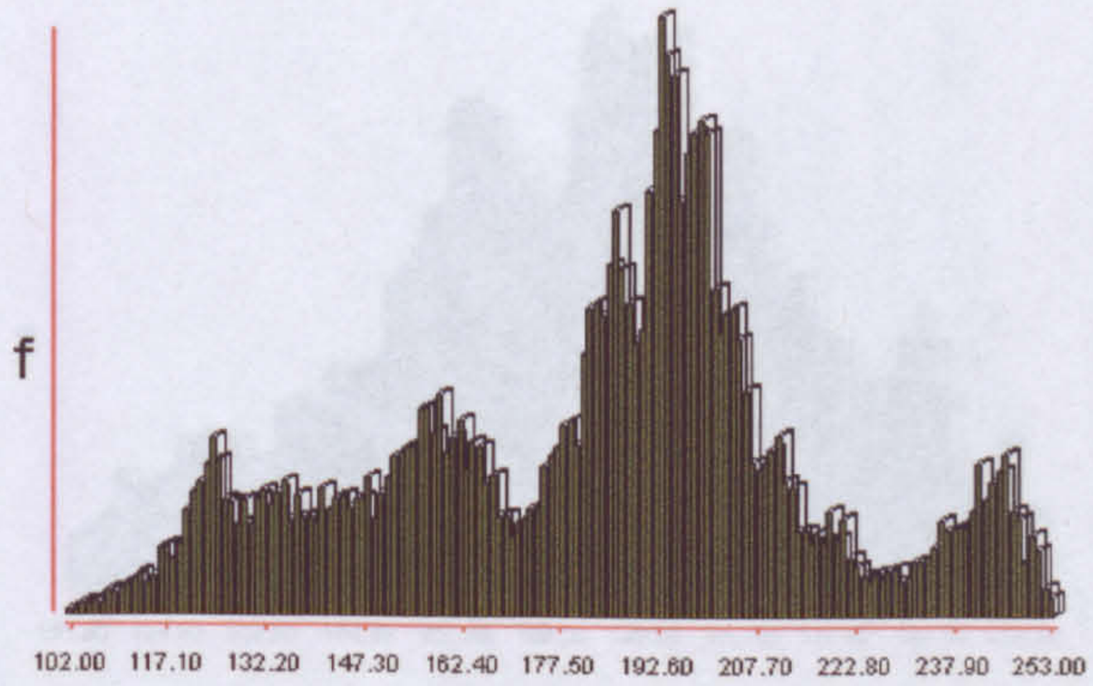

Histogram of
TEMPHIST

Class width :	1.0000
Display minimum :	102.0000
Display maximum :	253.0000
Actual minimum :	59.0000
Actual maximum :	255.0000
Mean :	182.7423
Stand. Deviation :	32.4854
df :	13055

based on 13056
values within range (out of 13100)

Figure C-3 Spectral signature of grey soil road

Bare ground

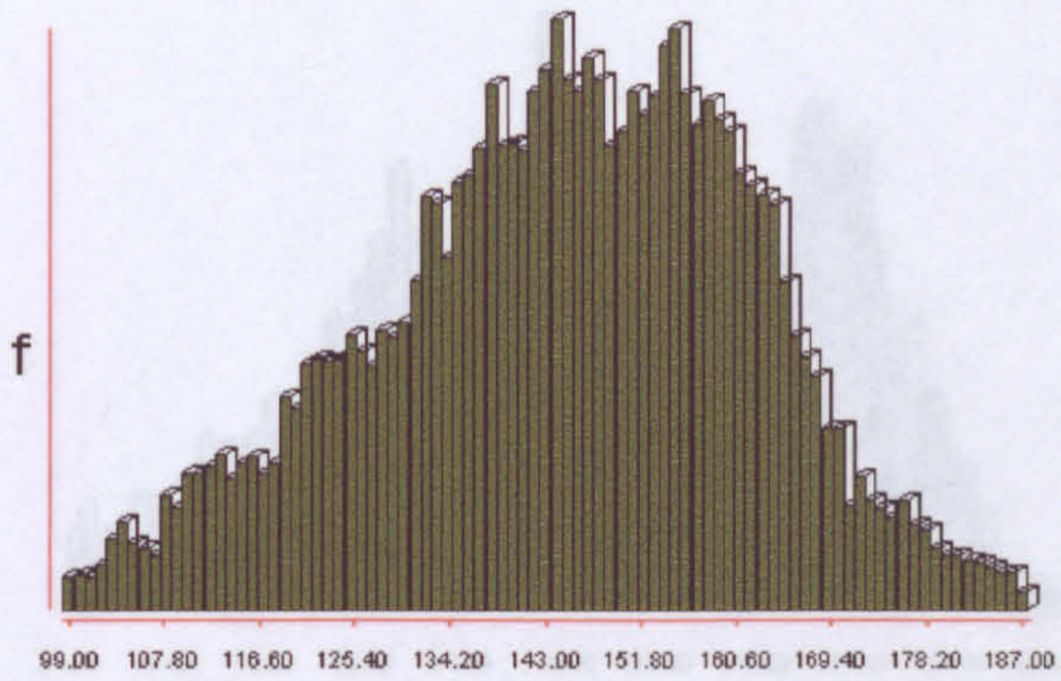

Histogram of
TEMPHIST

Class width :	1.0000
Display minimum :	99.0000
Display maximum :	187.0000
Actual minimum :	52.0000
Actual maximum :	201.0000
Mean :	144.5480
Stand. Deviation :	17.1928
df :	13482

based on 13483
values within range (out of 13682)

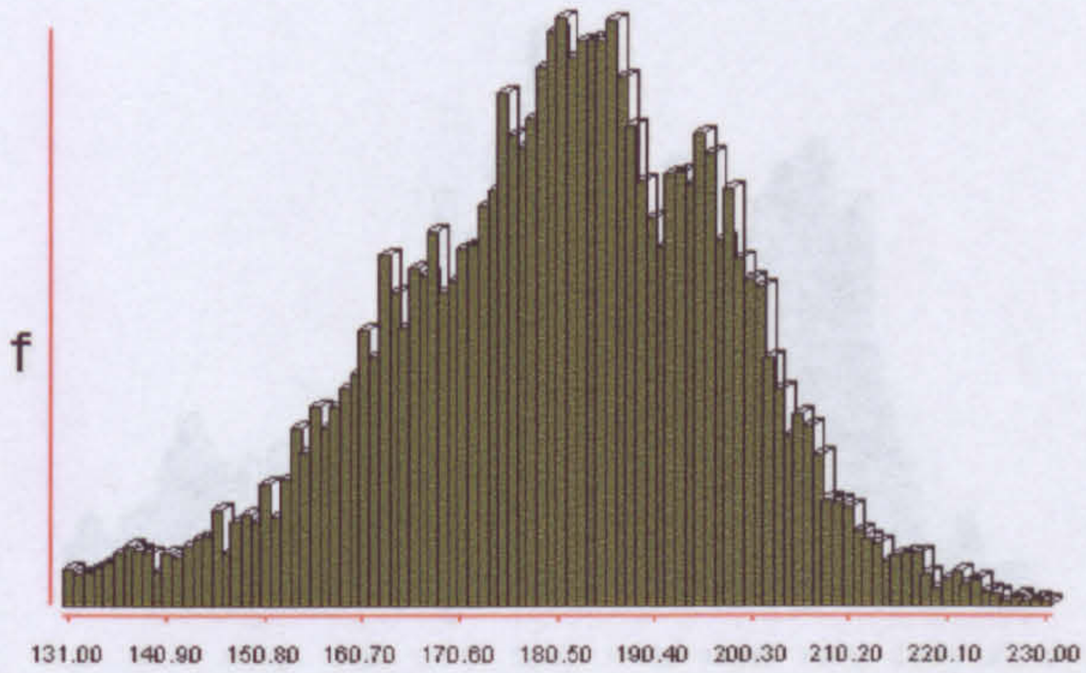

Histogram of
TEMPHIST

Class width :	1.0000
Display minimum :	131.0000
Display maximum :	230.0000
Actual minimum :	64.0000
Actual maximum :	232.0000
Mean :	180.4008
Stand. Deviation :	16.8910
df :	13460

based on 13461
values within range (out of 13682)

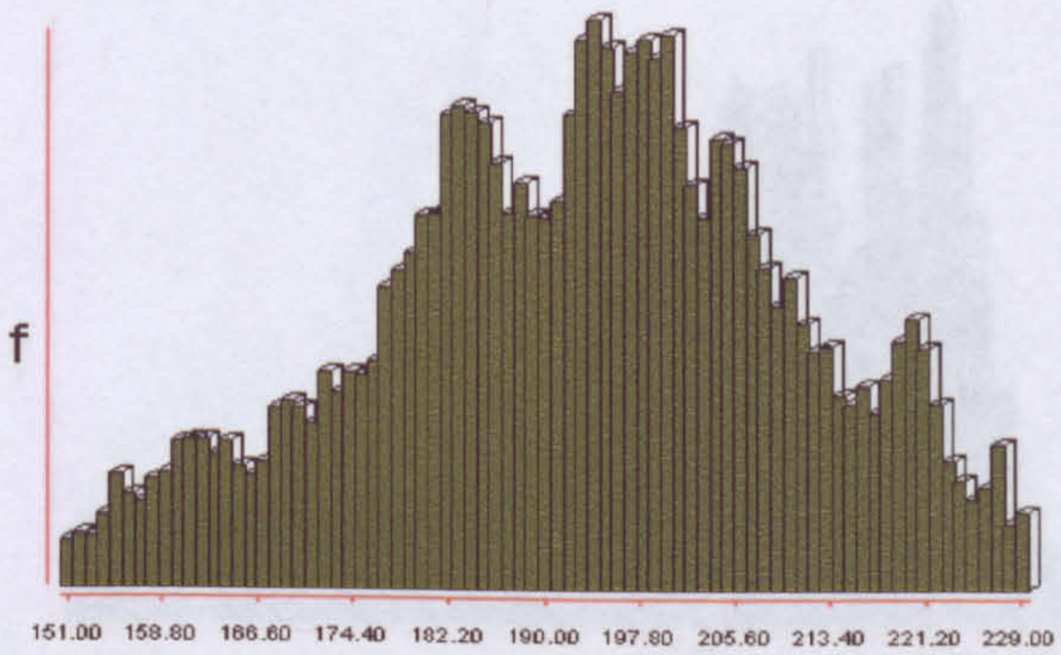

Histogram of
TEMPHIST

Class width :	1.0000
Display minimum :	151.0000
Display maximum :	229.0000
Actual minimum :	49.0000
Actual maximum :	246.0000
Mean :	192.8828
Stand. Deviation :	17.0413
df :	12921

based on 12922
values within range (out of 13682)

Figure C-4 Spectral signature of bare ground

Ploughed red soil

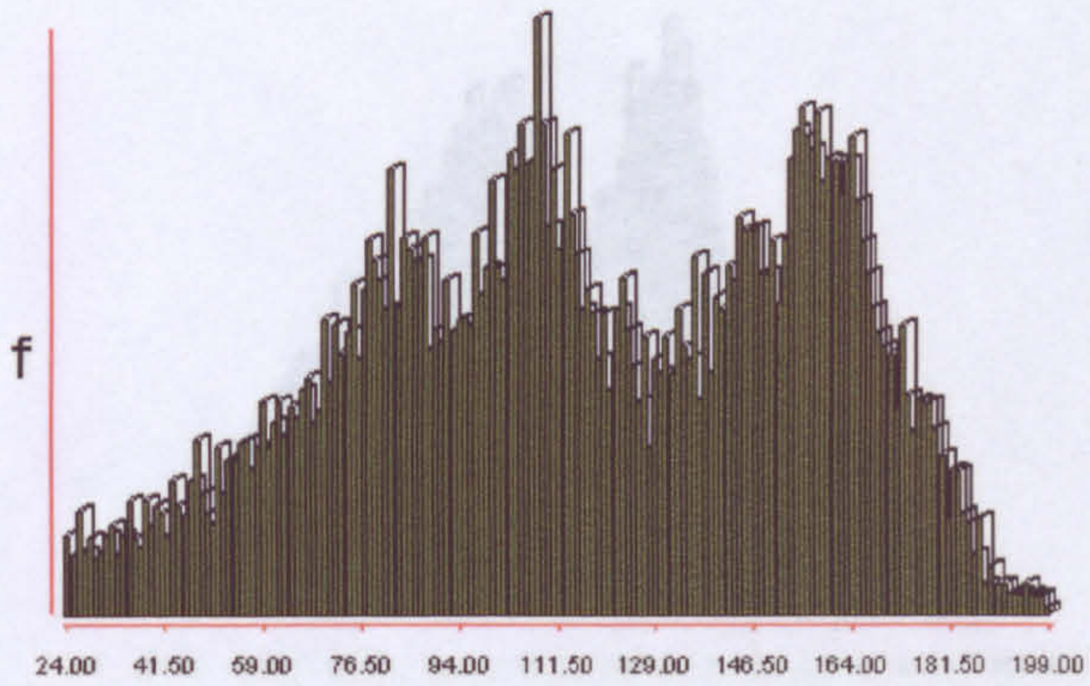

Histogram of
TEMPHIST

Class width :	1.0000
Display minimum :	24.0000
Display maximum :	199.0000
Actual minimum :	0.0000
Actual maximum :	205.0000
Mean :	116.2086
Stand. Deviation :	39.5979
df :	10777

based on 10778
values within range (out of 10982)

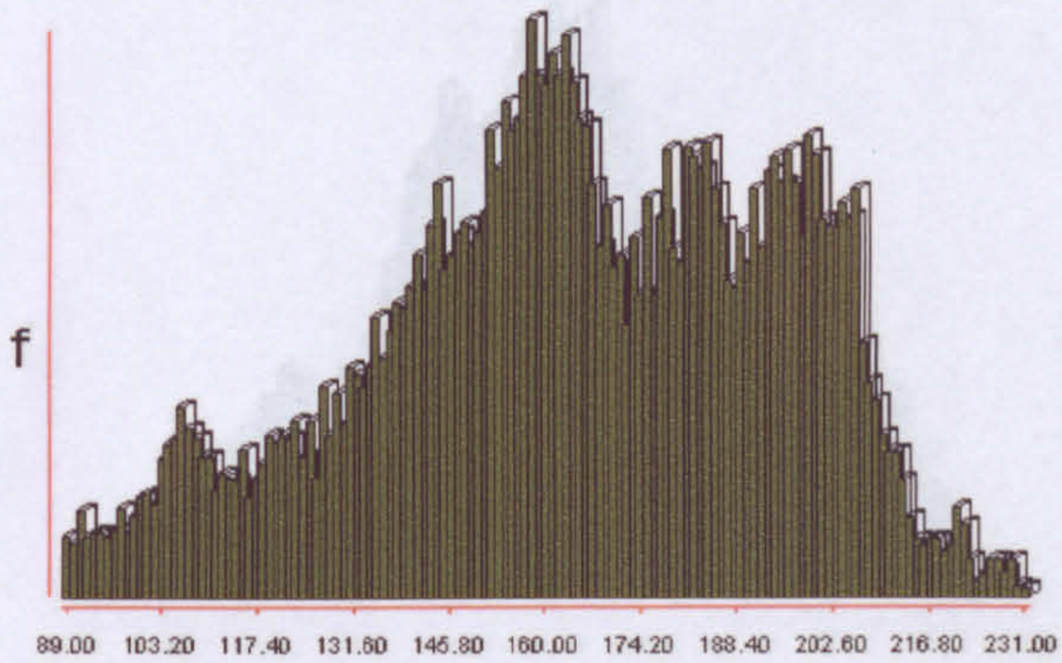

Histogram of
TEMPHIST

Class width :	1.0000
Display minimum :	89.0000
Display maximum :	231.0000
Actual minimum :	9.0000
Actual maximum :	237.0000
Mean :	164.1937
Stand. Deviation :	30.0148
df :	10531

based on 10532
values within range (out of 10982)

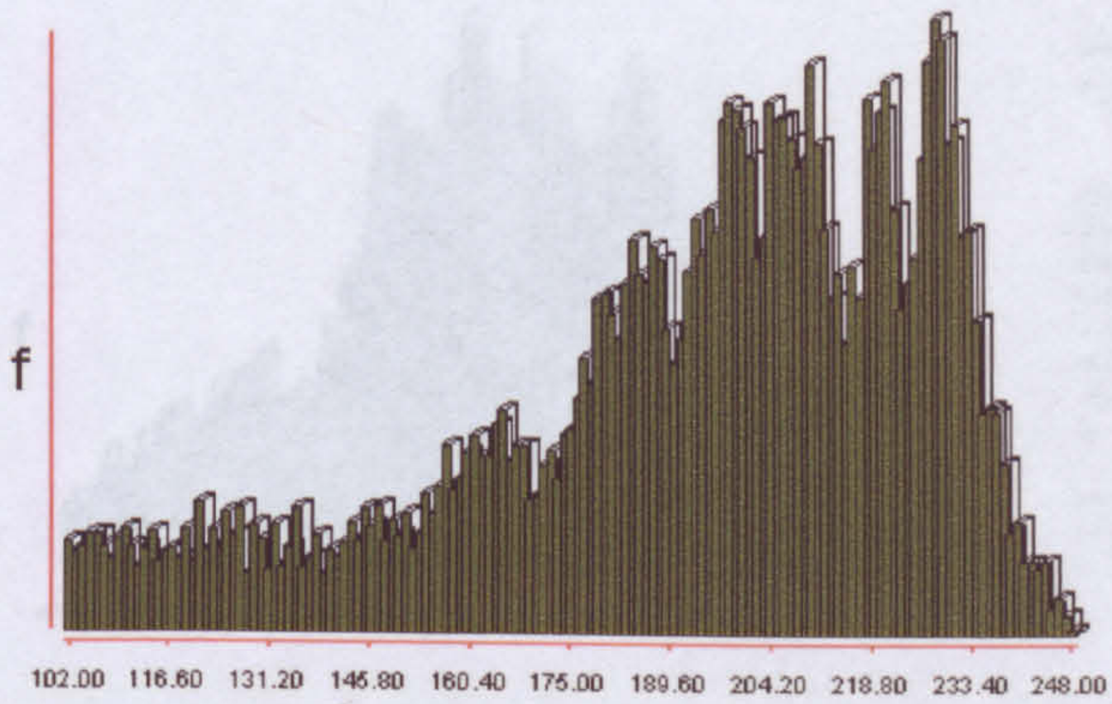

Histogram of
TEMPHIST

Class width :	1.0000
Display minimum :	102.0000
Display maximum :	248.0000
Actual minimum :	0.0000
Actual maximum :	248.0000
Mean :	192.8095
Stand. Deviation :	33.2916
df :	10127

based on 10128
values within range (out of 10982)

Figure C-5 Spectral signature of ploughed red soil

Red soil matorral

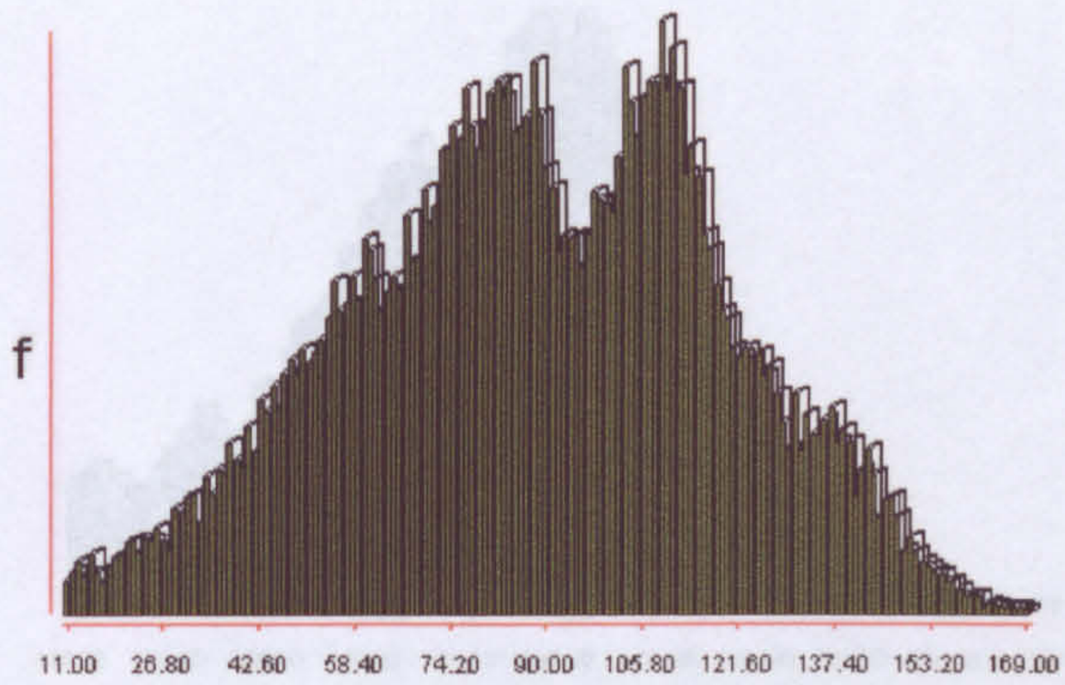

Histogram of
TEMPHIST

Class width :	1.0000
Display minimum :	11.0000
Display maximum :	169.0000
Actual minimum :	0.0000
Actual maximum :	175.0000
Mean :	88.2512
Stand. Deviation :	30.2487
df :	20251

based on 20252
values within range (out of 20384)

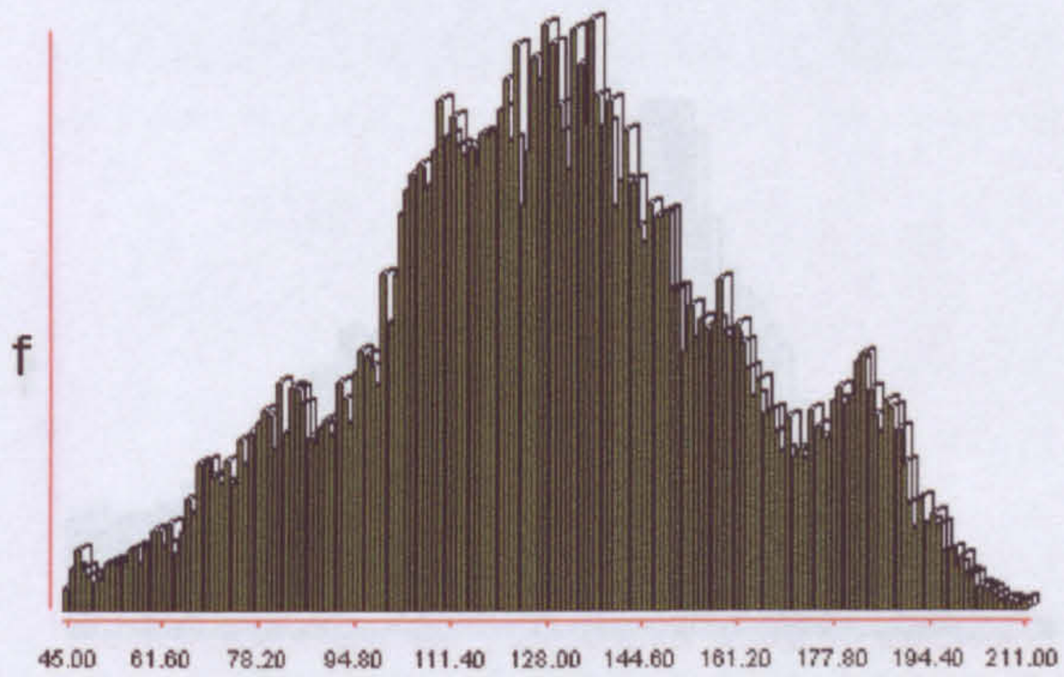

Histogram of
TEMPHIST

Class width :	1.0000
Display minimum :	45.0000
Display maximum :	211.0000
Actual minimum :	0.0000
Actual maximum :	217.0000
Mean :	128.3466
Stand. Deviation :	32.4282
df :	20094

based on 20095
values within range (out of 20384)

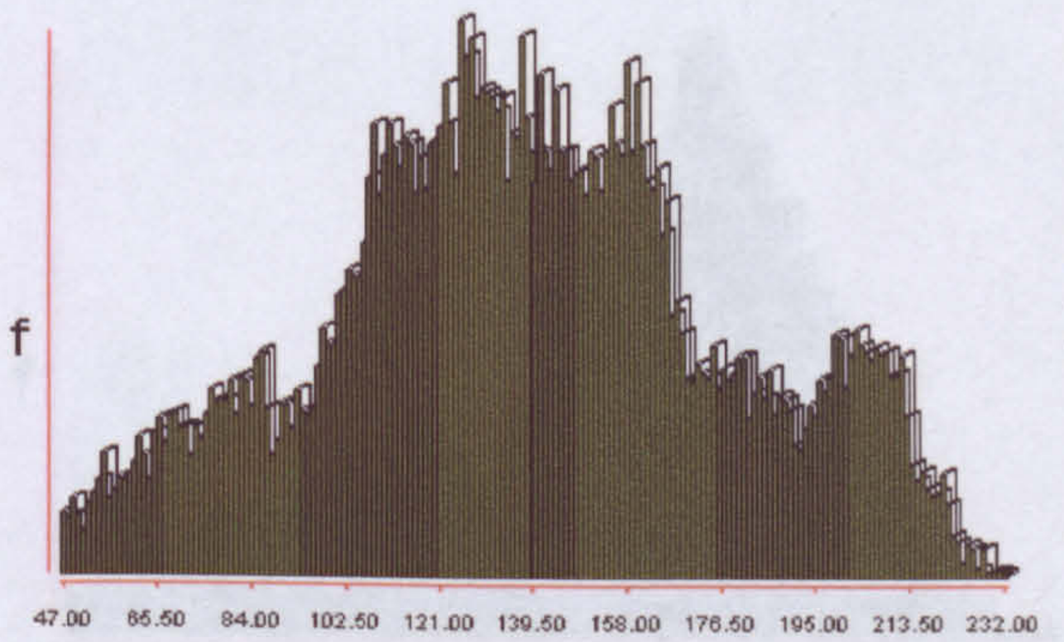

Histogram of
TEMPHIST

Class width :	1.0000
Display minimum :	47.0000
Display maximum :	232.0000
Actual minimum :	0.0000
Actual maximum :	234.0000
Mean :	137.7933
Stand. Deviation :	39.6551
df :	19570

based on 19571
values within range (out of 20384)

Figure C-6 Spectral signature of red soil matorral

Red soil river

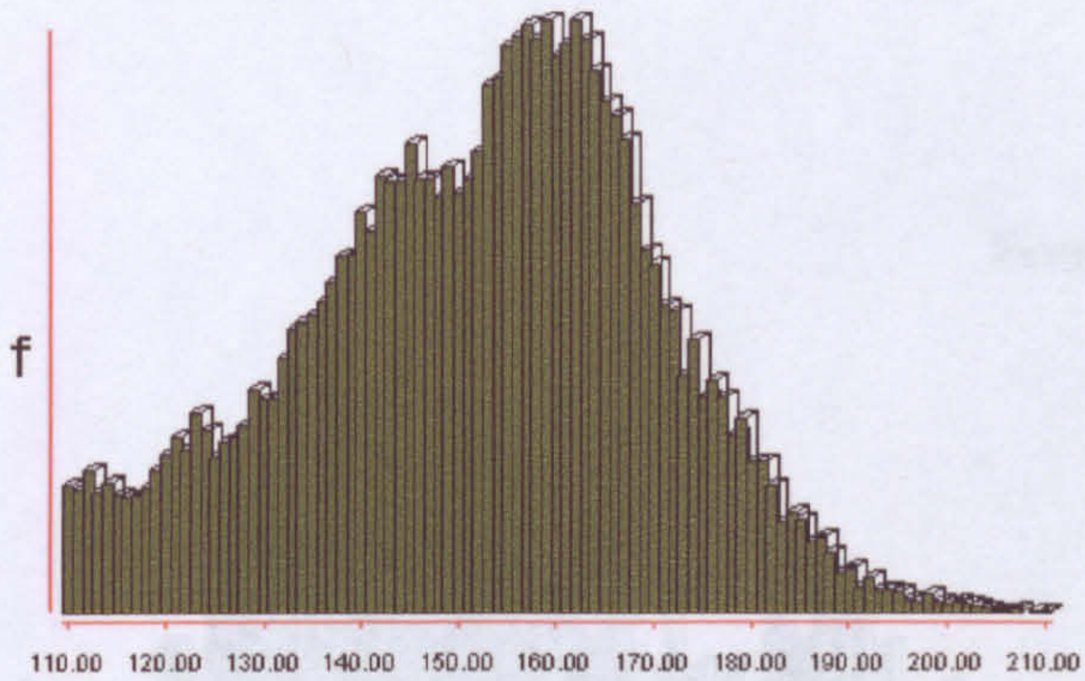

Histogram of
TEMPHIST

Class width :	1.0000
Display minimum :	110.0000
Display maximum :	210.0000
Actual minimum :	35.0000
Actual maximum :	210.0000
Mean :	151.8265
Stand. Deviation :	17.8110
df :	23058

based on 23059
values within range (out of 24930)

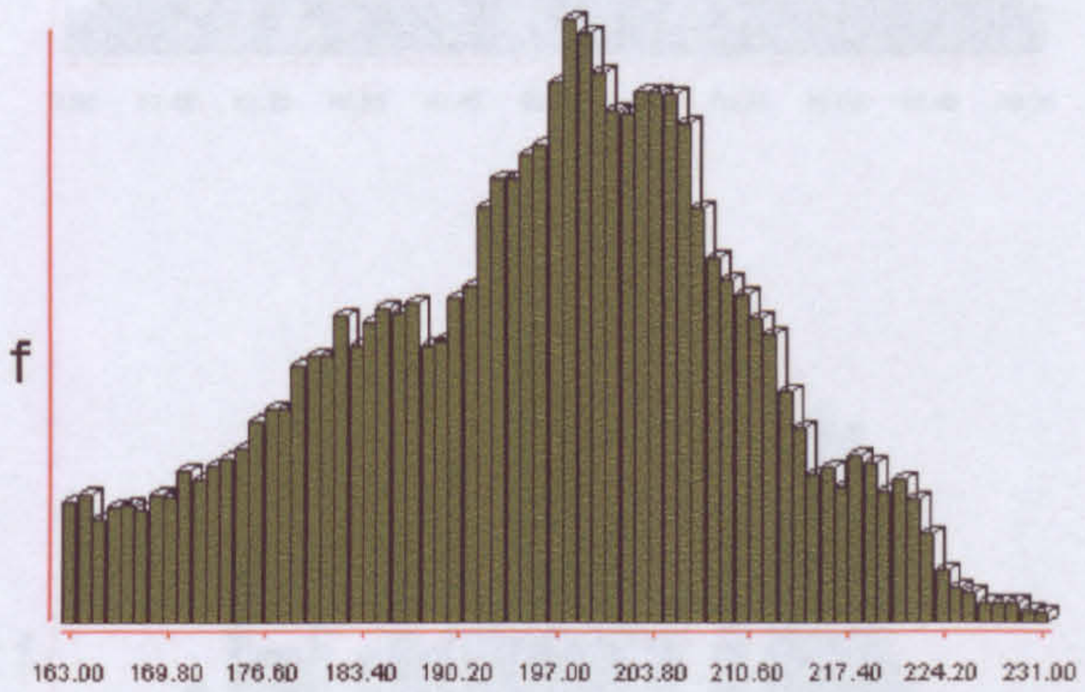

Histogram of
TEMPHIST

Class width :	1.0000
Display minimum :	163.0000
Display maximum :	231.0000
Actual minimum :	93.0000
Actual maximum :	235.0000
Mean :	195.6806
Stand. Deviation :	13.9584
df :	22233

based on 22234
values within range (out of 24930)

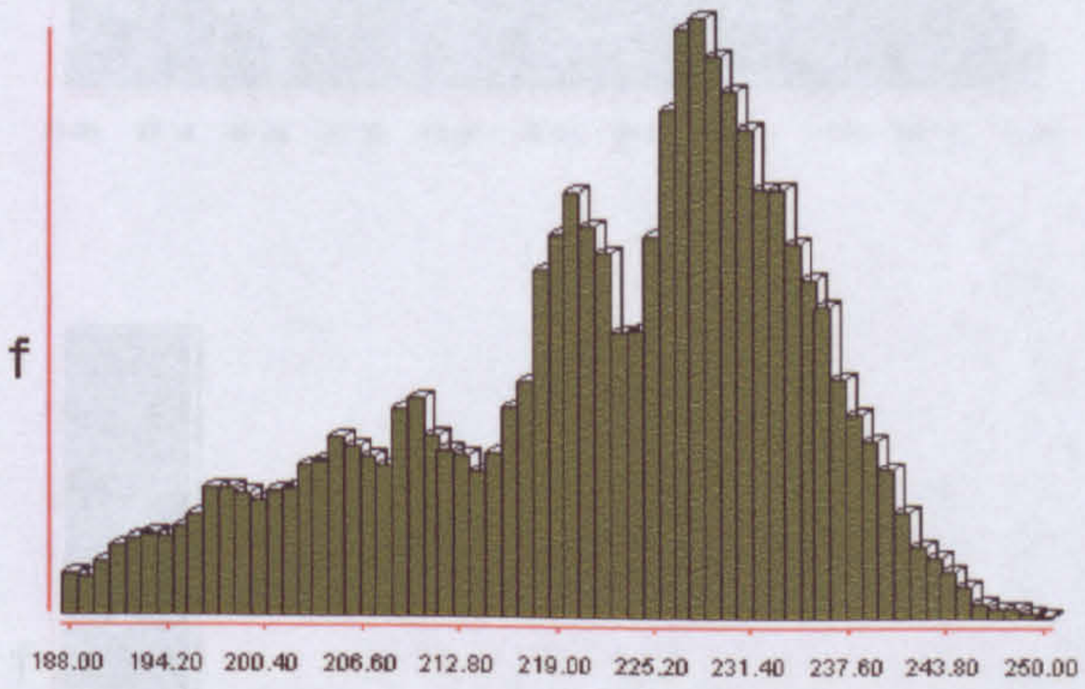

Histogram of
TEMPHIST

Class width :	1.0000
Display minimum :	188.0000
Display maximum :	250.0000
Actual minimum :	112.0000
Actual maximum :	253.0000
Mean :	221.6516
Stand. Deviation :	12.6279
df :	24131

based on 24132
values within range (out of 24930)

Figure C-7 Spectral signature of red soil river

Trees

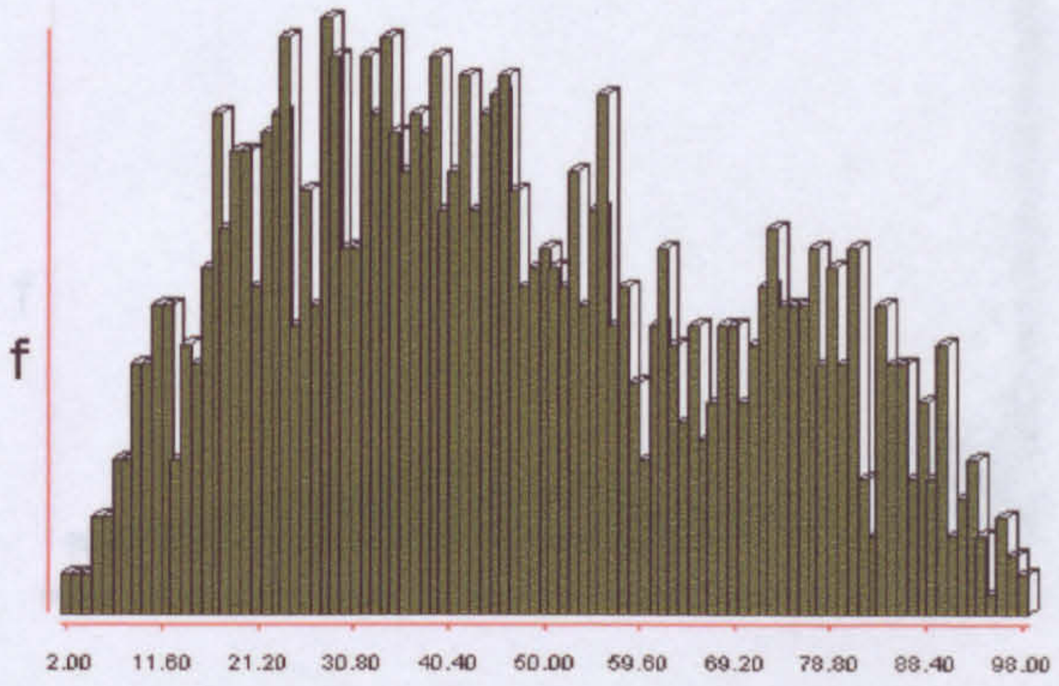

Histogram of
TEMPHIST

Class width :	1.0000
Display minimum :	2.0000
Display maximum :	98.0000
Actual minimum :	0.0000
Actual maximum :	118.0000
Mean :	45.8465
Stand. Deviation :	23.0907
df :	1562

based on 1563
values within range (out of 1614)

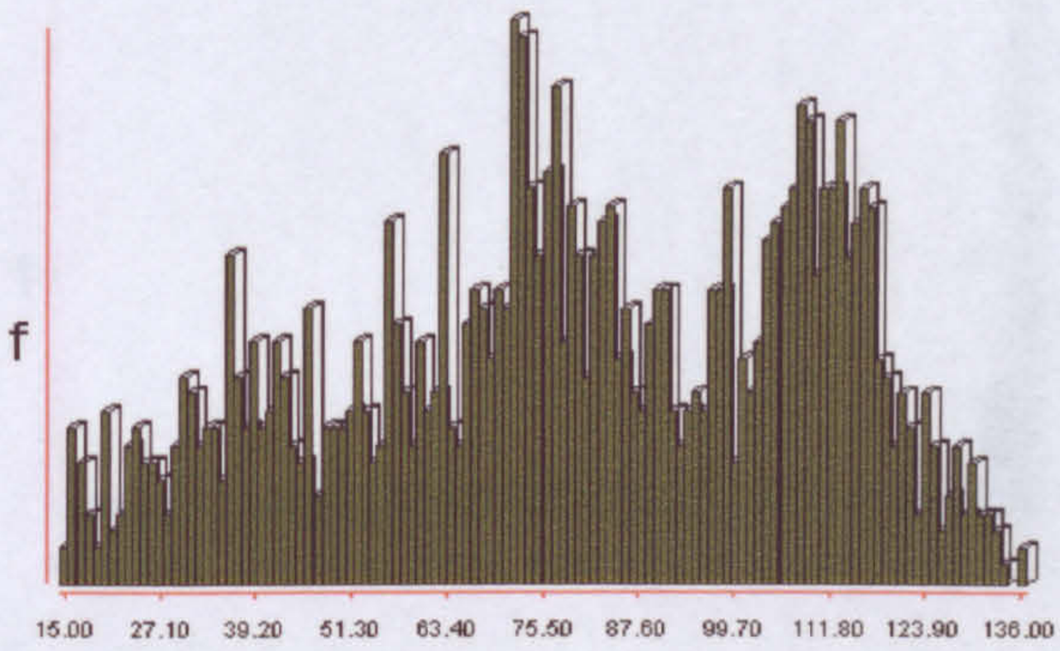

Histogram of
TEMPHIST

Class width :	1.0000
Display minimum :	15.0000
Display maximum :	136.0000
Actual minimum :	0.0000
Actual maximum :	156.0000
Mean :	79.1241
Stand. Deviation :	29.5201
df :	1554

based on 1555
values within range (out of 1614)

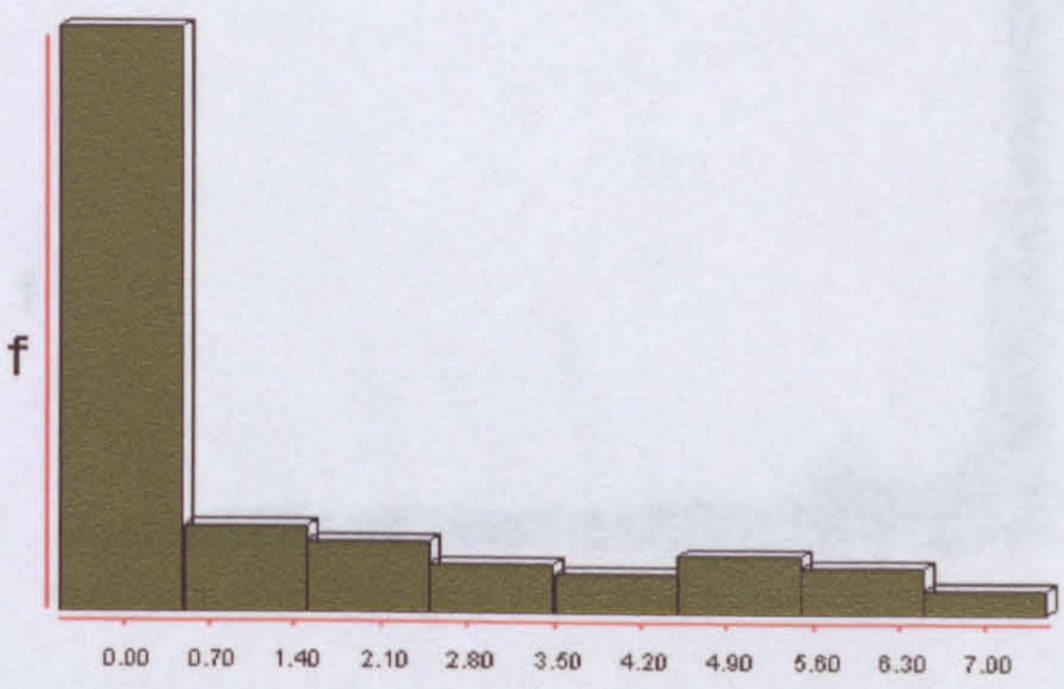

Histogram of
TEMPHIST

Class width :	1.0000
Display minimum :	0.0000
Display maximum :	7.0000
Actual minimum :	0.0000
Actual maximum :	140.0000
Mean :	1.2568
Stand. Deviation :	2.0223
df :	591

based on 592
values within range (out of 1614)

Figure C-8 Spectral signature of trees

Unpaved white road

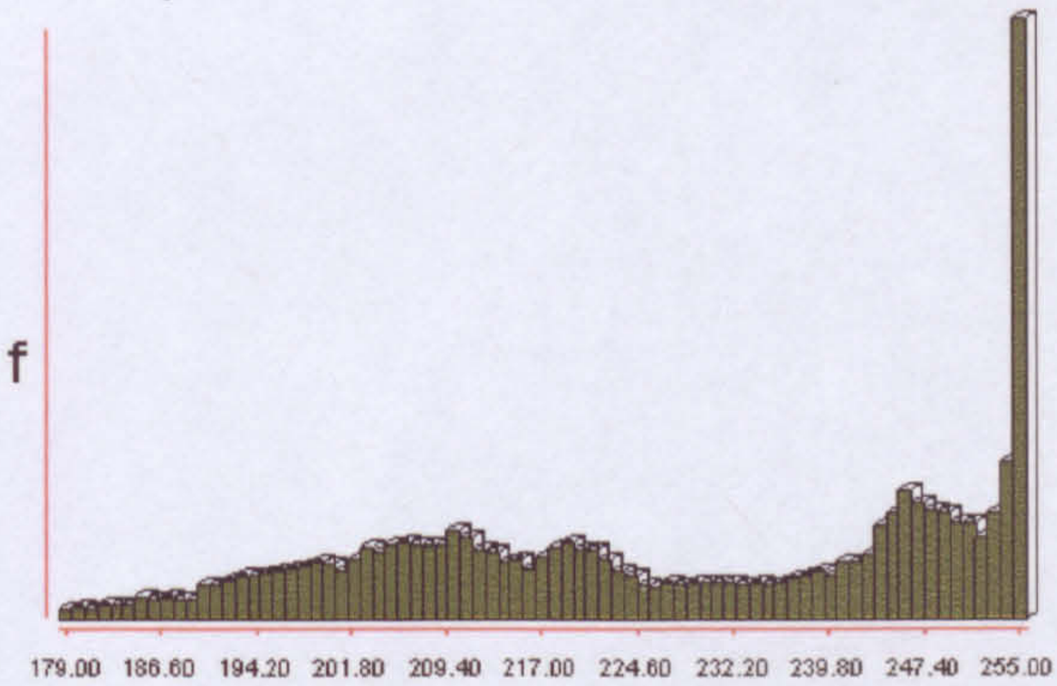

Histogram of
TEMPHIST

Class width :	1.0000
Display minimum :	179.0000
Display maximum :	255.0000
Actual minimum :	128.0000
Actual maximum :	255.0000
Mean :	227.8394
Stand. Deviation :	22.0915
df :	14545

based on 14546
values within range (out of 14678)

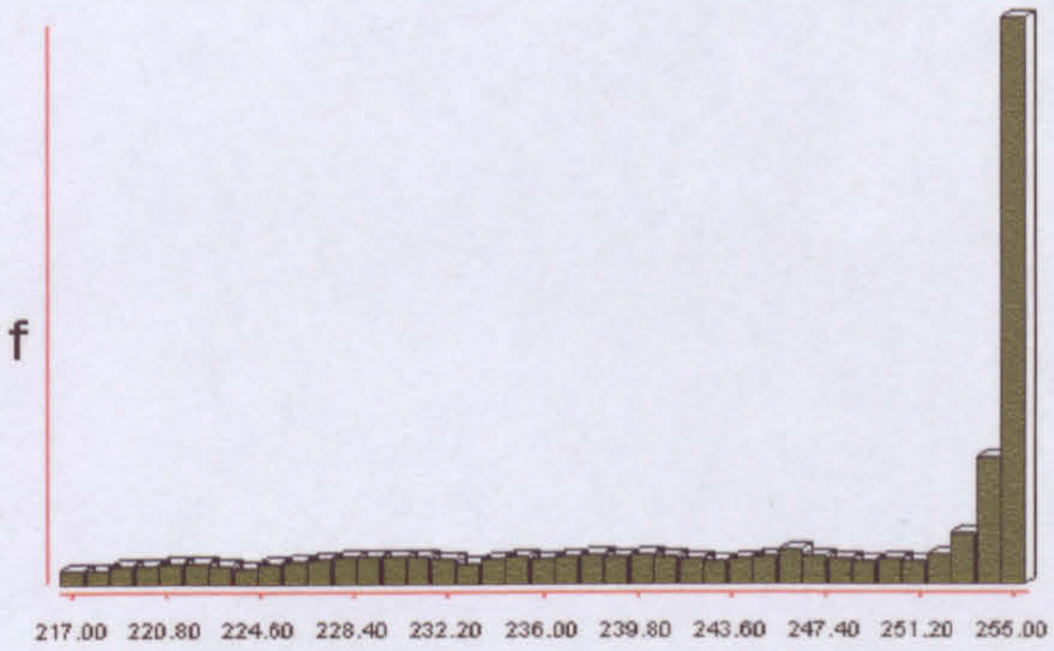

Histogram of
TEMPHIST

Class width :	1.0000
Display minimum :	217.0000
Display maximum :	255.0000
Actual minimum :	189.0000
Actual maximum :	255.0000
Mean :	244.9228
Stand. Deviation :	11.7848
df :	14301

based on 14302
values within range (out of 14678)

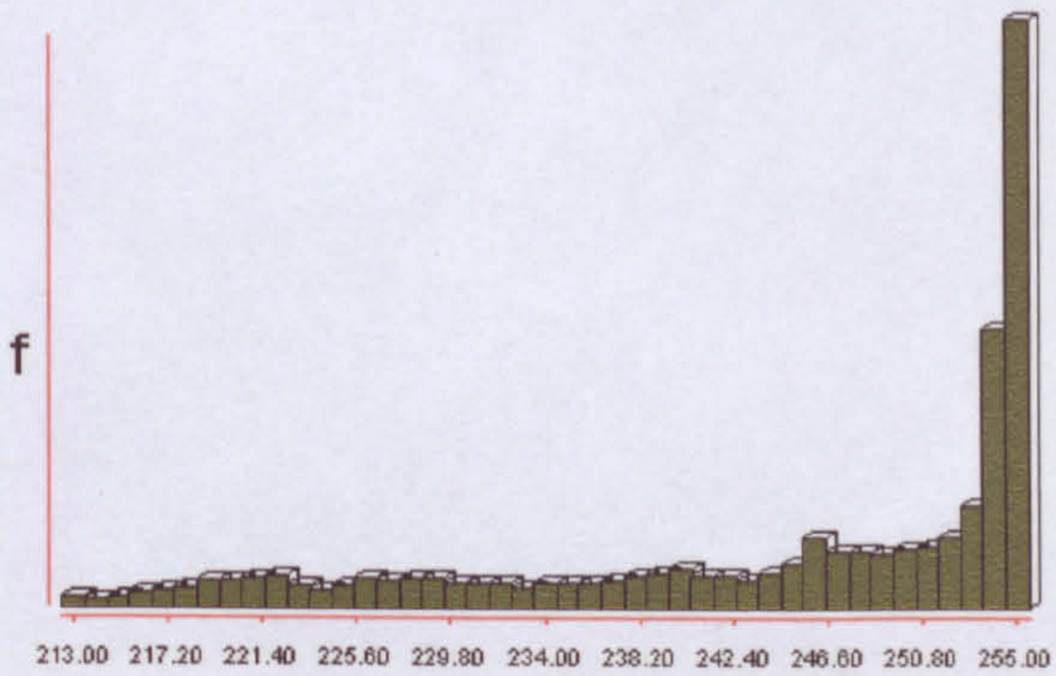

Histogram of
TEMPHIST

Class width :	1.0000
Display minimum :	213.0000
Display maximum :	255.0000
Actual minimum :	172.0000
Actual maximum :	255.0000
Mean :	244.8457
Stand. Deviation :	12.0234
df :	14421

based on 14422
values within range (out of 14678)

Figure C-9 Spectral signature of unpaved white road